

Frontiers in chemistry: Rising stars 2022

Edited by

Yunping Qiu, Rosalia Maria Cigala, Daniele Contini, Juqin Zeng,
Zhongzheng Yu, Alberto Rota, Sen Wang, M. Nageeb Rashed,
Marianna Pannico, Carlos D. S. Brites, Fidele Tugizimana, Uttam Pal,
Guigen Li, Essa M. Saied, Tsuyoshi Minami, Xiao-Peng He,
Ou Chen, Basem Moosa and Clemens Zwergel

Published in

Frontiers in Chemistry



FRONTIERS EBOOK COPYRIGHT STATEMENT

The copyright in the text of individual articles in this ebook is the property of their respective authors or their respective institutions or funders. The copyright in graphics and images within each article may be subject to copyright of other parties. In both cases this is subject to a license granted to Frontiers.

The compilation of articles constituting this ebook is the property of Frontiers.

Each article within this ebook, and the ebook itself, are published under the most recent version of the Creative Commons CC-BY licence. The version current at the date of publication of this ebook is CC-BY 4.0. If the CC-BY licence is updated, the licence granted by Frontiers is automatically updated to the new version.

When exercising any right under the CC-BY licence, Frontiers must be attributed as the original publisher of the article or ebook, as applicable.

Authors have the responsibility of ensuring that any graphics or other materials which are the property of others may be included in the CC-BY licence, but this should be checked before relying on the CC-BY licence to reproduce those materials. Any copyright notices relating to those materials must be complied with.

Copyright and source acknowledgement notices may not be removed and must be displayed in any copy, derivative work or partial copy which includes the elements in question.

All copyright, and all rights therein, are protected by national and international copyright laws. The above represents a summary only. For further information please read Frontiers' Conditions for Website Use and Copyright Statement, and the applicable CC-BY licence.

ISSN 1664-8714
ISBN 978-2-8325-4050-3
DOI 10.3389/978-2-8325-4050-3

About Frontiers

Frontiers is more than just an open access publisher of scholarly articles: it is a pioneering approach to the world of academia, radically improving the way scholarly research is managed. The grand vision of Frontiers is a world where all people have an equal opportunity to seek, share and generate knowledge. Frontiers provides immediate and permanent online open access to all its publications, but this alone is not enough to realize our grand goals.

Frontiers journal series

The Frontiers journal series is a multi-tier and interdisciplinary set of open-access, online journals, promising a paradigm shift from the current review, selection and dissemination processes in academic publishing. All Frontiers journals are driven by researchers for researchers; therefore, they constitute a service to the scholarly community. At the same time, the *Frontiers journal series* operates on a revolutionary invention, the tiered publishing system, initially addressing specific communities of scholars, and gradually climbing up to broader public understanding, thus serving the interests of the lay society, too.

Dedication to quality

Each Frontiers article is a landmark of the highest quality, thanks to genuinely collaborative interactions between authors and review editors, who include some of the world's best academicians. Research must be certified by peers before entering a stream of knowledge that may eventually reach the public - and shape society; therefore, Frontiers only applies the most rigorous and unbiased reviews. Frontiers revolutionizes research publishing by freely delivering the most outstanding research, evaluated with no bias from both the academic and social point of view. By applying the most advanced information technologies, Frontiers is catapulting scholarly publishing into a new generation.

What are Frontiers Research Topics?

Frontiers Research Topics are very popular trademarks of the *Frontiers journals series*: they are collections of at least ten articles, all centered on a particular subject. With their unique mix of varied contributions from Original Research to Review Articles, Frontiers Research Topics unify the most influential researchers, the latest key findings and historical advances in a hot research area.

Find out more on how to host your own Frontiers Research Topic or contribute to one as an author by contacting the Frontiers editorial office: frontiersin.org/about/contact

Frontiers in chemistry: Rising stars 2022

Topic editors

Yunping Qiu — Albert Einstein College of Medicine, United States

Rosalía Maria Cigala — University of Messina, Italy

Daniele Contini — Institute of Atmospheric Sciences and Climate, Department of Earth System Sciences and Technologies for the Environment, National Research Council (CNR), Italy

Juqin Zeng — Italian Institute of Technology (IIT), Italy

Zhongzheng Yu — University of Cambridge, United Kingdom

Alberto Rota — University of Modena and Reggio Emilia, Italy

Sen Wang — State Key Laboratory of Coal Conversion, Institute of Coal Chemistry, Chinese Academy of Sciences (CAS), China

M. Nageeb Rashed — Aswan University, Egypt

Marianna Pannico — Institute of Polymers, Composite and Biomaterials, Department of Chemical Sciences and Materials Technologies, National Research Council (CNR), Italy

Carlos D. S. Brites — University of Aveiro, Portugal

Fidele Tugizimana — Omnia, South Africa

Uttam Pal — S.N. Bose National Centre for Basic Sciences, India

Guigen Li — Texas Tech University, United States

Essa M. Saied — Humboldt University of Berlin, Germany

Tsuyoshi Minami — The University of Tokyo, Japan

Xiao-Peng He — East China University of Science and Technology, China

Ou Chen — Brown University, United States

Basem Moosa — King Abdullah University of Science and Technology, Saudi Arabia

Clemens Zwergel — Sapienza University of Rome, Italy

Citation

Qiu, Y., Cigala, R. M., Contini, D., Zeng, J., Yu, Z., Rota, A., Wang, S., Rashed, M. N., Pannico, M., Brites, C. D. S., Tugizimana, F., Pal, U., Li, G., Saied, E. M., Minami, T., He, X.-P., Chen, O., Moosa, B., Zwergel, C., eds. (2023). *Frontiers in chemistry: Rising stars 2022*. Lausanne: Frontiers Media SA. doi: 10.3389/978-2-8325-4050-3

Table of contents

- 05 **Editorial: Frontiers in Chemistry: rising stars 2022**
Carlos D. S. Brites, Daniele Contini, Xiao-Peng He, Tianqing Liu, Basem Moosa, Marianna Pannico, Mohamed Nageeb Rashed, Yunping Qiu and Clemens Zwergel
- 08 **Innovation in identifying metabolites from complex metabolome—Highlights of recent analytical platforms and protocols**
Shi Qiu, Sifan Guo, Qiang Yang, Yiqiang Xie, Songqi Tang and Aihua Zhang
- 11 **Qualitative and quantitative studies on two commercial specifications of *Polygonatum odoratum***
Yi Nan, Haizhen Liang, Xu Pang, Wei Zheng, Yuhao Shi, Xiaojuan Chen, Jie Zhang, Juan Song and Baiping Ma
- 22 **From PERK to RIPK1: Design, synthesis and evaluation of novel potent and selective necroptosis inhibitors**
Camilla Scarpellini, Sophie Valembois, Kenneth Goossens, Mike Vadi, Caroline Lanthier, Greta Klejborowska, Pieter Van Der Veken, Hans De Winter, Mathieu J. M. Bertrand and Koen Augustyns
- 37 **Single point mutations at the S129 residue of α -synuclein and their effect on structure, aggregation, and neurotoxicity**
Esha Pandit, Lopamudra Das, Anoy Kumar Das, Sandip Dolui, Saumen Saha, Uttam Pal, Animesh Mondal, Joydeep Chowdhury, Subhas C. Biswas and Nakul C. Maiti
- 51 **Mitochondria-targeted organic sonodynamic therapy agents: concept, benefits, and future directions**
Eunbin Hwang, Minjae Yun and Hyo Sung Jung
- 64 **Synthetic strategies to access silacycles**
Fengjuan Chen, Luo Liu and Wei Zeng
- 83 **RNA-protein complexes and force field polarizability**
Hanna Baltrukevich and Piia Bartos
- 97 **Development of the first geldanamycin-based HSP90 degraders**
Silas Wurnig, Melina Vogt, Julian Hogenkamp, Niklas Dienstbier, Arndt Borkhardt, Sanil Bhatia and Finn K. Hansen
- 107 **Nanoplasmonic biosensors for precision medicine**
Yiran Xiao, Zongming Zhang, Shi Yin and Xingyi Ma
- 120 **Kinetics and product identification of water-dissolved nitroguaiacol photolysis under artificial sunlight**
Ajda Delić, Urša Skube, Martin Šala and Ana Kroflič

- 132 **3D porous polymers for selective removal of CO₂ and H₂ storage: experimental and computational studies**
Muath S. Al-Bukhari, Ismail Abdulazeez, Mahmoud M. Abdelnaby, Isam H. Aljundi and Othman Charles S. Al Hamouz
- 145 **Thermodynamic insights into selenium oxyanion removal from synthetic flue gas desulfurization wastewater with temperature-swing solvent extraction**
Michael S. Meissner, Vy H. T. Nguyen, Imen Bousrih, Van T. C. Le, Alex Frickenstein, Giang V. Le and Ngoc T. Bui



OPEN ACCESS

EDITED AND REVIEWED BY

Gang Ma,
Hebei University, China

*CORRESPONDENCE

Carlos D. S. Brites,
✉ carlos.brites@ua.pt
Daniele Contini,
✉ d.contini@isac.cnr.it
Xiao-Peng He,
✉ xphe@ecust.edu.cn
Tianqing Liu,
✉ michelle.tianqing.liu@gmail.com
Basem Moosa,
✉ basem.moosa@kaust.edu.sa
Marianna Pannico,
✉ marianna.pannico@ipcb.cnr.it
Mohamed Nageeb Rashed,
✉ mnashed@hotmail.com
Yunping Qiu,
✉ yunping.qiu@einsteinmed.edu
Clemens Zwergel,
✉ clemens.zwergel@uniroma1.it

†These authors have contributed equally
to this work

RECEIVED 06 November 2023

ACCEPTED 13 November 2023

PUBLISHED 20 November 2023

CITATION

Brites CDS, Contini D, He X-P, Liu T,
Moosa B, Pannico M, Rashed MN, Qiu Y
and Zwergel C (2023), Editorial: Frontiers
in Chemistry: rising stars 2022.
Front. Chem. 11:1334117.
doi: 10.3389/fchem.2023.1334117

COPYRIGHT

© 2023 Brites, Contini, He, Liu, Moosa,
Pannico, Rashed, Qiu and Zwergel. This is
an open-access article distributed under
the terms of the [Creative Commons
Attribution License \(CC BY\)](#). The use,
distribution or reproduction in other
forums is permitted, provided the original
author(s) and the copyright owner(s) are
credited and that the original publication
in this journal is cited, in accordance with
accepted academic practice. No use,
distribution or reproduction is permitted
which does not comply with these terms.

Editorial: Frontiers in Chemistry: rising stars 2022

Carlos D. S. Brites^{1*†}, Daniele Contini^{2*†}, Xiao-Peng He^{3*†},
Tianqing Liu^{4*†}, Basem Moosa^{5*†}, Marianna Pannico^{6*†},
Mohamed Nageeb Rashed^{7*†}, Yunping Qiu^{8*†} and
Clemens Zwergel^{9*†}

¹Phantom-G, Department of Physics, CICECO—Aveiro Institute of Materials, University of Aveiro, Aveiro, Portugal, ²Institute of Atmospheric Sciences and Climate, ISAC-CNR, Lecce, Italy, ³Key Laboratory for Advanced Materials and Joint International Research Laboratory of Precision Chemistry and Molecular Engineering, Feringa Nobel Prize Scientist Joint Research Center, Frontiers Center for Materiobiology and Dynamic Chemistry, School of Chemistry and Molecular Engineering, East China University of Science and Technology, Shanghai, China, ⁴NICM Health Research Institute, Western Sydney University, Westmead, NSW, Australia, ⁵Smart Hybrid Materials (SHMs) Laboratory, Advanced Membranes and Porous Materials Center, Division of Physical Sciences and Engineering, King Abdullah University of Science and Technology (KAUST), Thuwal, Saudi Arabia, ⁶National Research Council of Italy, Institute for Polymers, Composites and Biomaterials, Pozzuoli, Italy, ⁷Faculty of Science, Aswan University, Aswan, Egypt, ⁸Department of Medicine, Albert Einstein College of Medicine, Bronx, NY, United States, ⁹Department of Drug Chemistry and Technologies, Sapienza University of Rome, Rome, Italy

KEYWORDS

rising stars, chemical sciences, analytical chemistry, medicinal chemistry, organic chemistry

Editorial on the Research Topic Frontiers in Chemistry: rising stars 2022

As guest editors of the 2022 Edition of our *Frontiers in Chemistry* “Rising Stars” article collection, we are delighted to showcase a collection of high-quality work of internationally recognized researchers in the early stages of their independent careers, spanning from analytical chemistry over medicinal chemistry to organic chemistry. In the present Research Topic, not only in original articles were submitted, but also numerous reviews are highlighting the latest progress in the field of chemistry in its broadest sense.

The review of [Qiu et al.](#) reported the different studies on the high-throughput mass spectrometry metabolomics analytical platforms and software for identifying metabolites and delineating their contribution. These include metabolic profiling of candidate metabolites with different techniques, which include LC/MS, open-source software Skyline tool mass spectrometry (MS), NOREVA that facilitate optimizing the multiclass metabolomic data processing, and the online MetaboAnalyst platform, which is a tool for high-resolution mass spectrometry spectra processing.

The rhizome of *Polygonatum odoratum* (PO) can be used to treat diabetes and cough. The chemical identification of its two major commercial specifications for this traditional Chinese medicine: Xiangyuzhu (XPO) and Guanyuzhu (GPO), is to be established. In their original research article, [Nan et al.](#) developed a comprehensive qualitative and quantitative procedure to differentiate these two specifications. The methods combined ultra-high-performance liquid chromatography-quadrupole time-of-flight mass spectrometry (UHPLC-Q-TOF/MS) and UPLC-charged aerosol detection (UHPLC-CAD). The authors discovered that the concentration ratio of timosaponin H1/polygodoroside G is a potential biomarker to differentiate these two specifications.

In their work, Pandit et al. focused on the impact of a single point mutation, particularly in the dynamic C-terminal region of the α -synuclein or alpha-synuclein (aS) protein whose aggregates are linked to Parkinson's disease. Their study demonstrated that mutating a crucial residue in the C-terminal region of aS with a residue promoting helix formation reduced the protein's aggregation and harmful effects on neuronal cells.

Scarpellini et al. explored the chemical space around their previously described compound GSK2656157, a known highly potent inhibitor of Protein Kinase (PKR) like ER Kinase (PERK). The structurally related Receptor-Interacting serine/threonine-Protein Kinase 1 (RIPK1) has been identified as a major cause of inflammation and, as a result, of inflammatory pathologies. Their structural optimization of the GSK2656157 scaffold resulted in a new class of more selective RIPK1 inhibitors. Based on the structure-activity relationship reported in the literature, they hypothesized that substituent insertion on the para position of the pyridinyl ring would reduce the interactions with PERK. Subsequent synthesis and evaluation of various para-substituted analogs proved their hypothesis and revealed UAMC3861 as the best compound with a potent RIPK1 inhibitory activity and good selectivity over PERK. Furthermore, UAMC3861 possesses the ability to inhibit RIPK1-dependent apoptosis and necroptosis in an *in vitro* inflammation model.

In their work, Chen et al. discussed the incorporation of silicon (Si) elements into carbon-based compounds, resulting in unique biological and physical-chemical properties. This review provides a summary of recent advancements in silacycle synthesis, including the use of transition metal-catalytic and photocatalytic strategies with various silicon-containing starting materials. It also highlights the mechanistic aspects and features of these developed reaction methodologies.

Precision medicine requires efficient and informative diagnostic tools to deeply understand diseases at molecular levels. Nanoplasmonic sensing is one of the techniques that showed great potential in providing high sensitivity and real-time information to characterize patients for personalized treatment. In this review article, Xiao et al. described the advantages and disadvantages of different nanoplasmonic and analysis-based sensing, the integration of multiple technologies, and the application and future development of nanoplasmonic biosensors in precision medicine. The great sensitivities of nanoplasmonic biosensors allow us to observe and quantify single molecular binding events. With further development, the next generations of nanoplasmonic technology will enrich the information and knowledge for precision medicine.

Nitroguaiacols, organic compounds released into the atmosphere from biomass burning, photolyze under sunlight to form various products, including chromophores. Delić et al. investigated the photolysis kinetics and product formation of two nitroguaiacols, 4-nitroguaiacol (4NG) and 5-nitroguaiacol (5NG), under artificial sunlight. Delić et al. found that 5NG photolysis is slower than 4NG photolysis and produces more chromophores, suggesting that 5NG has a stronger potential for secondary BrC formation. Their findings suggest that 5NG may be a more important precursor to secondary BrC (potent ozone-depleting substances) formation than 4NG. This study provides new insights into the photochemistry of nitroguaiacols and their potential role in forming secondary BrCs in the atmosphere.

Due to its minimal invasiveness and high tissue penetration depth, sonodynamic therapy (SDT) has recently emerged as a promising phototherapeutic modality for cancer. In their review, Hwang et al. summarized the recent progress in the design and synthesis of mitochondria-targeted organic SDT agents capable of being activated by ultrasound to generate cytotoxic reactive oxygen species in deep tumor regions. They also discussed the current challenges and future directions of developing organic SDT agents suitable for clinical settings.

Baltrukovich and Bartos performed Molecular Dynamics (MD) simulations, investigating the interactions and dynamics of, in their case, RNA and various proteins at the atomic level. To date, there have only been a few studies conducted on the simulation of complexes of RNA and proteins in MD simulations. In their paper, they examined the differences in force fields when simulating complexes of RNA and proteins. Specifically, they tested and compared three Non-Polarizable Force Fields (NPFs). All tested models can be used to simulate RNA and protein complexes; however, the NPF needs to be adapted to the research question.

Wurnig et al. designed, synthesized, and evaluated a geldanamycin-based degrader of heat shock protein 90 (HSP90) using the PROTAC strategy to fight cancer. PROTACs degrade the target protein rather than inhibiting it. This strategy is highly relevant in HSP90-related biology as, despite the initial clinical promise, resistance and dose-limiting toxicities have prevented classical HSP90 inhibitors from being used as anticancer drugs. Their best peptide degrader (compound 3a) effectively reduced HSP90 α and HSP90 β levels, providing a promising novel approach to target HSP90-driven diseases such as specific forms of cancer.

The work of Meissner et al. investigates the application of temperature-swing solvent extraction (TSSE) as a cost-effective and versatile technology for effectively removing selenium oxyanions and traces of mercury in the presence of high contents of chloride and sulfate. The study shows that TSSE might provide a technological solution with a high deionization potential for the industry in complying with regulations for discharge streams from coal-fired power facilities.

Al-Bukahri et al. reported a Polycondensation of tetrakis (4-aminophenyl) methane with pyrrole and phenazine, yielding newly designed 3D porous polymers. The novel polymers exhibited permanent porosity, with BET surface areas of 575 and 389 m²/g, respectively. Solid-state NMR spectroscopy, Fourier-transform infrared (FT-IR) spectroscopy, and thermogravimetric analysis were used to investigate the structure (TGA). The adsorption capacities of the synthesized polymers for CO₂ and H₂ were determined to be 1.85 and 2.10 mmol/g, respectively. The significance of the synthesized polymers lies in their CO₂/N₂ selectivity, which is 43 and 51, respectively. At 1 bar and 77 K, the polymers demonstrated promising hydrogen storage capacities of 66 cm³/g (0.6 wt%) and 87 cm³/g (0.8 wt%), respectively.

"Frontiers in Chemistry: Rising Stars" is a prestigious compilation of research articles and reviews that showcases the work of upcoming researchers in the field of chemistry. Within this Research Topic, we have seen numerous articles from young promising scientists from all over the world exhibiting the numerous facets of chemistry. The innovative research presented herein has been recognized for its potential to drive advancements and shape the future of the discipline. The publication provides a

platform for these emerging scientists to share their findings and insights, which not only contribute to the current body of knowledge in chemistry but also pave the way for innovative discoveries. It acknowledges their significant achievements and celebrates their potential to become future leaders in the field.

Author contributions

CB: Writing–original draft, Writing–review and editing. DC: Writing–original draft, Writing–review and editing. X-PH: Writing–original draft, Writing–review and editing. TL: Writing–review and editing. BM: Writing–original draft, Writing–review and editing. MP: Writing–original draft, Writing–review and editing. MR: Writing–original draft, Writing–review and editing. YQ: Writing–original draft, Writing–review and editing. CZ: Writing–original draft, Writing–review and editing.

Conflict of interest

The authors declare that the research was conducted in the absence of any commercial or financial relationships that could be construed as a potential conflict of interest.

The authors declared that they were an editorial board member of Frontiers, at the time of submission. This had no impact on the peer review process and the final decision.

Publisher's note

All claims expressed in this article are solely those of the authors and do not necessarily represent those of their affiliated organizations, or those of the publisher, the editors and the reviewers. Any product that may be evaluated in this article, or claim that may be made by its manufacturer, is not guaranteed or endorsed by the publisher.



OPEN ACCESS

EDITED BY

M. Nageeb Rashed,
Aswan University, Egypt

REVIEWED BY

Kirk L. Pappan,
Owlstone Medical Ltd., United Kingdom

*CORRESPONDENCE

Yiqiang Xie,
✉ xieyiqiang@hainmc.edu.cn
Songqi Tang,
✉ tangsongqi@hainmc.edu.cn
Aihua Zhang,
✉ aihuatcm@163.com

SPECIALTY SECTION

This article was submitted to Analytical Chemistry, a section of the journal Frontiers in Chemistry

RECEIVED 22 December 2022

ACCEPTED 16 January 2023

PUBLISHED 25 January 2023

CITATION

Qiu S, Guo S, Yang Q, Xie Y, Tang S and Zhang A (2023), Innovation in identifying metabolites from complex metabolome—Highlights of recent analytical platforms and protocols. *Front. Chem.* 11:1129717. doi: 10.3389/fchem.2023.1129717

COPYRIGHT

© 2023 Qiu, Guo, Yang, Xie, Tang and Zhang. This is an open-access article distributed under the terms of the [Creative Commons Attribution License \(CC BY\)](#). The use, distribution or reproduction in other forums is permitted, provided the original author(s) and the copyright owner(s) are credited and that the original publication in this journal is cited, in accordance with accepted academic practice. No use, distribution or reproduction is permitted which does not comply with these terms.

Innovation in identifying metabolites from complex metabolome—Highlights of recent analytical platforms and protocols

Shi Qiu¹, Sifan Guo², Qiang Yang², Yiqiang Xie^{1*}, Songqi Tang^{1*} and Aihua Zhang ^{1,2*}

¹International Advanced Functional Omics Platform, Scientific Experiment Center, Hainan Medical University, Haikou, China, ²Graduate School, Heilongjiang University of Chinese Medicine, Harbin, China

Metabolites are closely intertwined genotypes that can provide clear information about the final phenotype. The high-throughput analysis platform used to identify candidate metabolites and describe their contributions can help to quickly detect metabolic characteristics from large spectral data, which may lead to peak data preprocessing, statistical analysis and functional interpretation. Developing a comprehensive strategy for discovering and verifying bioactive metabolites can provide a large number of new functional biomarkers, and then more closely reveal their functional changes, which has relevant biological significance for disease diagnosis and prognosis treatment.

KEYWORDS

metabolites, functional biomarkers, metabolic pathway, metabolomics, diagnosis

In 2022, five studies on high-throughput mass spectrometry metabolomics analytical platforms and softwares for identifying metabolites and delineating their contribution were published in Nature Protocols (Fu et al., 2022; Horvath et al., 2022; Kilgour et al., 2022; Kirkwood et al., 2022; Pang et al., 2022). These studies have shown metabolic profiling of candidate metabolites as a dominant technology that enables rapid detection of the metabolic features in the spectral data, which may be followed by spectral and peak data preprocessing, statistical analysis and functional interpretation. These five publications facilitated the extraction of chemical signals, contributed to identification of novel metabolites and differential metabolites, and discovered new functional biomarkers related metabolites leading to better diagnosis, prognosis and treatment.

Metabolites are the final downstream products of protein translation and gene transcription or cellular perturbations to the proteome, genome or transcriptome, which serve as potential key links between genotype and environment and can provide a clear image of the final phenotype. Small-molecule metabolites can provide insights into unique metabolic mechanisms and therapeutic targets of diseases, and lead to personalized applications of metabolic phenotypes. Furthermore, metabolite identification or metabolic pathway changes will help to understand the pathophysiology of the disease and assist in determining therapeutic targets. Metabolomes are comprehensively characterized by measuring the small metabolites in cells, biofluids, organs, or other biological systems, and represents the upstream input from the environment and the downstream output from the genome. In particular, due to the huge complexity of metabolome, there is urgency to develop various powerful tools to facilitate spectral data processing and interpretation that help to identify bioactive metabolites. Identification of small molecule metabolite is one of the most important processes in the discovery stage and can be performed by a range of established innovative technologies

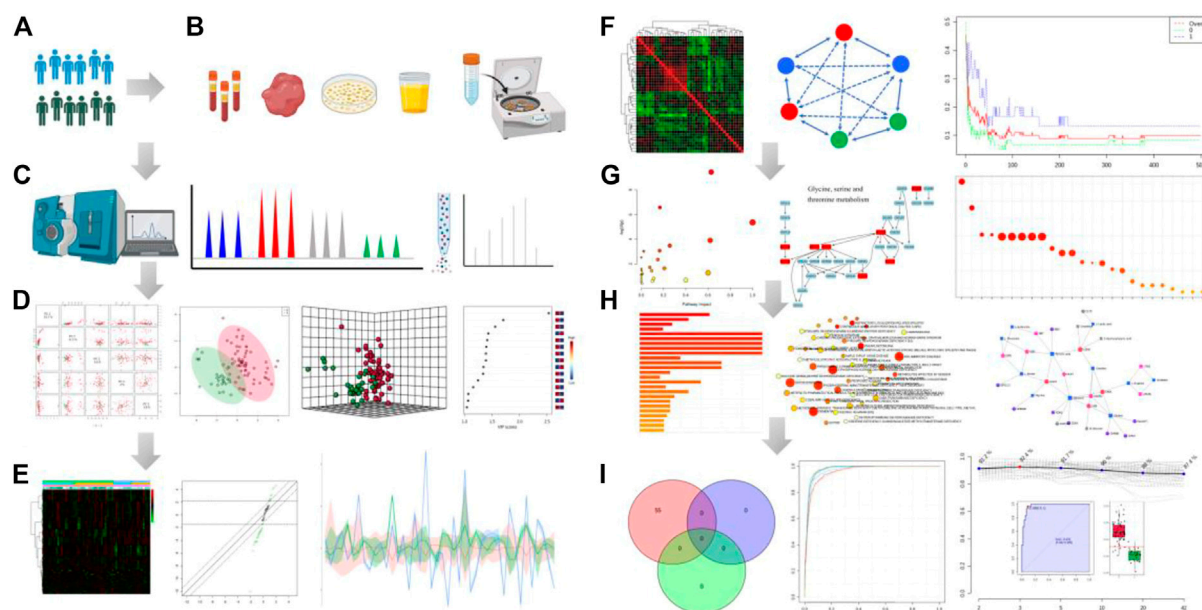


FIGURE 1

Analytical workflow of typical metabolomic analysis. It includes several basic steps: experimental design (A), sample collection (B), metabolite profiling (C), data analysis (D–F), functional interpretation (G, H) and potential application of the integrated datasets (I). Step (A) The experimental design based on phenotype analysis or diagnosis and treatment. Step (B) Sample preparation through deproteinization and/or centrifugation of biofluids. Step (C) Metabolite separation on a column (chromatography) and detection of analyte signal through MS or NMR spectroscopy. Metabolites can be identified on the basis of a combination of retention time and MS signature. Step (D) The data pre-processing and normalization of raw signals. Then, pattern recognition analysis and computational methods after data collection. Step (E) Expression analysis of the differential metabolites by which data is filtered for significant biomarkers of interest. Heatmap plot shows the differential metabolites in the statistical analysis function. Step (F) Clustering correlation patterns analysis among different data sets. Step (G) Pathway enrichment overview. Circle size and color are based on the pathway size and *p*-value. Step (H) The enriched metabolism pathway and joint pathway analysis in the correlation network. Step (I) Analysis model of diagnosis, prognosis and treatment based on the candidate metabolite features using classical univariate and multivariate ROC curve analyses. All images were obtained using the example data provided by the MetaboAnalyst 5.0 and figures also created by BioRender.

(Figure 1). Therefore, it is highly demanded to expand metabolites coverage, and optimize workflow by assessing multiple metabolic signals as possible to understand the biological role of metabolites. This minireview provides a brief overview and highlights of these five recent articles.

Recently, a study published in *Nature Protocols* by Horvath *et al.* developed a LC/MS quantitative analytical platform for liquid chromatography-tandem mass spectrometry metabolomics method for targeting analysis and monitoring the content change of microbially derived short-chain fatty acids and neurotransmitters from the bacterial cultures, organoid cultures and *in vivo* samples (Horvath *et al.*, 2022). This method has been customized for the targeted metabolite measurements of different microbial subsets and growth media. It can comprehensively specifically identify microbial signals within the host, and evaluate the relationship between microbial colonization and neurotransmitters of gut-brain axis *in vivo* and *in vitro* (media and organoids) models, reveal the contributions of microbes to host neurotransmitters, and dissect the important bidirectional connections, between commensal microbes and host. In this study, the authors demonstrated a systematic approach to reveal how the bacteria regulate the CNS and gut, provide valuable information by determining the specific pathways into the functional mechanisms that specific microbes influence host metabolism (Horvath *et al.*, 2022). In regard to cellular metabolism, Kilgour *et al.*, focused on performing identification of general metabolic characteristics for specific cell

populations by high-dimensional flow cytometry and MS-based metabolite profiling. They shared the general workflow of biological sample collection and storage (i.e., blood, tumor, and ascites) and cell enrichment analysis to uncover the unique metabolic difference in the tumor microenvironment (Kilgour *et al.*, 2022). Furthermore, it can be applied to reveal credible information on the bioindicators during cellular processes and functional metabolic mechanisms in different cell types under extensive experimental conditions.

Kirkwood and colleagues have analyzed lipidome data by the open-source software *Skyline* tool to improve the capabilities of lipid characterization and annotation beyond traditional mass spectrometry (MS)-based approaches (Kirkwood *et al.*, 2022). Importantly, they expanded capabilities of lipid molecule discovery, identification, quantification and annotation validation by integrating multidimensional liquid chromatography, mass spectrometry, ion mobility spectrometry, collision-induced dissociation and library editing. Pang *et al.*, have used the online *MetaboAnalyst* platform (www.metaboanalyst.ca) to conduct high-resolution mass spectrometry spectra processing, statistical analysis of complex metabolic datasets, and joint-pathway analysis of multi-omics integration (Pang *et al.*, 2022). It can provide a largely automated workflow for functional interpretation and analysis to identify critical features through efficient optimization of spectra processing parameters by default settings. This platform allocates small metabolites to biological pathways and enhances sensitivity and versatility of metabolites, precisely facilitates exploration of overall

metabolic changes that related to disease alteration, from whole organisms to single cells, and offers invaluable insights into the metabolic function and targets. Fu et al., have applied NOREVA to facilitate optimizing the multiclass metabolomic data processing (Fu et al., 2022). This protocol includes data filtering and imputation, correction, transformation, normalization and performance assessment. Open source code is fully provided in this protocol, allowing users to customize and improve NOREVA functions. Interestingly, according to the size of the analysis data, the execution time can vary from a few minutes to several hours.

Taken together, these helpful studies provide the technical advances for identifying active metabolites and greatly broaden the coverage level of metabolites for exploring metabolic altered dimensions of diseases. The described analytical platforms and software tools provide some advantages in the sensitivity, dynamic range, reproducibility, time-saving and throughput for the combination of qualitative and quantitative. Rapid analysis of complex metabolome requires the specialized tools for the preprocessing raw data followed by multivariate statistical analysis, omics data mining and bioinformatics integration and functional interpretation. In this setting, *MetaboAnalyst* includes numerous modules for metabolite enrichment and relevant metabolic pathway analysis with pathophysiological mechanism by establishing the network interaction and visualization map (Pang et al., 2022).

Despite these tremendous advances, at present, no single analytical method can fulfill the mission of identification of entire metabolome in the large sample sizes. Future works aimed at developing the integrated strategy for enhancing the accuracy of discovering a list of biologically active metabolites with pathological basis of diseases, could provide a large number of the relatively abundant ions and acquire more reliable identifications, and then shed light on the functional changes of small molecule metabolites more closely. Moreover, it should establish multi-cycle training optimization models of experimental and clinical studies to validate the overall prediction performance of particular metabolite bioactivity and relevant biological significance for disease diagnosis and prognostic

treatment that are worthy of further exploration. In the future, the integrated use of computational algorithms, artificial intelligence, and big data mining method will improve the precise identification ability of metabolites for resulting optimization and verification.

Author contributions

SQ, YX, and AZ participated in study design, contributed to method development and wrote the manuscript. SQ, ST, SG, and QY provided advises on method development and analysis and contributed to manuscript generation.

Acknowledgments

The authors are grateful for the generous support from the Program of Natural Science Foundation of State (Grant Nos 81973745 and 82104733), Talent Lift Engineering Project of China TCM Association (QNRC2-B06), Natural Science Foundation of Heilongjiang Province (YQ 2019H030). We also thank BioRender and MetaboAnalyst for the figure preparation.

Conflict of interest

The authors declare that the research was conducted in the absence of any commercial or financial relationships that could be construed as a potential conflict of interest.

Publisher's note

All claims expressed in this article are solely those of the authors and do not necessarily represent those of their affiliated organizations, or those of the publisher, the editors and the reviewers. Any product that may be evaluated in this article, or claim that may be made by its manufacturer, is not guaranteed or endorsed by the publisher.

References

- Fu, J., Zhang, Y., Wang, Y., Zhang, H., Liu, J., Tang, J., et al. (2022). Optimization of metabolomic data processing using NOREVA. *Nat. Protoc.* 17, 129–151. doi:10.1038/s41596-021-00636-9
- Horvath, T. D., Haidacher, S. J., Engevik, M. A., Luck, B., Ruan, W., Ihekweazu, F., et al. (2022). Interrogation of the mammalian gut-brain axis using LC-MS/MS-based targeted metabolomics with *in vitro* bacterial and organoid cultures and *in vivo* gnotobiotic mouse models. *Nat. Protoc.* doi:10.1038/s41596-022-00767-7
- Kilgour, M. K., MacPherson, S., Zacharias, L. G., LeBlanc, J., Babinszky, S., Kowalchuk, G., et al. (2022). Principles of reproducible metabolite profiling of enriched lymphocytes in tumors and ascites from human ovarian cancer. *Nat. Protoc.* 17, 2668–2698. doi:10.1038/s41596-022-00729-z
- Kirkwood, K. I., Pratt, B. S., Shulman, N., Tamura, K., MacCoss, M. J., MacLean, B. X., et al. (2022). Utilizing Skyline to analyze lipidomics data containing liquid chromatography, ion mobility spectrometry and mass spectrometry dimensions. *Nat. Protoc.* 17, 2415–2430. doi:10.1038/s41596-022-00714-6
- Pang, Z., Zhou, G., Ewald, J., Chang, L., Hacariz, O., Basu, N., et al. (2022). Using MetaboAnalyst 5.0 for LC-HRMS spectra processing, multi-omics integration and covariate adjustment of global metabolomics data. *Nat. Protoc.* 17, 1735–1761. doi:10.1038/s41596-022-00710-w



OPEN ACCESS

EDITED BY

Yunping Qiu,
Albert Einstein College of Medicine,
United States

REVIEWED BY

Kunming Qin,
Jiangsu Ocean University, China
Changgen Feng,
MTC Industries, Inc., United States

*CORRESPONDENCE

Baiping Ma,
✉ mabaiping@sina.com

SPECIALTY SECTION

This article was submitted to Analytical Chemistry, a section of the journal Frontiers in Chemistry

RECEIVED 17 January 2023

ACCEPTED 08 February 2023

PUBLISHED 23 February 2023

CITATION

Nan Y, Liang H, Pang X, Zheng W, Shi Y, Chen X, Zhang J, Song J and Ma B (2023), Qualitative and quantitative studies on two commercial specifications of *Polygonatum odoratum*. *Front. Chem.* 11:1146153. doi: 10.3389/fchem.2023.1146153

COPYRIGHT

© 2023 Nan, Liang, Pang, Zheng, Shi, Chen, Zhang, Song and Ma. This is an open-access article distributed under the terms of the [Creative Commons Attribution License \(CC BY\)](#). The use, distribution or reproduction in other forums is permitted, provided the original author(s) and the copyright owner(s) are credited and that the original publication in this journal is cited, in accordance with accepted academic practice. No use, distribution or reproduction is permitted which does not comply with these terms.

Qualitative and quantitative studies on two commercial specifications of *Polygonatum odoratum*

Yi Nan^{1,2}, Haizhen Liang¹, Xu Pang¹, Wei Zheng¹, Yuhao Shi^{1,2}, Xiaojuan Chen¹, Jie Zhang¹, Juan Song¹ and Baiping Ma^{1,2*}

¹Beijing Institute of Radiation Medicine, Beijing, China, ²Graduate School, Tianjin University of Traditional Chinese Medicine, Tianjin, China

The rhizoma of *Polygonatum odoratum* (PO) is used to treat yin injuries of the lung and stomach in traditional Chinese medicine. The chemical constituents of this herb are steroidal saponins, homoisoflavanones, and alkaloids. Xiangyuzhu (XPO) and Guanyuzhu (GPO) are available in the market as two specifications of the commodity. Nonetheless, systematic research on the identification and comparison of chemical constituents of these two commercial specifications is yet lacking. Herein, an integrated method combining ultra-high-performance liquid chromatography-quadrupole time-of-flight mass spectrometry (UHPLC-Q-TOF/MS) with ultra-high-performance liquid chromatography-charged aerosol detection (UHPLC-CAD) was employed for the comprehensively qualitative and quantitative analyses of PO. A total of 62 compounds were identified by UHPLC-Q-TOF/MS, among which 13 potential chemical markers were screened out to distinguish two commercial specifications. Subsequently, the absolute determination method for polygodoside G, polygonatunoside F, and timosaponin H1 was established and validated by UHPLC-CAD. The contents of the three compounds were 13.33–236.24 µg/g, 50.55–545.04 µg/g, and 13.34–407.83 µg/g, respectively. Furthermore, the ratio of timosaponin H1/polygodoside G could be applied to differentiate the two specifications. Samples with a ratio <2 are considered XPO and >5 are considered GPO. Therefore, the above results provide a valuable means for the quality control of PO.

KEYWORDS

Polygonatum odoratum, UHPLC-Q-TOF/MS, UHPLC-CAD, commercial specification, quality control

1 Introduction

Plants of genus *Polygonatum* have been extensively used as traditional Chinese medicine. The Chinese Pharmacopoeia records the rhizome of *Polygonatum odoratum* (PO) as a yin-nourishing medicine “Yuzhu”, which can be used for the treatment of diabetes and cough (Zhao et al., 2020; Li et al., 2021). PO is widely distributed in the temperate regions of Eurasia (Xia et al., 2022), growing in the forest or on the shady slopes of mountains (Feng et al., 2022). The major chemical constituents of PO are steroidal saponins, homoisoflavanones, alkaloids, and polysaccharides (Zhao et al., 2018; Zhao et al., 2019). In recent years, PO has gained increasing attention (Ning et al., 2018; Wang H J et al., 2018; Pang et al., 2021; Zhou

et al., 2021), but there is no systematic study on the chemical identification of PO. Xiangyuzhu (XPO) and Guanyuzhu (GPO) are available in the market as two main commercial specifications with different origins and prices. In the book “*Standard compilation of authentic medicinal materials*,” the appearance of XPO is thick, long, translucent, and light yellow in color, and that from Hunan is considered an authentic medicinal material, which occupies the majority of the Chinese market. GPO is a wild product in Northeast China, Inner Mongolia, and Hebei, and its cost is lower than XPO. Nonetheless, XPO is more frequently used as the raw material of dietary supplements, while GPO is more inclined to medicinal use. Currently, the quality control of PO was the only focus on the polysaccharide content (Jing et al., 2022), whereas some studies have pointed out that the polysaccharide content of GPO is higher than that of XPO (Tian et al., 2014). However, no comparison has been made between the other small molecule chemicals of these two commercial specifications to date. Therefore, it is essential to develop a specific method to distinguish the two commercial specifications in terms of chemical ingredients.

Ultra-high-performance liquid chromatography-quadrupole time-of-flight mass spectrometry (UHPLC-Q-TOF/MS) is a capital analytical tool with good resolution, excellent sensitivity, and strong structural characterization capability and has also been used in the qualitative analysis of *Polygonatum* genus (Huang et al., 2020; Sui et al., 2022). Off-line solid phase extraction (SPE) has been used in the pretreatment of complex samples to remove polysaccharides that cannot be retained on C18 columns and enrich targeted components for analysis (Li et al., 2019). The present study aimed to establish a qualitative method by coupling off-line SPE with UHPLC-Q-TOF/MS to characterize PO in positive and negative ion modes. The measured molecular weight plus the fragment ion information obtained by MS/MS could identify the structures of the chemical components (Zhao et al., 2013). Multivariate statistical analyses [for example, principal component analysis (PCA), orthogonal partial least squares discriminant analysis (OPLS-DA), and variable importance in the projection (VIP) plot] were used to identify the potential differential components among XPO and GPO (Pan et al., 2021).

As an aerosol-based universal detector, charged aerosol detector (CAD) can be characterized by high sensitivity, broad dynamic range, less interanalyte response variability, and improved reproducibility, which has gained increasing popularity for LC analysis of organic compounds with poor UV chromophores (Haidar Ahmad et al., 2019; Zheng et al., 2022). The fitting method of regression equation relies on the concentration range. In many cases, the linearity of CAD response is sufficient over the range of interest (Pawellek et al., 2021). Due to its high sensitivity, the limit of detection (LOD) and limit of quantification (LOQ) may be at the nanogram level (Zhang et al., 2019). Saponins are a class of active components used as key quality control indicators for content determination in many studies (Zhang et al., 2019; Nan et al., 2021). The furostol saponin polygonatumoside F showed the higher content in the PO samples and may be served as the chemical marker for quality control (Liu et al., 2018). In the present study, the other two components polygodoraside G and timosaponin H1 were screened out as major chemical markers in XPO and GPO. In order to assess the quality of PO, UHPLC-CAD method was used, and a

content ratio of timosaponin H1/polygodoraside G was proposed to differentiate the two commercial specifications of PO.

2 Materials and methods

2.1 Materials and reagents

Acetonitrile (HPLC grade) was purchased from Fisher Scientific Co. (Loughborough, United Kingdom). Distilled water was purchased from Watsons. Formic acid (HPLC grade) was purchased from Acros Co. Ltd. (NJ, United States). The other reagents of analytical grade were also obtained commercially (Beijing, China).

A total of 27 batches of representative PO were collected or purchased from Hunan (XPO, S1-S14) and Heilongjiang (GPO, S15-S27) provinces of China. The identity of all samples was confirmed by Prof. Bao-lin Guo of the Institute of Medicinal Plant Development, Chinese Academy of Medical Science&Peking Union. A total of 22 reference standards (purity >95%), polygodoraside A-H, typaspidoside H, typaspidoside L, polygonatumoside F, timosaponin H1, (25S)-26-O-(β -D-glucopyranosyl)-furost-5-en-3 β ,22 α ,26-triol 3-O- β -D-glucopyranosyl-(1 \rightarrow 2)- β -D-glucopyranosyl-(1 \rightarrow 4)- β -D-glucopyranoside, officinalisnin II, 25-*epi*-officinalisnin II, (3R)-5,7-dihydroxy-6,8-dimethyl-3-(4'-hydroxybenzyl)-chroman-4-one, (3R)-5,7-dihydroxy-6-methyl-8-methoxy-3-(4'-hydroxybenzyl)-chroman-4-one, (3R)-5,7-dihydroxy-6-methyl-3-(4'-hydroxybenzyl)-chroman-4-one, *N-trans-p*-coumaroyloctopamine, *N-trans-feruloyloctopamine*, (E)-3-(4-hydroxy-3-methoxybenzylidene)-4-(4-hydroxyphenyl)-pyrrolidin-2-one, and 3-(4-hydroxy-3-methoxy-phenyl)-acrylic acid carboxymethyl ester, were isolated in our laboratory and their structures were confirmed by comparing their MS and NMR spectral data with those described previously (Pang et al., 2020).

2.2 Preparation of samples and standard solutions

An equivalent of 1.0 g accurately weighed fine powder (<40 mesh) of each sample was mixed with 20 mL of 70% ethanol was added. After ultrasonication for 60 min, the solutions were cooled to room temperature, and the weight loss was replaced with 70% aqueous EtOH. Then, the solutions were filtered through a 0.45 μ m membrane before quantitative analysis. A volume of 10 mL of the supernatant was concentrated under reduced pressure and diluted to 4 mL with deionized water. A solid-phase extraction cartridge (C18-SPE, 6 mL) was activated with 10 mL of methanol, rinsed with 10 mL of water, and then reconstituted in 4 mL solution to load the sample; first, 10 mL water was used for elution, followed by 4 mL of 95% ethanol. Finally, the ethanol eluate was collected and filtered through a 0.22- μ m membrane for qualitative analysis.

The stock solutions of 22 standard references were prepared in acetonitrile at a final concentration of 0.1 mg/mL and analyzed by UHPLC-Q-TOF/MS. All the solutions were stored at 4°C for further study.

2.3 Qualitative analysis by UHPLC-Q-TOF/MS

UHPLC-Q-TOF/MS analysis was performed on an ACQUITY UHPLC™ system (Waters Corp. Milford, MA, United States) coupled with a Synapt G1 MS system (Waters Corp. Manchester, United Kingdom). A Waters ACQUITY UHPLC HSS T3 column (100 × 2.1 mm, 1.8 μm) was used for the analysis with the column temperature at 40°C. The mobile phases were water with 0.1% formic acid (A) and acetonitrile (B). The gradient used was as follows: 0–2 min, 5%→15% B; 2–18 min, 15%→37% B; 18–25 min, 37%→50% B; 25–27 min, 50% B; 27–28 min, 50%→5% B and 28–30 min, 5% B. The flow rate was 0.5 mL/min. The injection volume of the sample was 5 μL.

The data acquisition mode was MS^E. The data were obtained at 50–1500 Da. The source temperature was 100°C, the desolvation temperature was 450 °C with desolvation gas flow 850 L/h, leucine enkephaline was used as lock mass, and the capillary voltage was 3 kV. At low CE scan, the cone voltage was 30 V for ESI, and the collision energy was 6 eV (trap) and 4 eV (transfer), while it was 40–60 eV ramp (trap) and 12 eV (transfer) for ESI[−] and 15–25 eV ramp (trap) and 12 eV (transfer) for ESI⁺. The instrument was controlled by MassLynx 4.1 software (Waters Corp.).

2.4 Quantitative analysis by UHPLC-CAD analysis

UHPLC-CAD analysis was performed on the Thermo Vanquish UHPLC system (ThermoFisher Scientific, Germering, Bavaria, Germany). A Waters ACQUITY™ UHPLC HSS T3 column (100 × 2.1 mm, 1.8 μm) was used at a column temperature at 40°C, and the sample temperature was 10°C. The mobile phases were water with 0.1% formic acid (A) and acetonitrile (B). The gradient was as follows: 0–3 min, 10%→20% B; 3–12 min, 20% B; 12–13 min, 20%→22% B; 13–24 min, 22% B; 24–25 min, 22%→95% B; 25–27 min, 95% B; 27–28 min, 95%→10% B; 28–30 min, 10% B. The injection volume of the sample was 5 μL. The data collection was 5, and the filtration was for 3.6 s.

2.5 Validation of UHPLC-CAD analysis

The linearity of regression curves was tested by diluting the mixed stock solution to a series of concentrations of working solutions, and each was subjected to UHPLC analysis. The lower LODs and LOQs were determined by analyzing the serially diluted reference solutions of each compound until the signal-to-noise (S/N) proportion was about 3 and 10, respectively. The samples were analyzed in six replicates. The stability was tested by analyzing the sample solutions at different time points (0, 2, 4, 6, 8, 12, and 24 h). The RSD values of peak areas were calculated to examine the precision, repeatability, and stability of the quantitative method. Its accuracy was evaluated by recovery experiments. A specific amount of individual reference standards was spiked into PO sample. Five fortified samples were extracted and analyzed as described above. The recovery value (%) was calculated by the

following equation: recovery (%) = 100 × (detected amount – original amount)/spiked amount.

2.6 Multivariate analysis

The ESI-MS^E centroid data were processed by MarkerLynx version 4.1 (Waters Corp. Manchester, United Kingdom). The analysis included deconvolution, alignment, and data reduction to obtain a list of mass and retention time pairs with the corresponding areas for all the detected peaks from each file in the dataset. The processed data list was then imported by the PCA and OPLS-DA. All the test groups were discriminated in the PCA to investigate whether different groups could be separated. The method parameters were as follows: retention time range, 1–25 min; mass range, 100–1500 Da; mass tolerance, 0.02 Da; 6.00 for noise elimination level, 5% of the base peak intensity of minimum intensity; 0.20 min for RT tolerance. Moreover, isotopic peaks were excluded from analysis. Then, OPLS-DA was carried out to discriminate the ions contributing to the classification of the samples. The results were visualized in a score plot to show group clusters, and a VIP plot showed variables contributing to the classification.

3 Results and discussion

3.1 Characterization of chemical compounds in PO

To obtain satisfactory separation and high analytical efficiency, a series of preliminary experiment conditions, including chromatographic column particle size, mobile phase composition, and column temperature, were optimized. Various columns, such as ACQUITY UHPLC BEH C18 (2.1 mm × 100 mm, 1.7 μm) and CORTECS T3 (2.1 mm × 100 mm, 1.6 μm) were compared. Finally, the result was obtained on UHPLC HSS T3 column (100 × 2.1 mm, 1.8 μm). The acetonitrile-water system showed better separation and a more satisfactory peak shape than the methanol-water system. Moreover, 0.1% formic acid was added to the ACN-water system to enhance the peak capacity and improve the peak shape of saponins and flavonoids. The column showed excellent separation performance at 40°C.

Simultaneously, for the identification of the chemical components in PO by UHPLC-Q-TOF/MS, the MS parameters, such as ionization mode, capillary voltage, and different collision energy ranges, were optimized. The herbal extract samples were analyzed in the positive and negative ion modes with the same LC conditions. As shown in [Supplementary Table S1](#), 62 compounds were identified from the PO extract tentatively. The characterization was validated by the data of high-resolution mass spectrometry ([Figure 1](#)). The combination of the measured molecular weight with the fragment ion information obtained by collision-induced dissociation (CID) identified the structures and deduced that alkaloids, flavonoids, and steroidal saponins were the major constituents of the components.

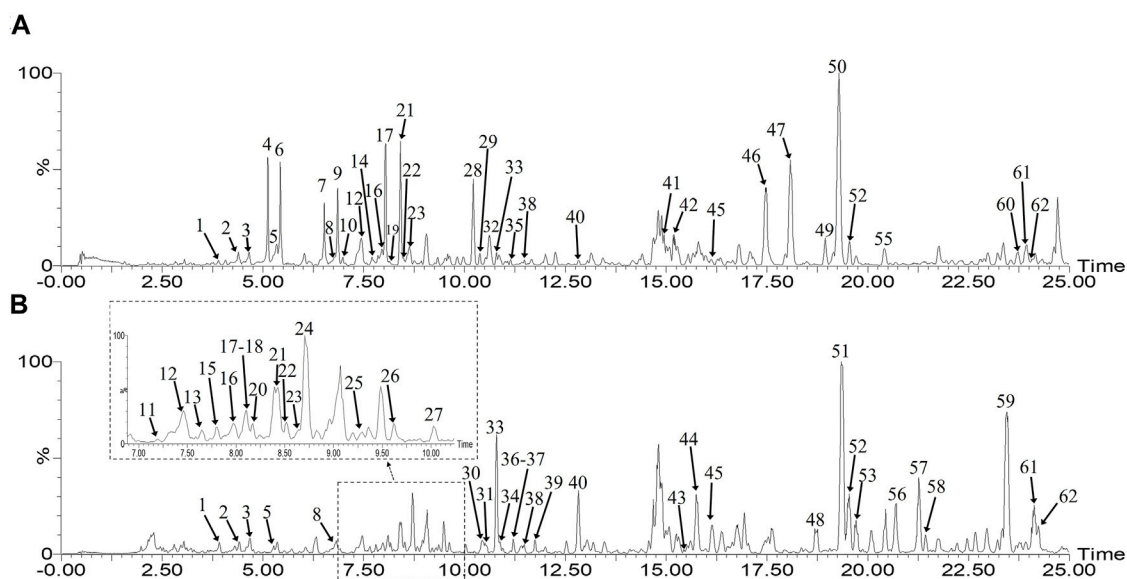


FIGURE 1
Base peak ion (BPI) chromatograms of XPO (A) and GPO (B) in the negative mode by UHPLC-Q-TOF/MS.

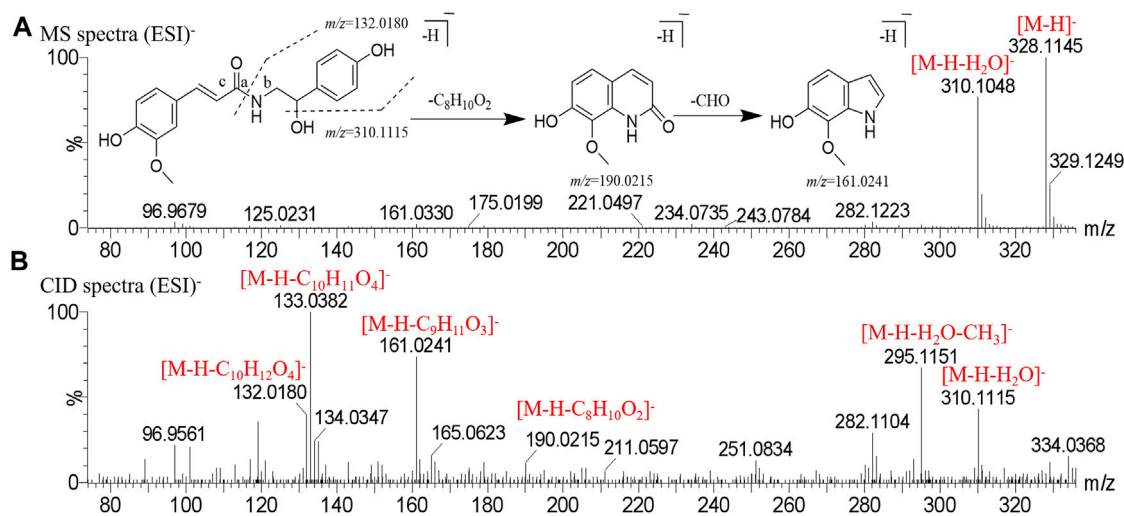


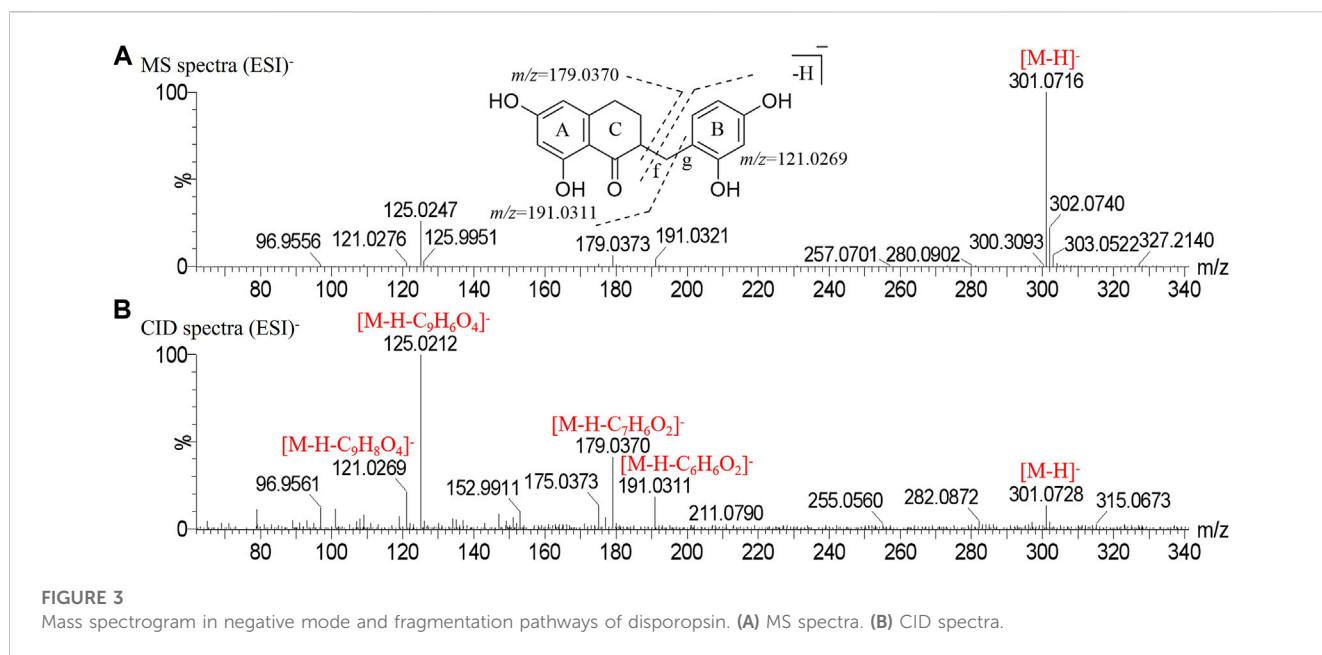
FIGURE 2
Mass spectrogram in negative mode and fragmentation pathways of *N-cis*-feruloyloctopamine. (A) MS spectra. (B) CID spectra.

3.1.1 Alkaloid derivatives

Alkaloids are nitrogen-containing basic organic compounds existing in nature. A total of four pairs of alkaloid components were identified in [Supplementary Table S1](#); their ion chromatographic signals were well-displayed in positive and negative ion modes. Each group of alkaloids had *cis* and *trans* structures, and the isomers could be determined by referring to the retention time of reference materials.

Peak two produced a deprotonated molecular ion at m/z 328.1145 $[M-H]^-$ and m/z 310.1048 $[M-H-H_2O]^-$ in the MS^1 spectrum. In the CID spectrum, the peak produced the fragment ion at m/z 161.0241 $[M-H-C_9H_{11}O_3]^-$ was broken at the b bond

resulting from McFarland's rearrangement cleavage, and also obtained the fragment ion m/z 190.0215 $[M-H-C_8H_{10}O_2]^-$; then, a molecule of CHO was removed to obtain the fragment ion m/z 132.0180 $[M-H-C_{10}H_{12}O_4]^-$ was generated by the cleavage of the bond based on the loss of a molecule of H_2O and McFarland's rearrangement. Peak two was tentatively identified as *N-cis*-feruloyloctopamine. The comparison of retention time showed that the alkaloids with the *cis* structure peaked more than those with *trans* structures. Also, other alkaloids were identified by this rule, and the mass spectrogram in the negative mode and the cracking pathway are shown in [Figure 2](#).



3.1.2 Flavonoids

The homoisoflavanones of PO are critical bioactive compounds (Wang Y et al., 2018; Xia G. H. et al., 2021; Xia G. H. et al., 2021), and the potential biosynthetic pathway for isoflavonoid formation has been defined in the PO (Zhang et al., 2020). It can generate characteristic fragment ions by RAD cleavage in the C ring at high energy levels (Ying et al., 2020), and the bond connecting the two sides of the methylene group between the B and C rings is broken to form other characteristic fragment ions.

Peak 32 produced a deprotonated molecular ion at m/z 301.0716 $[M-H]^-$ in the MS¹ spectrum. In the CID spectrum, the peak produced characteristic fragment ions m/z 179.0370 $[M-H-C_7H_6O_2]^-$ and m/z 121.0269 $[M-H-C_9H_8O_4]^-$ due to α -cleavage at the f bond (Ren et al., 2021) and the characteristic fragment ion m/z 191.0311 $[M-H-C_6H_6O_2]^-$ due to α -cleavage at the g bond. Finally, peak 32 was determined to be disporopsin, and the mass spectrogram in the negative mode and the potential cracking pathway are shown in Figure 3.

3.1.3 Steroidal saponins

Diosgenin and yamogenin are the main parent nucleus types in PO, and the C-3 position is often substituted by 3-4 sugar groups. The sugar group mainly consists of arabinose, glucose, xylose, and rhamnose. The negative ion mode displays deglycosylation fragments, while the positive ion mode presents patent ion characteristic fragments. Thus, these compounds could be identified by the combination of the positive and negative ion modes.

Peak 60 produced a deprotonated molecular ion at m/z 1061.5176 $[M-H]^-$ in the MS¹ spectrum. In the negative CID spectrum, the peak produced the fragment ions at m/z 899.4650 $[M-H-Glc]^-$, m/z 737.4129 $[M-H-Glc-Glc]^-$, and m/z 575.3652 $[M-H-Glc-Glc-Glc]^-$. In the positive CID spectrum, the peak produced the fragment ions at m/z 739.5706 $[M + H-Glc-Glc]^+$, m/z 577.4858 $[M + H-Glc-Glc-Glc]^+$, and m/z

415.3997 $[M + H-Glc-Glc-Glc-Gal]^+$. The presence of the characteristic ion m/z 271.2585 $[M + H-Glc-Glc-Glc-Gal-C_8H_{16}O_2]^+$ means that the composition is the same as the parent nucleus of 3-O- β -D-glucopyranosyl-(1 \rightarrow 2)-[β -D-xylopyranosyl-(1 \rightarrow 3)]- β -D-glucopyranosyl (1 \rightarrow 4)- β -D-galacopyranosyl-diosgenin, and the peak is finally determined to be 3-O- β -D-glucopyranosyl-(1 \rightarrow 2)-[β -D-glucopyranosyl-(1 \rightarrow 3)]- β -D-glucopyranosyl (1 \rightarrow 4)- β -D-galacopyranosyl-diosgenin. The mass spectrogram in the positive, negative mode and possible cracking pathway are shown in Figure 4.

3.1.4 Acetylated steroidal saponins

Acetylated steroidal saponins are primary metabolites that have been reported in the same genus of plants (Ahn et al., 2006). The position of the acetyl group is not fixed and could appear in the C-1 position or the sugar group inside the C-3 position. Such compounds mainly exist in GPO, and it is feasible to classify such compounds by the presence of a neutral loss of 42 Da in the mass spectrum.

For example, peak 36 produced a deprotonated molecular ion at m/z 1253.595 $[M-H]^-$ in the MS¹ spectrum. Typically, we observed that the precursor ion sheds 42 Da of m/z 1211.5792 $[M-H-COCH_2]^-$ in the CID spectrum. The peak produced the fragment ions at m/z 1079.5385 $[M-H-COCH_2-Xyl]^-$, m/z 1049.5275 $[M-H-COCH_2-Glc]^-$, m/z 917.4746 $[M-H-COCH_2-Glc-Xyl]^-$, and m/z 755.4301 $[M-H-COCH_2-2Glc-Xyl]^-$. The most fragment ion peaks are the same as timosaponin H1, which is the hydroxyacetylated precursor compound acetyl-timosaponin H1. The mass spectrogram in the negative mode of acetyl-timosaponin H1 and timosaponin H1 are shown in Supplementary Figure S1.

3.1.5 Identification of novel compounds

The summary of the chromatographic rules of reference substances could be used to deduce the structure of unknown

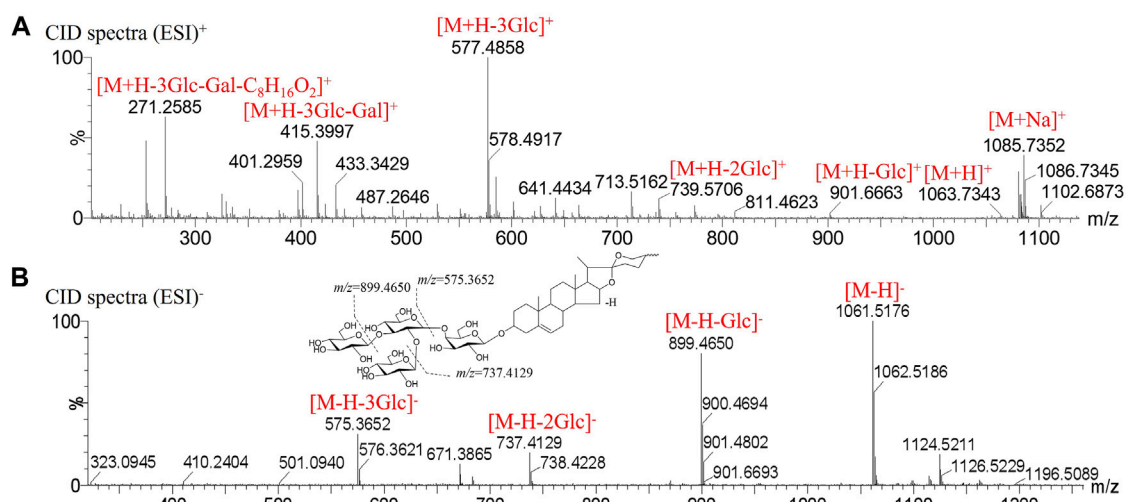


FIGURE 4

Mass spectrogram in positive, negative mode and fragmentation pathways of 3-O- β -D-glucopyranosyl-(1 \rightarrow 2)-[β -D-glucopyranosyl-(1 \rightarrow 3)]- β -D-glucopyranosyl (1 \rightarrow 4)- β -D-galactopyranosyl-diosgenin. (A) CID spectra in positive mode. (B) CID spectra in negative mode.

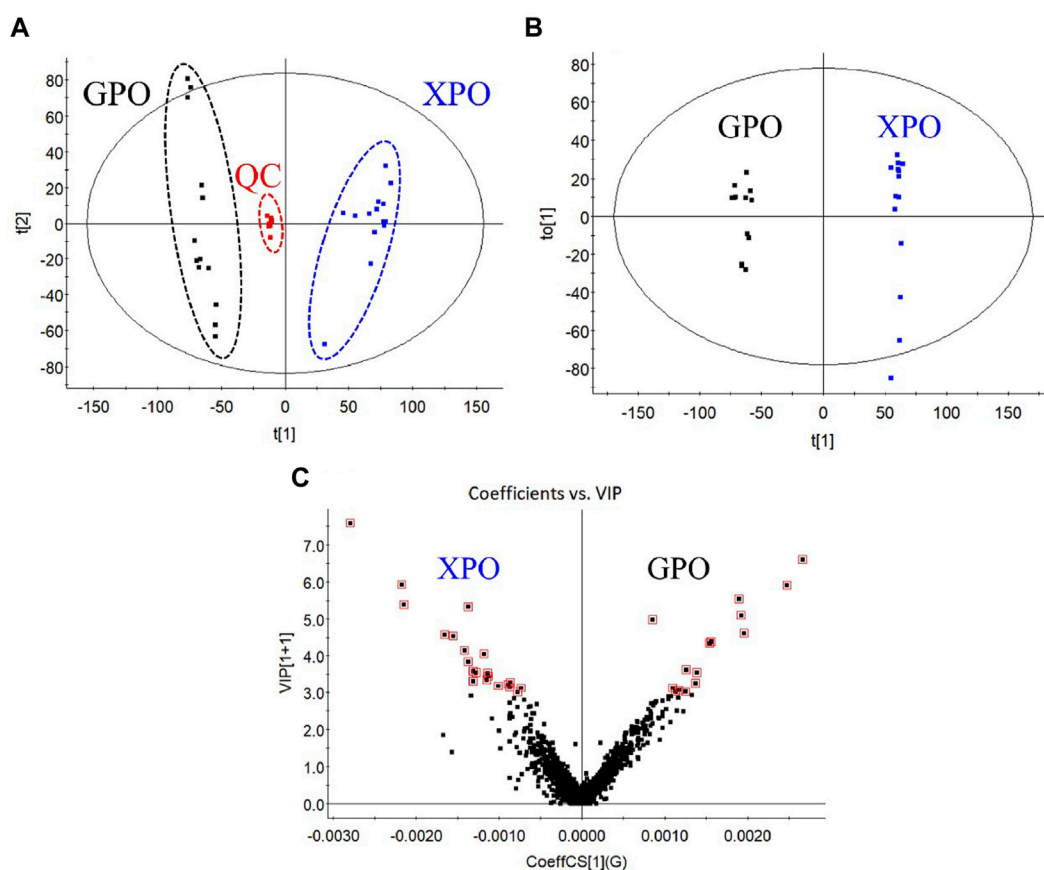


FIGURE 5

PCA score plot (A), OPLS-DA score plot (B), and VIP plot (C) of XPO and GPO.

TABLE 1 Selected markers responsible for discriminating two commercial specifications of PO.

Peak No.	t_R (min)	[M-H] ⁻	Identification	Main existing groups
17	8.03	1257.5757	Polygodoraside G	XPO
24	8.71	933.4652	Isomer of (25 <i>R</i> , 22 ξ)-hydroxylwattanoside C	GPO
28	10.21	741.4414	(22 <i>S</i>)-cholest-5-ene-1 β ,3 β ,16 β ,22-tetrol-1- <i>O</i> - α - <i>L</i> -rhamnopyranosyl-16- <i>O</i> - β -D-glucopyranoside	XPO
33	10.79	1211.5667	Timosaponin H1	GPO
40	12.82	609.3631	Polygonatumoside G	GPO
42	15.19	1061.5146	Isomer of 3- <i>O</i> - β -D-glucopyranosyl-(1 \rightarrow 2)-[β -D-glucopyranosyl-(1 \rightarrow 3)]- β -D-glucopyranosyl (1 \rightarrow 4)- β -D-galactopyranosyl-diosgenin	XPO
46	17.47	299.0952	(3 <i>R</i>)-5,7-dihydroxy-6-methyl-3-(4'-hydroxybenzyl)-chroman-4-one	XPO
47	18.1	329.1043	(3 <i>R</i>)-5,7-dihydroxy-6-methyl-8-methoxy-3-(4'-hydroxybenzyl)-chroman-4-one	XPO
50	19.29	313.1061	(3 <i>R</i>)-5,7-dihydroxy-6,8-dimethyl-3-(4'-hydroxybenzyl)-chroman-4-one	XPO
51	19.35	329.1071	Isomer of (3 <i>R</i>)-5,7-dihydroxy-6-methyl-8-methoxy-3-(4'-hydroxybenzyl)-chroman-4-one	GPO
56	20.69	299.0875	Isomer of (3 <i>R</i>)-5,7-dihydroxy-6-methyl-3-(4'-hydroxybenzyl)-chroman-4-one	GPO
57	21.28	753.4075	3 β -hydroxy-25 <i>S</i> -spirost-3- <i>O</i> - β -D-glucopyranosyl (1 \rightarrow 4)- β -D-galactopyranoside	GPO
59	23.46	313.1019	Isomer of (3 <i>R</i>)-5,7-dihydroxy-6,8-dimethyl-3-(4'-hydroxybenzyl)-chroman-4-one	GPO

Peak numbers were consistent with [Supplementary Table S1](#).

compounds to identify novel compounds. For example, the retention time of compounds with the glucose terminal group is less than that of xylose, and peak 7 can be inferred from this rule. The retention time of peak 7 was close to polygodoraside F and produced a deprotonated molecular ion at m/z 1255.5535 [M-H]⁻ in the MS¹ spectrum. In the CID spectrum, the peak produced the fragment ions at m/z 931.4557 [M-H-Glc-Glc]⁻, m/z 769.3910 [M-H-Glc-Glc-Glc]⁻, and m/z 571.3401 [M-H-Glc-Glc-Glc-Glc-2H₂O]⁻; these fragments were the same as those of polygodoraside F, and the retention time is relatively close. Therefore, it is inferred that there is difference between peak 7 and polygodoraside F in only the terminal sugar group; the peak 7 is finally determined to be polygodoraside F-Xyl + Glc. The mass spectrogram in the negative mode of polygodoraside F-Xyl + Glc and polygodoraside F are shown in [Supplementary Figure S2](#).

As a result, 62 compounds were identified from PO tentatively, including 43 steroidal saponins, 11 flavonoids, 8 alkaloids, and 10 possible new components.

3.2 Discrimination of PO samples with two commercial specifications by PCA and OPLS-DA analysis

Multivariate statistical analysis was carried out on the metabolite data to discriminate the two commercial specifications of PO. First, the obtained multivariate dataset of 27 batches of samples was analyzed by PCA. The results showed that the samples from different specifications were classified into two categories

([Figure 5A](#)), indicating a great variation in the chemical profile between XPO and GPO.

Then, the OPLS-DA model and VIP plot ([Figure 5C](#)) were established to identify the key markers that contribute to the differences between XPO and GPO, and a remarkable separation between these two specifications was also observed in the OPLS-DA score plot ([Figure 5B](#)). The model displayed 99% of the variation in the response Y (class) ($R^2Y = 99\%$) and also predicted 97% of the variations in the response Y ($Q^2Y = 97\%$). Therefore, the model could satisfactorily distinguish between the two species of samples. The VIP values (VIP >3.5) from OPLS-DA model were utilized to identify the potential differentiated variables, and 13 robust known chemical markers (including 6 flavonoids and 7 steroidal saponins) between XPO and GPO were selected and listed ([Table 1](#)). Isomer of (25*R*,22 ξ)-hydroxylwattanoside C (peak 24) and 3 β -hydroxy-25*S*-spirost-3-*O*- β -D-glucopyranosyl (1 \rightarrow 4)- β -D-galactopyranoside (peak 57) only existed in GPO samples, and their presence could be used to determine the commercial specification of PO. The differences in other components were differentiated in the content. For example, (1) compared to polygodoraside G (peak 17), no hydroxyl substitution was observed at the C-14 position of the parent nucleus of timosaponin H1 (peak 33). Peak 17 was a high content in XPO samples, while peak 33 was high in GPO samples; (2) polygonatumoside G (peak 40) was the product of deglycosylation of peak 17 with higher content in GPO samples; (3) as representative isoflavonoids components, (3*R*)-5,7-dihydroxy-6-methyl-3-(4'-hydroxybenzyl)-chroman-4-one (peak 46), (3*R*)-5,7-dihydroxy-6-methyl-8-methoxy-3-(4'-hydroxybenzyl)-chroman-4-one (peak 47), and (3*R*)-5,7-dihydroxy-6,8-dimethyl-3-(4'-hydroxybenzyl)-chroman-4-one

TABLE 2 Calibration curves, linear range, LOD, LOQ, recovery, precision, repeatability, and stability of three investigated analytes in PO.

No	Analyte	Calibration equation	r^2	Range (μg/mL)	LOD (ng)	LOQ (ng)	Recovery (%)	Precision (%)	Stability (%)	Repeatability (%)
1	Polygodoraside G	$Y = -104.67X^2 + 30.31X$	0.9999	0.23–30.00	0.04	2.00	105.10	0.83	1.83	2.75
2	Polygonatumoside F	$Y = -76.39X^2 + 32.44X$	0.9998	0.47–60.00	0.12	2.00	97.38	1.05	1.05	2.98
3	Timosaponin H1	$Y = -9.55X^2 + 27.68X$	0.9999	0.23–30.00	0.10	4.00	106.76	0.86	2.70	2.13

TABLE 3 Contents of three compounds in 27 batches of PO and the ratio of timosaponin H1/polygodoraside G.

Sample No.	Polygodoraside G (μg/g)	Polygonatumoside F (μg/g)	Timosaponin H1 (μg/g)	Total contents (μg/g)	Timosaponin H1/polygodoraside G
S1	109.03	96.39	16.62	222.04	0.15
S2	183.84	143.21	22.65	349.69	0.12
S3	73.18	50.55	13.97	137.70	0.19
S4	163.35	395.47	203.70	762.53	1.25
S5	67.80	75.76	19.28	162.83	0.28
S6	236.24	545.04	224.27	1005.55	0.95
S7	71.93	107.22	18.65	197.80	0.26
S8	72.69	56.02	13.34	142.06	0.18
S9	77.25	89.23	18.65	185.12	0.24
S10	179.74	404.75	145.79	730.27	0.81
S11	162.55	325.77	107.93	596.24	0.66
S12	95.22	93.21	19.31	218.00	0.20
S13	95.33	102.00	20.67	150.04	0.22
S14	71.04	63.06	15.94	563.50	0.22
S15	22.60	387.31	362.65	772.57	16.05
S16	13.33	438.48	407.83	859.64	30.60
S17	14.64	157.63	176.92	349.19	12.08
S18	29.98	285.11	281.11	596.19	9.38
S19	14.61	344.13	354.10	712.85	24.23
S20	14.66	287.17	295.84	597.67	20.18
S21	17.98	357.04	379.69	754.71	21.12
S22	18.65	282.42	262.43	563.50	14.07
S23	19.99	306.54	248.56	575.10	12.43
S24	27.33	340.59	335.93	703.85	12.29
S25	14.65	215.78	192.47	422.89	13.14
S26	25.31	470.98	271.79	768.08	10.74
S27	23.98	408.34	216.50	648.82	9.03

(peak 50) showed high contents in XPO samples. These chemical markers make it possible to distinguish the two groups of PO samples; then, two conspicuously characteristic markers,

polygodoraside G and timosaponin H1, were selected for further quantitative analysis to evaluate the quality of PO from two specifications.

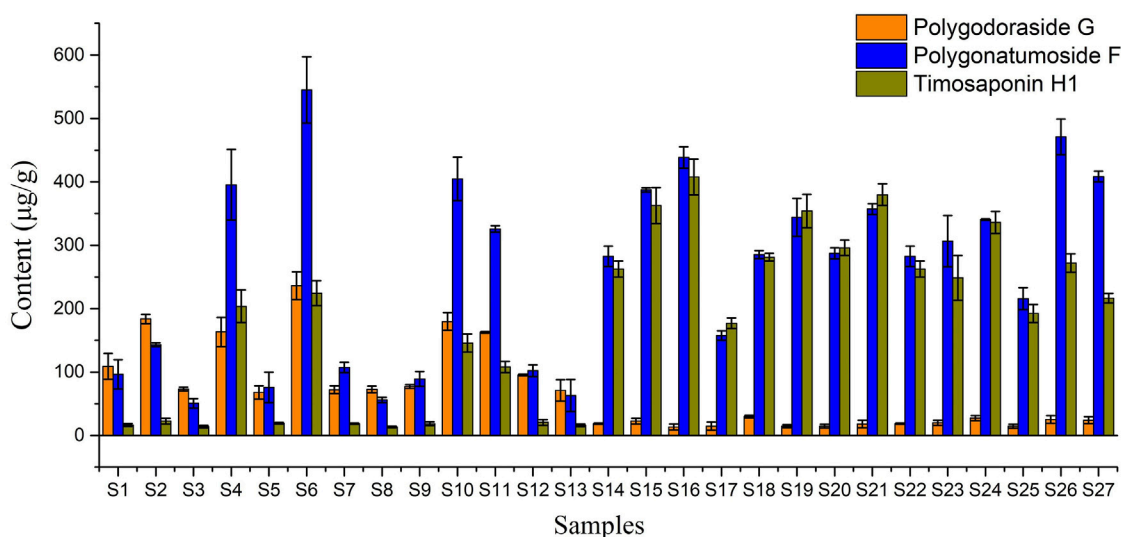


FIGURE 6
Contents of the three compounds in 27 batches of PO.

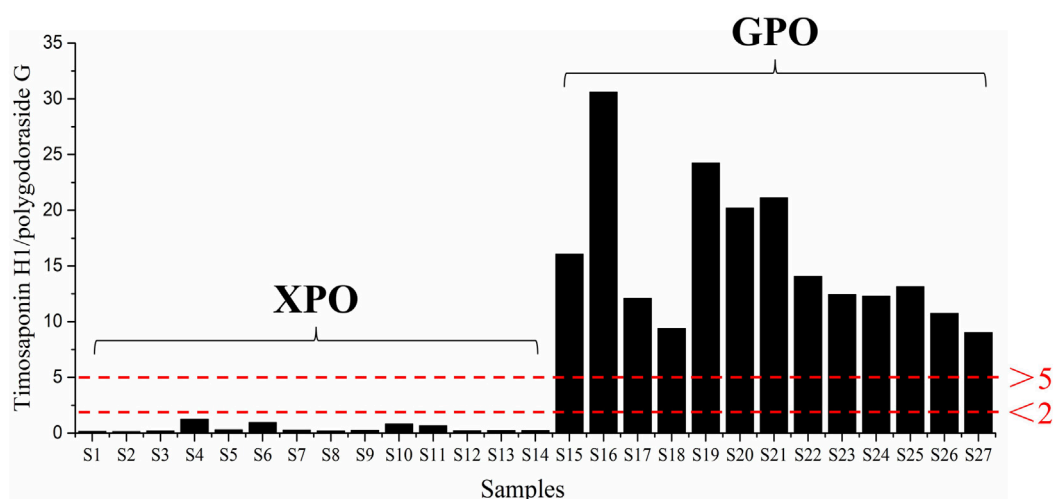


FIGURE 7
Ratio of timosaponin H1/polygodoraside G in 27 batches of PO.

3.3 Quantitative analysis of the PO samples by UHPLC-CAD with two commercial specifications

The furostolal saponin polygonatumoside F showed the higher content in all PO samples and thus could serve as the chemical marker for quality control, while the other components polygodoraside G and timosaponin H1 were screened out as chemical markers in XPO and GPO. To further understand the variation in the contents of the main steroidal saponins, a UHPLC-CAD approach was developed for the quantitative analysis of three furostanol saponins (polygodoraside G, polygonatumoside F, and timosaponin H1) in 27 samples with

two commercial specifications; the chemical structures showed in [Supplementary Figure S3](#).

The performance of Waters ACQUITY BEH C18 and ACQUITY CORTECS T3 was compared. Polygodoraside G and polygonatumoside F could be separated by Waters ACQUITY™ HSS T3. Therefore, the ACQUITY™ HSS T3 column was used for further separation. The column temperature and injection volume were also considered, and finally, the gradient was optimized under the condition of isocratic elution for the separation of the compounds. Subsequently, the established method was validated. The regression equations of the three analytes were calculated in the form of $Y = aX^2 + bX + c$; X and Y indicated the concentrations of the compound and the corresponding peak area, respectively. A good

linear correlation of the three analytes was gained ($r^2 > 0.999$) with a specific concentration range. Due to the high sensitivity of CAD, the LOD and LOQ were in the nanogram level. The results of the method validation are summarized in Table 2. The data indicated that the UHPLC-CAD method possessed good accuracy with recoveries from 97.38% to 106.76%, and all the RSDs of precision, stability, and repeatability were $<3\%$.

Then, the developed UHPLC-CAD method was applied to determine the three targeted compounds in different batches of PO samples (Supplementary Figure S4). Each sample was determined in triplicate, and the contents of targeted analytes are presented in Table 3. The contents of polygodoroside G, polygonatumoside F, and timosaponin H1 ranged from 13.33 to 236.24 $\mu\text{g/g}$, 50.55–545.04 $\mu\text{g/g}$, and 13.34–407.83 $\mu\text{g/g}$, respectively. Considering the total content of the three compounds (Figure 6), the quality of GPO was stable in the range of 349.19–859.64 $\mu\text{g/g}$, while the quality of different batches of XPO varied greatly, and the total content was 137.70–1005.55 $\mu\text{g/g}$. Moreover, polygonatumoside F was the main characteristic compound in the samples of PO. The average content of polygonatumoside F in XPO was 195.49 $\mu\text{g/g}$ and was lower in GPO with 329.35 $\mu\text{g/g}$, indicating that GPO should be focused upon from the perspective of saponin content. In addition, polygodoroside G was present in XPO with an average content of 113.04 $\mu\text{g/g}$, and that in GPO was 19.82 $\mu\text{g/g}$, while timosaponin H1 was mainly present in XPO with an average content of 78.85 $\mu\text{g/g}$ and that in GPO was 291.22 $\mu\text{g/g}$; the content ratio of the two compounds in different specifications differed markedly. Therefore, it can be concluded that the samples with a ratio <2 of timosaponin H1/polygodoroside G were considered as XPO, and >5 were considered as GPO (Figure 7). In conclusion, the absolute content of the main characteristic components in PO has been investigated. We found that XPO and GPO have significant differences in the quality of medicinal materials. Thus, timosaponin H1/polygodoroside G seems to be a promising indicator to distinguish the two commercial specifications.

4 Conclusion

In order to understand the chemical composition of PO comprehensively, an effective and sensitive UHPLC-Q-TOF/MS method was developed for the characterization of PO with two commercial specifications. A total of 62 components were identified, of which 13 robust known chemical markers (including 6 flavonoids and 7 steroidal saponins) were screened out to differentiate Xiangyuzhu (XPO) and Guanyuzhu (GPO). A simultaneous determination method for polygodoroside G, polygonatumoside F, and timosaponin H1 was established and validated by UHPLC-CAD before applying it to determine the differences in the contents of the three components in XPO and GPO samples. The ratio of timosaponin H1/polygodoroside G can be used as an indicator to distinguish the two commercial specifications of PO. The samples with a ratio <2 are considered XPO and >5 are considered GPO.

In this study, the qualitative analysis and quantitative analysis of PO were carried out to elucidate the composition. The findings provided a method for distinguishing the two commercial specifications of PO in the market and laid a theoretical foundation for the appropriate utilization of the resources.

Data availability statement

The original contributions presented in the study are included in the article/Supplementary Material, further inquiries can be directed to the corresponding author.

Author contributions

YN and BM conceived and designed the experiments. YN and XP performed the experiments. YN and BM conceived and designed the experiments. YN and XP performed the experiments. YN and YS analyzed the data, and WZ contributed to the manuscript preparation. HL, JZ, XC, and JS reviewed the manuscript. All authors reviewed the results and approved the final manuscript.

Funding

This study was financially supported by the National Natural Science Foundation of China (82074008).

Conflict of interest

The authors declare that the research was conducted in the absence of any commercial or financial relationships that could be construed as a potential conflict of interest.

Publisher's note

All claims expressed in this article are solely those of the authors and do not necessarily represent those of their affiliated organizations, or those of the publisher, the editors and the reviewers. Any product that may be evaluated in this article, or claim that may be made by its manufacturer, is not guaranteed or endorsed by the publisher.

Supplementary material

The Supplementary Material for this article can be found online at: <https://www.frontiersin.org/articles/10.3389/fchem.2023.1146153/full#supplementary-material>

References

- Ahn, M.-J., Kim, C. Y., Yoon, K.-D., Ryu, M. Y., Cheong, J. H., and Chin, Y.-W. (2006). Steroidal saponins from the rhizomes of *Polygonatum sibiricum*. *Polyg. Sib. J. Not. Prod.* 69, 360–364. doi:10.1021/np050394d
- Feng, C. J., Li, Q., Fan, M., Xu, M. L., Zhao, X. F., and Wang, X. (2022). High performance liquid chromatography fingerprint and chemical pattern recognition of wild *Polygonatum odoratum* in Gansu Province. *Chin. Med. Mat.* 45, 1203–1208. doi:10.13863/j.issn1001-4454.2022.05.028
- Haidar Ahmad, I. A., Blasko, A., Tam, J., Variankaval, N., Halsey, H. M., and Hartman, R. (2019). Revealing the inner workings of the power function algorithm in charged aerosol detection: A simple and effective approach to optimizing power function value for quantitative analysis. *J. Chromatogr. A* 1603, 1–7. doi:10.1016/j.chroma.2019.04.017
- Huang, Z. Z., Du, X., Ma, C. D., Zhang, R. R., Gong, W. L., and Liu, F. (2020). Identification of antitumor active constituents in *Polygonatum sibiricum* flower by UPLC-Q-TOF-MS^E and network pharmacology. *ACS Omega* 5, 29755–29764. doi:10.1021/acsomega.0c03582
- Jing, Y. S., Yan, M., Zhang, Y. W., Zhang, R. J., Wang, F. F., Zheng, Y. G., et al. (2022). HPLC fingerprint analysis of polysaccharides from different accessions of *Polygonatum odoratum*. *Polyg. Odoratum. Nat. Prod. Res.* 1-5, 1–5. doi:10.1080/14786419.2022.2102626
- Li, J., Wang, Y. Q., Mei, X. D., Liu, Z. H., Song, S., and Ma, T. (2019). Characterization of chemical constituents in aqueous extracts and fermentation broth from *Polygonati Rhizoma* by UHPLC-LTQ-Orbitrap MS combined with solid phase extraction. *Chin. Tradit. Herb. Drugs* 50, 3029–3043. doi:10.7501/j.issn.0253-2670.2019.13.006
- Li, X. L., Ma, R. H., Zhang, F., Ni, Z. J., Thakur, K., Wang, S. Y., et al. (2021). Evolutionary research trend of *polygonatum* species: A comprehensive account of their transformation from traditional medicines to functional foods. *Crit. Rev. Food Sci. Nutr.* 1–18. doi:10.1080/10408398.2021.1993783
- Liu, Q. B., Li, W., Nagata, K., Fu, H. W., Okada, S., Tanabe, I., et al. (2018). Isolation, structural elucidation, and liquid chromatography–mass spectrometry analysis of steroidal glycosides from *Polygonatum odoratum*. *Polyg. Odoratum. J. Agric. Food Chem.* 66, 521–531. doi:10.1021/acs.jafc.7b04488
- Nan, Y., Zheng, W., Ma, F. X., Sun, X. G., Zhao, Y., and Zhang, J. (2021). Simultaneous determination of mangiferin and timosaponin BII of *Anemarrhenae Rhizoma* by HPLC-CAD. *Chin. J. Pharm. Anal.* 41, 111–116. doi:10.16155/j.0254-1793.2021.01.13
- Ning, D., Jin, M., Xv, T., Sun, J. K., and Li, M. (2018). Homoisoflavanone-1 isolated from *Polygonatum odoratum* arrests the cell cycle and induces apoptosis in A549 cells. *Oncol. Lett.* 16, 3545–3554. doi:10.3892/ol.2018.9085
- Pan, J. Q., Zheng, W., Pang, X., Zhang, J., Chen, X. J., Yuan, M., et al. (2021). Comprehensive investigation on ginsenosides in different parts of a garden-cultivated ginseng root and rhizome. *Molecules* 26, 1696. doi:10.3390/molecules26061696
- Pang, X., Zhao, J. Y., Liu, N., Chen, M. H., Zheng, W., Zhang, J., et al. (2021). Anthraquinone analogues with inhibitory activities against influenza A virus from *Polygonatum odoratum*. *Polyg. Odoratum. J. Asian Nat. Prod. Res.* 23, 717–723. doi:10.1080/10286020.2020.1779707
- Pang, X., Zhao, J. Y., Wang, Y. J., Zheng, W., Zhang, J., Chen, X. J., et al. (2020). Steroidal glycosides, homoisoflavanones and cinnamic acid derivatives from *Polygonatum odoratum* and their inhibitory effects against influenza A virus. *Fitoterapia* 146, 104689. doi:10.1016/j.fitote.2020.104689
- Pawellek, R., Muellner, T., Gamache, P., and Holzgrabe, U. (2021). Power function setting in charged aerosol detection for the linearization of detector response - optimization strategies and their application. *J. Chromatogr. A* 1637, 461844. doi:10.1016/j.chroma.2020.461844
- Quan, L. T., Wang, S. C., and Zhang, J. (2015). Chemical constituents from *Polygonatum odoratum*. *Polyg. Odoratum. Biochem. Syst. Ecol.* 58, 281–284. doi:10.1016/j.bse.2014.12.019
- Ren, H. M., Deng, Y. L., Zhang, J. L., Ye, X. W., Xia, L. T., and Liu, M. M. (2020). Research progress on processing history evolution, chemical components and pharmacological effects of *Polygonati Rhizoma*. *Chin. J. Chin. Mater Med.* 45, 4163–4182. doi:10.19540/j.cnki.cjmm.20200522.601
- Ren, H. M., Zhang, J. L., Deng, Y. L., Ye, X. W., Xia, L. T., and Liu, M. M. (2021). Analysis of chemical constitutions of *Polygonatum cyrtoneura* dried rhizomes before and after processing based on UPLC-Q-TOF-MS. *Chin. J. Exp. Tradit. Med. Form.* 27, 110–121. doi:10.13422/j.cnki.syfjx.20202147
- Sui, Z. Y., Hou, P. Y., and Wang, B. (2022). Rapid identification of the components in *Polygonatum odoratum* based on UHPLC-Q-orbitrap platform. *Chin. Pharm.* 25, 626–630. doi:10.19962/j.cnki.issn1008-049X.2022.04.011
- Tian, W. Z., Li, H. N., and Sun, T. (2014). Studies on the comparison for polysaccharide between *Polygonatum* and *Polygonatum*. *Genseng Res.* 26, 33–35. doi:10.19403/j.cnki.1671-1521.2014.04.010
- Wang, H. J., Fowler, M., Messenger, D., Terry, L. A., Gu, X. L., Zhou, L. X., et al. (2018). Homoisoflavanones are potent glucose transporter 2 (GLUT2) inhibitors: A potential mechanism for the glucose-lowering properties of *Polygonatum odoratum*. *Polyg. Odoratum. J. Agric. Food Chem.* 66, 3137–3145. doi:10.1021/acs.jafc.8b00107
- Wang, Y., Fei, Y. Q., Liu, L. R., Xiao, Y. H., Pang, Y. L., Kang, J. H., et al. (2018). *Polygonatum odoratum* polysaccharides modulate gut microbiota and mitigate experimentally induced obesity in rats. *Int. J. Mol. Sci.* 19, 3587. doi:10.3390/ijms19113587
- Xia, G. H., Li, X. H., Zhang, Z., and Jiang, Y. H. (2021b). Effect of food processing on the antioxidant activity of flavones from *Polygonatum odoratum* (Mill.) Druce. *Open Life Sci.* 16, 92–101. doi:10.1515/biol-2021-0010
- Xia, G. H., Li, X. H., Zhang, Z., and Jiang, Y. H. (2021a). Effects of fermentation treatments on *Polygonatum odoratum* flavones' antioxidant activities. *Saudi J. Biol. Sci.* 28, 5011–5016. doi:10.1016/j.sjbs.2021.01.026
- Xia, M. Q., Liu, Y. J., Liu, J., Chen, D. H., Shi, Y., Chen, Z. X., et al. (2022). Out of the Himalaya-Hengduan mountains: Phylogenomics, biogeography and diversification of *polygonatum* mill. (Asparagaceae) in the northern hemisphere. *Mol. Phylogenet. Evol.* 169, 107431. doi:10.1016/j.ympev.2022.107431
- Ying, C. Y., Zhang, C., Sun, M. Q., Lin, L., and Liu, J. X. (2020). Mass spectrometric fragmentation pathways of three ginkgo biloba flavonoids using HPLC-Q-TOF/MS. *J. Chin. Mass Spectrom. Soc.* 41, 57–65. doi:10.7538/zpxb.2019.0011
- Zeng, T., Tang, Y. R., Li, B., Tasneem, S., Yuan, H. W., Jia, Y. Z., et al. (2020). Chemical characterization of constituents from *Polygonatum cyrtoneura* Hua and their cytotoxic and antioxidant evaluation. *Nat. Prod. Res.* 34, 2482–2489. doi:10.1080/14786419.2018.1543682
- Zhang, C. E., Liang, L. J., Yu, X. H., Wu, H., Tu, P. F., and Ma, Z. J. (2019). Quality assessment of *Astragali Radix* from different production areas by simultaneous determination of thirteen major compounds using tandem UV/charged aerosol detector. *J. Pharm. Biomed. Anal.* 165, 233–241. doi:10.1016/j.jpba.2018.12.015
- Zhang, S. X., Shi, Y. Y., Shan, C. M., Zhao, L. Q., Ma, K. L., and Huang, L. Q. (2020). Analysis of the transcriptome of *Polygonatum odoratum* (tll.) druce uncovers putative genes involved in isoflavonoid biosynthesis. *J. Plant Biol.* 63, 217–228. doi:10.1007/s12374-020-09246-6
- Zhao, J., Wang, Y. Z., Yang, W. Z., Yang, M. Q., and Zhang, J. Y. (2019). Research progress in chemical constituents in plants of *Polygonatum* and their pharmacological effects. *Chin. J. Chin. Mater Med.* 44, 1989–2008. doi:10.19540/j.cnki.cjmm.20190222.006
- Zhao, P., Li, X., Wang, Y., Yan, L. Y., Guo, L. P., Huang, L. Q., et al. (2020). Characterisation and saccharide mapping of polysaccharides from four common *Polygonatum* spp. *Carbohydr. Polym.* 233, 115836. doi:10.1016/j.carbpol.2020.115836
- Zhao, P., Zhao, C. C., Li, X., Gao, Q. Z., Huang, L. Q., Xiao, P. G., et al. (2018). The genus *polygonatum*: A review of ethnopharmacology, phytochemistry and pharmacology. *J. Ethnopharmacol.* 214, 274–291. doi:10.1016/j.jep.2017.12.006
- Zhao, Y., Kang, L., Yu, H., Zhang, J., Xiong, C., Pang, X., et al. (2013). Structure characterization and identification of steroidal saponins from the rhizomes of *Anemarrhena asphodeloides* by ultra performance liquid chromatography and hybrid quadrupole time-of-flight mass spectrometry. *Int. J. Mass Spectrom.* 341–342, 7–17. doi:10.1016/j.ijms.2013.03.005
- Zheng, W., Zhou, M., Chai, R. P., Liang, H. Z., Zhang, J., Zhao, Y., et al. (2022). Quality analysis of hawthorn leaves (the leaves of *Crataegus pinnatifida* Bge. var major N.E.Br.) in different harvest time. *Phytochem. Anal.* 33, 1147–1155. doi:10.1002/pca.3166
- Zhou, D., Feng, Y., Li, W., Liu, B., Liu, X., Sun, L., et al. (2021). Cytotoxic steroidal glycosides from *Polygonatum odoratum* (Mill.) Druce. *Phytochem.* 191, 112906. doi:10.1016/j.phytochem.2021.112906



OPEN ACCESS

EDITED BY

Clemens Zwergel,
Sapienza University of Rome, Italy

REVIEWED BY

Piia Bartos,
University of Eastern Finland, Finland
Sveva Pelliccia,
University of Naples Federico II, Italy

*CORRESPONDENCE

Koen Augustyns,
✉ koen.augustyns@uantwerpen.be

[†]These authors share senior authorship

SPECIALTY SECTION

This article was submitted to Medicinal and Pharmaceutical Chemistry, a section of the journal Frontiers in Chemistry

RECEIVED 06 February 2023

ACCEPTED 28 March 2023

PUBLISHED 07 April 2023

CITATION

Scarpellini C, Valembois S, Goossens K, Vadi M, Lanthier C, Klejborowska G, Van Der Veken P, De Winter H, Bertrand MJM and Augustyns K (2023), From PERK to RIPK1: Design, synthesis and evaluation of novel potent and selective necroptosis inhibitors. *Front. Chem.* 11:1160164. doi: 10.3389/fchem.2023.1160164

COPYRIGHT

© 2023 Scarpellini, Valembois, Goossens, Vadi, Lanthier, Klejborowska, Van Der Veken, De Winter, Bertrand and Augustyns. This is an open-access article distributed under the terms of the [Creative Commons Attribution License \(CC BY\)](https://creativecommons.org/licenses/by/4.0/). The use, distribution or reproduction in other forums is permitted, provided the original author(s) and the copyright owner(s) are credited and that the original publication in this journal is cited, in accordance with accepted academic practice. No use, distribution or reproduction is permitted which does not comply with these terms.

From PERK to RIPK1: Design, synthesis and evaluation of novel potent and selective necroptosis inhibitors

Camilla Scarpellini¹, Sophie Valembois¹, Kenneth Goossens¹, Mike Vadi^{2,3}, Caroline Lanthier¹, Greta Klejborowska¹, Pieter Van Der Veken¹, Hans De Winter¹, Mathieu J. M. Bertrand^{2,3†} and Koen Augustyns^{1*†}

¹Laboratory of Medicinal Chemistry, Department of Pharmaceutical Sciences, Faculty of Pharmaceutical, Biomedical and Veterinary Sciences, University of Antwerp, Antwerp, Belgium, ²Vlaams Instituut voor Biotechnologie (VIB) Center for Inflammation Research, Ghent, Belgium, ³Laboratory Cell Death and Inflammation, Department of Biomedical Molecular Biology, Ghent University, Ghent, Belgium

Receptor-Interacting serine/threonine-Protein Kinase 1 (RIPK1) emerged as an important driver of inflammation and, consequently, inflammatory pathologies. The enzymatic activity of RIPK1 is known to indirectly promote inflammation by triggering cell death, in the form of apoptosis, necroptosis and pyroptosis. Small molecule Receptor-Interacting serine/threonine-Protein Kinase 1 inhibitors have therefore recently entered clinical trials for the treatment of a subset of inflammatory pathologies. We previously identified GSK2656157 (GSK'157), a supposedly specific inhibitor of protein kinase R (PKR)-like ER kinase (PERK), as a much more potent type II Receptor-Interacting serine/threonine-Protein Kinase 1 inhibitor. We now performed further structural optimisation on the GSK'157 scaffold in order to develop a novel class of more selective Receptor-Interacting serine/threonine-Protein Kinase 1 inhibitors. Based on a structure-activity relationship (SAR) reported in the literature, we anticipated that introducing a substituent on the *para*-position of the pyridinyl ring would decrease the interaction with PERK. Herein, we report a series of novel GSK'157 analogues with different *para*-substituents with increased selectivity for Receptor-Interacting serine/threonine-Protein Kinase 1. The optimisation led to UAMC-3861 as the best compound of this series in terms of activity and selectivity for Receptor-Interacting serine/threonine-Protein Kinase 1 over PERK. The most selective compounds were screened *in vitro* for their ability to inhibit RIPK1-dependent apoptosis and necroptosis. With this work, we successfully synthesised a novel series of potent and selective type II Receptor-Interacting serine/threonine-Protein Kinase 1 inhibitors based on the GSK'157 scaffold.

KEYWORDS

RIPK1 inhibitor, necroptosis, regulated cell death, inflammation, type II kinase inhibitor, PERK (PKR-like endoplasmic reticulum kinase)

1 Introduction

Cell death is increasingly recognised as an important driver of inflammation, and is consequently believed to be at the origin of various inflammatory diseases when improperly regulated (Newton et al., 2021). A subset of innate immune receptors can trigger the dismantlement of the cell, and the resulting cell death can promote the production of pro-inflammatory mediators by activating immune receptors on neighbouring effector cells. Next to apoptosis, which is generally considered immunologically silent, lytic forms of cell death, such as apoptosis-driven secondary necrosis, necroptosis and pyroptosis, release intracellular factors, known as danger-associated molecular patterns (DAMPs), that activate immune receptors and induce inflammatory responses. In addition, the death of epithelial cells can also affect the functionality of bodily barriers, and thereby trigger/exacerbate inflammation through the sensing of pathogen-associated molecular patterns (PAMPs) from microbes that have breached the barriers. Accumulating evidence indicates that genetic targeting of cell death can revert the inflammatory pathology state in various mouse models of acute and chronic inflammatory diseases. Hence, drugs that inhibit cell death are currently under investigation as potential therapies for human inflammatory and autoimmune diseases. Among these drugs, pharmacological inhibitors of the receptor-interacting serine/threonine protein kinase 1 (RIPK1) have entered clinical trials for the treatment of autoimmune diseases (psoriasis, ulcerative colitis and rheumatoid arthritis), as well as some cancers and neurological disorders (Mifflin et al., 2020).

RIPK1 functions as a central signalling node downstream of several immune receptors, where it can paradoxically function as a scaffold to promote cell survival or as an active kinase to trigger cell death (Delanghe et al., 2020). RIPK1 has been best studied in the context of tumour necrosis factor (TNF) signalling. Binding of TNF to TNFR1 induces recruitment of RIPK1 to the cytosolic tail of the receptor, an initial step in the assembly of the receptor signalling complex (Complex I). Within this complex, RIPK1 functions as a ubiquitylated scaffold that contributes to the activation of the MAPK and NF- κ B signalling pathways, which collectively promote transcription of pro-inflammatory and pro-survival genes. Kinases from the MAPK and NF- κ B pathway, including MK2 and IKK α / β , signal back to RIPK1 to maintain it in an inactive prosurvival state (Dondelinger et al., 2015; 2017; 2019; Jaco et al., 2017; Menon et al., 2017; Lafont et al., 2018; Xu et al., 2018). Consequently, conditions that affect proper activation of these kinases remove the brake on RIPK1, which can then autophosphorylate on Ser166, dissociate from complex I and promote assembly of the cytosolic caspase-8 activating complex (complex II) that triggers apoptosis induction. Caspase-8 activation by RIPK1 was also recently reported to induce cleavage and activation of the pore forming molecule gasdermin D (GSDMD) in macrophages, thereby promoting induction of a specific form of pyroptosis (Orning et al., 2018; Chen et al., 2021). Furthermore, conditions that prevent activation of caspase-8 in Complex II (e.g., by the use of the pan-caspase inhibitor zVAD.fmk) induce further recruitment of RIPK3 and MLKL to complex II, now called the necrosome, leading to RIPK3 activation, phosphorylation of MLKL by RIPK3, and subsequent necroptosis induction (Rodriguez et al., 2016; Mompea et al., 2018; Weber et al., 2018; Klöditz and Fadeel,

2019). The enzymatic activity of RIPK1 is therefore capable of inducing three distinct forms of cell death, which have all been linked to inflammation (Mifflin et al., 2020). Consequently, the importance of specific targeting RIPK1 to prevent chronic inflammatory processes has emerged.

The first RIPK1 inhibitor described in the literature was necrostatin-1 (Nec-1) in 2005 (Figure 1) (Degterev et al., 2005). It served as a valuable tool compound to study RIPK1 structure and to demonstrate the implication of RIPK1 kinase-dependent cell death in animal models of human diseases (Xie et al., 2013). Particularly, the co-crystallization of Nec-1s, a stable form of Nec-1, with the kinase domain of RIPK1 demonstrated the typical type III kinases inhibitor mode of interaction, with binding to the specific RIPK1 allosteric pocket formed by the DLG-out conformation and without interacting with the hinge region (Wang et al., 2006; Zheng et al., 2008; Takahashi et al., 2012). Since then, several additional RIPK1 inhibitors have been reported (Martens et al., 2020; Chen et al., 2022; Shi et al., 2022). Among them, a class of compounds featuring a benzoxazepinone core emerged with GSK2882481 (Clark et al., 2009; Harris et al., 2016), but interspecies differences were observed when comparing humans to non-primate RIPK1, probably due to the different amino acids featured by the enzyme affecting protein flexibility (Berger et al., 2015; Harris et al., 2017). This class of compound was further optimised aiming to develop a drug with suitable oral bioavailability. The lead optimisation led to the discovery of GSK2982772 (GSK'772) which is currently in phase IIb clinical trial for the treatment of ulcerative colitis, psoriasis, and rheumatoid arthritis (Weisel et al., 2017).

Among the different RIPK1-inhibitors available in the literature (Figure 1), the type II class has been less investigated in disease models and in clinic (Martens et al., 2020; Chen et al., 2022; Shi et al., 2022). In the type II RIPK1 inhibitors family, tyrosine kinase inhibitor (TKI) ponatinib and its analogues, and sorafenib are reported as dual inhibitors for both RIPK1 and RIPK3 (Fauster et al., 2015; Martens et al., 2017). Compound 27 (cpd27) showed promising pharmacokinetics properties but low kinase selectivity (Harris et al., 2013). PN10 is a hybrid compound which combines the structures of Nec-1 and ponatinib (Najjar et al., 2015). This strategy increased specificity and selectivity of the analogue retaining the interaction with the allosteric pocket of Nec-1 and the interaction with the hinge region of ponatinib as type II kinases inhibitors. Besides, GSK identified a class of dual inhibitors represented by GSK2593067 and GSK2593074 which completely blocked necroptosis in both human and murine cells as type II inhibitors (Zhou et al., 2019).

We previously reported that two commonly used Protein kinase R (PKR)-like ER kinase (PERK) inhibitors, GSK2606414 (GSK'414) and GSK2656157 (GSK'157), were actually potent inhibitors of RIPK1 (Rojas-Rivera et al., 2017). Interestingly, and in comparison to the above mentioned RIPK1 inhibitors, GSK'157 appeared to function as a type II kinases inhibitor of RIPK1 (Axten et al., 2013). A kinome scan performed for both, GSK'414 and GSK'157 suggested a good selectivity profile. GSK'414 was screened against a panel of 294 kinases at 10 μ M with an inhibition of 20 kinases with more than 85%, while the optimised analogue GSK'157 inhibited 17 out of 300 kinases with more than 80% at the same concentration. The reported structure-

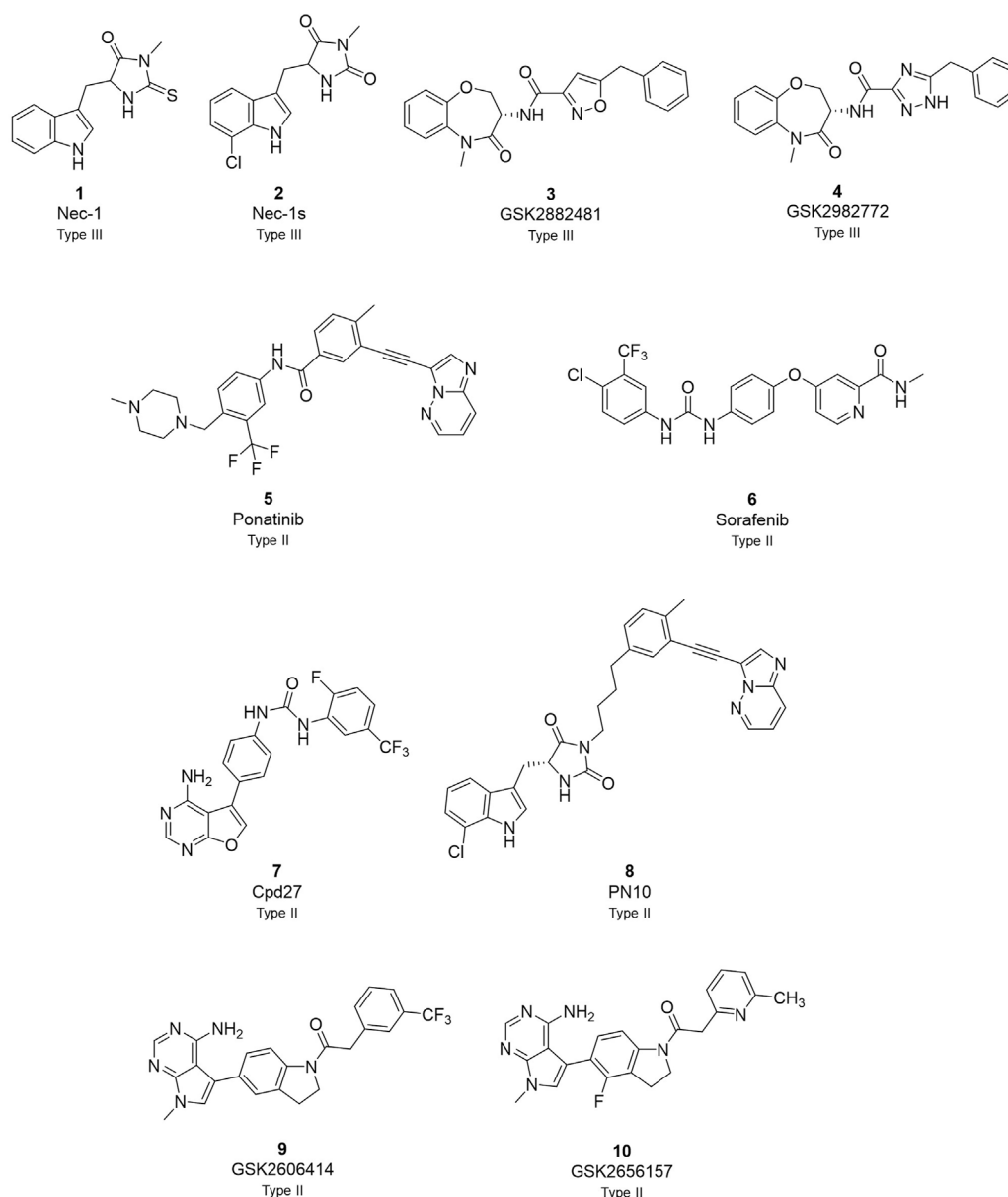


FIGURE 1
Overview of currently known RIPK1 inhibitors.

activity relationship (SAR) suggested that derivatisation of the corresponding *para*-position of the pyridinyl ring could reduce affinity for PERK (Axten et al., 2012; 2013). Moreover, recent molecular modelling studies confirmed the different nature of the C-alpha helix domain in RIPK1 with the presence of an additional lipophilic pocket compared to PERK (Chintha et al., 2019). We investigated the structural differences between PERK and RIPK1 and we verified the presence of an extra pocket with additional space to place the *para*-substituent. We hypothesised that this *para*-substituent would reduce the affinity for PERK and at the same time, keep or enhance the affinity for RIPK1. Based on these assumptions, we herein report the design, synthesis and biological evaluation of novel GSK157 analogues with increased selectivity for RIPK1 over PERK (Figure 2).

2 Materials and methods

2.1 Chemicals and instruments

Unless otherwise stated, laboratory reagent grade solvents were used. Reagents were obtained from various commercial sources and were used without any prior purification. Characterisation of all compounds was done with ^1H and ^{13}C NMR and mass spectrometry. NMR spectra were recorded with a 400 MHz Bruker Avance III Nanobay spectrometer with Ultrashield. All obtained spectra were analysed using MestReNova analytical chemistry software. Chemical shifts are displayed in ppm and coupling constants are shown in hertz (Hz). ES mass spectra were obtained from an Esquire 3000plus Ion Trap Mass Spectrometer from Bruker Daltonics. The

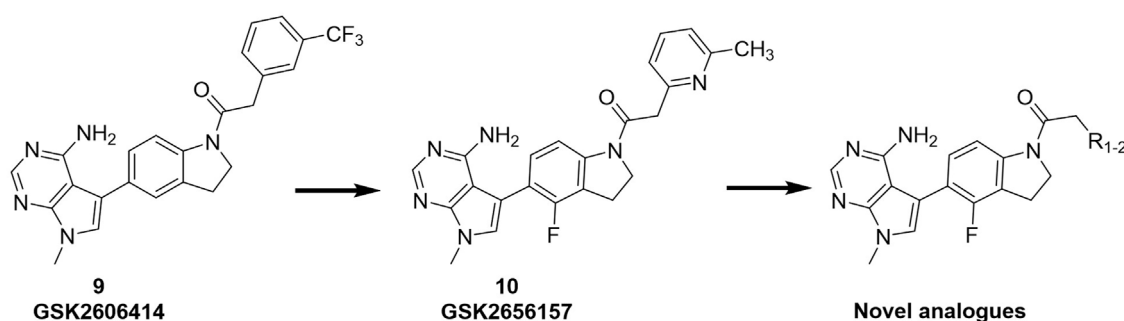


FIGURE 2

Overview of the novel GSK157 analogues featuring a substituent on corresponding para-position or the pyridinyl or aryl moiety.

UPLC (ultra performance liquid chromatography), used to quantify the purity of the products, was an ACQUITY UPLC H-Class system with a TUV detector Waters coupled to an MS detector Waters Qda. Waters Acquity UPLC BEH C18 1.7 μm , 2.1 mm \times 50 mm column was used. The eluent was composed of two different solvents. Solvent C consisted of water with 0.1% formic acid, solvent D was acetonitrile. For most of the experiments, unless stated otherwise, the general method was used. The column was first equilibrated for 0.15 min with a mixture of 95% solvent C and 5% solvent D. After that, solvent D was increased linearly to 100% over 1.75 min before being held constant for 0.25 min, followed by a mixture of 95% solvent C and 5% solvent D for 0.75 min (flow rate 0.7 mL/min). All mass spectra were recorded over a m/z range of 100–1000. The wavelength for UV detection was 254 nm. Method II starts with equilibration of column for 0.15 min with a mixture of 95% solvent C and 5% solvent D. After that, solvent D was increased linearly to 100% over 2.50 min before being held constant for 0.75 min, followed by a mixture of 95% solvent C and 5% solvent D for 0.75 min (flow rate 0.7 mL/min). Key target compounds for the activity were analyzed by high resolution mass spectrometry: 10 μL of each sample (concentration = 10^{-5} M) was injected using the CapLC system (Waters, Manchester, United Kingdom) and electrosprayed using a standard electrospray source. Samples were injected with an interval of 5 min. Positive ion mode accurate mass spectra (HRMS) were acquired using a Q-TOF II instrument (Waters, Manchester, United Kingdom). The MS was calibrated prior to use with a 0.2% H_3PO_4 solution. The spectra were lock mass corrected using the known mass of the nearest H_3PO_4 cluster. During the chemical synthesis, flash purification was performed when necessary on a Biotage ISOLERA One flash system equipped with an internal variable dual-wavelength diode array detector (200–400 nm). For the normal phase, purifications SNAP cartridges (10–340 g, flow rate of 10–100 mL/min) were used and reversed-phase purifications were done making use of KP-C18 or Buchi EcoFlex C18 cartridges. Dry sample loading was done by self-packing sample cartridges using Celite[®] 545. Gradients used varied for each purification. The following section comprises the synthetic procedures and analytical data for all compounds reported in this manuscript. Several synthesis procedures that were used in the preparation of intermediates and final products are summarized

here as “General Procedures”. The purities of all final products were found to be >95%. Analyses indicated by the symbols of the elements or functions were within $\pm 0.4\%$ of the theoretical values.

2.2 Antibodies and reagents

Antibodies and reagents were purchased from the following companies: anti-PERK (Cell Signaling Technology; no. 3192), anti-RIPK1 (BD Biosciences Laboratories; no. 610459), pPERK (Cell Signaling Technology; no. #3179), pRIPK1 (Cell Signaling Technology; no. #31122 (for S166) or ThermoFischer, custom made (for S166/T169)), Tunicamycin (Tm; Sigma-Aldrich, St Louis, MO, United States; no. T7765), Tubulin (Abcam, no. ab21058), 9-Epimer-11,12-dihydro-(5Z)-7-Oxozeanol ((5Z)-7-Oxozeanol or TAK1 inhibitor (TAK1i); AnalytiCon Discovery GmbH, Potsdam, Germany; no. NP-0009245), Carbobenzyloxy-valyl-alanyl-aspartyl-[O-methyl]-fluoromethylketone or zVAD.fmk (Bachem, Bubendorf, Switzerland; no. N-1510), GSK2656157 (ApexBio, Boston, MA, United States; no. B2175.). Recombinant human TNF- α is produced and purified to at least 99% homogeneity in the laboratory of VIB in Gent.

2.3 Cell culture

Mouse embryonic fibroblasts (MEFs) were isolated from C57Bl6/J E12.5 embryos according to standard protocol and immortalized by transfection of an SV40 large T-expressing construct. Ripk3^{+/+} and Ripk3^{-/-} MEFs have been isolated from littermate embryos of Ripk3 \pm pregnant females and have been described previously (Vanlangenakker et al., 2011; Dondelinger et al., 2013). The MEFs cells were cultured in Dulbecco's modified Eagle's medium supplemented with 10% fetal calf serum, L-glutamine (200 mM), sodium pyruvate (400 mM), penicillin (100 IU/mL), and streptomycin (0.1 mg/mL) in normoxic conditions (5% CO_2). HT-29 cells were cultured in McCoy's modified medium supplemented with 10% fetal calf serum, L-glutamine (200 mM), sodium pyruvate (400 mM), penicillin (100 IU/mL), and streptomycin (0.1 mg/mL) in normoxic conditions (5% CO_2).

2.4 Cell-death analysis

The cell-death measurements were carried out using a Fluostar Omega fluorescence plate reader (BMG Labtech, Ortenberg, Germany) with temperature and atmosphere-controlled settings, as previously reported (Grootjans et al., 2016). In brief, the cells were seeded in duplicate at 10,000 cells per well in a 96-well adherent plate and incubated overnight at 37°C with 5% CO₂. The next day, the cells were pretreated for 30 min with 1/10 dilution series of the indicated compounds ranging from 1 μM to 0.01 nM in the presence of 2.5 μM Sytox Green (Invitrogen, Waltham, MA, United States; no. S7020) and 50 μM zVAD.fmk. All the compound stock solutions were prepared in DMSO at 200 μM concentration. After stimulating the cells with human TNF at 20 ng/mL the plate was transferred to the incubator. Sytox Green intensity was measured in function of time at 0, 14 and 24 h with an excitation filter of 485 nm, an emission filter of 520 nm. The cell death was calculated by subtracting the background fluorescence from the induced Sytox Green fluorescence and by dividing the obtained result by the maximal fluorescence (minus the background fluorescence) obtained by permeabilization of the cells by using Triton X-100 at a final concentration of 0.1%. Curves were plotted in GraphPad 9 for the IC₅₀ calculation.

2.5 KinaseProfiler™ assay (eurofins cerep)

RIPK1 (h) is incubated with 8 mM MOPS pH 7.0, 0.2 mM EDTA, 0.33 mg/mL myelin basic protein, 10 mM Magnesium acetate and [γ-³²P-ATP] (specific activity and concentration as required). The reaction is initiated by the addition of the Mg/ATP mix. After incubation for 120 min at room temperature, the reaction is stopped by the addition of phosphoric acid to a concentration of 0.5%. An aliquot of the stopped reaction is spotted onto a filter and washed four times for 4 min in 0.425% phosphoric acid and once in methanol prior to drying and scintillation counting.

2.6 Immunoblotting

MEFs were seeded in 6-well plates at a density of 300,000 cells/well in 2 mL. The next day, the cells were suspended in 1 mL of medium and pre-treated for 30 min with the indicated compounds at 1/5 dilutions series for PERK ranging from 5 to 0.04 μM and 1 μg/mL of Tm followed by 4 h treatment with 20 ng/mL of hTNF. For RIPK1, the cells were pre-treated at 1/10 dilutions series ranging from 10 to 0.01 nM, 50 μM zVAD.fmk and 1 μM TAK1 before stimulation with 20 ng/mL of hTNF for 2.5 h. Then, the cells were washed two times with 1 mL of ice-cold PBS before lysis in 0.2 mL of Laemmli buffer 1x (10% (w/v) SDS, 50% glycerol, 0.5% bromophenol blue, 250 mM Tris-HCl pH 6.8) and 250 mM of dithiothreitol (DTT). The cell lysate was then collected and boiled at 95 °C for 10 min and stored at -20°C. Proteins expression was later monitored by immunoblotting.

2.7 Molecular docking

Molecular docking was carried out using Glide (Chen et al., 2018). The input structures for PERK and RIPK1 were extracted

from the Protein Data Bank (PDB ID: 4M7I and 4NEU, respectively) (Saur et al., 2021). Missing loops were modelled using MODELLER v10.2 (Fiser and Sali, 2003), and the structures were prepared using the Protein Preparation Wizard in Maestro (Madhavi Sastry et al., 2013). Ligands were prepared using the LigPrep module of Maestro, assuming a physiological pH of 7.4. Docking in Glide was performed with the OPLS2005 force field using the extra precision protocol. The binding site was defined based on the inhibitors present in the respective crystal structures. Docking was initially done unconstrained, but due to unrealistic poses being generated for PERK, core constraints were added to the adenylyl mimetic to ensure kinase-inhibitor-like docking poses by constraining its distance to the hinge region. Otherwise, default settings were kept.

3 Results

3.1 Compounds design

According to the design strategy mentioned above, a series of 17 novel analogues presenting *para*-substituted pyridinyl (18–29) and aryl (30–34) groups were designed and synthesised. Different halogens together with small alkyls such as methyl and trifluoromethyl were introduced in both pyridinyl (18–22) and aryl (30–34) analogues. Specifically for the pyridinyl compounds, additional small groups were added with different polarity (23 with -O-CH₃, 26 with -OH and the 4-pyridinyl analogue 27) and these were compared with compounds 24, 28 and 29 featuring bulkier moieties (5-cyclopropyl, 5-benzyl and 5-phenyl). The molecules were then tested for their selectivity profile against PERK and RIPK1 by Western blot. Afterwards, their cell death inhibitory activity was quantified by fluorometric cell death assay and finally compound UAMC-3861 (22) was selected for further biological characterisation (Grootjans et al., 2016).

3.2 Chemistry

The novel library was synthesised following the synthetic route reported for GSK'414 and GSK'157 (Axten et al., 2012; 2013). The common intermediate 17 was synthesised from the commercially available 4-fluoroindole as depicted in Figure 3. After the reduction of the 4-fluoroindole 11 to the corresponding indoline 12, the secondary amine group was Boc-protected (13) before allylic bromination with the *N*-bromosuccinimide (14). Finally, the reaction with the bis(pinacolato) diboron led to the corresponding boronic ester intermediate that was then used in a Suzuki–Miyaura coupling reaction with 5-Bromo-7-methyl-7*H*-pyrrolo [2,3-*d*]pyrimidin-4-amine (38) synthesised as reported in Figure 4. Briefly, the conditions for the methylation of the 4-chloro-7*H*-pyrrolo [2,3-*d*]pyrimidine (35) NH and the following bromination were modified compared to the route of Axten M. J. et al. As reported in the experimental section (Axten et al., 2013). After the Suzuki–Miyaura coupling, the intermediate 16 was deprotected under acidic conditions and the free indoline

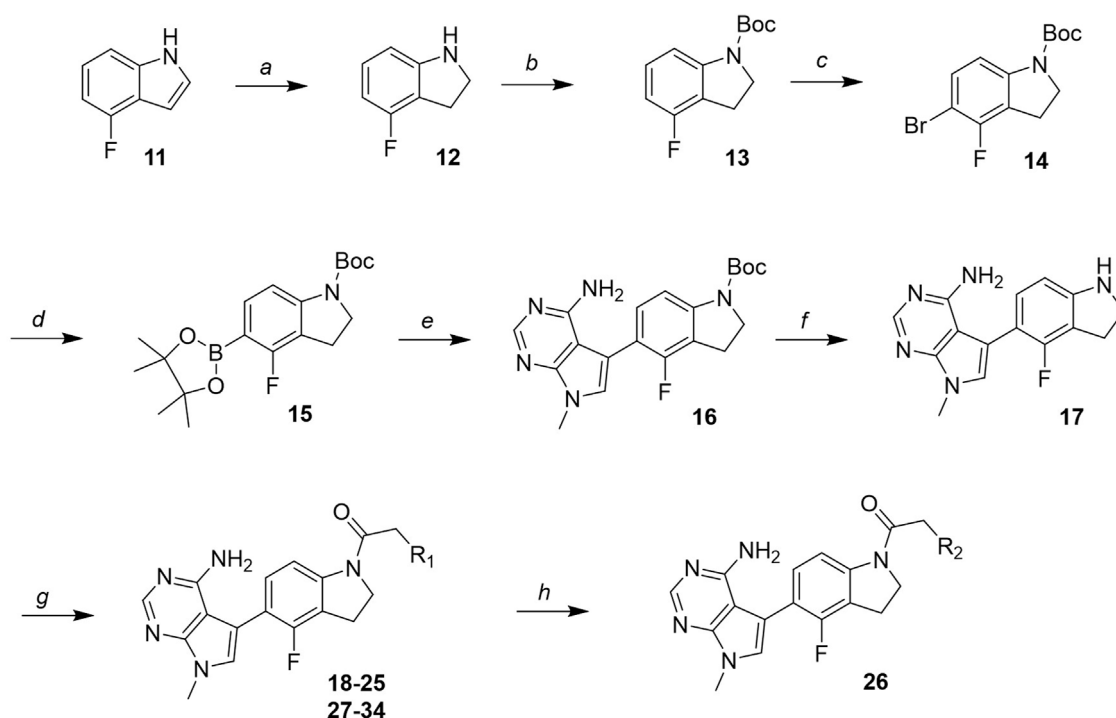


FIGURE 3

Synthesis of the common intermediate **17** based on GSK'157 synthetic route followed by amide coupling to obtain novel RIPK1 inhibitors **18–34**. Reagents and conditions: (a) 4-fluoro-1H-indole, NaBH₃CN, AcOH, 0°C, 10 min, rt, 1 h; (b) Boc₂O, DMAP, DCM, rt, 48 h; (c) NBS, DCM, rt, 1 h; (d) bis(pinacolato) diboron, KOAc, 1,4-dioxane, water, 80°C for 16 h (e) (t-Bu)₃PHBF₄, Pd₂(dba)₃, 90°C, 2 h; (f) HCl in 1,4-dioxane 4N, 1,4-dioxane, rt, 16 h; (g) HATU, corresponding carboxylic acid, DIPEA, DMF, rt, 16 h; (h) **23**, BBr₃, DCM, 0°C, 48 h.

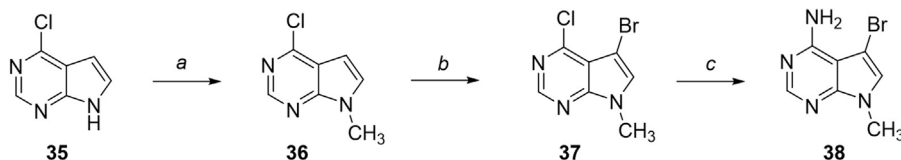


FIGURE 4

Synthesis of the coupling reagent 5-bromo-7-methyl-7H-pyrrolo [2,3-*d*]pyrimidin-4-amine. Reagents and conditions: (a) 4-chloro-7H-pyrrolo [2,3-*d*]pyrimidine, Cs₂CO₃, CH₃I, DMF, 1 h, rt; (b) NBS, DCM, 0°C, 1 h, rt, 3 h; (c) NH₃ aq 30%, 120°C, 48 h.

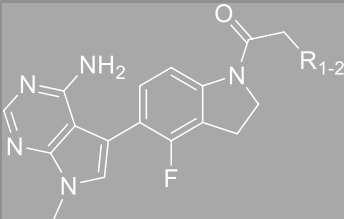
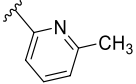
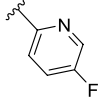
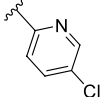
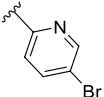
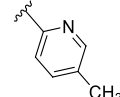
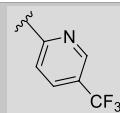
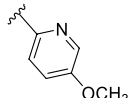
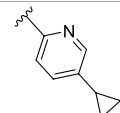
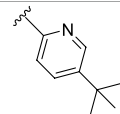
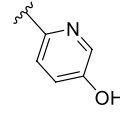
was coupled with different aryl acetic acids to obtain the desired final compounds (**18–25** and **27–34**). The corresponding acetic acids were either commercially available or synthesised as reported in the experimental section. To obtain the hydroxy **26**, the methoxy group of compound **23** was demethylated in presence of borontribromide (BBr₃). The corresponding R₁₋₂ groups are reported in Table 1.

3.3 Biological characterisation

The compounds were first tested for their abilities to inhibit PERK and RIPK1 enzymatic activities in mouse embryonic fibroblasts (MEFs). To do so, we monitored, by immunoblot, the effects of the compounds on the autophosphorylation of PERK and RIPK1.

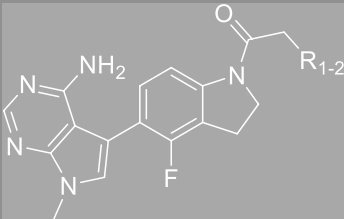
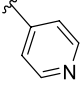
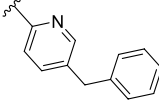
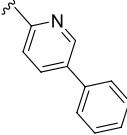
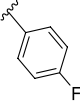
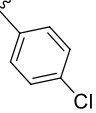
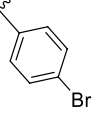
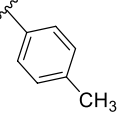
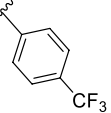
Activation of PERK was induced by stimulation of the cells with Tunicamycin, as previously reported (Bull and Thiede, 2012). More precisely, the immortalised MEFs were pre-incubated for 30 min with the analogues **18–34** at different concentrations (0.04, 0.2, 1, and 5 μM) prior to 4 h stimulation with Tunicamycin (1 μg/mL). As shown in Figures 5A–J, 12 out of the 17 compounds did not inhibit PERK at the tested concentrations while GSK'157 inhibited the autophosphorylation of PERK in a concentration range of 200–1000 nM. Their activities were evaluated by comparing the intensity of the signal to unstimulated MEFs (considered as zero phosphorylation) and Tunicamycin stimulated cells (considered as 100% PERK phosphorylation). The 12 compounds (**18–20**, **22–29** and **34**) that had lost their inhibitory capacity on PERK were then tested for their ability to inhibit RIPK1 as shown in Figures 6A–H. Activation and autophosphorylation of RIPK1 was induced by stimulating the cells with TNF in the

TABLE 1 Structures of the novel synthesised analogues and their corresponding IC₅₀.

					
Name	R ₁₋₂	cLogP ^a	PERK inhibition (nM) ^b	RIPK1 inhibition (nM) ^c	IC ₅₀ necroptosis (nM) ^d
10		2.57	200–1000	0.1–1	0.42
GSK'157					
18		2.58	> 5000	≥ 10	13.5
UAMC-4006					
19		3.04	> 5000	1–10	2.5
UAMC-4005					
20		3.21	> 5000	1–10	3.2
UAMC-4004					
21		2.95	1000–5000	≥ 10	37.6
UAMC-3715					
22		3.32	> 5000	1–10	2.9
UAMC-3861					
23		2.28	≥ 5000	≥ 10	39
UAMC-4111					
24		3.22	> 5000	≥ 10	33.5
UAMC-4235					
25		3.98	> 5000	≥ 10	40
UAMC-3863					
26		2.14	≥ 5000	≥ 10	2526
UAMC-4112					

(Continued on following page)

TABLE 1 (Continued) Structures of the novel synthesised analogues and their corresponding IC₅₀.

					
Name	R ₁₋₂	cLogP ^a	PERK inhibition (nM) ^b	RIPK1 inhibition (nM) ^c	IC ₅₀ necroptosis (nM) ^d
27		2.05	> 5000	≥ 10	3025
UAMC-4217					
28		4.53	≥ 5000	≥ 10	62
UAMC-3862					
29		4.09	> 5000	≥ 10	n.a.
UAMC-4233					
30		3.41	1000–5000	0.1–1	0.01
UAMC-4114					
31		3.88	1000–5000	0.1–1	0.4
UAMC-4116					
32		4.04	1000–5000	1–10	0.3
UAMC-4113					
33		3.78	1000–5000	≥ 10	n.a.
UAMC-4115					
34		4.15	≥ 5000	1–10	1.1
UAMC-4003					

n.a. = not active, IC₅₀ >10 μM.^aLogP calculated with Collaborative Drug Discovery Inc. CDD Vault® software.^bIC₅₀ estimated from a Western blot expressed in nM. Immortalized MEFs were pretreated for 30 min with increasing concentrations of GSK157 and the indicated compounds and stimulated with tunicamycin (Tm) (1 μg/ml) for 4 h.^cIC₅₀ estimated from a Western blot expressed in nM. Immortalized MEFs were pretreated for 30 min with zVAD.fmk (50 μM), TAK1i (1 μM) and the indicated compounds and then stimulated for 2.5 h with hTNF (20 ng/ml).^dIC₅₀ values are calculated from measurements at least in duplicate. RIPK1 kinase-dependent necroptosis was induced in immortalized MEFs by 30 min pretreatment with pan-caspases inhibitor zVAD-fmk (50 μM) and increasing concentrations of the indicated compounds then stimulated by hTNF (20 ng/ml). The TNF-mediated necroptosis was measured at 24 h post-stimulation by Sytox Green positivity. Analogues 30–33 retain activity for PERK at the higher concentration 1000–5000 nM.

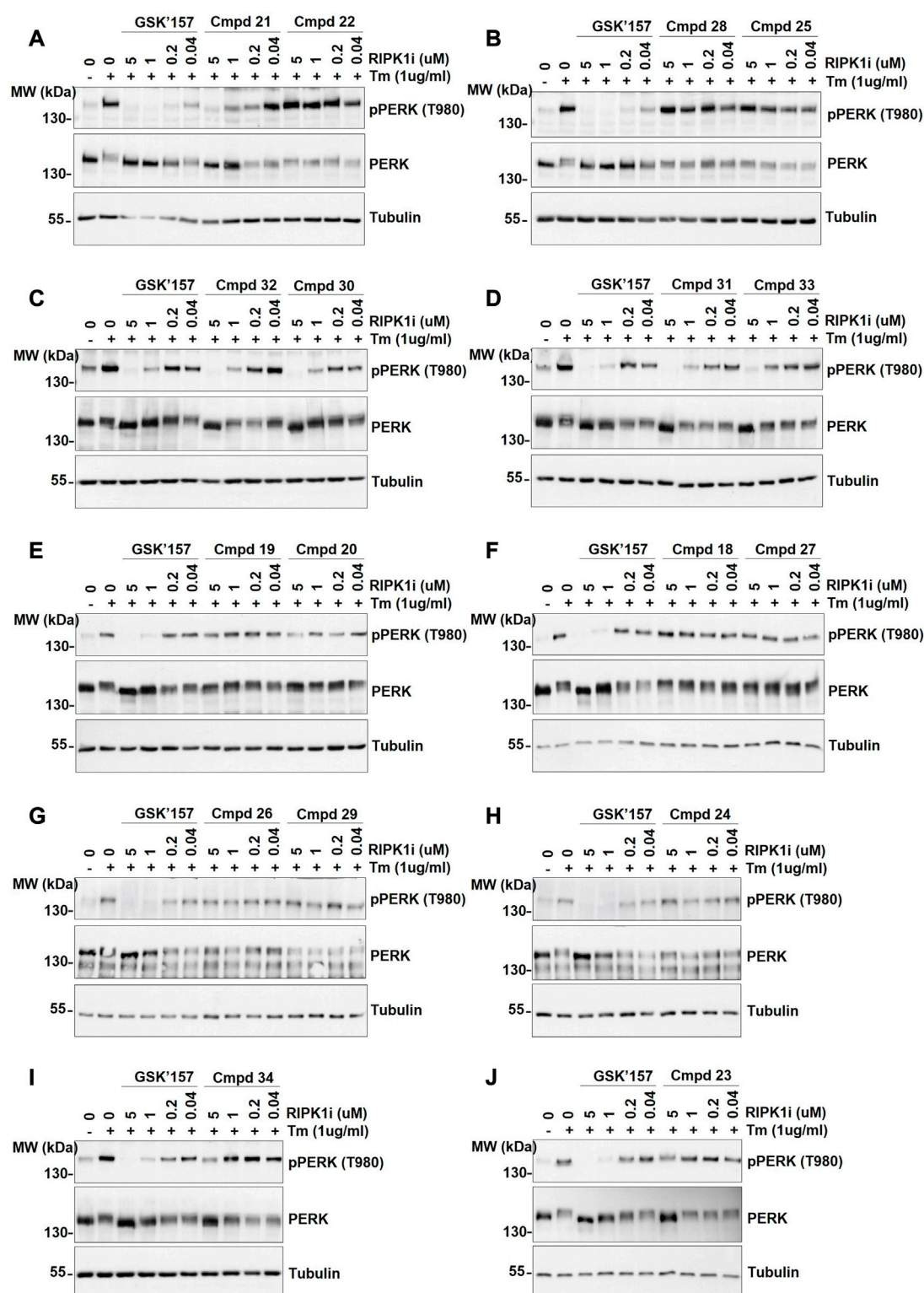


FIGURE 5

The effect of GSK'157 in comparison with compounds (cmpd) 18–34 on PERK autophosphorylation is reported in figures (A–J). Immortalized MEFs were pretreated for 30 min with increasing concentrations of GSK'157 and the indicated compounds and stimulated with tunicamycin (Tm) (1 μ g/ml) for 4 h. The cell lysates were then immunoblotted as indicated.

presence of TAK1 inhibitor and of the pan-caspases inhibitor zVAD.fmk, a well established necroptotic trigger (Vanlangenakker et al., 2011). The MEFs were pre-incubated for 30 min with the

different compounds (0.01 nM–1000 nM) and then stimulated with human TNF (20 ng/ml) for 2.5 h. Similar to the PERK assessment, IC₅₀ values for RIPK1 inhibition were estimated as a range of concentrations,

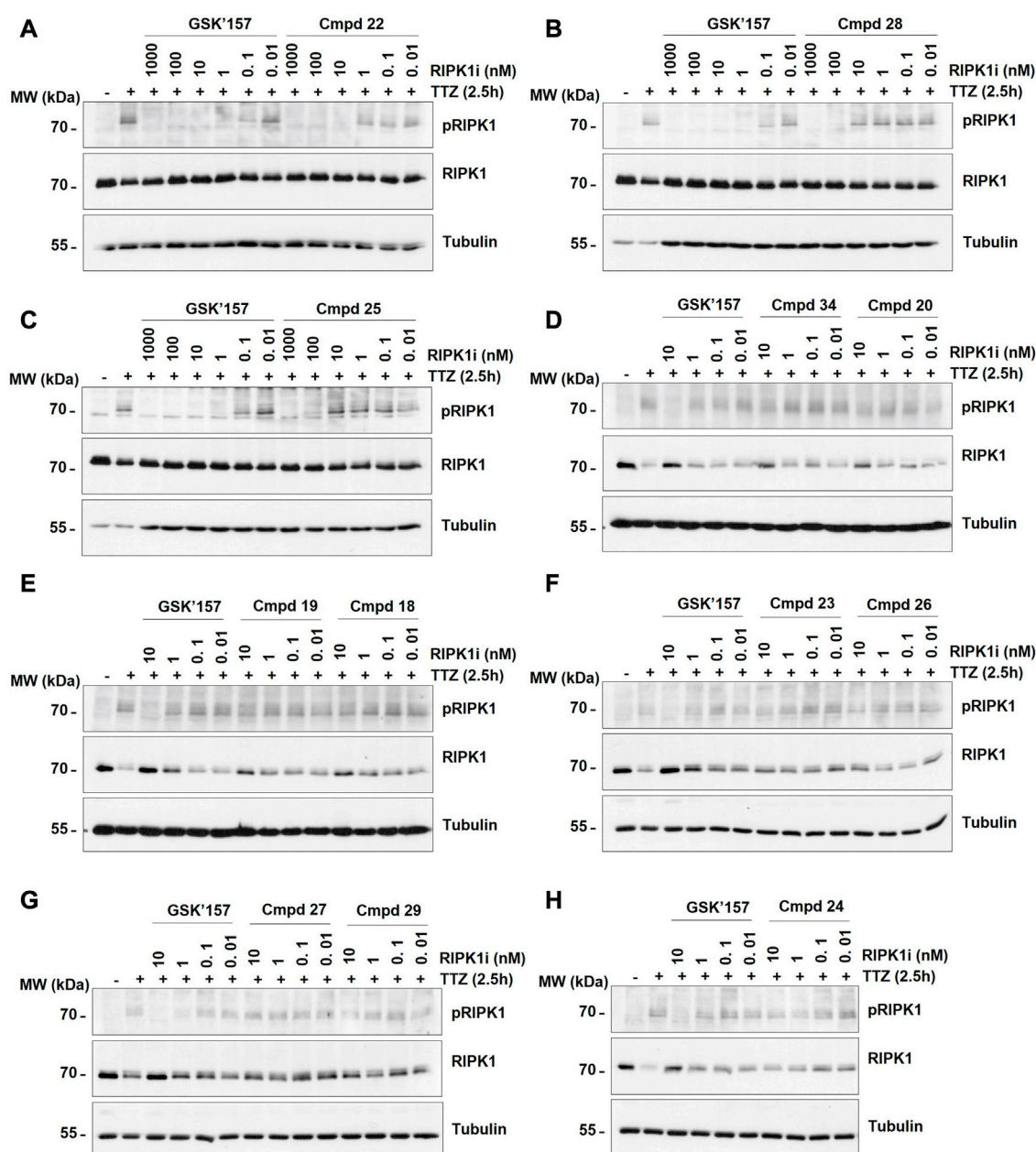


FIGURE 6

The effect of GSK'157 in comparison with compounds (cmpd) 18–20, 22–29 and 34 (not-active on PERK) on RIPK1 autophosphorylation (pS166) is reported in figures (A–H). Immortalized MEFs were pretreated for 30 min with zVAD.fmk (50 μ M), TAK1i (1 μ M) and the indicated compounds and then stimulated for 2.5 h with h TNF (20 ng/mL). TTX = hTNF + TAK1i + zVAD.fmk. The cell lysates were then immunoblotted as indicated.

and are reported in Table 1. These experiments provide an estimation of the specificity of our analogues against PERK and RIPK1 in comparison to the benchmark GSK'157 already reported as a potent PERK and RIPK1 inhibitor.

Consequently, the compounds were evaluated for their potential protection of RIPK1-mediated necroptosis following human TNF stimulation. The corresponding IC_{50} are reported in Table 1. The library was screened in MEFs cells due to their sensibility to TNF-induced necroptosis as described in the literature (Vanlangenakker et al., 2011). The IC_{50} values were calculated based on the cell response measured over 24 h by Sytox Green positivity.

4 Discussion

The series of novel compounds were screened for their activity to selectively inhibit RIPK1 kinase-dependent necroptosis (Table 1) and their inhibitory effect on PERK and RIPK1 autophosphorylation (Figure 5A–J and 6A–H). The novel analogues were compared with the benchmark GSK'157 which was confirmed as one of the most potent RIPK1 inhibitors currently available (IC_{50} = 0.42 nM). The compounds with a *para*-substituted-pyridinyl moiety (18–29) showed negligible PERK inhibition in contrast to GSK'157. Similar results were observed for the *para*-phenyl series (30–34), but to a lesser extent. The

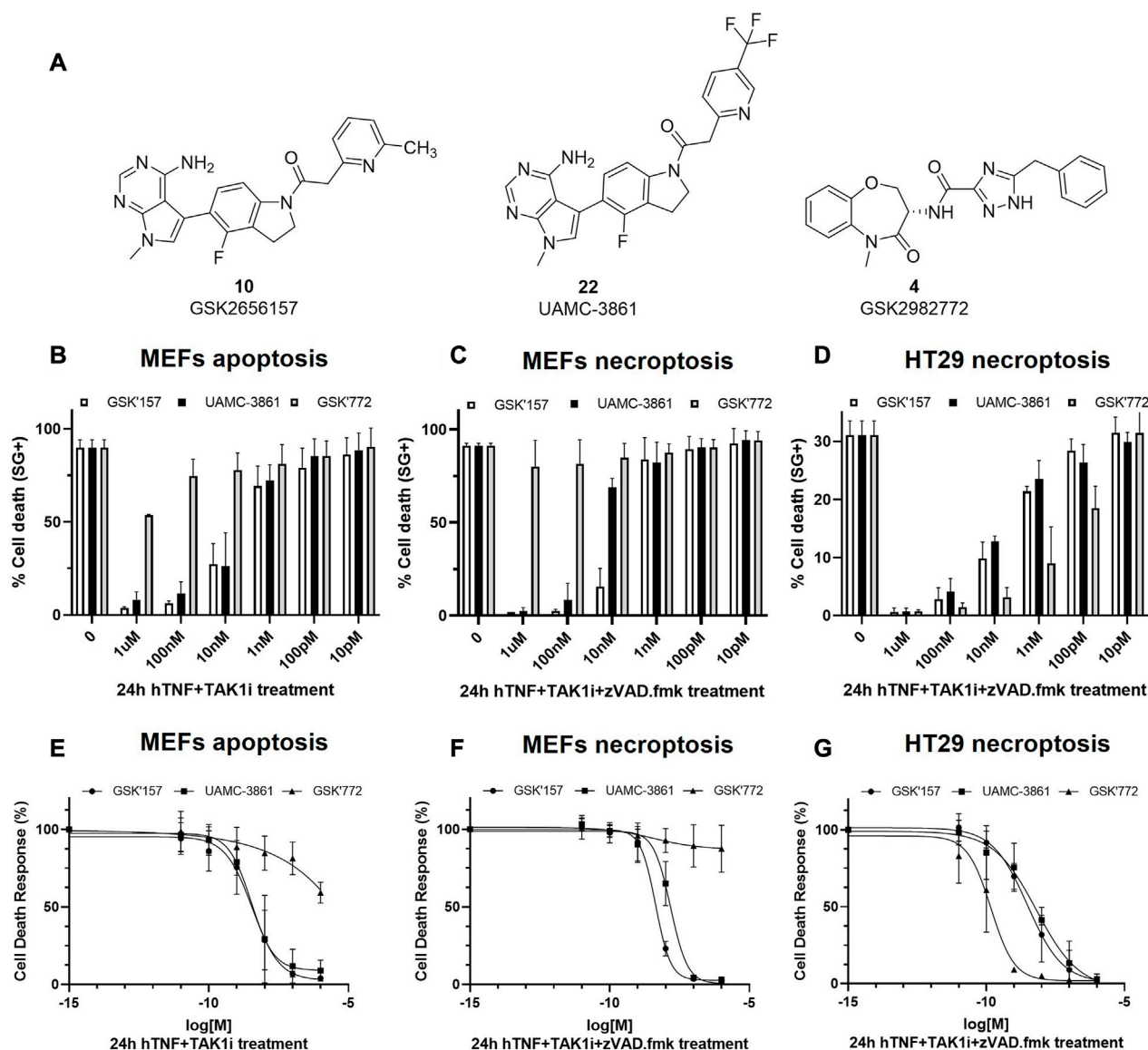


FIGURE 7

RIPK1-dependent cell death inhibition in mouse and human cells for GSK'157, UAMC-3861 and GSK'772. (A) Chemical structures of the compounds that were tested *in vitro* for RIPK1-dependent apoptosis and necroptosis. (B,C) MEFs and (D) HT-29 were pre-treated for 30 min with increasing concentrations of the indicated compounds. RIPK1 kinase-dependent apoptosis was induced by TAK1i + hTNF (100 pg/mL) and RIPK1 kinase-dependent necroptosis by zVAD.fmk + TAK1i + hTNF (100 pg/mL) and hTNF + zVAD.fmk (20 ng/mL). Cell death was measured over time by Sytox Green positivity (SG+) and the results are presented as mean \pm SEM of three independent experiments. (E–G) MEFs and HT-29 were pre-treated for 30 min with increasing concentrations of the indicated compounds. In presence or absence of TAK1i (1 μ M) and/or zVAD.

results confirmed the detrimental role of the *para*-substituent for PERK potency. In contrast, these compounds retained or even improved RIPK1 inhibition compared to GSK'157.

The IC_{50} value for necroptosis inhibition of the analogues substituted with halogen (F, Cl and Br) resulted in potent compounds. Compound **18** with the fluorine (IC_{50} = 13.5 nM) was less potent than the corresponding analogues **19** (IC_{50} = 2.5 nM) and **20** (IC_{50} = 3.2 nM), featuring a chlorine and bromide, respectively. The methyl analogue **21** was less potent (IC_{50} = 37 nM), whereas the corresponding trifluoromethyl (**22**, IC_{50} = 2.9 nM) is similar in potency to chlorine (**19**) and bromine

(**20**). The introduction of methoxy (**26**), cyclopropyl (**24**) and *tert*-butyl (**25**) resulted in compounds that were equipotent to the methyl analogue **21**. Polar substitutions such as the *para*-hydroxy (**26**) and a shift of the ring nitrogen of the pyridine ring (**27**) were detrimental for necroptosis inhibition (IC_{50} > 2 μ M). This result confirms the high-hydrophobic nature of the RIPK1-allosteric pocket. Similarly, the insertion of bulky substituents such as benzyl and phenyl (**28** and **29**) negatively affects the activity of the analogues.

Furthermore, when a halogen was introduced on the corresponding *para* position of phenyl series, the activity increased notably with IC_{50} values <0.5 nM. Compound **30** with

TABLE 2 Overview of the IC₅₀ values of compounds GSK'157, UAMC-3861 and GSK'772 in mouse and human cells.

	Apoptosis hTNF + TAK1i	Necroptosis hTNF + zVAD.fmk	Necroptosis hTNF + TAK1i + zVAD.fmk	Necroptosis hTNF + TAK1i + zVAD.fmk	hRIPK1 inhibition
	MEFs	MEFs	MEFs	HT-29	-
Name	IC ₅₀ (nM) ^a	IC ₅₀ (nM) ^a	IC ₅₀ (nM) ^a	IC ₅₀ (nM) ^a	IC ₅₀ (nM) ^{a,c}
GSK'157	3.7	0.7	4.4	3.1	53
UAMC-3861	3.3	1.06	15	6.5	139
GSK'772	n.a ^b	n.a ^b	n.a ^b	0.2	36

^aIC₅₀ values are calculated from measurements at least in duplicate.

^bn. a. = not active, IC₅₀ > 100 nM.

^cThe IC₅₀ values are determined based on 9 concentrations (0.0001 μM–1.0 μM) in presence of 10 μM ATP (Supporting Information).

fluorine is the most potent compound of the entire series (IC₅₀ = 0.01 nM), with 40-fold higher potency than GSK'157. To the best of our knowledge, this is the most potent necroptosis inhibitor ever reported (Martens et al., 2020; Chen et al., 2022; Shi et al., 2022). However, compared to the corresponding pyridinyl analogues (18–20), the phenyl analogues 30–32 retained some PERK inhibition, albeit at concentration higher than 1 μM which still results in excellent selectivity. Surprisingly, the introduction of a *para*-methyl substituent on the phenyl ring (33) resulted in a complete loss of necroptosis inhibition. The corresponding trifluoromethyl analogue (34, IC₅₀ = 1.1 nM) was again a potent necroptosis inhibitor. This striking difference in potency between the methyl and trifluoromethyl analogue was also seen in the pyridinyl series (21 and 22), although less prominent.

Compound 22 (UAMC-3861) was preferably selected for further characterisation. We chose an analogue that showed no PERK inhibition at the highest concentration tested (5 μM) combined with a single-digit nanomolar necroptosis inhibition. Compounds 19 and 20 also meet these criteria. However, different studies suggested that the trifluoromethyl moiety improves the interaction with the hydrophobic allosteric pocket of RIPK1 (Liu and Gray, 2006; Harris et al., 2013).

The selected compound 22 together with GSK'157 and the clinically most advanced RIPK1 inhibitor GSK'772, were tested for necroptosis and apoptosis inhibition in murine MEFs and human HT-29 cells (Figures 7A–G; Table 2). Moreover, the three compounds were tested for inhibition of hRIPK1 (Table 2).

It was previously reported that the binding of hTNF to TNFR1 can induce RIPK1 kinase-dependent apoptosis and necroptosis (Jin and El-Deiry, 2006; Vanlangenakker et al., 2011). In MEFs, TNF together with the pan caspases inhibitor zVAD.fmk induces RIPK1-dependent necroptosis while TNF together with TAK1 inhibitor induces RIPK1 kinase-dependent apoptosis. We also included the conditions selected for the Western blot experiments, where necroptosis was induced by the combination of hTNF, zVAD.fmk and TAK1 inhibitor.

In RIPK1 kinase-dependent necroptosis induced with hTNF + zVAD.fmk in mouse cells (MEFs) GSK'157 and UAMC-3861 showed similar potency. As expected, when necroptosis was induced with the stronger condition in MEFs cells (hTNF + TAK1 + zVAD.fmk), the IC₅₀ values decreased from 6-fold

(GSK'157) to 14-fold (UAMC-3861). As previously reported by Harris P. A. et al., GSK'772 is confirmed to be a species-specific inhibitor with no activity in mouse RIPK1-dependent necroptosis (Harris et al., 2017). To induce necroptosis in human colorectal adenocarcinoma cell line (HT-29) together with hTNF and the pan caspases inhibitor zVAD.fmk, TAK1 inhibitor is also needed. The high potency of the human necroptosis inhibitor GSK'772 (IC₅₀ = 0.2 nM) is confirmed while GSK'157 (IC₅₀ = 3.1 nM) and UAMC-3861 (IC₅₀ = 6.5 nM) are less potent, but still in the same single-digit nanomolar range as observed in mouse cells. Only necroptosis conditions were tested in HT-29 since the cell line is not sensitive to RIPK1-dependent apoptosis as reported in the literature (Kong et al., 2018).

A similar trend in inhibitory potency for GSK'772, GSK'157 and UAMC-3861 was also confirmed in the enzymatic assay against human RIPK1 (Table 2).

4.1 Docking study

UAMC-3861 was further studied for its mode of interaction with both RIPK1 and PERK in a computational study using molecular docking (Figures 8A–F). This was done in comparison with the binding mode of GSK'157. In RIPK1, UAMC-3861 is able to form an extra methionine interaction with the trifluoromethyl-pyridinyl substituent. Moreover, the amide group of UAMC-3861 interacted with the backbone amine of Asp156 while the gatekeeper Met92 and Met67 formed methionine-aromatic interactions with the 4-fluoroindoline ring, and the trifluoromethyl-pyridinyl substituent, respectively. In addition, the docking study also confirms the high hydrophobicity of the RIPK1 allosteric pocket, since the CF₃ moiety is surrounded by Met66, Met67 (C-helix), Leu70, Val75 (loop following C-helix), Leu129, Val134 (catalytic loop), and Leu159 (after DLG) as seen in Figure 8A. In PERK (Figure 8B), a stabilisation of the pyridinyl substituent was detected through the interaction between the pyridinyl ring and the backbone amine of Phe162. In addition, a methionine-aromatic interaction between the gatekeeper Met887 and the pyridinyl substituent was observed. When we compared the different poses of the substituent, in RIPK1 the pyridinyl is situated between the C-helix, the DLG-motif, and the

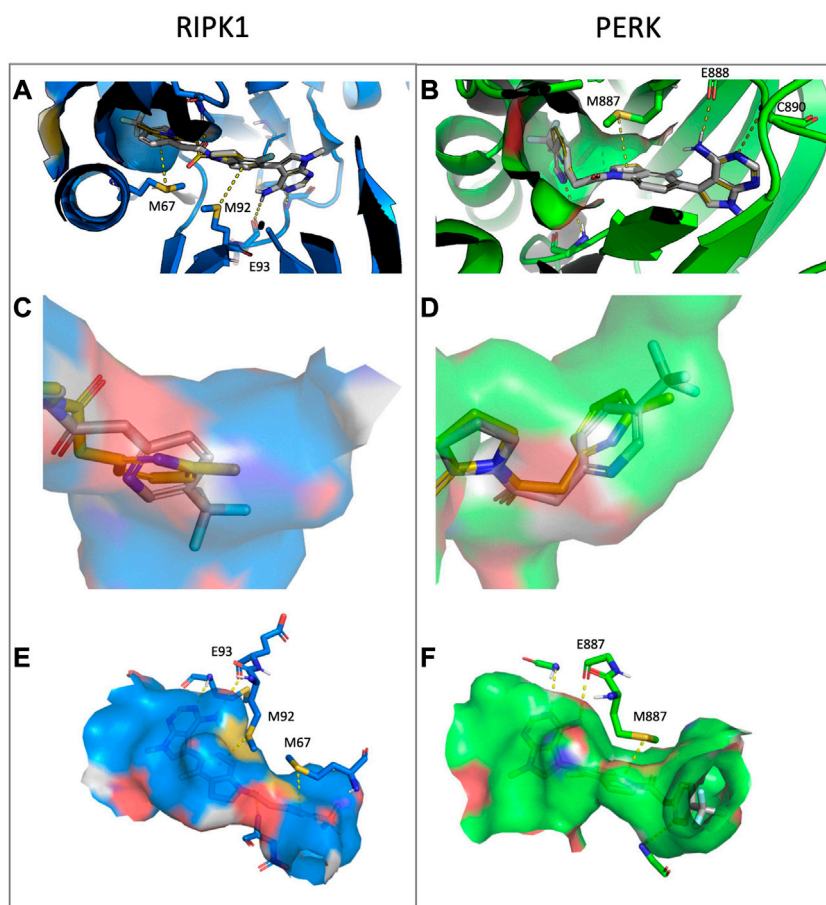


FIGURE 8

Docking of compound UAMC-3861 (grey sticks) and GSK'157 (yellow lines) in RIPK1 (blue) and PERK (green) (A–B), representation of the allosteric pockets of RIPK1 and PERK with GSK'157 and UAMC-3861 (C–D) and surface representation of the binding pocket for RIPK1 (blue) and PERK (green) and the different interactions with UAMC-3861 (E–F). (A) In RIPK1, UAMC-3861 is able to interact with the gatekeeper Met92 and tend to form a methionine-aromatic interaction with 4-fluorindoline ring. (B) In PERK, the trifluoromethyl-pyridinyl substituent is surrounded by a less hydrophobic environment. The pyridinyl substituent forms a methionine-aromatic interaction with the gatekeeper Met887. (C) Zoom on the allosteric pocket of RIPK1 where the positions of the pyridinyl moieties of GSK'157 and UAMC-3861 are compared. (D) Zoom on the allosteric pocket of PERK where the different orientations of the pyridinyl rings are compared. (E,F) The trifluoromethyl-pyridinyl moiety occupied a different pocket in RIPK1 (E) and PERK (F). While for the latter the binding site is slightly solvent-exposed, for RIPK1 the pocket is buried, featuring a more hydrophobic profile due to the presence of three Leu, two Val, and Met (not shown in detail).

activation loop; for PERK it is between the C-helix and the beta-sheet domain. The different interactions for GSK'157 methyl-pyridinyl and the corresponding trifluoromethyl-pyridinyl of UAMC-3861 are depicted in Figure 8C (RIPK1) and 8D (PERK). In Figures 8E,F, the different nature of the two allosteric pockets is illustrated. The allosteric pocket of PERK (green) is partly solvent-exposed, differently from the more hydrophobic one of RIPK1 (blue), which is buried inside the protein. Superposition of the docking poses in RIPK1 onto PERK and *vice versa* shows that neither docking pose is compatible with the other protein. In particular, the UAMC-3861 docking pose is incompatible with PERK due to steric clashes with the DFG-motif which impede the pyridinyl substituent from binding to the analogous RIPK1 allosteric binding pocket. Instead, the substituent is forced into a different, more solvent-exposed pocket, which is more unfavourable for binding of hydrophobic moieties. Concludingly, this docking study confirmed that the *para*-substituted pyridine ring is favourable for binding to RIPK1 whereas it is detrimental for binding to PERK.

5 Conclusion

The role of TNF-mediated inflammation and cell death in different pathologies is widely recognised. Particularly, the TNF inflammatory cascade can induce inflammation and the release of cytokines through the activation of RIPK1-dependent apoptosis or necroptosis. The previously reported work in which GSK'157, a well-known PERK inhibitor, was revealed as a potent RIPK1 inhibitor opened the door to further optimisation of the chemical structure to enhance RIPK1 selectivity over PERK (Rojas-Rivera et al., 2017). Moreover, a kinome scan reported by Axten J.M. et al. For GSK'157 suggested a good selectivity profile of the compound, even though RIPK1 was not included in the panel. In this study we confirmed the hypothesis that the potency and selectivity for RIPK1 could be increased by derivatising the corresponding *para*-position of the GSK'157 pyridinyl ring (Axten et al., 2013; Chintla et al., 2019). In addition, based on the mode of interaction of

GSK'157 this should result in a typical type II kinases inhibitor, a less explored class of RIPK1 inhibitors. We compared the potency of a *para*-substituted pyridinyl series (**18–29**) with the corresponding phenyl series (**30–34**). This demonstrates the importance of the pyridine ring to increase the selectivity for RIPK1 over PERK. Moreover, a smaller size of the *para*-substituent positively affected the potency for RIPK1. The hydrophobic nature of the RIPK1 allosteric pocket accommodating the *para*-substituted pyridine ring was confirmed, particularly considering the dramatic decrease of potency for the analogues having polar *para* substituents. To the best of our knowledge, the *para*-fluoro phenyl analogue (**30**) is the most potent necroptosis inhibitor described with an $IC_{50} = 0.01$ nM. However, since this compound retained some PERK inhibition at higher concentrations, we selected UAMC-3861 (**22**) for further evaluation in both murine and human cell lines. UAMC-3861 was confirmed as a highly potent compound with single digit nanomolar IC_{50} values for the inhibition of RIPK1-dependent necroptosis in both mouse and human cells as well as for the inhibition of RIPK1 dependent apoptosis in mouse cells. Compared with the clinical RIPK1 inhibitor GSK'772, UAMC-3861 is slightly less potent in human cells, but it has the advantage of potency in mouse cells in which GSK'772 is inactive. This suggests that UAMC-3861 will be an excellent tool compound to study RIPK1-dependent cell death in mouse models with the potential to translate to human cell lines.

Data availability statement

The original contributions presented in the study are included in the article/**Supplementary Materials**, further inquiries can be directed to the corresponding author.

Author contributions

CS wrote the manuscript, synthesised the compounds and performed the biological characterisation. SV synthesised the compounds. KG performed the molecular docking. MV contribute to the biological characterisation. CL, GK, PV, and HW revised the manuscript. MB and KA conceived the topic, supervised the work and critically revised the manuscript.

References

- Axten, J. M., Medina, J. R., Feng, Y., Shu, A., Romeril, S. P., Grant, S. W., et al. (2012). Discovery of 7-methyl-5-(1-((3-(trifluoromethyl)phenyl)acetyl)-2,3-dihydro-1H-indol-5-yl)-7H-pyrrolo[2,3-d]pyrimidin-4-amine (GSK2606414), a potent and selective first-in-class inhibitor of protein kinase R (PKR)-like endoplasmic reticulum kinase (PERK). *J. Med. Chem.* 55, 7193–7207. doi:10.1021/jm300713s
- Axten, J. M., Romeril, S. P., Shu, A., Ralph, J., Medina, J. R., Feng, Y., et al. (2013). Discovery of GSK2656157: An optimized PERK inhibitor selected for preclinical development. *ACS Med. Chem. Lett.* 4, 964–968. doi:10.1021/ml400228e
- Berger, S., Harris, P., Nagilla, R., Kasparcova, V., Hoffman, S., Swift, B., et al. (2015). Characterization of GSK'963: A structurally distinct, potent and selective inhibitor of RIP1 kinase. *Cell Death Discov.* 1, 15009. doi:10.1038/cddiscovery.2015.9
- Bull, V. H., and Thiede, B. (2012). Proteome analysis of tunicamycin-induced ER stress. *Electrophoresis* 33, 1814–1823. doi:10.1002/elps.201100565
- Chen, K. W., Demarco, B., Ramos, S., Heilig, R., Goris, M., Graczyk, J. P., et al. (2021). RIPK1 activates distinct gasdermins in macrophages and neutrophils upon pathogen blockade of innate immune signaling. *Proc. Natl. Acad. Sci. U. S. A.* 118, e2101189118–e2101189119. doi:10.1073/pnas.2101189118
- Chen, L., Zhang, X., Ou, Y., Liu, M., Yu, D., Song, Z., et al. (2022). Advances in RIPK1 kinase inhibitors. *Front. Pharmacol.* 13, 1123234. doi:10.3389/fphar.2022.976435
- Chen, Y., Ke, G., Ma, Y., Zhu, Z., Liu, M., Liu, Y., et al. (2018). A synthetic light-driven substrate channeling system for precise regulation of enzyme cascade activity based on DNA origami. *J. Am. Chem. Soc.* 140, 8990–8996. doi:10.1021/jacs.8b05429

Funding

This work was supported by the European Union's Horizon 2020 research and innovation programme under the Marie Skłodowska-Curie grant agreement No. 765608. This research was also funded by the University of Antwerp, BOF DOCPRO grant no.44874 and FWO-EOS Research project no. 36579. Research in the group of MB is financially supported by the Vlaams Instituut voor Biotechnologie (VIB), by Ghent University (iBOF ATLANTIS), by grants from the Fonds voor Wetenschappelijk Onderzoek Vlaanderen (FWO) (G035320N, G044518N, EOS G0G6618N, EOS G0I5722N) and from the Flemish Government (Methusalem BOF09/01M00709 and BOF16/MET_V/007 - attributed to P. Vandenabeele).

Acknowledgments

We would like to thank Frontiers in Chemistry for allowing us to share our research in Frontiers in Chemistry: Rising Stars 2022.

Conflict of interest

The authors declare that the research was conducted in the absence of any commercial or financial relationships that could be construed as a potential conflict of interest.

Publisher's note

All claims expressed in this article are solely those of the authors and do not necessarily represent those of their affiliated organizations, or those of the publisher, the editors and the reviewers. Any product that may be evaluated in this article, or claim that may be made by its manufacturer, is not guaranteed or endorsed by the publisher.

Supplementary material

The Supplementary Material for this article can be found online at: <https://www.frontiersin.org/articles/10.3389/fchem.2023.1160164/full#supplementary-material>

- Chintha, C., Carlesso, A., Gorman, A. M., Samali, A., and Eriksson, L. A. (2019). Molecular modeling provides a structural basis for PERK inhibitor selectivity towards RIPK1. *RSC Adv.* 10, 367–375. doi:10.1039/c9ra08047c
- Clark, M. A., Acharya, R. A., Arico-muendel, C. C., Belyanskaya, S. L., Benjamin, D. R., Carlson, N. R., et al. (2009). Design, synthesis and selection of DNA-encoded small-molecule libraries. *Nat. Chem. Biol.* 5, 647–654. doi:10.1038/nchembio.211
- Degterev, A., Huang, Z., Boyce, M., Li, Y., Jagtap, P., Mizushima, N., et al. (2005). Chemical inhibitor of nonapoptotic cell death with therapeutic potential for ischemic brain injury. *Nat. Chem. Biol.* 1, 112–119. doi:10.1038/nchembio711
- Delanghe, T., Dondelinger, Y., and Bertrand, M. J. M. (2020). RIPK1 kinase-dependent death: A symphony of phosphorylation events. *Trends Cell Biol.* 30, 189–200. doi:10.1016/j.tcb.2019.12.009
- Dondelinger, Y., Aguilera, M. A., Goossens, V., Dubuisson, C., Grootjans, S., Dejardin, E., et al. (2013). RIPK3 contributes to TNFR1-mediated RIPK1 kinase-dependent apoptosis in conditions of cIAP1/2 depletion or TAK1 kinase inhibition. *Cell Death Differ.* 20, 1381–1392. doi:10.1038/cdd.2013.94
- Dondelinger, Y., Delanghe, T., Priem, D., Wynosky-Dolfi, M. A., Sorobetea, D., Rojas-Rivera, D., et al. (2019). Serine 25 phosphorylation inhibits RIPK1 kinase-dependent cell death in models of infection and inflammation. *Nat. Commun.* 10, 1729. doi:10.1038/s41467-019-09690-0
- Dondelinger, Y., Delanghe, T., Rojas-Rivera, D., Priem, D., Delvaeye, T., Bruggeman, I., et al. (2017). MK2 phosphorylation of RIPK1 regulates TNF-mediated cell death. *Nat. Cell Biol.* 19, 1237–1247. doi:10.1038/ncb3608
- Dondelinger, Y., Jouan-Lanhout, S., Divert, T., Theatre, E., Bertin, J., Gough, P. J., et al. (2015). NF- κ B-Independent role of ikk α /ikk β in preventing RIPK1 kinase-dependent apoptotic and necroptotic cell death during TNF signaling. *Mol. Cell* 60, 63–76. doi:10.1016/j.molcel.2015.07.032
- Fauster, A., Rebsamen, M., Huber, K. V. M., Bigenzahn, J. W., Stukalov, A., Lardeau, C. H., et al. (2015). A cellular screen identifies ponatinib and pazopanib as inhibitors of necroptosis. *Cell Death Dis.* 6, e1767. doi:10.1038/cddis.2015.130
- Fiser, A., and Sali, A. (2003). ModLoop: Automated modeling of loops in protein structures. *Bioinformatics* 19, 2500–2501. doi:10.1093/bioinformatics/btg362
- Grootjans, S., Hassannia, B., Delrue, I., Goossens, V., Wiernicki, B., Dondelinger, Y., et al. (2016). A real-time fluorometric method for the simultaneous detection of cell death type and rate. *Nat. Protoc.* 11, 1444–1454. doi:10.1038/nprot.2016.085
- Harris, P. A., Bandyopadhyay, D., Berger, S. B., Campobasso, N., Capriotti, C. A., Cox, J. A., et al. (2013). Discovery of small molecule RIP1 kinase inhibitors for the treatment of pathologies associated with necroptosis. *ACS Med. Chem. Lett.* 4, 1238–1243. doi:10.1021/ml400382p
- Harris, P. A., Berger, S. B., Jeong, J. U., Nagilla, R., Bandyopadhyay, D., Campobasso, N., et al. (2017). Discovery of a first-in-class receptor interacting protein 1 (RIP1) kinase specific clinical candidate (GSK2982772) for the treatment of inflammatory diseases. *J. Med. Chem.* 60, 1247–1261. doi:10.1021/acs.jmedchem.6b01751
- Harris, P. A., King, B. W., Bandyopadhyay, D., Berger, S. B., Campobasso, N., Capriotti, C. A., et al. (2016). DNA-encoded library screening identifies benzo[b][1,4]oxazepin-4-ones as highly potent and monoselective receptor interacting protein 1 kinase inhibitors. *J. Med. Chem.* 59, 2163–2178. doi:10.1021/acs.jmedchem.5b01898
- Jaco, I., Annibaldi, A., Lalaoui, N., Wilson, R., Tenev, T., Laurien, L., et al. (2017). MK2 phosphorylates RIPK1 to prevent TNF-induced cell death. *Mol. Cell* 66, 698–710.e5. doi:10.1016/j.molcel.2017.05.003
- Jin, Z., and El-Deiry, W. S. (2006). Distinct signaling pathways in TRAIL-versus tumor necrosis factor-induced apoptosis. *Mol. Cell Biol.* 26, 8136–8148. doi:10.1128/mcb.00257-06
- Klöditz, K., and Fadeel, B. (2019). Three cell deaths and a funeral: Macrophage clearance of cells undergoing distinct modes of cell death. *Cell Death Discov.* 5, 65. doi:10.1038/s41420-019-0146-x
- Kong, Q., Lv, J., Yan, S., Chang, K., and Wang, G. (2018). A novel naphthyridine derivative, 3u, induces necroptosis at low concentrations and apoptosis at high concentrations in human melanoma A375 cells. doi:10.3390/ijms19102975
- Lafont, E., Draber, P., Rieser, E., Reichert, M., Kupka, S., de Miguel, D., et al. (2018). TBK1 and IKK ϵ prevent TNF-induced cell death by RIPK1 phosphorylation. *Nat. Cell Biol.* 20, 1389–1399. doi:10.1038/s41556-018-0229-6
- Liu, Y., and Gray, N. S. (2006). Rational design of inhibitors that bind to inactive kinase conformations. *Nat. Chem. Biol.* 2, 358–364. doi:10.1038/nchembio799
- Madhavi Sastry, G., Adzhigirey, M., Day, T., Annabhimoju, R., and Sherman, W. (2013). Protein and ligand preparation: Parameters, protocols, and influence on virtual screening enrichments. *J. Comput. Aided. Mol. Des.* 27, 221–234. doi:10.1007/s10822-013-9644-8
- Martens, S., Hofmans, S., Declercq, W., Augustyns, K., and Vandenabeele, P. (2020). Inhibitors targeting RIPK1/RIPK3: Old and new drugs. *Trends Pharmacol. Sci.* 41, 209–224. doi:10.1016/j.tips.2020.01.002
- Martens, S., Jeong, M., Tonnus, W., Feldmann, F., Hofmans, S., Goossens, V., et al. (2017). Sorafenib tosylate inhibits directly necrosome complex formation and protects in mouse models of inflammation and tissue injury. *Cell Death Dis.* 8, e2904. doi:10.1038/cddis.2017.298
- Menon, M. B., Gropengießer, J., Fischer, J., Novikova, L., Deuretzbacher, A., Lafera, J., et al. (2017). P38 MAPK/MK2-dependent phosphorylation controls cytotoxic RIPK1 signalling in inflammation and infection. *Nat. Cell Biol.* 19, 1248–1259. doi:10.1038/ncb3614
- Mifflin, L., Ofengeim, D., and Yuan, J. (2020). Receptor-interacting protein kinase 1 (RIPK1) as a therapeutic target. *Nat. Rev. Drug Discov.* 19, 553–571. doi:10.1038/s41573-020-0071-y
- Mompea, M., Li, W., Li, J., Laage, S., Siemer, A. B., Bozkurt, G., et al. (2018). The structure of the necrosome RIPK1-RIPK3 core, a human hetero-amyloid signaling complex. *Cell* 173, 1244–1253.e10. doi:10.1016/j.cell.2018.03.032
- Najjar, M., Suebsuwong, C., Ray, S. S., Thapa, R. J., Maki, J. L., Nogusa, S., et al. (2015). Structure guided design of potent and selective ponatinib-based hybrid inhibitors for RIPK1. *Cell Rep.* 10, 1850–1860. doi:10.1016/j.celrep.2015.02.052
- Newton, K., Dixit, V. M., and Kayagaki, N. (2021). Dying cells fan the flames of inflammation. *Sci.* (80-) 374, 1076–1080. doi:10.1126/SCIENCE.ABI5934
- Orning, P., Weng, D., Starheim, K., Ratner, D., Best, Z., Lee, B., et al. (2018). Pathogen blockade of TAK1 triggers caspase-8-dependent cleavage of gasdermin D and cell death. *Sci.* (80-) 362, 1064–1069. doi:10.1126/science.aau2818
- Rodriguez, D. A., Weinlich, R., Brown, S., Guy, C., Fitzgerald, P., Dillon, C. P., et al. (2016). Characterization of RIPK3-mediated phosphorylation of the activation loop of MLKL during necroptosis. *Cell Death Differ.* 23, 76–88. doi:10.1038/cdd.2015.70
- Rojas-Rivera, D., Delvaeye, T., Roelandt, R., Nerinckx, W., Augustyns, K., Vandenabeele, P., et al. (2017). When PERK inhibitors turn out to be new potent RIPK1 inhibitors: Critical issues on the specificity and use of GSK2606414 and GSK2656157. *Cell Death Differ.* 24, 1100–1110. doi:10.1038/cdd.2017.58
- Saur, I. M. L., Panstruga, R., and Schulze-Lefert, P. (2021). NOD-Like receptor-mediated plant immunity: From structure to cell death. *Nat. Rev. Immunol.* 21, 305–318. doi:10.1038/s41577-020-00473-z
- Shi, K., Zhang, J., Zhou, E., Wang, J., and Wang, Y. (2022). Small-molecule receptor-interacting protein 1 (RIP1) inhibitors as therapeutic agents for multifaceted diseases: Current medicinal chemistry insights and emerging opportunities. *J. Med. Chem.* 1, 14971–14999. doi:10.1021/acs.jmedchem.2c01518
- Takahashi, N., Duprez, L., Grootjans, S., Cauwels, A., Nerinckx, W., Duhadaway, J. B., et al. (2012). Necrostatin-1 analogues: Critical issues on the specificity, activity and *in vivo* use in experimental disease models. *Cell Death Dis.* 3, e437. doi:10.1038/cddis.2012.176
- Vanlangenakker, N., Bertrand, M. J. M., Bogaert, P., Vandenabeele, P., and Vanden Berghe, T. (2011). TNF-induced necroptosis in L929 cells is tightly regulated by multiple TNFR1 complex I and II members. *Cell Death Dis.* 2, e230. doi:10.1038/cddis.2011.111
- Wang, K., Li, J., Degterev, A., Hsu, E., Yuan, J., and Yuan, C. (2006). Structure – activity relationship analysis of a novel necroptosis inhibitor, Necrostatin-5. *Bioorg. Med. Chem. Lett.* 17, 1455–1465. doi:10.1016/j.bmcl.2006.11.056
- Weber, K., Roelandt, R., Bruggeman, I., Estornes, Y., and Vandenabeele, P. (2018). Nuclear RIPK3 and MLKL contribute to cytosolic necrosome formation and necroptosis. *Commun. Biol.* 1, 6–13. doi:10.1038/s42003-017-0007-1
- Weisel, K., Scott, N. E., Thompson, D. J., Votta, B. J., Madhavan, S., Povey, K., et al. (2017). Randomized clinical study of safety, pharmacokinetics, and pharmacodynamics of RIPK1 inhibitor GSK2982772 in healthy volunteers. *Pharmacol. Res. Perspect.* 5, e00365. doi:10.1002/prp2.365
- Xie, T., Peng, W., Liu, Y., Yan, C., Maki, J., Degterev, A., et al. (2013). Structural basis of RIP1 inhibition by necrostatins. *Structure* 21, 493–499. doi:10.1016/j.str.2013.01.016
- Xu, D., Jin, T., Zhu, H., Chen, H., Ofengeim, D., Zou, C., et al. (2018). TBK1 suppresses RIPK1-driven apoptosis and inflammation during development and in aging. *Cell* 174, 1477–1491.e19. doi:10.1016/j.cell.2018.07.041
- Zheng, W., Degterev, A., Hsu, E., Yuan, J., and Yuan, C. (2008). Structure-activity relationship study of a novel necroptosis inhibitor, necrostatin-7. *Bioorg. Med. Chem. Lett.* 18, 4932–4935. doi:10.1016/j.bmcl.2008.08.058
- Zhou, T., Wang, Q., Phan, N., Ren, J., Yang, H., Feldman, C. C., et al. (2019). Identification of a novel class of RIP1/RIP3 dual inhibitors that impede cell death and inflammation in mouse abdominal aortic aneurysm models. *Cell Death Dis.* 10, 226. doi:10.1038/s41419-019-1468-6



OPEN ACCESS

EDITED BY

Christelle Hureau,
Centre National de la Recherche
Scientifique, France

REVIEWED BY

Jonathan Pansieri,
University of Oxford, United Kingdom
Daniela Valensin,
University of Siena, Italy

*CORRESPONDENCE

Nakul C. Maiti,
✉ ncmaiti@iicb.res.in

[†]These authors have contributed equally
to this work and share first authorship

RECEIVED 17 January 2023

ACCEPTED 10 May 2023

PUBLISHED 26 May 2023

CITATION

Pandit E, Das L, Das AK, Dolui S, Saha S,
Pal U, Mondal A, Chowdhury J, Biswas SC
and Maiti NC (2023), Single point
mutations at the S129 residue of α -
synuclein and their effect on structure,
aggregation, and neurotoxicity.
Front. Chem. 11:1145877.
doi: 10.3389/fchem.2023.1145877

COPYRIGHT

© 2023 Pandit, Das, Das, Dolui, Saha, Pal,
Mondal, Chowdhury, Biswas and Maiti.
This is an open-access article distributed
under the terms of the [Creative
Commons Attribution License \(CC BY\)](#).
The use, distribution or reproduction in
other forums is permitted, provided the
original author(s) and the copyright
owner(s) are credited and that the original
publication in this journal is cited, in
accordance with accepted academic
practice. No use, distribution or
reproduction is permitted which does not
comply with these terms.

Single point mutations at the S129 residue of α -synuclein and their effect on structure, aggregation, and neurotoxicity

Esha Pandit^{1†}, Lopamudra Das^{1†}, Anoy Kumar Das², Sandip Dolui¹,
Saumen Saha¹, Uttam Pal¹, Animesh Mondal¹,
Joydeep Chowdhury³, Subhas C. Biswas² and Nakul C. Maiti^{1*}

¹Structural Biology and Bioinformatics Division, Indian Institute of Chemical Biology, Council of Scientific and Industrial Research, Kolkata, India, ²Cell Biology and Physiology Division, CSIR-Indian Institute of Chemical Biology, Kolkata, India, ³Department of Physics, Jadavpur University, Kolkata, India

Parkinson's disease is an age-related neurological disorder, and the pathology of the disease is linked to different types of aggregates of α -synuclein or alpha-synuclein (aS), which is an intrinsically disordered protein. The C-terminal domain (residues 96–140) of the protein is highly fluctuating and possesses random/disordered coil conformation. Thus, the region plays a significant role in the protein's solubility and stability by an interaction with other parts of the protein. In the current investigation, we examined the structure and aggregation behavior of two artificial single point mutations at a C-terminal residue at position 129 that represent a serine residue in the wild-type human aS (wt aS). Circular Dichroism (CD) and Raman spectroscopy were performed to analyse the secondary structure of the mutated proteins and compare it to the wt aS. Thioflavin T assay and atomic force microscopy imaging helped in understanding the aggregation kinetics and type of aggregates formed. Finally, the cytotoxicity assay gave an idea about the toxicity of the aggregates formed at different stages of incubation due to mutations. Compared to wt aS, the mutants S129A and S129W imparted structural stability and showed enhanced propensity toward the α -helical secondary structure. CD analysis showed proclivity of the mutant proteins toward α -helical conformation. The enhancement of α -helical propensity lengthened the lag phase of fibril formation. The growth rate of β -sheet-rich fibrillation was also reduced. Cytotoxicity tests on SH-SY5Y neuronal cell lines established that the S129A and S129W mutants and their aggregates were potentially less toxic than wt aS. The average survivability rate was ~40% for cells treated with oligomers (presumably formed after 24 h of incubation of the freshly prepared monomeric protein solution) produced from wt aS and ~80% for cells treated with oligomers obtained from mutant proteins. The relative structural stability with α -helical propensity of the mutants could be a plausible reason for their slow rate of oligomerization and fibrillation, and this was also the possible reason for reduced toxicity to neuronal cells.

KEYWORDS

amyloid, fibrillization, secondary structure, alpha-synuclein, neurotoxicity, Raman

Introduction

Parkinson's disease (PD) is one of the most prevalent neurodegenerative disorders, and it affects the nervous system that controls the movement of human body parts. Typical clinical features of the diseases comprise tremor, muscle rigidity, dysarthria, dysphagia, and impaired balance (Schapira et al., 2017). The pathological hallmark of PD includes progressive loss of nigrostriatal dopamine neurons, swollen dystrophic neurites, and characteristic amyloid inclusions, called Lewy bodies (Xu et al., 2016). The filamentous intracellular inclusions are protein aggregates found in other neural disorders like dementia and multiple system atrophy (MSA) (Aniszewska et al., 2022). Along with proteins like p62 and ubiquitin, the chief component of the Lewy bodies is found to be α -synuclein (aS) (Spillantini et al., 1997). aS also contributes to the fibrillization of amyloid- β and tau, two key proteins linked to Alzheimer's disease (AD) (Guo et al., 2013).

aS is a water soluble protein and largely found in the brain (Burré, 2022). It is a member of the synuclein family which also includes other proteins like β - and γ -synuclein (Kuusisto et al., 2003). This protein is abundantly expressed in the nervous system and is often localized at the presynaptic nerve terminals (Hawk et al., 2019). Even though the biological role and function of this protein are still an enigma, it is believed that the protein has a chaperone-like function and control release of neurotransmitters and it has effects on the SNARE complex (Maroteaux et al., 1988; Burré et al., 2010; Wang et al., 2018). aS consists of 140 amino acid residues; however, it does not have a defined globular and well folded structure. It thus belongs to the intrinsically disordered protein (IDP) family (Alderson and Markley, 2013). Earlier reports suggest that the protein is present in an unfolded monomeric conformation in the cytosol and may have a stable α -helical conformation when bound to phospholipids (Burré et al., 2014). The protein has three distinct regions with a defined role in the protein structure and functions (Marvian et al., 2020). The positively charged N-terminal domain (residues 1–60) includes seven series of 11 amino acid (AA) repeats; each repeat contains a highly conserved KTKEGV hexamer motif (Bartels et al., 2010). These are similar to repeats present in the highly conserved α -helical domain of apolipoproteins. These repeats play a role in the lipid–protein interaction (Romero et al., 1997). The core region (residues 61–95), also known as the NAC (non-A β -amyloid component) domain, can form a cross β -sheet structure and is significantly involved in the aggregation process and fibril event of this highly soluble protein (Fields et al., 2019).

The C-terminal domain (residues 96–140) is the acidic tail of the protein, with low hydrophobicity and a high net negative charge, and possesses random and highly fluctuating conformation (Das et al., 2014; Schapira et al., 2017). The region contains binding sites that are involved in protein–protein interactions and a common binding interface for metal ions (Pal et al., 2016a). Some residues in this region are also much prone to post translational modifications (PTMs) (Schmid et al., 2013; Burré et al., 2018; González et al., 2019; Zhang et al., 2019; Liu et al., 2020). It is reported that the C-terminal domain has similarities with the α -crystalline domain of small heat shock proteins (Kim et al., 2004), which indicates its protective role in keeping the protein out of the degradation process (McLean et al., 2002; Cox et al., 2018; Jia

et al., 2019). This region interacts with the NAC domain of the protein to inhibit and prevent its aggregation (Emamzadeh, 2016; Stephens et al., 2020). Moreover, calcium binding in this region modulates the protein interaction with synaptic vesicles (Lautenschläger et al., 2018). aS thus maintains a unique stability between its folded patches (rich with residues prone to aggregate, non-A β -amyloid component (NAC)) and highly disordered C-terminal regions in the solution state at physiological pH. The presence of such dynamic and flexible disordered regions in the protein may confer suitable plasticity to interact efficiently with several targets inside the cellular system. However, certain changes in the microenvironment cause misfolding of the protein, and it becomes the starting point of the aggregation process (Pal et al., 2016b). *In vitro* measurements also found that the mutations modulate protein aggregation and amyloid formation to a significant extent. For instance, A30P aggravates oligomerization, whereas E46K completely alters the fiber structure. Single point mutation or monogenic disorder is not very uncommon. Sickle cell anemia is a good example of such a case that leads to aggregation of hemoglobin, and it is due to a substitution of valine for glutamic acid in the structure of the β -chain hemoglobin molecule. It has also been demonstrated that the change in the chirality of an amino acid from L to D influences the aggregation kinetics (Chandra et al., 2017). In addition, for aS, several point mutations such as A18T, A29S, A30P, E46K, H50Q, G51D, A53E, and A53T are identified and it was observed that the rate of aggregation varies in each case (Appel-Cresswell et al., 2013; Lázaro et al., 2014; Flagmeier et al., 2016). For example, A30P greatly accelerates aS fibrillation, whereas E46K alters the core structure of the fibril (Chartier-Harlin et al., 2004). Interestingly, most of these mutations are present in the N-terminal end of the protein. The mutation in the C-terminal of the protein can also lead to a change in the protein–protein interaction, which may further affect the protein stability, change in conformation, and overall aggregation processes.

Our investigation was focused on the serine residue at position 129 (S129), which is found to be highly phosphorylated (89%) in aS present (Okochi et al., 2000; Fujiwara et al., 2002; Takahashi et al., 2003; Anderson et al., 2006) in the Lewy bodies. However, only 5% of the same residue was phosphorylated in the healthy brain samples. This phosphorylation, thus, assumed to have a significant effect on the aS aggregation pattern and subcellular distribution of the protein (Gonçalves and Outeiro, 2013; Pinho et al., 2019). Therefore, several investigations were carried out with S129A mutant protein (that prevents phosphorylation due to the lack of the serine residue at this position) to examine the role of phosphorylation on aggregation and toxic behavior to neuronal cells (Smith et al., 2005; McFarland et al., 2009; Lázaro et al., 2014; Oueslati, 2016; Ghanem et al., 2022). A study on the SH-SY5Y cell line by Smith et al. (2005), however, on the contrary, showed formation of less inclusion bodies inside the cell in the case of S129A mutation (Gasteiger et al., 2005). Thus, the study indicated that replacement of the residue with alanine reduced the aggregation behavior of the protein. However, what structural changes the S129A mutation brings and how that affects aggregation behavior of the protein were not known. Our interest was focused on deriving the structural information on the mutant protein and correlating this information with aggregation behavior of the protein in this altered

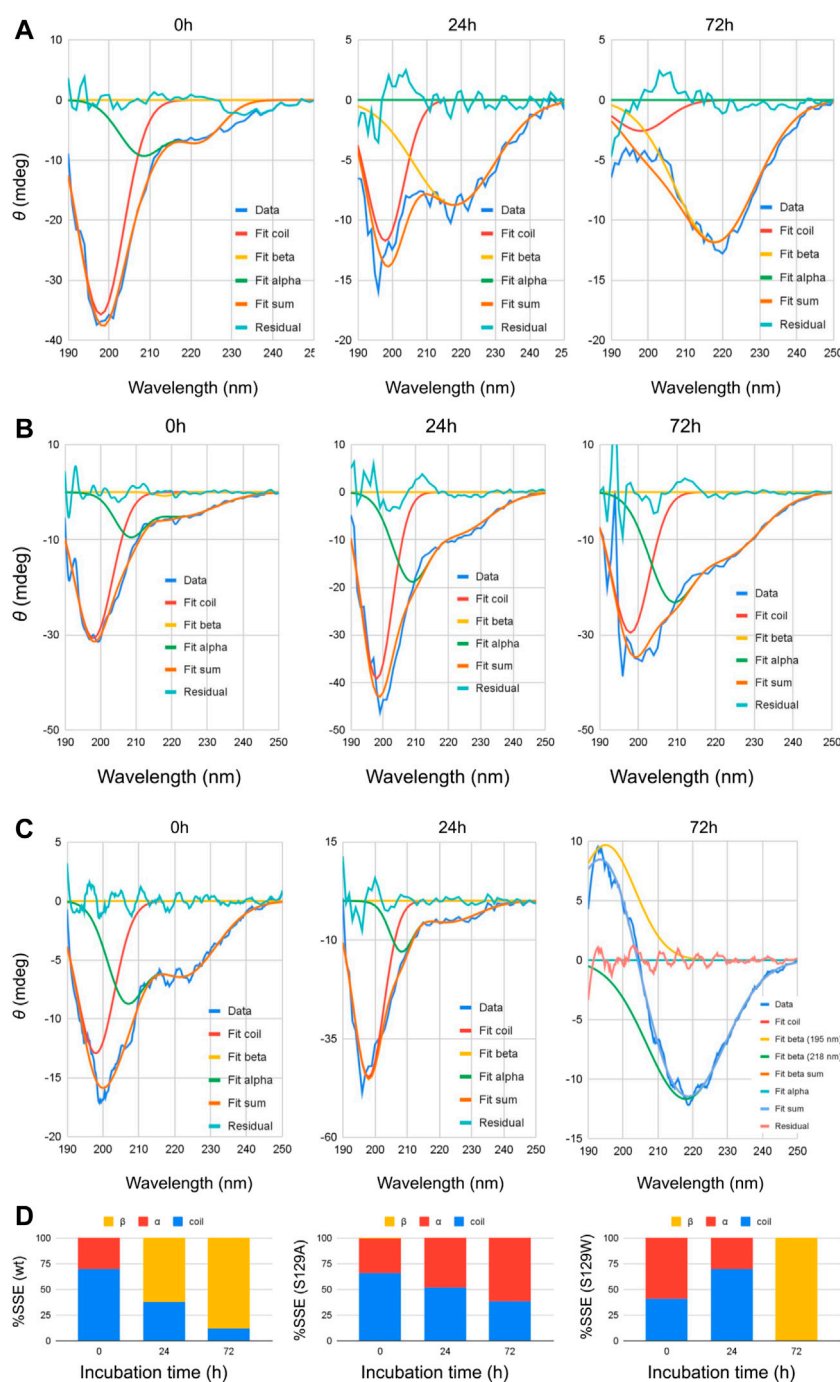


FIGURE 1

Circular dichroism spectra of wt and mutant alpha synucleins and spectral deconvolution. One Gaussian at 198 nm is fitted for random coil and one at 218 nm for beta sheets. Two Gaussians at 208 and 222 nm are fitted for alpha helix, and the sum of the two is shown as "Fit alpha." Summation of all the fitted Gaussians and the residuals are also shown. (A) CD spectra of wild-type aSn protein at different time points of incubation. (B) Circular dichroism spectra of S129A α -synuclein at different time points of incubation. (C) Circular dichroism spectra of S129W α -synuclein at different time points of incubation. For 72 h, a positive peak is observed at 195 nm, which is a signature of the beta-sheet. One Gaussian is additionally fitted for the beta-sheet in this spectrum. Summation of all the fitted Gaussians and the residuals are also shown. (D) Changes in the secondary structural composition over the period of incubation for wt and the mutants.

situation. Thus, it gave us the opportunity to explore the role of this unique residue and associated structure in aggregation behavior of aS in an ambient solution condition. We prepared two recombinant artificial single point mutants of aS: S129W and S129A and investigated the

protein secondary structure of the mutant proteins by CD and Raman spectroscopic methods. Furthermore, our investigation correlated the aggregation behavior of the protein with the alteration of the protein secondary structure in two mutant proteins. The derived results were

TABLE 1 Deconvolution of CD spectra.

Sample	Fitting		0 h				24 h				72 h			
	Peak	Remark	Depth	HWHM	Area	% Area	Depth	HWHM	Area	% Area	Depth	HWHM	Area	% Area
wt	198	Random	35.74	6.5	611	69	11.73	6.25	193	38	2.58	8.13	55	12
	208	Alpha	9	6.5	154	31	0	0	0	0	0	0	0	0
	222		6.76	6.5	116		0	0	0		0	0	0	
	218	Beta	0	0	0	0	8.74	13.79	317	62	11.83	12.76	397	88
S129A	198	Random	30.67	6.22	502	66	39.21	5.62	580	52	29.58	5.64	439	38
	208	Alpha	7.42	4.84	95	34	15.07	6.43	255	48	18.2	6.61	317	62
	222		5.15	11.97	162		8.75	12.32	284		13.44	11.14	394	
	218	Beta	0.79	2.96	6	1	0	0	0	0	0	0	0	0
S129W	198	Random	12.92	6.06	206	41	44.84	5.54	654	70	0	0	0	0
	208	Alpha	7.07	5.94	111	59	11.03	4.15	120	30	0	0	0	0
	222		6.4	11.06	186		5.51	11.36	165		0	0	0	
	218	Beta	0	0	0	0	0	0	0	0	11.68	13.17	405	100

compared to wt aS. In S129A, essentially, the polar side chain is replaced with a nonpolar methyl group and it was found that it drastically reduces the aggregation propensity of α -synuclein. Insertion of tryptophan residue in this position also produced interesting results. We further investigated the toxic effect on neuronal (SH-SY5Y) cell lines. The study established that increase in α -helicity in the secondary structure of the mutant proteins slowed down the aggregation and caused less damage to neuronal cells.

Results and discussion

Stability and their spectroscopic signatures of α -synuclein mutants

Established protocols were used to prepare and purify both the wild (wt aS) and mutant (S129A and S129W) human aS (Luth et al., 2015). The purity of the prepared protein solution in aqueous buffer was judged based on SDS-PAGE and mass spectroscopy analyses (Supplementary Figures S1A, S1B). Both the data confirmed the mass of the three proteins was ~14 kDa. Absorbance and fluorescence spectra of freshly prepared protein solutions were recorded (Supplementary Figures S2A, S2B). The absorbance band appeared at ~276 nm for wt aS and both the mutant proteins (Supplementary Figure S2A). Supplementary Figures S1B shows the fluorescence spectra of aqueous protein solutions at ambient conditions (20 mM phosphate buffer solution, pH 7.4). The wt aS and S129A showed fluorescence emission maxima at 302 nm, while the S129W mutant showed the peak at 356 nm. Lack of Trp residue in wild aS and S129A variant was indicated by very weak fluorescence at 302 nm due to four tyrosine residues present in the protein backbone. However, the strong fluorescence peak at 356 nm for S129W was caused due to substituted tryptophan. The emission Trp fluorescence is very sensitive to the polarity of the surrounding microenvironment of the tryptophan residue. Solvent-exposed Trp residues exhibit fluorescence

peaks at around 350 nm; however, in the hydrophobic cavity of folded protein, the residue yields fluorescence at ~342 nm (Vivian and Callis, 2001). The fluorescence peak position at 356 nm indicated that the tryptophan was well exposed to the solvent environment in the mutant protein, S129W.

Secondary structural changes during aggregation by circular dichroism spectroscopy

Circular dichroism (CD) spectroscopic measurement is an excellent way to determine the nature of the secondary structure and unfolding/folding properties of proteins *in vitro*. Changes in CD spectra correlate any alterations of the protein secondary structure. Our CD analysis with wt aS shows a primarily random coil structure with a strong negative CD band at 198 nm (Figure 1). Deconvolution of the spectrum, however, revealed the presence of some α -helical signatures in the protein secondary structure. Computation of the area under the curves showed 31% α -helix and 69% random/disordered conformation in wt aS (Table 1). After 24 h of incubation, the random coil signature was decreased from 69% to 38%. However, the β -sheet signature became prominent (62%). After subsequent incubation for 72 h, the presence of random coil further reduced to 12% and the protein attained mostly (88%) β -sheet conformation, confirming formation of compact and well-defined β -sheet rich amyloid fibrils. The initial structure of S129A was very similar to that of the wt aS (Figure 1). However, upon incubation for 24 h, the helical signature of mutant protein increased from 34% to 48% and finally to 62% (Table 1). No major β -sheet signature was observed. This result indicated that the substitution of the serine 129 residue with alanine enhanced the propensity of helix formation in its oligomeric states. The S129W mutant in the monomeric state itself showed more α -helical patterns

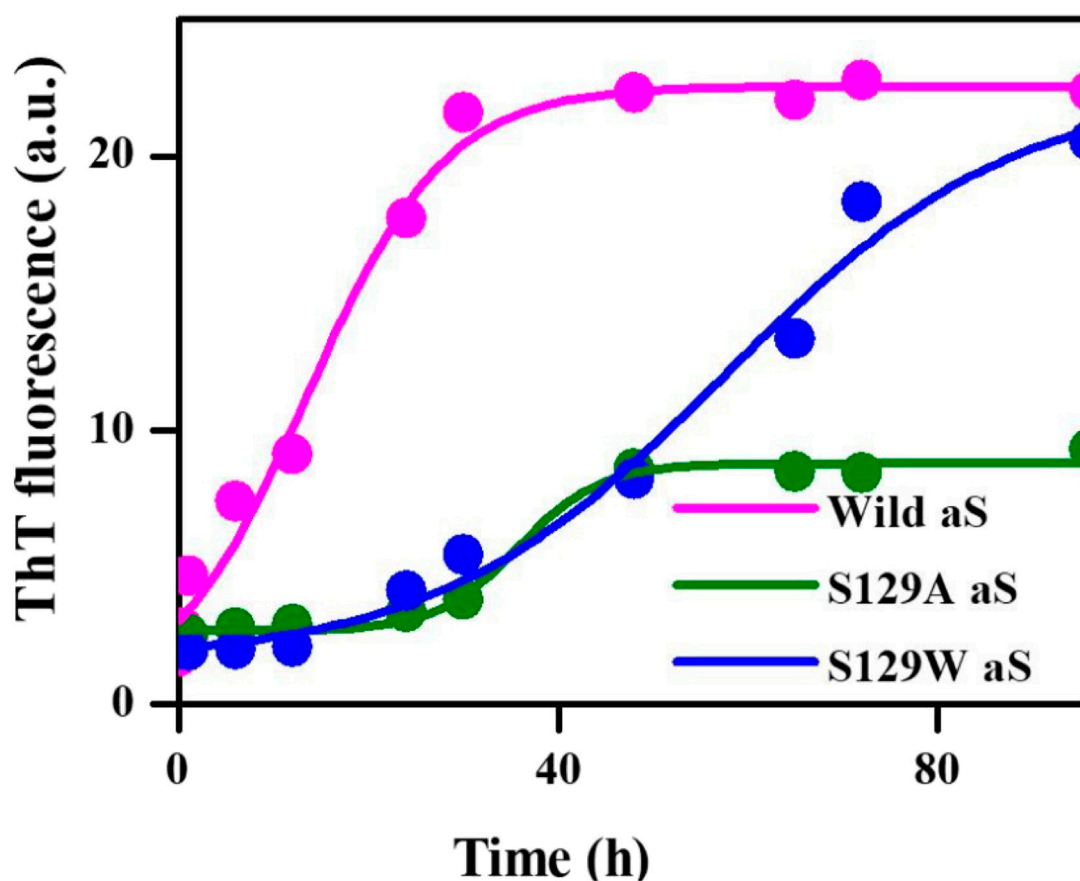


FIGURE 2

Time-dependent ThT fluorescence assay for determining the fibril formation growth kinetics of wild-type α -synuclein (wt aS) and the mutant variants (S129A and S129W). For each incubated sample, at different time points of incubation, 20 μ L of the incubated solution was mixed with 500 μ L of ThT solution ($\sim 20 \mu$ M) and the ThT fluorescence was measured, and the sample was excited at 440 nm. The magenta line is the fit of Eq. 1 to the data points obtained for wt aS. Similarly, the olive line is the fit of Eq. 1 to the data points obtained for S129A, and the blue line is a fit of Eq. 1 to the data points obtained for S129W.

than the wild-type and the S129A mutants (Figure 1; Table 1). After 24 h of incubation, some decrease in the helical signature was observed; however, no β -sheet signature was apparent. However, after 72 h of incubation, the mutant attained mostly a β -sheet structure. It was also confirmed by ThT fluorescence assay, as discussed in the following section.

Aggregation kinetics of α -synucleins by thioflavin T fluorescence assay and atomic force microscopy

Thioflavin T (ThT) assay was performed to measure the fibrillization kinetics of both the mutant and wild-type aS. ThT is a fluorescence dye and is often used to monitor *in vitro* amyloid fibril formation. Upon binding to amyloid fibrils, ThT emits a strong fluorescence signal at ~ 485 nm when excited at 450 nm (Voropai et al., 2003) Figure 2 shows the time-dependent ThT fluorescence assay for determining the fibril formation growth kinetics of wt aS and the mutant variants (S129A and S129W). The increment of fluorescence intensity for wt aS was faster than both the mutant aS. ThT fluorescence intensity was gradually increasing depending

upon the incubation time of the protein solution, until it reached a plateau by ~ 40 h. The fluorescence intensity subsequently remained steady until 90 h (Figure 2). The mechanism of the enhanced ThT fluorescence signal upon binding to β -sheet-rich fibrils has been attributed to the rotational immobilization of the central C-C bond of ThT, which connects its benzothiazole and aniline rings (Stsiapura et al., 2007; Srivastava et al., 2010). On the other hand, the lack of properly formed amyloid fibrils is indicated by weak fluorescence signals of the dye molecules present in the solution. ThT kinetics data, according to the protocol reported by Meisl et al. (2016), to understand the type of elongation as the slopes of the ThT kinetics graphs, differ significantly for the two mutant aS compared to the wild-type proteins. The wt aS showed nucleation-dependent elongation. It depends only on the concentration of free monomers. Thus, based on the fluorescence enhancement and incubation time, the fitted equation (Eq. 1) to the data suggested that fibril formation reached to its half maxima ($t_{1/2}$) at 13.6 h; the apparent rate constant (K_{app}) of fibrillation of wt aS was 0.13 h^{-1} . In contrast, the ThT fluorescence, in the presence of incubated S129W, increased at a slower rate than wild-type aS (wt aS). No significant rise in ThT fluorescence was observed up to 24 h. However, after 24 h of incubation, gradual increment of ThT fluorescence was

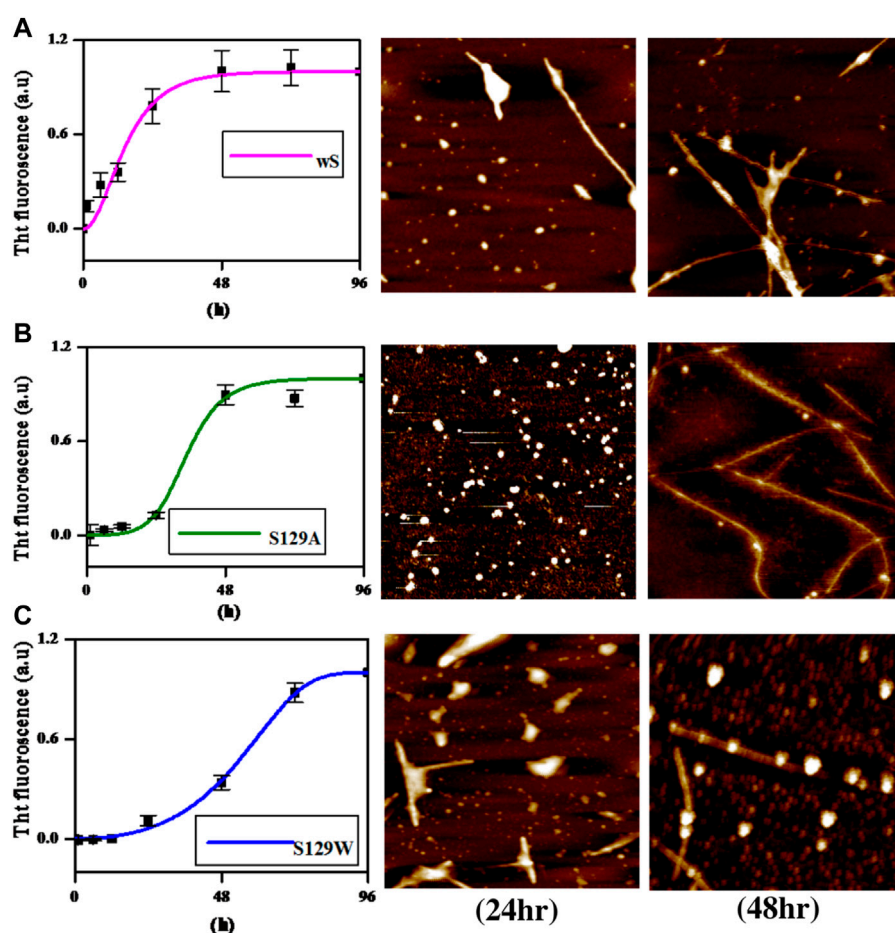


FIGURE 3

Different elongation kinetics of wt, S129A, and S129W aS proteins as obtained from AmyloFit and surface morphology of α -synuclein aggregates formed at different time points, as observed by atomic force microscopy. (A) Nucleation elongation kinetics for wild-type aS and AFM images obtained at 24 and 72 h. (B) Secondary nucleation-based elongation kinetics for S129A and AFM images obtained at 24 and 72 h. (C) Fragmentation-dominated elongation kinetics for S129W and AFM images obtained at 24 and 72 h. All AFM images are of dimension $2.5 \mu\text{m} \times 2.5 \mu\text{m}$.

observed and it was attributed to the formation of aggregates with beta-sheet conformation. The $t_{1/2}$ and apparent rate constant (K_{app}) of fibrillation for this mutant also were measured by fitting the data points using Eq. 1, and the values were 59 and 0.06 h^{-1} , respectively. Under the same conditions, S129A also showed a slow process of fibrillization. It has a prolonged lag phase and the half maxima ($t_{1/2}$) of 35 h, and the apparent rate constant (K_{app}) of fibrillation was 0.23 h^{-1} .

AFM (atomic force microscopy) was further engaged to visualize the morphological features of the aggregates produced in the processes of fibrillation. At 24 h of incubation, the wild protein showed the formation of protofibrils along with oligomers (Figure 3A). An average mean height of spherical oligomers was $\sim 6.4 \text{ nm}$. For the same time period of incubation, S129A and S129W yielded oligomers of diameters of ~ 3.8 and $\sim 5.0 \text{ nm}$, respectively. Fibrils were visible for all the three variants of proteins at 72 h of incubation. The wild protein produced a mesh-like fibrillar network with an average mean height of 6.08 nm (Figure 3A). It was also observed that both the mutants produced protofibrillar structures. The S129A mutant produced very thin fibrils (Figure 3B), and the

S129W mutant showed thicker protofibrils with oligomers still visible (Figure 3C). The average mean height of fibrils produced from S129A and S129W were 5.8 and 6.3 nm , respectively, as shown in Figure 3. The average mean height of all the oligomers and fibril samples is calculated taking an average sample size between 5 and 8 (Supplementary Figure S3A, S3B; Supplementary Table S1A). The fibril lengths for each species were $\sim 2.5 \mu\text{m}$, and no significant difference was observed.

Structural features of the protein and their aggregates from the Raman spectral signature

Raman spectroscopy is used to study the structural features of proteins and peptides in different stages of aggregation and fibrillation (Apetri et al., 2006; Kurouski et al., 2015; Flynn et al., 2018). Figures 4A, B show the Raman signature of the monomer and fibril of wt aS, S129W, and S129A. The most structure-sensitive amide I band of proteins appears at $1620\text{--}1700 \text{ cm}^{-1}$, and the amide III band is often

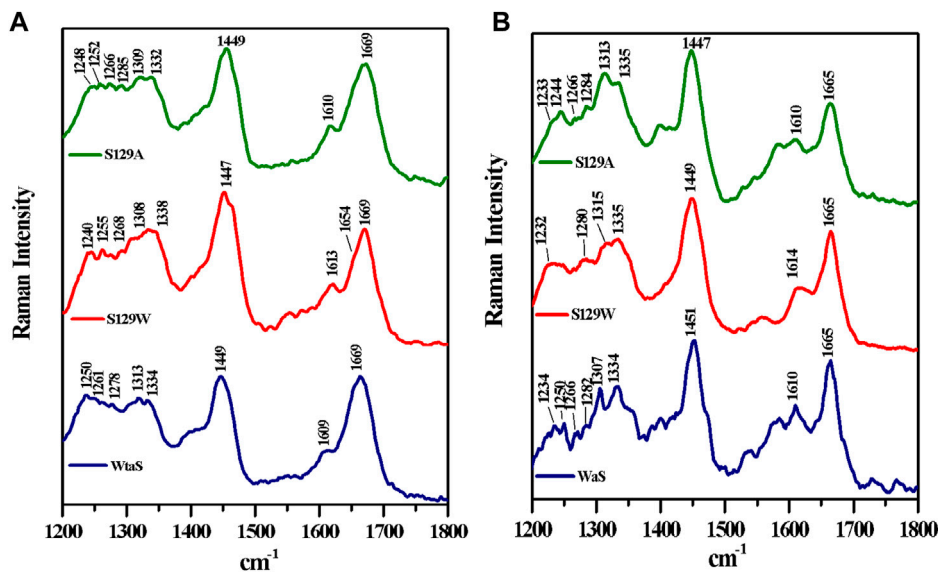


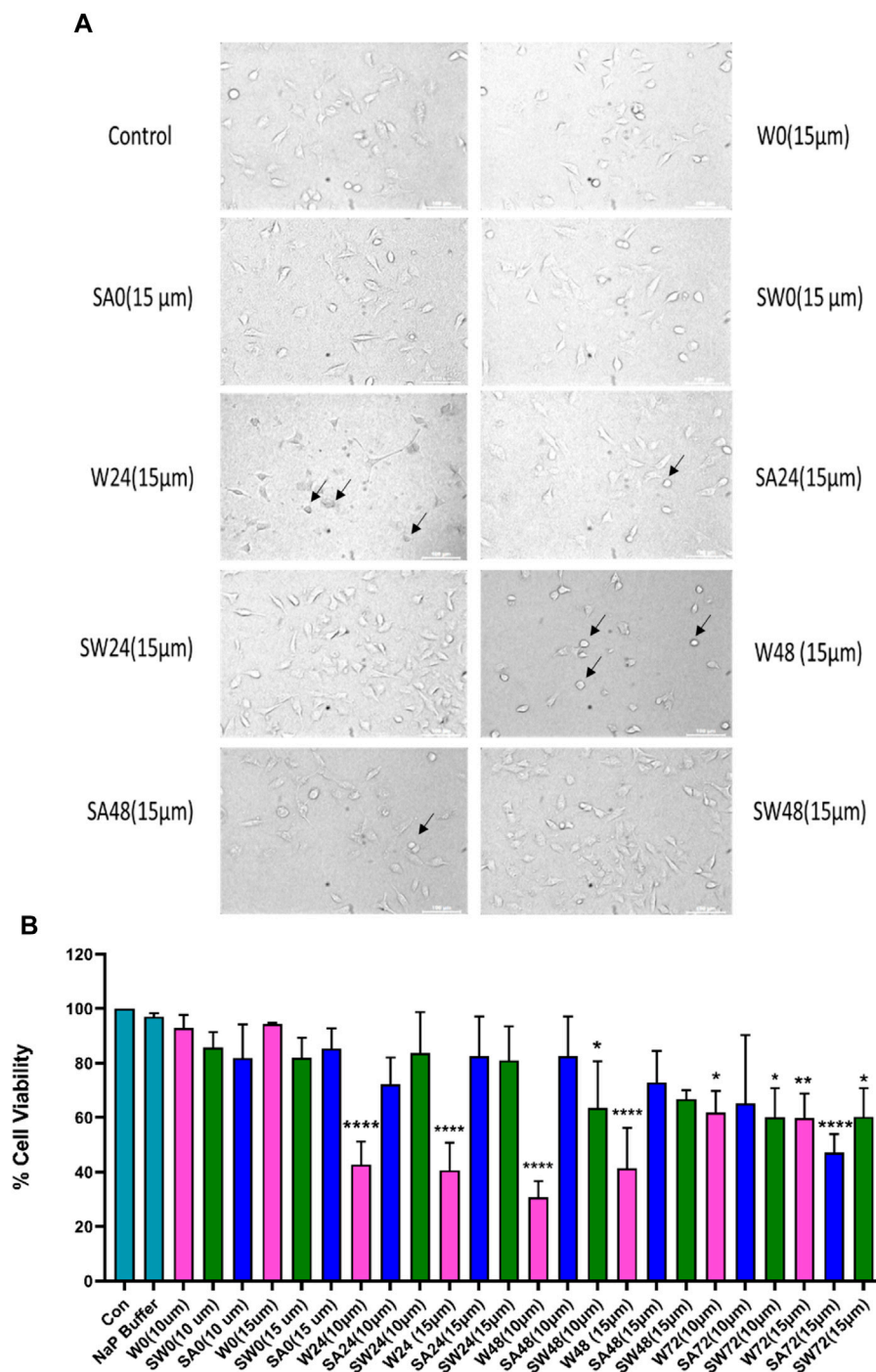
FIGURE 4
Raman spectra of wild and two mutants of alpha synuclein, their monomer, and fibril in the frequency range of 1200–1800 cm^{-1} by 532-nm laser. Both monomer (A) and fibril (B) solution were prepared in 20 mM sodium phosphate buffer pH 7.4 and dropped cast on a glass coverslip, and spectra were recorded at room temperature (25 °C) after being air dried. Laser power at the source was 50 mW at the sample.

TABLE 2 Raman vibrational bands (cm^{-1}) of alpha-synuclein as the monomer and fiber states.

wt aS (monomer)	S129A aS (monomer)	S129W aS (monomer)	wt aS (fiber)	S129A aS (fiber)	S129W aS (fiber)	Modes of Raman vibration
—	—	—	1,234	—	1,232	Amide III, β -sheet
—	—	1,239	—	1,244	1,247	Amide III, random coil
1,250	1,252	1,255	1,250	—	—	Amide III, random coil
1,261	1,266	1,268	1,266	1,266	1,265	Amide III, α -helix
1,278	1,285	—	1,282	1,284	1,280	Amide III, α -helix
1,313	1,309	1,308	1,307	1,313	1,315	CH ₂ twist
1,334	1,332	1,338	1,334	1,335	1,335	CH ₂ twist
1,449	1,449	1,447	1,451	1,447	1,449	CH ₂ , CH ₃ deformation
1,609	1,610	1,613	1,610	1,610	1,614	Tyr
—	—	—	1,665	1,665	1,665	Amide I, β -sheet
1,669	1,669	1,669	—	—	—	Amide I, random coil

observed at the 1200–1320 cm^{-1} frequency range. The Raman peaks of the protein samples are listed in Table 2. The Raman spectrum of freshly prepared wt aS in its fairly monomeric state showed a broad amide I band centered at 1669 cm^{-1} with a full width at half maxima (FWHM) of 55 cm^{-1} . It suggested a highly fluctuating secondary structure, similar to previously reported data (Maiti et al., 2004). The amide I band became quite narrow (FWHM 37 cm^{-1}), and it was from 1669 cm^{-1} to 1665 cm^{-1} , which was consistent with progressive increases in the ordered secondary structure, primarily the β -sheet conformations in this case. The Raman signature of the S129A monomer is shown in Figure 4A. It also exhibited a broad amide I Raman band at 1669 cm^{-1}

with an FWHM of 62 cm^{-1} . It also suggested the presence of conformational heterogeneity in its secondary structure. In S129A fibrils (Figure 4B), the Raman amide I band becomes somewhat narrow (FWHM 46 cm^{-1}) along with a shift in peak position from 1669 to 1665 cm^{-1} , indicating appearance of the ordered secondary structure. The S129W monomer amide I band shows an FWHM of 53 cm^{-1} , whereas in S129W fibrils, the Raman amide I band became narrow (FWHM 38 cm^{-1}), and there was a shift in the band position from 1669 to 1665 cm^{-1} , which also suggested the presence of ordered secondary structural conformation such as the β -sheet. However, further investigation indicated broad shoulders near 1655 cm^{-1} for

**FIGURE 5**

Cytotoxicity evaluation of wild-type and mutant aS proteins using MTT assay. Wild-type and mutant protein oligomers were incubated for 0, 24, 48, and 72 h, and then, their effects were checked for viability of SH-SY5Y neuroblastoma cells. **(A)** Representative microscopic images of SH-SY5Y cells after 24 h treatment of different variants of wild-type and mutant proteins. Cells were treated with 15 μM concentration for imaging purposes. Arrows indicate dead cells. **(B)** Cells were treated with two different concentrations of oligomer variants (10 μM and 15 μM) and incubated for 24 h, followed by MTT assay. All experiments were performed in triplicate, and the relative cell viability (%) was expressed as a percentage relative to the untreated cell (control) as mean ± SEM in a bar diagram where *, $p \leq 0.05$; **, $p \leq 0.01$; ***, $p \leq 0.001$; ****, $p \leq 0.0001$ compared to control. NaP, sodium phosphate buffer; W0, W24, W48, and W72, wild-type alpha synuclein incubated for 0, 24, 48, and 72 h, respectively; SW0, SW24, SW48, and SW72 mutant S129W alpha-synuclein incubated for 0, 24, 48, and 72 h, respectively; SA0, SA24, SA48, and SA72 mutant S129A alpha-synuclein incubated for 0, 24, 48, and 72 h, respectively.

both the mutants. Amide I band analysis suggested that wt aS and both the mutant variants may contain multiple secondary structures which are dynamic in nature. An exact differentiation of the structural content

in the different variants of the protein was difficult. However, a broader shoulder near 1655 cm^{-1} clearly suggested presence of residues in the α -helical space. Fibrils formed from the S129A mutant showed a greater

TABLE 3 Average cell survivability rate of SH-SY5Y cells when treated with different concentrations of oligomers formed by wt aS and S129A aS and S129W aS collected at different time points of incubation.

Treatment used	Average
Control	100
Sodium phosphate buffer	97.03
wt aS (0 h, 10 μ M)	92.9
wt aS (0 h, 15 μ M)	94.3
S129A aS (0 h, 10 μ M)	81.8
S129A aS (0 h, 15 μ M)	85.3
S129W aS (0 h, 10 μ M)	85.7
S129W aS (0 h, 15 μ M)	81.9
wt aS (24 h, 10 μ M)	42.67
wt aS (24 h, 15 μ M)	40.62
S129A aS (24 h, 10 μ M)	72.2
S129A aS (24 h, 15 μ M)	82.48
S129W aS (24 h, 10 μ M)	83.6
S129W aS (24 h, 15 μ M)	80.94
wt aS (48 h, 10 μ M)	30.77
wt aS (48 h, 15 μ M)	41.46
S129A aS (48 h, 10 μ M)	82.5
S129A aS (48 h, 15 μ M)	72.83
S129W aS (48 h, 10 μ M)	63.4
S129W aS (48 h, 15 μ M)	66.8
wt aS (72 h, 10 μ M)	61.7
wt aS (72 h, 15 μ M)	59.8
S129A aS (72 h, 10 μ M)	65
S129A aS (72 h, 15 μ M)	41
S129W aS (72 h, 10 μ M)	60
S129W aS (72 h, 15 μ M)	60

band width (FWHM 46 cm^{-1}) than the width observed for wt aS and S129W. It suggested a less compact β -sheet structure of the fibrils produced from S129A. It was also reflected in less amount of ThT fluorescence at an equilibrium/steady state of condition after 72 h (Figure 3B).

The amide III region (1200–1320 cm^{-1}) also provides some signature of the protein conformations. The band originated due to in-phase N–H deformation and C–N stretching. Recent articles by Dolui et al. and references therein provide the details of band positions. All the three variants of aS (wt aS, S129A, and S129W) showed a weak band at $\sim 1252 \text{ cm}^{-1}$ (precisely for wt aS, the band was at 1250 cm^{-1} , for S129W 1255 and 1252 cm^{-1} for S129A). The amide III band near 1250 cm^{-1} is assigned to mainly disordered or poly-L-proline conformation (Dolui et al., 2020 and the references therein). The shoulder band position near 1278 and 1261 cm^{-1} sometimes

indicated the presence of α -helical conformation. These bands were present with slight variation in all the three forms of the monomeric proteins (Figure 4A). Upon fibril formation, the β -sheet signature band appeared near 1234 cm^{-1} ; however, the band position for S129A was much weaker. However, the weak intensity and contribution of vibrational bands originating from the side chain of amino acid residues in this region render precise structural component analysis difficult and it was avoided.

Cytotoxicity evaluation of wild and mutated alpha synuclein using MTT assay

Studying the cell viability of SH-SY5Y cells upon exposure to different aS species has been extensively used in recent times (Mahapatra et al., 2019). It helps in accessing the toxicity of aggregates formed at different time points of incubation. It has been shown that extracellular aS fibrils are very often transported to neurons and play a significant role in aS pathology (Honarmand et al., 2019). Adding incubated samples of aS aggregates to neural cells helps in mimicking the prion-like nature of aggregated aS protein (Brundin et al., 2010). Several studies have also reported that aS oligomers and intermediates formed during aggregation are more toxic than fibrillar structures (Winner et al., 2011). Intrigued by that information, we investigated the cytotoxic effect of aggregates of wt aS and S129A aS and S129W aS in neuronal SH-SY5Y cells. The cells were treated with the oligomers, protofibrils, and fibers of different concentration in a time-dependent manner. Cells treated with early forms of aggregates formed by wild-type protein showed a considerably higher level of cytotoxicity than mutant variants (Figures 5A, B; Table 3). With respect to control, cells treated with wild-type protein aggregates collected after 24 and 48 h of incubation showed significant amount of cell death compared to cells treated with aggregates of mutated proteins collected from a similar time point of incubation, which showed much higher survivability. Cell death for wt aS-treated samples is highest when aggregates formed after 24 h of incubation are used to treat the cells (only $\sim 40\%$ cells survived compared to $\sim 80\%$ in case of both mutant proteins). Cells treated with aggregates formed by mutated variants obtained after 24 h of incubation show negligible cell death. The MTT assay results thus indicate that S129A and S129W point mutations in aS make it less toxic toward neuronal cells probably by reducing oligomer formation due to imparted stability of the monomeric states. In addition, it is interesting to see how the aggregates formed after 72 h of incubation are affecting the cell's survivability. In case of wild-type protein, after 72 h of incubation, the percentage of cell survivability goes up ($\sim 60\%$ compared to $\sim 40\%$ cell survival seen in case of treatment with oligomers.) This aligns with the previous finding of fibrils being less toxic than oligomers. We can also conclude that in the case of wild aS, most oligomers form protofibrils and fibrils after 72 h of incubation, which is also confirmed by ThT and AFM data. However, in case of mutant proteins, the cell survivability decreases when treatment is performed with samples collected after 72 h of incubation ($\sim 60\%$ in case of both mutant proteins S129A and S129W), which is significantly less than treatments performed with samples collected from 24 to 48 h of incubation. Cells incubated for 24 h with aggregated samples (prepared after 72 h of incubation) were

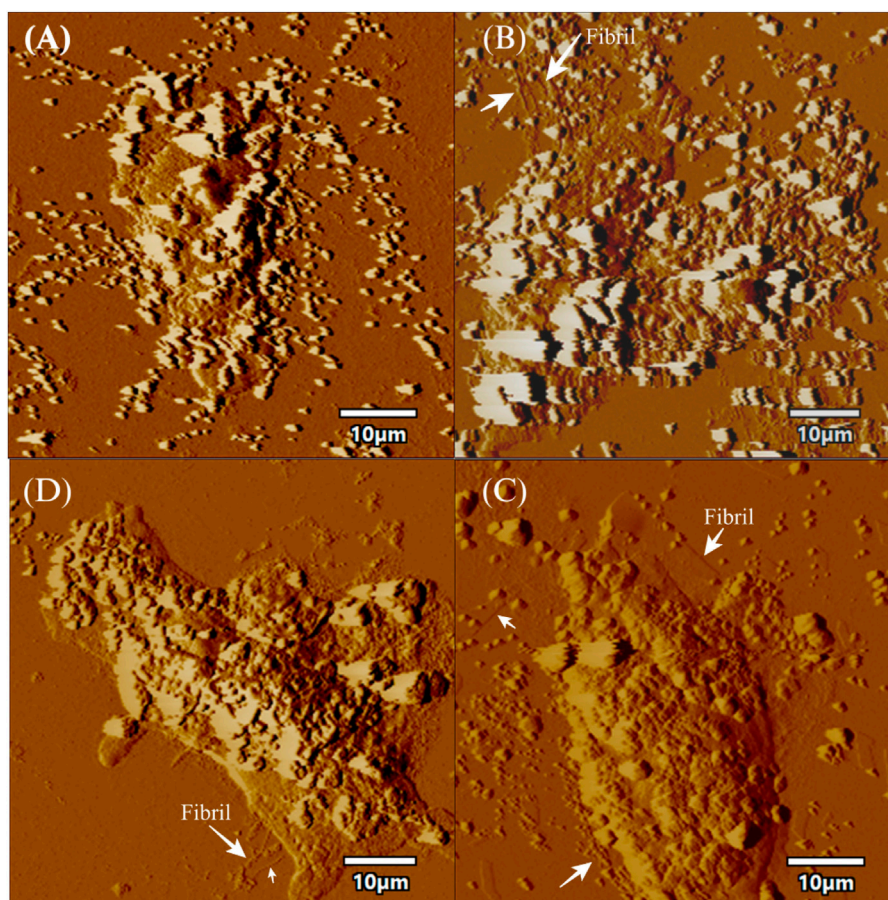


FIGURE 6

AFM topographic images of SH-SY5Y cells in presence of fibrils. The figure displays topographic images acquired through atomic force microscopy (AFM) of SH-SY5Y cells. SH-SY5Y cells were incubated for 24 h using 72 h incubated aS. Then, the cells were processed for AFM, which (A) depicts control cells without any alpha-synuclein (aS) fibrils, while (B) shows SH-SY5Y cells in the presence of wild-type aS fibrils. (C) shows SH-SY5Y cells exposed to the S129A aS fibril, and (D) displays SH-SY5Y cells exposed to the S129W aS fibril. In all panels, the presence of fibrils is indicated with a white arrow. Scale bar = 10 μ m.

also observed under AFM (Figure 6). This indicates that there was a probability that these fibrils were more toxic in nature, which leaves scope for further studies.

Conclusion

Our current investigation established how single point mutation, particularly in the highly dynamic C-terminal region, makes profound impacts on the aS structure, dynamics, and formation-specific aggregates of distinct morphologies. The study was focused on the S129 sequence position in the C-terminal soluble domain of aS. We found that replacement of this hydrophilic serine residue with alanine (considered as the most helix promoting residue), which is eventually a replacement of the polar side chain with a non-polar methyl group, reduced the aggregation propensity of aS significantly and hindered the formation of a very compact β -sheet structure. Similarly, replacing the serine residue with hydrophobic tryptophan (has both helix and β -sheet propensity) affects the aggregation processes; the lag phase of aggregation lengthened compared to wt aS. It was, thus, established

that increased hydrophobicity/helix-forming propensity in the C-terminal domain provided stability to the monomeric form of the protein, slowing down both oligomerization and subsequent fiber formation processes. ThT fluorescence assay CD and Raman spectral analysis all suggested β -sheet-rich compact fibrils for wt aS and S129W after 72 h of incubation, although β -sheets may not be very compact for S129A due to the presence of alanine, a helix promoting residue. The results, thus, established that mutation of an important residue in the soluble tail of aS with the helix-promoting residue reduced its aggregation and neurotoxic effect on neuronal cells.

Materials and methods

Expression and purification of wild-type and mutant α -synuclein

The plasmid containing aS gene was gifted by Hilal Lashuel (Addgene plasmid # 36046). aS was overexpressed in *E. coli* BL21 (DE3) using plasmid pT7-7 encoded with wild-type human aS gene,

following a previously published protocol. For the S129A and S129W mutated variants, the vector was constructed by replacing the codon AGT for serine 129 with GCC, which encodes alanine, and TGG, which encodes tryptophan (obtained from GenScript). Overexpression of mutant proteins was conducted in *E. coli* BL21 (DE3), following a similar protocol as the wild-type protein. Bacterial cells were cultured overnight at 37 °C in Luria Broth in the presence of ampicillin (100 µg/mL) as a selection agent. Overnight primary culture was followed by a secondary culture in LB under the same conditions. Once the optical density (OD) of the secondary culture reached 0.6, 1 mM isopropyl-β-D-thiogalactopyranoside (IPTG) was added for the induction of the protein overexpression. Bacterial pellets were harvested by centrifugation at 10000 rpm for 15 min at 4 °C. The pellets were resuspended in a TEN buffer composed of 30 mM Tris pH 7.5, 10 mM ethylenediaminetetraacetate, and 100 mM NaCl along with 1 mM phenylmethanesulfonyl fluoride for cell lysis. The lysate was then heated at 75 °C for 10 min and then centrifuged at 18000 rpm, and the supernatant enriched in aS was collected. The supernatant was transferred to a fresh tube, and streptomycin sulfate (136 µL of 10% solution/mL of the supernatant) and acetic acid (glacial, 228 µL/mL of supernatant) were added to it, followed by another centrifugation for 15 min. aS was then purified by fractional precipitation. Established protocols for the precipitation method were followed for protein purification for both wt aS and mutated aS variants.⁵⁴ The supernatant was subjected to ammonium sulfate precipitation (4 °C, 1:1 v/v saturated ammonium sulfate: water) and centrifuged for an hour. The pellet was collected and washed with 2 mL of 50% ammonium sulfate solution. The washed pellet was resuspended in 100 mM ammonium acetate solution, which was added gradually until a cloudy solution was formed, followed by ethanol precipitation. Ethanol precipitation was conducted once more followed by a final resuspension in 100 mM ammonium acetate solution. Overnight dialysis was performed in water at 4 °C, followed by freezing and lyophilization. The purity of the protein was checked using SDS-PAGE and MALDI analysis (S2A, S2B).

Induction of aggregation *in vitro*

To obtain oligomers and fibrils, lyophilized protein was dissolved in a 20 mM phosphate buffer (pH 7.4), and the concentration was adjusted by measuring UV absorption at 276 nm. Using the known extinction coefficient of 5960 M⁻¹cm⁻¹ at 276 nm for pure aS, a final concentration of 350 µM protein was prepared for all the samples that were set for incubation. The samples were incubated under constant shaking 700 rpm at 37 °C in a BR Biochem Thermo Mixer (BITH-100). Aliquots of incubated samples of wS and mS were extracted at certain intervals of incubation for spectroscopic and microscopic analyses.

Circular dichroism spectroscopy

The far-UV circular dichroism (CD) spectra (190–250 nm) were recorded on a JASCO J-815 spectropolarimeter (Jasco)

equipped with a Peltier temperature control unit, using a 1-mm path length cuvette. All of the CD measurements were performed at room temperature (~25 °C), and the buffer background was subtracted. For each sample, three scans were averaged. Then, 350 µM aS stock was prepared by dissolving the lyophilized powder in a 20 mM sodium phosphate buffer with 0.01% sodium azide solution and incubated under constant shaking (700 rpm) at 37 °C. For the CD analysis, prior to spectral acquisition, 15 µL of the stock solution was dissolved in 500 µL of 20 mM sodium phosphate buffers to get a diluted solution of aS with a final concentration of ~10 µM.

Spectral deconvolution was performed by fitting Gaussians at the known peak positions for random coil (189 nm, negative band), alpha helix (208 and 222 nm, negative bands), and beta sheet (218 nm, negative band) using Fityk curve fitting and peak fitting software, and the peak depth/height and half width at half maximum (HWHM) for the fitted Gaussians are listed in Table 1. Area under the curves was computed using the equation: Depth*FWHM/0.76, where FWHM = 2*HWHM.

Thioflavin T fluorescence assay

For ThT fluorescence measurement, a stock solution of 5 mM ThT was prepared in 20 mM sodium phosphate buffer (pH 7.4) and fluorescence measurements were performed using a 10-mm path length quartz cuvette. To measure aggregation kinetics, aliquots of the incubated samples were extracted at certain intervals and diluted with 20 mM sodium phosphate buffer pH 7.4 to a final concentration of 3 µM. The ThT solution was added from 5 mM stock to this oligomer solution to obtain a final concentration of 20 µM ThT. The sample was then mixed thoroughly for acquisition of fluorescence emission spectra. Fluorescence spectra over the 450–560 nm wavelength range were obtained using the PTI fluorescence spectrophotometer with the excitation monochromator set at 440 nm and excitation/emission slits at 5 nm. The averages of three consecutive readings were considered for each sample. The ThT fluorescence peak intensity at 482 nm was plotted against incubation time of the aS samples, and the following equation (Eq. 1) was fitted to the data to analyze aggregation kinetics:

$$F(t) = F_{\max} / (1 + \text{Exp}(-k(t - t_{1/2}))), \quad (1)$$

where F is the ThT fluorescence intensity at time t, t_{1/2} is the lag time, k is the apparent rate constant, and F_{max} is the maximum fluorescence intensity. k, t_{1/2}, and F_{max} are obtained by fitting the equation to F vs. t data.

Further analysis of the slopes of ThT kinetics data was conducted using the Amylofit⁵⁸ webserver (<https://amylofit.com/>).

Atomic force microscopy imaging

For the atomic force microscopy (AFM) study, aliquots were taken from the incubated samples after 24 and 48 h of incubation and diluted to 3.5 µM with distilled water. The diluted sample was then drop-casted on a freshly cleaned muscovite mica substrate and kept at room temperature for drying. Upon drying, the sample was

imaged immediately with a tapping mode of AFM using a Pico plus 5500 AFM (Agilent Technologies, United States) with a piezo scanner having a maximum range of 9 μm . The images were captured with a scan speed of 0.5 line/sec. For image processing, PicoView software was used. The images of cells treated with fibrils were taken using Asylum Research MFP-3D-BIO AFM (Oxford Instruments).

Raman spectroscopy

Raman spectra were recorded using a CTR-300 Raman spectrometer (model from Technos Instruments), which was fitted with a Nikon microscope and 300-mm focal length triple grating monochromator associated with CCD. The grating used was 600 grooves/mm. Then, 20 μL of the incubated protein samples was placed as a droplet onto a glass coverslip and air dried to obtain spectra. A $\sim 50\text{-mW}$ (at source) argon ion laser (532 nm) was focused on the protein-enriched droplet using a $\times 20$ microscope objective (NA = 0.4) of the microscope on the sample. No damage or spectral modifications were observed in the samples under these ambient conditions. The Raman vibrational modes' wavenumbers were calibrated with 520 cm^{-1} of silica wafer focused under the $\times 20$ objective lens, and spectral resolution was found to be $\sim 1\text{ cm}^{-1}$. Spectra were recorded over 370–4000 cm^{-1} with a typical accumulation time of 100 s. Spectra were processed with GRAMS/A1 software.

Cell viability assay (MTT assay)

SH-SY5Y is a human-derived cell line sub-cloned from the original cell line named SK-N-SH. The SH-SY5Y neuron model was created from the original SK-N-SH neuroblastoma cell phenotype, which came from a bone marrow biopsy sample of a patient who was 4 years old at the time of capture. The cell line was obtained from NCL, Pune. Cell culture media was prepared using Dulbecco's modified Eagle's medium (DMEM) with 10% fetal bovine serum (FBS) and 1% penicillin–streptomycin (PS). The cells were cultured in an incubator with 5% carbon dioxide at 37 °C. Then, the cells were processed for cell viability assay. The cell viability assay was carried out using the principle of reduction of 3-(4,5-dimethylthiazol-2-yl)-2,5-diphenyltetrazolium bromide (MTT) by viable cells. For this, the cells were seeded in 96-well plates at 60,000 cells/well and maintained in 200 μL of DMEM supplemented with 10% FBS and 1% PS for 24 h at 37 °C. The cells were treated with different concentrations of monomers/aggregated species. After treatment, the cells were incubated for 24 h at 37 °C and 5% CO_2 , followed by the MTT reduction assay, which was performed as previously described (Banerji et al., 2013). 6-OHDA (6-hydroxydopamine) is used as positive control as it is a standard chemical used in Parkinson's model. All experiments were performed in triplicate, and the relative cell viability (%) was expressed as a percentage relative to the untreated cell control. Statistical data analysis was performed using one-way ANOVA

analysis (Tukey's *post hoc* test) in the GraphPad Prism 9 software, where ns, non-significant; *, $p \leq 0.05$; **, $p \leq 0.01$; ***, $p \leq 0.001$; ****, $p \leq 0.0001$.

Data availability statement

The raw data supporting the conclusion of this article will be made available by the authors, without undue reservation.

Author contributions

EP and LD conceptualized the project and performed recombinant protein expression, purification, aggregation studies, spectroscopic studies, analyzed the data, and drafted the manuscript. SD performed the molecular dynamics study. AD performed the MTT assay. AM helped with the purification of recombinant proteins. SS and JC helped with the spectroscopic studies. SB helped in analysis of cell viability studies. UP and NM helped in data analysis and edited the manuscript. All authors contributed to the article and approved the submitted version.

Acknowledgments

EP thanks the Council of Scientific and Industrial Research (CSIR), India, for a fellowship. The authors thank the Director and central instrument facility of CSIR-IICB for providing all the instrument facilities.

Conflict of interest

The authors declare that the research was conducted in the absence of any commercial or financial relationships that could be construed as a potential conflict of interest.

Publisher's note

All claims expressed in this article are solely those of the authors and do not necessarily represent those of their affiliated organizations, or those of the publisher, the editors, and the reviewers. Any product that may be evaluated in this article, or claim that may be made by its manufacturer, is not guaranteed or endorsed by the publisher.

Supplementary material

The Supplementary Material for this article can be found online at: <https://www.frontiersin.org/articles/10.3389/fchem.2023.1145877/full#supplementary-material>

References

- Alderson, T. R., and Markley, J. L. (2013). Biophysical characterization of α -synuclein and its controversial structure. *Intrinsically Disord. Proteins* 1, e26255. doi:10.4161/idp.26255
- Anderson, J. P., Walker, D. E., Goldstein, J. M., Laat, R., Banducci, K., Caccavello, R. J., et al. (2006). Phosphorylation of ser-129 is the dominant pathological modification of α -synuclein in familial and sporadic Lewy body disease *. *J. Biol. Chem.* 281, 29739–29752. doi:10.1074/jbc.M600933200
- Aniszewska, A., Bergström, J., Ingelsson, M., and Ekmark-Lewén, S. (2022). Modeling Parkinson's disease-related symptoms in alpha-synuclein overexpressing mice. *Brain Behav.* 12, e2628. doi:10.1002/brb3.2628
- Apetri, M. M., Maiti, N. C., Zagorski, M. G., Carey, P. R., and Anderson, V. E. (2006). Secondary structure of α -synuclein oligomers: Characterization by Raman and atomic force microscopy. *J. Mol. Biol.* 355, 63–71. doi:10.1016/j.jmb.2005.10.071
- Appel-Cresswell, S., Vilarino-Guell, C., Encarnacion, M., Sherman, H., Yu, L., Shah, B., et al. (2013). Alpha-synuclein p.H50Q, a novel pathogenic mutation for Parkinson's disease. *Mov. Disord.* 28, 811–813. doi:10.1002/mds.25421
- Banerji, B., Pramanik, S. K., Pal, U., and Maiti, N. C. (2013). Potent anticancer activity of cystine-based dipeptides and their interaction with serum albumins. *Chem. Cent. J.* 7 (91), 91. doi:10.1186/1752-153x-7-91
- Bartels, T., Ahlstrom, L. S., Leftin, A., Kamp, F., Haass, C., Brown, M. F., et al. (2010). The N-terminus of the intrinsically disordered protein α -synuclein triggers membrane binding and helix folding. *J. J.* 99, 2116–2124. doi:10.1016/j.bpj.2010.06.035
- Brundin, P., Melki, R., and Kopito, R. (2010). Prion-like transmission of protein aggregates in neurodegenerative diseases. *Nat. Rev. Mol. Cell Biol.* 11, 301–307. doi:10.1038/nrm2873
- Burré, J. (2022). The synaptic function of α -synuclein. *J. Park. Dis.* 5, 699–713. doi:10.3233/jpd-150642
- Burré, J., Sharma, M., and Südhof, T. C. (2018). Cell Biology and pathophysiology of α -synuclein. *Cold Spring Harb. Perspect. Med.* 8, a024091. doi:10.1101/cshperspect.a024091
- Burré, J., Sharma, M., and Südhof, T. C. (2014). α -Synuclein assembles into higher-order multimers upon membrane binding to promote SNARE complex formation. *Proc. Natl. Acad. Sci.* 111, E4274–E4283. doi:10.1073/pnas.1416598111
- Burré, J., Sharma, M., Tssetsenis, T., Buchman, V., Etherton, M. R., and Südhof, T. C. (2010). α -Synuclein promotes SNARE-complex assembly *in vivo* and *in vitro*. *Science* 329, 1663–1667. doi:10.1126/science.1195227
- Chandra, B., Korn, A., Maity, B. K., Adler, J., Rawat, A., Krueger, M., et al. (2017). Stereoisomers probe steric zippers in amyloid- β . *J. Phys. Chem. B* 121, 1835–1842. doi:10.1021/acs.jpcc.6b12332
- Chartier-Harlin, M.-C., Kachergus, J., Roumier, C., Mouroux, V., Douay, X., Lincoln, S., et al. (2004). α -synuclein locus duplication as a cause of familial Parkinson's disease. *Engl* 364, 1167–1169. doi:10.1016/s0140-6736(04)17103-1
- Cox, D., Whiten, D. R., Brown, J. W. P., Horrocks, M. H., San Gil, R., Dobson, C. M., et al. (2018). The small heat shock protein Hsp27 binds α -synuclein fibrils, preventing elongation and cytotoxicity. *J. Biol. Chem.* 293, 4486–4497. doi:10.1074/jbc.m117.813865
- Das, S., Pal, U., Das, S., Bagga, K., Roy, A., Mrigwani, A., et al. (2014). Sequence complexity of amyloidogenic regions in intrinsically disordered human proteins. *PLoS ONE* 9, e89781. doi:10.1371/journal.pone.0089781
- Dolui, S., Mondal, A., Roy, A., Pal, U., Das, S., Saha, A., et al. (2020). Order, disorder, and reorder state of lysozyme: Aggregation mechanism by Raman spectroscopy. *J. Phys. Chem. B* 124, 50–60. doi:10.1021/acs.jpcc.9b09139
- Emamzadeh, F. N. (2016). Alpha-synuclein structure, functions, and interactions. *J. Res. Med. Sci. Off. J. Isfahan Univ. Med. Sci.* 21, 29. doi:10.4103/1735-1995.181989
- Fields, C. R., Bengoa-Vergniory, N., and Wade-Martins, R. (2019). Targeting alpha-synuclein as a therapy for Parkinson's disease. *Front. Mol. Neurosci.* 12. doi:10.3389/fnmol.2019.00299
- Flagmeier, P., Meisl, G., Vendruscolo, M., Knowles, T. P. J., Dobson, C. M., Buell, A. K., et al. (2016). Mutations associated with familial Parkinson's disease alter the initiation and amplification steps of α -synuclein aggregation. *Proc. Natl. Acad. Sci.* 113, 10328–10333. doi:10.1073/pnas.1604645113
- Flynn, J. D., McGlinchey, R. P., Walker, R. L., and Lee, J. C. (2018). Structural features of α -synuclein amyloid fibrils revealed by Raman spectroscopy. *J. Biol. Chem.* 293, 767–776. doi:10.1074/jbc.m117.812388
- Fujiwara, H., Hasegawa, M., Dohmae, N., Kawashima, A., Masliha, E., Goldberg, M. S., et al. (2002). α -Synuclein is phosphorylated in synucleinopathy lesions. *Nat. Cell Biol.* 4, 160–164. doi:10.1038/ncb748
- Gasteiger, E., Hoogland, C., Gattiker, A., Duvaud, S., Wilkins, M. R., Appel, R. D., et al. (2005). "Protein identification and analysis tools on the ExPASy server," in the proteomics protocols handbook. *J. M. Walk. (Humana Press)* 22, 571–607. doi:10.1385/1-59259-890-0%3A571
- Ghanem, S. S., Majbour, N. K., Vaikath, N. N., Ardah, M. T., Erskine, D., Jensen, N. M., et al. (2022). α -Synuclein phosphorylation at serine 129 occurs after initial protein deposition and inhibits seeded fibril formation and toxicity. *Proc. Natl. Acad. Sci.* 119, e2109617119. doi:10.1073/pnas.2109617119
- Gonçalves, S., and Outeiro, T. F. (2013). Assessing the subcellular dynamics of alpha-synuclein using photoactivation microscopy. *Mol. Neurobiol.* 47, 1081–1092. doi:10.1007/s12035-013-8406-x
- González, N., Arcos-López, T., König, A., Quintanar, L., Menacho Márquez, M., Outeiro, T. F., et al. (2019). Effects of alpha-synuclein post-translational modifications on metal binding. *J. Neurochem.* 150, 507–521. doi:10.1111/jnc.14721
- Guo, J. L., Covell, D. J., Daniels, J. P., Iba, M., Stieber, A., Zhang, B., et al. (2013). Distinct α -synuclein strains differentially promote tau inclusions in neurons. *Cell* 154, 103–117. doi:10.1016/j.cell.2013.05.057
- Hawk, B. J. D., Khounlo, R., and Shin, Y.-K. (2019). Alpha-synuclein continues to enhance SNARE-dependent vesicle docking at exorbitant concentrations. *Front. Neurosci.* 13, 216. doi:10.3389/fnins.2019.00216
- Honarmand, S., Dabirmanesh, B., Amanlou, M., and Khajeh, K. (2019). The interaction of several herbal extracts with α -synuclein: Fibril formation and surface plasmon resonance analysis. *PLOS ONE* 14, e0217801. doi:10.1371/journal.pone.0217801
- Jia, C., Ma, X., Liu, Z., Gu, J., Zhang, X., Li, D., et al. (2019). Temperature-dependent electrical transport properties of individual NiCo₂O₄ nanowire. *Neurosci* 13, 1124. doi:10.1186/s11671-018-2844-3
- Kim, T. D., Choi, E., Rhim, H., Paik, S. R., and Yang, C.-H. (2004). α -Synuclein has structural and functional similarities to small heat shock proteins. *Biochem. Biophys. Res. Commun.* 324, 1352–1359. doi:10.1016/j.bbrc.2004.09.208
- Kurouski, D., Duyn, R. P. V., and Lednev, I. K. (2015). Exploring the structure and formation mechanism of amyloid fibrils by Raman spectroscopy: A review. *Analyst* 140, 4967–4980. doi:10.1039/c5an00342c
- Kuusisto, E., Parkkinen, L., and Alafuzoff, I. (2003). Morphogenesis of Lewy bodies: Dissimilar incorporation of alpha-synuclein, ubiquitin, and p62. *J. Neuropathol. Exp. Neurol.* 62, 1241–1253. doi:10.1093/jnen/62.12.1241
- Lautenschläger, J., Stephens, A. D., Fusco, G., Ströhl, F., Curry, N., Zacharopoulou, M., et al. (2018). C-terminal calcium binding of α -synuclein modulates synaptic vesicle interaction. *Nat. Commun.* 9, 712. doi:10.1038/s41467-018-03111-4
- Lázaro, D. F., Rodrigues, E. F., Langohr, R., Shahpasandzadeh, H., Ribeiro, T., Guerreiro, P., et al. (2014). Systematic comparison of the effects of alpha-synuclein mutations on its oligomerization and aggregation. *PLOS Genet.* 10, e1004741. doi:10.1371/journal.pgen.1004741
- Liu, C., Liu, K., Wang, C., Liu, H., Wang, H., Su, H., et al. (2020). Elucidating heterogeneous photocatalytic superiority of microporous porphyrin organic cage. *Nat. Commun.* 11, 1047. doi:10.1038/s41467-020-14831-x
- Luth, E. S., Bartels, T., Dettmer, U., Kim, N. C., and Selkoe, D. J. (2015). Purification of α -synuclein from human brain reveals an instability of endogenous multimers as the protein approaches purity. *Biochemistry* 54, 279–292. doi:10.1021/bi501188a
- Mahapatra, A., Sarkar, S., Biswas, S. C., and Chattopadhyay, K. (2019). An aminoglycoside antibiotic inhibits both lipid-induced and solution-phase fibrillation of α -synuclein *in vitro*. *Chem. Commun.* 55, 11052–11055. doi:10.1039/c9cc04251b
- Maiti, N. C., Apetri, M. M., Zagorski, M. G., Carey, P. R., and Anderson, V. E. (2004). Raman spectroscopic characterization of secondary structure in natively unfolded Proteins: α -synuclein. *J. Am. Chem. Soc.* 126, 2399–2408. doi:10.1021/ja0356176
- Maroteaux, L., Campanelli, J. T., and Scheller, R. (1988). Synuclein: A neuron-specific protein localized to the nucleus and presynaptic nerve terminal. *J. Neurosci. Off. J. Soc. Neurosci.* 8, doi:10.1523/JNEUROSCI.08-08-02804.1988
- Marvan, A. T., Aliakbari, F., Mohammad-Beigi, H., Ahmadi, Z. A., Mehrpooyan, S., Lermyte, F., et al. (2020). The status of the terminal regions of α -synuclein in different forms of aggregates during fibrillization. *J. Biol. Macromol.* 155, 543–550. doi:10.1016/j.ijbiomac.2020.03.238
- McFarland, N. R., Fan, Z., Xu, K., Schwarzschild, M. A., Feany, M. B., Hyman, B. T., et al. (2009). α -Synuclein S129 phosphorylation mutants do not alter nigrostriatal toxicity in a rat model of Parkinson disease. *J. Neuropathol. Exp. Neurol.* 68, 515–524. doi:10.1097/nen.0b013e3181a24b53
- McLean, P. J., Kawamata, H., Shariff, S., Hewett, J., Sharma, N., Ueda, K., et al. (2002). TorsinA and heat shock proteins act as molecular chaperones: Suppression of alpha-synuclein aggregation. *J. Neurochem.* 83, 846–854. doi:10.1046/j.1471-4159.2002.01190.x
- Meisl, G., Kirkegaard, J., Arosio, P., Michaels, T. C. T., Vendruscolo, M., Dobson, C. M., et al. (2016). Molecular mechanisms of protein aggregation from global fitting of kinetic models. *Nat. Protoc.* 11, 252–272. doi:10.1038/nprot.2016.010
- Okochi, M., Walter, J., Koyama, A., Nakajo, S., Baba, M., Iwatsubo, T., et al. (2000). Constitutive phosphorylation of the Parkinson's disease associated alpha-synuclein. *J. Biol. Chem.* 275, 390–397. doi:10.1074/jbc.275.1.390

- Oueslati, A. (2016). Implication of alpha-synuclein phosphorylation at S129 in synucleinopathies: What have we learned in the last decade? *J. Park. Dis.* 6, 39–51. doi:10.3233/jpd-160779
- Pal, U., Maity, M., Khot, N., Das, S., Das, S., Dolui, S., et al. (2016a). Statistical insight into the binding regions in disordered human proteome. *J. Proteins Proteomics* 7, 47–60.
- Pal, U., Roy, A., Das, S., Das, S., Kundu, M., Bagga, K., et al. (2016b). Origin of protein aggregation: Identification of some characteristic traits in structured and intrinsically disordered proteins. *J. Proteins Proteomics* 7, 259–268.
- Pinho, R., Paiva, I., Jerčić, K. G., Fonseca-Ornelas, L., Gerhardt, E., Fahlbusch, C., et al. (2019). Nuclear localization and phosphorylation modulate pathological effects of alpha-synuclein. *Hum. Mol. Genet.* 28, 31–50. doi:10.1093/hmg/ddy326
- Romero, P., Obradovic, Z., Kissinger, C., Villafranca, J. E., and Dunker, A. K. (1997). "Identifying disordered regions in proteins from amino acid sequence," in Proceedings of International Conference on Neural Networks, Houston, TX, USA, 12–12 June 1997, 90–95.
- Schapira, A. H. V., Chaudhuri, K. R., and Jenner, P. (2017). Non-motor features of Parkinson disease. *Nat. Rev. Neurosci.* 18, 435–450. doi:10.1038/nrn.2017.62
- Schmid, A. W., Fauvet, B., Moniatte, M., and Lashuel, H. A. (2013). Alpha-synuclein post-translational modifications as potential biomarkers for Parkinson disease and other synucleinopathies. *Mol. Cell. Proteomics* 12, 3543–3558. doi:10.1074/mcp.r113.032730
- Smith, W. W., Margolis, R. L., Li, X., Troncoso, J. C., Lee, M. K., Dawson, V. L., et al. (2005). Alpha-synuclein phosphorylation enhances eosinophilic cytoplasmic inclusion formation in SH-SY5Y cells. *J. Neurosci.* 25, 5544–5552. doi:10.1523/JNEUROSCI.0482-05.2005
- Spillantini, M. G., Schmidt, M. L., Lee, V. M., Trojanowski, J. Q., Jakes, R., and Goedert, M. (1997). α -Synuclein in Lewy bodies. *Nature* 388, 839–840. doi:10.1038/42166
- Srivastava, A., Singh, P. K., Kumbhakar, M., Mukherjee, T., Chattopadhyay, S., Pal, H., et al. (2010). Identifying the bond responsible for the fluorescence modulation in an amyloid fibril sensor. *Eur. J.* 16, 9257–9263. doi:10.1002/chem.200902968
- Stephens, A. D., Zacharopoulou, M., Moons, R., Fusco, G., Seetaloo, N., Chiki, A., et al. (2020). Extent of N-terminus exposure of monomeric alpha-synuclein determines its aggregation propensity. *Nat. Commun.* 11, 2820. doi:10.1038/s41467-020-16564-3
- Stsiapura, V. I., Maskevich, A. A., Kuzmitsky, V. A., Turoverov, K. K., and Kuznetsova, I. M. (2007). Computational study of thioflavin T torsional relaxation in the excited state. *J. Phys. Chem. A* 111, 4829–4835. doi:10.1021/jp070590o
- Takahashi, M., Kanuka, H., Fujiwara, H., Koyama, A., Hasegawa, M., Miura, M., et al. (2003). Phosphorylation of alpha-synuclein characteristic of synucleinopathy lesions is recapitulated in alpha-synuclein transgenic *Drosophila*. *Neurosci. Lett.* 336, 155–158. doi:10.1016/s0304-3940(02)01258-2
- Vivian, J. T., and Callis, P. R. (2001). Mechanisms of tryptophan fluorescence shifts in proteins. *Biophys. J.* 80, 2093–2109. doi:10.1016/s0006-3495(01)76183-8
- Voropai, E. S., Samtsov, M. P., Kaplevskii, K. N., Maskevich, A. A., Stepuro, V. I., Povarova, O. I., et al. (2003). Spectral properties of thioflavin T and its complexes with amyloid fibrils. *J. Appl. Spectrosc.* 70, 868–874. doi:10.1023/b:japs.0000016303.37573.7e
- Wang, C., Ma, Z., Yan, D.-Y., Liu, C., Deng, Y., Liu, W., et al. (2018). Alpha-synuclein and calpains disrupt SNARE-mediated synaptic vesicle fusion during manganese exposure in SH-SY5Y cells. *Cells* 7, 258. doi:10.3390/cells7120258
- Winner, B., Jappelli, R., Maji, S. K., Desplats, P. A., Boyer, L., Aigner, S., et al. (2011). *In vivo* demonstration that α -synuclein oligomers are toxic. *Proc. Natl. Acad. Sci.* 108, 4194–4199. doi:10.1073/pnas.1100976108
- Xu, L., Pu, J., Li, Y., Wang, L., and Gao, C. (2016). Alpha-synuclein in Parkinson's disease: From pathogenetic dysfunction to potential clinical application. *Park. Dis.* 1720621. 10–18. doi:10.1016/j.chroma.2016.11.005
- Zhang, J., Li, X., and Li, J.-D. (2019). The roles of post-translational modifications on α -synuclein in the pathogenesis of Parkinson's diseases. *Front. Neurosci.* 13. doi:10.3389/fnins.2019.00381



OPEN ACCESS

EDITED BY

Xiao-Peng He,
East China University of Science and
Technology, China

REVIEWED BY

Mingle Li,
Korea University, Republic of Korea
Adam Sedgwick,
University of Oxford, United Kingdom

*CORRESPONDENCE

Hyo Sung Jung,
✉ hs0101j@uhs.ac.kr

[†]These authors have contributed equally
to this work

RECEIVED 25 April 2023

ACCEPTED 30 May 2023

PUBLISHED 08 June 2023

CITATION

Hwang E, Yun M and Jung HS (2023),
Mitochondria-targeted organic
sonodynamic therapy agents: concept,
benefits, and future directions.
Front. Chem. 11:1212193.
doi: 10.3389/fchem.2023.1212193

COPYRIGHT

© 2023 Hwang, Yun and Jung. This is an
open-access article distributed under the
terms of the [Creative Commons
Attribution License \(CC BY\)](#). The use,
distribution or reproduction in other
forums is permitted, provided the original
author(s) and the copyright owner(s) are
credited and that the original publication
in this journal is cited, in accordance with
accepted academic practice. No use,
distribution or reproduction is permitted
which does not comply with these terms.

Mitochondria-targeted organic sonodynamic therapy agents: concept, benefits, and future directions

Eunbin Hwang^{1†}, Minjae Yun^{2†} and Hyo Sung Jung^{2*}

¹Department of Gerontology (AgeTech-Service Convergence Major), Graduate School of East-West Medical Science, Kyung Hee University, Yongin, Republic of Korea, ²Department of Biomedical & Chemical Sciences, Hyupsung University, Hwasung, Republic of Korea

Sonodynamic therapy (SDT) is an emerging and potentially less invasive therapeutic approach for cancer that employs ultrasound (US)-sensitive agents combined with US irradiation to generate cytotoxic reactive oxygen species (ROS) in deep tumor regions. Among various cellular organelles, the mitochondria are particularly susceptible to ROS, making them an attractive target for SDT. Organic-based SDT agents with mitochondria-targeting affinity have gained considerable interest as potential alternatives to conventional SDT agents, offering significant advantages in the field of SDT. However, to date, a comprehensive review focusing on mitochondria-targeted SDT agents has not yet been published. In this review, we provide an overview of the general concept, importance, benefits, and limitations of mitochondria-targeted organic SDT agents in comparison to conventional SDT methods. Finally, we discuss the current challenges and future directions for the design and development of efficient SDT agents. By addressing these issues, we aim to stimulate further research and advancements in the field of mitochondria-targeted SDT, ultimately facilitating the translation of these agents into clinical applications.

KEYWORDS

sonodynamic therapy, mitochondria-targeting, organic-based agents, cancer therapy, reactive oxygen species

1 Introduction

Sonodynamic therapy (SDT) represents a newly-emerging treatment modality in clinical settings that offers the possibility of less-invasive and selective eradication of deep-seated tumors (Son et al., 2020). SDT is based on ultrasound (US) irradiation of US-sensitive agents (also called SDT agents), that when in the presence of O₂ or water, generates cytotoxic reactive oxygen species (ROS), thereby activating apoptosis of cancer cells. Simultaneously, the shear force activated by the US-mediated cavitation effect damages cancer cells through mechanical stress (Rengeng et al., 2017). While several studies have focused on finding or developing SDT agents, traditional SDT agents have shown limited therapeutic effects and safety concerns (Son et al., 2020; Zhang et al., 2021). Therefore, there is still a need for more advanced SDT agents and proven technologies for clinical application.

Organic-based agents offer satisfactory biocompatibility and are easy to prepare/modify, making them an attractive option to improve the therapeutic outcomes through enhanced or targeted cytotoxic ROS (Xing et al., 2021). However, major ROS typically have a very short half-life (singlet oxygen (¹O₂) and superoxide (•O₂): 10⁻⁶ s; hydroxyl radical (•OH): 10⁻⁹ s) (Rubio

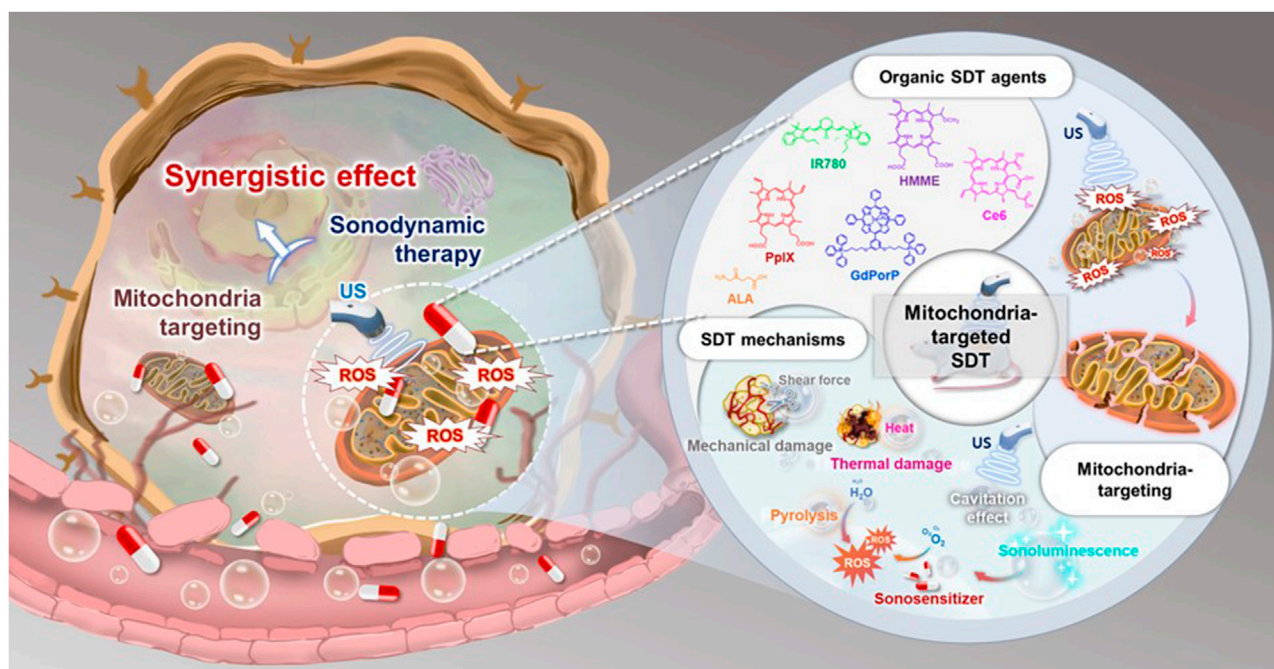


FIGURE 1
Overview of mitochondria-targeted organic SDT agents.

and Cerón, 2021), limiting their action to sites of production (<20 nm), which are much smaller than the size of cancer cells (Kim et al., 2014). This poses a significant challenge that needs to be overcome to fully harness the benefits of SDT. Therefore, delivering organic SDT agents to cancer cells, particularly to critical subcellular organelles vulnerable to ROS, could be a promising strategy to improve SDT therapeutic outcomes. Considering this, substantial efforts have been devoted to studying of new organic SDT agents, especially those capable of delivering ROS to specific affected biological sites, such as mitochondria, in a precise manner (Fulda et al., 2010).

Mitochondria, as preferential organelle targets for improved therapeutic outcomes, not only play a key role in tumor apoptosis or survival but are also highly susceptible to excessive ROS generated by SDT (Lockman et al., 2010; Bacellar et al., 2019; Chen et al., 2019). Mitochondria-targeted US-sensitive organic agents have recently gained attention as a potential complement to traditional agents, offering important advantages such as enhanced antitumor efficacy (Zhang et al., 2020; Li et al., 2022), activation of antitumor immune responses (Ren et al., 2021; Shi et al., 2023), and overcoming multiple SDT challenges (e.g., metastasis) (Han et al., 2021; Ji et al., 2021). These agents can also serve as multimodal approaches, combining SDT with other imaging-guided modalities such as photoacoustic (PA) imaging, magnetic resonance (MR) imaging, fluorescence (FL) imaging, etc. (Zhang et al., 2019; Ren et al., 2021). Targeting ligands in the mitochondria of cancer cells involve triphenylphosphonium (TPP) (Song et al., 2019), which has been applied in SDT agents utilizing hematoporphyrin monomethyl ether (HMME) (Chen et al., 2017), chlorin e6 (Ce6) (Cao et al., 2023), among others, as the sonodynamic payload. Furthermore, some US-sensitive agents, such as IR780 (Zhang et al., 2019) and protoporphyrin IX (PpIX)

(Xie et al., 2017), as well as adipocyte-derived organelle lipid droplets (LDs) (Shi et al., 2023), with inherent mitochondria-targeting affinity, are being investigated for this purpose.

Ideally, mitochondria-targeted organic SDT agents should meet the following significant requirements (Figure 1): 1) achieving excellent anticancer efficacy by selecting high-efficiency organic SDT agents; 2) appropriately modifying the agents using suitable methods for US-mediated ROS generation targeting both tumor cells and specific mitochondria, through modifications in the composition of the agents, introducing mitochondria-targeting moieties to the agents and creating activatable agents for mitochondria specific environments; 3) minimizing the dark toxicity of agents; 4) rapid disintegration after SDT application to avoid adverse effects; and 5) easy preparation and modification at a low cost.

Despite several reports on newly-emerging agents with mitochondrial affinity in recent years, no comprehensive review papers regarding these agents have been published thus far. Therefore, this review focuses on the recent advances in mitochondrial SDT agents, covering their general principle, importance, benefits, and challenges compared to the traditional SDT methods. We herein summarize the agent types, experimental conditions, *in vitro* anticancer efficacies, and their therapeutic strategies, as shown in Table 1.

2 Working principle of sonodynamic therapy

SDT agents can be activated by several mechanisms, including light-induced sonoluminescence (SL), increased acoustic cavitation,

TABLE 1 Mitochondria-targeted organic SDT agents for cancer therapy.

SDT agent	Probe construction	US irradiation	Cell viability (off-target vs. mitochondria-targeted SDT)	Therapeutic strategy	Reference
IR780	PFP/IR780 core-shell nanodroplets (IR780-NDs)	3 min	<40% for IR780-NDs vs. >90% for NDs (w/o IR780) cell viability of 4T1 cells at 121 µg/mL	Combination of mitochondria-targeted SDT, deep penetration, and FL/PA imaging visualization	Zhang et al. (2019)
		650 kHz			
		2.4 W/cm ²			
IR780	R162/IR780 TPP-based lipid bilayer (MLipRIR NPs)	1 min	16.4% for MLipRIR NPs vs. 27.6% for LipRIR NPs (w/o TPP) cell viability of 4T1 cells at 1 µg/mL (R162 conc.)	Combination of mitochondrial SDT and immunotherapy (w/R162)	Ren et al. (2021)
		1.0 MHz			
		1.5 W/cm ²			
		50% duty cycle			
IR780	HSA-NO/FDC nano-formulation (PIH-NO)	1 min	30% for PIH-NO vs. 50% for PIH (w/o HSA-NO) and 70% for IH (w/o HSA-NO and FDC) cell viability of 4T1 cells at 4 µg/mL (IR780 conc.)	Combination of mitochondria-targeted SDT and gas therapy (w/HSA-NO and FDC)	Ji et al. (2021)
		1.0 MHz			
		1.5 W/cm ² 50% duty cycle			
IR780	IR780/CPI-613/adipocyte-derived organelle LDs (CPI-613/IR780@LDs)	1 min	<40% for CPI-613/IR780@LDs cell viability of both normoxic and hypoxic Panc02 cells at 20 µmol/L	Combination of mitochondria-targeted SDT and metabolic modulation therapy (w/CPI-613)	Shi et al. (2023)
		1 MHz			
		0.5 W/cm ²			
		50% duty cycle			
ALA	ALA/2-DG/MB	5 min	33.2% for ALA/2-DG/MB vs. 49.2% for ALA/2-DG cell viability of HepG2 cells at 2 mmol/L (2-DG)	Combination of mitochondria-targeted SDT, metabolic modulation therapy (w/2-DG), and US-stimulated microbubble therapy (w/MB)	Xie et al. (2017)
		3 MHz			
		2 W/cm ²			
		60% duty cycle			
HMME	HMME/TPP-Chol liposome (HMME-Lipo-TPP)	3 min	~32% for HMME-Lipo-TPP vs. ~44% for HMME-Lipo (w/o TPP) cell viability of MCF-7 cells at 20 µg/mL	US-assisted increased cancer cells mitochondria delivery	Chen et al. (2017b)
		1 MHz			
		0.5 W/cm ²			
Ce6	TPP-Ce6/PL/EV (EV (TPP-Ce6/PL))	1 min	~6.5% for EV (TPP-Ce6/PL) vs. ~30% for EV (TPP-Ce6) and ~70% for TPP-Ce6 cell viability of MCF-7 cells at 10 µM (TPP-Ce6 (or Ce6) conc.)	Combination of mitochondria-targeted SDT and chemotherapy (w/PL)	Cao et al. (2023)
		1 MHz			
		0.3 W/cm ²			
IR780/HMME	IR780/HMME/GOx/PLGA core-shell nano-formulation (IHG@P)	30 s	8.48% for IHG@P vs. ~68% for starvation therapy alone and ~58% for SDT therapy alone cell viability of 4T1 cells at 60 µg/mL (PLGA conc.)	Combination of mitochondria-targeted dual SDT agent therapy, starvation therapy (w/GOx), and FL/PA imaging visualization	Zhang et al. (2020)
		2 W/cm ²			
IR780/Ce6	PEG-IR780/Ce6 nano-micelle (PEG-IR780@Ce6)	3 min	35% for PEG-IR780@Ce6 vs. 85% for free Ce6 and 43% for PEG-IR780 cell viability of MDA-MB-231 cells at 40 µg/mL	Mitochondria-targeted dual SDT agent therapy	Han et al. (2021)
		1 MHz			
		0.6 W/cm ²			
		50% duty rate)			
Gd(III)-porphyrinate	TPP-Gd(III) porphyrinate/MAL-PEG- <i>b</i> -PDPA pH-responsive nanomicelle (RPGdP)	1 min	25% for RPGdP vs. 65% for RPGd (w/o TPP) cell viability of H22 cancer cells at 80 µg/mL	Combination of mitochondria-targeted SDIT and MR imaging visualization	Li et al. (2022)
		1 MHz			
		1.5 W/cm ²			

[Abbreviation] PFP: perfluoropentane, NDs: nanodroplets, w/o: without, PA: photoacoustic, FL: fluorescence, MR: magnetic resonance, R162: glutamate dehydrogenase 1 inhibitor, TPP: triphenylphosphonium, conc.: concentration, HSA-NO: human serum albumin-based NO donor, FDC: perfluorodecalin, CPI-613: FDA-approved TCA cycle inhibitor, LDs: lipid droplets, w/: with, ALA: 5-aminolevulinic acid, 2-DG: glycolysis inhibitor 2-deoxyglucose, MB: microbubble, HMME: hematoporphyrin monomethyl ether, Chol: cholesterol, Ce6: Chlorin e6, PL: prooxidant piperlongumine, EV: extracellular vesicle, GOx: glucose oxidase, PLGA: polylactic-co-glycolic acid, SDIT: sonodynamic immunotherapy SDT: sonodynamic therapy.

and pyrolytic reactions. During SDT, ultrasonic waves create cavitation bubbles that absorb the energy of the sound waves. As the energy is released, the bubbles collapse, generating a high-pressure-high-temperature environment of over 81 MPa and 10,000 K in the affected area.

First, this phenomenon produces SL, which can excite the electron orbitals of the SDT agent via sound energy transfer; SL can generate electron holes, which can subsequently pair with the generated ROS, such as $\bullet\text{O}_2$, $\bullet\text{OH}$, or $^1\text{O}_2$ (Saksena and Nyborg, 1970).

Second, increased acoustic cavitation directly excites the agents to generate two types of ROS by different reactions (Costley et al., 2015; Canavese et al., 2018): 1) the energy released from excited SDT agents to the singlet ground state can be transferred to ambient oxygen to generate $^1\text{O}_2$, which is considered a major mediator of SDT; 2) excited-state SDT agents can react directly with other adjacent substrates or oxygens to convert hydrogen atoms into free radicals.

Third, the collapse of cavitation bubbles also provides enough energy to pyrolyze water and subsequently generate hydroxyl radicals ($\bullet\text{OH}$) (Riesz et al., 1992). Furthermore, the locally elevated temperature and the cavitation energy can decompose the SDT agent and generate free radicals, such as $\bullet\text{O}_2$ and $\bullet\text{OH}$ (Qian et al., 2016).

Ultimately, the produced ROS causes increased oxidative stress, resulting in irreversible cellular damage. Moreover, the shear forces and heat generated by the collapse of cavitation bubbles in the focal region result in severe mechanical and heat-shock damage to the cell membrane and cytoskeleton, culminating in cancer cell apoptosis.

3 General principle of mitochondria targeting

Mitochondria, commonly referred to as the cell's powerhouse, are double-membrane cell organelles with their own double-stranded circular mitochondrial DNA (mtDNA) (Murphy et al., 2018). The mitochondrial transmembrane potential (MTP) value is around -140 mV in the normal cell inner membrane, while it is significantly increased in tumor cells (~ 220 mV) (Huang et al., 2021). Therefore, SDT agents with strong delocalized positive potential and lipophilicity can effectively cross the cancer mitochondrial lipid bilayer membrane and accumulate within the mitochondria by hundreds of folds due to the high negative inner membrane potential. Mitochondrial disruption regulates the endogenous pathway to apoptosis, promoting caspase 3 expression and the production of cytochrome c, the main effectors of cell apoptosis (Bhatti et al., 2017).

Precise targeting of cancer cell mitochondria using SDT agents has already been accomplished in several studies (Chen et al., 2017; Xie et al., 2017; Zhang et al., 2019; Zhang et al., 2020; Han et al., 2021; Li et al., 2022; Cao et al., 2023). TPP, with a strong positive potential and lipophilicity, is the most frequently used agent for this purpose (Song et al., 2019). Additionally, a few US-sensitive agents such as IR780 (Zhang et al., 2019) and PpIX (Xie et al., 2017), and adipocyte-derived organelle LDs (Shi et al., 2023), with their inherent targeting ability, are being explored. Moreover, a variety of agents can be delivered to the mitochondria for SDT using various techniques (Li

and Huang, 2020). For example, small molecule ligands such as glycyrrhetic acid and guanidine can be used, as well as mitochondrial penetrating peptides, Szeto–Schiller peptides, and mitochondrial targeting sequences. Additionally, vehicle-type mitochondrial targeted systems such as MITO-Porter vehicles can be utilized for this purpose.

4 Mitochondria-targeted organic SDT agents

4.1 IR780-based SDT agents

IR780 is a lipophilic heptamethine cyanine agent with lipophilic properties that has been clinically employed in FL/PA imaging-guided procedures (Li et al., 2018). IR780 exhibits an inherent ability to target tumor cells and mitochondria, allowing for deep tumor penetration without the need for additional mitochondria-targeting moieties due to its lipophilic cationic property (Wang et al., 2014). Additionally, IR780 demonstrates significant SDT properties (Chen et al., 2017); however, it is characterized by limited water solubility and poor photostability. Despite these limitations, the combination of IR780 with FL/PA imaging approaches holds promise for imaging-guided SDT in deep tumors (Cheng et al., 2015).

In 2019, Zhang et al. (2019) developed IR780-loaded nanodroplets (IR780-NDs) with a well-designed core-shell structure (core: perfluoropentane (PFP); shell: IR780), enabling a US-mediated multifunctional IR780-NDs SDT system with deep penetration, mitochondrial targeting, and simultaneous FL/PA/US imaging abilities (Figure 2). Under US irradiation (3 min, 650 kHz, 2.4 W/cm^2), IR780-NDs penetrated from the tumor surface to its core through the acoustic droplet vaporization (ADV) effect of PFP (Mura et al., 2013; Ho et al., 2017), demonstrating excellent depth of penetration. In comparison to NDs (without IR780), IR780-loaded NDs selectively accumulated in and were activated by mitochondria (0.87 vs. -0.15 Pearson coefficient value, respectively). This targeted accumulation can induce oxidative stress through US-mediated ROS production and resulted in apoptosis of 4T1 cells ($<40\%$ vs. $>90\%$ cell viability, respectively, at $121\text{ }\mu\text{g/mL}$). Moreover, the efficacy of IR-780 NDs was evaluated in 4T1 tumor mouse models, demonstrating enhanced SDT, including FL/US/PA imaging abilities, likely attributed to the mitochondria-targeted SDT effect in cancer cells and amplified by the unique ADV effect of PFP.

Immunogenic cell death (ICD) is a form of cell death that stimulates the release of tumor-specific antigens and danger-associated molecular patterns (DAMPs), triggering a systemic antigen-mediated antitumor immune response (Krysko et al., 2012). Recent studies have suggested that ICD has the potential to enhance the efficacy of SDT (Yue et al., 2019; Li X. et al., 2022). In 2021, Ren et al. (2021) employed mitochondrial-targeting liposomal nanoparticles (MLipRIR NPs) to combine FL/PA multimodal imaging and SDT, reinforced by ICD (Figure 3). The NPs were developed by encapsulating R162 (glutamate dehydrogenase 1 inhibitor) and IR780 within a mitochondria-targetable lipid bilayer, efficiently entering the 4T1 cell and specifically targeting the mitochondria through a TPP moiety modification on the NPs surface. Under US irradiation, IR780 released from MLipRIR NPs generated high levels of ROS, impeding mitochondrial respiration

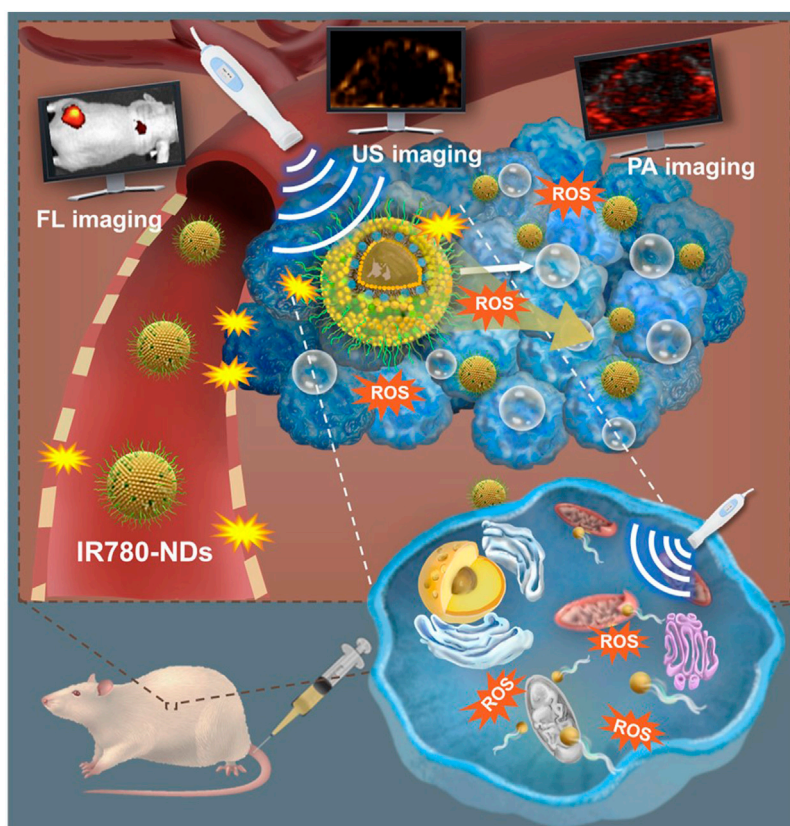


FIGURE 2

Schematic illustration of US-mediated multifunctional IR780-NDs SDT system for deep penetration, mitochondrial targeting, and simultaneous FL/PA/US imaging. Reprinted with permission from ref (Zhang et al., 2019). Copyright (2019) American Chemical Society.

and leading to local glutathione (GSH) consumption. In addition, the co-released R162 inhibited glutamate dehydrogenase 1 (GDH1) by interfering with the anaplerotic use of glutamine in the mitochondrial TCA cycle (Jin et al., 2015). These effects induced ferroptosis of cancer cells through lipid peroxide accumulation, effectively activating ICD. MLipRIR NPs also demonstrated superior US-mediated cytotoxicity in 4T1 cells (16.4% cell viability; R162 concentration = 1 $\mu\text{g/mL}$) relative to LipRIR NPs without TPP moiety modification (27.6% cell viability; R162 concentration = 1 $\mu\text{g/mL}$) under US irradiation (1 min, 1.0 MHz, 1.5 W/cm², 50% duty cycle). By leveraging the bimodal imaging capabilities of MLipRIR NPs, *in vivo* FL/PA multimodal imaging was successfully conducted in the 4T1 mouse models. Furthermore, studies in 4T1 mouse models showed that MLipRIR NPs efficiently reduced tumor size and mitigated severe side effects of cancer treatment on other tissues.

Ji et al. (2021) developed mitochondria-targeted formulations (PIH-NO) by encapsulating IR780 in a human serum albumin-based NO donor (HSA-NO) and an oxygen-carrier perfluorodecalin (FDC), a type of perfluorocarbon (PFC) (Figure 4). PIH-NO accumulated in the 4T1 cell mitochondria (PC = 0.76), leading to mitochondrial dysfunction, relief of hypoxia, and amplified ICD through ROS production, enhanced by the explosive release of NO and O₂ upon US irradiation. Notably, significant cytotoxicity was observed in the PIH-NO (30% cell viability; equivalent

IR780 concentration = 4 $\mu\text{g/mL}$) compared to PIH (without NO donor) (50% cell viability; equivalent IR780 concentration = 4 $\mu\text{g/mL}$) and IH (without NO donor and oxygen-carrier) (70% cell viability; equivalent IR780 concentration = 4 $\mu\text{g/mL}$) under US irradiation conditions (1 min, 1.0 MHz, 1.5 W/cm², 50% duty cycle). Furthermore, observations in 4T1 mouse models indicated that PIH-NO effectively reduced tumor size and significantly decreased the number of pulmonary metastatic nodules. Hence, this study demonstrated the potential of gas transportation to amplify mitochondrial SDT, enhancing its therapeutic efficacy, inducing anticancer immune responses and preventing metastasis.

Shi et al. (2023) developed a novel approach for mitochondrial SDT using adipocyte-derived organelle LDs as carrier agents with an inherent affinity for mitochondria (Figure 5). The developed LDs (CPI-613/IR780@LDs), contained IR780 and CPI-613, a FDA-approved TCA cycle inhibitor. By synergistically inhibiting the mitochondrial TCA cycle and enhancing ROS production at the tumor site, the combination of mitochondrial SDT and CPI-613 enabled efficient mitochondrial SDT in Panc02 tumors. Additionally, combining mitochondrial SDT and anti-PD-1-mediated immunotherapy reinforced the immune response in Panc02 tumors. CPI-613/IR780@LDs demonstrated significantly increased cell cytotoxicity, overcoming the limited efficacy of SDT induced by the hypoxia in the tumor microenvironment (TME) after US irradiation (1 min, 1 MHz, 0.5 W/cm², 50% duty

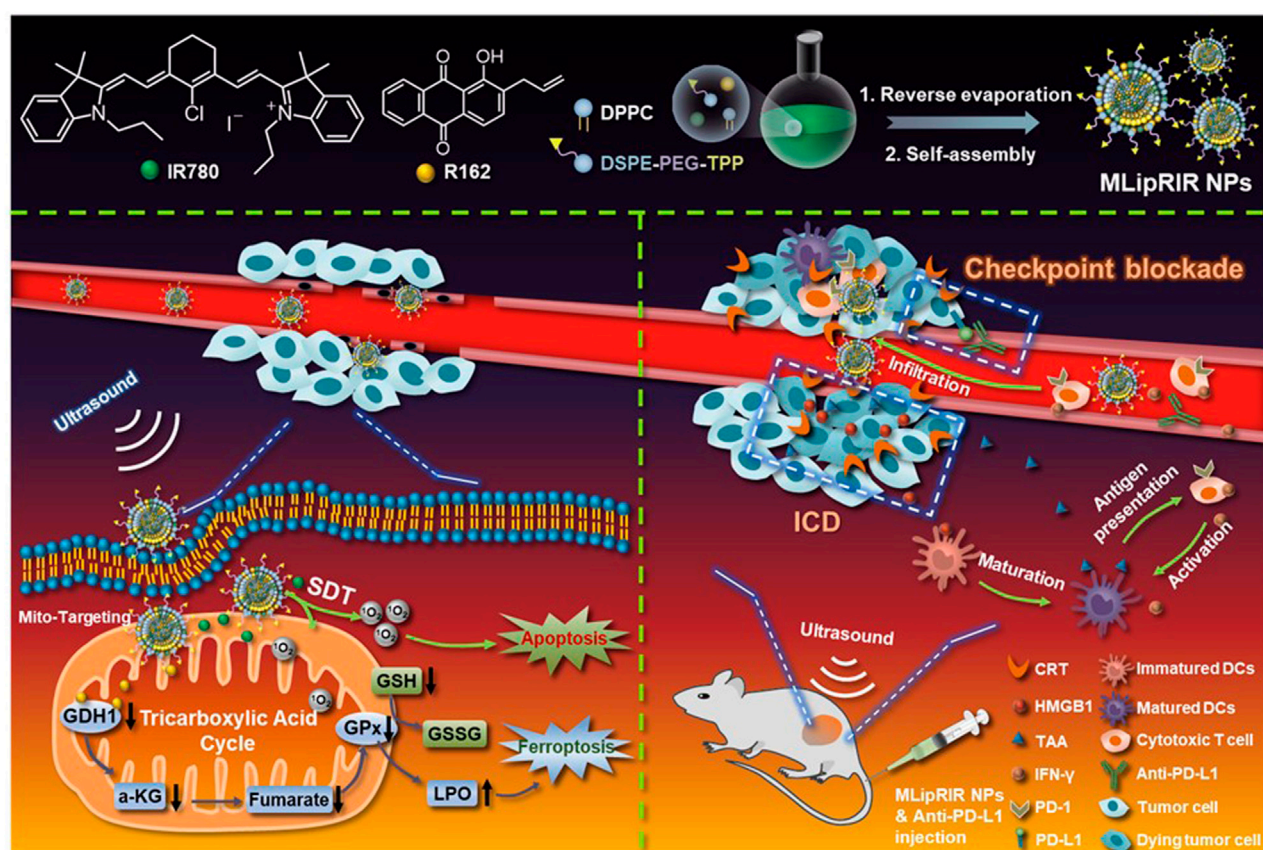


FIGURE 3

Schematic illustration of mitochondrial-targeting liposomal nanoparticles (MLipRIR NPs) for both FL/PA multimodal imaging and SDT reinforced by ICD. Adapted with permission from ref. (Ren et al., 2021). 2021, Ivspring International Publisher.

cycle) in both normoxic and hypoxic Panc02 cells (<40% cell viability of both normoxic and hypoxic Panc02 cells; CPI-613 concentration: 154.24 $\mu\text{mol/L}$, and IR780 concentration: 20 $\mu\text{mol/L}$). This approach successfully attenuated the progression of primary and metastatic tumors in Panc02-bearing mouse models.

4.2 5-Aminolevulinic acid-based SDT agent

The 5-aminolevulinic acid (ALA) is a powerful SDT agent that is converted to PpIX and delivers it to the heme synthetic root of cancer mitochondria. Previous studies have explored the use of ALA-based SDT for various cancers (Li et al., 2015; Wu et al., 2019).

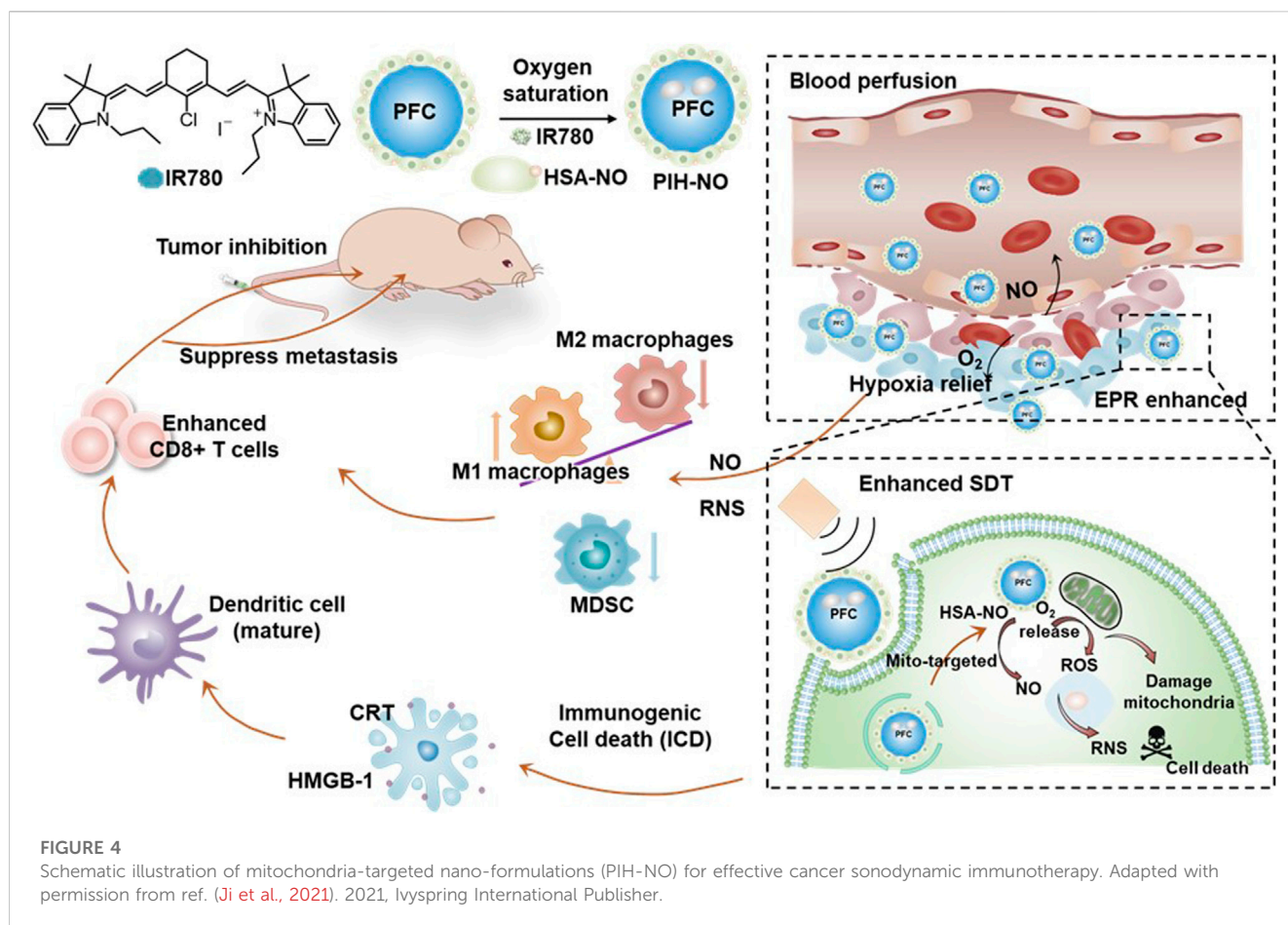
Cancer cells rely on two main pathways for the energy production: mitochondrial aerobic oxidation and cytoplasmic anaerobic glycolysis (Fu et al., 2019a; Fu et al., 2019b). Mitochondria-targeted SDT inhibits the mitochondrial aerobic oxidation process by generating an excessive amount of ROS, thus impacting tumor cell growth. However, this approach alone may have limitations because tumor cells can still obtain energy through anaerobic glycolysis (Wang et al., 2017). To address this, Xie et al. (2017) demonstrated the synergistic effect of combining ALA, a precursor of PpIX, the glycolysis inhibitor 2-deoxyglucose (2-DG), and microbubbles (MBs). Upon cell internalization, PpIX induced

by ALA selectively accumulated in the mitochondria of the HepG2 cells. Furthermore, US irradiation (5 min, 3 MHz, 2 W/cm², 60% duty rate) resulted in a potentiated therapeutic outcome with the combination system compared to both the ALA combined with 2-DG and MB (33.2%; 2-DG concentration = 2 mmol/L) and the ALA combined with 2-DG alone (49.2%; 2-DG concentration = 2 mmol/L). This study demonstrated that SDT enhanced with the glycolytic inhibitor 2-DG induces cell death in HepG2 cells, and MB enhances the outcome of SDT. However, further research is needed to investigate SDT application *in vivo*.

4.3 Hematoporphyrin monomethyl ether-based SDT agent

HMME, a derivative of PpIX, is commonly used as a photodynamic agent. However, it can also be activated by US irradiation to effectively generate ROS for SDT (Tian et al., 2009). Due to its hydrophobic nature, HMME is typically loaded into liposomes.

Chen M. et al. (2017) developed a mitochondria-targeting liposomal formulation of HMME modified with TPP (HMME-Lipo-TPP) and investigated its efficacy for SDT (Figure 6). The



formulation specifically targets mitochondria in MCF-7 cells and rapidly releases HMME upon US irradiation (3 min, 1 MHz, 0.5 W/cm²), leading to the production of ROS and induction of cell apoptosis. The cytotoxicity of HMME-Lipo-TPP in MCF-7 cells was superior to that of non-targeted controls (HMME-Lipo) under similar experimental conditions (~32% vs. ~44% cell viability, respectively, at 20 µg/mL). Although the *in vitro* characteristic of HMME-Lipo-TPP outperformed those of HMME-Lipo, further studies *in vivo* are required to validate its efficacy.

4.4 Chlorin e6-based SDT agent

Ce6 is a second-generation SDT agent that has been widely used to overcome the limitations of conventional agents, such as limited tumor targeting ability and slow clearance from normal tissues (Klyta et al., 2011). However, Ce6 still has drawbacks, including inefficient intracellular accumulation and low tumor specificity, limiting its SDT efficacy.

Cao et al. (2023) used a mitochondria-targeted approach using Ce6-loaded extracellular vesicles (EVs) (EV (TPP-Ce6)) to create a biocompatible and efficient mitochondria-targeting SDT (Figure 7). EVs have demonstrated clinical applicability as effective carriers for delivering SDT agents to tumor cells (Kalluri et al., 2020; Moller, 2020). In this study, Ce6 was conjugated with a TPP ligand and encapsulated within EVs. This formulation significantly increased

the mitochondrial uptake of Ce6 (0.58 for EV (TPP-Ce6) vs. 0.31 for Ce6 Mander's overlap coefficient). Under US irradiation (1 min, 1 MHz, 0.3 W/cm²), EV (TPP-Ce6) exhibited higher sonocytotoxicity in MCF-7 cells than Ce6 alone (~30% for EV (TPP-Ce6) vs. ~70% for TPP-Ce6 cell viability; TPP-Ce6 (or Ce6) concentration = 10 µM, EVs concentration = 4.96×10^{10} EVs/mL). Furthermore, the co-encapsulation of prooxidant piperlongumine (PL) into EV (TPP-Ce6) demonstrated the most effective tumor inhibition through the synergistic effect of chemo-SDT under similar experimental conditions (~6.5% cell viability; TPP-Ce6 (or Ce6) concentration = 10 µM, PL concentration = 3 µg/mL, EVs concentration = 4.96×10^{10} EVs/mL). Animal studies in MCF-7 cell mouse models demonstrated that this system significantly reduced tumor growth and, importantly, minimized side effects on other tissues.

4.5 IR780/hematoporphyrin monomethyl ether-based SDT agent

Zhang et al. (2020) reported a synergistic approach combining FL/PA bimodal imaging, mitochondria-targeted SDT, and starvation therapy using a combination of IR780 and HMME for FL/PA imaging and SDT and glucose oxidase (GOx) for starvation therapy (Figure 8). The system employed core/shell structured poly(lactic-co-glycolic acid) (PLGA) nano-formulations (IHG@P),

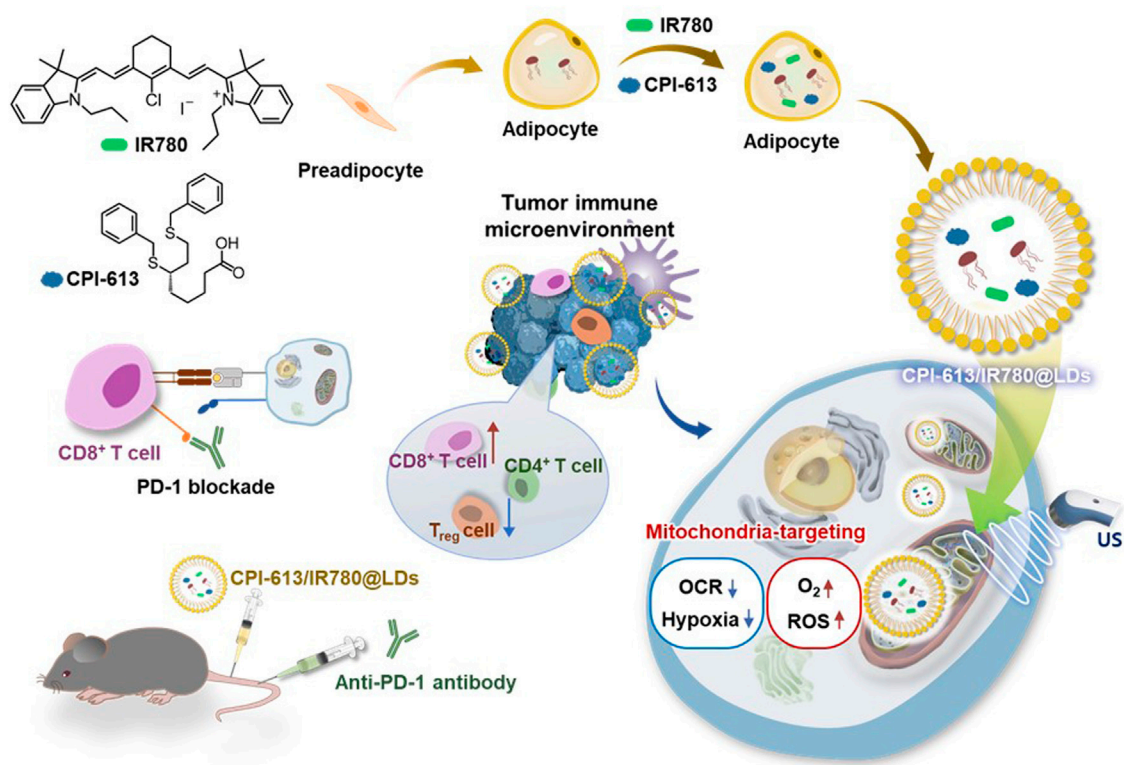


FIGURE 5
Schematic illustration of a novel approach for mitochondrial SDT using adipocyte-derived organelle LDs as carrier agents with an inherent affinity for mitochondria.

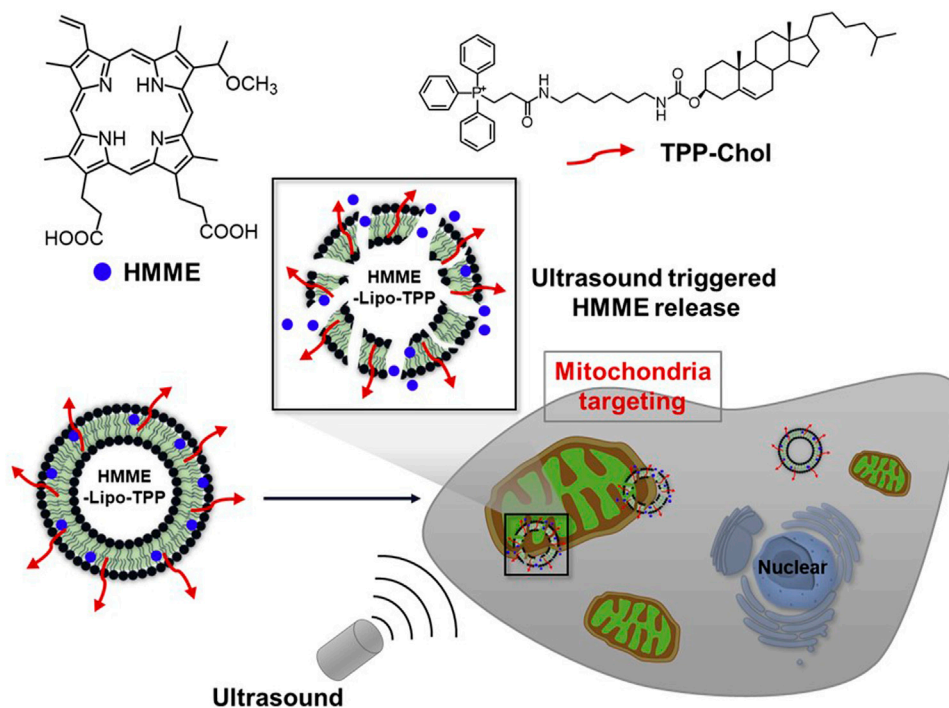


FIGURE 6
Schematic illustration of a mitochondria-targeting liposomal formulation of HMME modified with TPP (HMME-Lipo-TPP) for effective SDT. Reprinted with permission from (Chen et al., 2017), Copyright 2017 Elsevier.

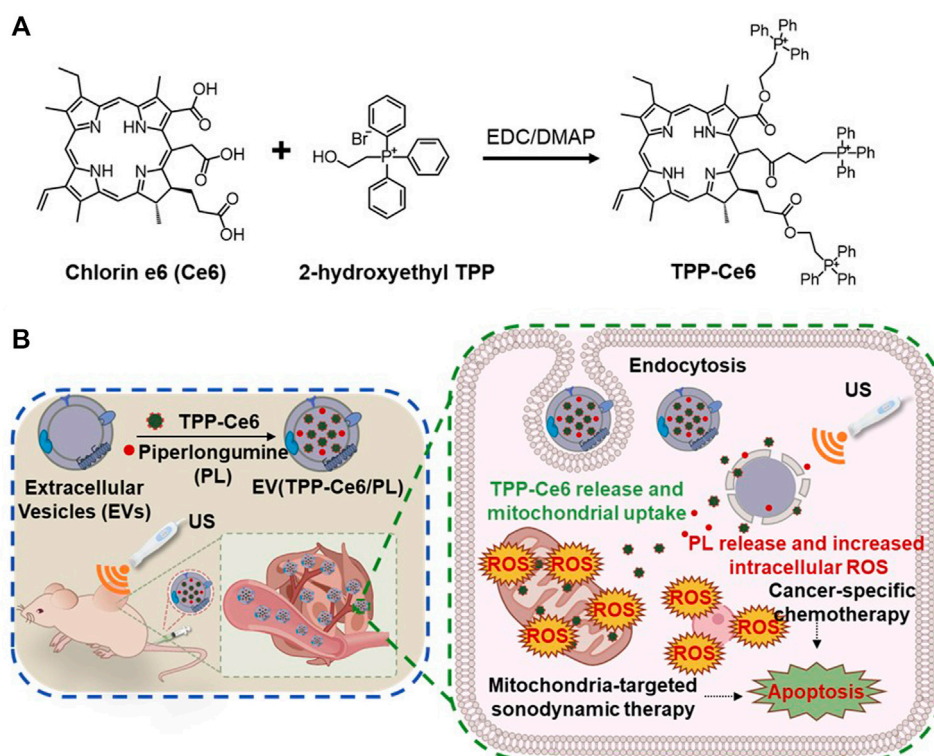


FIGURE 7

(A) Synthetic pathway of TPP-Ce6. (B) Schematic illustration of the mitochondria-targeted Ce6/PL-loaded extracellular vesicle (EV) (EV TPP-Ce6/PL) for biocompatible and efficient mitochondria-targeting chemo-SDT. Reprinted with permission from (Cao et al., 2023), Copyright 2023 Elsevier.

which consisted of GOx in the core and IR780 and HMME in the shell. This nano-formulation efficiently penetrated into 4T1 tumor cells, targeting the mitochondria, due to the inherent affinity of IR780 (PC = 0.806). As an adjuvant therapy, the GOx-mediated starvation therapy effectively suppressed cytosolic anaerobic glycolysis, limiting the energy supply of cancer cells and inducing tumor apoptosis. Under US irradiation (30 s, 2 W/cm²), the IHG@P group (8.48% Cell viability; PLGA concentration = 60 µg/mL) demonstrated the most significant 4T1 cancer cell apoptosis compared to the groups receiving starvation therapy alone (~68% cell viability; PLGA concentration = 60 µg/mL) or SDT therapy alone (~58% cell viability; PLGA concentration = 60 µg/mL) groups. Additionally, IHG@P was used for *in vivo* FL/PA multifunctional imaging of 4T1 cell mouse models, showing similar synergistic effects of SDT and starvation therapy.

4.6 IR780/chlorin e6-based SDT agent

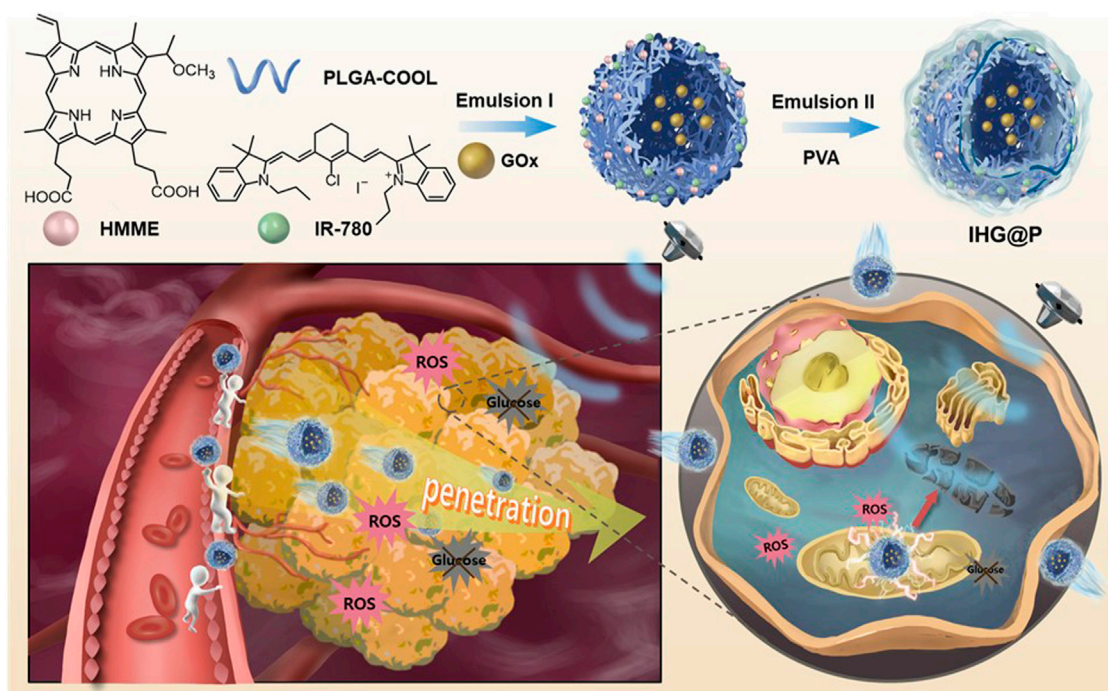
Triple-negative breast cancer (TNBC) is a highly aggressive breast cancer subtype with limited treatment options and a high metastasis rate, posing considerable challenges for effective therapy (O'Reilly et al., 2015). To address this issue, Han et al. (2021) developed a novel SDT complex nano-micelle (PEG-IR780@Ce6) for the efficient treatment of TNBC. This nano-micelle combines two sono-sensitizing agents, PEGylated IR780 (PEG-IR780) and Ce6 (Figure 9) and exhibited enhanced uptake by MDA-MB-231 TNBC

cells compared to PEG-IR780 or free Ce6 alone. The nano-micelle was efficiently delivered and accumulated in the mitochondria of MDA-MB-231 cells, resulting in ROS generation at the tumor site upon US irradiation. *In vitro* SDT experiments demonstrated the superior anticancer effects of PEG-IR780@Ce6 compared to PEG-IR780 or free Ce6 alone, highlighting its potential for sonodynamic TNBC therapy (3 min, 1 MHz, 0.6 W/cm², 50% duty rate) (35% for PEG-IR780@Ce6 vs. 85% for free Ce6 and 43% for PEG-IR780 cell viability, at 40 µg/mL). Furthermore, *in vivo* SDT results demonstrated that PEG-IR780@Ce6 effectively eradicated TNBC tumors, along with significant suppression of the invasion and migration, while exhibiting minimal side effects.

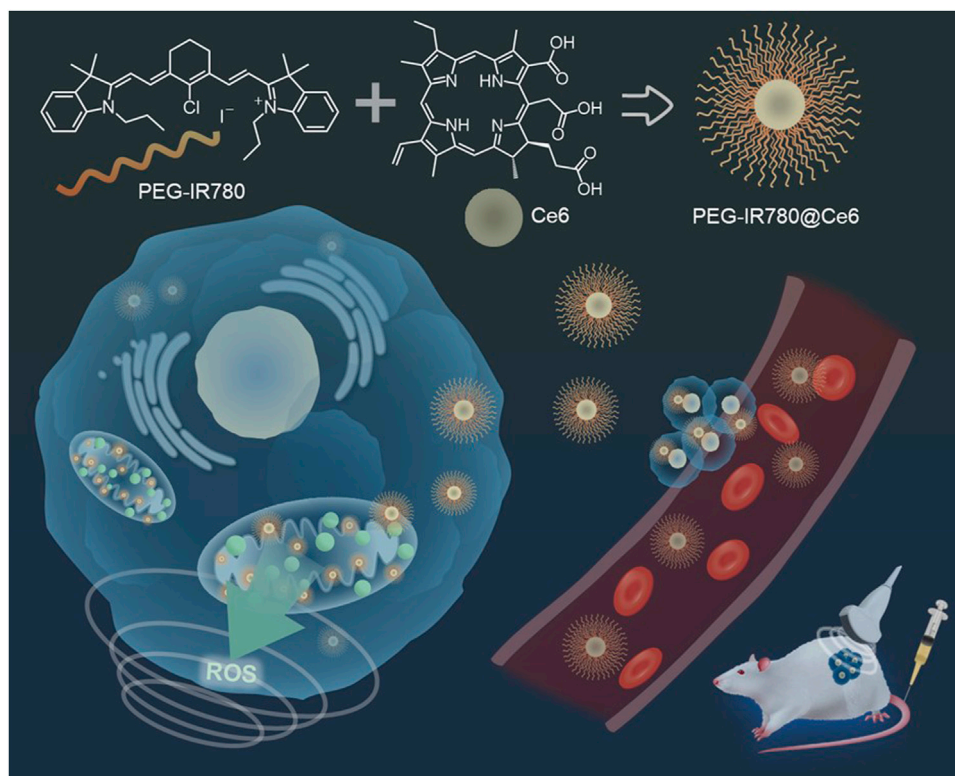
4.7 Gadolinium (III) porphyrinate-based SDT agent

To achieve effective sonodynamic immunotherapy (SDIT), it is crucial to enhance the level of ICD induction of current SDT agent-based inducers (Zhang et al., 2018). Therefore, the development of a new SDT agent with the potential to promote high ROS production and with mitochondrial targeting ability is timely and necessary.

Li et al. (2022) introduced a novel SDT agent called TPP-conjugated gadolinium (III) porphyrinate (GdPorP), which offers several advantages including high-efficiency ROS production, active mitochondrial targeting, and good MR contrast (Figure 10). To enhance tumor-targeting affinity and biocompatibility, GdPorP was

**FIGURE 8**

Schematic illustration of the core/shell structured PLGA nano-formulations (IHG@P), consisting of two sono-sensitizing agents (IR780 and HMME) and GOx, combining mitochondria-targeted dual SDT agent therapy, starvation therapy, and FL/PA imaging visualization. Reprinted with permission from Wiley (Zhang et al., 2020).

**FIGURE 9**

Schematic illustration of the new type of SDT complex nano-micelle (PEG-IR780@Ce6) for the treatment of triple-negative breast cancer (TNBC). Reprinted with permission from (Han et al., 2021), Copyright 2021 Elsevier.

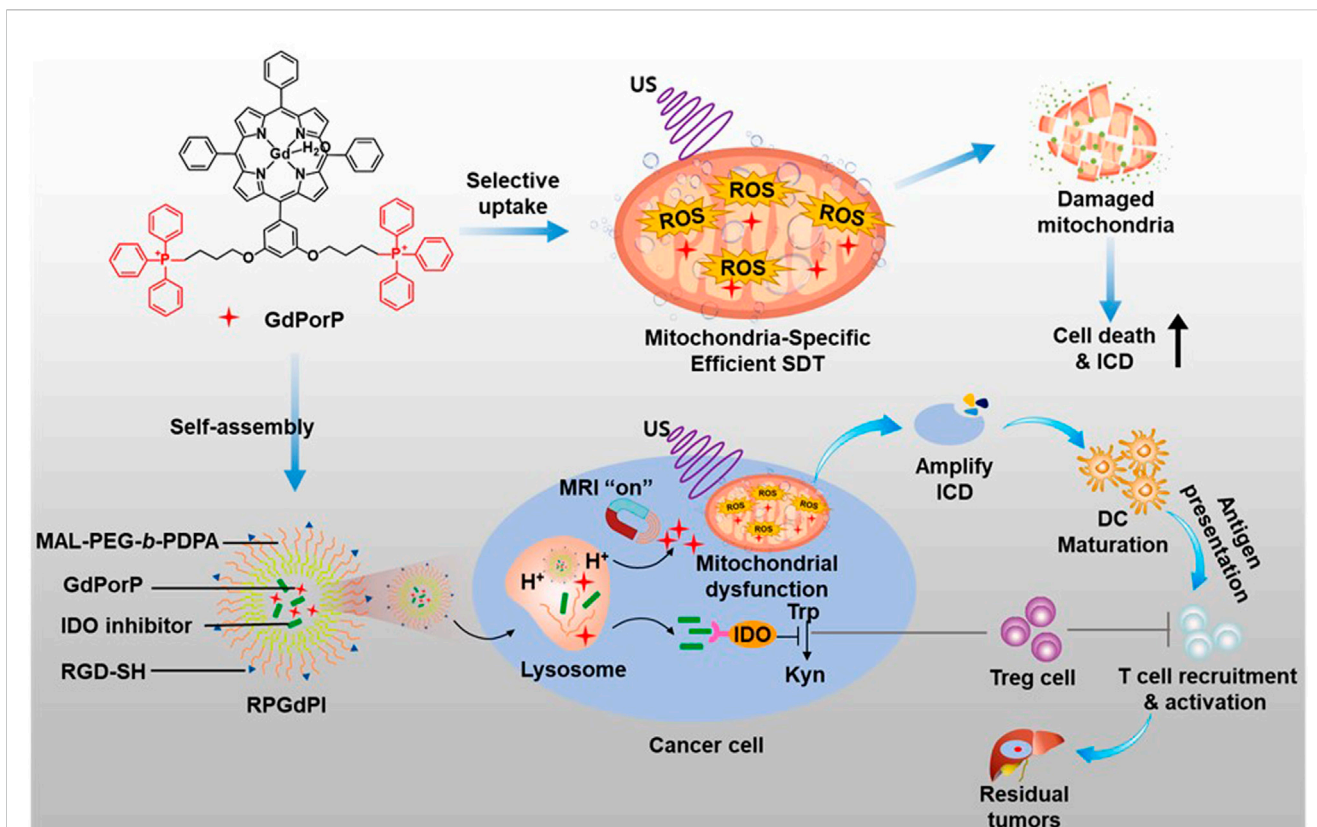


FIGURE 10

Schematic illustration of the TPP-conjugated gadolinium (III) porphyrinate (GdPorP) for high-efficiency ROS production, active mitochondrial targeting, and suitable MR contrast. Reprinted with permission from (Li et al., 2022), Copyright 2022 Elsevier.

coated with MAL-PEG-*b*-PDPA, forming pH-responsive nanomicelles (RPGdP). Upon delivery to H22 cancer cells, GdPorP accumulated in the cancer cell mitochondria ($PC = 0.93$), leading to increased cell death and amplifying ICD. Significant cell cytotoxicity was observed using RPGdP compared to the TPP-free RPGd upon the US irradiation (1 min, 1 MHz, 1.5 W/cm^2). To further enhance the *in vivo* SDIT efficacy of this system, the authors incorporated an indolamine 2,3-dioxygenase (IDO) inhibitor within the RPGdP, resulting in a nanopharmaceutical named RPGdPI. In H22 orthotopic liver tumor mouse models, RPGdPI effectively suppressed the growth of deep-seated primary tumors and induced significant antitumor effects by reversing the immunosuppressive tumor microenvironment.

5 Conclusion and outlook

Mitochondria play a crucial role in energy production and are closely related to cell apoptosis. Mitochondria-targeted SDT systems offer significant advantages over traditional SDT agents by enabling precise and localized production of ROS in ROS-susceptible mitochondrial regions. These systems have demonstrated antitumor efficacy, activation of antitumor immune responses, reduced adverse effects, lower agent doses, mild US irradiation, and the ability to overcome SDT challenges such as metastasis.

Mitochondria-targeted SDT agents have been extensively investigated in recent years, and some agents could bring new insights into the next SDT methods for clinical application.

US-mediated SDT agents with the mitochondria-targeting ability and efficient ROS production effect can induce increased oxidative stress in cancer cells under US irradiation. Several agents, such as HMME, IR780, Ce6, GdPorP, and PpIX derived from ALA, have demonstrated excellent efficacy in US-mediated SDT. Triphenylphosphoniums and adipocyte-derived organelles are commonly used for mitochondrial targeting in SDT. In addition, US-active agents such as IR780 and PpIX, with inherent mitochondria-targeting ability are also utilized for this purpose.

Considerable progress has been made in the development of mitochondrial SDT agents through various approaches, including US-responsive deep tumor penetration, improved cancer/mitochondria delivery with US assistance, US-related enhanced anticancer immune responses, and multimodal strategies combining SDT accompanied by other imaging-guided techniques [e.g., photoacoustic (PA) imaging, MR imaging, fluorescence (FL) imaging, etc.]. Combination therapies, such as mitochondria-targeted SDT and immunotherapy (e.g., R162), gas therapy (e.g., HSA-NO, FDC), metabolic modulation therapy (e.g., 2-DG, CPI-613), chemotherapy (e.g., PL), starvation therapy (e.g., GOx), dual SDT agent therapy (e.g., IR780/HMME, IR780/Ce6), and US-stimulated microbubble therapy (e.g., MB), are being

explored to amplify the benefits of each treatment modality. However, despite the remarkable advances in the field of biomedical SDT, further development of SDT agents and proven technologies for clinical application are still needed. Clinical applications of these SDT agents are currently lacking owing to the novelty of the field.

Several challenges and areas for improvement exist in the field of SDT: 1) while mitochondria-targeted SDT has shown significant potential, there is a limited number of studies focusing on other cell organelles such as the nucleus, ER, lysosomes, and Golgi apparatus; 2) there is a need for improved methods to manufacture well-defined, organelle-targeting agents on a large scale; 3) a universal treatment approach for various types of tumors has not been established, as SDT agents generally target the general features of cancer organelles; 4) the lack of standardized methods to evaluate SDT efficacy makes it challenging to compare the properties of various types of SDT agents; 5) studies on the biocompatibility of the by-products remaining after SDT treatment with commonly used agents are still lacking.

In conclusion, there is a need for the development of more biocompatible systems using non-toxic, biodegradable agents with improved organelle targeting abilities. Further biological and pharmacokinetic studies are also necessary. As research into improved SDT agents continues, various approaches are expected to be explored for targeted SDT therapy, leading to meaningful research outcomes and potential clinical translation in the future. Continued efforts in this area hold promise for the advancement of SDT and its application in clinical settings in a foreseeable future.

References

- Bacellar, I. O. L., and Baptista, M. S. (2019). Mechanisms of photosensitized lipid oxidation and membrane permeabilization. *ACS Omega* 4, 21636–21646. doi:10.1021/acsomega.9b03244
- Bhatti, J. S., Bhatti, G. K., and Reddy, P. H. (2017). Mitochondrial dysfunction and oxidative stress in metabolic disorders - a step towards mitochondria based therapeutic strategies. *Biochim. Biophys. Acta - Mol. Basis Dis.* 1863, 1066–1077. doi:10.1016/j.bbdis.2016.11.010
- Canavese, G., Ancona, A., Racca, L., Canta, M., Dumontel, B., Barbaresco, F., et al. (2018). Nanoparticle-assisted ultrasound: A special focus on sonodynamic therapy against cancer. *Chem. Eng. J.* 340, 155–172. doi:10.1016/j.cej.2018.01.060
- Cao, T. G. N., Hoang, Q. T., Hong, E. J., Kang, S. J., Kang, J. H., Ravichandran, V., et al. (2023). Mitochondria-targeting sonosensitizer-loaded extracellular vesicles for chemosonodynamic therapy. *J. Control. Release* 354, 651–663. doi:10.1016/j.jconrel.2023.01.044
- Chen, C., Ni, X., Jia, S., Liang, Y., Wu, X., Kong, D., et al. (2019). Massively evoking immunogenic cell death by focused mitochondrial oxidative stress using an AIE luminogen with a twisted molecular structure. *Adv. Mat.* 31, 1904914. doi:10.1002/adma.201904914
- Chen, J., Luo, H., Liu, Y., Zhang, W., Li, H., Luo, T., et al. (2017a). Oxygen-self-produced nanoplateform for relieving hypoxia and breaking resistance to sonodynamic treatment of pancreatic cancer. *ACS Nano* 11, 12849–12862. doi:10.1021/acsnano.7b08225
- Chen, M., Xu, A., He, W., Ma, W., and Shen, S. (2017b). Ultrasound triggered drug delivery for mitochondria targeted sonodynamic therapy. *J. Drug Deliv. Sci. Technol.* 39, 501–507. doi:10.1016/j.jddst.2017.05.009
- Cheng, Y., Cheng, H., Jiang, C., Qiu, X., Wang, K., Huan, W., et al. (2015). Perfluorocarbon nanoparticles enhance reactive oxygen levels and tumour growth inhibition in photodynamic therapy. *Nat. Commun.* 6, 8785. doi:10.1038/ncomms9785
- Costley, D., Mc Ewan, C., Fowley, C., McHale, A. P., Atchison, J., Nomikou, N., et al. (2015). Treating cancer with sonodynamic therapy: A review. *Int. J. Hyperth.* 31, 107–117. doi:10.3109/02656736.2014.992484
- Fu, L.-H., Hu, Y.-R., Qi, C., He, T., Jiang, S., Jiang, C., et al. (2019a). Biodegradable manganese-doped calcium phosphate nanotheranostics for traceable cascade reaction-enhanced anti-tumor therapy. *ACS Nano* 13, 13985–13994. doi:10.1021/acsnano.9b05836
- Fu, L.-H., Qi, C., Hu, Y.-R., Lin, J., and Huang, P. (2019b). Glucose oxidase-instructed multimodal synergistic cancer therapy. *Adv. Mat.* 31, 1808325. doi:10.1002/adma.201808325
- Fulda, S., Galluzzi, L., and Kroemer, G. (2010). Targeting mitochondria for cancer therapy. *Nat. Rev. Drug Discov.* 9, 447–464. doi:10.1038/nrd3137
- Han, X., Song, Z., Zhou, Y., Zhang, Y., Deng, Y., Qin, J., et al. (2021). Mitochondria-targeted high-load sound-sensitive micelles for sonodynamic therapy to treat triple-negative breast cancer and inhibit metastasis. *Mat. Sci. Eng. C* 124, 112054. doi:10.1016/j.msec.2021.112054
- Ho, Y.-J., and Yeh, C.-K. (2017). Theranostic performance of acoustic nanodroplet vaporization-generated bubbles in Tumor Intertissue. *Theranostics* 7, 1477–1488. doi:10.7150/thno.19099
- Huang, M., Myers, C. R., Wang, Y., and You, M. (2021). Mitochondria as a novel target for cancer chemoprevention: Emergence of mitochondrial targeting agents. *Cancer Prev. Res. (Phila.)* 14, 285–306. doi:10.1158/1940-6207.CAPR-20-0425
- Ji, C., Si, J., Xu, Y., Zhang, W., Yang, Y., He, X., et al. (2021). Mitochondria-targeted and ultrasound-responsive nanoparticles for oxygen and nitric oxide codelivery to reverse immunosuppression and enhance sonodynamic therapy for immune activation. *Theranostics* 11, 8587–8604. doi:10.7150/thno.62572
- Jin, L., Li, D., Alesi, G. N., Fan, J., Kang, H.-B., Lu, Z., et al. (2015). Glutamate dehydrogenase 1 signals through antioxidant glutathione peroxidase 1 to regulate redox homeostasis and tumor growth. *Cancer Cell* 27, 257–270. doi:10.1016/j.ccell.2014.12.006
- Kalluri, R., and LeBleu, V. S. (2020). The biology, function, and biomedical applications of exosomes. *Science* 367, eaau6977. doi:10.1126/science.aau6977
- Kim, S., Tachikawa, T., Fujitsuka, M., and Majima, T. (2014). Far-red fluorescence probe for monitoring singlet oxygen during photodynamic therapy. *J. Am. Chem. Soc.* 136, 11707–11715. doi:10.1021/ja504279r
- KlytaM.Ostasiewicz, P., Jurczyszyn, K., Duś, K., Latos-Grażyński, L., Pacholska-Dudziak, E., et al. (2011). Vacata- and divacataporphyrin: New photosensitizers for application in photodynamic therapy-an *in vitro* study. *Lasers Surg. Med.* 43, 607–613. doi:10.1002/lsm.21086

Author contributions

HJ designed this project, wrote and revised the manuscript. EH and MY jointly reviewed the results and summarized the data. All authors contributed to the article and approved the submitted version.

Funding

This work was supported by the Hyupsung University Research Grant of 2021 (2021-0039).

Conflict of interest

The authors declare that the research was conducted in the absence of any commercial or financial relationships that could be construed as a potential conflict of interest.

Publisher's note

All claims expressed in this article are solely those of the authors and do not necessarily represent those of their affiliated organizations, or those of the publisher, the editors and the reviewers. Any product that may be evaluated in this article, or claim that may be made by its manufacturer, is not guaranteed or endorsed by the publisher.

- Krysko, Dmitri. V., Garg, A. D., Kaczmarek, A., Krysko, O., Agostinis, P., and Vandenabeele, P. (2012). Immunogenic cell death and DAMPs in cancer therapy. *Nat. Rev. Cancer* 12, 860–875. doi:10.1038/nrc3380
- Li, Q., and Huang, Y. (2020). Mitochondrial targeted strategies and their application for cancer and other diseases treatment. *J. Pharm. Investig.* 50, 271–293. doi:10.1007/s40005-020-00481-0
- Li, W., Peng, J., Yang, Q., Chen, L., Zhang, L., Chen, X., et al. (2018). α -Lipoic acid stabilized DTX/IR780 micelles for photoacoustic/fluorescence imaging guided photothermal therapy/chemotherapy of breast cancer. *Biomater. Sci.* 6, 1201–1216. doi:10.1039/c8bm00096d
- Li, X., Zeng, Q., Zhang, R., Li, J., Xing, D., and Zhang, T. (2022). Mitochondria-specific gadolinium (III) porphyrinate as efficient ROS generator for MRI visualization and sonodynamic-immunotherapy of deep localized tumors. *Chem. Eng. J.* 450, 138210. doi:10.1016/j.ccej.2022.138210
- Li, Y., Zhou, Q., Hu, Z., Yang, B., Li, Q., Wang, J., et al. (2015). 5-Aminolevulinic acid-based sonodynamic therapy induces the apoptosis of osteosarcoma in mice. *PLoS One* 10, e0132074. doi:10.1371/journal.pone.0132074
- Lockman, P. R., Mittapalli, R. K., Taskar, K. S., Rudraraju, V., Gril, B., Bohn, K. A., et al. (2010). Heterogeneous blood–tumor barrier permeability determines drug efficacy in experimental brain metastases of breast cancer. *Clin. Cancer Res.* 16, 5664–5678. doi:10.1158/1078-0432.CCR-10-1564
- Möller, A., and Lobb, R. J. (2020). The evolving translational potential of small extracellular vesicles in cancer. *Nat. Rev. Cancer* 20, 697–709. doi:10.1038/s41568-020-00299-w
- Mura, S., Nicolas, J., and Couvreur, P. (2013). Stimuli-responsive nanocarriers for drug delivery. *Nat. Mat.* 12, 991–1003. doi:10.1038/nmat3776
- Murphy, M. P., and Hartley, R. C. (2018). Mitochondria as a therapeutic target for common pathologies. *Nat. Rev. Drug Discov.* 17, 865–886. doi:10.1038/nrd.2018.174
- O'Reilly, E. A., Gubbins, L., Sharma, S., Tully, R., Guang, M. H. Z., Weiner-Gorzel, K., et al. (2015). The fate of chemoresistance in triple negative breast cancer (TNBC). *BBA Clin.* 3, 257–275. doi:10.1016/j.bbaci.2015.03.003
- Qian, X., Zheng, Y., and Chen, Y. (2016). Micro/nanoparticle-augmented sonodynamic therapy (SDT): Breaking the depth shallow of photoactivation. *Adv. Mat.* 28, 8097–8129. doi:10.1002/adma.201602012
- Ren, J., Zhou, J., Liu, H., Jiao, X., Cao, Y., Xu, Z., et al. (2021). Ultrasound (US)-activated redox dyshomeostasis therapy reinforced by immunogenic cell death (ICD) through a mitochondrial targeting liposomal nanosystem. *Theranostics* 11, 9470–9491. doi:10.7150/thno.62984
- Rengeng, L., Qianyu, Z., Yuehong, L., Zhongzhong, P., and Libo, L. (2017). Sonodynamic therapy, a treatment developing from photodynamic therapy. *Photodiagnosis Photodyn. Ther.* 19, 159–166. doi:10.1016/j.pdpdt.2017.06.003
- Riesz, P., and Kondo, T. (1992). Free radical formation induced by ultrasound and its biological implications. *Free Radic. Biol. Med.* 13, 247–270. doi:10.1016/0891-5849(92)90021-8
- Rubio, C. P., and Cerón, J. J. (2021). Spectrophotometric assays for evaluation of reactive oxygen species (ROS) in serum: General concepts and applications in dogs and humans. *BMC Vet. Res.* 17, 226. doi:10.1186/s12917-021-02924-8
- Saksena, T. K., and Nyborg, W. L. (1970). Sonoluminescence from stable cavitation. *J. Chem. Phys.* 53, 1722–1734. doi:10.1063/1.1674249
- Shi, Z., Wang, X., Luo, J., Zeng, Y., Wen, Q., Hong, Y., et al. (2023). RNA sequencing-based optimization of biological lipid droplets for sonodynamic therapy to reverse tumor hypoxia and elicit robust immune response. *Nano Res.* 16, 7187–7198. doi:10.1007/s12274-022-5340-0
- Son, S., Kim, J. H., Wang, X., Zhang, C., Yoon, S. A., Shin, J., et al. (2020). Multifunctional sonosensitizers in sonodynamic cancer therapy. *Chem. Soc. Rev.* 49, 3244–3261. doi:10.1039/c9cs00648f
- Song, J., Lin, C., Yang, X., Xie, Y., Hu, P., Li, H., et al. (2019). Mitochondrial targeting nanodrugs self-assembled from 9-O-octadecyl substituted berberine derivative for cancer treatment by inducing mitochondrial apoptosis pathways. *J. Control. Release* 294, 27–42. doi:10.1016/j.jconrel.2018.11.014
- Tian, Z., Quan, X., Xu, C., Dan, L., Guo, H., and Leung, W. (2009). Hematoporphyrin monomethyl ether enhances the killing action of ultrasound on osteosarcoma *in vivo*. *J. Ultrasound Med.* 28, 1695–1702. doi:10.7863/jum.2009.28.12.1695
- Wang, Q., Zhang, X., Huang, L., Zhang, Z., and Dong, S. (2017). GOx@ZIF-8(NiPd) nanoflower: An artificial enzyme system for tandem catalysis. *Angew. Chem. Int. Ed.* 56, 16082–16085. doi:10.1002/anie.201710418
- Wang, Y., Liu, T., Zhang, E., Luo, S., Tan, X., and Shi, C. (2014). Preferential accumulation of the near infrared heptamethine dye IR-780 in the mitochondria of drug-resistant lung cancer cells. *Biomaterials* 35, 4116–4124. doi:10.1016/j.biomaterials.2014.01.061
- Wu, S.-K., Santos, M. A., Marcus, S. L., and Hynynen, K. (2019). MR-guided focused ultrasound facilitates sonodynamic therapy with 5-aminolevulinic acid in a rat glioma model. *Sci. Rep.* 9, 10465. doi:10.1038/s41598-019-46832-2
- Xie, R., Xu, T., Zhu, J., Wei, X., Zhu, W., Li, L., et al. (2017). The combination of glycolytic inhibitor 2-deoxyglucose and microbubbles increases the effect of 5-aminolevulinic acid-sonodynamic therapy in liver cancer cells. *Ultrasound Med. Biol.* 43, 2640–2650. doi:10.1016/j.ultrasmedbio.2017.06.031
- Xing, X., Zhao, S., Xu, T., Huang, L., Zhang, Y., Lan, M., et al. (2021). Advances and perspectives in organic sonosensitizers for sonodynamic therapy. *Coord. Chem. Rev.* 445, 214087. doi:10.1016/j.ccr.2021.214087
- Yue, W., Chen, L., Yu, L., Zhou, B., Yin, H., Ren, W., et al. (2019). Checkpoint blockade and nanosonosensitizer-augmented noninvasive sonodynamic therapy combination reduces tumour growth and metastases in mice. *Nat. Commun.* 10, 2025. doi:10.1038/s41467-019-09760-3
- Zhang, L., Yi, H., Song, J., Huang, J., Yang, K., Tan, B., et al. (2019). Mitochondria-targeted and ultrasound-activated nanodroplets for enhanced deep-penetration sonodynamic cancer therapy. *ACS Appl. Mat. Interfaces* 11, 9355–9366. doi:10.1021/acsami.8b21968
- Zhang, Q., Bao, C., Cai, X., Jin, L., Sun, L., Lang, Y., et al. (2018). Sonodynamic therapy-assisted immunotherapy: A novel modality for cancer treatment. *Cancer Sci.* 109, 1330–1345. doi:10.1111/cas.13578
- Zhang, R., Zhang, L., Ran, H., Li, P., Huang, J., Tan, M., et al. (2020). A mitochondria-targeted anticancer nanoplateform with deep penetration for enhanced synergistic sonodynamic and starvation therapy. *Biomater. Sci.* 8, 4581–4594. doi:10.1039/D0BM00408A
- Zhang, Y., Zhang, X., Yang, H., Yu, L., Xu, Y., Sharma, A., et al. (2021). Advanced biotechnology-assisted precise sonodynamic therapy. *Chem. Soc. Rev.* 50, 11227–11248. doi:10.1039/d1cs00403d



OPEN ACCESS

EDITED BY

Jianrong Steve Zhou,
Peking University, China

REVIEWED BY

Dongbing Zhao,
Nankai University, China
Zheng Xu,
Hangzhou Normal University, China

*CORRESPONDENCE

Wei Zeng,
✉ zengwei@scut.edu.cn

RECEIVED 05 April 2023

ACCEPTED 24 May 2023

PUBLISHED 15 June 2023

CITATION

Chen F, Liu L and Zeng W (2023),
Synthetic strategies to access silacycles.
Front. Chem. 11:1200494.
doi: 10.3389/fchem.2023.1200494

COPYRIGHT

© 2023 Chen, Liu and Zeng. This is an open-access article distributed under the terms of the [Creative Commons Attribution License \(CC BY\)](#). The use, distribution or reproduction in other forums is permitted, provided the original author(s) and the copyright owner(s) are credited and that the original publication in this journal is cited, in accordance with accepted academic practice. No use, distribution or reproduction is permitted which does not comply with these terms.

Synthetic strategies to access silacycles

Fengjuan Chen, Luo Liu and Wei Zeng*

Key Laboratory of Functional Molecular Engineering of Guangdong Province, School of Chemistry and Chemical Engineering, South China University of Technology, Guangzhou, China

In comparison with all-carbon parent compounds, the incorporation of Si-element into carboskeletons generally endows the corresponding sila-analogues with unique biological activity and physical-chemical properties. Silacycles have recently shown promising application potential in biological chemistry, pharmaceuticals industry, and material chemistry. Therefore, the development of efficient methodology to assemble versatile silacycles has aroused increasing concerns in the past decades. In this review, recent advances in the synthesis of silacycle-system are briefly summarized, including transition metal-catalytic and photocatalytic strategies by employing arylsilanes, alkylsilane, vinylsilane, hydrosilanes, and alkynylsilanes, etc. as starting materials. Moreover, a clear presentation and understanding of the mechanistic aspects and features of these developed reaction methodologies have been high-lighted.

KEYWORDS

cyclization, silacycles, transition-metal catalysis, photocatalysis, organocatalysis, silaarenes

1 Introduction

Nonmetallic Si-element which constitutes almost 30% of the mass of earth's crust in silica and silicates exists extensively in our planet. As is well-known that aza-, oxa-, or thia-organic molecules are commonly encountered in many natural products and pharmaceuticals, but sila-organic molecules are not readily available in nature. Compared with all-carbon organic compounds, sila-analogues generally possess unique bioactive and photophysical properties (Förster et al., 2014; Pujals et al., 2006; Lippert et al., 2009) due to that silicon element has larger covalent radius (r_{Si} vs. r_{C} : 111 p.m. vs 67 p.m.) and less electronegativity (χ_{Si} vs. χ_{C} : 1.74 eV vs. 2.50 eV) different from carbon atom (Allred and Rochow, 1958). For instance, some representative examples of therapeutically potential silacycles are described in Figure 1. However, incorporating Si-element into all-carbon skeletons and heterocyclic systems has not been well-established. The main reason is that extra 3d orbitals of silicon element easily interact with heteroatoms and metal ions to form hypervalent five- or six-coordinated intermediates (Breit et al., 2013; Shen et al., 2017), leading to decomposition of organosilanes (Akiyama and Imazeki, 1997; Fleming and Winter 1998). Meanwhile, transmetalation between sila-compounds and metal catalysts can often occur to make the silane-based chemical reactions show poor chemoselectivity (Chen et al., 2021; Pawley et al., 2022). Therefore, the development of versatile strategies to access various organosilanes has recently aroused increasing concerns. To date, the scope, mechanism, and applications for intermolecular silylations of alkanes, alkenes, arenes, diazo-compounds, and alkynes, etc., have been widely explored, and the corresponding studies involved transition metal-catalysis and photocatalysis have also been summarized

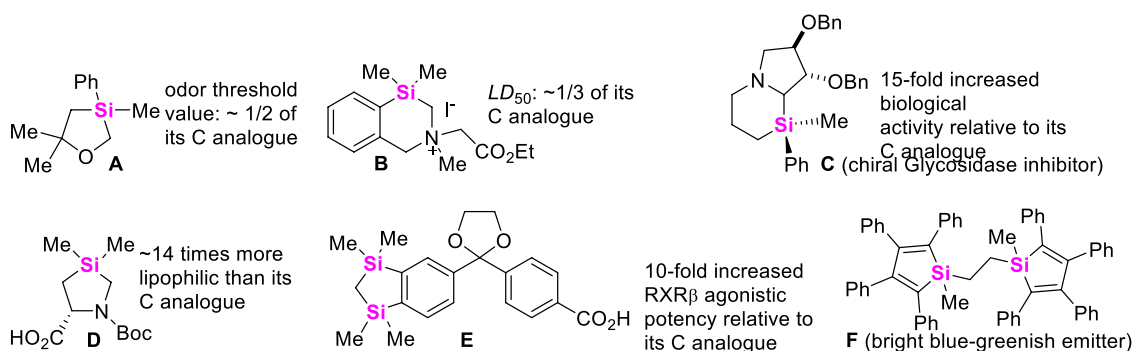


FIGURE 1

The difference in of biological activity and photophysical properties between the representative silacycles and their all-carbon analogues.

by different research groups (Cheng and Hartwig, 2015; Li et al., 2015; Xu et al., 2015; Van Hoveln et al., 2019; Keipour et al., 2017; Chatgililoglu et al., 2018; Huang W S et al., 2022). However, no comprehensive review about synthetical strategies of silacycles through C-C bond and C-heteroatom bond formation reactions has been published. This review will focus on the assembly of unique structural silacyclic skeletons through intermolecular and intramolecular coupling-cyclization of alkylsilanes, arylsilanes, alkynylsilanes, vinylsilanes, and hydrosilanes, etc., with different coupling-reagents.

2 Synthetic strategy of silacycles via C-Si σ bond functionalization

C-Si σ bond is commonly encountered in many organic sila-molecules. Therefore, the development of C-Si bond cleavage-based transformation will provide a novel platform to assemble silacycles with high step-economy. Generally, C-Si bonds include strained C-Si σ bonds and unstrained C-Si σ bonds. The cleavage of C-Si bonds catalyzed by transition metal is still in its infancy because of the unmet challenges on reactivity, selectivity, and substrate scope.

2.1 Coupling-cyclization by catalytic cleavage of the strained C-Si σ bond activation

The scope of strained C-Si bond cleavage is primarily restricted to the silacycles with a small ring size such as silacyclobutanes (SCBs), in which strain release can provide thermodynamic driving forces. In these regards, Oshima and Yorimitsu early reported a Pd-catalyzed intermolecular cycloaddition of SCBs with enones, in which coupling-cyclization of SCBs with enones under Pd-catalysis conditions could smoothly proceed via formal cycloaddition to yield the corresponding eight-membered ring (Hirano et al., 2008). The reaction was first triggered by the initial oxidative addition (O. A.) of SCBs to Pd (0) catalysts, producing

palladasilacyclopentane which was then trapped by a, β -unsaturated ketones (Scheme 1A).

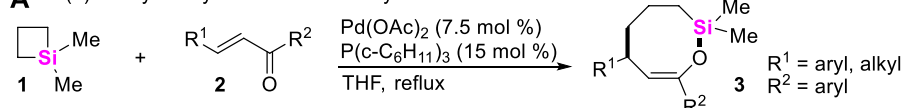
Possibly encouraged by Oshima's work (Hirano et al., 2008), in 2011, Hayashi and Shintani developed a Pd-catalyzed enantioselective desymmetrization of SCBs through an intramolecular coupling-cyclization, in which alkyne-tethered SCBs **4** were used as starting material, and 5,5',6,6',7,7',8,8'-octahydro-1,10-binaphthyl phosphoramidite (**L**₁) was utilized as a chiral ligand (Shintani et al., 2011). This transformation provided an efficient approach to access chiral silacycles **5** featuring tetraorganosilicon stereocenter (Scheme 1B). The overall process for this transformation starts with the oxidative addition of a C-Si bond of silacyclobutane from **4** to Pd (0) catalysts, giving 1-pallada-2-silacyclopentanes **A**. Intermediates **A** then undergo an intramolecular insertion of the alkyne to form 1-pallada-4-sila-2-cycloheptenes **B**, followed by the subsequent reductive elimination (R. E.) to produce compounds **5** along with regeneration of Pd (0)-catalysts. Meanwhile, β -H elimination from intermediate **B** gives alkenylpalladium hydride species **C**, and successive reductive elimination results in the formation of byproducts **6**.

Subsequently, Hayashi and Shintani further developed a Pd-catalyzed intermolecular desymmetrization of SCBs with alkynes almost using the same reaction conditions (Shintani et al., 2012), assembling Si-stereogenic 1-sila-2-cyclohexenes. The reaction mechanism possibly proceeds through Path A, in which oxidative addition of a C-Si σ bond of SCBs **7** to Pd (0) gives 1-pallada-2-silacyclopentane **A**. **A** species then undergo insertion of alkynes **8** to produce 1-pallada-4-sila-2-cycloheptenes **B**, the reductive elimination of **B** leads to the formation of products **9** along with regeneration of Pd (0)-catalysts. Alternatively, coordination of **8** to Pd (0) could precede cleavage of the C-Si σ bond of **7** as shown in Path B. Subsequent transmetalation (or σ -bond metathesis) of **7** can provide the same intermediates **B**, which eventually give silacycles **9** and Pd (0)-catalysts by reductive elimination (Scheme 1C). Of course, the detailed experiments and DFT calculation about this transformation were further performed by Xu, confirming that Path B (Scheme 1C) is reasonable (Zhang

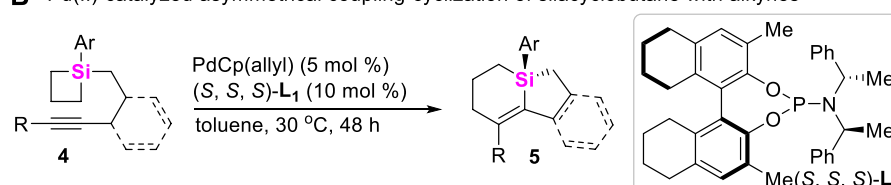
Q W et al., 2016). In 2021, the similar transformation of Rh/Cu-catalyzed coupling-cyclization of SCBs with arylpropiolate-type internal alkynes was also achieved by Xu (Wang X C et al., 2021). In 2022, Song developed a Rh (I)-catalyzed intermolecular asymmetric coupling-cyclization of sipsilacyclobutanes **10** with terminal alkynes

11 to produce spirosilabicyclohexenes **12** with up to 96% ee (Scheme 1D) (Chen et al., 2022). Meanwhile, Song still utilized allenates **13** and **14** as coupling reagents to react with silacyclobutanes **7** to furnish 2- or 3-(*E*)-enoate-substituted silacyclohexenes **15** and **16** (up to 80% ee) in the presence of chiral phosphoramidite **L₃** (Scheme 1E) (Tang et al., 2022).

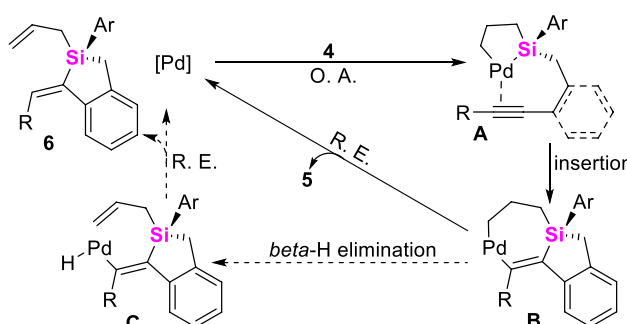
A Pd(II)-catalyzed cycloaddition of silacyclobutanes with enones



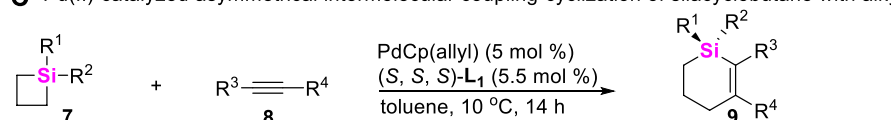
B Pd(II)-catalyzed asymmetrical coupling-cyclization of silacyclobutane with alkynes



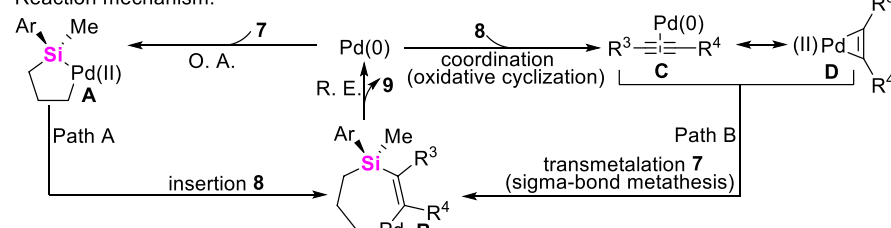
Reaction mechanism:



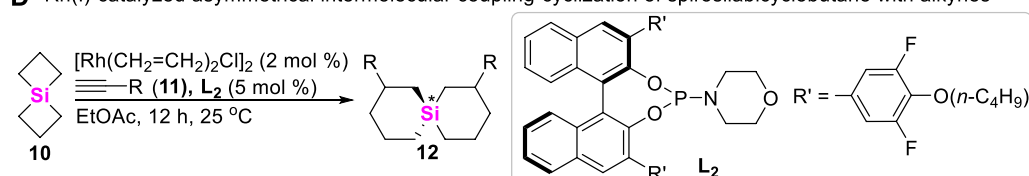
C Pd(II)-catalyzed asymmetrical intermolecular coupling-cyclization of silacyclobutane with alkynes



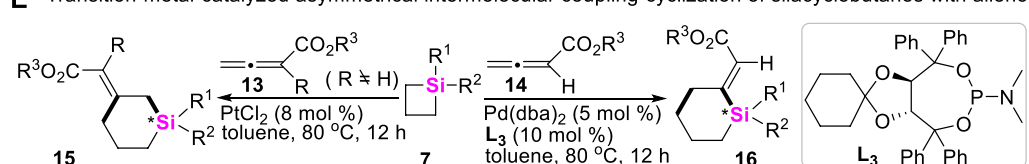
Reaction mechanism:



D Rh(I)-catalyzed asymmetrical intermolecular coupling-cyclization of spiroilabicyclobutane with alkynes



E Transition metal-catalyzed asymmetrical intermolecular coupling-cyclization of silacyclobutanes with allenates



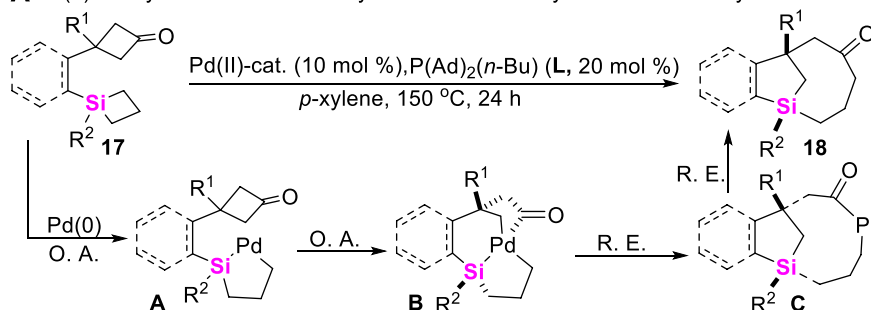
SCHEME 1

Transition metal-catalyzed coupling-cyclization of silacyclobutanes with alkenes, alkynes and allenates.

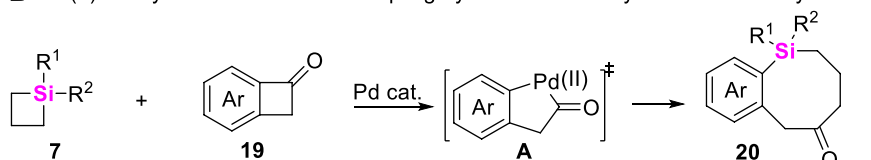
Besides that a, β -unsaturated ketones and alkynes could be employed to couple with SCBs via C-Si σ bond cleavage, cycloketones, cyclopropenones, arenes, and trisylhydrazones were also demonstrated to be efficient coupling-partners. In this vein,

Murakami successively developed Pd-catalyzed intramolecular and intermolecular coupling-strategies of cyclobutanones with SCBs to construct complex structural benzosilacycles through σ -bond exchange process. For the intramolecular coupling-cyclization of cyclobutanone-

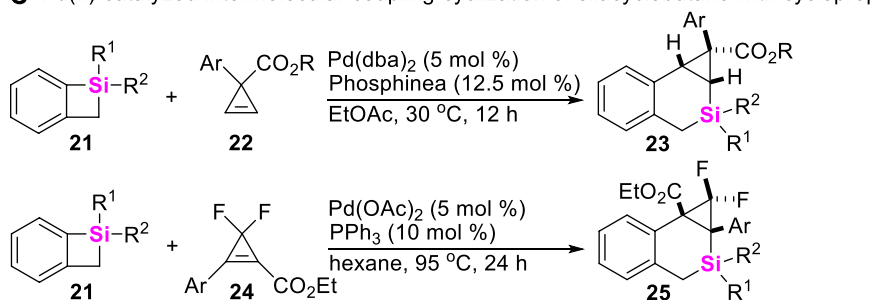
A Pd(II)-catalyzed intramolecular cycloaddition of silacyclobutanes with cyclobutanones



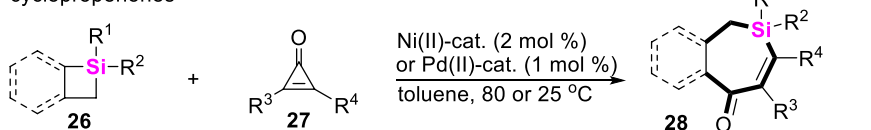
B Pd(II)-catalyzed intermolecular coupling-cyclization of silacyclobutane with cyclobutanones



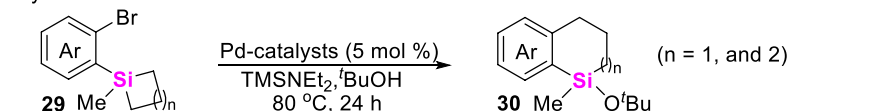
C Pd(II)-catalyzed intermolecular coupling-cyclization of silacyclobutane with cyclopropenes



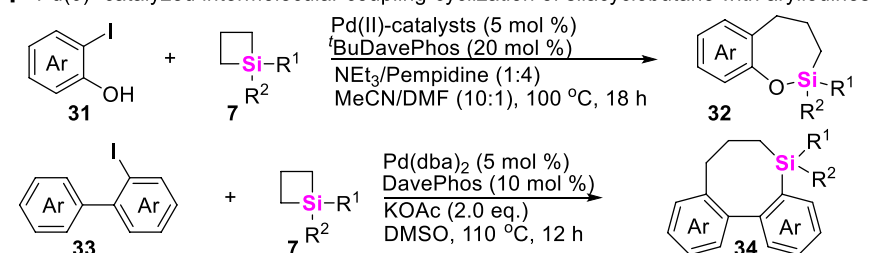
D Pd(II)- or Ni(II)-catalyzed intermolecular coupling-cyclization of silacyclobutane with cyclopropenones



E Pd(0)-catalyzed intramolecular coupling-cyclization of silacyclobutane with arylbromides



F Pd(0)-catalyzed intermolecular coupling-cyclization of silacyclobutane with arylidines

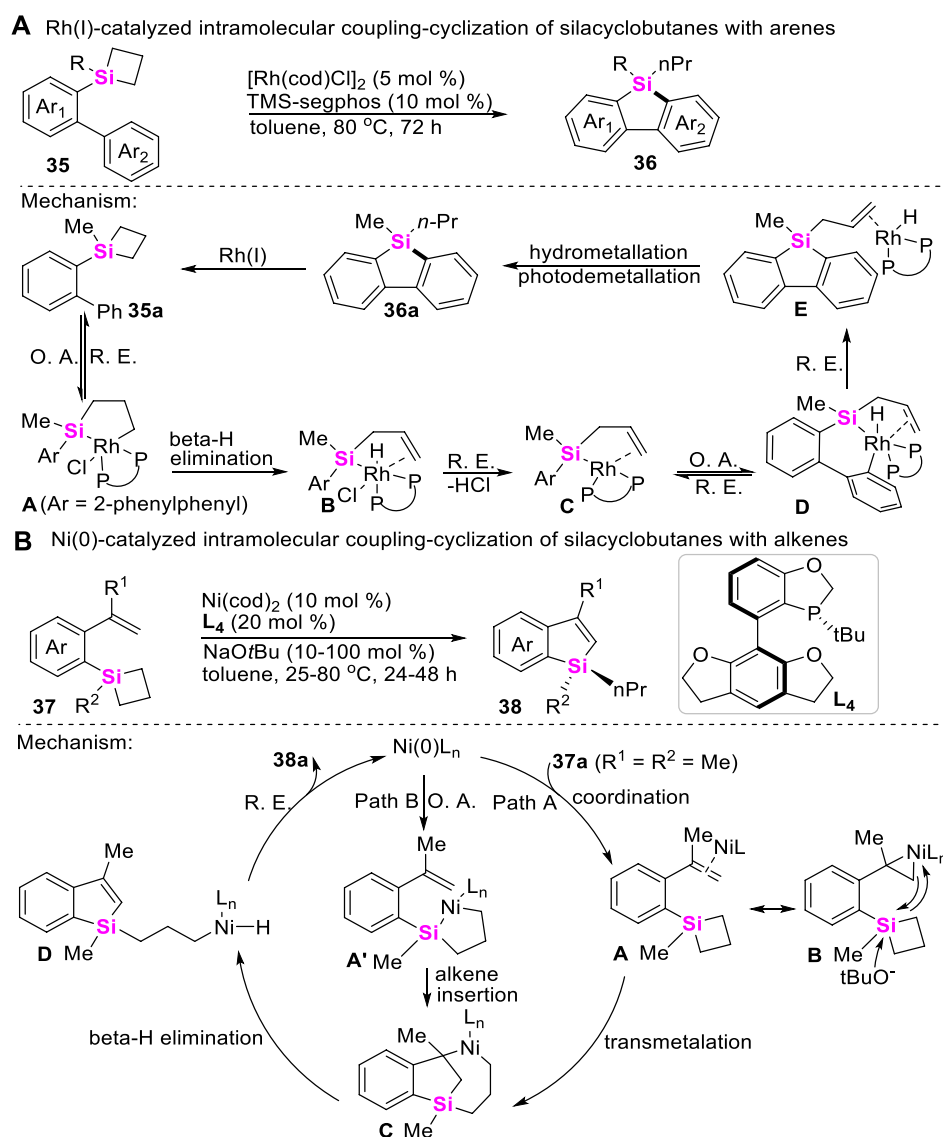


SCHEME 2

Transition metal-catalyzed coupling-cyclization of silacyclobutanes with cycloketones, cyclopropenes, and arylhalides.

containing SCBs **17** (Ishida et al., 2014), the key step is involved the oxidative addition of Pd (0) onto Si-C σ bond of silacyclobutane moiety to generate silapalladacycles **A** (Scheme 2A). On the contrary, for the intermolecular coupling-cyclization of cyclobutanones **19** with SCBs **7** (Okumura et al., 2017), the control experiments confirmed that the oxidative addition of Pd (0) onto C-C bond of cycloketone moiety to generate palladacycle (II) intermediates (**A**) prefer to occur (Scheme 2B). Based on the similar reaction mechanism, Xu and co-workers developed a Pd (II)-catalyzed [4 + 2] annulation of cyclopropenes with benzosilacyclobutanes to rapidly assemble silabicyclo [4.1.0] heptanes **23** and **25** in which cyclopropenes include *gem*-difluorocyclopropenes **24** (Scheme 2C) (Wang W et al., 2021; Xu et al., 2022). Meanwhile, Zhao still found Pd (II)- or Ni (II)-catalytic system could rapidly enable the intermolecular coupling-cyclization of silacyclobutanes **26** with cyclopropenones **27** (Scheme 2D) and aryl halides **29**, **31**, and **33** (Schemes 2E–G), furnishing silacycles **28**, **30**, **32**, and **34** (Zhao et al., 2018a; Qin et al., 2020; Qin et al., 2021; Wang X et al., 2021).

Meanwhile, the more challenging Rh-catalyzed intramolecular coupling-cyclization of SCBs with Csp²-H bonds has recently been achieved to make π -conjugated siloles with good regioselectivities by He (Zhang J et al., 2016). As shown in Scheme 3A, this transformation undergoes sequential C-Si bond and aryl Csp²-H bond activation process, and the catalytic cycle involves a rarely endocyclic β -hydride elimination of five-membered metallacycles **A**, which after reductive elimination gave rise to a Si-Rh^I species **B** that is capable of C-H activation. Apart from the Rh-catalysts, Zhao further developed a Ni (0)-catalyzed asymmetric intramolecular coupling-cyclization of alkene and SCBs to make enantioenriched silicon-stereogenic benzosiloles by utilizing *ortho*-vinylaryl silacyclobutanes **37** as substrates (Zhang et al., 2021). Two distinct pathways of this transformation are proposed. Path A begins with the coordination of the nickel (0) catalyst with alkene moiety to generate η^2 -coordinated complex **A** or **B**, then followed by an



SCHEME 3

Transition metal-catalyzed coupling-cyclization of silacyclobutanes with Csp²-H bonds.

alkoxide-promoted transmetalation, β -hydride elimination, and reductive elimination to produce the desired benzosilacycles **38**. In the contrast, Path B involves the oxidative addition of C-Si bond on SCB and sequential intramolecular insertion of an alkene moiety (Scheme 3B).

More recently, Wang reported a highly efficient Pd (II)-catalyzed carbene insertion into C-Si bonds of SCBs **7** to deliver silacyclopentanes **40** with excellent enantioselectivity by using trisylhydrazones **39** as carbenoid precursors (Huo et al., 2021). This reaction features with wide substrate scope and high tolerance of functional groups. Mechanistic studies including DFT calculations suggest a catalytic cycle involving oxidative addition of Pd to strained C-Si bonds, carbenoid migratory insertion, and reductive elimination (Scheme 4). Moreover, the roles of the chiral ligand **L**₅ in controlling the reaction enantioselectivity are also elucidated.

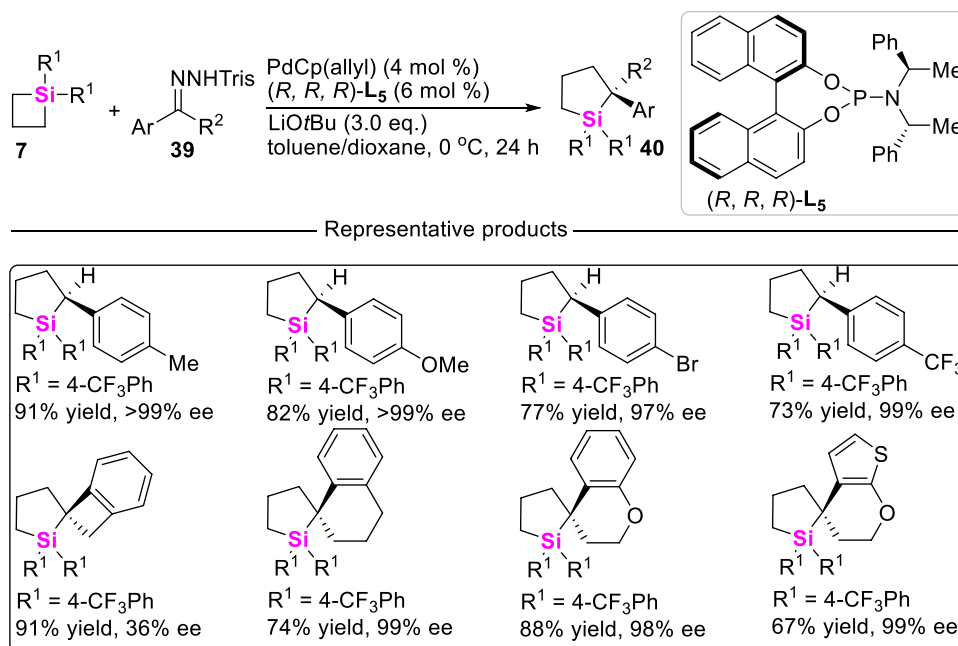
2.2 Coupling-cyclization by catalytic cleavage of the unstrained Si-C σ bond activation

In comparison with the strained C-Si bonds, unstrained C-Si σ bonds possess higher thermodynamic stability. Therefore, the inert C-Si bond cleavage generally requires the use of stoichiometric amounts of either organomagnesium (van Klink et al., 2002) or organolithium reagents (Yu et al., 2008) and harsh reaction conditions. Nevertheless, transition metal-catalyzed C-Si σ bond activation provides an alternative mild approach to enable C-Si σ bond cleavage. In these regards, Chatani first reported an Rh (I)-catalyzed benzosilole synthesis in

2009 through the coupling-cyclization of 2-silylphenylboronic acids with alkynes (Tobisu et al., 2009). The corresponding mechanism starts from the formation of arylrhodium intermediates **A**, generated by the transmetalation of arylboronic acids **41** to rhodium hydroxide Rh (I)OH, and adds across alkynes **8** to form the vinylrhodium intermediates **B**, which subsequently undergo oxidative addition at a trimethylsilyl group to afford intermediates **C**, producing benzosilole products **42** and methyl-rhodium **D** through reductive elimination. Meanwhile, protonolysis of **D** regenerates the catalytically active Rh (I)OH (Scheme 5A). By using the similar strategy, Xi, He, Ogoshi, and Zhao successively developed Pd-, Rh-, and Ni-catalyzed coupling-cyclization of unstrained C-Si σ bonds with alkynes (Schemes 5B, 5C), aldehydes (Scheme 5D), and alkenes (Scheme 5E), providing various synthetic methods to construct complex structural benzosiloles **45** (Liang et al., 2012) and **47** (Zhang et al., 2014), benzoxasiloles **49** (Hoshimoto et al., 2014), and spiro-silacycles **51** (Shi et al., 2022).

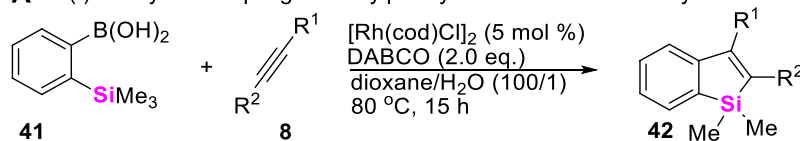
3 Synthetic strategy of silacycles via Si-H σ bond functionalization

Hydrosilanes belong to readily accessible organosilanes which possess versatile reactivity. So, the cross-coupling of hydrosilanes with alkanes, arenes, alkenes, and alkynes could provide an alternative strategy to form C-Si bonds. Among them, transition metal-catalyzed C-H/Si-H coupling and hydrosilylation of unsaturated hydrocarbons represent two main chemical transformations to assemble silacycles.

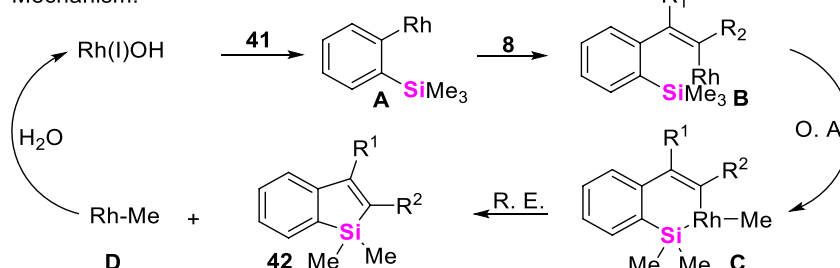
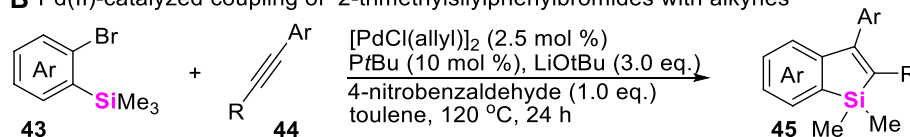
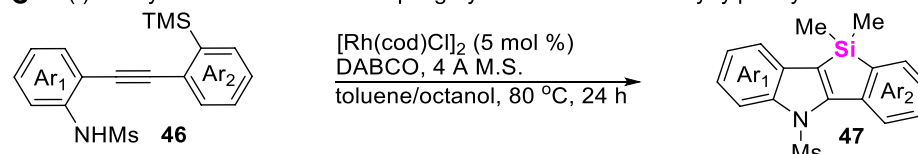
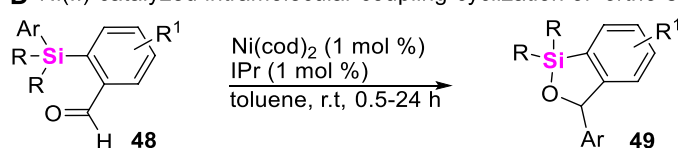
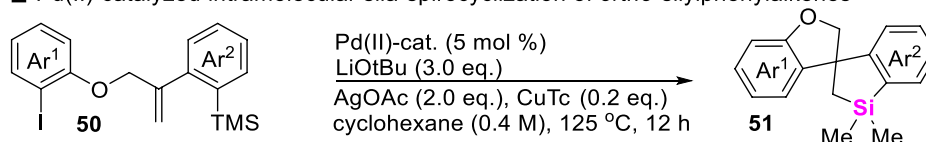


SCHEME 4

Pd (II)-catalyzed carbene insertion into C-Si bonds of silacyclobutanes.

A Rh(I)-catalyzed coupling of 2-silylphenylboronic acids with alkynes

Mechanism:

**B** Pd(II)-catalyzed coupling of 2-trimethylsilylphenylbromides with alkynes**C** Rh(I)-catalyzed intermolecular coupling-cyclization of *ortho*-alkynylphenylamines**D** Ni(II)-catalyzed intramolecular coupling-cyclization of *ortho*-silylphenylaldehydes**E** Pd(II)-catalyzed intramolecular sila-spirocyclization of *ortho*-silylphenylalkenes

SCHEME 5

Transition metal-catalyzed unstrained C-Si bond activation.

Meanwhile, hydrosilanes including dihydrosilanes and monohydrosilanes are also the most common precursors of chiral tetraorganosilicons, and the development of synthetic methodology for chiral silacycles which are derived from hydrosilanes, has become more challenging.

3.1 Intramolecular coupling-cyclization of Si-H bonds with alkanes

As is well-known, Csp³-H bond functionalization is one of the most useful and versatile strategies for constructing organic molecules. In comparison with Csp²-H bond and Csp³-H bond, the reactivity of alkyl Csp³-H bond is inert. Therefore, examples of Csp³-H/Si-H coupling reactions are very rare.

The pioneer studies on transition metal-catalyzed Csp³-H/Si-H bond coupling reaction were mainly performed by Hartwig, but most of these transformations suffered from high reaction temperatures (135°C ~ 200 °C) (Tsukada and Hartwig, 2005). In 2010, Takai and co-workers reported Rh (I)-catalyzed Csp²-H/Si-H coupling reaction to produce the mixture of silafluorene 53 and dibenzo [b, d]silane 54 by using *ortho*-arylphenylsilanes including 33 as starting materials (Scheme 6A) (Ureshino et al., 2010). Subsequently, they further found that increasing the reaction temperature could chemoselectively enable Csp³-H/Si-H coupling under the same catalytical system, giving dibenzo [b, d]silane 56 as a sole intermolecular coupling-cyclization product by using *ortho*-alkylphenylsilanes as starting materials (Kuninobu et al., 2013a). The proposed mechanism was involved in the oxidative addition of the Si-H bond to Rh (I)-catalysts,

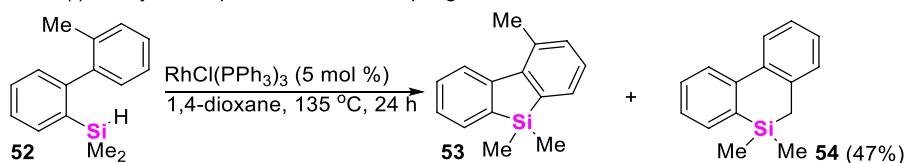
then undergoing Si-H bond activation and σ -bond metathesis to form cyclorhodiumates **B** and **C**, respectively. Subsequently, reductive elimination of intermediate **B** or **C** produces benzosilacycle **56** and regenerates the Rh (I)-catalyst (Scheme 6B). To our satisfaction, Takai continued to optimize these reaction parameters by utilizing phosphorus ligand and 3,3-dimethyl-1-butene as additional additives, significantly lowering the reaction temperatures from 180°C to 50°C (Murai et al., 2015).

Possibly encouraged by Takai's work, Huang further explored the synthetic approach to access 1,3-sila-heterocycles through methoxyl or aminomethyl Csp³-H/Si-H coupling of arylalkylhydrosilanes **57**

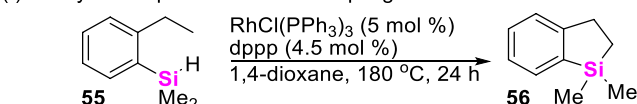
(Fang et al., 2017), and found that PCP Pincer-Ru(II)- and PCP Pincer-Ir (III)-catalyzed intramolecular cyclization could rapidly assemble 1,3-sila-heterocycles **58** via intermolecular σ -bond metathesis process (Scheme 6C). As for the more challenging Csp³-H/Si-H coupling of trialkylhydrosilanes **59**, Gevorgyan developed an Ir(I)-catalyzed and pyridine-chelation-assisted Csp³-H silylation strategy of an unactivated C (sp³)-H bonds to produce silolanes **60** with good to excellent yields (Ghavytadze et al., 2014), in which different linear alkyl chains were well-tolerated in this reaction conditions (Scheme 6D).

Although chiral Si-atoms are not naturally occurring, these organosilanes show great application potential, especially in the

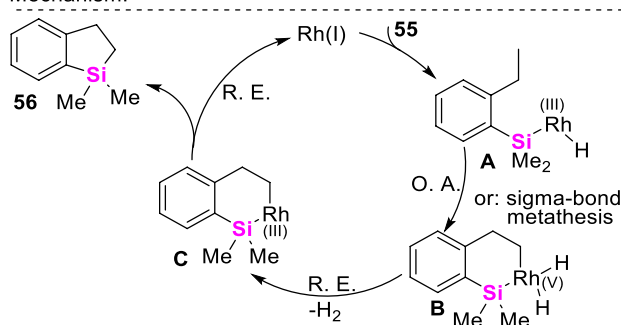
A Rh(I)-catalyzed Csp²-H/Si-H bond coupling



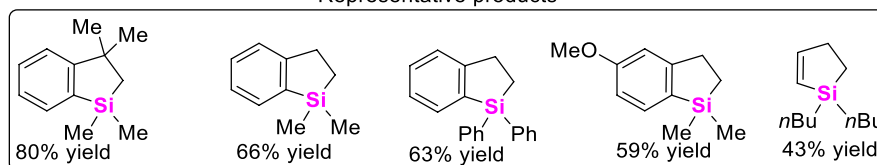
B Rh(I)-catalyzed Csp³-H/Si-H bond coupling



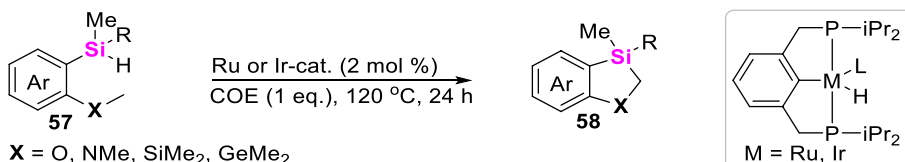
Mechanism:



Representative products

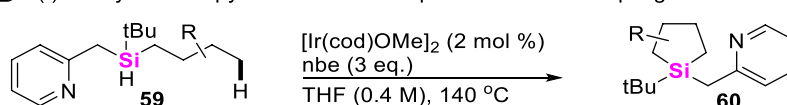


C Pincer-Ru(II)- and Ir(III)-catalyzed methoxyl and aminomethyl Csp³-H/Si-H bond coupling



X = O, NMe, SiMe₂, GeMe₂

D Ir(I)-catalyzed and pyridine-directed Csp³-H/Si-H bond coupling of linear alkyl chains



SCHEME 6

Transition metal-catalyzed Csp³-H/Si-H bond coupling reaction.

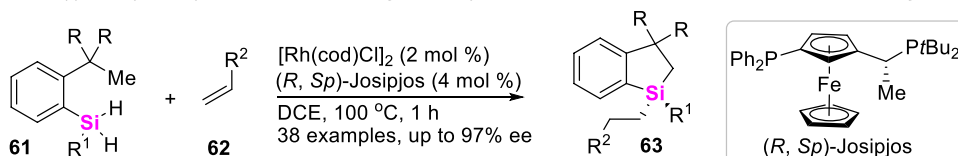
field of life sciences and material chemistry. To date, the approach to access chiral sila-compounds through $\text{Csp}^3\text{-H/Si-H}$ coupling reaction is very limited. Albeit Takai ever achieved an asymmetric $\text{Csp}^3\text{-H}$ silylation toward silicon-stereogenic center, the corresponding enantiomeric excess (ee) values of spirosilabiindanes did not exceed 40% (Murai et al., 2015). Recently, He utilized Rh (I)/chiral Josiphos-catalytic system, successively realized intramolecular asymmetric $\text{Csp}^3\text{-H/Si-H}$ coupling-reaction of dihydrosilanes, constructing silicon-stereogenic dihydrobenzosiloles (Scheme 7A) (Yang et al., 2020) and dihydrodibenzosilines (Scheme 7B) (Guo et al., 2021) with excellent enantioselectivity (up to 97% ee values).

3.2 Intramolecular coupling-cyclization of Si-H bonds with arenes

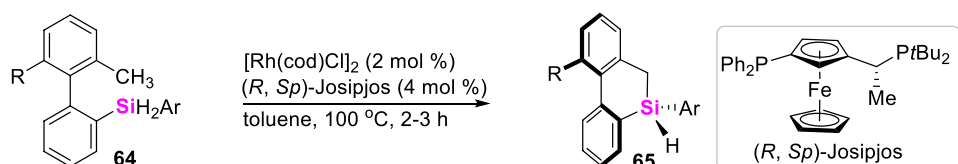
Silicon-containing π -conjugated molecules can be utilized in the areas of electro- and photo-luminescence, the

intramolecular coupling-cyclization of aryl $\text{Csp}^2\text{-H}$ bonds with Si-H bonds has therefore been widely explored to furnish silaarenes. Usually, the present synthetic methods to access benzosilacycles are mainly focused on the set-up of different reaction systems, including arylsilanes and catalysts. The reaction mechanism was generally involved in the oxidative addition of low-valent metal ions including Rh (I) and Ir (I) to Si-H bond of hydrosilanes **66**, followed by the sequential aryl $\text{Csp}^2\text{-H}$ bond activation and reductive elimination process to afford diverse silaarenes **67** (Scheme 8A). The earlier study about transition metal-catalyzed aryl $\text{Csp}^2\text{-H/Si-H}$ coupling-reaction was reported by Takai in 2010 (Ureshino et al., 2010). Takai and co-workers utilized $\text{RhCl}(\text{PPh}_3)_3$ as catalysts, and employed biarylmonehydrosilanes as substrates to rapidly assemble silafluorenes through Rh (I)-catalyzed double activation of Si-H and C-H bonds with dehydrogenation. Since then, Hartwig (Li et al., 2014), Shi (Su et al., 2017), Zhao (Zhao et al., 2018b), and Xu (Lin et al., 2017) also realized Ir (I)-catalyzed intramolecular dehydrogenation-coupling of aryl $\text{Csp}^2\text{-H}$ bonds with monohydrosilanes **68**, **70**, and **72**, producing azo-silacycles **69** (Scheme 8B), oxa-silacycles **71** (Scheme 8C) and cyclic disiloxanes **73** (Scheme 8D), respectively.

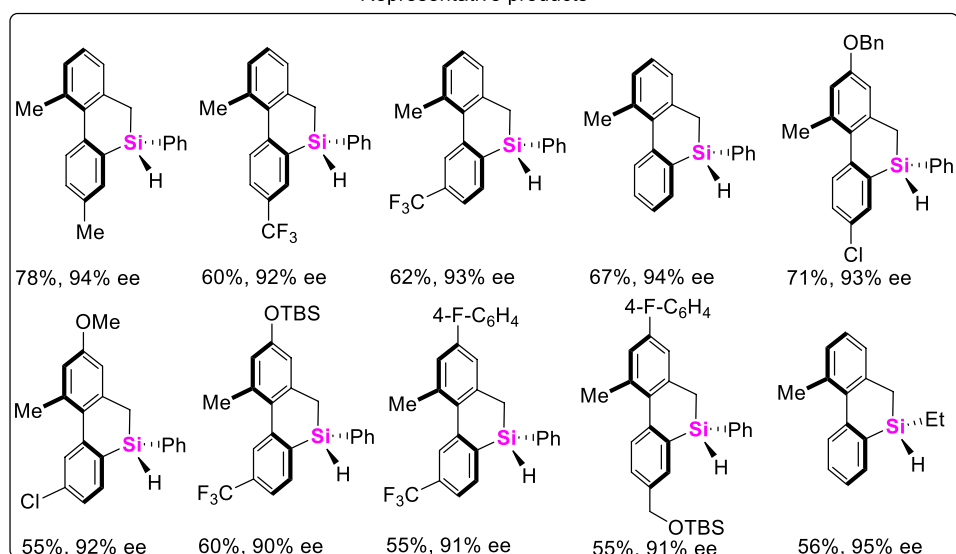
A Rh(I)-catalyzed synthesis of Si-stereogenic dihydrobenzosiloles via $\text{Csp}^3\text{-H/Si-H}$ bond coupling



B Rh(I)-catalyzed synthesis of silicon-stereogenic dihydrodibenzosilines via $\text{Csp}^3\text{-H/Si-H}$ bond coupling



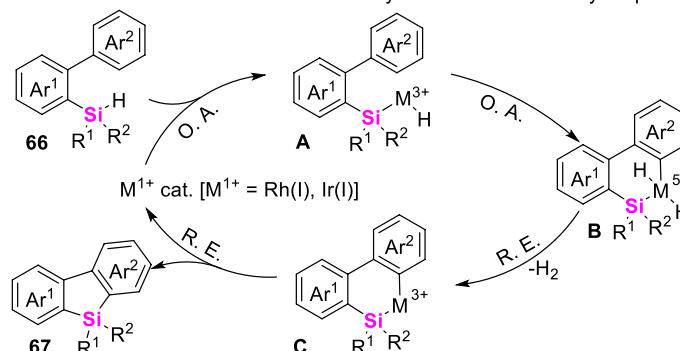
Representative products



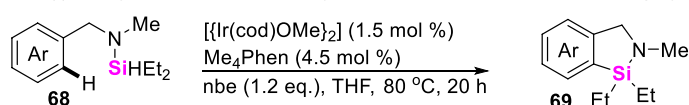
SCHEME 7

Transition metal-catalyzed asymmetric $\text{Csp}^3\text{-H/Si-H}$ bond coupling reactions.

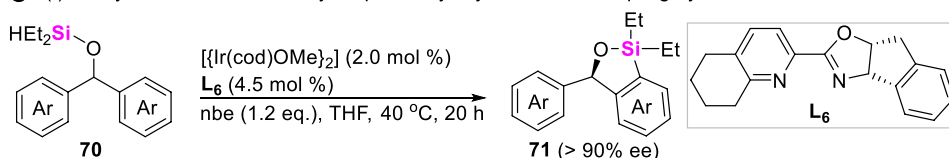
A The general reaction mechanism of the metal-catalyzed intramolecular aryl Csp²-H/Si-H bond coupling



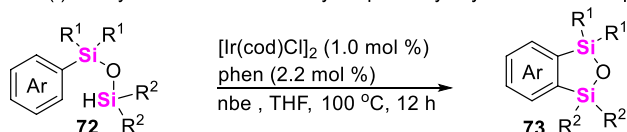
B Ir(I)-catalyzed intramolecular aryl Csp²-H/amino Si-H bond coupling-cyclization



C Ir(I)-catalyzed intramolecular aryl Csp²-H/alkoxy Si-H bond coupling-cyclization



D Ir(I)-catalyzed intramolecular aryl Csp²-H/silyloxy Si-H bond coupling-cyclization



SCHEME 8

Transition metal-catalyzed intramolecular aryl Csp²-H/Si-H bond coupling reactions.

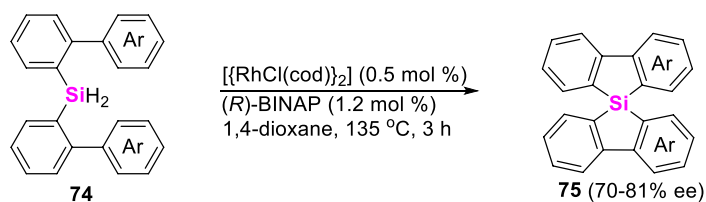
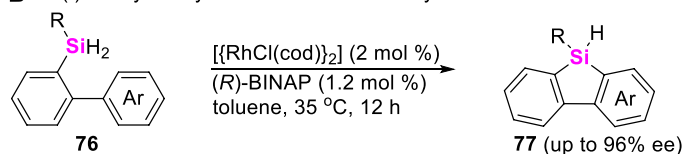
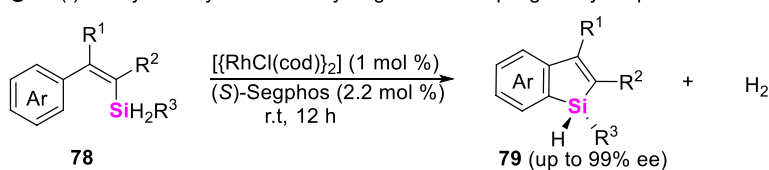
Of course, Takai still found Rh (I)-salts possess excellent catalytical activity to allow for dehydrogenation-coupling between aryl Csp²-H bonds and dihydrosilanes. For example, in 2013, Takai and coworkers developed an intramolecular asymmetric coupling-cyclization of bis (biphenyl) bihydrosilanes **74** in the presence of {[RhCl(cod)]₂} and chiral (*R*)-binap (Kuninobu et al., 2013b), providing spirosilabifluorenes **75** in 73%–95% yields (Scheme 9A). Encouraged by this work, W. He (Scheme 9B) and C. He (Scheme 9C) further realized the construction of stereogenic silicon benzosilacycles by using aryldihydrosilanes **76** and vinyldihydrosilanes **78** as starting material in the presence of Rh (I)-catalysts and chiral diphosphine ligands, excellent enantioselectivities of chiral benzosilacycles **77** and **79** were up to >99% ee (Ma et al., 2021; Yuan et al., 2021).

Besides that transition metal Rh (I)- and Ir (I)-catalysts could efficiently enhance the cross-coupling of aryl Csp³-H bonds with hydrosilanes, Studer and Li also found that oxidants-promoted aryl Csp²-H bond/Si-H coupling could easily occur to deliver benzosilacycles **80** in good reaction conversions (Scheme 10). This transformation is generally involved in the homolysis of oxidants such as DTBP and

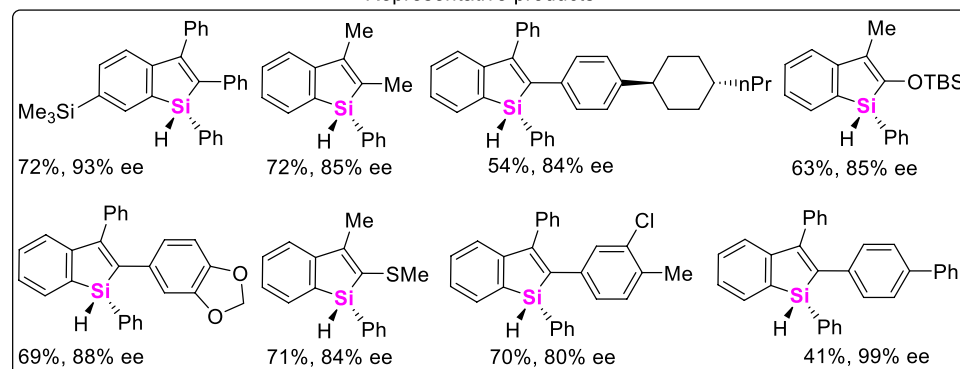
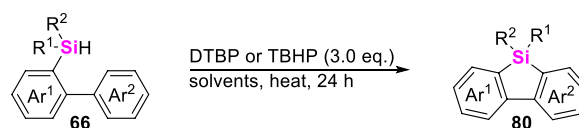
TBHP to produce alkoxy radicals, which then abstracted the H atom from monohydrosilanes to form Si-centered radicals. Finally, the radical-cyclization between Si-centered radicals and arenes gave 9-silafluorene skeletons (Leifert and Studer, 2015; Xu et al., 2015).

3.3 Intramolecular coupling-cyclization of Si-H bonds with alkenes and alkynes

Despite the rich history of the synthesis of silacycles, the method of intramolecular coupling-cyclization of hydrosilanes with alkenes or alkynes has been significantly lacking. To date, only Nakamura in 2008 reported a Me₃SnLi-promoted intramolecular coupling-cyclization of hydrosilanes with alkynes to produce benzosiloles (Ilies et al., 2008), in which nucleophilic addition of Et₃SnLi to alkynes was involved (Scheme 11A). Subsequently, Nakamura further found that strong base KH could also promote the same transformation by using (2-alkynylphenyl)monohydrosilanes as substrates (Scheme 11A) (Ilies et al., 2009). By utilizing the similar substrates, Xu realized a Rh-catalyzed dynamic kinetic

A Rh(I)-catalyzed intramolecular dehydrogenation-coupling of aryl Csp²-H bonds with dihydrosilanes**B** Rh(I)-catalyzed synthesis of chiral monohydrosilanes**C** Rh(I)-catalyzed asymmetric dehydrogenation-coupling of aryl Csp²-H bonds with vinylhydrosilanes

Representative products

**SCHEME 9**Rh-catalyzed intramolecular asymmetric dehydrogenation-coupling of aryl Csp²-H bonds with dihydrosilanes.**SCHEME 10**Oxidant-promoted intramolecular dehydrogenation-coupling of aryl Csp²-H bonds with hydrosilanes.

asymmetric intramolecular hydrosilylation with “silicon-centered” racemic hydrosilanes in the presence of chiral ligand SiMOS-Phos, providing silicon-stereogenic benzosiloles in excellent ee values (Scheme 11B) (Tang et al., 2020; Zeng et al., 2022). By the way, the Pt (0)-catalyzed intermolecular hydrosilylation of OH-containing acetylenes **89** with dihydrosilanes **90** was also achieved in 2018 by Xu to allow for assembling silyloxycycles and cyclic siloxanes **91** (Scheme 11C) (Long et al., 2018). In 2020, the transition metal-catalysis

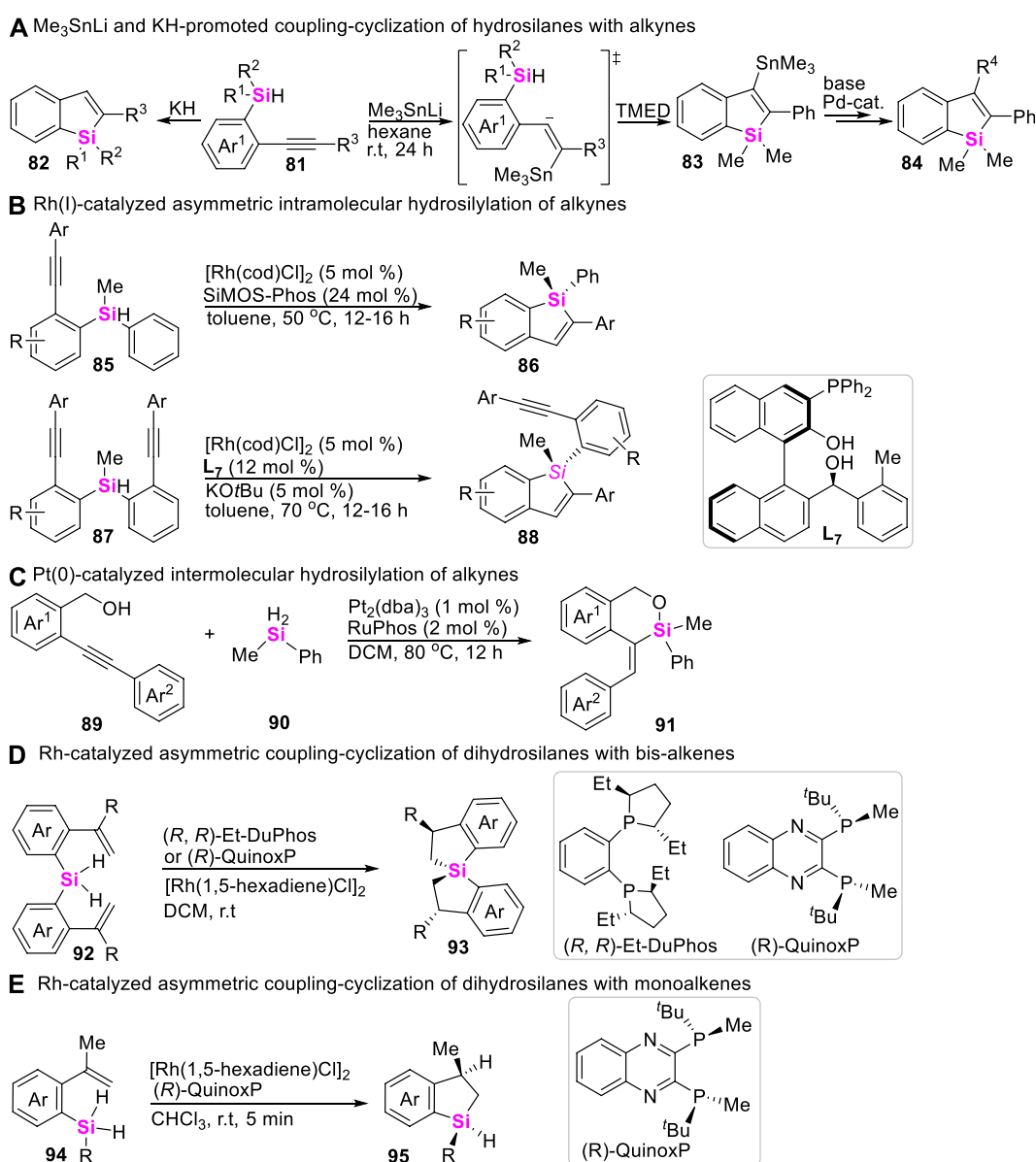
strategy has been gradually developed by Wang to assemble benzosilacycles through intramolecular coupling-cyclization of monohydrosilanes with alkenes. The intramolecular coupling-cyclization of bis-(alkenyl)dihydrosilanes (Chang et al., 2020) and mono-(alkene)dihydrosilanes (Huang Y H et al., 2022) could smoothly proceed in the presence of Rh (I)-catalysts and chiral ligands, producing spiro-silabiindanes (Scheme 11D) and monohydro-benzosilacycles (Scheme 11E) with good to excellent ee values, respectively.

4 Synthetic strategy of silacycles via coupling-cyclization of vinylsilanes

Although vinylsilanes have been widely used in the Hiyama cross-coupling reaction to make C-C bonds with the release of the silyl group, transition metal-catalyzed Mizoroki-Heck reaction of vinylsilanes with aryl halides can form new C-C bonds at the β -position of vinylsilane and keep silyl moiety untouched. Therefore, the development of intramolecular Mizoroki-Heck coupling-cyclization of vinylsilanes may provide an efficient approach to access silacycles. Unfortunately, the examples involving vinylsilane which participated in the Mizoroki-Heck reaction are rarely

reported. To date, only Xi and Teen successively reported Pd-catalyzed intramolecular coupling-cyclization of vinylsilanes with aryl Csp²-X bonds (X = Br and I) to assemble benzosilacycles (Scheme 12A) (Teng and Keese, 1999; Ouyang et al., 2012).

Aryl migration via Smiles rearrangement is a powerful tool for the synthesis of polycyclic arenes. However, the modes of radical Smiles rearrangement are very limited. More recently, Zeng reported a novel photo-catalyzed cycloaromatization of *ortho*-alkynylaryl vinylsilanes **99** with arylsulfonyl azides **100** for delivering naphthyl-fused benzosiloles **101**, various *ortho*-alkynylaryl vinylsilanes including *ortho*-alkynylaryl allylsilanes and arylsulfonyl azides are well-allowed for this



SCHEME 11

Intramolecular coupling-cyclization of Si-H bonds with alkenes and alkynes.

reaction system (Chen et al., 2021). The corresponding reaction mechanism features a unique combination of cascade S-N/C-S bond cleavages and α -silyl radical Smiles rearrangement, in which silyl hyperconjugation effect (the so-called β -effect) plays a key role in controlling the regioselective coupling-cyclization (Scheme 12B). Post-synthetic applications indicate that these silaarenes show promising potential in luminescent materials.

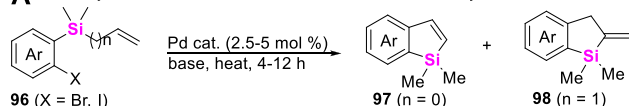
5 Synthetic strategy of silacycles via coupling-cyclization of alkynylsilanes

Alkynylsilanes belong to versatile synthons, possessing characteristic reactivity. Therefore, the development of alkynylsilane-based coupling-cyclization has aroused increasing concerns in the assembly of silacycles. In these regards, Nozaki utilized silicon-containing diynes **102** as substrates, explored the reactivity of Rh-catalyzed intramolecular alkynylsilylation of alkynes to produce enyne-functionalized dibenzosilacycles **103** (Shintani et al., 2015), this transformation was involved in sequential oxidative-addition, *syn*-insertion and reductive elimination process (Scheme 13A). Subsequently, Nozaki continued to design and synthesize prochiral triynes **104** and developed an Rh-catalyzed asymmetric [2 + 2 + 2] cycloaddition of silicon-containing

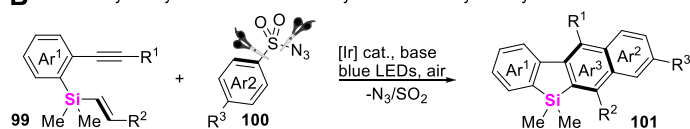
prochiral triynes with isocyanates to afford silicon-stereogenic silicon-bridged arylpyridinones **105** (Shintani et al., 2016), high yields and enantioselectivities have been achieved by employing an axially chiral monophosphine ligand (Scheme 13B). Meanwhile, transition metal-catalyzed intramolecular coupling-cyclization of alkynylsilanes with aryl Csp²-X bonds (X = Br, I, etc.) could also provide an alternated approach to access silacycles. Possibly encouraged by the research work from Teen (Teng and Keese, 1999) and Ouyang (Ouyang et al., 2012) groups, Donnard utilized *ortho*-alkynylsilylalkyl aryl halides as substrates, realized the Pd (II)-catalyzed of coupling-cyclization of alkynylsilanes **96** with aryl boronic acids (Scheme 13C), rapidly assembling vinylation benzosiloles **106** (Wagner et al., 2017). More recently, Zeng developed an efficient Pd/Rh-cooperatively catalyzed arylalkynylation of *ortho*-alkynylsilylalkyl aryl halides **107** with α -alkynylalcohols **108**, merging an alkynylidene moiety into benzosilacycle **109** (Chen et al., 2021). The corresponding mechanistic investigations demonstrated that the relay trimetallic transmetalation played a pivotal role in governing this transformation (Scheme 13D).

On the other hand, alkynylsilanes can also undergo 1,2-silicon migration under transition metal-catalytic systems (Kanno et al., 2016). Employing these reaction characteristics, Tanaka reported an Rh(I)/biphep complex catalyzed cycloisomerization of 2-(alkynylsilyl-ethynyl)phenols **110**,

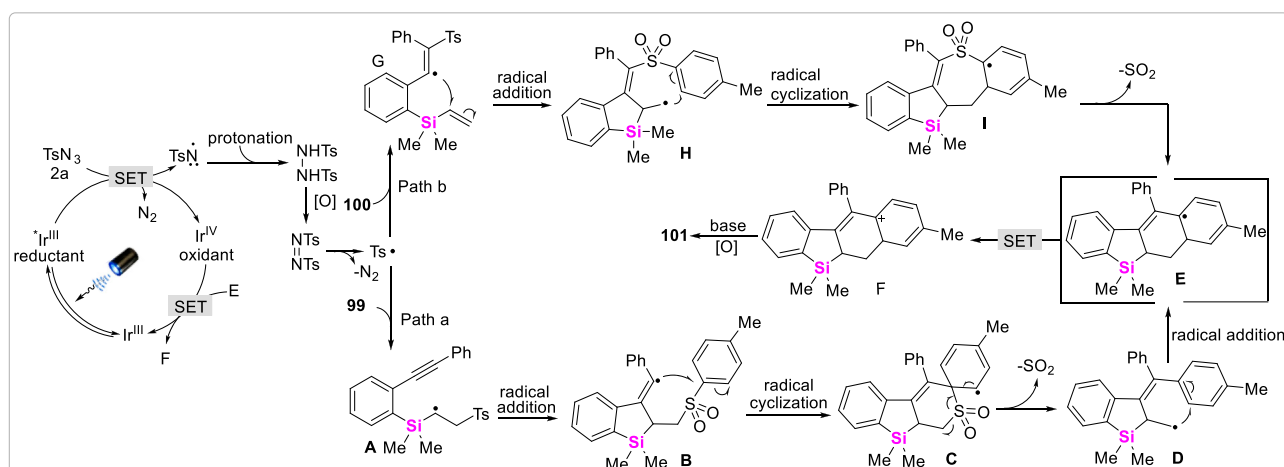
A Pd-catalyzed intramolecular Mizoroki-Heck reaction of vinylsilanes



B Photocatalyzed cycloaromatization of vinylsilanes with arylsulfonylazides

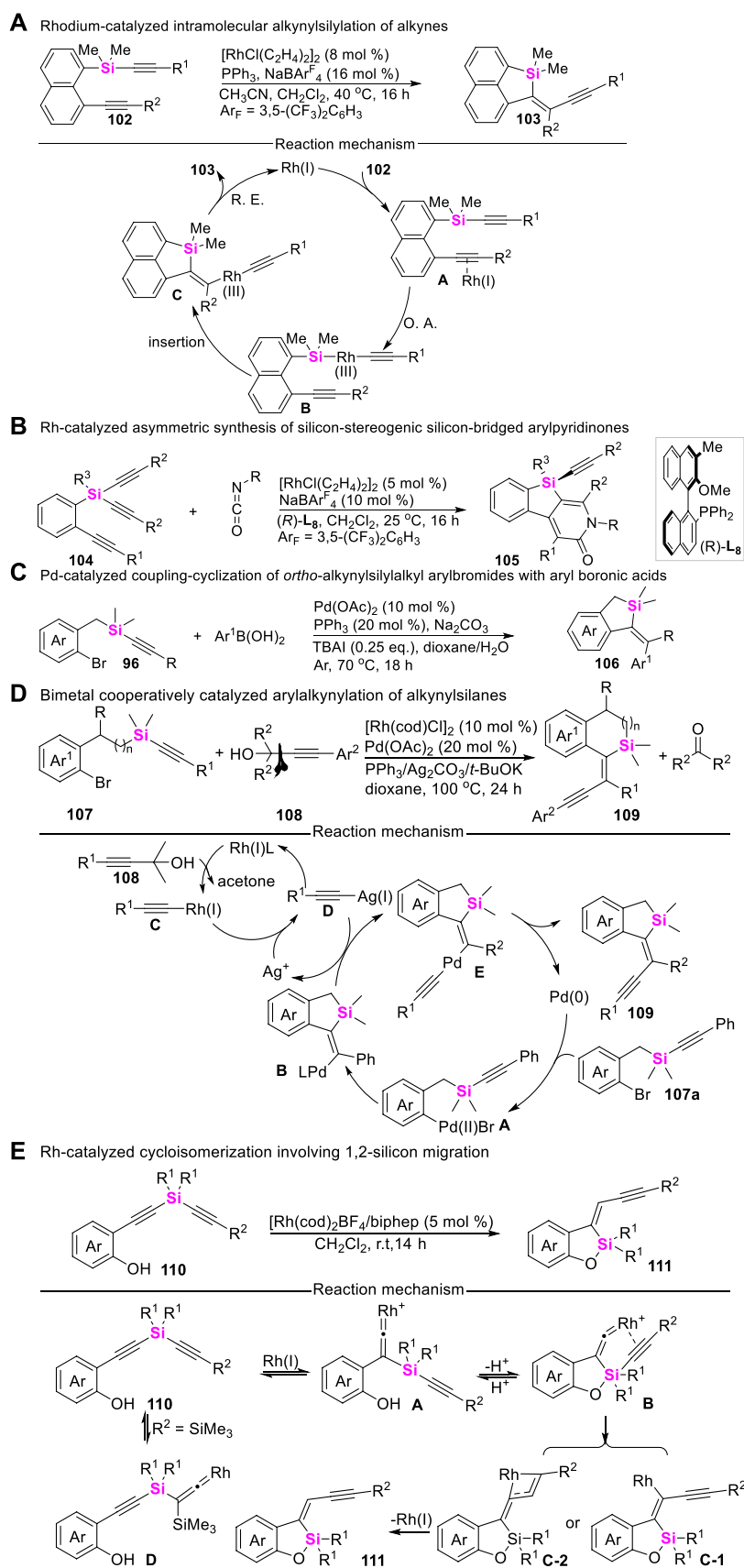


Reaction mechanism



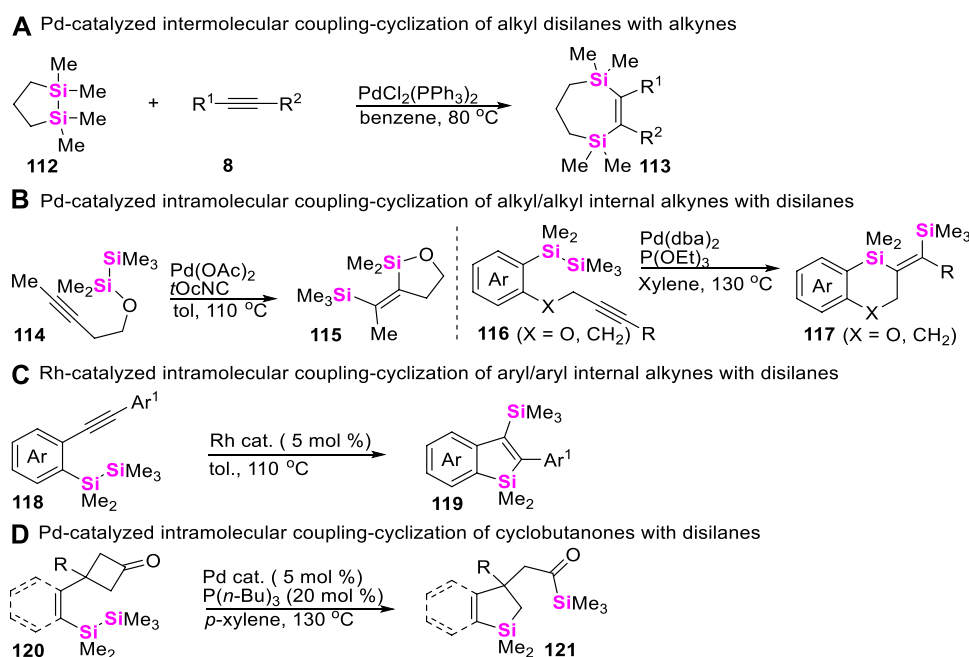
SCHEME 12

Coupling-cyclization of vinylsilanes.



SCHEME 13

Coupling-cyclization of alkynylsilanes.



SCHEME 14

Coupling-cyclization of disilanes with alkynes and cyclobutanones.

leading to the formation of alkynylmethylidene-benzoxasiloles **111** through concomitant silicon and carbon migration (Namba et al., 2017). This novel cycloisomerization possibly proceeds via the formation of Rh-vinylidenes through 1,2-silicon migration, followed by 1,3-carbon (alkyne) migration via the formation of hypervalent silicon centers (Scheme 13E).

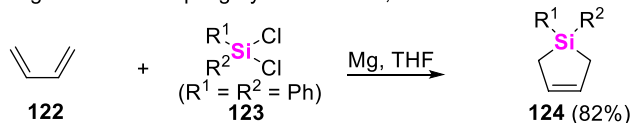
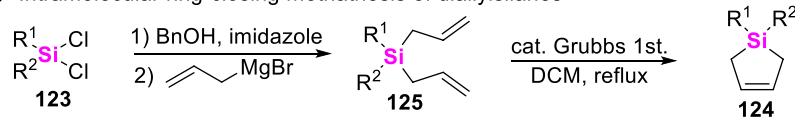
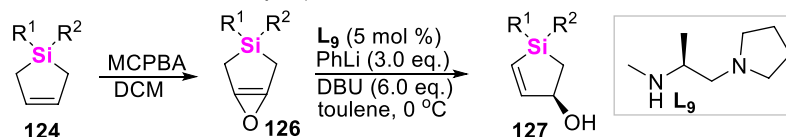
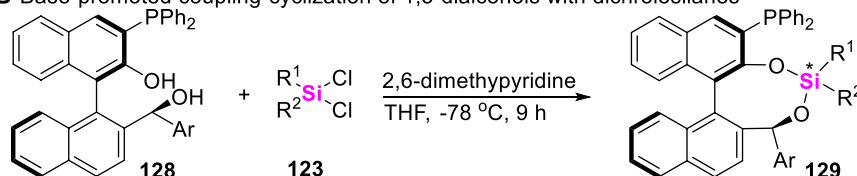
6 Synthetic strategies of silacycles via Si-Si σ bond activation of disilanes

The relatively weak Si-Si σ bond (ca. 54 kcal/mol) (Sanderson, 1983) suggests that disilanes could be converted into $\text{Si-M}^{n+2}\text{-Si}$ species via low-valent metal-based oxidative addition. Thus, the addition of intermetallic $\text{Si-M}^{n+2}\text{-Si}$ σ -bonds to alkynes can provide an efficient route for the preparation of silacycles. In these regards, the first example was evidenced by Sakurai et al., 1975, that a strained cyclic disilane **112** can react with activated alkynes **8** in the presence of Pd(II)-catalysts to provide disilyl-cycloheptenes **113** (Scheme 14A). Encouraged by this pioneering work, different disilanes were successively designed and synthesized to react with alkynyl moieties via intramolecular coupling-cyclization. For examples, Ito and Matsuda reported Pd-catalyzed intramolecular *syn* bis-silylation of alkyl/alkyl internal alkynes (Ito et al., 1991; Ahmad et al., 2017), providing straightforward access to a large set of *syn*-disilylated olefins **115** and **117** (Scheme 14B). In 2012, Matsuda and co-workers (Matsuda and Ichioka, 2012) utilized Rh (I)-catalysts to enable an intramolecular bis-silylation of aryl/aryl internal alkynes **118** into silylbenzosilanes **119** (Scheme 14C). Of course, apart

from the coupling-cyclization of disilanes with alkynes, Pd-catalyzed intramolecular σ -bond metathesis between disilanes with cyclobutanones was also investigated by Murakami (Ishida et al., 2012) to furnish an acylsilane-tethered silaindane skeletons **121** (Scheme 14D).

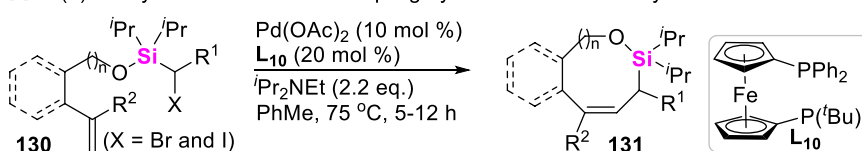
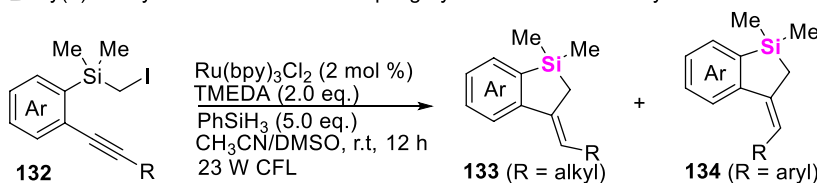
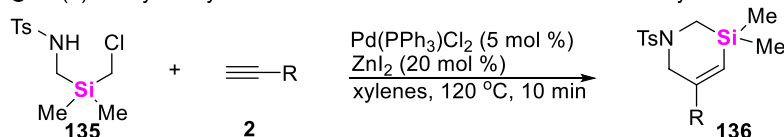
7 Synthetic strategy of silacycles via cross-coupling of 1,3-dienes with dichlorosilanes and intramolecular ring-closing metathesis of diallylsilanes

Silacyclopentenes belong to versatile precursors of silacycles. In 2001, Kozmin reported an Mg-mediated cyclosilylation of butadiene **122** with dichlorodiphenylsilane **123** to produce silacyclopentene **124** (Scheme 15A) (Liu and Kozmin, 2001). Recently, Tomooka and Igawa developed an alternative approach to access silacyclopentenes **124** through successive diallylation of dichlorosilanes **123** and ring-closing metathesis of diallylsilanes **125** (Scheme 15B). These silacyclopentenes **124** could be further oxidized to furnish epoxide **126** by 3-chloro-peroxybenzoic acid (MCPBA), followed by post-modification to afford chiral silacyclopentenols **127** and other multi-functionalized silacycles (Scheme 15C), featuring with interesting biological activity (Igawa et al., 2016; Igawa et al., 2017). By the way, it should be noted that dichlorosilanes could also easily react with 1,5-dialcohols **128** under base conditions to produce dioxasilanes **129** (Scheme 15D) (Bai et al., 2017).

A Mg-mediated coupling-cyclization of 1,3-dienes with dichlorosilanes**B** Intramolecular ring-closing metathesis of diallylsilanes**C** Post-modification of silacyclopentenes**D** Base-promoted coupling-cyclization of 1,5-dialcohols with dichlorosilanes

SCHEME 15

Synthetic strategies of silacyclopentenes.

A Pd(II)-catalyzed intramolecular coupling-cyclization of halomethylsilanes with alkenes**B** Ru(II)-catalyzed intramolecular coupling-cyclization of halomethylsilanes with alkynes**C** Pd(II)-catalyzed cycloaddition of 3-silaazetidines with terminal alkynes

SCHEME 16

Coupling-cyclization of halomethylsilanes with unsaturated hydrocarbons.

8 Synthetic strategy of silacycles via cross-coupling of halomethylsilanes with unsaturated hydrocarbons

To date, besides that these organosilicon compounds including silacyclobutanes, aryl/alkylsilanes, hydrosilanes, halosilanes,

alkynylsilanes, vinylsilanes, allylsilanes and disilanes which have been successfully employed to couple with different coupling-reagents to make various silacycle skeletons, other novel silyl sources have also aroused wide concerns. In this regard, Gevorgyan designed and made halomethylsilyl ether-tethered alkenes **130**, and found that these halomethylsilanes can undergo intramolecular coupling-

cyclization under Pd (II)-catalysis system to afford allylic silyloxycycles **131** via Heck reaction (Scheme 16A) (Parasram et al., 2014). Two years later, Song developed photo-catalyzed intramolecular coupling-cyclization of iodomethylsilanes with alkynes to produce 5-exo-cyclization products (Lin et al., 2016), in which alkyl-substituted internal alkynes lead to *Z*-benzosilolines **132**, aryl-substituted internal alkynes result in *E*-benzosiloline **134** (Scheme 16B). More recently, Song still further found that 3-silaazetidines can be easily prepared *in situ* from diverse air-stable precursors ($\text{RSO}_2\text{NHCH}_2\text{SiR}_2\text{CH}_2\text{Cl}$ **135**) (Scheme 16C), and this silyl source could easily undergo an intermolecular coupling-cyclization with terminal alkynes **2** in the presence of Pd (II)-catalysts, producing 3-silatetrahydropyridines **136** and diverse silaazacycle derivatives (Wang X et al., 2021).

9 Conclusion and perspectives

In summary, the methods for rapid assembly of silacycles are valuable to the fields of synthetic chemistry, material science, and biological chemistry. Therefore, the discovery of new reagents and new synthetic methodologies plays an important role in the development of organosilane chemistry. To date, the coupling-reaction between hydrosilanes with unsaturated hydrocarbons, alkanes, and arenes has been well-established; meanwhile, the studies on C-Si σ bond activation- and Si-Si σ bond activation-based coupling-cyclization have also obtained significant progress. By contrast, silylenoid-involved coupling-cyclization is very rarely reported. Although several silylenoid precursors such as di-*tert*-butyldiazidosilanes (Welsh et al., 1988), diamidodichlorosilanes (Denk et al., 1994), and cyclohexene-derived silacyclopropanes (Driver et al., 2002) have been reported, their applications in the construction of silacycles are very limited. Thus, a major goal for the future focus of this field is the development of silylenoid-based new organic reactions,

which will be believed to provide a versatile strategy to access more complex structural silacycles.

Author contributions

FC: investigation and editing; LL: investigation; WZ: supervision, writing—review. All authors contributed to the article and approved the submitted version.

Funding

This work is supported by the NSFC (No. 22271100), KARDPGP (No. 2020B010188001), GBABRF (No. 2023A1515010070), and CPSF (No. 2021M701243) for financial support.

Conflict of interest

The authors declare that the research was conducted in the absence of any commercial or financial relationships that could be construed as a potential conflict of interest.

Publisher's note

All claims expressed in this article are solely those of the authors and do not necessarily represent those of their affiliated organizations, or those of the publisher, the editors and the reviewers. Any product that may be evaluated in this article, or claim that may be made by its manufacturer, is not guaranteed or endorsed by the publisher.

References

- Ahmad, M., Gaumont, A. C., Durandetti, M., and Maddaluno, J. (2017). Direct syn addition of two silicon atoms to a $\text{C}\equiv\text{C}$ triple bond by Si-Si bond activation: Access to reactive disilylated olefins. *Angew. Chem. Int. Ed.* 56, 2504–2508. doi:10.1002/ange.201611719
- Akiyama, T., and Imazeki, S. (1997). Base promoted preparation of alkenylsilanes from allylsilanes. *Chem. Lett.* 10, 1077–1078. doi:10.1246/cl.1997.1077
- Allred, A. L., and Rochow, E. G. (1958). A scale of electronegativity based on electrostatic force. *J. Inorg. Nucl. Chem.* 5, 264–268. doi:10.1016/0022-1902(58)80003-2
- Bai, X. Y., Zou, J. F., Chen, M. Y., Xu, Z., Li, L., Cui, Y. M., et al. (2017). Lewis-base-mediated diastereoselective silylations of alcohols: Synthesis of silicon-stereogenic dialkoxysilanes controlled by chiral aryl BINOLs. *Chem. Asian J.* 12, 1730–1735. doi:10.1002/asia.201700640
- Breit, N. C., Szilvasi, T., Suzuki, T., Gallego, D., and Inoue, S. (2013). From a zwitterionic phosphasilene to base stabilized silyliumylidene-phosphide and bis(silylene) complexes. *J. Am. Chem. Soc.* 135, 17958–17968. doi:10.1021/ja409720c
- Chang, X., Ma, P. L., Chen, H. C., Li, C. Y., and Wang, P. (2020). Asymmetric synthesis and application of chiral spirosilabindanes. *Angew. Chem. Int. Ed.* 59, 9022–9025. doi:10.1002/ange.202002289
- Chatgililoglu, C., Ferreri, C., Landais, Y., and Timokhin, V. I. (2018). Thirty years of $(\text{TMS})_3\text{SiH}$: A milestone in radical-based synthetic chemistry. *Chem. Rev.* 118, 6516–6572. doi:10.1021/acs.chemrev.8b00109
- Chen, F., Shao, Y., Li, M., Yang, C., Su, S. -J., Jiang, H. F., et al. (2021). Photocatalyzed cycloaromatization of vinylsilanes with arylsulfonfylazides. *Nat. Commun.* 12, 3304. doi:10.1038/s41467-021-23326-2
- Chen, H., Peng, J., Pang, Q., Du, H., Huang, L., Gao, L., et al. (2022). Enantioselective synthesis of spirosilabicyclohexenes by asymmetric dual ring expansion of spirosilabicyclobutane with alkynes. *Angew. Chem. Int. Ed.* 61, e202212889. doi:10.1002/anie.202212889
- Chen, X., Li, M. K., Liu, Z. P., Yang, C., Xie, H. S., Hu, X. W., et al. (2021). Bimetal cooperatively catalyzed arylalkynylation of alkynylsilanes. *Org. Lett.* 23, 6724–6728. doi:10.1021/acs.orglett.1c02283
- Cheng, C., and Hartwig, J. F. (2015). Catalytic silylation of unactivated C-H bonds. *Chem. Rev.* 115, 8946–8975. doi:10.1021/cr5006414
- Denk, M., Lennon, R., Hayashi, R., West, R., Belyakov, A. V., Verne, H. P., et al. (1994). Synthesis and structure of a stable silylene. *J. Am. Chem. Soc.* 116, 2691–2692. doi:10.1021/ja00085a088
- Driver, T. G., Franz, A. K., and Woerpel, K. A. (2002). Diastereoselective silacyclopropanations of functionalized chiral alkenes. *J. Am. Chem. Soc.* 124, 6524–6525. doi:10.1021/ja020183k
- Fang, H., Hou, W., Liu, G., and Huang, Z. (2017). Ruthenium-catalyzed site-selective intramolecular silylation of primary C-H bonds for synthesis of sila-heterocycles. *J. Am. Chem. Soc.* 139, 11601–11609. doi:10.1021/jacs.7b06798
- Fleming, I., and Winter, S. B. D. (1998). Stereocontrol in organic synthesis using silicon-containing compounds. A formal synthesis of prostaglandins controlling the stereochemistry at C-15 using a silyl-to-hydroxy conversion following a stereochemically convergent synthesis of an allylsilane. *J. Chem. Soc. Perkin Trans.* 17, 2687–2700. doi:10.1039/a804276d
- Förster, B., Bertermann, R., Kraft, P., and Tacke, R. (2014). Sila-rhubafuran and derivatives: Synthesis and olfactory characterization of novel silicon-containing odorants. *Organometallics* 33, 338–346. doi:10.1021/om401070c

- Ghahvatzade, N., Melkonyan, F. S., Gulevich, A. V., Huang, C., and Gevorgyan, V. (2014). Conversion of 1-alkenes into 1,4-diols through an auxiliary-mediated formal homoallylic C-H oxidation. *Nat. Chem.* 6, 122–125. doi:10.1038/nchem.1841
- Guo, Y., Liu, M. M., Zhu, X., Zhu, L., and He, C. (2021). Catalytic asymmetric synthesis of silicon-stereogenic dihydrodibenzosilines: Silicon central-to-axial chirality relay. *Angew. Chem. Int. Ed.* 60, 14006–14010. doi:10.1002/ange.202103748
- Hirano, K., Yorimitsu, H., and Oshima, K. (2008). Palladium-catalyzed formal cycloaddition of silacyclobutanes with enones: Synthesis of eight-membered cyclic silyl enolates. *Org. Lett.* 10, 2199–2201. doi:10.1021/ol800603z
- Hoshimoto, Y., Yabuki, H., Kumar, R., Suzuki, H., Ohashi, M., and Ogoshi, S. (2014). Highly efficient activation of organosilanes with η^2 -aldehyde nickel complexes: Key for catalytic syntheses of aryl-vinyl- and alkynyl-benzoxasiloles/efficient activation of organosilanes with η^2 -aldehyde nickel complexes: Key for catalytic syntheses of aryl-vinyl- and alkynyl-benzoxasiloles. *J. Am. Chem. Soc.* 136, 16752–16755. doi:10.1021/ja510089c
- Huang, W. S., Wang, Q., Yang, H., and Xu, L. (2022). State-of-the-art advances in enantioselective transition-metal-mediated reactions of silacyclobutanes. *Synthesis* 54, 5400–5408. doi:10.1055/a-1929-4890
- Huang, Y. H., Wu, Y., Zhu, Z., Zheng, S., Ye, Z., Peng, Q., et al. (2022). Enantioselective synthesis of silicon-stereogenic monohydrosilanes by rhodium-catalyzed intramolecular hydrosilylation. *Angew. Chem. Int. Ed.* 61, e202113052. doi:10.1002/anie.202113052
- Huo, J., Zhong, K., Xue, Y., Lyu, M., Ping, Y., Liu, Z., et al. (2021). Palladium-catalyzed enantioselective carbene insertion into carbon–silicon bonds of silacyclobutanes. *J. Am. Chem. Soc.* 143, 12968–12973. doi:10.1021/jacs.1c05879
- Igawa, K., Kuroo, A., Yoshihiro, D., Yamanaka, Y., and Tomooka, K. (2017). Synthesis of stereoselectively functionalized silacyclopentanes. *Synlett* 28, 2445–2448. doi:10.1055/s-0036-1590826
- Igawa, K., Yoshihiro, D., Abe, Y., and Tomooka, K. (2016). Enantioselective synthesis of silacyclopentanes. *Angew. Chem. Int. Ed.* 55, 5908–5912. doi:10.1002/ange.201511728
- Ilies, L., Tsuji, H., and Nakamura, E. (2009). Synthesis of benzo[b]siloles via KH-promoted cyclization of (2-alkynylphenyl)silanes. *Org. Lett.* 11, 3966–3968. doi:10.1021/ol9015282
- Ilies, L., Tsuji, H., Sato, Y., and Nakamura, E. (2008). Modular synthesis of functionalized benzosiloles by Tin-mediated cyclization of (o-alkynylphenyl)silane. *J. Am. Chem. Soc.* 130, 4240–4241. doi:10.1021/ja800636g
- Ishida, N., Ikemoto, W., and Murakami, M. (2014). Cleavage of C–C and C–Si σ -bonds and their intramolecular exchange. *J. Am. Chem. Soc.* 136, 5912–5915. doi:10.1021/ja502601g
- Ishida, N., Ikemoto, W., and Murakami, M. (2012). Intramolecular σ -bond metathesis between carbon–carbon and silicon–silicon bonds. *Org. Lett.* 14, 3230–3232. doi:10.1021/ol301280u
- Ito, Y., Sugimoto, M., and Murakami, M. (1991). Palladium (II) acetate-tert-alkyl isocyanide as a highly efficient catalyst for the inter- and intramolecular bis-silylation of carbon–carbon triple bonds. *J. Org. Chem.* 56, 1948–1951. doi:10.1021/jo00005a055
- Kanno, H., Nakamura, K., Noguchi, K., Shibata, Y., and Tanaka, K. (2016). Rhodium-catalyzed cycloisomerization of 2-silylphenyl phenols and anilines via 1,2-silicon migration. *Org. Lett.* 18, 1654–1657. doi:10.1021/acs.orglett.6b00529
- Keipour, H., Carreras, V., and Thierry Ollevier, T. (2017). Recent progress in the catalytic carbene insertion reactions into the silicon–hydrogen bond. *Org. Biomol. Chem.* 15, 5441–5456. doi:10.1039/c7ob00807d
- Kuninobu, Y., Nakahara, T., Takeshima, H., and Takai, K. (2013a). Rhodium-catalyzed intramolecular silylation of unactivated C(sp³)-H bonds. *Org. Lett.* 15, 426–428. doi:10.1021/ol303353m
- Kuninobu, Y., Yamauchi, K., Tamura, N., Seiki, T., and Takai, K. (2013b). Rhodium-catalyzed asymmetric synthesis of spiro[3.5]heptene derivatives. *Angew. Chem. Int. Ed.* 52, 1560–1562. doi:10.1002/ange.201207723
- Leifert, D., and Studer, A. (2015). 9-Silafluorenes via Base-Promoted Homolytic Aromatic Substitution (BHAS) – the Electron as a Catalyst/fluorenes via base-promoted homolytic aromatic substitution (BHAS) – the electron as a catalyst. *Org. Lett.* 17, 386–389. doi:10.1021/ol503574k
- Li, L., Zhang, Y., Gao, L., and Song, Z. (2015). Recent advances in C–Si bond activation via a direct transition metal insertion. *Tetrahedron Lett.* 56, 1466–1473. doi:10.1016/j.tetlet.2015.01.184
- Li, Q., Driess, M., and Hartwig, J. F. (2014). Iridium-catalyzed regioselective silylation of aromatic and benzylic C–H bonds directed by a secondary amine. *Angew. Chem. Int. Ed.* 53, 8471–8474. doi:10.1002/anie.201404620
- Liang, Y., Geng, W., Wei, J., and Xi, Z. (2012). Palladium-catalyzed intermolecular coupling of 2-silylaryl bromides with alkynes: Synthesis of benzosiloles and heteroarene-fused siloles by catalytic cleavage of the C(sp³)-Si bond. *Angew. Chem. Int. Ed.* 51, 1970–1973. doi:10.1002/ange.201108154
- Lin, X., Gan, Z., Lu, J., Su, Z., Hu, C., Zhang, Y., et al. (2016). Visible light-promoted radical cyclization of silicon-tethered alkyl iodide and phenyl alkyne. An efficient approach to synthesize benzosilolines/efficient approach to synthesize benzosilolines. *Chem. Commun.* 52, 6189–6192. doi:10.1039/c6cc00635c
- Lin, Y., Jiang, K. -Z., Cao, J., Zheng, Z. -Z., Xu, Z., Cui, Y. -M., et al. (2017). Iridium-catalyzed intramolecular C–H silylation of siloxane-tethered arene and hydrosilane: Facile and catalytic synthesis of cyclic siloxanes. *Adv. Synth. Catal.* 359, 2247–2252. doi:10.1002/adsc.201700160
- Lippert, W. P., Burschka, C., Götz, K., Kaupp, M., Ivanova, D., Gaudon, C., et al. (2009). Silicon analogues of the RXR-selective retinoid agonist SR11237 (BMS649): Chemistry and Biology. *ChemMedChem* 4, 1143–1152. doi:10.1002/cmdc.200900090
- Liu, D., and Kozmin, S. A. (2001). Catalytic enantioselective isomerization of silacyclopentene oxides: New strategy for stereocontrolled assembly of acyclic polyols. *Angew. Chem. Int. Ed.* 40, 4757–4759. doi:10.1002/1521-3773(20011217)40:24<4757::aid-anie4757>3.0.co;2-s
- Long, P. W., Bai, X. F., Ye, F., Li, L., Xu, Z., Yang, K. F., et al. (2018). Construction of six-membered silacyclic skeletons via platinum-catalyzed tandem hydrosilylation/cyclization with dihydrosilanes. *Adv. Synth. Catal.* 360, 2825–2830. doi:10.1002/adsc.201800456
- Ma, W., Liu, L. -C., An, K., He, T., and He, W. (2021). Rhodium-catalyzed synthesis of chiral monohydrosilanes by intramolecular C–H functionalization of dihydrosilanes. *Angew. Chem. Int. Ed.* 60, 4245–4251. doi:10.1002/anie.202013041
- Matsuda, T., and Ichioka, Y. (2012). Rhodium-catalyzed intramolecular trans-bis-silylation of alkynes to synthesize 3-silyl-1-benzosiloles. *Org. Biomol. Chem.* 10, 3175–3177. doi:10.1039/c2ob25242b
- Mu, Q.-C., Chen, J., Xia, C.-G., and Xu, L.-W. (2018). Synthesis of silacyclobutanes and their catalytic transformations enabled by transition-metal complexes. *Coord. Chem. Rev.* 374, 93–113. doi:10.1016/j.ccr.2018.06.015
- Murai, M., Takeshima, H., Morita, H., Kuninobu, Y., and Takai, K. (2015). Acceleration effects of phosphine ligands on the rhodium-catalyzed dehydrogenative silylation and germylation of unactivated C(sp³)-H bonds/effects of phosphine ligands on the rhodium-catalyzed dehydrogenative silylation and germylation of unactivated C(sp³) –H bonds. *J. Org. Chem.* 80, 5407–5414. doi:10.1021/acs.joc.5b00920
- Namba, T., Kawauchi, S., Shibata, Y., Kanno, H., and Tanaka, K. (2017). Synthesis of alkynylmethylidene-benzoxasiloles through a rhodium-catalyzed cycloisomerization involving 1,2-silicon and 1,3-carbon migration. *Angew. Chem. Int. Ed.* 56, 3050–3054. doi:10.1002/ange.201612560
- Okumura, S., Sun, F., Ishida, N., and Murakami, M. (2017). Palladium-catalyzed intermolecular exchange between C–C and C–Si σ -bonds. *J. Am. Chem. Soc.* 139, 12414–12417. doi:10.1021/jacs.7b07667
- Ouyang, K., Liang, Y., and Xi, Z. (2012). Construction of benzosiloles, Six- and Eight-membered silacyclic skeletons, via a Pd-catalyzed intramolecular Mizoroki-Heck reaction of vinylsilanes. *Org. Lett.* 14, 4572–4575. doi:10.1021/ol302040j
- Parasram, M., Iaroshenko, V. O., and Gevorgyan, V. (2014). Endo-selective Pd-catalyzed silyl methyl Heck reaction. *J. Am. Chem. Soc.* 136, 17926–17929. doi:10.1021/ja5104525
- Pawley, S. B., Conner, A. M., Omer, H. M., and Watson, D. A. (2022). Development of a general method for the Hiyama-Denmark cross-coupling of tetrasubstituted vinyl silanes. *ACS Catal.* 12, 13108–13115. doi:10.1021/acscatal.2c03981
- Pujals, S., Fernández-Carneado, J., Kogan, M. J., Martínez, J., Cavellier, F., and Giralt, E. (2006). Replacement of a proline with silaproline causes a 20-fold increase in the cellular uptake of a pro-rich peptide. *J. Am. Chem. Soc.* 128, 8479–8483. doi:10.1021/ja060036c
- Qin, Y., Han, J. L., Ju, C. W., and Zhao, D. (2020). Ring expansion to 6-7- and 8-membered benzosilacycles through strain-release silicon-based cross-coupling. *Angew. Chem. Int. Ed.* 59, 8559–8563. doi:10.1002/ange.202001539
- Qin, Y., Li, L., Liang, J. Y., Li, K., and Zhao, D. (2021). Silacyclization through palladium-catalyzed intermolecular silicon-based C(sp³)-C(sp³) cross-coupling. *Chem. Sci.* 12, 14224–14229. doi:10.1039/d1sc04180k
- Sakurai, H., Kamiyama, Y., and Nakadaira, Y. (1975). Chemistry of organosilicon compounds 79 Novel [sigma + pi] reactions of hexaorganodisilanes with acetylenes catalyzed by palladium complexes. *J. Am. Chem. Soc.* 97, 931–932. doi:10.1021/ja00837a061
- Sanderson, R. T. (1983). Electronegativity and bond energy. *J. Am. Chem. Soc.* 105, 2259–2261. doi:10.1021/ja00346a026
- Shen, L., Zhao, K., Doitomi, K., Ganguly, R., Li, Y. X., Shen, Z. L., et al. (2017). Lewis acid-catalyzed selective [2 + 2]-cycloaddition and dearomatizing cascade reaction of aryl alkynes with acrylates. *J. Am. Chem. Soc.* 139, 13570–13578. doi:10.1021/jacs.7b07997
- Shi, Y., Shi, X., Zhang, J., Qin, Y., Li, B., and Zhao, D. (2022). Sila-spirocyclization involving unstrained C(sp³)-Si bond cleavage. *Nat. Commun.* 13, 6697. doi:10.1038/s41467-022-34466-4
- Shintani, R., Kurata, H., and Nozaki, K. (2015). Rhodium-catalyzed intramolecular alkynylsilylation of alkynes. *Chem. Commun.* 51, 11378–11381. doi:10.1039/c5cc04172d

- Shintani, R., Moriya, K., and Hayashi, T. (2012). Palladium-catalyzed desymmetrization of silacyclobutanes with alkynes: Enantioselective synthesis of silicon-stereogenic 1-sila-2-cyclohexenes and mechanistic considerations. *Org. Lett.* 14, 2902–2905. doi:10.1021/ol301191u
- Shintani, R., Moriya, K., and Hayashi, T. (2011). Palladium-catalyzed enantioselective desymmetrization of silacyclobutanes: Construction of silacycles possessing a tetraorganosilicon stereocenter. *J. Am. Chem. Soc.* 133, 16440–16443. doi:10.1021/ja208621x
- Shintani, R., Takano, R., and Nozaki, K. (2016). Rhodium-catalyzed asymmetric synthesis of silicon-stereogenic silicon-bridged arylpyridinones. *Chem. Sci.* 7, 1205–1211. doi:10.1039/c5cs03767k
- Su, B., Zhou, T.-G., Li, X.-W., Shao, X.-R., Xu, P.-L., Wu, W.-L., et al. (2017). A chiral nitrogen ligand for enantioselective, iridium-catalyzed silylation of aromatic C-H bonds. *Angew. Chem. Int. Ed.* 56, 1092–1096. doi:10.1002/anie.201609939
- Tang, R. H., Xu, Z., Nie, Y. X., Xiao, X. Q., Yang, K. F., Xie, J. L., et al. (2020). Catalytic asymmetric *trans*-selective hydrosilylation of bisalkynes to access AIE and CPL-active silicon-stereogenic benzosiloles. *iScience* 23, 101268. doi:10.1016/j.isci.2020.101268
- Tang, X., Zhang, Y., Tang, Y., Li, Y., Zhou, J., Wang, D., et al. (2022). Ring expansion of silacyclobutanes with allenates to selectively construct 2- or 3-(*E*)-enoate-substituted silacyclohexenes. *ACS Catal.* 12, 5185–5196. doi:10.1021/acscatal.1c05831
- Teng, Z., and Keese, Y. (1999). Palladium-induced intramolecular coupling reactions of some alkenyl(*o*-iodobenzyl)silanes. *Helv. Chim. Acta.* 82, 515–521. doi:10.1002/(sici)1522-2675(19990407)82:4<515::aid-hlca515>3.0.co;2-y
- Tobisu, M., Onoe, M., Kita, Y., and Chatani, N. (2009). Rhodium-catalyzed coupling of 2-silylphenylboronic acids with alkynes leading to benzosiloles: Catalytic cleavage of the carbon-silicon bond in trialkylsilyl groups. *J. Am. Chem. Soc.* 131, 7506–7507. doi:10.1021/ja9022978
- Tsukada, N., and Hartwig, J. F. (2005). Intermolecular and intramolecular, platinum-catalyzed, acceptorless dehydrogenative coupling of hydrosilanes with aryl and aliphatic methyl C-H bonds. *J. Am. Chem. Soc.* 127, 5022–5023. doi:10.1021/ja050612p
- Ureshino, T., Yoshida, T., Kuninobu, T., and Takai, K. (2010). Rhodium-catalyzed synthesis of silafluorene derivatives via cleavage of Silicon-Hydrogen and Carbon-Hydrogen bonds/fluorene derivatives via cleavage of silicon-hydrogen and carbon-hydrogen bonds. *J. Am. Chem. Soc.* 132, 14324–14326. doi:10.1021/ja107698p
- Van Klink, G. P. M., de Boer, H. J. R., Schat, G., Akkerman, O. S., Bickelhaupt, F., and Spek, A. L. (2002). Carbanions as intermediates in the formation of grignard reagents. *Organometallics* 21, 2119–2135. doi:10.1021/om011083a
- Wagner, P., Gulea, M., Suffert, J., and Donnard, M. (2017). Synthesis of benzo[*c*]silole derivatives bearing a tetrasubstituted exocyclic C=C double bond by palladium-catalyzed domino reactions. *Chem. Eur. J.* 23, 7458–7462. doi:10.1002/chem.201701736
- Wang, W., Zhou, S., Li, L., He, Y., Dong, X., Gao, L., et al. (2021). 3-Silaazetidine: An unexplored yet versatile organosilane species for ring expansion toward silaazacycles. *J. Am. Chem. Soc.* 143, 11141–11151. doi:10.1021/jacs.1c04667
- Wang, X. B., Zheng, Z. Z., Xie, J. L., Gu, X. W., Mu, Q. C., Yin, G. W., et al. (2020). Controllable Si-C bond activation enables stereocontrol in the palladium-catalyzed [4 + 2] annulation of cyclopropenes with benzosilacyclobutanes. *Angew. Chem. Int. Ed.* 59, 790–797. doi:10.1002/anie.201913060
- Wang, X. C., Wang, H. R., Xu, X., and Zhao, D. (2021). Ring expansion to 8-membered silacycles through formal cross-dimerization of 5-membered palladacycles with silacyclobutanes. *Eur. J. Org. Chem.* 2021, 3039–3042. doi:10.1002/ejoc.202100535
- Wang, X. X., Huang, S. S., Zhang, F. J., Xie, J. L., Li, Z., Xu, Z., et al. (2021). Multifunctional P-ligand-controlled “silicon-centered” selectivity in Rh/Cu-catalyzed Si-C bond cleavage of silacyclobutanes. *Org. Chem. Front.* 8, 6577–6584. doi:10.1039/d1qo01386f
- Welsh, K. M., Michl, J., and West, R. (1988). The photochemistry of matrix-isolated di-*tert*-butyldiazidosilane. observation of di-*tert*-butylsilylene and *N*, *N'*-di-*tert*-butylsilanediiimine. *J. Am. Chem. Soc.* 110, 6689–6696. doi:10.1021/ja00228a014
- Wilkinson, J. R., Nuyen, C. E., Carpenter, T. S., Harruff, S. R., and Van Hoveln, R. (2019). Copper-catalyzed carbon-silicon bond formation. *ACS Catal.* 9, 8961–8979. doi:10.1021/acscatal.9b02762
- Xu, H., Fang, X. J., Huang, W. S., Xu, Z., Li, L., Ye, F., et al. (2022). Catalytic regio- and stereoselective silicon-carbon bond formations on unsymmetric *gem*-difluorocyclopropenes by capture of silyl metal species. *Org. Chem. Front.* 9, 5272–5280. doi:10.1039/d2qo00943a
- Xu, L., Zhang, S., and Li, P. (2015). Synthesis of silafluorenes and silaindenes via silyl radicals from arylhydrosilanes: Intramolecular cyclization and intermolecular annulation with alkynes/fluorenes and silaindenes via silylradicals from arylhydrosilanes: Intramolecular cyclization and intermolecular annulations with alkynes. *Org. Chem. Front.* 2, 459–463. doi:10.1039/c5qo00012b
- Yang, B., Yang, W., Guo, Y., You, L., and He, C. (2020). Enantioselective silylation of aliphatic C-H bonds for the synthesis of silicon-stereogenic dihydrobenzosiloles. *Angew. Chem. Int. Ed.* 59, 22401–22406. doi:10.1002/ange.202009912
- Ye, F., and Xu, L. W. (2021). A glimpse and perspective of current organosilicon chemistry from the view of hydrosilylation and synthesis of silicon-stereogenic silanes. *Synlett* 32, 1281–1288. doi:10.1055/a-1408-6795
- Ye, F., Xu, Z., and Xu, L. W. (2021). The Discovery of multifunctional chiral P ligands for the catalytic construction of quaternary carbon/silicon and multiple stereogenic centers. *Acc. Chem. Res.* 54, 452–470. doi:10.1021/acs.accounts.0c00740
- Yu, N., Wang, C., Zhao, F., Liu, L., Zhang, W.-X., and Xi, Z. (2008). Diverse reactions of 1,4-Dithio-1,3-dienes with nitriles: Facile access to tricyclic d1-bipyrrrolines, multiply substituted pyridines, siloles, and (Z,Z)-Dienylsilanes by tuning of substituents on the butadienyl skeleton. *Chem.-Eur. J.* 14, 5670–5679. doi:10.1002/chem.200701742
- Yuan, W., You, L., Lin, W., Ke, J., Li, Y., and He, C. (2021). Asymmetric synthesis of silicon-stereogenic monohydrosilanes by dehydrogenative C-H silylation. *Org. Lett.* 23, 1367–1372. doi:10.1021/acs.orglett.1c00029
- Zeng, Y., Fang, X. J., Tang, R. H., Xie, J. Y., Zhang, F. J., Xu, Z., et al. (2022). Rhodium-catalyzed dynamic kinetic asymmetric hydrosilylation to access silicon-stereogenic center. *Angew. Chem. Int. Ed.* 61, e202214147. doi:10.1002/anie.202214147
- Zhang, J., Xu, J. Z., Zheng, Z. J., Xu, Z., Cui, Y. M., Cao, J., et al. (2016). Palladium-catalyzed desymmetrization of silacyclobutanes with alkynes to silicon-stereogenic silanes: A density functional theory study. *Chem. Asian J.* 11, 2867–2875. doi:10.1002/asia.201600709
- Zhang, J., Yan, N., Ju, C. W., and Zhao, D. (2021). Nickel(0)-catalyzed asymmetric ring expansion toward enantioenriched silicon-stereogenic benzosiloles. *Angew. Chem. Int. Ed.* 60, 25927–25932. doi:10.1002/ange.202111025
- Zhang, Q. W., An, K., and He, W. (2014). Rhodium-catalyzed tandem cyclization/Si-C activation reaction for the synthesis of siloles. *Angew. Chem. Int. Ed.* 53, 5667–5671. doi:10.1002/anie.201400828
- Zhang, Q. W., An, K., Liu, L. C., Guo, S., Jiang, C., Guo, H., et al. (2016). Rhodium-catalyzed intramolecular C-H silylation by silacyclobutanes. *Angew. Chem. Int. Ed.* 55, 6427–6431. doi:10.1002/ange.201602376
- Zhao, W. T., Gao, F., and Zhao, D. (2018a). Intermolecular σ -bond cross-exchange reaction between cyclopropenones and (Benzo)silacyclobutanes: Straightforward access towards sila(benzo)cycloheptenones. *Angew. Chem. Int. Ed.* 57, 6329–6332. doi:10.1002/anie.201803156
- Zhao, W. T., Lu, Z. Q., Zheng, H., Xue, X. S., and Zhao, D. (2018b). Rhodium-catalyzed 2-arylphenol-derived six-membered silacyclization: Straightforward access toward dibenzooxasilines and silicon-containing planar chiral metallocenes. *ACS Catal.* 8, 7997–8005. doi:10.1021/acscatal.8b01992



OPEN ACCESS

EDITED BY

Clemens Zwergel,
Sapienza University of Rome, Italy

REVIEWED BY

Margherita Brindisi,
University of Naples Federico II, Italy
Gerardo Andres Cisneros,
University of North Texas, United States

*CORRESPONDENCE

Piia Bartos,
✉ Piia.Bartos@uef.fi

RECEIVED 05 May 2023

ACCEPTED 14 June 2023

PUBLISHED 22 June 2023

CITATION

Baltrukevich H and Bartos P (2023), RNA-
protein complexes and force
field polarizability.
Front. Chem. 11:1217506.
doi: 10.3389/fchem.2023.1217506

COPYRIGHT

© 2023 Baltrukevich and Bartos. This is an
open-access article distributed under the
terms of the [Creative Commons
Attribution License \(CC BY\)](#). The use,
distribution or reproduction in other
forums is permitted, provided the original
author(s) and the copyright owner(s) are
credited and that the original publication
in this journal is cited, in accordance with
accepted academic practice. No use,
distribution or reproduction is permitted
which does not comply with these terms.

RNA-protein complexes and force field polarizability

Hanna Baltrukevich¹ and Piia Bartos^{2*}

¹Faculty of Pharmacy, Jagiellonian University in Krakow, Kraków, Poland, ²School of Pharmacy, Faculty of Health Sciences, University of Eastern Finland, Kuopio, Finland

Molecular dynamic (MD) simulations offer a way to study biomolecular interactions and their dynamics at the atomistic level. There are only a few studies of RNA-protein complexes in MD simulations, and here we wanted to study how force fields differ when simulating RNA-protein complexes: 1) argonaute 2 with bound guide RNA and a target RNA, 2) CasPhi-2 bound to CRISPR RNA and 3) Retinoic acid-inducible gene I C268F variant in complex with double-stranded RNA. We tested three non-polarizable force fields: Amber protein force fields ff14SB and ff19SB with RNA force field OL3, and the all-atom OPLS4 force field. Due to the highly charged and polar nature of RNA, we also tested the polarizable AMOEBA force field and the ff19SB and OL3 force fields with a polarizable water model O3P. Our results show that the non-polarizable force fields lead to compact and stable complexes. The polarizability in the force field or in the water model allows significantly more movement from the complex, but in some cases, this results in the disintegration of the complex structure, especially if the protein contains longer loop regions. Thus, one should be cautious when running long-scale simulations with polarizability. As a conclusion, all the tested force fields can be used to simulate RNA-protein complexes and the choice of the optimal force field depends on the studied system and research question.

KEYWORDS

RNA, protein, simulation, molecular dynamics, polarization, force field

1 Introduction

Molecular dynamics (MD) simulations are routinely used to study the structure and dynamics of biomolecules at the atomistic level. Even though the models are by their very nature wrong in many ways, they are useful in showing us atomistic details of phenomena which cannot be directly observed experimentally (Berro, 2018). MD simulations have led to advances in drug and enzyme design and material science, and they have greatly increased our understanding of the interactions of biomolecules at the atomistic level.

During the last few years, RNA-protein complex simulations have started to appear in the literature (for example, Estarellas et al., 2015; Jiang et al., 2015; Kalia et al., 2015; Krepl et al., 2015; Krepl et al., 2021; Bhandare and Ramaswamy, 2016; Chang et al., 2016; Harikrishna and Pradeepkumar, 2017; Kong et al., 2017; Palermo et al., 2017; Bochicchio et al., 2018; Casalino et al., 2018; Kandeel and Kitade, 2018; Liu et al., 2018; Tan et al., 2018; Bissaro et al., 2020; Habibian et al., 2020; Saltalamacchia et al., 2020; Jing and Ren, 2022; Rinaldi et al., 2022). While this field is starting to gain interest, it is unfortunate to see that there are only a few studies published which use multiple force fields in studying RNA-protein complexes (Gallardo et al., 2022). The selection of force field and other simulation parameters depends on the studied system (Šponer et al., 2018), and thus some time should be spent testing suitable options for each study case. One could assume that

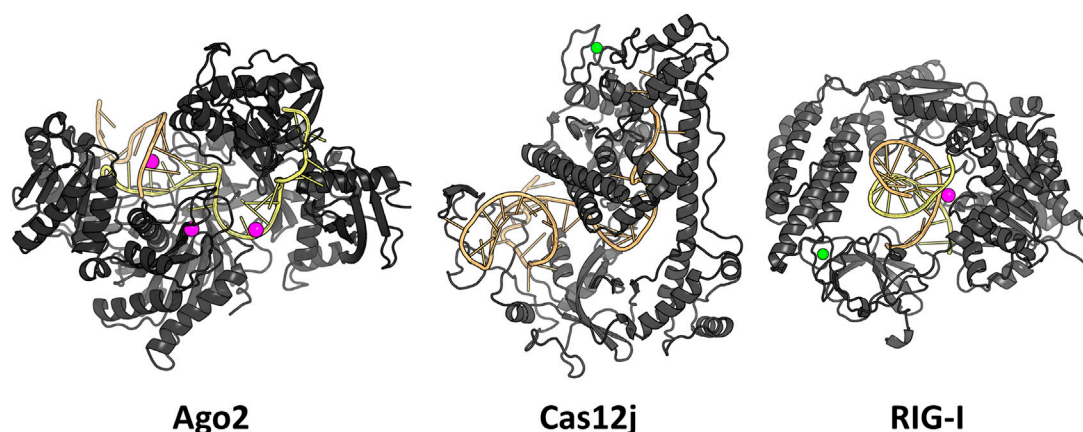


FIGURE 1

The studied RNA-protein complexes. Mg^{2+} ions are shown in magenta and Zn^{2+} ions in green.

polarizability of a force field could help in simulations containing RNA, as strong electrostatic interactions are in dominant role in these systems and one of the problems why it has been difficult to develop parameters for nucleic acids in the point-charge force fields (Zhang et al., 2018; Šponer et al., 2018; Cesari et al., 2019; Tucker et al., 2022). However, polarizable force fields are computationally demanding and thus a few orders of magnitude slower than the traditional force fields. In this study, we wanted to find if there are differences between traditional non-polarizable point-charge force fields and a polarizable force field when describing the RNA-protein complex interactions. A new polarizable water model for non-polarizable force fields (Xiong et al., 2022) was published during the preparation of this manuscript, and it was also included to illustrate a compromise between the extremes.

We examined three RNA-protein complexes: 1) argonaute 2 with bound guide RNA and a target RNA (Schirle et al., 2014), 2) CasPhi-2 bound to CRISPR RNA (Pausch et al., 2021) and 3) Retinoic acid-inducible gene I C268F in complex with double-stranded RNA (Lässig et al., 2018) (Figure 1). For simplicity, we will refer to these complexes with the abbreviations Ago2, Cas12j, and RIG-I, respectively. Ago2 forms the base of the RNA-induced silencing complex (RISC) which inhibits gene expression by binding to the mRNA guided by the short siRNA (Wang et al., 2009). Cas12j is an RNA-guided nuclease that initiates CRISPR RNA complementary double-stranded DNA unwinding and cleavage in bacteriophages (Pausch et al., 2021). RIG-I is a cytosolic receptor that recognizes viral double-stranded RNA molecules as an immune sensor (Lässig et al., 2018). These complexes were chosen because they included only protein and RNA chains, were cytosolic, relatively small (contained less than 8,000 of modeled non-hydrogen atoms), had not too many missing residues in their structures and all of them had a large interaction surface between the RNA(s) and the protein.

We tested the MD simulations of the three RNA-protein complexes using three traditional non-polarizable force fields: Amber RNA force field OL3 (Zgarbová et al., 2011) with protein force fields ff14SB (Maier et al., 2015) and ff19SB (Tian et al., 2020), the all-atom force field OPLS4 (Lu et al., 2021, 4), the polarizable

AMOEBA force field (Harger et al., 2017; Zhang et al., 2018) and the O3P polarizable water model (Xiong et al., 2022) with the ff19SB and OL3 force fields. The total simulation times for all systems were at least 1 μ s. It is possible to run reasonable RNA-protein complex simulations with any of the tested force fields and none of them outperforms the others in all cases. However, especially when running hundreds of ns-scale simulations with the polarizable force fields or water model, one should pay attention to the structural integrity of the complex. Overall, we recommend testing of different force field combinations to find a setup that works for both your system of interest and research question.

2 Methods

2.1 System preparation

The complexes 4W5O (Ago2), 7M5O (Cas12j), and 6PGG (RIG-I) were downloaded from the PDB (Protein Data Bank) (Schirle et al., 2014; Lässig et al., 2018; Pausch et al., 2021). The missing nucleotides in the PDB model 4W5O were built manually in PyMOL (Version 2.5.1) (The PyMOL Molecular Graphics System, 2000). The missing loops in the protein structure were modelled in BioLuminate (Schrödinger, 2021.3), and afterwards the built loops were refined using Prime (Schrödinger, 2021.3) (Schrödinger Release 2020-4: Glide, Schrödinger, LLC, New York, NY, 2020). Both terminal phosphates were deleted from the ends of RNA molecules. The bound ions (Zn^{2+} and/or Mg^{2+}) were retained. The models were prepared in Protein Preparation Wizard (Schrödinger version 2021-3): the water molecules were deleted beyond 5.0 Å from het groups, the states of het groups were generated using Epik in pH 7.4 \pm 2.0; the optimization of H-bonds was performed with PROPKA (Olsson et al., 2011; Søndergaard et al., 2011) in pH 7.4 followed by restrained minimization of them in OPLS4 (Lu et al., 2021, 4). The N-terminal of the proteins were not present in the crystal structures and they were omitted which is why Ago2 residue numbering starts from 22,

Cas12j starts from 53 and RIG-I starts from 29. All systems were then converted to Amber atom names using the `pdb4amber` script in the `AmberTools21`.

2.2 Amber simulations—OL3, ff14SB and ff19SB

The Amber simulation systems were prepared with the `tleap` tool of `AmberTools21` (Case et al., 2020). The RNA-protein complex was solvated with a water box with 10 Å buffer using 0.15M NaCl solution with SPCE or OPC water model for ff14SB and ff19SB protein force fields, respectively. The ions used parameters specified with the corresponding water model, and the RNA was parameterized with the RNA force field OL3 (Zgarbová et al., 2011). To use the larger timestep (4 fs), the hydrogen masses were repartitioned to the connected atoms using `ParmEd` software (Shirts et al., 2017, 5).

For the ff19SB (Tian et al., 2020, 19) simulations, the minimization and equilibration steps were following: 1) all non-water atoms constrained, 2) heavy atoms constrained, 3) protein back bone constrained and 4) no constraints. The constraint force was 50 kcal/mol in the minimizations and 10 kcal/mol in the equilibration simulations. The minimizations 1–4 used the steepest descent algorithm with a maximum of 10,000 steps. The equilibration steps 1–3 consisted of 400 ps simulations, and step 4 was a 4,000 ps simulation. In the first equilibration step, the system was heated to 310 K. The temperature and pressure were maintained with Langevin thermostat and Berendsen barostat in the equilibration simulations. For the ff14SB, steps 2–4 were used in the minimization procedure and steps 2 and 4 for the equilibration runs of 20 ps and 2,000 ps, respectively.

During the production runs for each system the NPT ensemble was used: the 1.0 bar pressure was maintained with the help of Monte Carlo barostat and 310 K temperature was controlled by Langevin thermostat. Frames were recorded every 0.1 ns. The files were made ready for analysis by aligning and centering the complex, stripping away water molecules and writing the output in the format of `xtc` (compressed Gromacs trajectory) using `cpptraj` tool. The Amber production simulations were 4*500 ns in length for both force fields, resulting in 2 μs of total simulation time for each Ago2 complex. For the RIG-I and Cas12j systems, the ff14SB + OL3 simulations had a runtime of 4*300 ns, totaling 1.2 μs, and the ff19SB + OL3 simulations were of similar length than those of Ago2.

2.3 Amber simulations—ff19SB and O3P

The simulations with O3P water were prepared similarly as the ff19SB + OL3 simulations with OPC water model, with a few exceptions. The water box of O3P water is not equilibrated, and thus the box buffer was increased to 12 Å. The increased buffer size lead to about the same number of water molecules that was present with the OPC simulations. The solvent box dimensions were then added using `tleap` to match the initial dimensions of the equilibrated OPC box from the previous simulations. To equilibrate this system more gently, the first equilibration simulation length was increased

from 400 ps to 1 ns. The production run parameters were similar to the other Amber simulations.

2.4 Desmond simulations—OPLS4

The Ago2 complex was solvated with truncated octahedron water box with 15 Å buffer using 0.15M NaCl solution with SPCE water model. The simulations in Desmond (Bowers et al., 2006) consisted of the default minimization and relaxation protocol and the production run applying Desmond default parameters as well: 2 fs timestep, ensemble class NPT with temperature 300 K controlled by Nose-Hoover chain thermostat and pressure 1.01325 bar maintained by Martyna-Tobias-Klein barostat, recording interval was set to 100 ps. The Desmond simulations of Ago2 complex were 8*250 ns in length, resulting in 2 μs of total simulation time. The smaller Cas12j and RIG-I complexes were placed in the cubic box with 12 Å buffer and solvated using 0.15M NaCl solution and SPCE water model. Both complexes were initially prepared with Protein Preparation Wizard and then processed with `pdb4amber` to preserve the naming of the atoms, which was important for the further `cpptraj` analysis. The Cas12j and RIG-I structures obtained in the following way were solvated and used for the Desmond simulations. However, due to absence of additional Protein Preparation Wizard step after using `pdb4amber` script, zero-order bonds to metals (Zn^{2+} and Mg^{2+}) were omitted, and therefore the movements of these ions were unconstrained during simulation of Cas12j and RIG-I complexes in OPLS4 force field. After default minimization and relaxation protocol, the production run was parametrized using default settings with the temperature and pressure changed to comply with Amber simulations: NPT ensemble class, temperature 310 K, pressure 1.0 bar and recording interval each 100 ps. The Desmond simulations of the Cas12j and RIG-I complexes were run in 4*500 ns replicas, total 2 μs of simulation time.

2.5 OpenMM simulations—AMOEBA

The RNA-protein complex solvated with the Amber protocol was used to start the AMOEBA simulations in OpenMM (Eastman et al., 2017). To avoid clashes and high energy conformations in this slower force field, we used the last frame of an Amber trajectory as the starting conformation for the Ago2 simulations. The Cas12j and RIG-I simulations were run from the same initial conformation as the other simulations, as we determined no major equilibration issues as with the Ago2 system. The systems were first minimized using Verlet Integrator with 1 ps timestep for a maximum of 100 iterations. The production simulations were run with the default parameters (polarization method “mutual” and convergence threshold $\epsilon = 0.01$) using Langevin integrator, 1/ps collision frequency and 2 fs timestep. We want to note that the rather large default convergence threshold has been changed to 0.00001 in later versions of OpenMM (our simulations were run in early 2022). We made a preliminary set of 10*10 ns simulations of Ago2 system to check for simulation stability, and then

TABLE 1 Average RMSD values (Å) in different simulations with corresponding standard deviations (SD).

Ago2	ff14SB + OL3	ff19SB + OL3	OPLS4	ff19SB + OL3+O3P _{water}	AMOEBA
Protein backbone	2.2 ± 0.3	2.8 ± 0.7	2.4 ± 0.4 Å	4.4 ± 0.9	3.0 ± 0.6
Guide RNA backbone	1.9 ± 0.3	1.8 ± 0.2	2.5 ± 0.4 Å	2.6 ± 0.4	2.5 ± 0.7
Target RNA backbone	2.1 ± 0.5	2.9 ± 1.0	3.7 ± 1.3 Å	3.1 ± 0.9	3.5 ± 1.2
Cas12j	ff14SB + OL3	ff19SB + OL3	OPLS4	ff19SB + OL3+O3P _{water}	AMOEBA
Protein backbone	4.0 ± 0.6	4.3 ± 0.7	5.1 ± 0.8	7.9 ± 2.2	5.7 ± 1.3
RNA backbone	3.7 ± 0.7	4.2 ± 1.0	5.7 ± 1.5	5.7 ± 1.4	4.4 ± 1.0
RIG-I	ff14SB + OL3	ff19SB + OL3	OPLS4	ff19SB + OL3+O3P _{water}	AMOEBA
Protein backbone	3.1 ± 0.4	2.6 ± 0.3	2.6 ± 0.3	7.3 ± 2.6	3.8 ± 0.7
RNA A + B backbone	2.0 ± 0.4	2.4 ± 0.5	3.1 ± 0.8	2.9 ± 0.9	2.1 ± 0.4

conducted a set of 10*100 ns simulations for all the systems that were used for the analysis. The simulation frames were saved every 0.02 ns.

2.6 Analysis of simulations—cpptraj

The resulting simulations were stripped from water atoms, wrapped into a single periodic box, centered around the protein and converted to .xtc-format to save disk space. These simulations are available in the Zenodo database. The stripped simulations were then analyzed using the in-house cpptraj scripts to calculate the RMSD, RMSF, PCA and hydrogen bond count. The simulation trajectories in .xtc format and their corresponding .pdb files have been uploaded into the Zenodo database under the following DOIs: 10.5281/zenodo.6605469 (Ago2 except for AMOEBA), 10.5281/zenodo.7694834 (Ago2 in AMOEBA), 10.5281/zenodo.7694878 (all Cas12j simulations) and 10.5281/zenodo.7695265 (all RIG-I simulations). The trajectories are wrapped into a single periodic boundary box, centered around the protein Cα atoms and the water molecules have been stripped out to conserve disk space.

3 Results

3.1 System flexibility and fluctuations—RMSD and RMSF

The flexibility of the protein and RNA strands was calculated using the root-mean-square deviation (RMSD) to the crystal structure. The results were calculated separately for the protein backbone (Cα, C, N, O atoms), guide RNA backbone (sugar + phosphate moieties) and target RNA backbone (sugar + phosphate moieties), and they are presented in [Table 1](#). The distribution of RMSD values in simulations is depicted at the kernel density estimate plots, which are smoothed versions of the histogram in [Figure 2](#), as well as at the time evolution graphs calculated from all the combined replicas in [Supplementary Figure S2](#). The root-mean-square fluctuations (RMSF) of Cα atoms of the protein and the P

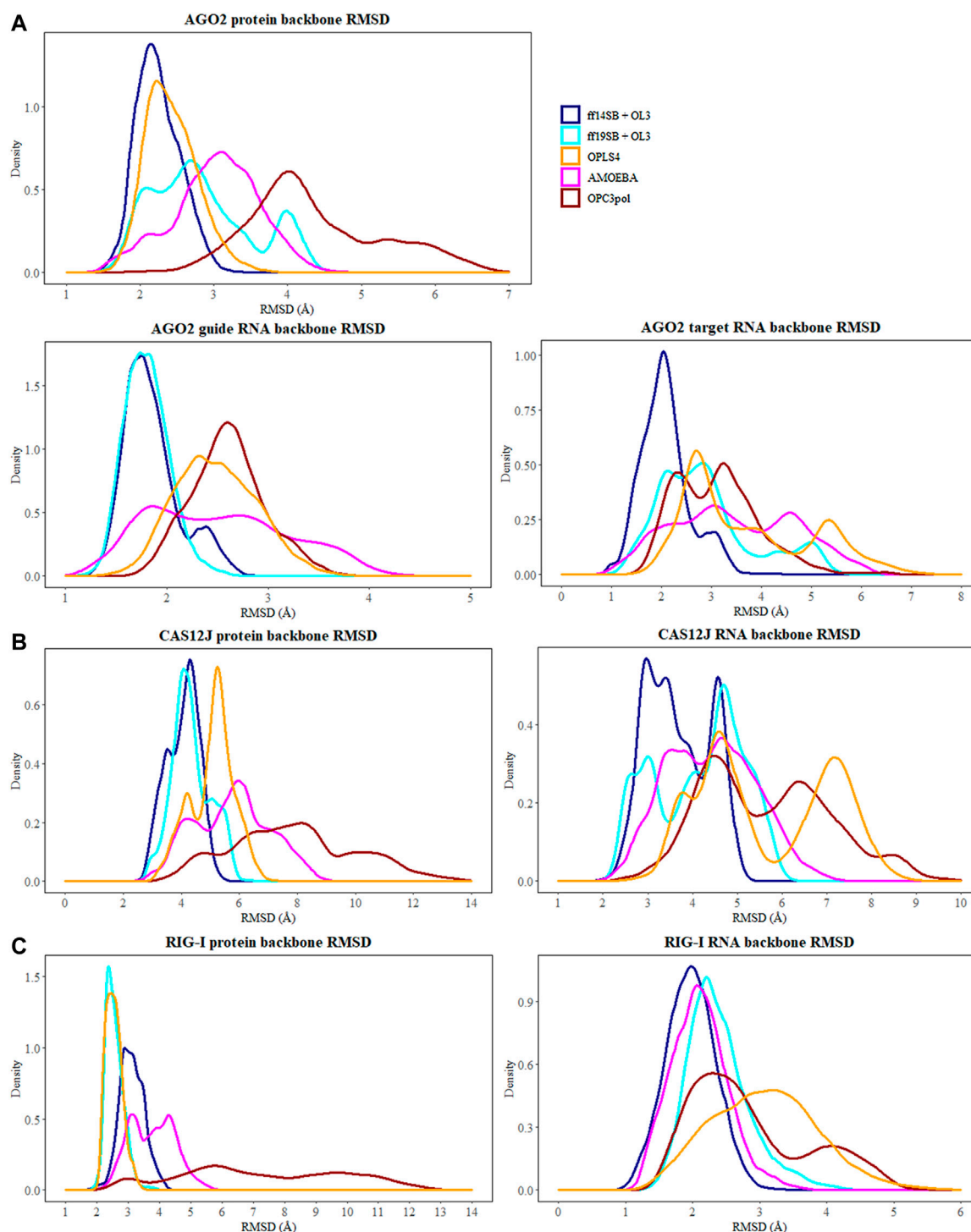
atoms of the RNA are shown in [Figure 3](#) and [Supplementary Figures S3–S5](#).

The simulations with the non-polarizable force fields display lower fluctuations than the simulations with the polarizable AMOEBA force field or the polarizable water model O3P. Indeed, the RMSD and RMSF values of O3P simulations clearly show that this water model leads to instability of the complex structure which can be confirmed by visual inspection of the trajectories. As the O3P simulations were run with similar parameters to ff19SB + OL3 simulation, it is likely that this instability is caused by the water model. However, in some of the AMOEBA simulations, similar structural integrity issues around the longer loop regions (residues 450–480 and 660–700) are observed on the Cas12j system ([Figure 4](#)).

3.2 Number of hydrogen bonds

The number of hydrogen bonds between the protein and the RNA and within RNA are shown in [Table 2](#) and [Figure 5](#) shows kernel density estimate plots. The hydrogen bond numbers for the crystal structures were calculated with both “strong” (donor-acceptor distance <3.0 Å and angle >135°) and “weak” hydrogen bond definition (accordingly, <3.5 Å and >120°), because the hydrogen bonding in the crystal structures was generally not agreeing with the stricter criteria. One possible reason for the low number of the hydrogen bonds in the initial structures might be relatively low resolution: 2.89 Å for RIG-I (X-ray) and 3.54 Å Cas12J (cryoEM) complexes. The discrepancy between the number of “strong” hydrogen bonds in the starting structure and the average from the simulations is especially clear in the case of Cas12J complex, which is the only cryoEM structure studied here. Ago2 complex is X-ray structure with 1.8 Å resolution, here the underestimated number of hydrogen bonds could be caused by the water mediating the hydrogen bonding, which could not be accessed by the calculation method we applied.

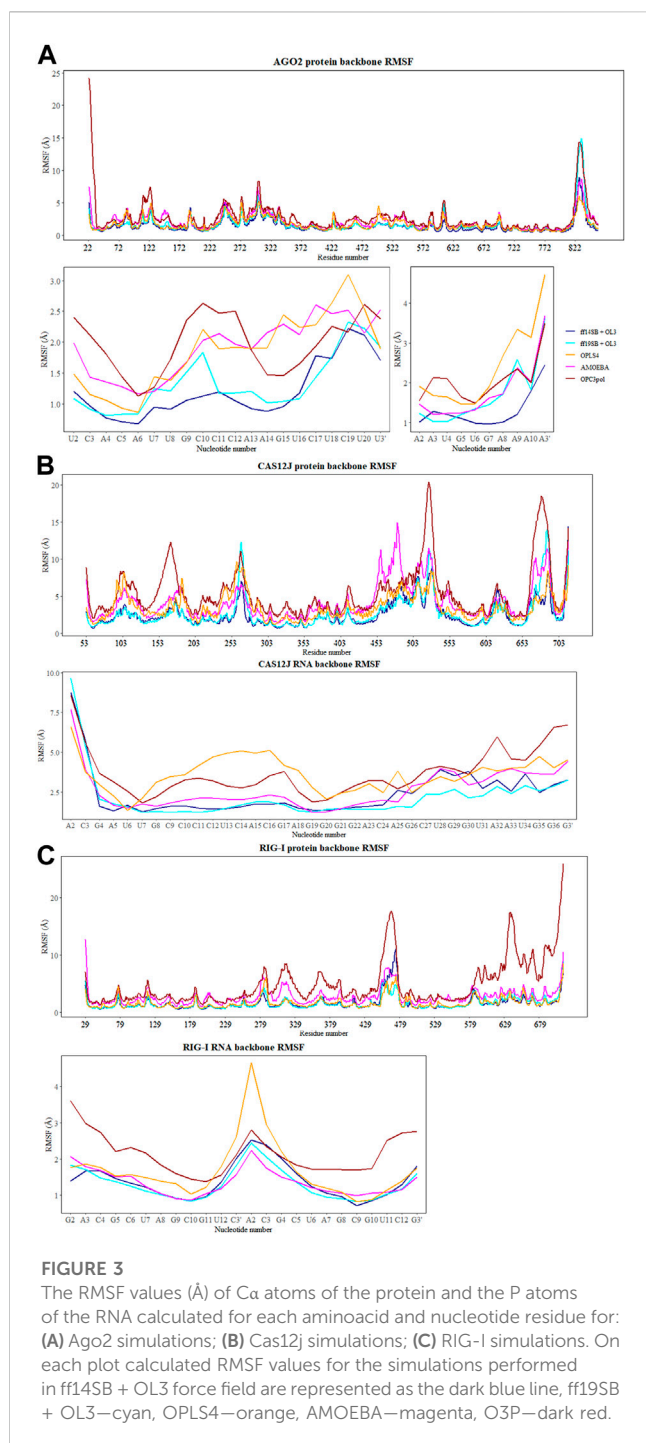
There are generally a few less intra-RNA hydrogen bonds observed in the Ago2 and RIG-I simulations than in the crystal structure ([Table 2](#)), and the difference is larger in the polarizable

**FIGURE 2**

The distribution of RMSD values (Å) depicted at the kernel density estimate plots for: **(A)** Ago2 simulations; **(B)** Cas12j simulations; **(C)** RIG-I simulations. On each plot calculated RMSD values for the simulations performed in ff14SB + OL3 force field are represented as the dark blue line, ff19SB + OL3—cyan, OPLS4—orange, AMOEBA—magenta, O3P—dark red.

force field. In Cas12j simulations, the non-polarizable force fields display about same number of intra-RNA hydrogen bonds that was observed in the crystal structure, and there are less hydrogen bonds observed in the AMOEBA simulations.

The protein-RNA hydrogen bond numbers display more variation. In the Ago2 system, the non-polarizable force fields display about the same number of hydrogen bonds as the crystal structure, and the AMOEBA and O3P water simulations display



less. In Cas12j system, ff14SB + OL3 and OPLS4 display more hydrogen bonds, ff19SB + OL3 and AMOEBA agree with crystal structure and O3P water simulations display less. In RIG-I simulations, the non-polarizable force fields agree with the crystal structure about the number of hydrogen bonds and the polarizable water model and AMOEBA display less hydrogen bonds.

These results indicate that the non-polarizable force fields stabilize the hydrogen bonding at the protein-RNA interface

which has been reported before (Estarellas et al., 2015; Šponer et al., 2018; Gallardo et al., 2022).

3.3 Ions

Bound ions can affect the structure of the protein and the protein-RNA complex. In this study, Ago2 system had a bound Mg^{2+} ion, Cas12j had a bound Zn^{2+} ion and RIG-I system had bound Mg^{2+} and Zn^{2+} ions. Mg^{2+} ion is important for the catalytic activity of Ago2, however, in the complex we investigated, Mg^{2+} is inactivated by an inhibitory coordination to the main chain carbonyl of V598 (Schirle et al., 2014). Cas12j has a cofactor Zn^{2+} bound to the zinc finger, which together with nuclease domains is proposed to assist in the recruitment of DNA for the Cas12j cleavage (Cui et al., 2008; Lässig et al., 2018). In RIG-I Zn^{2+} coordination site is essential for signaling, while Mg^{2+} is involved in the ATPase activity (Huang et al., 2020; Pausch et al., 2021).

In the Ago2 simulations, the Mg^{2+} ion stays in place in all the tested force fields (Supplementary Figure S1). In the Cas12j simulations, the Zn^{2+} ion stays in place in ff14SB + OL3 and AMOEBA force fields, in the other ones it unbinds. In the RIG-I simulations, the Mg^{2+} ion stays in place in the ff14SB + OL3, ff19SB + OL3 and AMOEBA simulations and unbinds in the others. The Zn^{2+} ion is fluctuating more, but it displays similar behavior. Based on these results, one should use constraints with the structurally important ions to keep them in place. Due to an error in the preparation process of Cas12j and RIG-I systems for the OPLS4 force field, we did not include the default zero-order bonds to metals. However, this mistake made it possible for us to compare the stability of the ion binding without a bias in these systems.

3.4 PCA analysis

The principal component analysis was conducted for the coordinates of the CA atoms of the protein and the P and C4' atoms of the RNA. The simulation frames plotted against the first two principal components (PC) are shown in Figure 6 on the left panel. On the right panel are shown the loadings of the atoms that were used to calculate the first PC. The PC loadings and weights show that the different force fields are generally not sampling a similar conformational space and the largest movements are not contributed by a certain part of the complex in all cases. The residue numbers that had the highest weights for the first PC are shown in Supplementary Table S1.

3.5 AGO2 results

AGO2 is a crucial component of the RNA-induced silencing complex (RISC) which when bound to an RNA molecule inhibits gene expression (Wang et al., 2009). The structure of AGO2 complex (4W5O) contains a protein of 859 residues (residues 1–21 not modeled), a guide RNA of 21 nucleotides and a target RNA of 11 nucleotides. The guide RNA binds to Ago2 mainly from the 5' end which contains the seed sequence

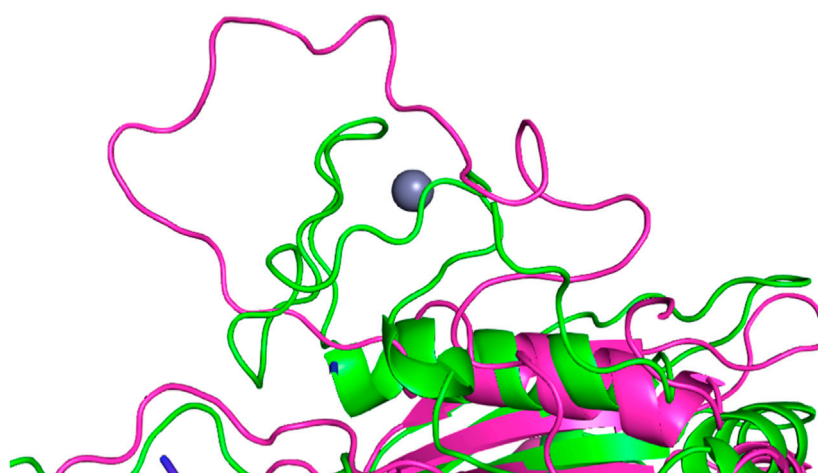


FIGURE 4

Structural integrity issue observed in the simulation with O3P water model simulations around the longer loop region (residues 660–700) in the Cas12j system. The starting structure is colored in green, the frame from the simulation in magenta. Zinc ion (in gray) bound by the mentioned above loop in the crystal structure unbinds in the first few ns of the simulation.

TABLE 2 The average number of hydrogen bonds within RNA and between RNA and protein in the simulation and their standard deviation (SD) during the simulations. Strong bond = Donor-acceptor distance <3.0 Å and angle >135°. *Weak bond = Donor-acceptor distance <3.5 Å and angle >120°.

Intra-RNA	Crystal	ff14SB + OL3	ff19SB + OL3	OPLS4	ff19SB + OL3+O3P _{water}	AMOEBa
Ago2	18 (20*)	11.5 ± 2.2	12.2 ± 2.1	12.2 ± 2.4	8.3 ± 2.8	10.4 ± 2.3
Cas12j	17 (22*)	23.6 ± 3.1	23.4 ± 3.0	24.2 ± 3.8	22.8 ± 3.3	14.1 ± 2.7
RIG-I	31 (34*)	24.3 ± 3.0	23.9 ± 3.1	24.5 ± 3.1	19.2 ± 4.2	19.5 ± 3.2
RNA-Protein	Crystal	ff14SB + OL3	ff19SB + OL3	OPLS4	ff19SB + OL3+O3P _{water}	AMOEBa
Ago2	33 (38*)	38.0 ± 4.4	35.3 ± 4.0	33.9 ± 4.1	30.7 ± 5.0	23.7 ± 5.2
Cas12j	17 (40*)	50.7 ± 5.8	42.9 ± 5.6	53.7 ± 5.0	31.2 ± 7.5	39.0 ± 5.9
RIG-I	10 (19*)	20.4 ± 3.5	18.3 ± 3.0	18.4 ± 3.1	9.8 ± 3.7	11.2 ± 3.4

(nucleotides 2–7) which are crucial to the binding to the complementary mRNA strand (Kehl et al., 2017). The 3' end of the guide RNA is bound to the most flexible part of Ago2, the PAZ domain (residues 235–348) (Jiang et al., 2015). The target RNA is mainly forming interactions with the guide RNA strand, with a few flanking nucleotides interacting with the Ago2 surface.

3.5.1 Fluctuations of the AGO2 system

In the Amber simulations, the protein is fluctuating more than either of the RNA strands. In the OPLS4 and AMOEBa force fields, the situation is the opposite, and the RNA fluctuates more than the protein. The fluctuations of the guide RNA are more pronounced in the polarizable force fields and around nucleotides 9–18 which are not tightly bound to the protein. Some of the RNA stabilization in OPLS4 force field is caused by an extra hydrogen bond forming between the guide RNA U1 and the target RNA A2 (Figure 7). For the protein, the longer loop regions around residues 110, 605 and 830 appear to fluctuate more in the Amber ff19SB + OL3 force field

and the O3P water systems, but otherwise the trends in the RMSF graph are similar in all the tested force fields (Figure 2; Supplementary Figure S3). The longer loops around residues 110 and 830 are very much fluctuating in the O3P simulations but this does not lead to overall structural instability in these 500 ns simulations. The Mg²⁺ ion in the AGO2 system is tightly bound between the protein and the RNA and it remains in its position in all simulations in all force fields.

3.5.2 Hydrogen bonds of the AGO2 system

The hydrogen bonds between the guide and target RNA base pairs remain stable in all tested force fields (Table 2; Figure 5). From these force fields, OPLS4 and ff19SB + OL3 match the crystal structure hydrogen bond count. In all the nonpolarizable force fields, there are on average more observed hydrogen bonds between the protein and the RNA than in the crystal structure. In the polarizable simulations, there are less hydrogen bonds than in the crystal structure. The complexes in polarizable conditions are not as compact as in the nonpolarizable

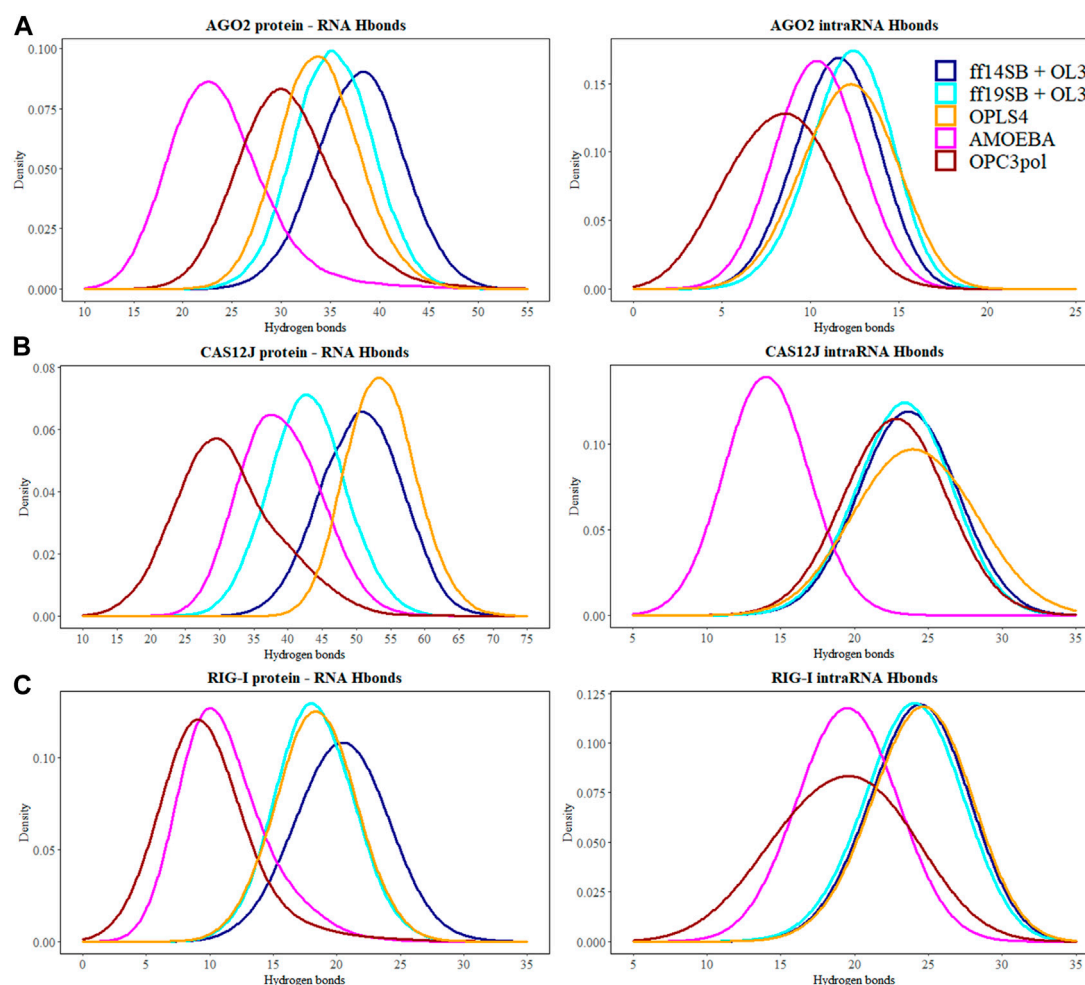


FIGURE 5

The number of hydrogen bonds between the protein and the RNA molecules are depicted at the kernel density estimate plots for: (A) Ago2 simulations; (B) Cas12j simulations; (C) RIG-I simulations. On each plot calculated H-bond values for the simulations performed in ff14SB + OL3 force field are represented as the dark blue line, ff19SB + OL3—cyan, OPLS4—orange, AMOEBA—magenta, O3P—dark red. Hydrogen bonds were calculated according to the definition of the strong bond assumed in this study—donor-acceptor distance <3.0 Å and angle D-H-A $>135^\circ$.

simulations. The complexes open more in these simulations, which increases the distances of the hydrogen bonds beyond our cutoff distance and lowers the number of hydrogen bonds.

3.5.3 Exploration of conformations in the AGO2 system—PCA

Figure 6 (right panel) shows the simulation frames are plotted against the first two PCs. In the case of AGO2, the distribution of PC1 and PC2 values are relatively similar within Amber force fields and OPLS4, and AMOEBA samples a slightly larger conformational space. O3P water simulations sample the largest conformational space, but these states are likely highly defined by the larger fluctuations of the terminals. Generally, there are two to three somewhat distinct conformational states observed in the PCA plots for the Ago2 system.

To observe which protein residues and RNA nucleotides have the highest effect on the first PC, we listed the top 10 residues based on their absolute PC weight (Figure 6A, right panel; Supplementary Table S1). The first PC is heavily affected by the flexible loop around

residue 830 in the Amber and AMOEBA force fields. Except for ff19SB + OL3, high weights are observed on residues around 300 which contains the second most flexible region in the AGO2 system, the PAZ domain that binds the 3' end of the RNA. ff19SB + OL3 and O3P simulations are the only simulations where one or two RNA atoms make it into the top weighing residues for PC1. In O3P simulations, the highest contributions are from either of the terminals of the protein which are also fluctuating more than in the other conditions. The N-terminal residues are also important for the AMOEBA PC1.

3.6 Cas12j results

Cas12j is an RNA-guided nuclease that bacteriophages use for DNA cutting and genome editing (Pausch et al., 2021). The structure of Cas12j (7M5O) contains a protein of 763 residues (residues 1–52 and 717–763 unmodeled) and a single-stranded crRNA molecule of

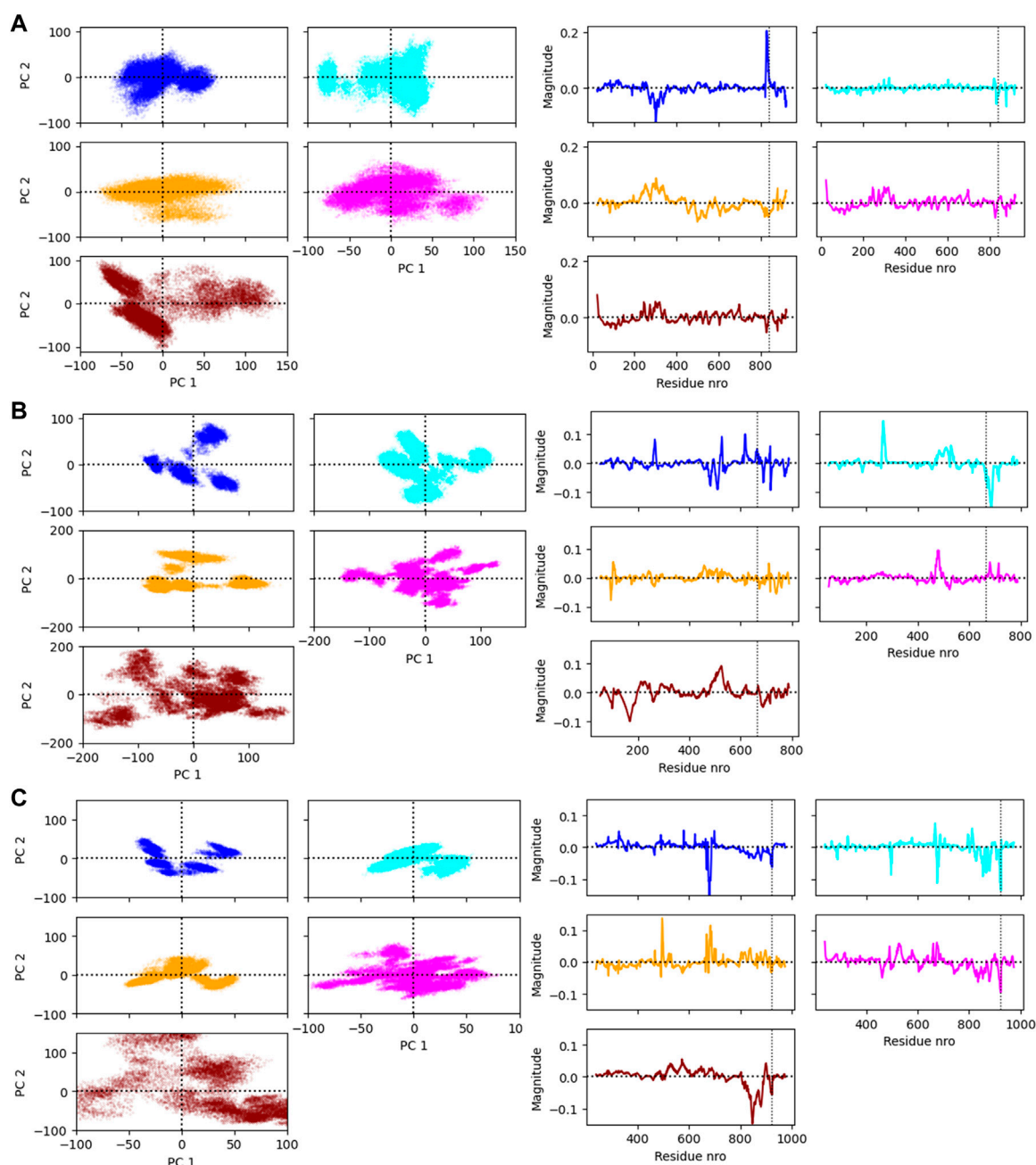


FIGURE 6

(A) The Ago2 simulation frames projected on the first two principal components (PC1 and PC2) and the loading values of the residues on PC1. (B) The Cas12j simulation frames projected on the PC1 and PC2 and the loading values of the residues on PC1. (C) The RIG-I simulation frames projected on the PC1 and PC2 and the loading values of the residues on PC1. The vertical line in the loading value plot indicates the start of the RNA. Note that there are two atoms analyzed per RNA nucleotide which changes the numbering of this region.

45 nucleotides. In addition, there is a Zn^{2+} ion bound in the zinc finger part of the protein. The crRNA forms a hairpin loop with the first 23 nucleotides, and it continues as a single stranded spacer region that is used to recognize the DNA sequence to be cut.

3.6.1 Fluctuations of the Cas12j system

The Cas12j system has overall higher RMSD values than the Ago2 system. The protein is not as compact and globular as Ago2 and there is more freedom of movement also for the RNA.

The higher RMSD values do not necessarily mean that the system is fluctuating more, as they could be a result of the initial structure being further away from a local energy minimum. Then, in the simulations the system adopts an energetically more favorable conformation which is by RMSD further away from the initial one and fluctuates around that conformation. As the deviations of the RMSD values are like those of Ago2, this seems to be the case with Cas12j. The Amber force fields display the least fluctuating protein and RNA, and the largest RMSD values are observed in the

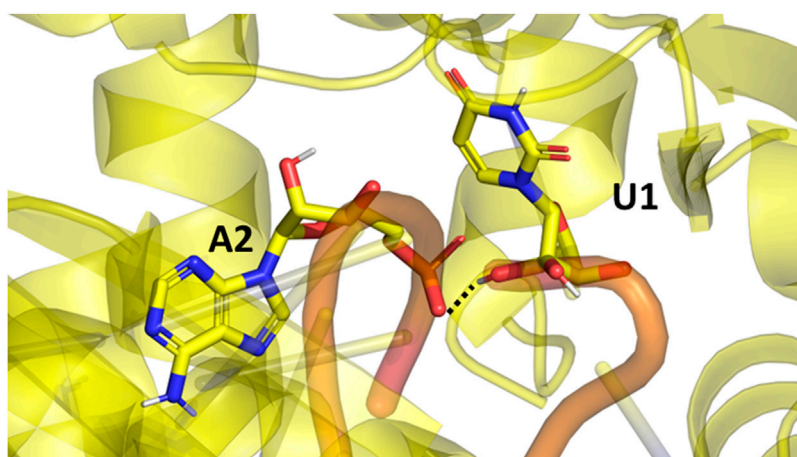


FIGURE 7

The extra hydrogen bond formed between the guide (U1) and target (A2) RNAs in the Ago2 system. This bond formed only in the OPLS4 simulations, and it was one of the reasons why OPLS4 simulations displayed lower RMSF and RMSD values.

AMOEBA and O3P systems for the protein and in the OPLS4 and O3P systems for the RNA. The Zn^{2+} ion stays in place in ff14SB + OL3 and AMOEBA force fields, in the other ones it unbinds. This leads to overall structural instability which is most obvious in the O3P simulations (Figure 4).

3.6.2 Hydrogen bonds of the Cas12j system

There are 22 intra-RNA hydrogen bonds in the Cas12j crystal structure (Table 2). The simulations have a similar number of hydrogen bonds, except for AMOEBA where the hydrogen bond number is lower. This result is a combination of slight structural instability issues and the generally more open and relaxed conformation of the complex that leads the hydrogen bonds to be longer than our relatively strict criteria.

There are 40 hydrogen bonds between the protein and the RNA in the preprocessed starting structure. From these force fields, the ff19SB + OL3 and AMOEBA closely match the initial hydrogen bond count. Like the Ago2 systems, in all the nonpolarizable force fields, there are on average more observed hydrogen bonds between the protein and the RNA than in the crystal structure. In the O3P water simulations where there are structural integrity issues, the number of hydrogen bonds drops by 9.

3.6.3 Exploration of conformations in the Cas12j system—PCA

The plots of PC1 and PC2 values show that Cas12j system adopts clearer distinct conformational states than the Ago2 system (Figure 6B, left panel). There are four to five different states in all the tested force fields. The PC analysis of O3P simulations shows a larger sampling of the conformational space which is due to the structural instability.

Based on the loadings graphs, the different force fields are not sampling similar conformational space. The Amber ff14SB + OL3 and ff19SB + OL3 force fields have the highest weights around the residues 265 and 510, and the 5' end of the RNA (Figure 6B, right panel; Supplementary Table S2). The loop of the RNA hairpin is located close to the flexible oligonucleotide binding domain (OBD) protein region around residue 265 and the movement of these interacting parts are connected. The first 3 nt of

the 5' end of the RNA are moving rather freely and not interacting with the protein which might explain their higher effect on the first PC in these force fields. Residue 510 is part of a long loop (508–537) which forms part of the second recognition domain (RecII) which can interact with the 3' end of the RNA. This RecII domain is also visible on the loadings plots of the polarizable force fields. The highest loadings in the OPLS4 force field are observed around the middle region of the RNA and around residue 100 which forms a loop in the first recognition domain (RecI).

3.7 RIG-I results

RIG-I is a protein that binds cytosolic viral RNA and ATP to trigger an immune response (Lässig et al., 2018). In this study, we used the C268F variant of RIG-I that can trigger the immune response without ATP. The crystal structure of RIG-I consists of a protein of 922 residues (residues 1–239 and 823–925 not modeled) which surrounds two identical RNA chains of 13 nucleotides that are bound into a double helical structure. There is also one Zn^{2+} and 1 Mg^{2+} ion bound in the complex.

3.7.1 Fluctuations of the RIG-I system

Similarly to the Ago2 systems, the protein is moving more than the RNA in the simulations (Table 1). The RMSD values are slightly higher than with the AGO2 system and lower than with the Cas12j system, indicating that the system remains relatively close to the initial conformation of the crystal structure. The RMSD values observed in the non-polarizable force fields are comparable to each other and AMOEBA simulations displays slightly elevated values. The O3P water model leads to structural integrity issues of the protein, starting from terminals and longer loop regions, similarly to the Cas12j system. This can be easily seen in Figure 2C where the distribution of protein RMSD values in the O3P simulations is very wide, whereas the RMSD in the other simulations remain comparable to the other protein systems. The RIG-I system has both a Zn^{2+} and a Mg^{2+} ion which behave

differently (Supplementary Figure S1). The Zn^{2+} ion unbinds from the protein in all the simulations except some of the AMOEBA simulations. The Mg^{2+} ion is stable, and it stays in its place in all the simulations except for OPLS4.

3.7.2 Hydrogen bonds of the RIG-I system

There are 31 strong RNA-RNA hydrogen bonds in the RIG-I crystal structure (Table 2). All simulations display at least six less hydrogen bonds on average, the polarizable O3P water model and AMOEBA both display on average less than 20 hydrogen bonds in total. This loss of hydrogen bonds is explained by the one or two base pairs breaking from each other at the end that is not bound on the protein.

There are 19 weak hydrogen bonds between the protein and the RNA in the preprocessed starting structure. The non-polarizable force fields closely match the hydrogen bond amount observed in the initial structure. The hydrogen bond number is significantly lower in the simulations with the polarizable water model O3P or the AMOEBA force field. This trend is similar to the other two studied systems.

3.7.3 Exploration of conformations in the RIG-I system—PCA

The PCA shows two to four somewhat distinct conformational states for the RIG-I system in the non-polarizable force fields (Figure 6C, left panel). The states are not very distinct in AMOEBA or O3P water model simulations and the O3P simulations sample a large conformational space due to the structural integrity issues.

The weights of the first PC (Figure 6C, right panel) display that the nonpolarizable force fields relatively well agree which parts of the RIG-I complex contribute most to the different conformations. All non-polarizable force fields display larger magnitude around residue 685 which is part of the long loop (residues 676–720) residing close to the catalytic site (around residue 268 which is mutated in our variant C268F) which normally binds ATP and a Mg^{2+} ion. The movements of this loop are required to access the catalytic site, and based on these simulations it seems that this loop is fluctuating a lot possibly to accommodate the ATP and Mg^{2+} binding. The ff19SB + OL3 has higher weight close to residue 439 which is a part of a smaller loop on the other side of the catalytic site. In the OPLS4 force field, higher weights are observed around residue 500 which is a smaller loop region connecting two helices. In all the non-polarizable force fields, the C terminus of the protein gets high weights. The C terminus of RIG-I contains long loop regions without many helical or sheet structures which makes it more structurally unstable than the rest of the protein. Also, it binds the Zn^{2+} ion which unbinds in many of the simulations leading to more structural instability. This is why the C terminal residues also get high weights in the polarizable force fields which tend to sample more conformations in these less structured regions. The effect of the RNA atoms for the PCA analysis is negligible.

4 Discussion

All the studied force fields can be used with RNA-protein complexes.

All force fields produced reasonable simulations without major artefacts that could be traced back to the parameterization of the force fields. The RNA-protein complexes are chemically and biologically special systems, for which there are no specifically tailored parameters in any currently available force field. Proteins and nucleic acids are chemically different which has led to force fields being developed for them separately or making compromises in the form of all-atom force fields. The comparison of force fields presented here is not perfect as it is missing CHARMM36 force field that has been discussed recently in the context of RNA-protein complexes (Gallardo et al., 2022). This, and other weaknesses are discussed in Supplementary Material Part 6.

4.1 Force field selection depends on the studied system

As described previously (Krepl et al., 2015), the choice of the protein and RNA force field depends on many factors of the studied system. There was no single force field that would outperform others in all of our studied complexes, and thus the selection of the force field should happen based on the studied system and the research question. Especially the flexibility of the system affected the force field performance in this study: the flexible Cas12j system displayed some structural instability with the AMOEBA force field and O3P water model, whereas this was not as obvious with the more stable and globular Ago2 system. The instability was most notably observed in the O3P water model simulations, where even some of the Ago2 systems displayed large fluctuations and lower number of hydrogen bonds. It is possible that the very recently published fine-tuned van der Waals parameters of the AMOEBA force field (Jing and Ren, 2022) would alleviate instability issue in the AMOEBA force field.

4.2 Structurally important ions might need constraints in any force field

Many protein RNA-complexes contain ions, which are crucial for protein activity. Ions as charged particles pose a challenge for the non-polarizable force fields which could be observed as the ions unbinding. The issues of ions in nonpolarizable force fields have been described many times before (for example, Leontyev and Stuchebrukhov, 2011; Bedrov et al., 2019; Kurki et al., 2022), and there are no easy solutions. Seeing that the ions sometimes unbind also in the polarizable force fields, the only feasible solution is to constrain the structurally important ions positionally unless one especially wants to study the ion unbinding.

4.3 Polarizability is computationally demanding and might induce structural instability

Using the polarizable force field comes with a significant computational cost. While the ff19SB + OL3 simulations

achieved a simulation speed of ~300 ns/day for the largest (Ago2) complex, the AMOEBA simulations only reached a simulation speed of ~4 ns/day. All simulations were run in a similar environment, on a single NVIDIA Volta V100 GPU on CSC's supercomputer Puhti. Due to this significant increase in computational cost, in some cases it might be more beneficial to use non-polarizable force fields with an enhanced sampling method to get reasonably accurate results. The polarizable water model O3P only minorly decreased the simulation speed (~280 ns/day).

The recently published polarizable water model O3P (Xiong et al., 2022) was not a very good choice for RNA-protein complex simulations. Just changing the water model without changing the simulation parameters or force fields lead to disorganized protein structures that were most prominent on Cas12j system. This water model is not likely the best choice for RNA-protein complexes before some further optimization of its parameters.

4.4 The nonpolarizable force fields stabilize the complexes and might hide rare conformational states

Even though both Amber simulation sets used the same RNA force field, the complexes behaved slightly differently with the different complexes. It is known that the Amber ff14SB force field underestimates helicity which in connection to 3-point water models leads to overly compact protein structures (Tian et al., 2020). This behavior is enhanced when RNA is bound to the protein, as the electrostatic interactions with the RNA backbone make the complex even more compact. Changing the protein force field to ff19SB and the water model to the 4-point OPC alleviate the problem, as the results show more flexible protein backbone movement (Onufriev and Izadi, 2018). OPLS4 and ff14SB + OL3 simulation sets used the older 3-point water model SPC/E. Even in the case of OPC water model, the electrostatic interactions of RNA with the protein and the other RNA strand are strong which leads to less freedom of movement to all biomolecules. The strong charge-charge interactions are a known issue in non-polarizable force fields (Yoo and Aksimentiev, 2016; Aksimentiev, 2018; Duboué-Dijon et al., 2020; Gallardo et al., 2022), for which there are no easy solutions.

Generally, only adjusting Lennard-Jones parameters, vdW parameters or changing the water model are proposed to help with the issue of strong electrostatic interactions (Nerenberg et al., 2012; Chen and García, 2013; Tan et al., 2018; Duboué-Dijon et al., 2020; Tian et al., 2020, 19). Electronic continuum correction approach can be used to adjust the charges of ions to enhance the ion representation in non-polarizable force fields (Duboué-Dijon et al., 2020). This methodology could be partially also employed on proteins, where the charged side chains are relatively distant from the backbone. However, in the case of RNA, the ribose-phosphate backbone is heavily charged and any simple modifications to the point charges would compromise the description of the backbone dihedrals which are directly related to the point charges.

5 Conclusion

Even though extensive effort has been put to parameterize the force fields for RNA and proteins, the RNA-protein complex simulations remain problematic because they need to provide reasonable interactions at the interface of these two chemically different molecules. This study further confirms that the force field and other simulation parameters selection is always dependent on the studied system. Based on our results all the tested non-polarizable force fields can be used to simulate RNA-protein complexes. However, all the non-polarizable force fields tended to make the complexes very compact which might prevent the formation of some biologically relevant conformations. To avoid this, and when the computational cost is not an issue, the polarizable force field AMOEBA could be preferred, but the polarizable O3P water model cannot be recommended for RNA-protein complex simulations. We perceive that the polarizable force fields are the future of biomolecular simulations also beyond the RNA-protein complexes after sufficient development of software and hardware makes them a computationally reasonable alternative.

Data availability statement

The datasets presented in this study can be found in online repositories. The names of the repository/repositories and accession number(s) can be found in the article/Supplementary Material.

Author contributions

HB conducted the Ago2 simulations in non-polarizable force fields, and Cas12j and RIG-I simulations in OPLS4, and wrote the analysis scripts. PB conducted the AMOEBA simulations and the Amber O3P simulations and participated in the analysis of the results. All authors contributed to the article and approved the submitted version.

Funding

This work was supported by Erasmus+ program which funded the research visit of HB at the University of Eastern Finland, during which most of the simulations were ran and analyzed. In addition, PB is funded by the competitive funding to strengthen university research profiles, 5th call, funding to University of Eastern Finland, funded by the Academy of Finland (grant number 325022). PB thanks Emil Aaltonen Foundation for project funding.

Acknowledgments

The authors thank CSC IT Center for Science for the computational resources and Professor Antti Poso for critical comments on the manuscript.

Conflict of interest

The authors declare that the research was conducted in the absence of any commercial or financial relationships that could be construed as a potential conflict of interest.

Publisher's note

All claims expressed in this article are solely those of the authors and do not necessarily represent those of their affiliated

organizations, or those of the publisher, the editors and the reviewers. Any product that may be evaluated in this article, or claim that may be made by its manufacturer, is not guaranteed or endorsed by the publisher.

Supplementary material

The Supplementary Material for this article can be found online at: <https://www.frontiersin.org/articles/10.3389/fchem.2023.1217506/full#supplementary-material>

References

- Bedrov, D., Piquemal, J. P., Borodin, O., MacKerell, A. D., Roux, B., and Schröder, C. (2019). Molecular dynamics simulations of ionic liquids and electrolytes using polarizable force fields. *Chem. Rev.* 119, 7940–7995. doi:10.1021/acs.chemrev.8b00763
- Berro, J. (2018). Essentially, all models are wrong, but some are useful—A cross-disciplinary agenda for building useful models in cell biology and biophysics. *Biophys. Rev.* 10, 1637–1647. doi:10.1007/s12551-018-0478-4
- Bhandare, V., and Ramaswamy, A. (2016). Structural dynamics of human Argonaute2 and its interaction with siRNAs designed to target mutant tdp43. *Adv. Bioinforma.* 2016, 1–13. doi:10.1155/2016/8792814
- Bissaro, M., Sturlese, M., and Moro, S. (2020). Exploring the RNA-recognition mechanism using supervised molecular dynamics (SuMD) simulations: Toward a rational design for ribonucleic-targeting molecules? *Front. Chem.* 8, 107. doi:10.3389/fchem.2020.00107
- Bochicchio, A., Krepl, M., Yang, F., Varani, G., Sponer, J., and Carloni, P. (2018). Molecular basis for the increased affinity of an RNA recognition motif with re-engineered specificity: A molecular dynamics and enhanced sampling simulations study. *PLOS Comput. Biol.* 14, 1006642. doi:10.1371/journal.pcbi.1006642
- Bowers, K. J., Chow, E., Xu, H., Dror, R. O., Eastwood, M. P., Gregersen, B. A., et al. (2006). "Scalable algorithms for molecular dynamics simulations on commodity clusters," in Proceedings of the 2006 ACM/IEEE conference on Supercomputing SC '06 (New York, NY, USA: Association for Computing Machinery), 84. doi:10.1145/1188455.1188544
- Casalino, L., Palermo, G., Spinello, A., Rothlisberger, U., and Magistrato, A. (2018). All-atom simulations disentangle the functional dynamics underlying gene maturation in the intron lariat spliceosome. *Proc. Natl. Acad. Sci.* 115, 6584–6589. doi:10.1073/pnas.1802963115
- Case, D. A., Belfon, K., Ben-Shalom, I. Y., Brozell, S. R., Cerutti, D. S., Cheatham, T. E., et al. (2020). *Amber 2020*. San Francisco: University of California.
- Cesari, A., Bottaro, S., Lindorff-Larsen, K., Banáš, P., Šponer, J., and Bussi, G. (2019). Fitting corrections to an RNA force field using experimental Data. *J. Chem. Theory Comput.* 15, 3425–3431. doi:10.1021/acs.jctc.9b00206
- Chang, S., Zhang, D. W., Xu, L., Wan, H., Hou, T. J., and Kong, R. (2016). Exploring the molecular basis of RNA recognition by the dimeric RNA-binding protein via molecular simulation methods. *RNA Biol.* 13, 1133–1143. doi:10.1080/15476286.2016.1223007
- Chen, A. A., and García, A. E. (2013). High-resolution reversible folding of hyperstable RNA tetraloops using molecular dynamics simulations. *Proc. Natl. Acad. Sci. U. S. A.* 110, 16820–16825. doi:10.1073/pnas.1309392110
- Cui, S., Eisenächer, K., Kirchhofer, A., Brzózka, K., Lammens, A., Lammens, K., et al. (2008). The C-terminal regulatory domain is the RNA 5'-triphosphate sensor of RIG-I. *Mol. Cell.* 29, 169–179. doi:10.1016/j.molcel.2007.10.032
- Duboué-Dijon, E., Javanainen, M., Delcroix, P., Jungwirth, P., and Martinez-Seara, H. (2020). A practical guide to biologically relevant molecular simulations with charge scaling for electronic polarization. *J. Chem. Phys.* 153, 050901. doi:10.1063/5.0017775
- Eastman, P., Swails, J., Chodera, J. D., McGibbon, R. T., Zhao, Y., Beauchamp, K. A., et al. (2017). OpenMM 7: Rapid development of high performance algorithms for molecular dynamics. *PLoS Comput. Biol.* 13, 1005659. doi:10.1371/journal.pcbi.1005659
- Estarellas, C., Otyepka, M., Koča, J., Banáš, P., Krepl, M., and Šponer, J. (2015). Molecular dynamic simulations of protein/RNA complexes: CRISPR/Csy4 endoribonuclease. *Biochimica Biophysica Acta (BBA) - General Subj.* 1850, 1072–1090. doi:10.1016/j.bbagen.2014.10.021
- Gallardo, A., Bogart, B. M., and Dutagaci, B. (2022). Protein–nucleic acid interactions for RNA polymerase II elongation factors by molecular dynamics simulations. *J. Chem. Inf. Model.* 62, 3079–3089. doi:10.1021/acs.jcim.2c00121
- Habibian, M., Hari Krishna, S., Fakhoury, J., Barton, M., Ageely, E. A., Cencic, R., et al. (2020). Effect of 2'-5'/3'-5' phosphodiester linkage heterogeneity on RNA interference. *Nucleic Acids Res.* 48, 4643–4657. doi:10.1093/nar/gkaa222
- Harger, M., Li, D., Wang, Z., Dalby, K., Lagardère, L., Piquemal, J. P., et al. (2017). Tinker-OpenMM: Absolute and relative alchemical free energies using AMOEBA on GPUs. *J. Comput. Chem.* 38, 2047–2055. doi:10.1002/jcc.24853
- Harikrishna, S., and Pradeepkumar, P. I. (2017). Probing the binding interactions between chemically modified siRNAs and human argonaute 2 using microsecond molecular dynamics simulations. *J. Chem. Inf. Model.* 57, 883–896. doi:10.1021/acs.jcim.6b00773
- Huang, X., Sun, W., Cheng, Z., Chen, M., Li, X., Wang, J., et al. (2020). Structural basis for two metal-ion catalysis of DNA cleavage by Cas12i2. *Nat. Commun.* 11, 5241. doi:10.1038/s41467-020-19072-6
- Jiang, H., Sheong, F. K., Zhu, L., Gao, X., Bernauer, J., and Huang, X. (2015). Markov state models reveal a two-step mechanism of miRNA loading into the human argonaute protein: Selective binding followed by structural Re-arrangement. *PLOS Comput. Biol.* 11, 1004404. doi:10.1371/journal.pcbi.1004404
- Jing, Z., and Ren, P. (2022). Molecular dynamics simulations of protein RNA complexes by using an advanced electrostatic model. *J. Phys. Chem. B* 126, 7343–7353. doi:10.1021/acs.jpcc.2c05278
- Kalia, M., Willkomm, S., Claussen, J. C., Restle, T., and Bonvin, A. M. J. J. (2015). Novel insights into guide RNA 5'-nucleoside/tide binding by human argonaute 2. *Int. J. Mol. Sci.* 17, 22. doi:10.3390/ijms17010022
- Kandeel, M., and Kitade, Y. (2018). Molecular dynamics and binding selectivity of nucleotides and polynucleotide substrates with EIF2C2/Ago2 PAZ domain. *Int. J. Biol. Macromol.* 107, 2566–2573. doi:10.1016/j.ijbiomac.2017.10.145
- Kehl, T., Backes, C., Kern, F., Fehlmann, T., Ludwig, N., Meese, E., et al. (2017). About miRNAs, miRNA seeds, target genes and target pathways. *Oncotarget* 8, 107167–107175. doi:10.18632/oncotarget.22363
- Kong, R., Xu, L., Piao, L., Zhang, D., Hou, T. J., and Chang, S. (2017). Exploring the RNA-bound and RNA-free human Argonaute-2 by molecular dynamics simulation method. *Chem. Biol. Drug Des.* 90, 753–763. doi:10.1111/cbdd.12997
- Krepl, M., Dendooven, T., Luisi, B. F., and Sponer, J. (2021). MD simulations reveal the basis for dimeric assembly of Hfq–RNA complexes. *J. Biol. Chem.* 296, 100656. doi:10.1016/j.jbc.2021.100656
- Krepl, M., Havrila, M., Stadlbauer, P., Banas, P., Otyepka, M., Pasulka, J., et al. (2015). Can we execute stable microsecond-scale atomistic simulations of protein–RNA complexes? *J. Chem. Theory Comput.* 11, 1220–1243. doi:10.1021/ct5008108
- Kurki, M., Poso, A., Bartos, P., and Miettinen, M. S. (2022). Structure of POPC Lipid Bilayers in OPLS3e Force Field. *J. Chem. Inf. Model.* 62, 6462–6474. doi:10.1021/acs.jcim.2c00395
- Lässig, C., Lammens, K., Gorenflo López, J. L., Michalski, S., Fetscher, O., and Hopfner, K. P. (2018). Unified mechanisms for self-RNA recognition by RIG-I Singleton-Merten syndrome variants. *Elife* 7, 38958. doi:10.7554/eLife.38958
- Leontyev, I., and Stuchebrukhov, A. (2011). Accounting for electronic polarization in non-polarizable force fields. *Phys. Chem. Chem. Phys.* 13, 2613–2626. doi:10.1039/c0cp01971b
- Liu, Y., Yu, Z., Zhu, J., Wang, S., Xu, D., and Han, W. (2018). Why is a high temperature needed by thermus thermophilus argonaute during mRNA silencing: A theoretical study. *Front. Chem.* 6, 223. doi:10.3389/fchem.2018.00223
- Lu, C., Wu, C., Ghoreishi, D., Chen, W., Wang, L., Damm, W., et al. (2021). OPLS4: Improving force field accuracy on challenging regimes of chemical space. *J. Chem. Theory Comput.* 17, 4291–4300. doi:10.1021/acs.jctc.1c00302
- Maier, J. A., Martinez, C., Kasavajhala, K., Wickstrom, L., Hauser, K. E., and Simmerling, C. (2015). ff14SB: Improving the accuracy of protein side chain and backbone parameters from ff99SB. *J. Chem. Theory Comput.* 11, 3696–3713. doi:10.1021/acs.jctc.5b00255
- Nerenberg, P. S., Jo, B., So, C., Tripathy, A., and Head-Gordon, T. (2012). Optimizing solute–water van der Waals interactions to reproduce solvation free energies. *J. Phys. Chem. B* 116, 4524–4534. doi:10.1021/jp2118373

- Olsson, M. H. M., Søndergaard, C. R., Rostkowski, M., and Jensen, J. H. (2011). PROPKA3: Consistent treatment of internal and surface residues in empirical pKa predictions. *J. Chem. Theory Comput.* 7, 525–537. doi:10.1021/ct100578z
- Onufriev, A. V., and Izadi, S. (2018). Water models for biomolecular simulations. *WIREs Comput. Mol. Sci.* 8, 1347. doi:10.1002/wcms.1347
- Palermo, G., Miao, Y., Walker, R. C., Jinek, M., and McCammon, J. A. (2017). CRISPR-Cas9 conformational activation as elucidated from enhanced molecular simulations. *Proc. Natl. Acad. Sci. U. S. A.* 114, 7260–7265. doi:10.1073/pnas.1707645114
- Pausch, P., Soczek, K. M., Herbst, D. A., Tsuchida, C. A., Al-Shayeb, B., Banfield, J. F., et al. (2021). DNA interference states of the hypercompact CRISPR-CasΦ effector. *Nat. Struct. Mol. Biol.* 28, 652–661. doi:10.1038/s41594-021-00632-3
- Rinaldi, S., Colombo, G., and Paladino, A. (2022). The dynamics of t1 adenosine binding on human Argonaute 2: Understanding recognition with conformational selection. *Protein Sci.* 31, e4377. doi:10.1002/pro.4377
- Saltalamacchia, A., Casalino, L., Borišek, J., Batista, V. S., Rivalta, I., and Magistrato, A. (2020). Decrypting the information exchange pathways across the spliceosome machinery. *J. Am. Chem. Soc.* 142, 8403–8411. doi:10.1021/jacs.0c02036
- Schirle, N. T., Sheu-Gruttadauria, J., and MacRae, I. J. (2014). Structural basis for microRNA targeting. *Science* 346, 608–613. doi:10.1126/science.1258040
- Schrödinger (2021). *Schrödinger Release 2021-3*. New York, NY: Schrödinger, LLC.
- Shirts, M. R., Klein, C., Swails, J. M., Yin, J., Gilson, M. K., Mobley, D. L., et al. (2017). Lessons learned from comparing molecular dynamics engines on the SAMPL5 dataset. *J. Comput. Aided Mol. Des.* 31, 147–161. doi:10.1007/s10822-016-9977-1
- Søndergaard, C. R., Olsson, M. H. M., Rostkowski, M., and Jensen, J. H. (2011). Improved treatment of ligands and coupling effects in empirical calculation and rationalization of pKa values. *J. Chem. Theory Comput.* 7, 2284–2295. doi:10.1021/ct200133y
- Šponer, J., Bussi, G., Krepl, M., Banáš, P., Bottaro, S., Cunha, R. A., et al. (2018). RNA structural dynamics as captured by molecular simulations: A comprehensive overview. *Chem. Rev.* 118, 4177–4338. doi:10.1021/acs.chemrev.7b00427
- Tan, D., Piana, S., Dirks, R. M., and Shaw, D. E. (2018). RNA force field with accuracy comparable to state-of-the-art protein force fields. *Proc. Natl. Acad. Sci.* 115, E1346–E1355. doi:10.1073/pnas.1713027115
- The PyMOL Molecular Graphics System (2000). *The PyMOL molecular Graphics system*. Schrödinger: LLC.
- Tian, C., Kasavajhala, K., Belfon, K. A. A., Raguette, L., Huang, H., Miguës, A. N., et al. (2020). ff19SB: Amino-Acid-Specific protein backbone parameters trained against quantum mechanics energy surfaces in solution. *J. Chem. Theory Comput.* 16, 528–552. doi:10.1021/acs.jctc.9b00591
- Tucker, M. R., Piana, S., Tan, D., LeVine, M. V., and Shaw, D. E. (2022). Development of force field parameters for the simulation of single- and double-stranded DNA molecules and DNA–protein complexes. *J. Phys. Chem. B* 126, 4442–4457. doi:10.1021/acs.jpcb.1c10971
- Wang, H. W., Noland, C., Siridechadilok, B., Taylor, D. W., Ma, E., Felderer, K., et al. (2009). Structural insights into RNA processing by the human RISC-loading complex. *Nat. Struct. Mol. Biol.* 16, 1148–1153. doi:10.1038/nsmb.1673
- Xiong, Y., Izadi, S., and Onufriev, A. V. (2022). Fast polarizable water model for atomistic simulations. *J. Chem. Theory Comput.* 18, 6324–6333. doi:10.1021/acs.jctc.2c00378
- Yoo, J., and Aksimentiev, A. (2016). Improved parameterization of amine–carboxylate and amine–phosphate interactions for molecular dynamics simulations using the CHARMM and AMBER force fields. *J. Chem. Theory Comput.* 12, 430–443. doi:10.1021/acs.jctc.5b00967
- Yoo, J., and Aksimentiev, A. (2018). New tricks for old dogs: Improving the accuracy of biomolecular force fields by pair-specific corrections to non-bonded interactions. *Phys. Chem. Chem. Phys.* 20, 8432–8449. doi:10.1039/C7CP08185E
- Zgarbová, M., Otyepka, M., Šponer, J., Mládek, A., Banáš, P., Cheatham, T. E., et al. (2011). Refinement of the Cornell et al. Nucleic Acids Force Field Based on Reference Quantum Chemical Calculations of Glycosidic Torsion Profiles. *J. Chem. Theory Comput.* 7, 2886–2902. doi:10.1021/ct200162x
- Zhang, C., Lu, C., Jing, Z., Wu, C., Piquemal, J. P., Ponder, J. W., et al. (2018). AMOEBA polarizable atomic multipole force field for nucleic acids. *J. Chem. Theory Comput.* 14, 2084–2108. doi:10.1021/acs.jctc.7b01169



OPEN ACCESS

EDITED BY

Clemens Zwergel,
Sapienza University of Rome, Italy

REVIEWED BY

Monica Viviano,
University of Salerno, Italy
Carlos Henrique Ramos,
State University of Campinas, Brazil

*CORRESPONDENCE

Finn K. Hansen,
✉ finn.hansen@uni-bonn.de
Sanil Bhatia,
✉ sanil.bhatia@med.uni-duesseldorf.de

[†]These authors have contributed equally
to this work and share first authorship

RECEIVED 09 May 2023

ACCEPTED 09 June 2023

PUBLISHED 28 June 2023

CITATION

Wurnig S, Vogt M, Hogenkamp J,
Dienstbier N, Borkhardt A, Bhatia S and
Hansen FK (2023), Development of the
first geldanamycin-
based HSP90 degraders.
Front. Chem. 11:1219883.
doi: 10.3389/fchem.2023.1219883

COPYRIGHT

© 2023 Wurnig, Vogt, Hogenkamp,
Dienstbier, Borkhardt, Bhatia and Hansen.
This is an open-access article distributed
under the terms of the [Creative
Commons Attribution License \(CC BY\)](#).
The use, distribution or reproduction in
other forums is permitted, provided the
original author(s) and the copyright
owner(s) are credited and that the original
publication in this journal is cited, in
accordance with accepted academic
practice. No use, distribution or
reproduction is permitted which does not
comply with these terms.

Development of the first geldanamycin-based HSP90 degraders

Silas Wurnig^{1†}, Melina Vogt^{2†}, Julian Hogenkamp²,
Niklas Dienstbier², Arndt Borkhardt², Sanil Bhatia^{2*} and
Finn K. Hansen^{1*}

¹Department of Pharmaceutical and Cell Biological Chemistry, Pharmaceutical Institute, University of Bonn, Bonn, Germany, ²Department of Pediatric Oncology, Hematology and Clinical Immunology, Medical Faculty, Heinrich Heine University Düsseldorf, Düsseldorf, Germany

Despite the early clinical promise, adverse events such as acquired resistance and dose-limiting toxicities have barred the widespread use of HSP90 inhibitors as anticancer drugs. A new approach involving proteolysis-targeting chimeras (PROTACs) to degrade the protein instead of inhibiting it may overcome these problems. In this work, we describe the design, synthesis, and evaluation of cereblon-recruiting geldanamycin-based HSP90 degraders based on the PROTAC technology. Our best degrader, **3a**, effectively decreased HSP90 α and HSP90 β levels in cells utilizing the ubiquitin–proteasome pathway.

KEYWORDS

cancer, cereblon, heat shock protein, Hsp90, PROTAC

1 Introduction

When cells encounter external stressors, such as radiation, heat, hypoxia, or infections, their vital processes need to remain unaffected. This crucial role in the cells is performed by a group of chaperone proteins known as heat shock proteins (HSPs) (Hoter et al., 2018). Cancer cells hijack these pathways to promote their survival and growth. Among the chaperone proteins, HSP of 90 kDa (HSP90) has been extensively studied, maintaining protein homeostasis by assisting in protein folding, stabilization, and degradation (Jackson, 2013; Schopf et al., 2017; Hoter et al., 2018; Biebl and Buchner, 2019). Client proteins of HSP90 fulfill essential roles in signaling cascades, including cell cycle, cell proliferation, differentiation, and apoptosis (Miyata et al., 2013). In mammalian cells, two dominant homologs are found in the cytoplasm: HSP90 α , the stress-inducible isoform, and HSP90 β , the constitutively expressed isoform (Jackson, 2013). Elevated levels of HSP90 have been found in a variety of cancer types, suggesting that HSP90 plays a central role in malignant cell survival and growth (Csermely et al., 1998; Mayer and Bukau, 1999; Bhatia et al., 2018; Park et al., 2020). For instance, enriched HSP90 expression in the therapy-resistant BCR-ABL1⁺ leukemia subgroup facilitates proper folding of BCR-ABL1 oncoprotein, providing a rationale to target leukemia cells via HSP90 inhibition-mediated BCR-ABL1 oncoprotein degradation (Bhatia et al., 2018). Therefore, the inhibition of HSP90 proteins represents a viable option for the development of new anticancer drugs (Birbo et al., 2021).

The different HSP90 isoforms (HSP90 α , HSP90 β , GRP94, and TRAP1) share a high sequence identity with respect to their N-terminal ATP binding pocket. This pocket is targeted by most inhibitors published to date (Park et al., 2020). Until now, over 15 HSP90 inhibitors with different pharmacological properties have entered clinical

trials (Jhaveri et al., 2014; Koren and Blagg, 2020). However, most of these inhibitors displayed poor risk–benefit profiles in the treatment of cancer. This is mostly attributed to dose-dependent hepatotoxicity, ocular toxicity, and the development of chemoresistance (Butler et al., 2015). Notably, the inhibition of HSP90 leads to a dose-dependent depletion of the client proteins, resulting in a heat shock response (HSR) induced by the heat shock factor 1 (HSF1). HSF1 is a transcription factor that, when activated, induces the production of HSP27, HSP40, and HSP70, which in turn protects the cells from apoptosis and cytotoxic stress (Park et al., 2020).

The protein can also be degraded using proteolysis-targeting chimeras (PROTACs) to circumvent problems occurring with traditional protein inhibition, such as overexpression of the target. This approach utilizes a chimeric molecule with an E3 ligase ligand and a warhead that specifically targets the desired protein of interest (POI) connected by a suitable linker moiety (Sosic et al., 2022). Due to the formation of an E3 ligase:PROTAC:POI ternary complex, the POI is recruited into the proximity of the E3 ligase system, leading to POI polyubiquitination and subsequent degradation via the proteasomal system (Sosic et al., 2022).

Geldanamycin (GM), which was isolated from the bacterium *Streptomyces hygroscopicus*, was originally identified as an Src kinase inhibitor (Miller et al., 1994). Further research demonstrated that geldanamycin is a potent inhibitor of HSP90. The ansamycin derivative containing a benzoquinone moiety binds to the N-terminal ATP binding pocket of HSP90 proteins (Deboer et al., 1970). Despite the high potency of GM, it has not progressed into the clinic due to its poor physicochemical properties and unacceptable adverse effects, such as high hepatotoxicity and ocular toxicity (Li et al., 2019). Thus, a series of more soluble and stable semi-synthetic GM analogs were developed. These compounds are characterized by a substitution of the methoxy group in position 17 by an amine-based sidechain such as 17-allylamino (17-AAG, tanespimycin) or 17-[2-(dimethylamino)ethyl]amino (17-DMAG, alvespimycin) (Li et al., 2019; Talaei et al., 2019). However, this also did not lead to success at the clinical level, particularly due to HSR induction and toxicity-related concerns (Butler et al., 2015). Consequently, the targeted degradation of HSP90 via PROTACs might provide an alternative approach to treating HSP90-driven diseases. Thus far, only one report on HSP90 degraders was published by Liu et al. (2022), in which the clinical candidate and purine-derivative BIIB021 was utilized as an HSP90 warhead. Herein, we report the design, synthesis, and evaluation of the first GM-based HSP90 degraders.

2 Materials and methods

2.1 Knock-in for generation of HSP90-HiBiT cell lines

Transfection was carried out using the Amaxa Nucleofection system (SF Cell Line Kit, cat. No. V4XC-2032) as previously described (Bhatia et al., 2022). For 2×10^5 K562 (BCR–ABL1+) leukemia cells, 100 pmol of Cas9 protein (Alt-R S. p. HiFi Cas9 nuclease V3, cat. No. 1081060; IDT) was mixed with

120 pmol of gRNA (crRNA:tracrRNA 1:1) and assembled for 20 min at room temperature. Afterward, ssODN was added, and the mixture was combined with the cell suspension (resuspended cells in Nucleofector solution SF) and the electroporation enhancer. The complete volume was gently transferred to the Nucleocuvette module, placed in the 4D-Nucleofector system, and electroporated using the program CA-137. Pre-warmed culture media were quickly added to the cells and transferred to a 96-well plate. Cells were expanded, and monoclonal selection of the edited cells was performed via a semi-solid methylcellulose medium (MethoCult™ H4100 STEMCELL, #04100) supplemented with FCS (Sigma-Aldrich, St. Louis, MO, United States) and penicillin/streptomycin (Invitrogen, Carlsbad, CA, United States). The Nano-Glo® HiBiT Lytic Detection System (#N3030; Promega) was used to measure the edited gene expression for selecting stable HSP90α/β-HiBiT tagged clones. Positive clones with stable and higher bioluminescence signals were selected and later subjected to Sanger sequencing to exclude random mutations in the *HSP90AA1* or *HSP90AB1* gene during the integration of HiBiT-tag. For experiments, 1×10^4 cells were incubated at indicated concentrations of PROTACs or inhibitor (geldanamycin) at 6 or 24 h time points. Therefore, the treated cells were mixed 1:1 with Nano-Glo® HiBiT Lytic reagent (containing LgBiT Protein (1:100) and Nano-Glo® HiBiT Lytic Substrate (1:50) in Nano-Glo® HiBiT Lytic Buffer). The mixture was incubated for 10 min at room temperature, and luminescence was measured using a Tecan Spark microplate reader. The background luminescence was measured using unedited cells and subtracted from all readings.

2.2 Fluorescence polarization assay

An evaluation of the binding affinity of compounds toward the ATP pocket of the HSP90 N-terminal domain (NTD) was determined by a competitive binding assay against FITC-labeled geldanamycin (GM) using the HSP90-NTD assay kit (cat. 50293, BPS Biosciences) as previously described (Bhatia et al., 2022). To this end, the inhibitor sample wells were filled with 15 µL of 1× HSP90 assay buffer, 5 µL of 40 mM DTT, 5 µL of 2 mg/ml BSA, 40 µL of H₂O, 5 µL of FITC-labeled GM (100 nM), and 10 µL of inhibitor at 10 µM or 1 µM. The reaction was initiated by adding 20 µL of HSP90 (17 ng/µL) and incubating at room temperature (protected from light) for 3 h with slow shaking. Background wells (master mix only), negative controls (FITC-labeled GM, buffer, and DMSO), and positive controls (FITC-labeled GM, buffer, DMSO, and HSP90) were also included within the assay plate. Fluorescence polarization was measured at a 470-nm excitation wavelength and 525-nm emission wavelength in a microtiter plate reader (Infinite M1000pro by Tecan). Polarization was calculated using $(III - G(I\bot))/(III + G(I\bot)) \times 1,000$ and a g-factor of 1.187. The percentage of HSP90-bound FITC-labeled GM was calculated using

$$P_{norm} = \frac{P_{inhibitor} - P_{neg}}{P_{pos} - P_{neg}} * 100.$$

2.3 Simple western immunoassay

Fluorescent (5×) master mix, DTT, and biotinylated ladder were prepared following the manufacturer's instructions (BioTechne). Lysates were diluted with 0.1× sample buffer and mixed 5:1 with fluorescent 5× master mix to obtain a target sample concentration of 0.40 µg/µL per well. Samples were then denatured for 5 min at 95°C in a PCR cycler (Gene AMP PCR System 2700, Applied Biosystems). The assay plate was loaded following the manufacturer's instructions and centrifuged for 5 min at 1,000 g at room temperature. The immunoassay was performed using a 12- to 230-kDa separation module with 25 cartridges (SM-W004, BioTechne). Lysates were separated for 25 min at 375 V, blocked for 5 min with antibody diluent 2, and incubated for 30 min with primary antibody and for 30 min with secondary antibody, subsequently. Primary antibody multiplex mix consisted of 1:100 anti-HSP90 (4877S, Cell Signaling Technology, Danvers, MA) and 1:50 anti-β-actin (MAB8929, R&D) diluted in antibody diluent 2. Signals were detected using a JESS anti-rabbit detection module (DM-001, BioTechne) multiplexed with an anti-mouse secondary NIR antibody (043-821, BioTechne).

List of antibodies used

Target	species	dilution (JESS)	cat. no.
β-actin	Mouse	1:50	MAB8929
HSP90 total	Rabbit	1:100	CST#4877
HSP90α	Rabbit	1:100	CST#8165
HSP90β	Rabbit	1:100	CST#5087

2.4 General information and chemistry

Chemicals were obtained from abcr GmbH, Acros Organics, Carbolution Chemicals, Sigma-Aldrich, TCI Chemicals, BLDpharm, or VWR and used without further purification. Technical grade solvents were distilled prior to use. For all HPLC purposes, acetonitrile in HPLC-grade quality (HiPerSolv CHROMANORM, VWR) was used. Water was purified with PURELAB® flex (ELGA VEOLIA). Air-sensitive reactions were carried out under an argon atmosphere utilizing standard Schlenk techniques. The uncorrected melting points were determined using a Büchi Melting Point M-560 apparatus. Thin-layer chromatography (TLC) was carried out on prefabricated plates (silica gel 60, F₂₅₄, Merck). Components were visualized either by irradiation with ultraviolet light (254 nm or 366 nm) or by staining appropriately. Column chromatography was carried out on silica gel (60 Å, 40–60 µm, Acros Organics). If no solvent is stated, an aqueous solution was prepared with demineralized water. Mixtures of two or more solvents are specified as “solvent A”/“solvent B,” 3/1, v/v, meaning that 100 ml of the respective mixture consists of 75 ml of “solvent A” and 25 ml of “solvent B.”

2.5 Nuclear magnetic resonance spectroscopy (NMR)

Proton (¹H), carbon (¹³C), and fluorine (¹⁹F) NMR spectra were recorded either on a Bruker AVANCE 500 MHz at a frequency of

500 MHz (¹H) and 126 MHz (¹³C) or a Bruker AVANCE III HD 600 MHz at a frequency of 600 MHz (¹H), 151 MHz (¹³C), and 565 MHz (¹⁹F). The chemical shifts are given in parts per million (ppm). As solvents, deuterated chloroform (CDCl₃), deuterated methanol (methanol-*d*₄), and deuterated dimethyl sulfoxide (DMSO-*d*₆) were used. The residual solvent signal (CDCl₃: ¹H NMR: 7.26 ppm, ¹³C NMR: 77.1 ppm; DMSO-*d*₆: ¹H NMR: 2.50 ppm, ¹³C NMR: 39.52 ppm; methanol-*d*₄: ¹H NMR: 3.31 ppm, 4.87 ppm, ¹³C NMR: 49.00 ppm) was used for calibration. The multiplicity of each signal is reported as singlet (s), doublet (d), triplet (t), multiplet (m), or combinations thereof. Multiplicities and coupling constants are reported as measured and might disagree with the expected values. For all final compounds, a racemic mixture of R and S thalidomide was used in the reaction; therefore, certain ¹H and ¹³C NMR signals can occur as two distinct sets of signals due to the presence of diastereomers. When methanol-*d*₆ was used, some NH and OH protons were undetectable due to the H/D exchange.

2.6 Mass spectrometry

High-resolution electrospray ionization mass spectra (HRMS-ESI) were acquired with a micrOTOF-Q mass spectrometer (Bruker) with ESI-source coupled with HPLC Dionex UltiMate 3,000 (Thermo Scientific). Low-resolution electrospray ionization mass spectra (LRMS-ESI) were acquired with an Advion expression® compact mass spectrometer (CMS) coupled with an automated TLC plate reader Plate Express® (Advion).

2.7 High-performance liquid chromatography (HPLC)

A Thermo Fisher Scientific UltiMate™ 3000 UHPLC system with a Nucleodur 100-5 C18 (250 × 4.6 mm, Macherey Nagel) with a flow rate of 1 ml/min and a temperature of 25°C or a 100-5 C18 (100 × 3 mm, Macherey Nagel) with a flow rate of 0.5 ml/min and a temperature of 25°C with an appropriate gradient was used. For preparative purposes, a Varian ProStar system with a Nucleodur 110-5 C18 HTec (150 × 32 mm, Macherey Nagel) column with 20 ml/min was used. Detection was implemented by UV absorption measurement at a wavelength of λ = 220 nm and λ = 250 nm. Bidest H₂O (A) and MeCN (B) were used as eluents with an addition of 0.1% TFA for eluent A. Purity: the purity of all final compounds was 95% or higher. Purity was determined via HPLC with Nucleodur 100-5 C18 (250 × 4.6 mm, Macherey Nagel) at 250 nm. After column equilibration for 5 min, a linear gradient from 5% A to 95% B in 7 min followed by an isocratic regime of 95% B for 10 min was used.

2.8 Synthesis

General procedures and data sheets for the final compounds are provided in the following. The data sheets for all intermediates can be found in the [Supplementary Materials](#).

2.8.1 General procedure A

The free diamine (2.0 eq.) was dissolved in ethanol (30 ml per g diamine) and cooled to 0°C. Di-*tert*-butyl dicarbonate (1.1 eq.) was added in small portions to the continuously stirred solution. Afterward, the solution was allowed to warm to room temperature and stirred overnight. After extraction with CH₂Cl₂ (3 × 75 ml), the combined organic phases were dried over Na₂SO₄ and filtered, and the solvent was removed under reduced pressure. The crude product was purified by column chromatography using CH₂Cl₂/MeOH (9/1, v/v) with 2% triethylamine.

2.8.2 General procedure B

The free diamine (2.0 eq.) was dissolved in CH₂Cl₂ (15 ml per g diamine) and cooled to 0°C. Di-*tert*-butyl dicarbonate (1.0 eq.) was added in small portions to the continuously stirred solution. Afterward, the solution was allowed to warm to room temperature and stirred overnight. After extraction with CH₂Cl₂ (3 × 75 ml), the organic phase was dried over Na₂SO₄ and filtered, and the solvent was removed under reduced pressure. The crude product was purified by column chromatography using CH₂Cl₂/MeOH (9/1, v/v) with 2% triethylamine.

2.8.3 General procedure C

The mono-Boc-protected diamine linker (1.0 eq.) was dissolved in DMSO (20 ml per g mono-Boc-protected diamine). *N,N*-Diisopropylethylamine (2.0 eq.) and 2-(2,6-dioxo-3-piperidinyl)-4-fluoro-1*H*-isindole-1,3(2*H*)-dione (1.0 eq.) were added, and the mixture was stirred at 90°C overnight. After cooling, the solution was poured onto half-saturated brine and extracted with ethyl acetate (3 × 50 ml). The combined organic phases were dried over Na₂SO₄, filtered, and concentrated under reduced pressure. The crude product was purified by column chromatography using a mixture of ethyl acetate and cyclohexane.

2.8.4 General procedure D

The Boc-protected thalidomide-linker building block was dissolved in a mixture of CH₂Cl₂ and TFA [3/1 (v/v)] and stirred at room temperature until TLC analysis showed complete conversion. After evaporation of the solvents, the TFA-amine salt was dissolved in 5 ml of dichloromethane. After the addition of *N,N*-diisopropylethylamine (8.0 eq.) and geldanamycin (1.0 eq.), the solution was stirred at room temperature overnight. After extraction with ethyl acetate (3 × 25 ml), the solution was dried over Na₂SO₄, filtered, and concentrated under reduced pressure. The crude product was purified by column chromatography using a mixture of CH₂Cl₂ and acetone.

2.8.5 General procedure E

The Boc-protected thalidomide-linker building block was dissolved in a mixture of CH₂Cl₂ and TFA [3/1 (v/v)] and stirred at room temperature until TLC analysis showed complete conversion. After evaporation of the solvents, the TFA-amine salt was dissolved in 5 ml of dichloromethane. After the addition of *N,N*-diisopropylethylamine (8.0 eq.) and geldanamycin (1.0 eq.), the solution was stirred at room temperature overnight. After extraction with ethyl acetate (3 × 25 ml), the solution was dried over Na₂SO₄, filtered, and concentrated under reduced pressure. The crude

product was purified by column chromatography using a mixture of cyclohexane and ethyl acetate.

2.8.6 (4*E*,6*Z*,8*S*,9*S*,10*E*,12*S*,13*R*,14*S*,16*R*)-19-((2-[2-(2-([2-(2,6-dioxopiperidin-3-yl)-1,3-dioxoisindolin-4-yl]amino)ethoxy)ethoxy]ethyl)amino)-13-hydroxy-8,14-dimethoxy-4,10,12,16-tetramethyl-3,20,22-trioxo-2-azabicyclo[16.3.1]docosa-1,4,6,10,18-pentaen-9-yl carbamate (3a)

3a was synthesized according to General Procedure D using **2a** as starting material (51 mg, 0.10 mmol, 2.0 eq.). The desired compound **3a** was obtained as a red-brown solid (25 mg, 0.03 mmol). Yield: 50%; mp: 122°C–129°C; R_f: 0.43 (CH₂Cl₂/acetone (3/1) (v/v)); HRMS-ESI (*m/z*): [M + H]⁺ calcd for C₄₇H₆₁N₆O₁₄⁺: 933.4240, found: 933.4240; ¹H NMR (600 MHz, methanol-*d*₄): *d* 7.55–7.48 (m, 1H), 7.15–7.06 (m, 1H), 7.06–7.01 (m, 1H), 7.01–6.97 (m, 1H), 6.95–6.88 (m, 1H), 6.65–6.57 (m, 1H), 5.90–5.82 (m, 1H), 5.66–5.59 (m, 1H), 5.23–5.14 (m, 1H), 5.03–4.93 (m, 1H), 4.55–4.48 (m, 1H), 3.82–3.64 (m, 10H), 3.61–3.56 (m, 1H), 3.50–3.41 (m, 3H), 3.35–3.32 (m, 3H), 3.28 (s, 3H), 2.89–2.79 (m, 1H), 2.77–2.64 (m, 4H), 2.37–2.27 (m, 1H), 2.14–2.06 (m, 1H), 2.00–1.96 (m, 3H), 1.80–1.70 (m, 4H), 1.70–1.53 (m, 2H), 1.00–0.93 (m, 6H); ¹³C NMR (151 MHz, methanol-*d*₄): *d* 211.4, 185.6, 185.6, 181.1, 181.0, 174.6, 174.6, 171.4, 171.4, 170.6, 170.6, 169.2, 159.1, 159.1, 148.2, 148.2, 146.7, 146.7, 142.6, 139.3, 137.9, 137.2, 135.4, 135.2, 134.5, 134.5, 133.8, 133.7, 132.9, 132.7, 129.6, 127.3, 127.2, 125.5, 118.3, 112.1, 112.1, 111.3, 110.1, 110.0, 109.3, 109.2, 83.0, 82.1, 82.0, 74.2, 74.2, 71.7, 71.6, 71.6, 70.7, 70.7, 70.6, 70.2, 70.2, 57.5, 57.5, 56.9, 56.1, 50.2, 50.2, 49.6, 49.4, 49.3, 49.1, 49.0, 48.9, 48.7, 48.6, 46.2, 46.1, 43.3, 43.3, 35.8, 35.5, 34.4, 34.3, 33.9, 33.7, 33.1, 32.3, 32.3, 32.1, 31.9, 30.9, 30.8, 30.5, 29.5, 23.9, 23.9, 23.7, 22.7, 20.9, 13.6, 13.5, 12.4.

2.8.7 (4*E*,6*Z*,8*S*,9*S*,10*E*,12*S*,13*R*,14*S*,16*R*)-19-((2-[2-(2-([2-(2,6-dioxopiperidin-3-yl)-1,3-dioxoisindolin-4-yl]amino)ethoxy)ethoxy]ethyl)amino)-13-hydroxy-8,14-dimethoxy-4,10,12,16-tetramethyl-3,20,22-trioxo-2-azabicyclo[16.3.1]docosa-1(21),4,6,10,18-pentaen-9-yl carbamate (3b)

3b was synthesized according to General Procedure D using **2b** as starting material (56 mg, 0.10 mmol, 2.0 eq.). The desired compound **3b** was obtained as a red-brown solid (28 mg, 0.03 mmol). Yield: 55%; mp: 117°C–119°C; R_f: 0.65 (CH₂Cl₂/acetone (1/1) (v/v)); HRMS-ESI (*m/z*): [M + Na]⁺ calcd for C₄₉H₆₄N₆O₁₅Na⁺: 999.4322, found: 999.4322; ¹H NMR (600 MHz, methanol-*d*₄): *d* 7.54–7.48 (m, 1H), 7.14–7.07 (m, 1H), 7.07–6.96 (m, 3H), 6.62 (d, *J* = 11.4 Hz, 1H), 5.90–5.83 (m, 1H), 5.64–5.59 (m, 1H), 5.22 (s, 1H), 5.05–4.99 (m, 1H), 4.55–4.50 (m, 1H), 3.74–3.64 (m, 14H), 3.62–3.56 (m, 1H), 3.50–3.43 (m, 3H), 3.35–3.32 (m, 3H), 3.30 (s, 3H), 2.89–2.82 (m, 1H), 2.78–2.65 (m, 4H), 2.34–2.26 (m, 1H), 2.15–2.10 (m, 1H), 2.01–1.97 (m, 3H), 1.74–1.71 (m, 4H), 1.68–1.53 (m, 2H), 0.98–0.93 (m, 6H); ¹³C NMR (151 MHz, methanol-*d*₄): *d* 211.7, 185.7, 181.0, 174.8, 171.5, 170.7, 170.6, 169.3, 159.1, 148.1, 146.8, 142.6, 137.9, 137.3, 135.3, 134.4, 133.8, 129.6, 127.2, 118.3, 118.3, 112.1, 111.2, 110.2, 109.2, 83.0, 81.9, 74.3, 71.7, 71.7, 71.7, 71.7, 71.6, 71.4, 70.6, 70.6, 70.6, 70.2, 57.5, 56.8, 56.0, 50.2, 49.6, 49.4, 49.3, 49.1, 49.0, 48.9, 48.7, 48.6, 46.3, 43.3,

35.8, 34.4, 33.6, 33.0, 32.2, 32.1, 30.7, 30.4, 29.6, 29.5, 23.9, 23.8, 23.7, 22.7, 20.9, 13.6, 12.5.

2.8.8 (4E,6Z,8S,9S,10E,12S,13R,14S,16R)-19-((3-[4-(3-([2-(2,6-dioxopiperidin-3-yl)-1,3-dioxoisindolin-4-yl]amino)propoxy)butoxy]propyl)amino)-13-hydroxy-8,14-dimethoxy-4,10,12,16-tetramethyl-3,20,22-trioxo-2-azabicyclo[16.3.1]docosa-1(21),4,6,10,18-pentaen-9-yl carbamate (3c)

3c was synthesized according to General Procedure D using **2c** as starting material (56 mg, 0.10 mmol, 2.0 eq.). The desired compound **3c** was obtained as a red-brown solid (40 mg, 0.04 mmol). Yield: 78%; mp: 145°C–150°C; R_f : 0.42 (CH₂Cl₂/acetone (3/1) (v/v)); HRMS-ESI (m/z): [M + H]⁺ calcd for C₅₁H₆₉N₆O₁₄⁺: 989.4833, found: 989.4866; ¹H NMR (600 MHz, methanol-*d*₄) δ 7.53–7.46 (m, 1H), 7.11–7.05 (m, 1H), 7.04–6.96 (m, 3H), 6.65–6.57 (m, 1H), 5.89–5.83 (m, 1H), 5.67–5.59 (m, 1H), 5.23–5.19 (m, 1H), 5.04–4.97 (m, 1H), 4.54–4.49 (m, 1H), 3.71–3.53 (m, 8H), 3.50–3.44 (m, 5H), 3.43–3.38 (m, 2H), 3.33 (s, 3H), 3.30–3.27 (m, 3H), 2.90–2.80 (m, 1H), 2.79–2.63 (m, 4H), 2.39–2.31 (m, 1H), 2.15–2.07 (m, 1H), 1.98 (s, 3H), 1.94–1.86 (m, 4H), 1.75–1.63 (m, 8H), 1.62–1.55 (m, 1H), 0.99–0.94 (m, 6H); ¹³C NMR (151 MHz, methanol-*d*₄) δ 211.8, 185.7, 185.7, 180.8, 180.8, 174.9, 174.8, 174.8, 171.5, 171.4, 170.7, 170.6, 170.6, 169.4, 169.3, 159.1, 159.1, 148.3, 148.2, 146.8, 142.8, 137.9, 137.2, 137.2, 135.3, 134.4, 133.8, 129.6, 127.2, 118.0, 117.9, 111.8, 110.9, 110.9, 109.4, 109.1, 83.0, 82.0, 74.2, 72.2, 72.2, 72.0, 71.9, 70.6, 70.3, 70.3, 69.6, 69.6, 57.5, 56.9, 56.9, 56.0, 50.2, 50.1, 49.6, 49.4, 49.3, 49.1, 49.0, 48.9, 48.7, 48.6, 45.6, 45.6, 41.4, 41.3, 41.2, 35.9, 34.4, 33.8, 33.0, 32.2, 32.1, 31.4, 30.9, 30.7, 30.6, 30.5, 30.5, 30.4, 30.4, 29.6, 29.5, 27.6, 27.6, 27.4, 23.8, 23.7, 22.7, 20.9, 14.3, 13.6, 12.5.

2.8.9 (4E,6Z,8S,9S,10E,12S,13R,14S,16R)-19-((3-{2-[2-(3-([2-(2,6-dioxopiperidin-3-yl)-1,3-dioxoisindolin-4-yl]amino)propoxy)ethoxy]propyl)amino]-13-hydroxy-8,14-dimethoxy-4,10,12,16-tetramethyl-3,20,22-trioxo-2-azabicyclo[16.3.1]docosa-1(21),4,6,10,18-pentaen-9-yl carbamate (3d)

3d was synthesized according to General Procedure D using **2d** as starting material (58 mg, 0.10 mmol, 2.0 eq.). The desired compound **3d** was obtained as a red-brown solid (41 mg, 0.04 mmol). Yield: 78%; mp: 123°C–132°C; R_f : 0.77 (CH₂Cl₂/acetone (1/1) (v/v)); HRMS-ESI (m/z): [M + H]⁺ calcd for C₅₁H₆₉N₆O₁₅⁺: 1,005.4815, found: 1,005.4815; ¹H NMR (600 MHz, methanol-*d*₄) δ 7.54–7.47 (m, 1H), 7.11–7.04 (m, 1H), 7.04–7.00 (m, 1H), 7.00–6.95 (m, 2H), 6.65–6.58 (m, 1H), 5.89–5.83 (m, 1H), 5.67–5.59 (m, 1H), 5.25–5.20 (m, 1H), 5.04–4.97 (m, 1H), 4.56–4.49 (m, 1H), 3.74–3.67 (m, 4H), 3.67–3.54 (m, 10H), 3.48–3.43 (m, 1H), 3.43–3.37 (m, 2H), 3.34 (s, 3H), 3.29–3.28 (m, 3H), 2.89–2.81 (m, 1H), 2.79–2.63 (m, 4H), 2.38–2.29 (m, 1H), 2.16–2.09 (m, 2H), 2.01–1.97 (m, 3H), 1.94–1.86 (m, 4H), 1.73 (s, 4H), 1.69–1.54 (m, 2H), 0.99–0.93 (m, 6H); ¹³C NMR (151 MHz, methanol-*d*₄) δ 211.8, 210.5, 185.7, 185.7, 180.8, 174.9, 174.8, 171.5, 171.5, 170.7, 170.6, 170.6, 169.3, 169.3, 159.1, 159.1, 159.1, 159.1, 148.2, 148.2, 146.8, 146.7, 142.8, 137.9, 137.3, 135.3, 134.4, 133.8, 132.8, 129.6, 127.2, 127.2, 118.0, 111.8, 111.8, 110.9, 110.8, 109.5, 109.1, 83.0, 82.0, 74.2, 71.6, 71.6, 71.6, 71.5, 71.5,

71.4, 70.6, 70.5, 70.5, 70.0, 69.9, 57.5, 57.5, 56.9, 56.1, 50.2, 50.1, 49.4, 49.3, 49.1, 49.0, 48.9, 48.7, 48.6, 45.3, 45.2, 45.2, 41.3, 41.2, 41.1, 35.9, 34.4, 33.8, 33.0, 32.2, 32.1, 30.9, 30.7, 30.7, 30.6, 30.5, 30.4, 30.4, 29.5, 23.9, 23.7, 22.7, 20.9, 14.3, 13.6, 12.5.

2.8.10 (4E,6Z,8S,9S,10E,12S,13R,14S,16R)-19-[(6-{[2-(2,6-dioxopiperidin-3-yl)-1,3-dioxoisindolin-4-yl]amino}hexyl)amino]-13-hydroxy-8,14-dimethoxy-4,10,12,16-tetramethyl-3,20,22-trioxo-2-azabicyclo[16.3.1]docosa-1(21),4,6,10,18-pentaen-9-yl carbamate (3e)

3e was synthesized according to General Procedure E using **2e** as starting material (47 mg, 0.10 mmol, 2.0 eq.). The desired compound **3e** was obtained as a red-brown solid (24 mg, 0.03 mmol). Yield: 52%; mp: 158°C–162°C; R_f : 0.64 (ethyl acetate); HRMS-ESI (m/z): [M + Na]⁺ calcd for C₄₇H₆₀N₆O₁₂Na⁺: 923.4167, found: 923.4161; ¹H NMR (600 MHz, methanol-*d*₄) δ 7.56–7.50 (m, 1H), 7.14–7.09 (m, 1H), 7.05–6.99 (m, 3H), 6.62 (t, J = 11.7 Hz, 1H), 5.90–5.84 (m, 1H), 5.62–5.57 (m, 1H), 5.24–5.20 (m, 1H), 5.06–5.01 (m, 1H), 4.56–4.51 (m, 1H), 3.63–3.58 (m, 1H), 3.55–3.51 (m, 2H), 3.49–3.44 (m, 1H), 3.33–3.32 (m, 3H), 3.30 (s, 3H), 2.89–2.82 (m, 1H), 2.78–2.64 (m, 4H), 2.35–2.25 (m, 1H), 2.15–2.08 (m, 1H), 1.72–1.61 (m, 6H), 1.60–1.53 (m, 2H), 1.53–1.43 (m, 5H), 1.36–1.26 (m, 6H), 1.01–0.94 (m, 6H); ¹³C NMR (151 MHz, methanol-*d*₄) δ 185.8, 185.8, 180.9, 180.9, 174.9, 174.8, 171.6, 171.6, 170.8, 170.8, 169.4, 169.4, 159.1, 159.1, 148.4, 148.3, 146.6, 142.8, 137.9, 137.3, 135.4, 134.4, 133.8, 133.8, 130.9, 130.4, 129.6, 127.8, 127.2, 118.1, 111.9, 111.9, 110.9, 109.6, 109.1, 83.0, 81.9, 77.4, 74.3, 72.2, 67.4, 62.0, 57.5, 56.8, 50.2, 50.2, 49.4, 49.3, 49.1, 49.0, 48.9, 48.7, 48.6, 46.3, 46.2, 46.2, 43.3, 43.3, 43.2, 43.1, 38.9, 35.8, 35.3, 34.5, 33.7, 33.0, 32.8, 32.2, 32.2, 31.8, 30.8, 30.8, 30.7, 30.7, 30.7, 30.6, 30.4, 30.3, 30.2, 30.1, 30.0, 28.1, 27.5, 27.4, 27.3, 26.9, 26.1, 23.8, 23.8, 23.7, 22.9, 22.7, 21.0, 20.9, 20.3, 19.9, 14.3, 13.6, 12.5.

2.8.11 (4E,6Z,8S,9S,10E,12S,13R,14S,16R)-19-[(8-{[2-(2,6-dioxopiperidin-3-yl)-1,3-dioxoisindolin-4-yl]amino}octyl)amino]-13-hydroxy-8,14-dimethoxy-4,10,12,16-tetramethyl-3,20,22-trioxo-2-azabicyclo[16.3.1]docosa-1(21),4,6,10,18-pentaen-9-yl carbamate (3f)

3f was synthesized according to General Procedure E using **2f** as starting material (50 mg, 0.10 mmol, 2.0 eq.). The desired compound **3f** was obtained as a red-brown solid (26 mg, 0.03 mmol). Yield: 52%; mp: 155°C–162°C; R_f : 0.28 (cyclohexane/ethyl acetate (1/3) (v/v)); HRMS-ESI (m/z): [M + Na]⁺ calcd for C₄₉H₆₄N₆O₁₂Na⁺: 951.4480, found: 951.4474; ¹H NMR (600 MHz, methanol-*d*₄) δ 7.57–7.51 (m, 1H), 7.14–7.09 (m, 1H), 7.07–7.00 (m, 3H), 6.62 (t, J = 11.4 Hz, 1H), 5.90–5.84 (m, 1H), 5.62–5.57 (m, 1H), 5.22 (s, 1H), 5.07–5.01 (m, 1H), 4.56–4.52 (m, 1H), 3.64–3.57 (m, 1H), 3.56–3.50 (m, 2H), 3.50–3.44 (m, 1H), 3.34 (s, 3H), 3.30 (s, 3H), 2.88–2.80 (m, 1H), 2.79–2.65 (m, 4H), 2.35–2.25 (m, 1H), 2.15–2.08 (m, 1H), 1.99 (s, 3H), 1.83–1.77 (m, 1H), 1.73 (s, 3H), 1.70–1.61 (m, 5H), 1.61–1.52 (m, 2H), 1.46–1.36 (m, 9H), 0.99–0.96 (m, 6H); ¹³C NMR (151 MHz, methanol-*d*₄) δ 185.8, 180.9, 174.8, 171.6, 170.8, 169.4, 159.1, 159.1, 148.4, 148.3, 146.6, 142.9, 137.9, 137.3, 135.3, 134.4, 133.8, 133.8, 132.5, 130.4, 129.7, 127.8, 127.2, 118.0, 115.8, 111.8, 110.9, 109.5, 109.1, 83.0, 81.9, 77.4, 74.3, 72.2, 67.4, 57.6, 56.8, 52.5, 50.2, 49.6, 49.4, 49.3, 49.1, 49.0, 48.9, 48.7, 48.6, 46.3, 46.3, 43.5,

43.4, 35.8, 34.5, 33.6, 33.1, 32.8, 32.2, 31.7, 30.8, 30.8, 30.7, 30.6, 30.4, 30.3, 30.2, 30.1, 30.1, 30.1, 30.1, 30.0, 29.1, 27.7, 27.7, 27.5, 27.5, 23.8, 23.7, 23.7, 23.0, 22.9, 22.7, 20.9, 20.3, 19.9, 19.3, 14.3, 13.7, 12.4.

2.8.12 (4E,6Z,8S,9S,10E,12S,13R,14S,16R)-19-[(10-[(2-(2,6-dioxopiperidin-3-yl)-1,3-dioxoisindolin-4-yl)amino]decyl)amino]-13-hydroxy-8,14-dimethoxy-4,10,12,16-tetramethyl-3,20,22-trioxo-2-azabicyclo[16.3.1]docosa-1(21),4,6,10,18-pentaen-9-yl carbamate (3g)

3g was synthesized according to General Procedure E using **2g** as starting material (53 mg, 0.10 mmol, 2.0 eq.). The desired compound **3g** was obtained as a red-brown solid (22 mg, 0.02 mmol). Yield: 44%; mp: 165°C–169°C; R_f : 0.22 (cyclohexane/ethyl acetate (1/3) (v/v)); HRMS-ESI (m/z): $[M + Na]^+$ calcd for $C_{51}H_{68}N_6O_{12}Na^+$: 979.4793, found: 979.4787; 1H NMR (600 MHz, methanol- d_4) δ 7.57–7.51 (m, 1H), 7.15–7.09 (m, 1H), 7.07–7.00 (m, 3H), 6.65–6.58 (m, 1H), 5.90–5.84 (m, 1H), 5.62–5.56 (m, 1H), 5.22 (s, 1H), 5.06–5.01 (m, 1H), 4.56–4.52 (m, 1H), 3.64–3.57 (m, 1H), 3.55–3.44 (m, 3H), 3.34 (s, 3H), 3.30 (s, 3H), 2.90–2.83 (m, 1H), 2.79–2.66 (m, 4H), 2.35–2.25 (m, 1H), 2.15–2.07 (m, 1H), 1.99 (s, 3H), 1.86–1.77 (m, 1H), 1.73 (d, $J = 1.3$ Hz, 3H), 1.70–1.61 (m, 5H), 1.60–1.52 (m, 2H), 1.47–1.34 (m, 13H), 1.03–0.95 (m, 6H); ^{13}C NMR (151 MHz, methanol- d_4) δ 185.8, 180.9, 174.8, 171.6, 170.8, 169.4, 159.1, 159.1, 148.4, 148.3, 146.6, 142.9, 137.9, 137.3, 135.3, 134.4, 133.9, 132.4, 129.7, 127.2, 118.0, 111.8, 110.9, 109.5, 109.1, 83.0, 81.9, 77.4, 74.4, 72.2, 67.4, 62.0, 57.6, 56.8, 50.2, 49.6, 49.4, 49.3, 49.1, 49.0, 48.9, 48.7, 48.6, 46.5, 46.3, 43.5, 43.4, 38.9, 35.8, 34.6, 33.6, 33.1, 32.8, 32.2, 32.2, 31.4, 30.8, 30.8, 30.7, 30.4, 30.3, 30.3, 30.2, 30.2, 30.1, 27.8, 27.6, 26.9, 23.8, 23.7, 22.9, 22.7, 20.9, 20.3, 19.9, 14.3, 13.7, 12.4.

2.8.13 (4E,6Z,8S,9S,10E,12S,13R,14S,16R)-13-hydroxy-8,14-dimethoxy-4,10,12,16-tetramethyl-19-[(2-[(2-[(2-(1-methyl-2,6-dioxopiperidin-3-yl)-1,3-dioxoisindolin-4-yl)amino]ethoxy)ethoxy]ethyl)amino]-3,20,22-trioxo-2-azabicyclo[16.3.1]docosa-1(21),4,6,10,18-pentaen-9-yl carbamate (nc-3a)

nc-3a was synthesized according to General Procedure D using **6** as starting material (52 mg, 0.10 mmol, 2.0 eq.). The desired

compound **nc-3a** was obtained as a red brown solid (10 mg, 0.01 mmol). Yield: 20%; mp: 123–130°C; R_f : 0.28 (cyclohexane/ethyl acetate (9/1) (v/v)); HRMS-ESI (m/z): $[M + Na]^+$ calcd for $C_{48}H_{62}N_6O_{14}Na^+$: 969.4222, found: 969.4216; 1H NMR (600 MHz, methanol- d_4) δ 7.55–7.49 (m, 1H), 7.13–7.08 (m, 1H), 7.08–7.03 (m, 1H), 7.03–6.98 (m, 1H), 6.98–6.93 (m, 1H), 6.62 (t, $J = 11.4$ Hz, 1H), 5.90–5.84 (m, 1H), 5.63–5.58 (m, 1H), 5.18 (s, 1H), 5.07–5.01 (m, 1H), 4.55–4.47 (m, 1H), 3.80–3.75 (m, 2H), 3.74–3.66 (m, 8H), 3.62–3.52 (m, 1H), 3.51–3.46 (m, 2H), 3.46–3.41 (m, 1H), 3.35 (s, 1H), 3.34–3.32 (m, 3H), 3.30–3.28 (m, 2H), 3.12 (s, 3H), 2.90–2.83 (m, 2H), 2.74–2.64 (m, 3H), 2.35–2.28 (m, 1H), 2.14–2.06 (m, 1H), 2.00 (s, 3H), 1.82–1.75 (m, 1H), 1.73 (s, 3H), 1.66–1.61 (m, 1H), 1.59–1.52 (m, 1H), 1.01–0.94 (m, 6H); ^{13}C NMR (151 MHz, methanol- d_4) δ 211.4, 185.7, 185.6, 181.0, 181.0, 173.7, 171.3, 170.7, 170.7, 170.6, 169.3, 169.3, 159.1, 148.2, 146.8, 142.6, 137.9, 137.2, 135.4, 134.5, 133.8, 133.8, 132.6, 130.9, 129.6, 127.2, 120.6, 118.3, 112.1, 111.3, 110.1, 109.2, 82.9, 82.0, 74.3, 73.4, 71.7, 71.7, 71.7, 71.4, 70.7, 70.6, 70.3, 70.3, 69.8, 69.8, 62.2, 57.5, 57.5, 56.8, 56.8, 56.8, 56.1, 50.9, 50.9, 49.8, 49.6, 49.4, 49.3, 49.1, 49.0, 48.9, 48.7, 48.6, 46.2, 46.2, 43.3, 43.3, 40.8, 40.7, 36.5, 35.7, 34.5, 33.6, 33.1, 32.6, 32.5, 32.1, 31.4, 30.8, 30.8, 30.6, 30.6, 30.5, 30.3, 29.5, 28.1, 27.4, 26.9, 25.6, 23.7, 23.1, 23.1, 22.7, 16.8, 14.3, 13.6, 13.6, 12.4.

3 Results

After analyzing the crystal structure of GM bound to human HSP90 α , we observed that the methoxy group at the 17-position is exposed to the solvent (Figure 1A). Therefore, this position can serve as a suitable exit vector for the assembly of PROTACs. This is further corroborated by the commercially available fluorescent probe FITC-GM, which is commonly used in fluorescence polarization assays to investigate the binding of HSP90 inhibitors to the *N*-terminal ATP binding pocket (Llauger-Bufi et al., 2003). As shown in Figure 1B, the FITC label was introduced via an alkyl linker into the 17-position of GM. The same position was utilized in the conjugation of GM with small molecules, such as estradiol, testosterone, and ferulic acid (Kuduk et al., 1999; Kuduk et al., 2000; Li et al., 2019). Hence, we designed a series of potential PROTACs by attaching a cereblon (CRBN)-recruiting, pomalidomide-derived ligand via various alkyl-

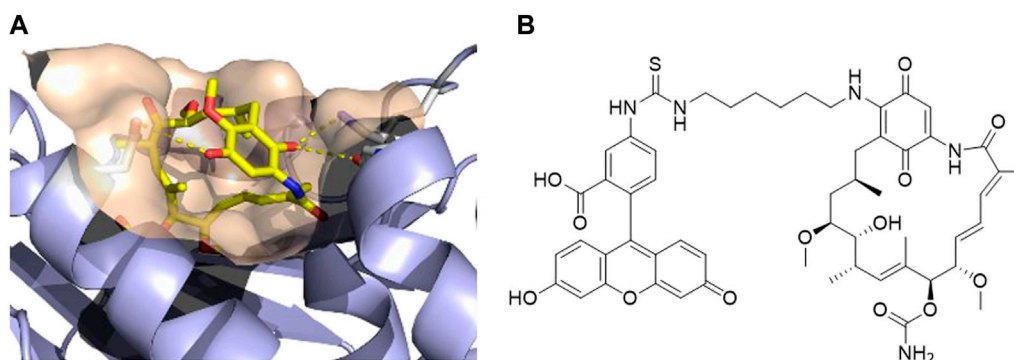


FIGURE 1
(A) Co-crystal structure of human HSP90 α in complex with geldanamycin (PDB ID: 1YET) (Stebbins et al., 1997). (B) Structure of the fluorescent probe FITC-geldanamycin (Llauger-Bufi et al., 2003).

or PEG-based linkers of different chain lengths into the 17-position of GM.

The synthesis of the potential HSP90 degraders is outlined in **Scheme 1**. First, the commercially available diamine linkers were dissolved in ethanol or dichloromethane. The addition of an excess of di-*tert*-butyl dicarbonate to the mixture at 0°C and stirring overnight gave mono-Boc protected diamines **1a–f** (see **Supplementary Materials** for synthetic details). In the next step, 2-(2,6-dioxo-piperidin-3-yl)-4-fluoroisoindoline-1,3-dione and diisopropylethylamine (DIPEA) were dissolved in DMSO. After the addition of the mono-Boc protected linkers, the reaction was heated to 90°C overnight, yielding the pomalidomide-linker derivatives **2a–h**. Finally, the target compounds were obtained by acidolytic Boc-deprotection followed by the substitution reaction of commercially available GM with the free amine of the pomalidomide-linker-NH₂ building blocks. In addition, a non-

degrading control compound was prepared by *N*-methylation of the glutarimide ring (see **Supplementary Materials** for synthetic details). After purification by column chromatography, the final PROTACs shown in **Table 1** were obtained in >95% purity.

At first, a pre-selection was made to determine which PROTAC is capable of degrading HSP90α, β, or both. For this purpose, K562 leukemia cells were treated with respective PROTACs at a fixed concentration (1 μM) and incubated for 24 h. Quantitative simple western immunoassays showed that **3a** with a PEG2-based linker induced the strongest degradation of HSP90α and HSP90β (**Supplementary Figure S1A**, **Supplementary Materials**). Consequently, this PROTAC was selected for further detailed biological experiments. The binding affinity was determined in a fluorescence polarization assay based on the displacement of the fluorescent probe FITC-GM to validate the binding of PROTAC to HSP90. **3a** was found to bind the ATP binding pocket of the HSP90α-

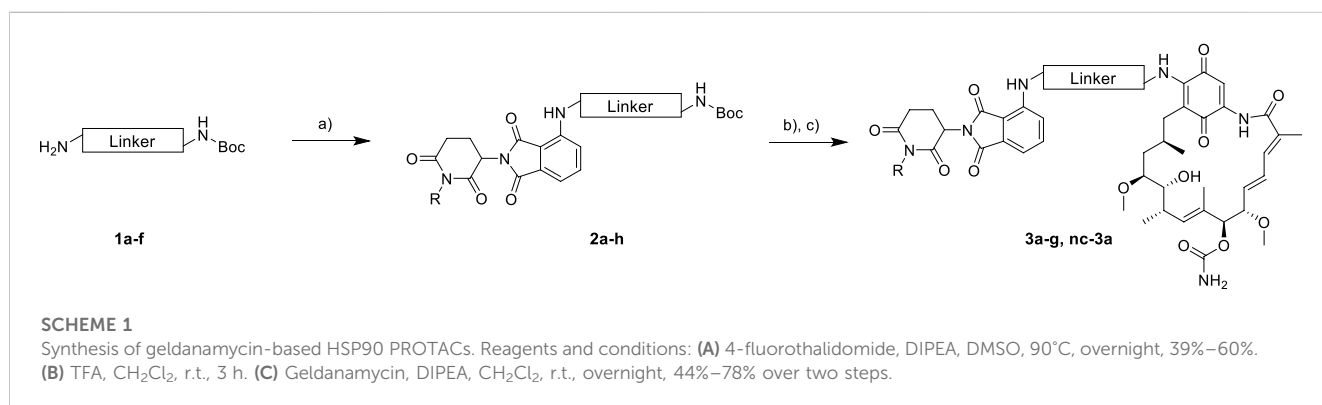


TABLE 1 Overview of the final compounds with their respective linkers.

Compound	Linker	R
3a		H
3b		H
3c		H
3d		H
3e		H
3f		H
3g		H
nc-3a		CH ³

N-terminal domain (NTD), with only slightly lower affinity than GM (Figure 2A). The degradation efficiency was investigated by automated capillary Western blot in a wide concentration range (Figures 2B,C and Supplementary Figures S1B,C; Supplementary Materials) to identify the optimal concentration range. HSP90 α was degraded, especially at low levels of **3a**, in a range between 30 nM and 125 nM. Further quantification revealed a degradation maximum (D_{MAX}) of 57% against HSP90 α (Figure 2B, Supplementary Figure S1B, Supplementary Materials). At higher concentrations from 188 nM, a renewed increase in HSP90 α was seen. Conversely, HSP90 β is more degraded with increasing concentration of **3a**, and a plateau is reached above 188 nM. Further quantification revealed a D_{max} for

HSP90 β of 34% (Figure 2C and Supplementary Figure S1C, Supplementary Materials). Next, we generated HSP90 α/β HiBiT-tagged models using CRISPR/Cas9 gene knock-in in K562 cells (Table 2) (Sinatra et al., 2022). This system allows the quantification of proteins down to endogenous levels. The degradation efficiency of HSP90 α/β after incubation of **3a** was then determined using a sensitive bioluminescent-based assay utilizing the HiBiT-LgBiT complementation technology. The concentration range for the HiBiT assay was picked based on the Western blot data and the incubation time from the kinetic studies, which showed that 24 h treatment of **3a** causes more degradation of HSP90 β than 6 h treatment (Supplementary Figure S1D,

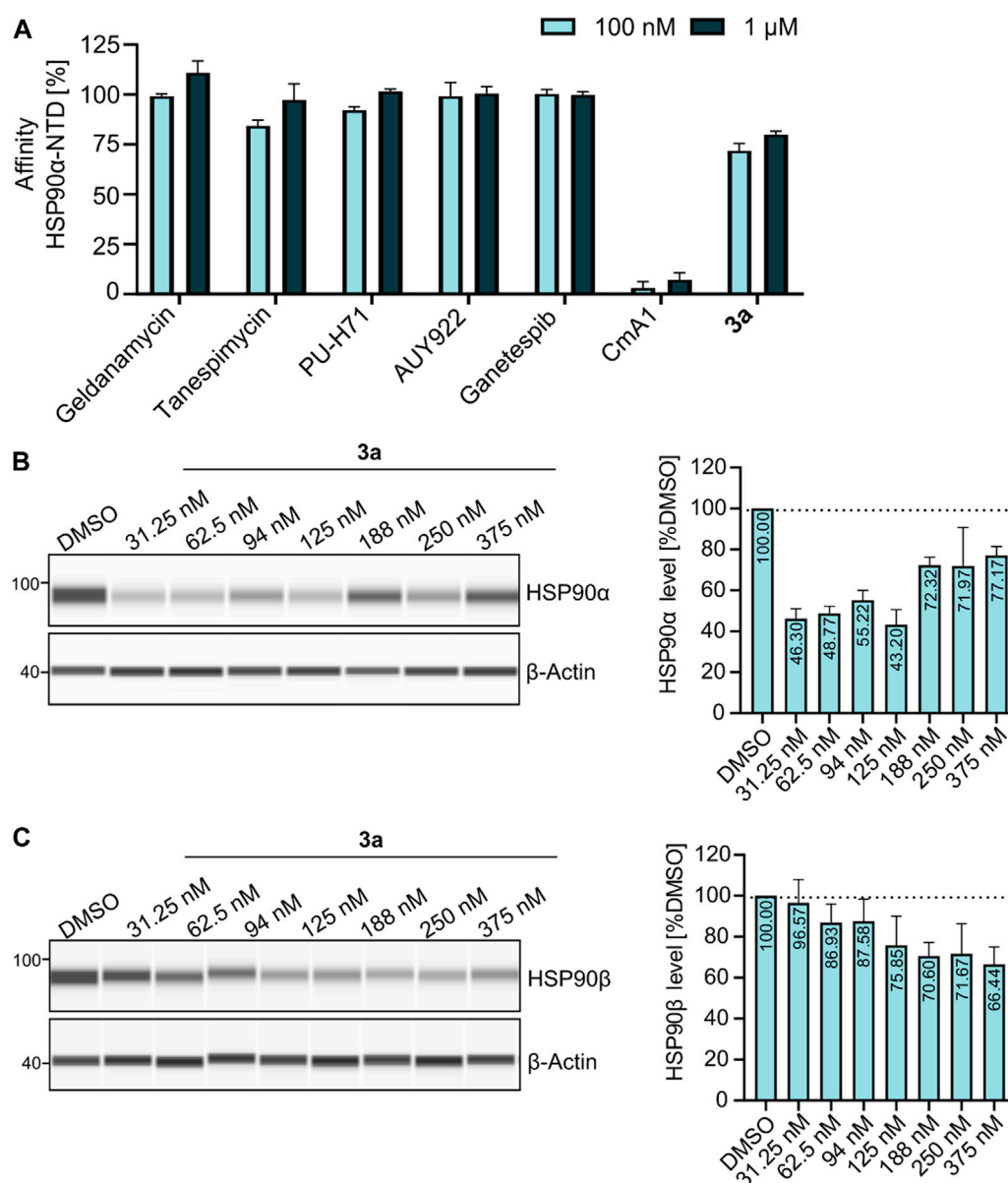


FIGURE 2

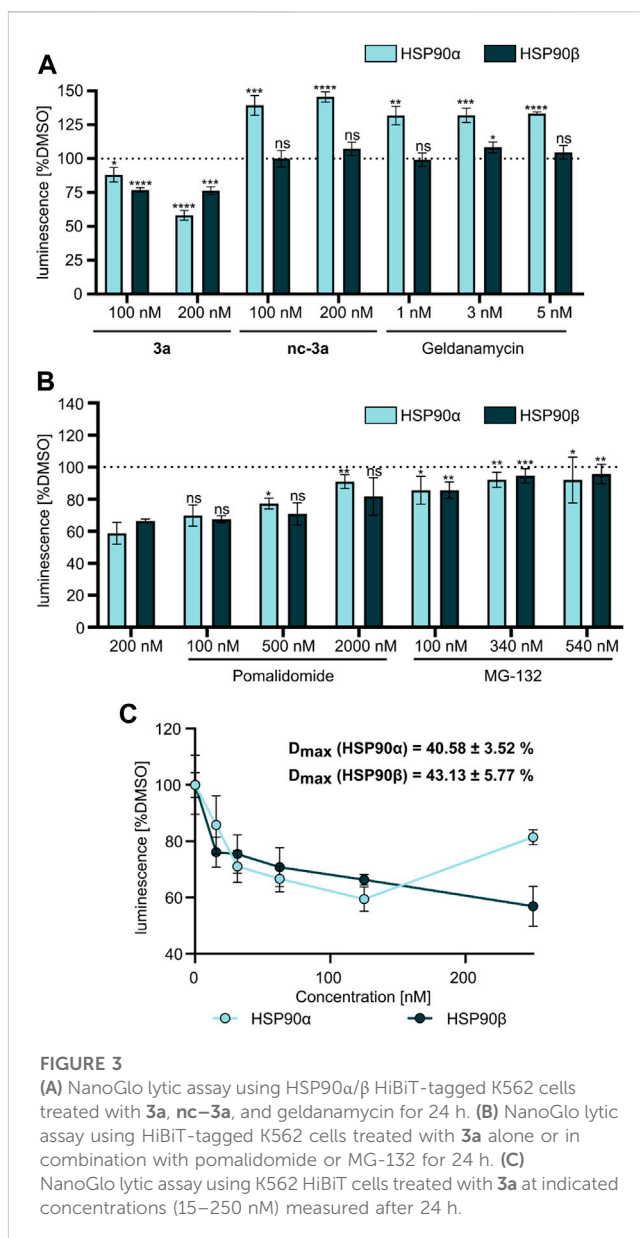
(A) Fluorescence polarization assay showing that **3a** is binding to HSP90 α -NTD as compared to other HSP90-NTD targeting inhibitors (geldanamycin, tanespimycin, PU-H71, AUY922, and ganetespib), whereas HSP90 C-terminal domain targeting inhibitor coumermycin A1 (CmA1) served as a negative control for the assay. Data were normalized using bound FITC-labeled geldanamycin (100 nM) as the negative control (0%), while free spinning or unbound FITC-labeled geldanamycin as the positive control (100%). (B–C) Exemplary JESS run with increasing concentrations of **3a**, showing the degradation of (B) HSP90 α and (C) HSP90 β .

TABLE 2 Trans-activating CRISPR RNA (crRNA) and repair template (single-stranded oligodeoxynucleotide or ssODN) sequences used to generate stable HSP90 α / β -HiBiT tagged knock-in cells. The left and the right homology arms for the respective target genes in the ssODN sequence are represented in upper case, separated by the HiBiT-tag, represented in lower case.

Construct	Sequence
crRNA <i>HSP90AA1</i> (HSP90α)	5'-AGUAGACUAAUCUCUGGCUGGUUUUAGAGC UAUGCU-3'
crRNA <i>HSP90AB1</i> (HSP90β)	5'-UCGCAUGGAAGAAGUCGAUUGUUUAGAGC UAUGCU-3'
tracrRNA	Universal 67mer
ssODN <i>HSP90AA1</i>	5'- TGCCACCCCTTGAAGGAGATGACGACACAT CACGCATGGAAGAAGTAGACgtgagcggctggcggctgt tcaagaagattagcTAATCTCTGGCTGAGGGATGACTTAA CCTGTTACGTA CTCTACAATTCCTC-3'
ssODN <i>HSP90AB1</i>	5'- TCCCCCTCTCGAGGGCGATGAGGATGCGT CTCGCATGGAAGAAGTCGATgtgagcggctggcggctgt tcaagaagattagcTAAGTTAGAAGTTCATAGTTGA AAAAC TTGTGCCCTTGATAGTGTCCCC-3'

Supplementary Materials). The non-degrading PROTAC analog **nc-3a** was used as control, which bears a methyl group at the glutarimide moiety of the pomalidomide. This substitution prevents the pomalidomide derivative from binding to its target cereblon, and therefore, **nc-3a** can only bind to HSP90. In the case of HSP90 β , the use of **nc-3a** led to no degradation, as expected, whereas, interestingly, a significant increase in the expression of the stress-inducible isoform HSP90 α was noticed. The same effect was also observed with the inhibitor GM, which also caused a significant increase in the HSP90 α expression (Figure 3A). Next, K562 cells were pretreated with the CRBN ligand pomalidomide followed by **3a** treatment to demonstrate that binding to CRBN is involved in the reduction of HSP90 protein levels. Increasing the concentration of pomalidomide resulted in a gradual rescue of HSP90 α degradation, while a weak trend in the HSP90 β rescue was noticed (Figure 3B). Furthermore, K562 cells were pre-incubated with the proteasome inhibitor MG-132 and subsequently treated with **3a**. This also resulted in the inhibition of HSP90 α / β degradation (Figure 3B), thereby confirming that the ubiquitin-proteasome system is involved in the observed degradation of HSP90 α / β . Taken together, these results indicate that the degradation of HSP90 is mediated *via* the ubiquitin-proteasome pathway. Using the HSP90-HiBiT system, a D_{\max} of 41% for HSP90 α and 43% for HSP90 β was determined for **3a** (Figure 3C). However, in line with the Western blot results, the HSP90 α level started to increase between 100 nM and 200 nM, compared to HSP90 β . The discrepancy in the degradation of HSP90 α and HSP90 β can be attributed to the fact that HSP90 α is an isoform that is induced under stressful conditions, whereas HSP90 β is a constitutively expressed isoform. At higher concentrations, besides acting as a degrader, **3a** can inhibit both HSP90 isoforms, which can induce cellular stress, resulting in the induction of the stress-inducible isoform HSP90 α , while HSP90 β levels remain unaffected.

In summary, we have designed and synthesized a first-in-class series of GM-based HSP90 degraders. The most promising PROTAC **3a** effectively degraded HSP90 α and HSP90 β levels *via* the ubiquitin–proteasome pathway. Using (endogenous) HSP90-labeled HiBiT–LgBiT complementation assay for the first time, we showed that **3a** was capable of downregulating HSP90, while normal



HSP90 inhibition by GM or the non-degrading control compound **nc-3a** led to a significant upregulation of the stress-inducible isoform HSP90 α . Thus, targeted degradation of HSP90 via GM-based PROTACs might provide an alternative approach to target HSP90-driven diseases.

Data availability statement

The raw data supporting the conclusion of this article will be made available by the authors, without undue reservation.

Author contributions

Conceptualization: SB and FH; data curation: SW, MV, JH, and ND; funding acquisition: AB, SB, and FH; investigation: SW, MV,

JH, and ND; project administration: SB and FH; resources: AB, SB, and FH; supervision: SB and FH; writing—original draft: SW and MV; and writing—review and editing: SB and FH. All authors contributed to the article and approved the submitted version.

Funding

This work was supported by the Open Access Publication Fund of the University of Bonn. This work was funded in part by the Düsseldorf School of Oncology (DSO-Netzwerkverbundes) and Forschungskommission (2021-19) HHU Düsseldorf to SB.

Acknowledgments

SB additionally acknowledges the financial support by Elterninitiative Kinderkrebsklinik e.V. AB acknowledges the financial support from Katharina-Hardt Foundation, Christiane and Claudia Hempel Foundation, and especially Löwenstern e.V. for funding Simple Western system (JESS).

References

- Bhatia, S., Diedrich, D., Frieg, B., Ahlert, H., Stein, S., Bopp, B., et al. (2018). Targeting HSP90 dimerization via the C terminus is effective in imatinib-resistant CML and lacks the heat shock response. *Blood* 3, 307–320. doi:10.1182/blood-2017-10-810986
- Bhatia, S., Spanier, L., Bickel, D., Dienstbier, N., Woloschin, V., Vogt, M., et al. (2022). Development of a first-in-class small-molecule inhibitor of the C-terminal Hsp90 dimerization. *ACS Cent. Sci.* 8, 636–655. doi:10.1021/acscentsci.2c00013
- Biebl, M. M., and Buchner, J. (2019). Structure, function, and regulation of the Hsp90 machinery. *Cold Spring Harb. Perspect. Biol.* 11, a034017. doi:10.1101/cshperspecta.034017
- Birbo, B., Madu, E. E., Madu, C. O., Jain, A., and Lu, Y. (2021). Role of HSP90 in cancer. *Int. J. Mol. Sci.* 19, 10317. doi:10.3390/ijms221910317
- Butler, L. M., Ferraldeschi, R., Armstrong, H. K., Centenera, M. M., and Workman, P. (2015). Maximizing the therapeutic potential of HSP90 inhibitors. *Mol. Cancer Res.* 11, 1445–1451. doi:10.1158/1541-7786.mcr-15-0234
- Csermely, P., Schnaider, T., Soti, C., Prohaszka, Z., and Nardai, G. (1998). The 90-kDa molecular chaperone family. *Pharmacol. Ther.* 79, 129–168. doi:10.1016/s0163-7258(98)00013-8
- Deboer, C., Meulman, P. A., Wnuk, R. J., and Peterson, D. H. (1970). Geldanamycin, a new antibiotic. *J. Antibiot.* 23, 442–447. doi:10.7164/antibiotics.23.442
- Hoter, A., El-Sabban, M. E., and Naim, H. I. (2018). The HSP90 family: Structure, regulation, function, and implications in health and disease. *Int. J. Mol. Sci.* 19, 2560. doi:10.3390/ijms19092560
- Jackson, S. E. (2013). Hsp90: Structure and function. *Top. Curr. Chem.* 328, 155–240. doi:10.1007/128_2012_356
- Jhaveri, K., Ochiana, S. O., Dunphy, M. P. S., Gerecitano, J. F., Corben, A. D., Peter, R. I., et al. (2014). Heat shock protein 90 inhibitors in the treatment of cancer: Current status and future directions. *Expert Opin. Investig. Drugs* 23, 611–628. doi:10.1517/13543784.2014.902442
- Koren, J., and Blagg, B. S. J. (2020). The right tool for the job: An Overview of Hsp90 inhibitors. *Adv. Exp. Med. Biol.* 1243, 135–146. doi:10.1007/978-3-030-40204-4_9
- Kuduk, S. D., Harris, C. R., Zheng, F. F., Sepp-Lorenzino, L., Ouerfelli, Q., Rosen, N., et al. (2000). Synthesis and evaluation of geldanamycin–testosterone hybrids. *Bioorg. Med. Chem. Lett.* 10, 1303–1306. doi:10.1016/s0960-894x(00)00208-0
- Kuduk, S. D., Zheng, F. F., Sepp-Lorenzino, L., Rosen, N., and Danishefsky, S. J. (1999). Synthesis and evaluation of geldanamycin–estradiol hybrids. *Bioorg. Med. Chem. Lett.* 9, 1233–1238. doi:10.1016/s0960-894x(99)00185-7
- Li, Z., Jia, L., Tang, H., Shen, Y., and Shen, C. (2019). Synthesis and biological evaluation of geldanamycin–ferulic acid conjugate as a potent Hsp90 inhibitor. *RSC Adv.* 9, 42509–42515. doi:10.1039/c9ra08665j
- Liu, Q., Tu, G., Hu, Y., Jiang, Q., Liu, J., Lin, S., et al. (2022). Discovery of BP3 as an efficacious proteolysis targeting chimera (PROTAC) degrader of HSP90 for treating breast cancer. *Eur. J. Med. Chem.* 228, 114013. doi:10.1016/j.ejmech.2021.114013
- Llauger-Bufi, L., Felts, S. J., Huezio, H., Rosena, N., and Chiosis, G. (2003). Synthesis of novel fluorescent probes for the molecular chaperone Hsp90. *Bioorg. Med. Chem. Lett.* 13, 3975–3978. doi:10.1016/j.bmcl.2003.08.065
- Mayer, M. P., and Bukau, B. (1999). Molecular chaperones: The busy life of Hsp90. *Curr. Biol.* 9, 322–325. doi:10.1016/s0960-9822(99)80203-6
- Miller, P., DiOrio, C., Moyer, M., Schnur, R. C., Bruskin, A., Cullen, W., et al. (1994). Depletion of the erbB-2 gene product p185 by benzoquinoid ansamycins. *Cancer Res.* 54, 2724–2730.
- Miyata, Y., Nakamoto, H., and Neckers, L. (2013). The therapeutic target Hsp90 and cancer hallmarks. *Curr. Pharm. Des.* 19, 347–365. doi:10.2174/138161213804143725
- Park, H.-K., Yoon, N. G., Lee, J.-E., Hu, S., Yoon, S., Kim, S. Y., et al. (2020). Unleashing the full potential of Hsp90 inhibitors as cancer therapeutics through simultaneous inactivation of Hsp90, Grp94, and TRAP1. *Exp. Mol. Med.* 52, 79–91. doi:10.1038/s12276-019-0360-x
- Schopf, F. H., Biebl, M. M., and Buchner, J. (2017). The HSP90 chaperone machinery. *Nat. Rev. Mol. Cell. Biol.* 18, 345–360. doi:10.1038/nrm.2017.20
- Sinatra, L., Yang, J., Schliehe-Diecks, J., Dienstbier, N., Vogt, M., Gebing, P., et al. (2022). Solid-phase synthesis of cereblon-recruiting selective histone deacetylase 6 degraders (HDAC6 PROTACs) with antileukemic activity. *J. Med. Chem.* 65, 16860–16878. doi:10.1021/acs.jmedchem.2c01659
- Sosic, I., Bricelj, A., and Steinebach, C. (2022). E3 ligase ligand chemistries: From building blocks to protein degraders. *Chem. Soc. Rev.* 51, 3487–3534. doi:10.1039/d2cs00148a
- Stebbins, C. E., Russo, A. A., Schneider, C., Rosen, N., Hartl, F. U., and Pavletich, N. P. (1997). Crystal structure of an hsp90–geldanamycin complex: Targeting of a protein chaperone by an antitumor agent. *Cell* 89, 239–250. doi:10.1016/s0092-8674(00)80203-2
- Talaei, S., Mellatyar, H., Asadi, A., Akbarzadeh, A., Sheervalilou, R., and Zarghami, N. (2019). Spotlight on 17-AAG as an Hsp90 inhibitor for molecular targeted cancer treatment. *Chem. Biol. Drug Des.* 93, 760–786. doi:10.1111/cbdd.13486

Conflict of interest

The authors declare that the research was conducted in the absence of any commercial or financial relationships that could be construed as a potential conflict of interest.

Publisher's note

All claims expressed in this article are solely those of the authors and do not necessarily represent those of their affiliated organizations or those of the publisher, the editors, and the reviewers. Any product that may be evaluated in this article, or claim that may be made by its manufacturer, is not guaranteed or endorsed by the publisher.

Supplementary material

The Supplementary Material for this article can be found online at: <https://www.frontiersin.org/articles/10.3389/fchem.2023.1219883/full#supplementary-material>



OPEN ACCESS

EDITED BY

Yunping Qiu,
Albert Einstein College of Medicine,
United States

REVIEWED BY

Lin Huang,
Shanghai Jiao Tong University, China
Guoliang Ke,
Hunan University, China

*CORRESPONDENCE

Xingyi Ma,
✉ maxy@hit.edu.cn

RECEIVED 21 April 2023

ACCEPTED 22 June 2023

PUBLISHED 06 July 2023

CITATION

Xiao Y, Zhang Z, Yin S and Ma X (2023),
Nanoplasmonic biosensors for
precision medicine.
Front. Chem. 11:1209744.
doi: 10.3389/fchem.2023.1209744

COPYRIGHT

© 2023 Xiao, Zhang, Yin and Ma. This is an open-access article distributed under the terms of the [Creative Commons Attribution License \(CC BY\)](#). The use, distribution or reproduction in other forums is permitted, provided the original author(s) and the copyright owner(s) are credited and that the original publication in this journal is cited, in accordance with accepted academic practice. No use, distribution or reproduction is permitted which does not comply with these terms.

Nanoplasmonic biosensors for precision medicine

Yiran Xiao¹, Zongming Zhang², Shi Yin³ and Xingyi Ma ^{1,2,3*}

¹School of Science, Harbin Institute of Technology, Shenzhen, Guangdong, China, ²Biosen International, Jinan, Shandong, China, ³Briteley Institute of Life Sciences, Yantai, Shandong, China

Nanoplasmonic biosensors have a huge boost for precision medicine, which allows doctors to better understand diseases at the molecular level and to improve the earlier diagnosis and develop treatment programs. Unlike traditional biosensors, nanoplasmonic biosensors meet the global health industry's need for low-cost, rapid and portable aspects, while offering multiplexing, high sensitivity and real-time detection. In this review, we describe the common detection schemes used based on localized plasmon resonance (LSPR) and highlight three sensing classes based on LSPR. Then, we present the recent applications of nanoplasmonic in other sensing methods such as isothermal amplification, CRISPR/Cas systems, lab on a chip and enzyme-linked immunosorbent assay. The advantages of nanoplasmonic-based integrated sensing for multiple methods are discussed. Finally, we review the current applications of nanoplasmonic biosensors in precision medicine, such as DNA mutation, vaccine evaluation and drug delivery. The obstacles faced by nanoplasmonic biosensors and the current countermeasures are discussed.

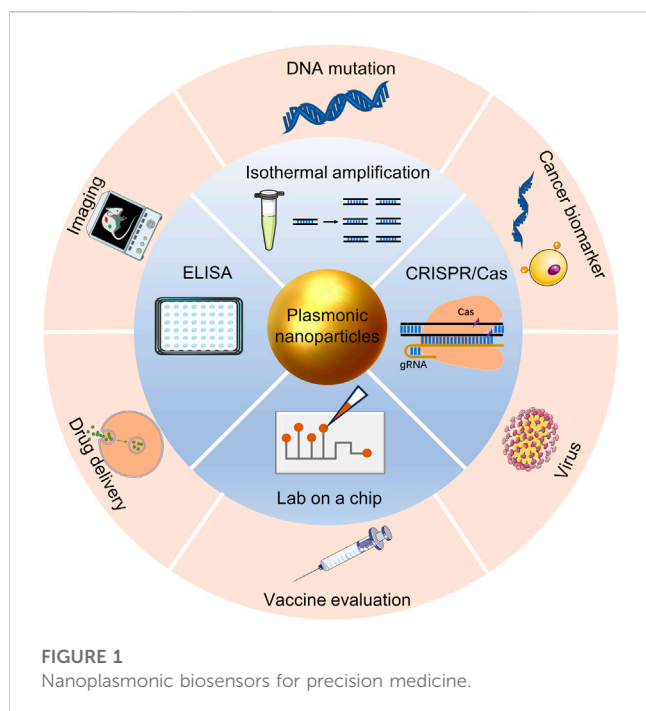
KEYWORDS

nanoplasmonic, biosensors, precision medicine, localized surface plasmon resonance, surface-enhanced Raman scattering, lab on a particle, CRISPR/Cas system, cancer diagnosis

1 Introduction

Precision medicine promises to improve health by considering individual variability in genetics, environment and lifestyle (Denny and Collins, 2021). This new medical model provides disease prevention and early diagnosis for patients by combining the latest molecular genetic detecting technologies. The molecular mechanisms of various diseases are revealed through the characterization of genetic material sequences and their products, for example, mutations in the BRCA1 and BRCA2 genes can cause patients to have an increased risk of developing breast and ovarian cancer (da Costa et al., 2020). Therefore, their detection provides a more in-depth and more comprehensive understanding of disease risk. The appropriate detection tools for the diagnosis of individual specific biological indicators help doctors interpret cases more accurately.

Precise diagnosis is a premise for precise treatment, and to meet its requirements, detection tools need high sensitivity, specificity and rapid analysis. Most importantly, it is possible to track and quantify individual information in living cells. Nanoplasmonic sensing is a high spatial resolution optical technique based on localized surface plasmon resonance (LSPR) (Akkilic et al., 2020). Since the scattered light of LSPR is very sensitive to the surrounding media, the binding of trace biochemical molecules to the nanoparticle (NP) surface leads to changes in the local refractive index. This change is reflected in the availability of label-free and real-time presentation on biological macromolecules (Ma et al., 2015). Thus, plasmonic nanoparticles (PNPs) can be used as light scattering



probes independent of each other for molecular detection as well as for the analysis of other interactions.

The optical properties of PNPs can be modified by changing their composition, shape and size, and different PNPs can be applied to different situations. Nanoparticles of gold (Au), silver (Ag), and copper (Cu) serve as typical plasmonic materials, which have significant light absorption capabilities in the visible region (Wang et al., 2023). Due to the electron oscillation, different shapes and sizes of nanoplasmonic, such as conventional particles, rods shells and stars, will be special optical phenomena derived from their heterogeneous geometry (Sharifi et al., 2019). By studying the dynamic behavior of nanoplasmonic at the single molecule level in real time, it is important for understanding the biological behavior of living cells and tissues and developing novel nanoplasmonic biosensors.

In this review, we describe the principles of nanoplasmonic biosensors, discuss the use of nanoplasmonic biosensors combined other detection tools and research progress in precision medicine in recent years, and provide an outlook on the challenges and future development of nanoplasmonic biosensors (Figure 1).

2 Nanoplasmonic sensing

2.1 Localized surface plasmon resonance

Precision medicine requires real-time, highly sensitive and *in situ* detection of important substances in living organisms, which poses new requirements for biosensing. In recent years, the rapid development of nanotechnology has provided new opportunities. Nanophotonics-based LSPR sensing enables ultramicroscopic structures, and this combination of the unique optical and electronic properties of nanomaterials has led to a wide range of

applications in medical diagnosis and treatment, molecular biology and cell biology (Su et al., 2017).

Both surface plasmon resonance (SPR) and LSPR are caused by the interaction of light with metal surfaces. When light travels through a dielectric (such as air or water) to a metal surface and interacts with certain metals (such as Au), collective oscillations of electrons in the conductive band take place at the metal-dielectric interface (Ma and Sim, 2020). If the light is confined to a very small area of the metal nanoparticle surface, it is called LSPR (Figure 2A). The LSPR is much shorter than the evanescent field of SPR. It shows that LSPR can only perceive distances of a few tens of nanometers compared to a micron perception range of the SPR (Jackman et al., 2017; Bousiakou et al., 2020). In other words, in biosensing, due to the large detection range of SPR, SPR may detect biomolecules that are not bound to the sensor surface, resulting in false positives (Figure 2B). Second, since SPR is difficult to satisfy the plasmon resonance condition, the momentum of light needs to be increased by adaptive optics (such as an optical prism) (Figure 2C) (Chauhan and Kumar Singh, 2021). This presents an engineering challenge and increases the complexity of the application.

2.2 Types of LSPR-based sensors

Most of the LSPR sensing is performed on gold nanoparticles (AuNPs) or silver nanoparticles (AgNPs). AuNPs and AgNPs are widely used because of the strong fluorescence quenching, resonance and oxidation resistance. (Navas and Soni, 2015; Fai and Kumar, 2021; Kurt et al., 2021). Most importantly, they can easily adsorb biomolecules such as proteins, nucleic acids and other substances, but still retain their optical properties. Stable nanoparticles can be used as sensors to monitor light signals that are triggered by biomolecular interactions through LSPR-sensitive devices.

There are various sensing detection principles based on LSPR, among which the typical types are the use of LSPR absorbance as a readout signal, resonance shifts resulting from local variations in refractive index (refractive index sensing) and field-enhanced characteristic optical radiation (for instance, surface-enhanced Raman scattering, SERS) (Su et al., 2017; Ma and Sim, 2020).

Nanoparticles utilizing LSPR absorbance as a readout signal are typically small in size, they are more stable in buffer, and shorten the time to detection. The extinction of nanoparticles is usually monitored by chromaticity change or UV-vis spectroscopy (Borghei and Hosseini, 2019). reported a naked eye reading method for the detection of miRNA derived from CdTe QDs photoinduced LSPR solubilized gold nanoparticles (Figure 3A). CdTe QDs brought effects on the extinction bands of AuNPs, and the association of various concentrations of miR-155 and CdTe QDs produced different extinction bands on AuNPs (Kumar et al., 2021). reported a sensitive fiber optic LSPR-based biosensor for the detection of *Shigella*. They utilized coatings of nanomaterials and molybdenum disulfide (MoS₂) to help excite localized plasma excitations.

According to the Mie theory, the plasma resonance frequency of noble metal nanoparticles frequency is closely related to the refractive index of the surrounding medium (Su et al., 2017). The scattering spectra will be shifted with refractive index changes. Nucleic acid sensing by scattering signal change is much larger

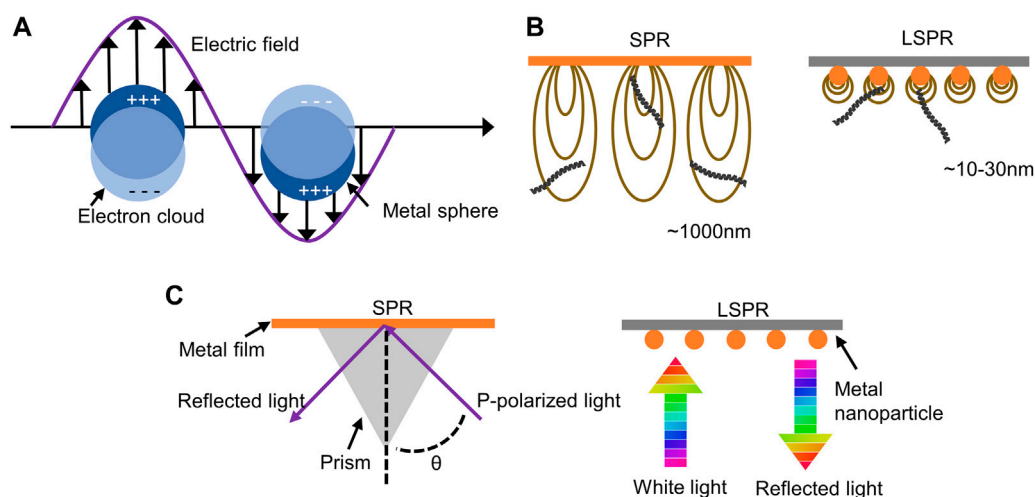


FIGURE 2

Advantages of LSPR technology compared to SPR. (A) Illustration of localized surface plasmon resonance. (B) The perception range in LSPR compared to SPR. (C) Differences between adaptive optics in LSPR and SPR.

than that by absorbance change. The size of AuNPs and AgNPs that are sensed by changes in scattering signal is usually larger than those that are detected by changes in absorbance. This is due to the fact that the nanoparticles need to be sufficiently energetic so that the light scattering signal of each particle can be observed under dark field microscopy (DFM) (Ma et al., 2019). reported a method for rapid identification of point mutations by a single bridge-like AuNP sensor synthesized by DNA guidance (Figure 3B). This high refractive index sensitive biosensor is capable of detecting protein-DNA interactions and detecting single point DNA mutations (Funari et al., 2020). developed an optical microfluidic sensing platform. Gold nanospikes in this platform were fabricated using an electrodeposition method to detect a certain of antibodies specific for SARS-CoV-2 spike protein in human plasma within 30 min. The LSPR wavelength peak shift of gold nanospikes varies with the concentration of antibodies at different targets, which is attributed to local refractive index changes due to antigen-antibody binding. In the same year (Versiani et al., 2020), carried out a nanosensor based on LSPR, which is able to differentiate serologically between dengue and Zika infections. Readings can be obtained in the ELISA-plate spectrophotometer without the need for specific equipment. In recent years, researchers have improved the refractive index sensitivity by improving the size and morphology of gold nanoparticles, and are gradually moving toward miniaturization in terms of experimental setup.

Since Raman analysis cannot detect molecules in ultra-low concentration solutions, surface-enhanced Raman was developed to improve the sensitivity of Raman detection (Zhang et al., 2019) (Balderas-Valadez et al., 2018). When the LSPR spectrum matches the absorption wavelength of the adsorbed molecules, some biosensors can detect Raman signals caused by plasma field enhancement effects, in addition to the signal of the intrinsic LSPR of the plasma. The capability of SERS to enhance the Raman signal by several magnitudes through plasma excitation has led to great scientific interest in knowing the foundation of this improvement (Langer et al., 2020). SERS has been used in

various ways for cancer diagnosis. Many research groups have attempted to use SERS in medical diagnostics to detect cancer biomolecules in blood, saliva and urine (Constantinou et al., 2022). (Moothanchery et al., 2022) group developed a fast single peak Raman technique for the diagnosis of epithelial ovarian cancer by haptoglobin, prognostic biomarkers. Haptoglobin concentration in ovarian cyst fluid can be tested and quantified using an *in vitro* based on Raman spectroscopy. Instead of using plasma nanoparticles to enhance the intrinsically weak Raman signal as described previously, this system is quantified by the pure Raman signal intensity of the TMB. Still, it can be seen that the development of low-cost and portable systems is the direction of SERS device development. However, logical multiplex assays with more than three biomarkers remain challenging (Gong et al., 2015). (Lin et al., 2021a) developed a 0.3 cm diameter nanogel matrix which can enhance and stabilize the Raman signal further. This nanogel substrate can capture SERS nanoparticles corresponding to the proteolytic activity of matrix metalloproteinases (MMP), assisting doctors to obtain low concentrations of target MMP to guide subsequent treatment. And more recently, SERS has been further developed in conjunction with AI for cancer diagnosis (Shin et al., 2023). demonstrated a liquid biopsy method combining AI and SERS to diagnose 6 early cancers through label-free analysis of plasma exosomes (Figure 3C). Recent papers have emphasized the need to continue the performance exploration not only in the structure of metallic nanomaterials, but also to focus on the integration, miniaturization and cost reduction of sensors for practical applications. In this regard, disposable, stand-alone integrated sensing's are perhaps the most practical.

3 Integration of nanoplasmonic with other methods

Local enhancement of optical fields displayed in metallic nanostructures has been used in a large number of research

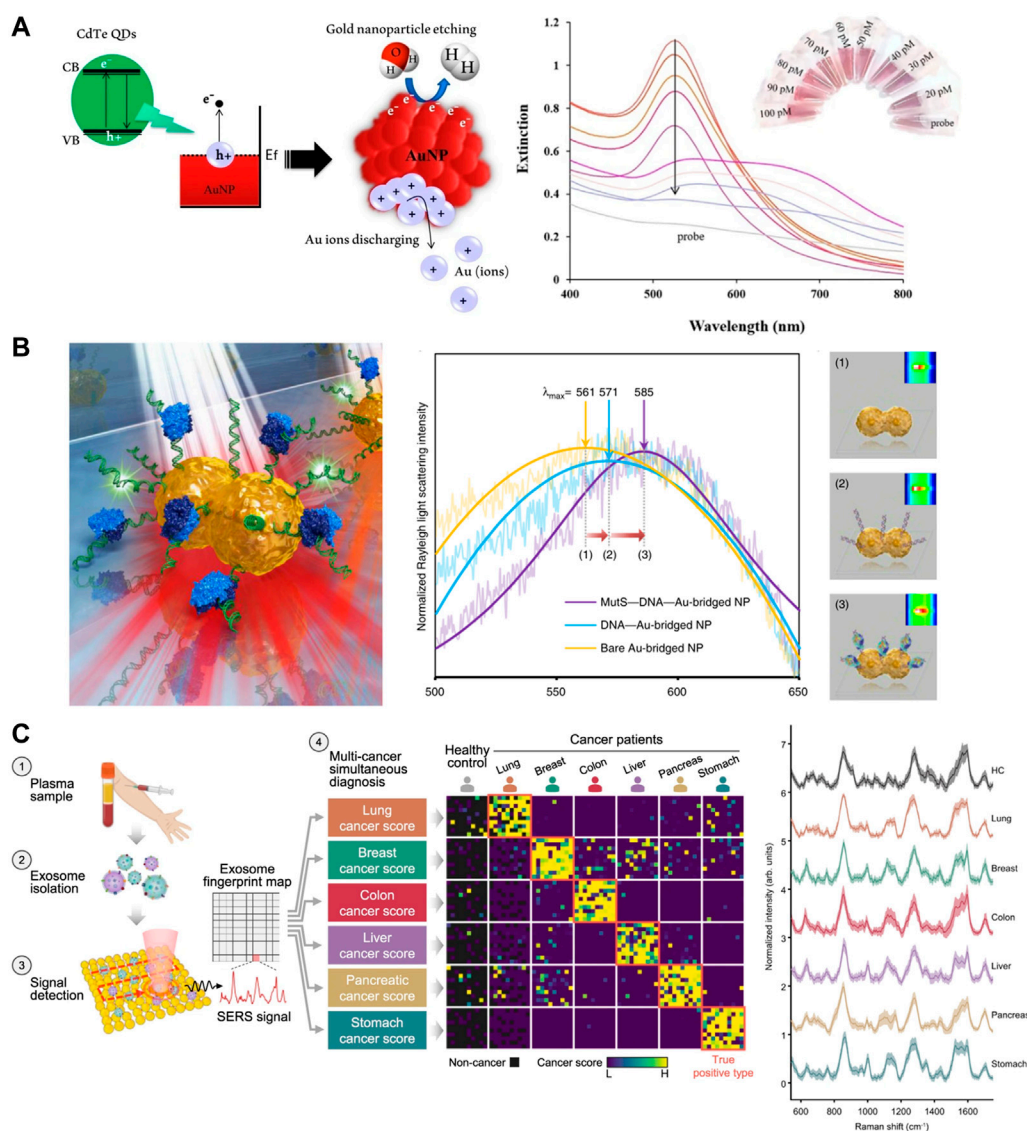


FIGURE 3

SERS sensors in cancer diagnosis. **(A)** Mechanism of dissolution plasmonic AuNPs with water splitting via hot-electron injection by using CdTe QDs photoinduction, and Extinction band of dsDNA-green QDs complex formed with miR-155 target (right). Reproduced with permission from (Borghesi and Hosseini, 2019). **(B)** Schematic illustration of single NP sensing for identifying single point DNA mutations (left) and LSPR λ_{\max} shifts (right). Reproduced with permission from (Ma et al., 2019). **(C)** One test-multi cancer using exosome-SERS-AI (left) and representative SERS spectra (right). Reproduced with permission from (Shin et al., 2023).

areas. In single molecule biosensing, PNP is one of the most researched label-free platforms with high sensitivity (Akkilic et al., 2020). Not only that, with the advancement of nano-plasmas, more biological diagnostics are integrated, greatly facilitating the development of crossover to different subjects.

3.1 Isothermal amplification

Mainstream isothermal amplification techniques include loop-mediated isothermal amplification (LAMP), recombinase polymerase amplification (RPA) and helicase-dependent amplification (HDA), etc (Zhao et al., 2015). The entire

process of isothermal amplification is always at one temperature, and rapid amplification of nucleic acids can be achieved by designing the appropriate specific primers and adding active enzymes. To facilitate and enhance their performance, various nanomaterials have been introduced in isothermal nucleic acid amplification, mainly for reaction enhancers, signal generation/amplification or surface loading carriers (Zhang et al., 2022).

Alafeef et al., 2021 reported a stepwise protocol for rapid and naked-eye molecular diagnosis of COVID-19 with RNA-free extraction nano-colorimetric testing. The binding of ASO, which is specific for the N-gene of SARS-CoV-2, to its target sequence leads to the aggregation of plasmonic AuNPs. Such high-specific

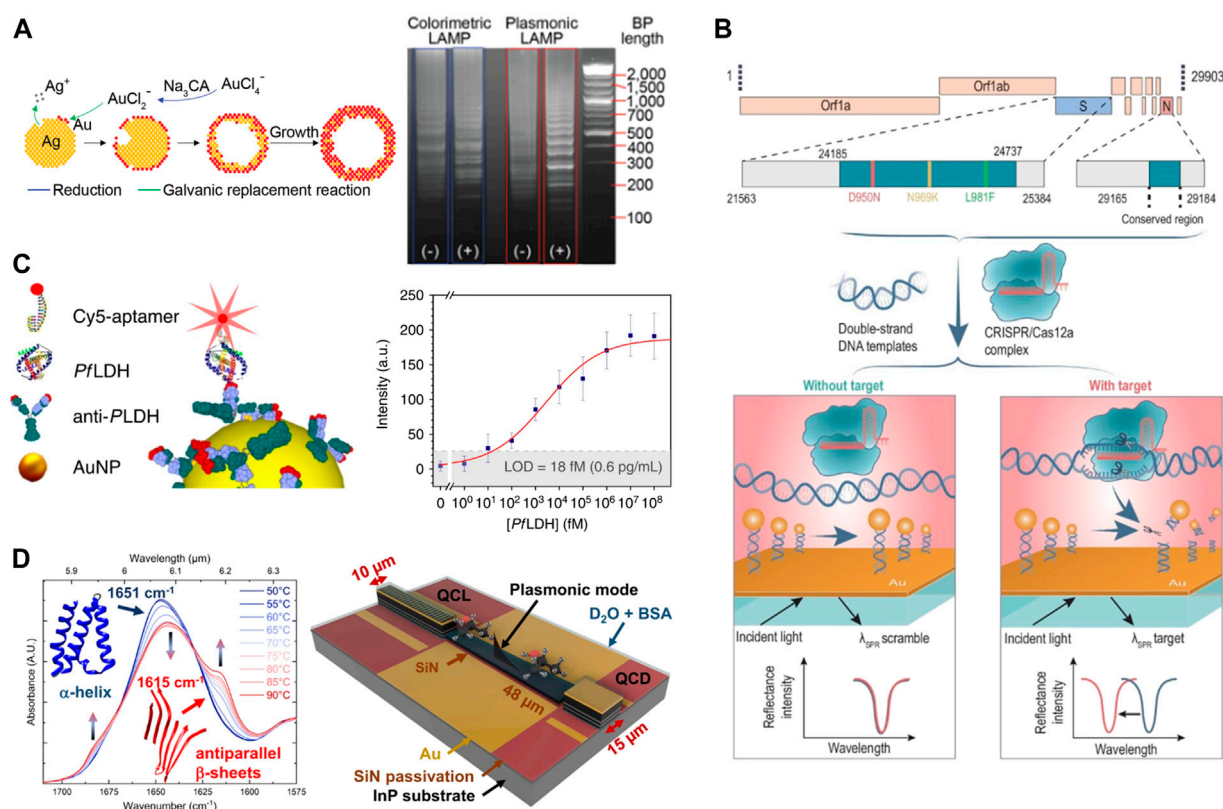


FIGURE 4

Nanoplasmonic integration strategy. (A) Schematic illustration of the Au-Ag shells growth based on galvanic replacement reaction (left) and gel images of plasmonic LAMP (right). Reproduced with permission from (Ye et al., 2022). (B) Scheme of MOPCS. Reproduced with permission from (Chen et al., 2022). (C) Sketch of the Ab-PfLDH-aptamer sandwich scheme (left) and calibration curve of the immunoassay for PfLDH (right). Reproduced with permission from (Minopoli et al., 2020). (D) FTIR spectrum of bovine serum albumin (BSA) (left) and schematic of the QCLD device (right). Reproduced with permission from (Hinkov et al., 2022).

aggregation processes resulted in an alteration of the plasmonic response of the nanoparticles. The following year (Ye et al., 2022), reported a powerful sensing method based on DNA hybridization of LAMP amplicons for nucleic acid detection, called Plasmonic LAMP. Au-Ag alloy nanoshells are developed as plasma sensors and display molecular weight standard patterns in gel images (Figure 4A). However, RPA exhibits a faster detection compared to the 75 min reaction time of the LAMP method described above (Woo et al., 2021). developed a plasmonic isothermal RPA array chip that can accomplish fast multiplex molecular detection. The 3D plasmonic substrates comprising AuNPs on intensive gold nanopillars show highly intensified iso-excited enhanced fluorescence of long RPA products.

The application of nanoplasmonic in isothermal amplification is extensive and effective. Because nanoplasmonic significantly increases the sensitivity to isothermal amplification. But traditional isothermal amplification requires purification of nucleic acids and gel electrophoresis, and although the amplification time is shortened, the results show that it takes a significant amount of time. Researchers expected to take advantage of the fast speed of isothermal amplification by combining it with nanoplasmonic and using fluorescence microscopy for simple

measurements. However, the overflow of nucleic acids during isothermal amplification and the lack of the complex laboratory equipment remain pressing issues.

3.2 CRISPR/Cas system

Recent advances in Clustered Regularly Interspaced Short Palindromic Repeats (CRISPR) and CRISPR associated (Cas) enzymes have exposed the distinctive incidental DNase activities of Cas (Zetsche et al., 2015; Chen et al., 2018). The widely known mechanism of CRISPR technology is the combination of a Cas enzyme with a guide RNA (gRNA). This complex can recognize and cleave site-specific DNA sequences by protospacer-adjacent motif (PAM). The rich variety and diverse properties of CRISPR/Cas systems make them important not only for gene editing, but also show great potential for single-molecule sensing.

In recent years, although different methods for detecting DNA mutations such as SPR and SERS have also been developed, these methods require expensive equipment and do not allow for point of care (POC) applications (Li et al., 2014; Moitra et al., 2022). (Zhou et al., 2022) developed a CRISPR/Cas9-based visual colorimetric

platform that specifically detects all single-base mutations. The visual effect was further enhanced by using HRP-gold nanoparticles complex (hGNPs) and biotin modified probes (Bioprobe) to hybridize with RCA products on top of magnetic separation. Similarly, in the same year (Chen et al., 2022), demonstrated a Methodologies of Photonic CRISPR Sensing (MOPCS) for rapid and specific diagnosis of the Omicron variant of SARS-CoV-2 (Figure 4B). The application of this single-base mutation recognition capability highlights the potential for subspecies precision detection applications, is a novel finding, and may replace PCR in future large-scale virus screening.

Besides that, the nanoplasmonic also plays a role in virus detection by enhancing color development (Li et al., 2019), described a new plasma-based CRISPR Cas12a assay for colorimetric detection of red-blotch infection. This sensing strategy generates a fast and specific colorimetric signal for nucleic acid amplicons by combining Cas12a's unique targeting-induced single-stranded DNase activity with plasma coupling of DNA-functionalized AuNPs. However, in tumor therapy, the direct combination of SHP2 and Elaiophyllin was further confirmed by SPR (Li et al., 2022). This contributes to a rational treatment strategy for ovarian cancer (Tao et al., 2022). synthesized multi-branched gold nanocomposites that not only have significant plasmon resonance in the NIR-II window but also control the delivery of CRISPR-Cas9 for synergistic gene photothermal therapy.

Nanoplasmonic is integrated with CRISPR may be the future trend of development. Firstly, compared to the traditional CRISPR strategy of signal amplification with the help of amplification, which is prone to aerosol contamination, nano-plasma combination achieves enhanced sensitivity under no amplification by a different way. Secondly, traditional nano-plasma sensing usually requires the use of precision and complex instruments, while CRISPR systems have great potential for visualization and *in situ* detection. With high sensitivity and accuracy, the characteristics of both are well complemented. It is exciting to note that in addition to diagnostic advances, the synergy of nanoplasmonic and Cas-led gene editing in therapeutic approaches has also yielded good results, which is driving the development of precision medicine.

3.3 ELISA

Enzyme-linked immunosorbent assay (ELISA) is a comprehensive technique that combines the immune reaction of antigens and antibodies with the efficient catalytic reaction of enzymes. A common feature of nanomaterials is the high specific surface, which has enabled the immobilization of probes and enhanced detection performance through increased sensitivity (Li et al., 2020). Exploring nanoplasmonic strategies for ultrasensitive detection of protein biomarkers appears to be more challenging than DNA detection.

Luan et al., 2020 reported that plasmonic nanoscale structures can be used as “add-on” tags for various bioassays, improving their signal-to-noise ratio and variable range without changing their workflow and reading devices. In the same year (Minopoli et al., 2020), described an isoelectric-enhanced fluorescent immunosensor to detect *Plasmodium falciparum* lactate dehydrogenase (PfLDH), specifically and ultrasensitively in whole blood (Figure 4C). The

biosensor achieves a detection limit of <1 pg/mL (<30 fM) without any sample pretreatment and has very high specificity. Also, (Li et al., 2020), designed a plasma nanoplatform with a catalytic hairpin assembly (CHA) amplification reaction and increased detection limit to 1.0×10^{-4} pg/mL. In the early diagnosis of hepatitis C virus (HCV) infection, the detection sensitivity was much better than that of commercial ELISA kits. And the 83.3% positivity rate of the plasmonic nanoplatform was higher than the 53.3% of ELISA. Plasmonic nanostructures are candidates for extending fluorescence detection limits to femtomolar levels and beyond.

Naked-eye detection, without any optical readout device, is another advantage of this sensing approach, which significantly reduces the cost of analysis and makes it feasible in resource-limited settings. Although the emerging plasmonic ELISA is a candidate diagnostic due to its unprecedented sensitivity and ease of handling, unimodal colorimetric readouts that rely primarily on the monodisperse or aggregated state of Au or Ag nanoparticles remain limited in clinical applications due to uncertain experimental and environmental factors leading to poor accuracy.

The future direction of nanoplasmonic biosensors relies on fast, sensitive, and fielded strategies that are not only useful for achieving single-molecule sensitivity *in vitro* bioassays and revealing molecular interactions within organisms, but are also suitable for large-scale applications. This requires the cross-application of multiple technologies and continuous improvement of detection devices to complement the obvious shortcomings of biosensors, thus showing greater potential for integration, portability, and standardization in nanoplasmonic biosensors. Surprisingly, with the advancement of biocompatible and long-term stable nanomaterials, tracking single target molecules will finally open new paths for precision diagnostics and therapeutics.

3.4 Lab on a chip

A microfluidic chip is one that manipulates or processes small amounts of fluid through channels of tens to hundreds of microns in size, and is also known as a lab on a chip (LOC). In recent years, advances in LOC technology have facilitated advances in miniaturized bioanalytical equipment (Whitesides, 2006; Liao et al., 2018). (Hinkov et al., 2022) presented a fully monolithic integrated mid-IR sensor which integrates all these functions into a miniaturized device (Figure 4D). By combining a laser, interaction zone, and detector on a single chip, and by using plasmonic waveguides that avoid the diffraction limitations typical of conventional chip-scale photonic systems. They achieved a next-generation fast liquid sensor of fingertip size ($<5 \times 5$ mm²) next-generation fast liquid sensor. However, due to the oversimplified nature of most optical architectures, miniaturized systems are usually far less capable than equivalent systems in desktop labs (Tua et al., 2023) developed a compact plasmonic “rainbow” chip for fast and accurate dual-function spectroscopic sensing that can outperform conventional portable spectrometers under certain conditions. The system has the potential to be integrated with smartphones and LOC systems to develop *in situ* analysis applications.

Although LOC has made substantial progress in improving detection throughput, reducing cost and time, and simplifying

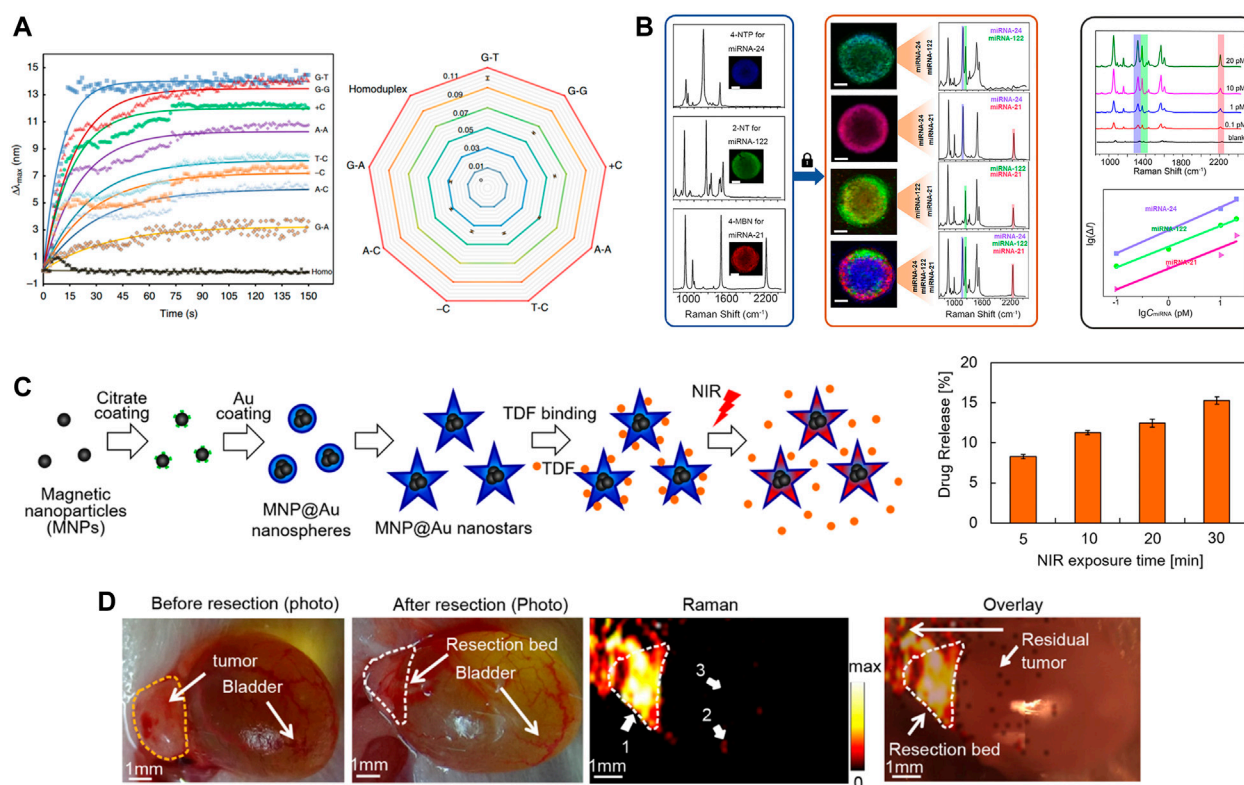


FIGURE 5

(A) Identification of the eight single point mutations. Reproduced with permission from (Ma et al., 2019). (B) Simultaneous detection of multiple miRNA targets. Reproduced with permission from (Lu et al., 2021). (C) Schematic diagram of MNP@Au nanostars synthesis steps, drug binding, and NIR-triggered drug release (left) and drug release after illumination with NIR. Reproduced with permission from (Tomitaka et al., 2020). (D) Intraoperative Raman imaging of residual microtumors after surgical resection of primary tumors. Reproduced with permission from (Qiu et al., 2018).

operation, the improvement of sensitivity in the integration of nanoplasmonic on microfluidic chips is still not negligible (Garcia-Lojo et al., 2020). produced SERS microfluidic chips by integrating plasmonic supercrystals within microfluidic channels for label-free and ultrasensitive detection (Wang et al., 2021). proposed the integration of nanorod arrays on microfluidic chips to be used for rapid and sensitive flow immunoassays of physiologically related macromolecules. Dense arrays of Au nanorods can be easily prepared by one-step oblique angle deposition, thus eliminating the requirement for advanced lithography methods.

4 Applications in precision medicine

4.1 DNA mutation

Genetic diagnosis (such as DNA mutations) for precise prevention and treatment presupposes the ability to accurately determine individual genetic information, thus genetic diagnosis is the foundation of precision medicine (Liu et al., 2020b). Current genetic testing is focused on tumor patients and rare single gene disease testing. In the future, as the expected cost of sequencing decreases from \$500 in 2021 to \$20 in 2030, genetic testing will

become a common test item in diagnosis for more scenarios such as common diseases and medication guidance (Denny and Collins, 2021).

Scientists believe that identifying specific point mutations, deficiencies and nucleic acid modifications is becoming increasingly important as many sequences are confirmed as clinical biomarkers (Koch et al., 2018; Luo et al., 2018). Gene mutations are related to 10%–30% of spontaneous cancers in a diverse range of tissues (Hollstein et al., 2017). Most approaches to identifying gene mutations depend on traditional sequencing (Schmitz et al., 2018). However, these measures are still complex, which limits their use in the clinic. With the development of nanoplasmonic biosensors, researchers expect to solve this challenge through the design of rational plasmonic nanostructures. They effectively improve refractive index sensitivity, making them more sensitive than nano-plasmas of the same size (Ma et al., 2019). reported a rapid method for identifying point mutations through a AuNP sensor (Figure 5A). DNA-directed gold crystals form structurally designed rod-like nanoparticles with bridges based on the structure. Such plasmonic nanoparticles achieve a high refractive index to monitor trace amounts of protein-DNA binding without interference. Similarly (Liu et al., 2020b), proposed to combine active plasmonic nanostructures,

SERS and polymerase chain reaction (PCR) to identify and classify BRAF wild type and V600E mutant genes using statistical tools. Among the four different shapes, the nanostar exhibited the highest SERS activity due to its highly anisotropic structure. Detection limits can be as low as 100 copies of the target DNA sequence.

In addition to high-precision detection of single-base mutations, because nanopores are sensitive to small changes in local refractive index, novel nanopore-based sequencing has been developed to open up new avenues for high-throughput nucleic acid sequencing (Garoli et al., 2019). Arif E. Cetin et al. describe a label-free sequencing platform integrated with a device based on lens-free imaging (Cetin et al., 2018). The spectral shift within the transmission resonance is triggered by a sharp decrease in the nanopore transmission response due to a mismatch in the spectral window upon attachment of streptavidin. This platform can reliably identify targeted deoxyribonucleic acids by monitoring plasma diffraction images. Nanopore sequencing will need to adapt the physical and chemical properties of solid-state nanopores and their compatibility with mass production in future developments to overcome the limitations of current electrical readouts and highlight potential advantages.

4.2 Cancer biomarker diagnosis

The diagnosis of cancer biomarkers is essential to achieve early disease prevention, monitoring progression and effectiveness of therapeutic interventions. Plasmonic sensors have demonstrated a wide array of analytical abilities, ranging from fast colorimetric readings generation to single molecule sensitivity at ultra-low sample volumes, which has allowed them to be increasingly explored in cancer biomarkers (Cathcart and Chen, 2020). A large number of biomarkers have been developed for cancer diagnosis, such as microRNA (miRNA), exosomes, circulating tumor DNA (ctDNA), and circulating tumor cells (CTCs) (Bellassai et al., 2019). For example, the presence of CTCs, whose phenotypic heterogeneity suggests different invasiveness, reveals the stage of cancer and metastasis (Poudineh et al., 2017). Among them, research on miRNA is progressing rapidly. There are now significant advances in miRNA applications of biosensors in breast, lung and colorectal cancers (Borghei and Hosseini, 2019; Wong et al., 2021; Azzouz et al., 2022; Ekiz Kanik et al., 2022). miRNA, a single-stranded non-coding RNA molecule of short length (usually about 18–25 nucleotides in length), have a critical role in apoptosis, proliferation, differentiation, invasion and migration of cells (Kappel and Keller, 2017). Therefore, miRNA is a potential and important indicator to distinguish benign and malignant tumors in certain contexts (Wong et al., 2021). However, miRNA detection is still complicated by the short length and low abundance of miRNAs and the high sequence similarity between members of the same family (D'Agata and Spoto, 2019). In principle, the operation of the plasma sensor relies on sensing changes in the local dielectric environment. miRNAs differing in sequence by only a single base are expected to show almost identical refractive indices, and thus should vary identically in the local dielectric environment.

Lu et al., 2021 reported the use of individual magnetic beads covered with a plasma layer as a multiplexed microreactor (Figure 5B). miRNA will result in the specific capture of the

corresponding SERS reporter GNP being specifically captured into the epithelial layer, which will greatly boost SERS signal caused by the target miRNA. This signal will be mapped by confocal Raman microscopy. This method achieves high precision g-sensing of sub-pM targets with multiplex detection. Subsequently, attomolar-level assays were reported (Ekiz Kanik et al., 2022), developed a highly sensitive and multiplexed digital microarray using plasmonic Au nanorods as markers to enable high-precision two microRNA (miRNA-451a and miRNA-223-3p) detection. Particle tracking addresses the sensitivity constraints of biomarkers in the existence of low-affinity but high-abundance background molecules. Both miRNAs are 10 attomolar and the total incubation time is reduced from 5 h to 35 min.

4.3 Virus detection

The spread and proliferation of viruses has emerged as a risk to global biosecurity, with the current COVID-19 pandemic as an example. SARS-CoV-2 is an RNA virus that can be transmitted not only by inhalation of viral particles in droplets discharged into the air, but also by aerosols carrying viral droplets that can survive for up to 3 h, and by daily personal contact with contaminated surfaces (Lewis, 2020; Prather et al., 2020). The high level of antigenic drift of SARS-CoV-2 may allow the viral pathogen to find additional modes of transmission and become more lethal (Yewdell, 2021). With thousands of different types or variants of SARS-CoV-2 around the world, the variability of the virus underscores the urgent need to design effective vaccines, develop early and rapid diagnostics, and effective antiviral and protective therapies (Yakoubi and Dhafer, 2023). In this regard, the field of nanotechnology can be a bridge between diagnosis and treatment in the fight against COVID-19 and can provide many solutions both outside and inside the host.

Nanoplasmonic have antiviral activity against former coronaviruses and numerous other kinds of viruses, and by studying the photoelectric and chemical characteristics of plasmonic nanoparticles showing surface plasmon resonance effects, they may offer novel perspectives to combat COVID-19 as a drug carrier that is part of an effective therapy for early detection. On the one hand, it is based on the detection of metal surfaces. For example (Huang et al., 2021), developed a method for one-step rapid and direct optical measurement of SARS-CoV-2 virus particles using a spike-in protein-specific nanoplasmonic biosensor, which requires almost no sample preparation. Sensitivity down to 15 vp/mL. On the other hand, the detection is based on self-assembled metal structures. For example (Funari et al., 2020), developed a label-free microfluidic sensing platform with gold nanospikes fabricated by electrodeposition, where the concentration of the target antibody can be associated with the LSPR wavelength peak shift of the gold nanospikes due to local refractive index changes caused by antigen-antibody binding. The platform achieves a limit of detection of ~0.08 ng/mL (~0.5p.m.). To further improve sensitivity (Qiu et al., 2020), used complementary DNA receptor-functionalized two-dimensional gold nanoislands (AuNIs) that can accurately distinguish selected sequences of SARS-CoV-2 by nucleic acid hybridization with a low detection limit of 0.22 p.m.

In terms of external conditions, existing personal protective equipment can actually be an effective measure to restrain the spreading of SARS-CoV-2, but there is no inherent antimicrobial effect can only temporarily protect the user (Yakoubi and Dhafer, 2023). Therefore, the development of anti-viral surface coatings and self-sterilizing surfaces to inactivate SARS-CoV-2 is an issue of high demand. In these respects, several researches have recently been presented highlighting the use of plasma metal nanoparticles in combination with polymers and textiles that play a role in decreasing the survival of viruses on the surface (Toledo et al., 2020; Ulucan-Karnak, 2021). Ordinary masks and N95 respirators usually lack self-sterilizing properties, and water droplets can still remain on the fibers (Zhong et al., 2020). reported plasma photothermal and superhydrophobic coatings on N95 respirators, where the superhydrophobic properties prevent the accumulation of respiratory droplets on the respirator surface and the presence of silver nanoparticles provides additional protection against microorganisms through the disinfection of silver ions. The plasmonic heating can raise the respirator surface temperature to more than 1 °C within 80 min of sunlight exposure. This approach offers greater long-term protection by enhancing the reusability and antimicrobial activity of the mask.

4.4 Evaluation of vaccine effectiveness

Although the COVID-19 vaccine has significantly transformed the struggle against pandemics, for many people there is hesitation to get vaccinated (Fischer et al., 2022). Detection of vaccines (adjuvants and antigens) is therefore critical for basic research in immunotherapy and may influence the extent to which people accommodate vaccines in the future (Shen et al., 2021). Meanwhile, the development of antibody assays is essential for monitoring and epidemic studies, evaluating the level and persistence of antibodies required for immunization, and assessing vaccine effectiveness. There appears to be less information on the evaluation of nanoplasmonic biosensors in terms of vaccine efficacy, probably because of difficulties such as assessing antibody maturation and distinguishing recent from old infections, but this is still very important.

Park et al., 2021 performed LSPR to evaluate real-time adsorption of bovine serum albumin (BSA) on alumina and silica surfaces using alumina- and silica-coated silver nanodiscs arrays with plasmonic properties. A more rigidly adherent BSA protein-based coating was formed on the surface of alumina-based nanomaterials. Helps guide the development of protein coatings for vaccines. Antibody and antibody affinity assays are also among the uses of plasma in vaccines (Liu et al., 2020a). simultaneously detected antibodies to the spindle S1 subunit and SARS-CoV-2 receptor binding domain in human serum and saliva by near-infrared fluorescence amplification of proton Au substrates, and quantified immunoglobulin affinities against coronavirus antigens from SARS-CoV-2, SARS-CoV-1, and common cold virus. The effectiveness and efficacy of most studies involving vaccines against mutant strains is unknown. In addition, the longer COVID-19 persists, the more likely new mutations which assist the virus to escape the immune response will appear. Therefore, further studies on different types of vaccines and cross-vaccination are needed.

4.5 Drug delivery

Due to the expanding imaging and diagnostic capabilities of nanoplasmonic biosensors in response to exterior stimulation, they are already being explored for on-demand drug detection (Asadishad et al., 2021), drug resistance analysis (Ouyang et al., 2023), drug attrition reduction (Lee et al., 2021), drug delivery (Figure 5C) (Tomitaka et al., 2020) and toxicological analysis (Masterson et al., 2021). Due to individual differences, such as medication history, age, and other factors, routine doses of medications may not be appropriate, which may lead to organ damage or other complications for the patient.

The number of nanomedicines currently available to patients is much lower than predicted by the field, in part because of the translational gap between animal and human studies (Mitragotri et al., 2017). Overcoming the patients' heterogeneous biological, microenvironmental and cellular barriers is also achieved through precision therapy (Mitchell et al., 2021). As a result, few of the approved nanomedicines are suggested as preferred treatments and many improve the condition of only a small percentage of patients. However, nanoplasmonic development can begin to optimize drug delivery in a more individualized way and enter the era of precision medicine. sweat usually contains large amounts of biochemical substances (such as electrolytes, metabolites, proteins, and drugs), and can reflect human physiological conditions (Xiao et al., 2023). achieved simultaneous monitoring of vital signs with sweat sampling and acetaminophen drugs. Some treatments with nanoplasmonic are intended to facilitate particle build-up and penetration by reshaping the tumor microenvironment, thereby improving drug efficacy or sensitizing tumors to specific therapies. For example (Chen et al., 2019), used photothermal NPs to improve the infiltration and activity of chimeric antigen receptor (CAR) T cells against solid tumors. Similarly (Wilson et al., 2016), reported that tumor-associated endothelial cells can be manipulated by microRNAs delivered by NPs that alter the tumor vascular system, thereby sensitizing the tumor to conventional cancer therapies.

In conclusion, the introduction of nanoplasmonic developed for specific patient populations can accelerate clinical translation. Advances in genome sequencing and biomarker diagnostics permit suitable choices for the treatment of patient-specific diseases, as mentioned earlier. The development of drug delivery for precision medicine should be a highly customizable process. Such well-designed methods enable the pharmacokinetics of therapeutic agents to be tuned to meet solubility, delivery or biodistribution requirements.

4.6 Molecular imaging

Nanoplasmonic in SPR and LSPR imaging are applied to microscopic imaging techniques in biology and biochemistry to improve key properties of fluorescence imaging (such as sensitivity and resolution) (Ahn et al., 2021). SPR and LSPR imaging are actively used in studies to monitor changes in surface properties with specific markers for functionalized imaging (such as DNA fixation/hybridization processes and antibody-antigen interactions) (Aoki et al., 2019; Zhou et al., 2019). In recent studies, improvements in

nanoplasmonic element-based fluorescence imaging have reached the level of super-resolution imaging, pushing the diffraction limit (Brettin et al., 2019). For example (Son et al., 2019), demonstrated that hyperlocalized near fields with plasmonic nanopore arrays (PNA) studied neuronal mitochondrial transport. Compared to conventional imaging techniques, PNAs create large arrays of hyperlocalized beams and allow sampling and extraction of 3D mitochondrial dynamics in almost real time. The resolution is improved by a factor of 12.7 compared to confocal fluorescence microscopy.

SERS-based nanoprobes are used as competitive imaging agents for *in vitro* and *in vivo* bioimaging due to their ultra-sensitivity, specificity, multiplicity, biocompatibility and photostability (Lin et al., 2021b). In addition to its use in cancer diagnosis, SERS has shown an increasingly important role in cancer treatment. On the one hand, there is growing evidence that SERS has become a new imaging tool to guide surgeons in pinpointing the margins of surgically removed tumors. On the other hand, there has been considerable interest in smart SERS-based therapeutic diagnostic platforms for SERS guidance. For example (Qiu et al., 2018), demonstrated intraoperative detection and eradication of residual microscopic lesions at the surgical margins, which relies on gap-enhanced Raman tags (GERTs)-based Raman imaging (Figure 5D). The low energy laser at 785 nm triggers a Raman signal that can be used for highly sensitive and photostable detection of microtumors. And the thermal effect of microtumor ablation is produced when switching between 808 nm high power lasers. However, since the expression of biomarkers in tumors is heterogeneous, attention should be paid to the issue of multiple molecular imaging of different disease-associated biomarkers.

5 Outlook and conclusion

Nanoplasmonic, a promising nanomaterial, has unique plasmonic and optical properties including absorption, scattering, and field enhancement. In this review, we disclose that nanoplasmonic biosensors have great potential for applications in precision medicine. The first part demonstrates specific sensing based on nanoplasmonic (such as SPR, LSPR and SERS) and analyzes their existing advantages and shortcomings. The second part reports on the integration of multiple technologies, including integrated isothermal amplification, CRISPR/Cas, lab on a chip and ELISA, which help to bridge the gaps of individual technologies. Based on the current situation, POC testing is more appropriate for these sensors than large-scale testing, although micro and portable sensors are appearing. In the final section we discuss the applications and trends of nanoplasmonic biosensors in precision medicine. In particular, the continuing COVID-19 pandemic has highlighted the need to find fast and reliable sensors. In fact, in a sense, virus pandemics and insurmountable cancers are driving the field of precision medicine sensing, especially plasmonic technology, as the requirement for rapid, dependable, mobile and inexpensive sensors becomes essential.

Despite the rapid development of nanoplasmonic with controlled optical properties, their large-scale utilization in medicine is still limited, probably due to i) the relatively high price of precious metals, ii) the low yield of materials with excellent properties, iii) the need for precise fabrication methods

to control different sizes and morphologies, iv) the unclear biological toxicity in physiological environments, and v) the complex matrix identification capabilities in complex matrices. In most applications, the optical properties of nanoplasmonic are strongly dependent on size, morphology, and interactions with each other, so care must be taken to adapt fabrication techniques to achieve well-controlled and highly productive plasmas with various structures. In order to be stable in maintaining optical properties, polymers and inorganic coatings have been successfully used with many effective surface modification strategies that contribute to chemical and biological stability. However, issues such as long-term biocompatibility and specific cytotoxic residues of nanoplasmonic under pathological conditions remain a challenge for clinical practice.

Several issues need to be addressed in nanoplasmonic integration technology. The first is the integration of nanoplasmonic biosensors with sample pre-processing units (such as separation and purification of samples) for eventual practical applications in POC as well as cost-effective sensors for mass production, and more ideally will be used to deliver advanced nanoplasmonic technology from the laboratory to the bedside. As a result, the need for plasma coupled to microfluidics for sample collection and processing will continue to grow. With development it can be expected that mobile and economical biosensors will be available. Secondly, while nanoplasmonic biosensors are very promising for detecting the redox activity of individual proteins or enzymes, they still face challenges due to the limitations of current amplification strategies. The application of nanopores will not only be applied to commercial DNA sequencing, but will also contribute to the study of protein binding and enzyme reaction kinetics.

In conclusion, nanoplasmonic biosensors have achieved significant advances and have shown sufficient sensitivity to observe even single molecular binding events. The quantification of biomolecular interactions at the single molecule level greatly expands the scope of biosensor and analytical techniques and allows access to potential heterogeneity in molecular properties. This heterogeneity may arise from the existence of various species in the sample or the presence of distinct conformations of the same species. However, transforming these encouraging advances in science to biosensor devices for daily life will require additional work on many aspects. The next-generation of nanoplasmonic technology will move out of the laboratory and translate into smart POC diagnostics that will shape the future of precision medicine.

Author contributions

XM conceived the concept of lab-on-a-particle and led the researches of nanoplasmonic biosensors. YX wrote the manuscript with input of ZZ and SY. All authors contributed to the article and approved the submitted version.

Funding

XM acknowledges the grants from Natural Science Foundations of Shenzhen (JCYJ20210324132815037, GXWD20220818171934001) and Guangdong (2022A1515220158), Department of Education of

Guangdong (2021KQNCX276, 2022ZDZX 2065), the Fundamental Research Funds for the Central Universities (Grant No. HIT.OCEF.2022040), Zhujiang Talents Programme (2021QN02Y120), China Postdoctoral Science Foundation (2017M621664), Qianjiang Talents Programme (QJD2002017), Taishan Industrial Experts Programme (TSCY202006001) and the Provincial Science Foundation for the Excellent Youth Scholars (2022HWYQ097).

Conflict of interest

ZZ and XM provide technical support to Biosen International.

References

- Ahn, H., Kim, S., Kim, Y., Kim, S., Choi, J. R., and Kim, K. (2021). Plasmonic sensing, imaging, and stimulation techniques for neuron studies. *Biosens. Bioelectron.* 182, 113150. doi:10.1016/j.bios.2021.113150
- Akkilic, N., Geschwindner, S., and Hook, F. (2020). Single-molecule biosensors: Recent advances and applications. *Biosens. Bioelectron.* 151, 111944. doi:10.1016/j.bios.2019.111944
- Alafeef, M., Moitra, P., Dighe, K., and Pan, D. (2021). RNA-extraction-free nano-amplified colorimetric test for point-of-care clinical diagnosis of COVID-19. *Nat. Protoc.* 16, 3141–3162. doi:10.1038/s41596-021-00546-w
- Aoki, H., Corn, R. M., and Matthews, B. (2019). MicroRNA detection on microsensor arrays by SPR imaging measurements with enzymatic signal enhancement. *Biosens. Bioelectron.* 142, 111565. doi:10.1016/j.bios.2019.111565
- Asadishad, T., Sohrabi, F., Hakimi, M., Ghazimoradi, M. H., Mahinroosta, T., Hamidi, S. M., et al. (2021). Effect of methadone and tramadol opioids on stem cells based on integrated plasmonic-ellipsometry technique. *J. Lasers Med. Sci.* 12, e46. doi:10.34172/jlms.2021.46
- Azzouz, A., Hejji, L., Kim, K. H., Kukkar, D., Souhail, B., Bhardwaj, N., et al. (2022). Advances in surface plasmon resonance-based biosensor technologies for cancer biomarker detection. *Biosens. Bioelectron.* 197, 113767. doi:10.1016/j.bios.2021.113767
- Balderas-Valadez, R. F., Estevez-Espinoza, J. O., Salazar-Kuri, U., Pacholski, C., Mochan, W. L., and Agarwal, V. (2018). Fabrication of ordered tubular porous silicon structures by colloidal lithography and metal assisted chemical etching: SERS performance of 2D porous silicon structures. *Appl. Surf. Sci.* 462, 783–790. doi:10.1016/j.apsusc.2018.08.120
- Bellaisai, N., D'Agata, R., Jungbluth, V., and Spoto, G. (2019). Surface plasmon resonance for biomarker detection: Advances in non-invasive cancer diagnosis. *Front. Chem.* 7, 570. doi:10.3389/fchem.2019.00570
- Borghesi, Y. S., and Hosseini, M. (2019). A new eye dual-readout method for MiRNA detection based on dissolution of gold nanoparticles via LSPR by CdTe QDs photoinduction. *Sci. Rep.* 9, 5453. doi:10.1038/s41598-019-41898-4
- Bousiakou, L. G., Gebavi, H., Mikac, L., Karapetis, S., and Ivanda, M. (2020). Surface enhanced Raman spectroscopy for molecular identification-a review on surface plasmon resonance (SPR) and localised surface plasmon resonance (LSPR) in optical nanobiosensing. *Croat. Chem. acta* 92, 479–494. doi:10.5562/cca3558
- Brettin, A., Abolmaali, F., Blanchette, K. F., McGinnis, C. L., Nesmelov, Y. E., Limberopoulos, N. I., et al. (2019). Enhancement of resolution in microspherical nanoscopy by coupling of fluorescent objects to plasmonic metasurfaces. *Appl. Phys. Lett.* 114, 131101. doi:10.1063/1.5066080
- Cathcart, N., and Chen, J. I. L. (2020). Sensing biomarkers with plasmonics. *Anal. Chem.* 92, 7373–7381. doi:10.1021/acs.analchem.0c00711
- Cetin, A. E., Iyidogan, P., Hayashi, Y., Wallen, M., Vijayan, K., Tu, E., et al. (2018). Plasmonic sensor could enable label-free DNA sequencing. *ACS Sens.* 3, 561–568. doi:10.1021/acssensors.7b00957
- Chauhan, M., and Kumar Singh, V. (2021). Review on recent experimental SPR/LSPR based fiber optic analyte sensors. *Opt. Fiber Technol.* 64, 102580. doi:10.1016/j.yofte.2021.102580
- Chen, J. S., Ma, E., Harrington, L. B., Da Costa, M., Tian, X., Palefsky, J. M., et al. (2018). CRISPR-Cas12a target binding unleashes indiscriminate single-stranded DNase activity. *Science* 360, 436–439. doi:10.1126/science.aar6245
- Chen, Q., Hu, Q., Dukhovlinova, E., Chen, G., Ahn, S., Wang, C., et al. (2019). Photothermal therapy promotes tumor infiltration and antitumor activity of CAR T cells. *Adv. Mater.* 31, 1900192. doi:10.1002/adma.201900192
- Chen, Z., Li, J., Li, T., Fan, T., Meng, C., Li, C., et al. (2022). A CRISPR/Cas12a-empowered surface plasmon resonance platform for rapid and specific diagnosis of the Omicron variant of SARS-CoV-2. *Natl. Sci. Rev.* 9, nwac104. doi:10.1093/nsr/nwac104
- Constantinou, M., Hadjigeorgiou, K., Abalde-Cela, S., and Andreou, C. (2022). Label-free sensing with metal nanostructure-based surface-enhanced Raman spectroscopy for cancer diagnosis. *ACS Appl. Nano Mater.* 5, 12276–12299. doi:10.1021/acsnm.2c02392
- D'Agata, R., and Spoto, G. (2019). Advanced methods for microRNA biosensing: A problem-solving perspective. *Anal. Bioanal. Chem.* 411, 4425–4444. doi:10.1007/s00216-019-01621-8
- Da Costa, E. S. C. S., Cury, N. M., Brotto, D. B., De Araujo, L. F., Rosa, R. C. A., Teixeira, L. A., et al. (2020). Germline variants in DNA repair genes associated with hereditary breast and ovarian cancer syndrome: Analysis of a 21 gene panel in the Brazilian population. *BMC Med. Genomics* 13, 21. doi:10.1186/s12920-019-0652-y
- Denny, J. C., and Collins, F. S. (2021). Precision medicine in 2030-seven ways to transform healthcare. *Cell.* 184, 1415–1419. doi:10.1016/j.cell.2021.01.015
- Ekiz Kanik, F., Celebi, I., Sevenler, D., Tanriverdi, K., Lortlar Ünlü, N., Freedman, J. E., et al. (2022). Attomolar sensitivity microRNA detection using real-time digital microarrays. *Sci. Rep.* 12, 16220. doi:10.1038/s41598-022-19912-z
- Fai, T., and Kumar, P. (2021). Revolution in the synthesis, physio-chemical and biological characterization of gold nanoplatform. *Curr. Pharm. Des.* 27, 2482–2504. doi:10.2174/1381612827666210127121347
- Fischer, I., Rubenstein, D. I., and Levin, S. A. (2022). Vaccination-hesitancy and global warming: Distinct social challenges with similar behavioural solutions. *R. Soc. Open Sci.* 9, 211515. doi:10.1098/rsos.211515
- Funari, R., Chu, K. Y., and Shen, A. Q. (2020). Detection of antibodies against SARS-CoV-2 spike protein by gold nanospikes in an opto-microfluidic chip. *Biosens. Bioelectron.* 169, 112578. doi:10.1016/j.bios.2020.112578
- Garcia-Lojo, D., Gomez-Grana, S., Martin, V. F., Solis, D. M., Taboada, J. M., Perez-Juste, J., et al. (2020). Integrating plasmonic supercrystals in microfluidics for ultrasensitive, label-free, and selective surface-enhanced Raman spectroscopy detection. *ACS Appl. Mater. Interfaces* 12, 46557–46564. doi:10.1021/acsmi.0c13940
- Garoli, D., Yamazaki, H., Maccaferri, N., and Wanunu, M. (2019). Plasmonic nanopores for single-molecule detection and manipulation: Toward sequencing applications. *Nano Lett.* 19, 7553–7562. doi:10.1021/acs.nanolett.9b02759
- Gong, T., Kong, K. V., Goh, D., Olivo, M., and Yong, K. T. (2015). Sensitive surface enhanced Raman scattering multiplexed detection of matrix metalloproteinase 2 and 7 cancer markers. *Biomed. Opt. Express* 6, 2076–2087. doi:10.1364/boe.6.002076
- Hinkov, B., Pilat, F., Lux, L., Souza, P. L., David, M., Schwaighofer, A., et al. (2022). A mid-infrared lab-on-a-chip for dynamic reaction monitoring. *Nat. Commun.* 13, 4753. doi:10.1038/s41467-022-32417-7
- Hollstein, M., Alexandrov, L. B., Wild, C. P., Ardin, M., and Zavadil, J. (2017). Base changes in tumour DNA have the power to reveal the causes and evolution of cancer. *Oncogene* 36, 158–167. doi:10.1038/onc.2016.192
- Huang, L., Ding, L., Zhou, J., Chen, S., Chen, F., Zhao, C., et al. (2021). One-step rapid quantification of SARS-CoV-2 virus particles via low-cost nanoplasmonic sensors in generic microplate reader and point-of-care device. *Biosens. Bioelectron.* 171, 112685. doi:10.1016/j.bios.2020.112685
- Jackman, J. A., Rahim Ferhan, A., and Cho, N. J. (2017). Nanoplasmonic sensors for biointerfacial science. *Chem. Soc. Rev.* 46, 3615–3660. doi:10.1039/c6cs00494f
- Kappel, A., and Keller, A. (2017). miRNA assays in the clinical laboratory: Workflow, detection technologies and automation aspects. *Clin. Chem. Lab. Med.* 55, 636–647. doi:10.1515/cclm-2016-0467

Publisher's note

All claims expressed in this article are solely those of the authors and do not necessarily represent those of their affiliated organizations, or those of the publisher, the editors and the reviewers. Any product that may be evaluated in this article, or claim that may be made by its manufacturer, is not guaranteed or endorsed by the publisher.

- Koch, A., Joosten, S. C., Feng, Z., De Ruijter, T. C., Draht, M. X., Melotte, V., et al. (2018). Analysis of DNA methylation in cancer: Location revisited. *Nat. Rev. Clin. Oncol.* 15, 459–466. doi:10.1038/s41571-018-0004-4
- Kumar, S., Guo, Z., Singh, R., Wang, Q., Zhang, B., Cheng, S., et al. (2021). MoS₂ functionalized multicore fiber probes for selective detection of *Shigella* bacteria based on localized plasmon. *J. Light. Technol.* 39, 4069–4081. doi:10.1109/jlt.2020.3036610
- Kurt, H., Pishva, P., Pehlivan, Z. S., Arsoy, E. G., Saleem, Q., Bayazit, M. K., et al. (2021). Nanoplasmonic biosensors: Theory, structure, design, and review of recent applications. *Anal. Chim. Acta* 1185, 338842. doi:10.1016/j.aca.2021.338842
- Langer, J., Aberasturi, D. J. D., Aizpuru, J., Alvarez-Puebla, R. A., Liz-Marzán, L. M., Baumberg, J. J., et al. (2020). Present and future of surface enhanced Raman scattering. *ACS Nano* 14, 28–117. doi:10.1021/acsnano.9b04224
- Lee, D., Park, D., Kim, I., Lee, S. W., Lee, W., Hwang, K. S., et al. (2021). Plasmonic nanoparticle amyloid corona for screening A β oligomeric aggregate-degrading drugs. *Nat. Commun.* 12, 639. doi:10.1038/s41467-020-20611-4
- Lewis, D. (2020). Is the coronavirus airborne? Experts can't agree. *Nature* 580, 175. doi:10.1038/d41586-020-00974-w
- Li, G. N., Zhao, X. J., Wang, Z., Luo, M. S., Shi, S. N., Yan, D. M., et al. (2022). Elaiophyllin triggers paraptosis and preferentially kills ovarian cancer drug-resistant cells by inducing MAPK hyperactivation. *Signal Transduct. Target Ther.* 7, 317. doi:10.1038/s41392-022-01131-7
- Li, X., Yin, C., Wu, Y., Zhang, Z., Jiang, D., Xiao, D., et al. (2020). Plasmonic nanoplasmon platform for point-of-care testing trace HCV core protein. *Biosens. Bioelectron.* 147, 111488. doi:10.1016/j.bios.2019.111488
- Li, Y., Mansour, H., Wang, T., Poojari, S., and Li, F. (2019). Naked-eye detection of grapevine red-blotch viral infection using a plasmonic CRISPR Cas12a assay. *Anal. Chem.* 91, 11510–11513. doi:10.1021/acs.analchem.9b03545
- Li, Y., Yan, Y., Lei, Y., Zhao, D., Yuan, T., Zhang, D., et al. (2014). Surface plasmon resonance biosensor for label-free and highly sensitive detection of point mutation using polymerization extension reaction. *Colloids Surf. B Biointerfaces* 120, 15–20. doi:10.1016/j.colsurfb.2014.04.007
- Liao, Z., Wang, J., Zhang, P., Zhang, Y., Miao, Y., Gao, S., et al. (2018). Recent advances in microfluidic chip integrated electronic biosensors for multiplexed detection. *Biosens. Bioelectron.* 121, 272–280. doi:10.1016/j.bios.2018.08.061
- Lin, D., Hsieh, C. L., Hsu, K. C., Liao, P. H., Qiu, S., Gong, T., et al. (2021a). Geometrically encoded SERS nanobarcodes for the logical detection of nasopharyngeal carcinoma-related progression biomarkers. *Nat. Commun.* 12, 3430. doi:10.1038/s41467-021-23789-3
- Lin, L., Bi, X., Gu, Y., Wang, F., and Ye, J. (2021b). Surface-enhanced Raman scattering nanotags for bioimaging. *J. Appl. Phys.* 129, 191101. doi:10.1063/5.0047578
- Liu, T., Hsiung, J., Zhao, S., Kost, J., Sreedhar, D., Hanson, C. V., et al. (2020a). Quantification of antibody avidities and accurate detection of SARS-CoV-2 antibodies in serum and saliva on plasmonic substrates. *Nat. Biomed. Eng.* 4, 1188–1196. doi:10.1038/s41551-020-00642-4
- Liu, Y., Lyu, N., Rajendran, V. K., Piper, J., Rodger, A., and Wang, Y. (2020b). Sensitive and direct DNA mutation detection by surface-enhanced Raman spectroscopy using rational designed and tunable plasmonic nanostructures. *Anal. Chem.* 92, 5708–5716. doi:10.1021/acs.analchem.9b04183
- Lu, X., Hu, C., Jia, D., Fan, W., Ren, W., and Liu, C. (2021). Amplification-free and mix-and-read analysis of multiplexed MicroRNAs on a single plasmonic microbead. *Nano Lett.* 21, 6718–6724. doi:10.1021/acs.nanolett.1c02473
- Luan, J., Seth, A., Gupta, R., Wang, Z., Rathi, P., Cao, S., et al. (2020). Ultrabright fluorescent nanoscale labels for the femtomolar detection of analytes with standard bioassays. *Nat. Biomed. Eng.* 4, 518–530. doi:10.1038/s41551-020-0547-4
- Luo, C., Hajkova, P., and Ecker, J. R. (2018). Dynamic DNA methylation: In the right place at the right time. *Science* 361, 1336–1340. doi:10.1126/science.aat6806
- Ma, X., and Sim, S. J. (2020). Single plasmonic nanostructures for biomedical diagnosis. *J. Mater. Chem. B* 8, 6197–6216. doi:10.1039/d0tb00351d
- Ma, X., Song, S., Kim, S., Kwon, M. S., Lee, H., Park, W., et al. (2019). Single gold-bridged nanoprobe for identification of single point DNA mutations. *Nat. Commun.* 10, 836. doi:10.1038/s41467-019-08769-y
- Ma, X., Truong, P. L., Anh, N. H., and Sim, S. J. (2015). Single gold nanoplasmonic sensor for clinical cancer diagnosis based on specific interaction between nucleic acids and protein. *Biosens. Bioelectron.* 67, 59–65. doi:10.1016/j.bios.2014.06.038
- Masterson, A. N., Hati, S., Ren, G., Liyanage, T., Manicke, N. E., Goodpaster, J. V., et al. (2021). Enhancing nonfouling and sensitivity of surface-enhanced Raman scattering substrates for potent drug analysis in blood plasma via fabrication of a flexible plasmonic patch. *Anal. Chem.* 93, 2578–2588. doi:10.1021/acs.analchem.0c04643
- Minopoli, A., Della Ventura, B., Lenyk, B., Gentile, F., Tanner, J. A., Offenhäusser, A., et al. (2020). Ultrasensitive antibody-aptamer plasmonic biosensor for malaria biomarker detection in whole blood. *Nat. Commun.* 11, 6134. doi:10.1038/s41467-020-19755-0
- Mitchell, M. J., Billingsley, M. M., Haley, R. M., Wechsler, M. E., Peppas, N. A., and Langer, R. (2021). Engineering precision nanoparticles for drug delivery. *Nat. Rev. Drug Discov.* 20, 101–124. doi:10.1038/s41573-020-0090-8
- Mitragotri, S., Lammers, T., Bae, Y. H., Schwendeman, S., De Smedt, S., Leroux, J. C., et al. (2017). Drug delivery research for the future: Expanding the nano horizons and beyond. *J. Control Release* 246, 183–184. doi:10.1016/j.jconrel.2017.01.011
- Moitra, P., Chaichi, A., Abid Hasan, S. M., Dighe, K., Alafeef, M., Prasad, A., et al. (2022). Probing the mutation independent interaction of DNA probes with SARS-CoV-2 variants through a combination of surface-enhanced Raman scattering and machine learning. *Biosens. Bioelectron.* 208, 114200. doi:10.1016/j.bios.2022.114200
- Moothanchery, M., Perumal, J., Mahyuddin, A. P., Singh, G., Choolani, M., and Olivo, M. (2022). Rapid and sensitive detection of ovarian cancer biomarker using a portable single peak Raman detection method. *Sci. Rep.* 12, 12459. doi:10.1038/s41598-022-13859-x
- Navas, M. P., and Soni, R. K. (2015). Laser-generated bimetallic Ag-Au and Ag-Cu core-shell nanoparticles for refractive index sensing. *Plasmonics* 10, 681–690. doi:10.1007/s11468-014-9854-5
- Ouyang, Y., Chen, Y., Shang, J., Sun, S., Wang, X., Huan, S., et al. (2023). Virus-like plasmonic nanoprobe for quick analysis of antiviral efficacy and mutation-induced drug resistance. *Anal. Chem.* 95, 5009–5017. doi:10.1021/acs.analchem.2c05464
- Park, H., Ma, G. J., Yoon, B. K., Cho, N. J., and Jackman, J. A. (2021). Comparing protein adsorption onto alumina and silica nanomaterial surfaces: Clues for vaccine adjuvant development. *Langmuir* 37, 1306–1314. doi:10.1021/acs.langmuir.0c03396
- Poudineh, M., Aldridge, P. M., Ahmed, S., Green, B. J., Kermanshah, L., Nguyen, V., et al. (2017). Tracking the dynamics of circulating tumour cell phenotypes using nanoparticle-mediated magnetic ranking. *Nat. Nanotechnol.* 12, 274–281. doi:10.1038/nnano.2016.239
- Prather, K. A., Wang, C. C., and Schooley, R. T. (2020). Reducing transmission of SARS-CoV-2. *Science* 368, 1422–1424. doi:10.1126/science.abc6197
- Qiu, G., Gai, Z., Tao, Y., Schmitt, J., Kullak-Ublick, G. A., and Wang, J. (2020). Dual-functional plasmonic photothermal biosensors for highly accurate severe acute respiratory syndrome coronavirus 2 detection. *ACS Nano* 14, 5268–5277. doi:10.1021/acsnano.0c02439
- Qiu, Y., Zhang, Y., Li, M., Chen, G., Fan, C., Cui, K., et al. (2018). Intraoperative detection and eradication of residual microtumors with gap-enhanced Raman tags. *ACS Nano* 12, 7974–7985. doi:10.1021/acsnano.8b02681
- Schmitz, R., Wright, G. W., Huang, D. W., Johnson, C. A., Phelan, J. D., Wang, J. Q., et al. (2018). Genetics and pathogenesis of diffuse large B-cell lymphoma. *N. Engl. J. Med.* 378, 1396–1407. doi:10.1056/nejmoa1801445
- Sharifi, M., Attar, F., Saboury, A. A., Akhtari, K., Hooshmand, N., Hasan, A., et al. (2019). Plasmonic gold nanoparticles: Optical manipulation, imaging, drug delivery and therapy. *J. Control Release* 311–312, 170–189. doi:10.1016/j.jconrel.2019.08.032
- Shen, S., Huang, Y., Sun, Y., and Zhang, W. (2021). Catechol-driven self-assembly to fabricate highly ordered and SERS-active glycoadjuvant patterns. *J. Mater. Chem. B* 9, 5039–5042. doi:10.1039/d1tb00833a
- Shin, H., Choi, B. H., Shim, O., Kim, J., Park, Y., Cho, S. K., et al. (2023). Single test-based diagnosis of multiple cancer types using Exosome-SERS-AI for early stage cancers. *Nat. Commun.* 14, 1644. doi:10.1038/s41467-023-37403-1
- Son, T., Lee, D., Lee, C., Moon, G., Ha, G. E., Lee, H., et al. (2019). Superlocalized three-dimensional live imaging of mitochondrial dynamics in neurons using plasmonic nanohole arrays. *ACS Nano* 13, 3063–3074. doi:10.1021/acsnano.8b08178
- Su, Y., Peng, T., Xing, F., Li, D., and Fan, C. (2017). Nanoplasmonic biological sensing and imaging. *Acta Chim. Sin. -Chinese Edition-* 75, 1036. doi:10.6023/a17060289
- Tao, W., Cheng, X., Sun, D., Guo, Y., Wang, N., Ruan, J., et al. (2022). Synthesis of multi-branched Au nanocomposites with distinct plasmon resonance in NIR-II window and controlled CRISPR-Cas9 delivery for synergistic gene-photothermal therapy. *Biomaterials* 287, 121621. doi:10.1016/j.biomaterials.2022.121621
- Toledo, G. G., Toledo, V. H., Lanfredi, A. J. C., Escote, M., Champi, A., Silva, M., et al. (2020). Promising nanostructured materials against enveloped virus. *Acad Bras Cienc* 92, 20200718. doi:10.1590/0001-3765202020200718
- Tomitaka, A., Arami, H., Ahmadvand, A., Pala, N., McGoron, A. J., Takemura, Y., et al. (2020). Magneto-plasmonic nanostars for image-guided and NIR-triggered drug delivery. *Sci. Rep.* 10, 10115. doi:10.1038/s41598-020-66706-2
- Tua, D., Liu, R., Yang, W., Zhou, L., Song, H., Ying, L., et al. (2023). Imaging-based intelligent spectrometer on a plasmonic rainbow chip. *Nat. Commun.* 14, 1902. doi:10.1038/s41467-023-37628-0
- Uluhan-Karnak, F. (2021). Nanotechnology-based antimicrobial and antiviral surface coating strategies. *Prosthesis* 3, 25–52. doi:10.3390/prosthesis3010005
- Versiani, A. F., Martins, E. M. N., Andrade, L. M., Cox, L., Pereira, G. C., Barbosa-Stanciolli, E. F., et al. (2020). Nanosensors based on LSPR are able to serologically differentiate dengue from Zika infections. *Sci. Rep.* 10, 11302. doi:10.1038/s41598-020-68357-9
- Wang, Y., Liu, X. L., Zhang, Q. Z., Wang, C., Huang, S. Y., Liu, Y. N., et al. (2023). Stable, cost-effective TiN-based plasmonic nanocomposites with over 99% solar steam generation efficiency. *Adv. Funct. Mater.* 33, 12301. doi:10.1002/adfm.202212301

- Wang, Y., Zhao, J., Zhu, Y., Dong, S., Liu, Y., Sun, Y., et al. (2021). Monolithic integration of nanorod arrays on microfluidic chips for fast and sensitive one-step immunoassays. *Microsyst. Nanoeng.* 7, 65. doi:10.1038/s41378-021-00291-w
- Whitesides, G. M. (2006). The origins and the future of microfluidics. *Nature* 442, 368–373. doi:10.1038/nature05058
- Wilson, R., Espinosa-Diez, C., Kanner, N., Chatterjee, N., Ruhl, R., Hipfinger, C., et al. (2016). MicroRNA regulation of endothelial TREX1 reprograms the tumour microenvironment. *Nat. Commun.* 7, 13597. doi:10.1038/ncomms13597
- Wong, C. L., Loke, S. Y., Lim, H. Q., Balasundaram, G., Chan, P., Chong, B. K., et al. (2021). Circulating microRNA breast cancer biomarker detection in patient sera with surface plasmon resonance imaging biosensor. *J. Biophot.* 14, 202100153. doi:10.1002/jbio.202100153
- Woo, A., Jung, H. S., Kim, D. H., Park, S. G., and Lee, M. Y. (2021). Rapid and sensitive multiplex molecular diagnosis of respiratory pathogens using plasmonic isothermal RPA array chip. *Biosens. Bioelectron.* 182, 113167. doi:10.1016/j.bios.2021.113167
- Xiao, J., Wang, J., Luo, Y., Xu, T., and Zhang, X. (2023). Wearable plasmonic sweat biosensor for acetaminophen drug monitoring. *ACS Sens.* 8, 1766–1773. doi:10.1021/acssensors.3c00063
- Yakoubi, A., and Dhafer, C. E. B. (2023). Advanced plasmonic nanoparticle-based techniques for the prevention, detection, and treatment of current COVID-19. *Plasmonics* 18, 311–347. doi:10.1007/s11468-022-01754-0
- Ye, H., Nowak, C., Liu, Y., Li, Y., Zhang, T., Bleris, L., et al. (2022). Plasmonic LAMP: Improving the detection specificity and sensitivity for SARS-CoV-2 by plasmonic sensing of isothermally amplified nucleic acids. *Small* 18, 2107832. doi:10.1002/smll.202107832
- Yewdell, J. W. (2021). Antigenic drift: Understanding COVID-19. *Immunity* 54, 2681–2687. doi:10.1016/j.immuni.2021.11.016
- Zetsche, B., Gootenberg, J. S., Abudayyeh, O. O., Slaymaker, I. M., Makarova, K. S., Essletzbichler, P., et al. (2015). Cpf1 is a single RNA-guided endonuclease of a class 2 CRISPR-Cas system. *Cell* 163, 759–771. doi:10.1016/j.cell.2015.09.038
- Zhang, C., Belwal, T., Luo, Z., Su, B., and Lin, X. (2022). Application of nanomaterials in isothermal nucleic acid amplification. *Small* 18, 2102711. doi:10.1002/smll.202102711
- Zhang, X., Zhang, H., Yan, S., Zeng, Z., Huang, A., Liu, A., et al. (2019). Organic molecule detection based on SERS in microfluidics. *Sci. Rep.* 9, 17634. doi:10.1038/s41598-019-53478-7
- Zhao, Y., Chen, F., Li, Q., Wang, L., and Fan, C. (2015). Isothermal amplification of nucleic acids. *Chem. Rev.* 115, 12491–12545. doi:10.1021/acs.chemrev.5b00428
- Zhong, H., Zhu, Z., You, P., Lin, J., Cheung, C. F., Lu, V. L., et al. (2020). Plasmonic and superhydrophobic self-decontaminating N95 respirators. *ACS Nano* 14, 8846–8854. doi:10.1021/acsnano.0c03504
- Zhou, J., Zeng, Y., Wang, X., Wu, C., Shao, Y., Gao, B. Z., et al. (2019). The capture of antibodies by antibody-binding proteins for ABO blood typing using SPR imaging-based sensing technology. *Sensors Actuators B Chem.* 304, 127391. doi:10.1016/j.snb.2019.127391
- Zhou, M., Wang, H., Li, C., Yan, C., Qin, P., and Huang, L. (2022). CRISPR/Cas9 mediated triple signal amplification platform for high selective and sensitive detection of single base mutations. *Anal. Chim. Acta* 1230, 340421. doi:10.1016/j.aca.2022.340421



OPEN ACCESS

EDITED BY

Carlos D. S. Brites,
University of Aveiro, Portugal

REVIEWED BY

Barbara Noziere,
Royal Institute of Technology, Sweden
Liu Jiangping,
Kunming University of Science and
Technology, China
Sasho Gligorovski,
Chinese Academy of Sciences (CAS),
China

*CORRESPONDENCE

Ana Kroflič,
✉ ana.kroflic@ki.si
Martin Šala,
✉ martin.sala@ki.si

RECEIVED 24 April 2023

ACCEPTED 05 July 2023

PUBLISHED 14 July 2023

CITATION

Delić A, Skube U, Šala M and Kroflič A
(2023), Kinetics and product
identification of water-dissolved
nitroguaiacol photolysis under
artificial sunlight.
Front. Chem. 11:1211061.
doi: 10.3389/fchem.2023.1211061

COPYRIGHT

© 2023 Delić, Skube, Šala and Kroflič. This
is an open-access article distributed
under the terms of the [Creative
Commons Attribution License \(CC BY\)](#).
The use, distribution or reproduction in
other forums is permitted, provided the
original author(s) and the copyright
owner(s) are credited and that the original
publication in this journal is cited, in
accordance with accepted academic
practice. No use, distribution or
reproduction is permitted which does not
comply with these terms.

Kinetics and product identification of water-dissolved nitroguaiacol photolysis under artificial sunlight

Ajda Delić^{1,2}, Urša Skube², Martin Šala^{2*} and Ana Kroflič^{1,2*}

¹Department of Catalysis and Chemical Reaction Engineering, National Institute of Chemistry, Ljubljana, Slovenia, ²Department of Analytical Chemistry, National Institute of Chemistry, Ljubljana, Slovenia

Nitroguaiacols are typical constituents of biomass-burning emissions, including absorbing aerosols which contribute to climate change. Although they are also harmful to humans and plants, their atmospheric fate and lifetimes are still very speculative. Therefore, in this work, the photolysis kinetics of aqueous-phase 4-nitroguaiacol (4NG) and 5-nitroguaiacol (5NG), and the resulting photo-formed products were investigated under artificial sunlight, observing also the effect of sunlight on the absorption properties of the solutions. We found the photolysis of 5NG slower than that of 4NG, whereas the absorbance in the visible range prevailed in the 5NG solutions at the end of experiments. Although we identified dinitroguaiacol as one of the 4NG photolysis products, which increased light absorption of 4NG-containing solutions, considerably more chromophores formed in the 5NG photolyzed solutions, implying its stronger potential for secondary BrC formation in the atmosphere. In general, denitration, carbon loss, hydroxylation, nitration, and carbon gain were characteristic of 4NG phototransformation, while carbon loss, hydroxylation, and carbon gain were observed in the case of 5NG. The photolysis kinetics was found of the first order at low precursor concentrations (<0.45 mM), resulting in their lifetimes in the order of days (125 and 167 h illumination for 4NG and 5NG, respectively), which suggests long-range transport of the investigated compounds in the atmosphere and proposes their use as biomass-burning aerosol tracer compounds.

KEYWORDS

4-nitroguaiacol, 5-nitroguaiacol, 2-methoxyphenol, secondary organic aerosol, photodegradation, atmospheric aqueous phase, atmospheric lifetime, brown carbon

1 Introduction

Nitrophenols (NPs, Ph-NO₂), i.e., nitrated compounds with the phenolic moiety in their structure, are common constituents of ambient air with known phytotoxic activity. In particular, NPs attract our attention because in the past, they have been linked with remote forest decline (Rippen *et al.*, 1987; Natangelo *et al.*, 1999), while eco- and cytotoxicity of NPs have also been confirmed in more recent studies (Subashchandrabose *et al.*, 2012; Pflieger and Kroflič, 2017; Majewska *et al.*, 2021). Moreover, particulate NPs, such as 4-nitrophenol, 4-nitrocatechol, methylnitrophenols, and nitroguaiacols (NGs) that are closely connected with lignin biomass burning have been shown predominant constituents of atmospheric brown carbon (BrC, near-UV and visible light-absorbing component of atmospheric aerosols), giving atmospheric aerosols typical yellow color and contributing to climate change by light absorption and subsequent warming of the atmosphere (Li *et al.*, 2021).

Airborne NPs can be directly emitted into the atmosphere during various types of fuel combustion or form in secondary atmospheric processes from diverse aromatic precursor

gases (Roger et al., 1992; Harrison et al., 2005; Kroflič et al., 2021). In general, NPs are semi-volatile in their nature, therefore they tend to partition between different atmospheric compartments, *i.e.*, gaseous, liquid and particulate phases (Sakakibara et al., 2022), each of them acting as a specific chemical reactor in which NPs interact with different reactive species and sunlight. Due to the chemical stability of NPs compared with their non-nitrated analogues (Grosjean, 1991), their residence time in the atmosphere is generally considered long, which intuitively implies long traveling distances from their emission sources (Kroflič et al., 2015a). However, especially photostability still needs to be evaluated for specific groups of NP compounds as photolysis kinetics and atmospheric lifetimes of many NPs are missing.

To date, environmentally relevant studies of nitrophenol photolysis have mostly focused on the formation of gaseous nitrous acid (HONO), which is the major source of hydroxyl radicals ($\bullet\text{OH}$) in the troposphere during early morning. Already 2 decades ago, direct photolysis of gas-phase *ortho*-nitrophenol (*o*-NP) was identified as a potential important source of ambient HONO, with possible further implications in the oxidative capacity of the atmosphere (Bejan et al., 2006). Later on, this photolysis reaction has been investigated in many laboratory (Bejan et al., 2007; Wei et al., 2008; Sangwan and Zhu, 2018), theoretical (Vereecken et al., 2016; Guo and Li, 2022), and combined experimental-theoretical studies (Cheng et al., 2009; Nitta et al., 2021), which further suggested that besides nitrogen release, $\bullet\text{OH}$ can also form directly during the photolytic degradation of gaseous *o*-NP, resulting in aromatic nitroso products. In a recent field study conducted in an urban environment, however, a minor role has been attributed to this second pathway (Cheng et al., 2021). Moreover, very recently, photolysis frequency of selected gas-phase NPs has been estimated from ambient measurements, resulting in their atmospheric lifetimes in the order of minutes (Peng et al., 2023), which contradicts the general belief that they are long-lived in the atmosphere. Finally, it has been shown that direct photolysis is the dominant degradation pathway of gas-phase *o*-NP in the atmosphere, corresponding to the photolysis lifetimes in the order of minutes compared with the estimated atmospheric $\bullet\text{OH}$ radical reaction lifetime of 193 h (Sangwan and Zhu, 2016). Although studies on gaseous NPs other than unsubstituted phenols are scarce, knowledge on the photolysis kinetics and mechanisms of environmentally relevant semi-volatile NPs in the atmospheric condensed phase is even poorer.

In contrast to the gas-phase photolysis pathways just described, it has been recently shown that *para*-nitrophenol (*p*-NP) photolyses more rapidly than the other nitrophenol isomers in aqueous solutions and viscous aqueous films, resulting in HONO and/or nitrite build-up similarly to the gas-phase *o*-NP (Barsotti et al., 2017). Chen and co-workers (2005) studied direct photolysis of all three nitrophenol isomers in aqueous solutions. Among the most important pathways leading to the observed photoproducts, excited triplet state formation followed by nitro-nitrite rearrangement was proposed, yielding the corresponding phenoxy radical and NO after the O–NO bond cleavage (Chen et al., 2005). In addition, the second pathway of photoinduced aqueous-phase nitrophenol denitration accompanied by the HONO release has been studied by several authors (Chen et al., 2005; Barsotti et al., 2017; Guo and Li, 2022). Different mechanisms have been proposed for this step, yielding

whole range of speculative reaction products. Alternatively, NO and NO₂ cannot be excluded as the ring-leaving groups as well (Barsotti et al., 2017; Guo and Li, 2022). Despite a few mechanistic studies conducted, to the best of our knowledge photolysis rates and/or atmospheric lifetimes of aqueous-phase NPs when exposed to sunlight are completely unknown.

Although guaiacol (2-methoxyphenol, GUA) is a common model compound for biomass-burning emissions, which is known to produce substantial amounts of toxic NG chromophores under specific conditions in the atmosphere (Kroflič et al., 2021), the photodegradation kinetics of its secondary nitrated products is still speculative in the literature (Iinuma et al., 2007; Lauraguais et al., 2014). Different aqueous-phase transformations of GUA under various atmospherically-relevant conditions have already been studied (Kroflič et al., 2015b; Slikboer et al., 2015; Kroflič et al., 2018; Yang et al., 2021), whereas atmospheric lifetimes of the formed NGs in a sense of their resistance to direct photolysis have never been determined to date. To elucidate the fate of biomass-burning NGs in the atmospheric waters, aqueous solutions containing 4- and 5-nitroguaiacol (4NG and 5NG, respectively) as atmospherically abundant NGs were investigated upon illumination by a solar simulator. The aim of the study was to evaluate the kinetics of their direct photolysis and identify the main products that retain the aromatic moiety at the end of experiment. This further allowed us to determine daytime atmospheric lifetimes due to aqueous-phase photolysis of the investigated compounds and identify characteristic pathways of direct NG phototransformations, which are summarized in schematic representations underlying primary and secondary reaction products formation.

2 Materials and methods

2.1 Materials

For the preparation of standard solutions and reaction mixtures, GUA (2-methoxyphenol, CAS: 90-05-1, Sigma), 4NG (2-methoxy-4-nitrophenol, CAS: 3251-56-7, Sigma Aldrich), 5NG (2-methoxy-5-nitrophenol, CAS: 636-93-1, Fluka), 4,6-dinitroguaiacol (46DNG; 2-methoxy-4,6-dinitrophenol, CAS: 4097-63-6, AKos GmbH) and 4-nitrocatechol (4NC; 4-nitrobenzene-1,2-diol, CAS: 3316-09-4, Fluka) were used. Their formulas and the corresponding deprotonated molecular ions are collected in [Supplementary Table S1](#). The purity of all standard compounds was $\geq 95\%$. Standard solutions and reaction mixtures were prepared with high-purity water (18.2 M Ω -cm) supplied by a Milli-Q water purification system.

Standard buffer solutions (pH 10, pH 7, pH 4, and pH 2) were used for two-point pH meter calibration and to preliminarily define the measurement range for the spectrophotometric determination of pK_a values. Sodium hydroxide (NaOH, 0.01 M and 0.1 M) and/or sulfuric acid (95%, H₂SO₄, 0.09 M) were used for the pH adjustment of standard solutions.

For HPLC analyses, methanol ($\geq 99.9\%$, Chromasolv for HPLC) and formic acid (98%–100%) were used for mobile phase preparation, while methanol ($\geq 99.9\%$, Chromasolv for LC/MS) and formic acid (98%–100%, LiChropur) were used for the unknown products identification with HPLC-MS/MS.

2.2 Methods

2.2.1 Photolysis experiments

Photolysis of diluted solutions containing 4NG and 5NG was carried out in a custom-made reactor using a LOT-Quantum Design Europe solar simulator equipped with an ozone-free Xenon short arc lamp operated at 250 W. Reaction mixtures at different initial concentrations were held at 19 cm from the light source in a round bottom flask made from the borosilicate DURAN® glass, partially submerged in a thermostated water bath at 25°C and thoroughly mixed by rotation. According to the instrument specifications, the produced irradiation was equivalent to approximately one sun (~1000 W/m²). Note at this point that DURAN® glass substantially absorbs light only below about 300 nm, which is comparable with stratospheric ozone, mimicking real atmospheric conditions. Emission spectrum of the Xenon lamp above and under the glass of the reactor flask together with the absorption spectra of 4NG and 5NG is shown in [Supplementary Figure S1](#).

As atmospheric waters are mostly acidic due to the presence of dissolved CO₂ and other water-soluble acids [pH values between 1.95 and 7.74 have been reported according to [Vidović et al. \(2018\)](#)], all starting reaction mixtures had their pH adjusted to around 5 with H₂SO₄. Each reaction mixture was kept under the light for at least 48 h, aliquots were taken at scheduled times and analyzed with a spectrophotometer and HPLC-UV/VIS-(MS/MS). Solution pH at the beginning and at the end of each experiment are given in [Supplementary Table S2](#). Starting solutions of 4NG and 5NG were all stable when kept in dark (an example of blank experiments is shown in [Supplementary Figure S2](#)).

2.2.2 Spectroscopic characterization of standard compounds and reaction mixtures

Spectroscopic measurements were performed with a Perkin Elmer Lambda 25 spectrophotometer with 1 nm resolution. Absorption spectra of standard solutions and reaction mixtures were recorded in the 200–700 nm range.

To assure that ionization of the studied phenolic compounds did not affect absorption spectra of the reaction mixtures, pK_a values of 4NG, 5NG, 46DNG, and GUA were determined prior to the photolysis experiments. Conditions used for the determination of pK_a values are collected in [Supplementary Table S2](#). Small amounts of NaOH were consecutively added to the standard solutions in H₂SO₄ in the investigated pH range. At each step, pH of the solution was measured with a pH meter (Iskra pH meter MA 5736) while moderately stirring and a sample aliquot was taken for the absorbance measurement at the wavelength specified in [Supplementary Table S3](#). The influence of sole NaOH and H₂SO₄ at the maximum added concentration was also tested and no absorbance of the investigated solvents at the characteristic wavelengths for model compounds was observed.

To obtain the pK_a of each compound, the acquired absorbance data were plotted against the corresponding pH and fitted by a model function shown in Eq. 4. The model function was derived from the Henderson–Hasselbalch Eq. 1 and the Beer–Lambert law (Eq. 2) by considering additivity of absorbances and the mass balance equation (Eq. 3; *i* denotes protonated (HA) and deprotonated (A[−]) molecular forms).

$$\text{pH} = \text{pK}_a + \log \frac{A^-}{HA} \quad (1)$$

$$A = \varepsilon \times l \times c = \sum A_i = \sum \varepsilon_i \times l \times c_i \quad (2)$$

$$c_{\text{tot}} = \sum c_i \quad (3)$$

$$A = A_{HA} - \frac{10^{\text{pH}-\text{pK}_a}}{1 + 10^{\text{pH}-\text{pK}_a}} \times (A_{HA} - A_{A^-}) \quad (4)$$

Three fitting parameters were always adjusted to give the lowest chi-square: absorbance of the completely protonated molecule (A_{HA}), absorbance of the completely deprotonated molecule (A_{A[−]}), and pK_a value of the compound.

2.2.3 Product studies

Concentrations of target compounds in the reaction mixture aliquots were determined with a Thermo Scientific Dionex Ultimate 3000 RS UHPLC system equipped with a diode-array detector (DAD) with the adaptation of the previously developed method ([Frka et al., 2016](#)). Sample components were separated on an Atlantis T3 column (3.0 × 150 mm, 3 μm particle size, Waters) at 30°C by an isocratic elution with a mobile phase consisting of methanol/water (50/50, v/v) containing 0.1% (v/v) formic acid at a flow rate of 0.4 mL/min and detected with a DAD detector at 275 nm (GUA), 345 nm (4NG and 5NG), and 380 nm (46DNG). After the separation, unknown peaks were further investigated with a mass spectrometer (4000 QTRAP system Applied Biosystems/MDS Sciex) by using negative polarity electrospray ionization [(−)ESI]. For identification and quantification purposes, MS/MS and selected reaction monitoring (SRM) experiments were performed. The parameters used in SRM experiments are listed in [Supplementary Table S4](#), whereas the declustering potential (DP) and the collision energy (CE) for the MS/MS experiments were selected in a similar range.

2.2.4 Atmospheric lifetimes

To determine the atmospheric lifetime (τ) of a substance, changes in chemical composition with time are important. The collected kinetic data were thus studied and most suitable kinetic laws were determined for each photolysis experiment using the initial rate method.

The atmospheric lifetime is defined as the time in which investigated compound's concentration drops to the 1/e of its original value, therefore it can only be determined for the first-order reactions (Eq. 5) as is shown in Eq. 6.

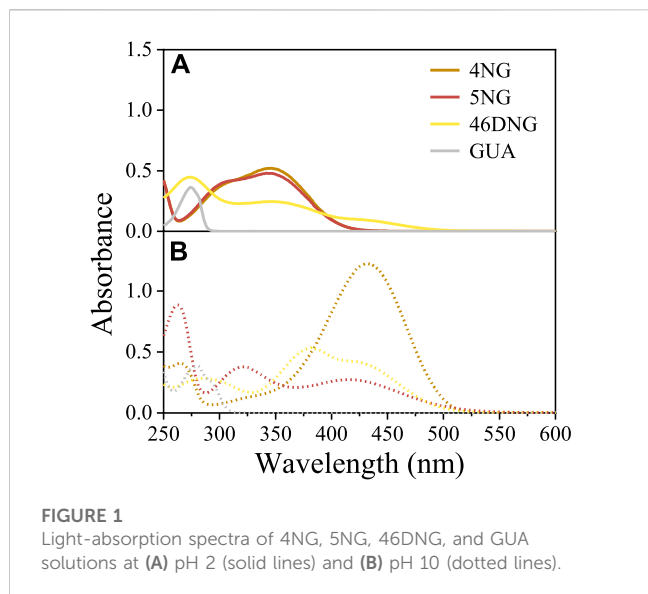
$$\ln \frac{[\text{NG}]}{[\text{NG}]_0} = -k_1 t \quad (5)$$

$$\tau = \frac{1}{k_1} \quad (6)$$

For the zero-order reactions (Eq. 7), universal τ cannot be defined because it always depends on the initial pollutant concentration.

$$[\text{NG}] = [\text{NG}]_0 - k_0 t \quad (7)$$

In the above equations, [NG]₀ and [NG] stand for compound's concentrations at the beginning and at a certain time *t* of the reaction, respectively, and *k*₀ and *k*₁ are the zero-order and first-order kinetic rate constants, respectively.



3 Results and discussion

3.1 Photo-spectroscopic characterization of standard solutions

Guaiacol only absorbs UV light (<310 nm) and the spectrum measured under acidic conditions (Figure 1A) compares very well with those found in the literature (Wang et al., 2019). On the other hand, NGs significantly absorb near UV and visible radiation (<450 nm and <500 nm for mono and dinitro compounds, respectively; Figure 1A), giving them yellow color characteristic of phenolic substances with nitro substituents. As the intensity of the color depends on the number and position of substituent nitro groups on the phenolic ring, especially 46DNG aqueous solutions are intensely yellow to brownish in color.

Nevertheless, besides the intrinsic chemical characteristics responsible for molecule's visible light absorption (i.e., chromophores), pH of the solution can also influence the absorption spectrum of a compound with specific structural features (e.g., possessing acidic phenolic group; Figure 1). Exploring the effect of pH on the spectroscopic behavior of nitroguaiacols indeed gave us important results. At pH 2, typical absorbance bands in the near UV region (280–400 nm) were characteristic of methoxyphenols with one nitro group (i.e., 4NG and 5NG), similar to their analogous *m*-nitrophenol (*m*-NP) and *o*-NP (Bailey-Darland et al., 2023), while 46DNG significantly absorbed light also in the visible part of the spectrum (above 400 nm) (Figure 1A). However, the deprotonated forms of all investigated compounds at pH 10 exhibited significant absorption in the visible range of the spectrum (Figure 1B).

By increasing the solution pH, a shift of characteristic absorbance bands towards longer wavelengths was observed (Figure 1) and a more intense yellow color appeared. Similar has been observed for monosubstituted nitrophenol isomers (Bailey-Darland et al., 2023) and the bathochromic effect of pH on the spectroscopic properties has also been reported for real atmospheric samples with high content of aromatic components (Mo et al., 2017).

TABLE 1 Comparison between the determined pKa values for guaiacols with the literature values of phenols; phenol (PhOH), *m*-nitrophenol (*m*-NP), *p*-nitrophenol (*p*-NP), and 2,4-dinitrophenol (DNP).

Compound	pKa (experimental)	pKa (literature)
4NG	6.4	
5NG	8.5	
46DNG	3.3	
GUA	10.0	9.98 ^a
PhOH		10.0 ^b
<i>m</i> -NP		8.4 ^b
<i>p</i> -NP		7.2 ^b
DNP		4.1 ^b

^aVarekova et al. (2011).

^bDewick (2013).

This is typically attributed to the dissociation of a proton from the acidic phenolic hydroxy group.

From our pH-dependent spectroscopic data shown in Supplementary Figure S3 we were further able to determine pKa values of the investigated compounds, which are lacking in the current literature. The determined pKa values are increasing in the following order: 46DNG < 4NG < 5NG < GUA. To elucidate the influence of the position of the nitro group on the pKa of nitrated GUA, we compare those to the pKa values of a series of nitrophenol isomers in Table 1.

The determined pKa of GUA corresponds very well to the estimated one by use of quantum chemical calculations (Varekova et al., 2011). Moreover, the order of pKa values for phenol and its nitro derivatives is similar to the one we obtained for GUA and NGs. While the pKa values for phenol and GUA as well as for *m*-NP and 5NG pairs are practically the same, somehow lower pKa were determined for 4NG and 46DNG compared to *p*-NP and 2,4-DNP, respectively. These discrepancies can be attributed to the electron-donating methoxy substituent in the case of NGs.

We can conclude from these data that >90% of 4NG and 5NG were in their protonated forms during the photolysis experiments, which were performed at pH 5 as a proxy of atmospheric aqueous phase. On the other hand, the formed 46DNG was mostly ionized during the experiments and could serve as a source of additional hydronium ions in the photolyzed 4NG solutions (see the text below).

3.2 Photolysis experiments

3.2.1 Spectrophotometric analysis

By measuring absorption spectra of the reaction mixtures in a timeframe of 52 h, we observed a decrease in absorbance of the characteristic bands for both 5NG and 4NG (Figure 2), implying original molecule degradation.

From these data it seems that the photolysis of 5NG progressed slower than that of 4NG, which is indicated by a lesser decrease in the characteristic absorbance band at 350 nm (Figure 2). Moreover, the measured spectra also imply that artificial sunlight significantly

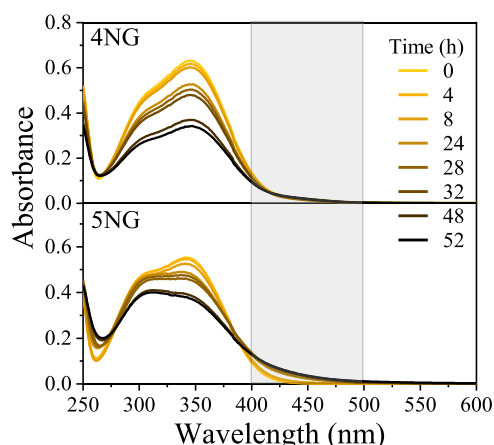


FIGURE 2
Absorption spectra of 4NG and 5NG photolysis solutions at different exposure times.

altered chemical composition of the reaction mixtures, which is evident from the gradual increase of absorbance at longer wavelengths for both investigated compounds that can be attributed to the formation of vis-absorbing products (>400 nm; marked with a gray box in Figure 2). Oppositely to the slower disappearance of the original molecular band, however, these products prevailed in the case of 5NG (there were either chromophores formed in larger amounts or those formed were more intensively colored), which was also confirmed by observing a more intense yellowish-brown color of the reaction mixture at the end of the experiment. Similar absorption spectra, including in the visible range, were characteristic of the simulated atmospheric aerosol from GUA in the high NO_x environment, particularly when formed at high relative humidity (Kroflíč et al., 2021). At the same time, the UVC region of the 5NG-illuminated spectra also changed significantly (note the isosbestic point at 278 nm), whereas the spectra of 4NG practically retained their original shape in this wavelength range. This part of the spectra, however, is not relevant for the atmosphere because the majority of light below 300 nm is absorbed by the stratospheric ozone anyways.

3.2.2 Product studies

For the product analyses we chose the samples at the end of each experiment, which eventually contained the highest quantity of the formed products with retained aromaticity. Based on the comparison of recorded HPLC-DAD spectra with standards, we found that GUA was absent in all reaction mixtures (or was below the detection limit), although it was expected to be formed in analogy with the *p*-NP photolysis (Chen et al., 2005). The obtained chromatographic peaks were further investigated by LC-MS/MS. Detailed product identification was performed by studying MS/MS fragmentation patterns of the identified deprotonated molecular ions $[\text{M} - \text{H}]^-$, which were compared with standards whenever possible. Fragmentation patterns of unknown compounds showed characteristic neutral losses of NO (-30), OH (-17), and sometimes CH_3 (-15) and CO (-28), pointing to the presence of aromatic nitro, methoxy, and hydroxy groups (Frka et al., 2016). Characteristic SRM transitions are collected in Supplementary Table S4.

Total ion chromatogram (TIC) of the 4NG photolyzed solution contains four peaks including five different components with characteristic molecular ions: m/z 213, 212, 184, 154, and 168 (Figure 3A). The identified molecular ions corresponding to peaks A–E were subjected to further fragmentation and the results are shown in Figure 3B.

The fragmentation pattern of m/z 154 eluted at 9 min (Figures 3B–b) shows characteristic neutral losses of NO (m/z 124) and OH (m/z 107), which fit with 4-nitrocatechol (4NC). Peak B found at the retention time (RT) of 14 min (molecular ion m/z 168) agrees with 4NG with the molar mass of 169 Da (Figures 3B–b). The identity of both compounds was confirmed by comparison with the corresponding standard compounds.

Although the compounds with m/z 212 (Figures 3B–c) and 184 (Figures 3B–d) could not be unequivocally confirmed, their structures are tentatively proposed in Supplementary Table S1 (refer here to compounds number 7 and 6, respectively). The fragmentation pattern of m/z 212 possibly points to the presence of the carboxylic group due to the neutral loss characteristic of CO_2 (-44) giving m/z 168 fragment.

The m/z 213 compound elutes at 17 min and from its fragmentation pattern (Figures 3B–e) neutral losses of CH_3 (m/z 154) and NO (m/z 124) could be identified, which agree with 46DNG. The identity of this compound was again additionally confirmed by comparison of its RT and MS/MS spectrum with the standard compound. As the acidity of 46DNG is stronger than that of the precursor molecules, this reaction pathway resulted in the concomitant release of H_3O^+ ions, which was confirmed by a drop in solution pH by the end of experiment (refer here to Supplementary Table S2). Furthermore, the drop in solution pH could also result from the nitrous acid release (Chen et al., 2005), which cannot be confirmed for our experimental system as it was not specifically targeted in this study. Moreover, there seem to be even more products eluted from the column soon after the solvent front (around RT = 5 min, Figure 3A), which we were unable to separate and identify with the applied methods.

The identified photodegradation pathways of water-dissolved 4NG under artificial sunlight are schematically represented in Figure 4.

Poor sensitivity of the HPLC analysis and the lack of ionization of non-nitrated phenols in the ESI source (e.g., GUA and other hydroxylated benzenes) prevented us from unequivocally confirming the photo-induced loss of the nitro group from the aromatic ring (note the dotted arrow for the pathway to GUA formation), which was previously observed by Chen and co-workers (2005) in the case of *p*-NP yielding phenol upon photolysis. On the other hand, intermediate denitration products, such as phenoxy radicals as proposed by other authors might have been formed as well (Barsotti et al., 2017), allowing for a plethora of possible final products, including oligomer formation, which were again out of reach of the implemented methods. Nevertheless, reactive nitrogen species (NO^\bullet , NO_2^\bullet and/or HONO) must have been formed in the solution yielding the detected 46DNG product in the subsequent reaction steps, which could only originate from 4NG as this was the only source of nitrogen added to the solutions. The most likely mechanism leading to the observed dinitrated product is through the formation of an $[\text{aromatic-OH}]^\bullet$ adduct and consequent water elimination to the corresponding phenoxy radical, followed by NO_2^\bullet .

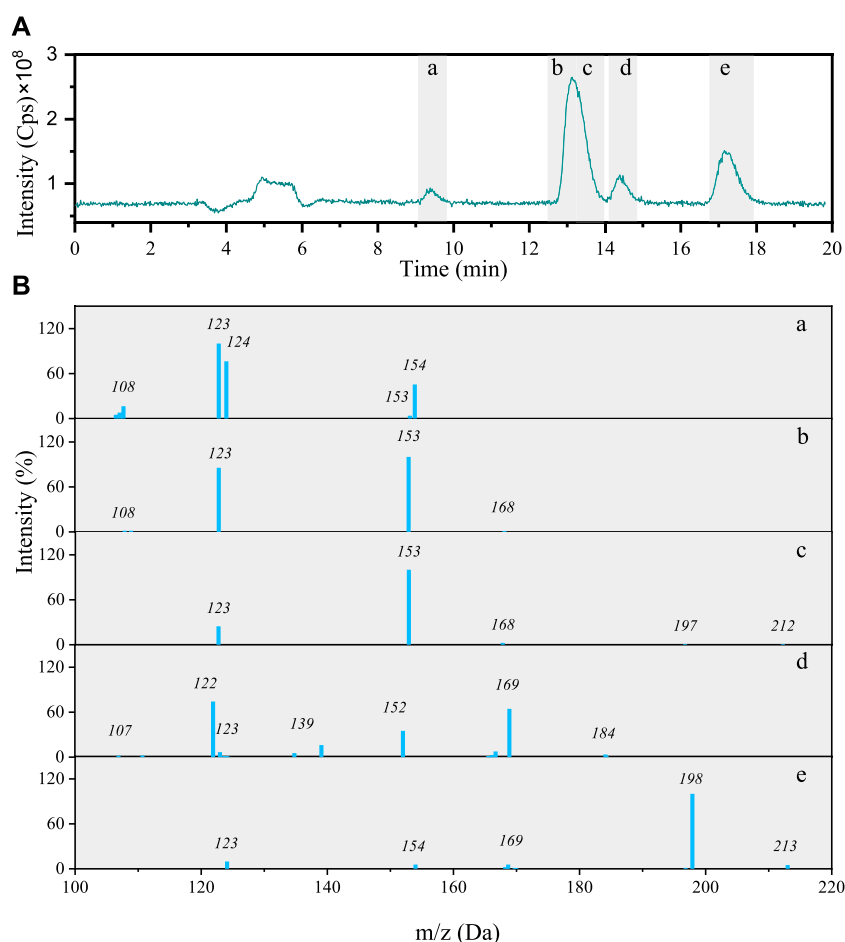


FIGURE 3

(A) Total ion chromatogram after 48 h photolysis of 4NG along with (B) MS/MS spectra of the separated compounds (a–e).

addition to 46DNG (Kroflíč et al., 2018). This, however, further implies that hydroxyl radicals were also present in the solutions and were either a direct product of 4NG photolysis (Guo and Li, 2022) or were secondarily formed in the solution by the photolysis of released reactive nitrogen species, such as NO_2^\bullet and HONO.

Products containing more than one hydroxyl group were also detected, similar to study of Chen and co-workers (Chen et al., 2005), and support the involvement of secondary $^\bullet\text{OH}$ chemistry in the investigated systems (refer here to the Unknown a in Figure 4). Phenolic hydroxylation in aqueous solutions is mostly described by $^\bullet\text{OH}$ addition to the aromatic ring and consecutive reaction with O_2 , followed by HO_2^\bullet elimination to the corresponding hydroxyphenol (Barzaghi and Herrmann, 2002). Moreover, *ipso*-attack of $^\bullet\text{OH}$ to the methoxy group-bearing C-atom followed by methanol elimination is proposed as the main mechanism of catechol formation from guaiacol (Aihara et al., 1993), which has also been observed in a multi-phase system as a proxy for atmospheric aerosols at high relative humidity (Kroflíč et al., 2021). On the other hand, the minor demethoxylation route starting with $^\bullet\text{OH}$ -assisted hydrogen abstraction and resulting in formaldehyde abstraction (Aihara et al., 1993) could lead to the Unknown b formation through the acid-catalyzed 4NG and

formaldehyde condensation followed by the oxidation in an oxygen atmosphere or by HONO. The reaction between formaldehyde and phenol, however, has never been confirmed under mild atmospheric conditions.

Total ion chromatogram of the 5NG photolyzed solution shows only three distinct peaks (Figure 5A) with $[\text{M} - \text{H}]^-$ molecular ions of m/z 198, 154, and 168, which were again subjected to further fragmentation as presented in Figure 5B.

The characteristic of the first chromatographic peak in Figure 5B is the molecular ion m/z 198, its fragmentation yielding fragments at m/z 183 (–15; neutral loss of CH_3), m/z 155 (–28; loss of CO) and m/z 125 (–30; consecutive neutral loss of NO). Its signal, however, is too small to allow for the identification with certainty. A possible molecular structure of the corresponding compound based on the MS/MS data alone is shown in Supplementary Table S1 (compound 8).

The peak at 9 min on the other hand corresponds to the same species also found in the 4NG sample, i.e., 4NC (compare fragmentation patterns in Figures 3A-a; Figures 5B-b). The peak at RT 11.7 min agrees with 5NG (Figures 5B-c), its fragmentation showing neutral losses of CH_3 (m/z 153) and NO (m/z 123), which was also confirmed by comparison with the standard compound.

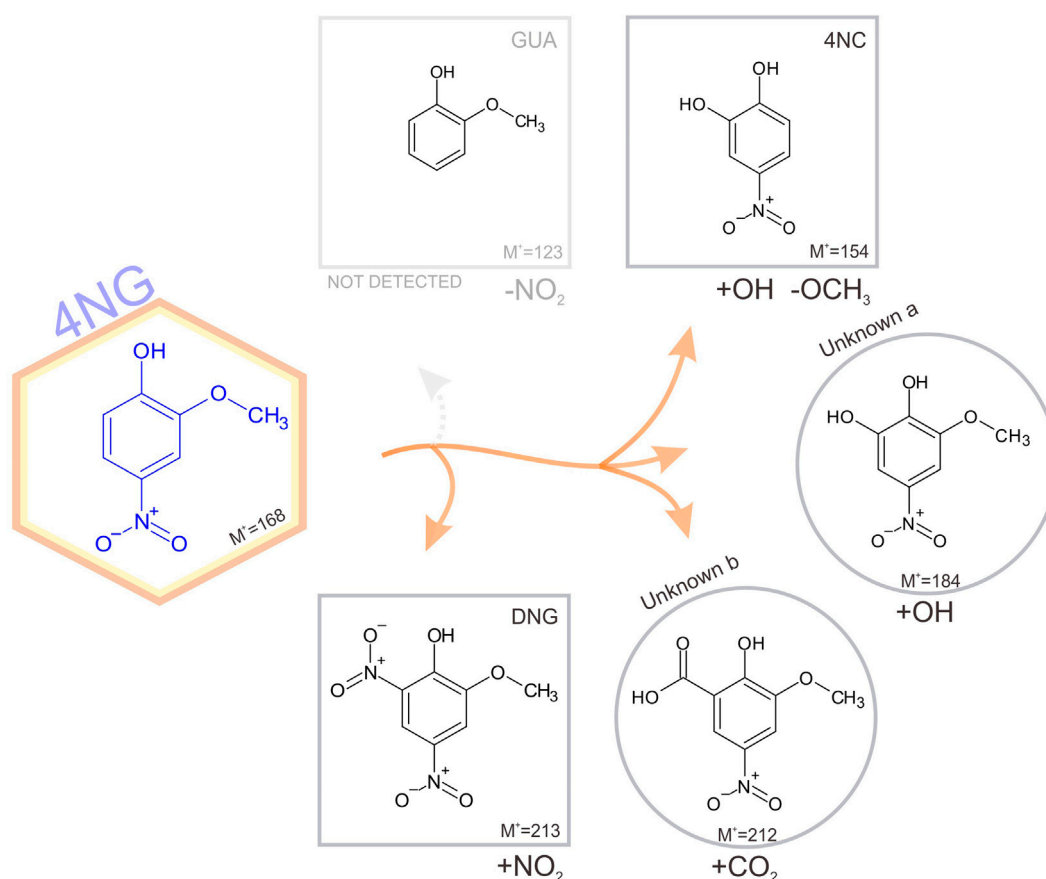


FIGURE 4

Schematic representation of identified pathways of 4NG photo-catalyzed transformations in an illuminated aqueous solution. Products shown in square boxes were confirmed by comparison with commercial standards; in round boxes, tentative structures are proposed based on the measured fragmentation patterns. Note, GUA (or its non-nitrated derivatives) were not detected, but must have been formed. The corresponding mechanisms are proposed in the text.

Schematic representation of 5NG photodegradation pathways is shown in Figure 6.

Lack of evidence for the possible 5NG denitration is in line with the previous study on *m*-NP photolysis (Chen et al., 2005). Again, the demethoxylated product (4NC) was observed, which must have involved the $\bullet\text{OH}$ chemistry as explained above. Moreover, similar to the industrial acid-catalyzed synthesis of phenol-formaldehyde resins (Lu et al., 2004), the Unknown c could be formed as a precursor to the carboxylated analogue observed in the 4NG solutions, stopping at this stage due to lower concentrations of oxidant species in the solution (e.g., HONO) as a result of slower photolysis rate. As already mentioned, this is only speculation and would need to be confirmed under atmospheric conditions.

As we previously showed that the absorption spectra of 5NG photolysed solutions changed more significantly than those of 4NG photolysed solutions, we can now attribute those changes to a small number of photoproducts with retained aromaticity and nitro substitution, or oligomer formation. On the other hand, in the case of 4NG photolysis, the more numerous products obviously possess comparable spectroscopic properties to the parent compound (or do not absorb in the investigated range at all), resulting in very limited changes in the absorption spectrum after the photolysis, except for the

altered peak intensity. This agrees with the proposed formation of non-nitrated phenols, which could not be unequivocally confirmed in our study, but must have been formed based on the evidence given above.

3.3 Kinetics

Figure 7 shows concentration changes during the photolysis of 4NG and 5NG containing aqueous solutions with time. At the same initial concentration, 5NG concentration decreased slower than the concentration of 4NG, which agrees with the spectroscopic data presented above and also with the studies performed on the nitrophenol isomers (Chen et al., 2005).

Most experimental data could be well described by linear functions ($r^2 \geq 0.97$), which means that during the photolysis experiments, changing reactant concentration had no effect on the reaction rate itself. Similarly, zero-order photolysis kinetics was also observed in the case of nitrophenol photolysis (Chen et al., 2005). In one specific case, however, the reaction rate increased after some time (0.45 mM 4NG solution; Figure 7), probably due to the formation of photosensitizer products (Felber et al., 2021), which are out of scope of this study.

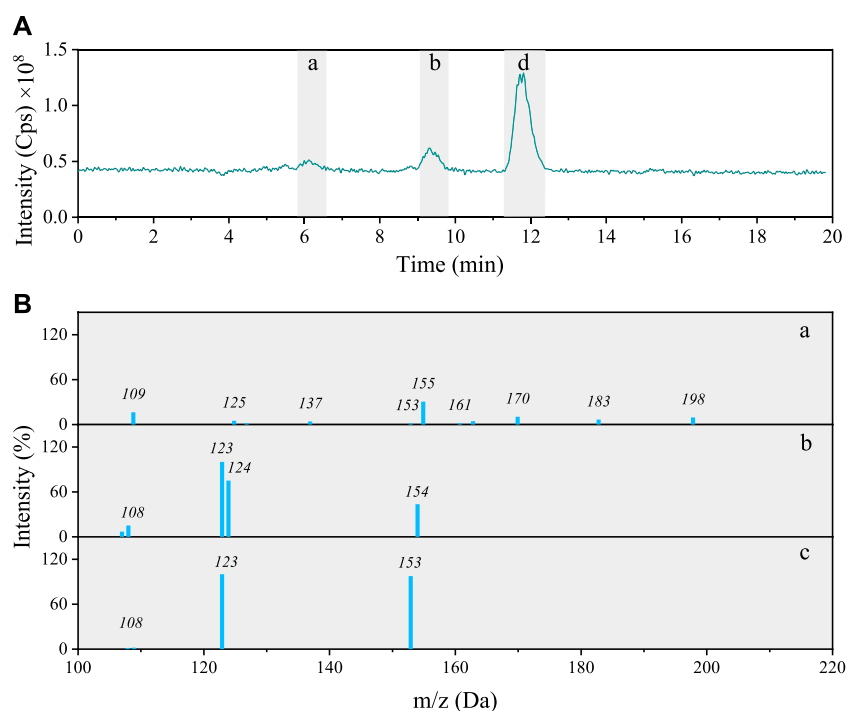


FIGURE 5

(A) Total ion chromatogram after 48 h photolysis of 5NG along with (B) MS/MS spectra of the separated compounds (a–c).

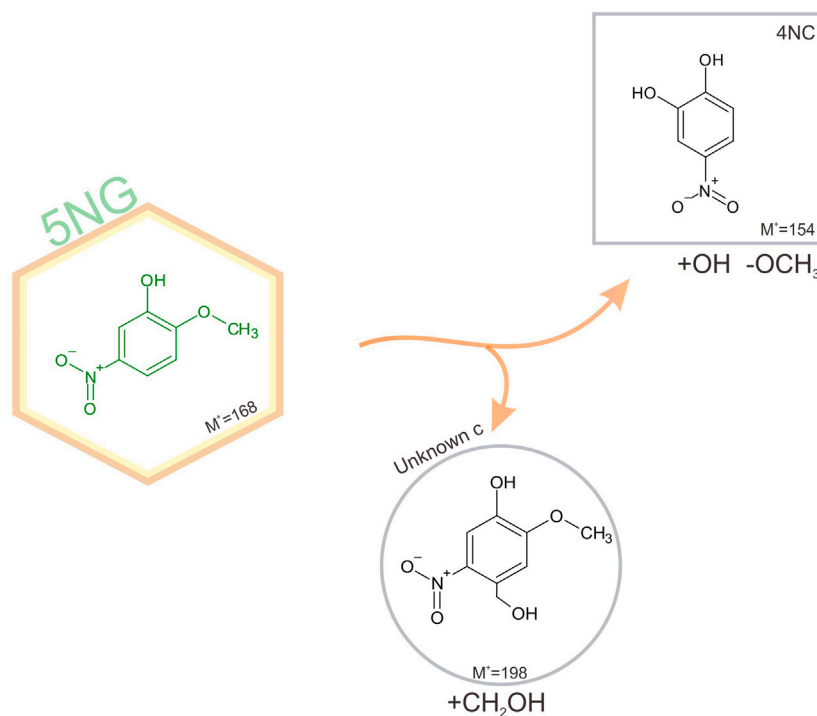
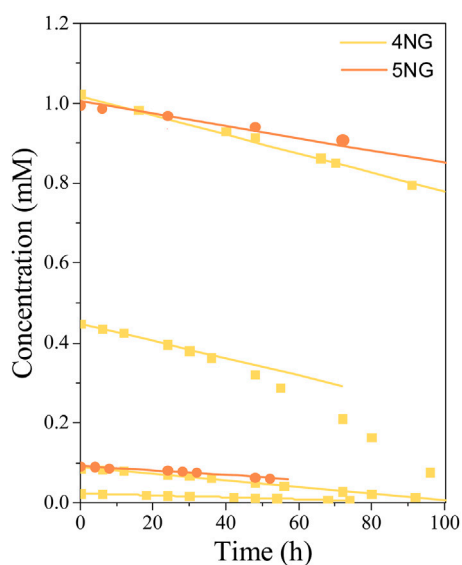


FIGURE 6

Schematic representation of identified pathways of 5NG photo-catalyzed transformations in an illuminated aqueous solution. Products shown in square boxes were confirmed by comparison with commercial standards; in round boxes, tentative structures are proposed based on the measured fragmentation patterns. The corresponding mechanisms are proposed in the text.

TABLE 2 Kinetic parameters for the photolysis of 4NG (1–4) and 5NG (5–6) in aqueous solutions irradiated with the artificial sunlight.

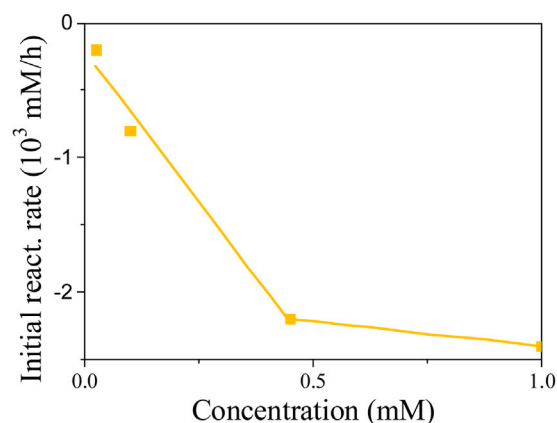
	Init. conc. (mM)	Reaction rate (mM/h)	r^2	Rate constant	Reaction order	Lifetime (h)
1	1.0	−0.0024	0.97	−0.002 mM/h	zero	—
2	0.45	−0.0022 ^a	0.99	−0.005 h ^{−1a}	cannot be determined	200 ^a
3	0.1	−0.0008	0.99	−0.008 h ^{−1}	pseudo-zero	125
4	0.025	−0.0002	0.99	−0.008 h ^{−1}	pseudo-zero	125
5	1.0	−0.0015	0.98	−0.0015 mM/h	zero	—
6	0.1	−0.0006	0.99	−0.006 h ^{−1}	pseudo-zero	167

^aOverestimated, see discussion.**FIGURE 7**

Concentration profiles of 4NG and 5NG photolysis at different initial concentrations during illumination with the artificial sunlight; symbols represent experimental data, while lines are linear fits through the (initial) experimental points.

The photolysis kinetics was evaluated by the initial rate method. Linear regression was used to estimate the reaction rates at the beginning of each experiment, while according to the zero-order kinetics, the slope of the line (i.e., the reaction rate) equals the kinetic rate constant. For most experimental conditions (0.025, 0.1, and 1.0 mM initial concentrations), these were representative reaction rate constants throughout the experiments, whereas the experiment at 0.45 mM 4NG showed some deviation from linearity, which was already mentioned before. The resulting zero-order kinetic parameters (Eq. 5) are gathered in Table 2. Our photolysis rates under the artificial sunlight are for two orders of magnitude lower than those determined for 0.1 mM solutions of *p*-NP and *m*-NP under the Mercury lamp, i.e. 0.0486 mM/h and 0.0151 mM/h, respectively (Chen et al., 2005).

Based on the linearity of response, one would easily conclude that 4NG photolysis is of zero-order kinetics and only depends on the photon flux to the solution. However, different slopes for

**FIGURE 8**

Initial reaction rates for different starting 4NG concentrations.

different experiments in Figure 7 suggest that the kinetics is of pseudo-zero order and that real reaction rate also depends on initial reactant concentration, which is demonstrated in Figure 8.

We found out at low reactant concentrations that the determined reaction rates are directly proportional to the corresponding reactant concentration at the beginning of each experiment, which agrees with the first-order kinetics. However, the slopes at 0.45 and 1.00 mM 4NG became equal, implying that the initial reactant concentration indeed ceases to have an effect on the reaction rate at high reactant concentrations, following real zero-order kinetics at those conditions.

Nevertheless, considering the effect of initial reactant concentration on the observed reaction rates, 4NG photolysis is of pseudo-zero order at low concentrations (<0.45 mM), the slope of the line indicating an apparent rate constant of the zero order ($k_{app} = k_0 = k_1 \cdot c_0$). Therefore, we were able to calculate the corresponding first-order rate constants for the three experimental systems (Table 2) and to further predict photolysis lifetimes in the atmospheric waters according to the Eq. 7. For the reaction regime of the lowest two concentrations, the lifetime was estimated at 125 h. However, the actual lifetime for 0.45 mM 4NG estimated at 200 h should be much shorter due to photosensitization reactions taking place in the solution. For concentrations higher

than this, it is impossible to calculate a unique lifetime as it depends on the reactant concentration itself as explained above.

Based on the 4NG photolysis results, photodegradation of 5NG is also expected to be of the pseudo-zero order at low reactant concentrations and of real zero order at high initial concentrations, although the borderline concentration for the change of the regime is not evident from our experimental data. We thus only estimated the lifetime for the lowest 0.1 mM concentration, which is with 167 h longer than that of 4NG, in line with our previous discussion.

Both atmospheric lifetimes are much longer than those observed for the gas-phase photolysis of NPs, which were determined in the order of minutes (Peng et al., 2023).

3.4 Atmospheric applications

The determined pKa values of the investigated compounds and their major photodegradation products were in the following order: 46DNG < 4NG < 5NG < GUA. Although we found light absorption by all investigated compounds is pH-dependent, 4NG and 5NG are expected to mostly contribute to the atmospheric light absorption by BrC under basic conditions, which is rarely relevant for the atmospheric aqueous phase. In contrast, 46DNG significantly absorbs visible light in a wide range of pH values (especially above pH 3.3) and is expected to respond to the changing secondary aerosol pH with changing atmospheric conditions. Acidic aqueous phase (pH < 5) is typical for liquid aerosols and cloud water in rural areas and polluted urban environments, whereas higher pH values (pH > 4) are more characteristic of atmospheric waters in very clean environments, expecting to enhance the atmosphere-heating effect of long-range transported NG aerosols in these sensitive regions.

We further found the photolysis of aqueous-phase 4NG under the artificial sunlight faster than that of 5NG; however, this was not resembled in the visible part of the recorded absorption spectra. More visible absorption was observed in the case of 5NG photolysis products at the end of experiments, implying its higher potential to contribute to atmospheric light absorption by secondary BrC aerosols.

The kinetics of 4NG and 5NG photolysis was of the pseudo-first order at low precursor concentrations and changed to the real zero-order above some marginal initial concentration (around 0.45 mM), which is expected to change upon addition of other light-absorbing species competing for the incoming photons with the target compounds. This, however, needs to be confirmed in future studies. Moreover, the effect of photosensitization was also observed that was out of scope of this study. At pH 5, atmospheric lifetimes of aqueous-phase 4NG and 5NG were determined at 125 and 167 h, respectively, which implies their potential damaging influence on the distant regions downwind from the emission sources. Such long atmospheric lifetimes also suggest 4NG and 5NG can be used as biomass-burning marker compounds.

The photolysis of both precursor molecules (4NG and 5NG) yielded photoproducts with preserved aromatic ring, $-\text{OCH}_3$, $-\text{OH}$, and $-\text{NO}_2$ groups. Based on the confirmed presence of 46DNG, which formed during the 4NG photolysis, the nitro group must have been detached from the 4NG aromatic ring (in a form of NO_2^\bullet and/

or HONO) and reacted further with another 4NG molecule. Chemical transformations involving secondary $^\bullet\text{OH}$ are further proposed, additionally pointing to the influence of both, direct and indirect photodegradation pathways to the observed precursor decays, involving also reactive species that formed in the solutions during the experiment. In short, denitration, carbon loss, hydroxylation, nitration, and carbon gain were characteristic of 4NG phototransformation, while carbon loss, hydroxylation, and carbon gain were observed in the case of 5NG. Although mechanisms underlying the observed reaction pathways are discussed based on the existing literature, these still need to be confirmed in future laboratory and field studies.

Data availability statement

The original contributions presented in the study are included in the article/Supplementary Material, further inquiries can be directed to the corresponding authors.

Author contributions

AD and US performed laboratory work and analyzed the acquired data. AD interpreted the data, wrote the original draft of the manuscript together with AK and took care of tables and figures. AK and MS designed the research, supervised the laboratory work and contributed to the interpretation of the results. All authors contributed to the article and approved the submitted version.

Funding

The authors acknowledge the financial support from the Slovenian Research Agency (research core funding Nos. P1-0034 and P2-0152).

Acknowledgments

AD acknowledges Faculty of Environmental Sciences, University of Nova Gorica for giving her the opportunity to conduct the research work at the National Institute of Chemistry and for awarding her with Master's degree.

Conflict of interest

The authors declare that the research was conducted in the absence of any commercial or financial relationships that could be construed as a potential conflict of interest.

Publisher's note

All claims expressed in this article are solely those of the authors and do not necessarily represent those of their

affiliated organizations, or those of the publisher, the editors and the reviewers. Any product that may be evaluated in this article, or claim that may be made by its manufacturer, is not guaranteed or endorsed by the publisher.

References

- Aihara, K., Urano, Y., Higuchi, T., and Hirobe, M. (1993). Mechanistic studies of selective catechol formation from *o*-methoxyphenols using a copper (II)-ascorbic acid-dioxygen system. *J. Chem. Society-Perkin Trans. 2*, 2165–2170. doi:10.1039/c29930002165
- Bailey-Darland, S., Krueger, T. D., and Fang, C. (2023). Ultrafast spectroscopies of nitrophenols and nitrophenolates in solution: From electronic dynamics and vibrational structures to photochemical and environmental implications. *Molecules* 28, 601. doi:10.3390/molecules28020601
- Barbott, F., Bartels-Rausch, T., De Laurentiis, E., Ammann, M., Brigante, M., Mailhot, G., et al. (2017). Photochemical formation of nitrite and nitrous acid (HONO) upon irradiation of nitrophenols in aqueous solution and in viscous secondary organic aerosol proxy. *Environ. Sci. Technol.* 51, 7486–7495. doi:10.1021/acs.est.7b01397
- Barzaghi, P., and Herrmann, H. (2002). A mechanistic study of the oxidation of phenol by OH/NO₂/NO₃ in aqueous solution. *Phys. Chem. Chem. Phys.* 4, 3669–3675. doi:10.1039/b201652d
- Bejan, I., Abd El Aal, Y., Barnes, I., Benter, T., Bohn, B., Wiesen, P., et al. (2006). The photolysis of ortho-nitrophenols: A new gas phase source of HONO. *Phys. Chem. Chem. Phys.* 8, 2028–2035. doi:10.1039/b516590c
- Bejan, I., Barnes, I., Olariu, R., Zhou, S. M., Wiesen, P., and Benter, T. (2007). Investigations on the gas-phase photolysis and OH radical kinetics of methyl-2-nitrophenols. *Phys. Chem. Chem. Phys.* 9, 5686–5692. doi:10.1039/b709464g
- Chen, B., Yang, C., and Goh, N. K. (2005). Direct photolysis of nitroaromatic compounds in aqueous solutions. *J. Environ. Sci.* 17, 598–604.
- Cheng, S. B., Zhou, C. H., Yin, H. M., Sun, J. L., and Han, K. L. (2009). OH produced from *o*-nitrophenol photolysis: A combined experimental and theoretical investigation. *J. Chem. Phys.* 130, 234311. doi:10.1063/1.3152635
- Cheng, X., Chen, Q., Li, Y., Huang, G., Liu, Y., Lu, S., et al. (2021). Secondary production of gaseous nitrated phenols in polluted urban environments. *Environ. Sci. Technol.* 55, 4410–4419. doi:10.1021/acs.est.0c07988
- Dewick, P. M. (2013). *Essentials of organic chemistry: For students of pharmacy, medicinal chemistry and biological chemistry*. West Sussex, England: John Wiley and Sons Ltd.
- Felber, T., Schaefer, T., He, L., and Herrmann, H. (2021). Aromatic carbonyl and nitro compounds as photosensitizers and their photophysical properties in the tropospheric aqueous phase. *J. Phys. Chem. A* 125, 5078–5095. doi:10.1021/acs.jpca.1c03503
- Frka, S., Šala, M., Kroflič, A., Huš, M., Čusak, A., and Grgić, I. (2016). Quantum chemical calculations resolved identification of methyl-nitrocatechols in atmospheric aerosols. *Environ. Sci. Technol.* 50, 5526–5535. doi:10.1021/acs.est.6b00823
- Grosjean, D. (1991). Atmospheric fate of toxic aromatic compounds. *Sci. Total Environ.* 100, 367–414. doi:10.1016/0048-9697(91)90386-S
- Guo, S., and Li, H. (2022). Photolysis of nitrophenols in gas phase and aqueous environment: A potential daytime source for atmospheric nitrous acid (HONO). *Environ. Sci. Atmos.* 3, 143–155. doi:10.1039/d2ea00053a
- Harrison, M. a. J., Barra, S., Borghesi, D., Vione, D., Arsene, C., and Iulian Olariu, R. L. (2005). Nitrated phenols in the atmosphere: A review. *Atmos. Environ.* 39, 231–248. doi:10.1016/j.atmosenv.2004.09.044
- Inuma, Y., Brüggemann, E., Gnauk, T., Müller, K., Andreae, M. O., Helas, G., et al. (2007). Source characterization of biomass burning particles: The combustion of selected European conifers, African hardwood, savanna grass, and German and Indonesian peat. *J. Geophys. Res. Atmos.* 112, D08209. doi:10.1029/2006JD007120
- Kroflič, A., Anders, J., Drventić, I., Mettke, P., Böge, O., Mutzel, A., et al. (2021). Guaiacol nitration in a simulated atmospheric aerosol with an emphasis on atmospheric nitrophenol formation mechanisms. *ACS Earth Space Chem.* 5, 1083–1093. doi:10.1021/acsearthspacechem.1c00014
- Kroflič, A., Grilc, M., and Grgić, I. (2015a). Does toxicity of aromatic pollutants increase under remote atmospheric conditions? *Sci. Rep.* 5, 8859. doi:10.1038/srep08859
- Kroflič, A., Grilc, M., and Grgić, I. (2015b). Unraveling pathways of guaiacol nitration in atmospheric waters: Nitrite, a source of reactive nitronium ion in the atmosphere. *Environ. Sci. Technol.* 49, 9150–9158. doi:10.1021/acs.est.5b01811
- Kroflič, A., Huš, M., Grilc, M., and Grgić, I. (2018). Underappreciated and complex role of nitrous acid in aromatic nitration under mild environmental conditions: The case of activated methoxyphenols. *Environ. Sci. Technol.* 52, 13756–13765. doi:10.1021/acs.est.8b01903
- Lauraguais, A., Coeur-Tourneur, C., Cassez, A., Deboudt, K., Fourmentin, M., and Choe, M. (2014). Atmospheric reactivity of hydroxyl radicals with guaiacol (2-methoxyphenol), a biomass burning emitted compound: Secondary organic aerosol formation and gas-phase oxidation products. *Atmos. Environ.* 86, 155–163. doi:10.1016/j.atmosenv.2013.11.074
- Li, X., Hu, M., Wang, Y., Xu, N., Fan, H., Zong, T., et al. (2021). Links between the optical properties and chemical compositions of Brown carbon chromophores in different environments: Contributions and formation of functionalized aromatic compounds. *Sci. Total Environ.* 786, 147418. doi:10.1016/j.scitotenv.2021.147418
- Lu, K. T., Luo, K. M., Lin, S. H., Su, S. H., and Hu, K. H. (2004). The acid-catalyzed phenol-formaldehyde reaction. *Process Saf. Environ. Prot.* 82, 37–47. doi:10.1205/09575820432277651
- Majewska, M., Khan, F., Pieta, I. S., Wróblewska, A., Szmigielski, R., and Pieta, P. (2021). Toxicity of selected airborne nitrophenols on eukaryotic cell membrane models. *Chemosphere* 266, 128996. doi:10.1016/j.chemosphere.2020.128996
- Mo, Y., Li, J., Liu, J., Zhong, G., Cheng, Z., Tian, C., et al. (2017). The influence of solvent and pH on determination of the light absorption properties of water-soluble Brown carbon. *Atmos. Environ.* 161, 90–98. doi:10.1016/j.atmosenv.2017.04.037
- Natangelo, M., Mangiapan, S., Bagnati, R., Benfenati, E., and Fanelli, R. (1999). Increased concentrations of nitrophenols in leaves from a damaged forest site. *Chemosphere* 38, 1495–1503. doi:10.1016/S0045-6535(98)00370-1
- Nitta, Y., Schalk, O., Igarashi, H., Wada, S., Tsutsumi, T., Saita, K., et al. (2021). Real-time probing of an atmospheric photochemical reaction by ultrashort extreme ultraviolet pulses: Nitrous acid release from *o*-nitrophenol. *J. Phys. Chem. Lett.* 12, 674–679. doi:10.1021/acs.jpclett.0c03297
- Peng, Y., Yuan, B., Yang, S., Wang, S., Yang, X., Wang, W., et al. (2023). Photolysis frequency of nitrophenols derived from ambient measurements. *Sci. Total Environ.* 869, 161810. doi:10.1016/j.scitotenv.2023.161810
- Pflieger, M., and Kroflič, A. (2017). Acute toxicity of emerging atmospheric pollutants from wood lignin due to biomass burning. *J. Hazard. Mater.* 338, 132–139. doi:10.1016/j.jhazmat.2017.05.023
- Rippen, G., Zietz, E., Frank, R., Knacker, T., and Klopffer, W. (1987). Do airborne nitrophenols contribute to forest decline. *Environ. Technol. Lett.* 8, 475–482. doi:10.1080/09593338709384508
- Roger, A., Aschmann, S. M., and Janet, A. (1992). Reactions of hydroxyl and nitrogen trioxide radicals with phenol, cresols, and 2-nitrophenol at 296 ± 2 K. *Environ. Sci. Technol.* 26, 1397–1403. doi:10.1021/es00031a018
- Sakakibara, K., Taira, M., Nagatomi, K., Kuriyama, G., Ohira, S. I., and Toda, K. (2022). Diurnal variations of gaseous and particulate nitrophenol isomers in the atmosphere monitored by using wet scrubbing online preconcentration. *Environ. Science-Atmospheres* 2, 1108–1119. doi:10.1039/d2ea00021k
- Sangwan, M., and Zhu, L. (2016). Absorption cross sections of 2-Nitrophenol in the 295–400 nm region and photolysis of 2-Nitrophenol at 308 and 351 nm. *J. Phys. Chem. A* 120, 9958–9967. doi:10.1021/acs.jpca.6b08961
- Sangwan, M., and Zhu, L. (2018). Role of methyl-2-nitrophenol photolysis as a potential source of OH radicals in the polluted atmosphere: Implications from laboratory investigation. *J. Phys. Chem. A* 122, 1861–1872. doi:10.1021/acs.jpca.7b11235
- Slkboer, S., Grandy, L., Blair, S. L., Nizkorodov, S. A., Smith, R. W., and Al-Abadleh, H. A. (2015). Formation of light absorbing soluble secondary organics and insoluble polymeric particles from the dark reaction of catechol and guaiacol with Fe(III). *Environ. Sci. Technol.* 49, 7793–7801. doi:10.1021/acs.est.5b01032
- Subashchandrabose, S. R., Megharaj, M., Venkateswarlu, K., and Naidu, R. (2012). P-nitrophenol toxicity to and its removal by three select soil isolates of microalgae: The role of antioxidants. *Environ. Toxicol. Chem.* 31, 1980–1988. doi:10.1002/etc.1931
- Varekova, R. S., Geidl, S., Ionescu, C. M., Skrehota, O., Kudera, M., Sehnal, D., et al. (2011). Predicting pK(a) values of substituted phenols from atomic charges:

Supplementary material

The Supplementary Material for this article can be found online at: <https://www.frontiersin.org/articles/10.3389/fchem.2023.1211061/full#supplementary-material>

Comparison of different quantum mechanical methods and charge distribution schemes. *J. Chem. Inf. Model.* 51, 1795–1806. doi:10.1021/ci200133w

Vereecken, L., Chakravarty, H. K., Bohn, B., and Lelieveld, J. (2016). Theoretical study on the formation of H- and O-atoms, HONO, OH, NO, and NO₂ from the lowest lying singlet and triplet states in ortho-nitrophenol photolysis. *Int. J. Chem. Kinet.* 48, 785–795. doi:10.1002/kin.21033

Vidović, K., Lašić Jurković, D., Šala, M., Kroflič, A., and Grgić, I. (2018). Nighttime aqueous-phase formation of nitrocatechols in the atmospheric condensed phase. *Environ. Sci. Technol.* 52, 9722–9730. doi:10.1021/acs.est.8b01161

Wang, Y., Ding, Z. X., Zhang, Y. H., Wei, C. Y., and Xie, Z. C. (2019). Luffa pretreated by plasma oxidation and acidity to be used as cellulose films. *Polymers* 11, 37. doi:10.3390/polym11010037

Wei, Q., Yin, H. M., Sun, J. L., Yue, X. F., and Han, K. L. (2008). The dynamics of OH channel in the 266 and 355 nm photodissociation of 2-nitrophenol. *Chem. Phys. Lett.* 463, 340–344. doi:10.1016/j.cplett.2008.08.080

Yang, J., Au, W. C., Law, H., Lam, C. H., and Nah, T. (2021). Formation and evolution of Brown carbon during aqueous-phase nitrate-mediated photooxidation of guaiacol and 5-nitroguaiacol. *Atmos. Environ.* 254, 118401. doi:10.1016/j.atmosenv.2021.118401



OPEN ACCESS

EDITED BY

Basem Moosa,
King Abdullah University of Science and
Technology, Saudi Arabia

REVIEWED BY

Himanshu Aggarwal,
Birla Institute of Technology and Science,
India
Stefan Chisca,
King Abdullah University of Science and
Technology, Saudi Arabia

*CORRESPONDENCE

Othman Charles S. Al Hamouz,
✉ othmanacs@kfupm.edu.sa

RECEIVED 22 July 2023

ACCEPTED 24 August 2023

PUBLISHED 07 September 2023

CITATION

Al-Bukhari MS, Abdulazeez I,
Abdelnaby MM, Aljundi IH and
Al Hamouz OCS (2023), 3D porous
polymers for selective removal of CO₂
and H₂ storage: experimental and
computational studies.
Front. Chem. 11:1265324.
doi: 10.3389/fchem.2023.1265324

COPYRIGHT

© 2023 Al-Bukhari, Abdulazeez,
Abdelnaby, Aljundi and Al Hamouz. This is
an open-access article distributed under
the terms of the [Creative Commons
Attribution License \(CC BY\)](#). The use,
distribution or reproduction in other
forums is permitted, provided the original
author(s) and the copyright owner(s) are
credited and that the original publication
in this journal is cited, in accordance with
accepted academic practice. No use,
distribution or reproduction is permitted
which does not comply with these terms.

3D porous polymers for selective removal of CO₂ and H₂ storage: experimental and computational studies

Muath S. Al-Bukhari¹, Ismail Abdulazeez²,
Mahmoud M. Abdelnaby³, Isam H. Aljundi^{2,4} and
Othman Charles S. Al Hamouz^{1,3*}

¹Chemistry Department, King Fahd University of Petroleum and Minerals, Dhahran, Saudi Arabia,

²Interdisciplinary Research Center for Membranes and Water Security, King Fahd University of Petroleum and Minerals, Dhahran, Saudi Arabia, ³Interdisciplinary Research Center for Hydrogen and Energy Storage, King Fahd University of Petroleum and Minerals, Dhahran, Saudi Arabia, ⁴Chemical Engineering Department, King Fahd University of Petroleum and Minerals, Dhahran, Saudi Arabia

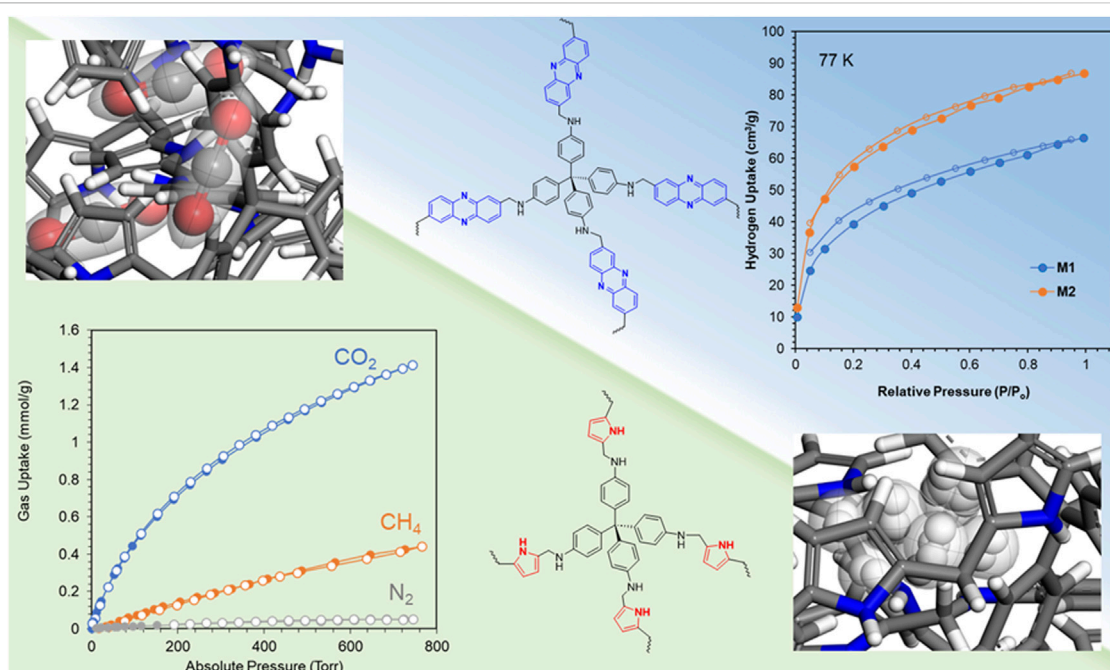
In this article, newly designed 3D porous polymers with tuned porosity were synthesized by the polycondensation of tetrakis (4-aminophenyl) methane with pyrrole to form **M1** polymer and with phenazine to form **M2** polymer. The polymerization reaction used *p*-formaldehyde as a linker and nitric acid as a catalyst. The newly designed 3D porous polymers showed permanent porosity with a BET surface area of 575 m²/g for **M1** and 389 m²/g for **M2**. The structure and thermal stability were investigated by solid ¹³C-NMR spectroscopy, Fourier-transform infrared (FT-IR) spectroscopy, and thermogravimetric analysis (TGA). The performance of the synthesized polymers toward CO₂ and H₂ was evaluated, demonstrating adsorption capacities of 1.85 mmol/g and 2.10 mmol/g for CO₂ by **M1** and **M2**, respectively. The importance of the synthesized polymers lies in their selectivity for CO₂ capture, with CO₂/N₂ selectivity of 43 and 51 for **M1** and **M2**, respectively. **M1** and **M2** polymers showed their capability for hydrogen storage with a capacity of 66 cm³/g (0.6 wt%) and 87 cm³/g (0.8 wt%), respectively, at 1 bar and 77 K. Molecular dynamics (MD) simulations using the grand canonical Monte Carlo (GCMC) method revealed the presence of considerable microporosity on **M2**, making it highly selective to CO₂. The exceptional removal capabilities, combined with the high thermal stability and microporosity, enable **M2** to be a potential material for flue gas purification and hydrogen storage.

KEYWORDS

3D porous polymers, global warming, flue gas purification, CO₂ capture, H₂ storage

1 Introduction

Global warming caused by the elevated levels of CO₂ has garnered significant attention in recent years. The elevated levels of CO₂ have become a serious problem due to their hazardous effects on the environment; these effects encompass a gradual increase in the temperature of the earth, resulting in droughts, fluctuations in the weather, and elevated oceanic water levels and ocean acidification (Feldman et al., 2015; Leal et al., 2018; Zakeri et al., 2022). During the last 40 years, the concentration of CO₂ has increased tremendously from 319 ppm to 414 ppm in 2021, setting a new record, and is estimated to increase to



GRAPHICAL ABSTRACT

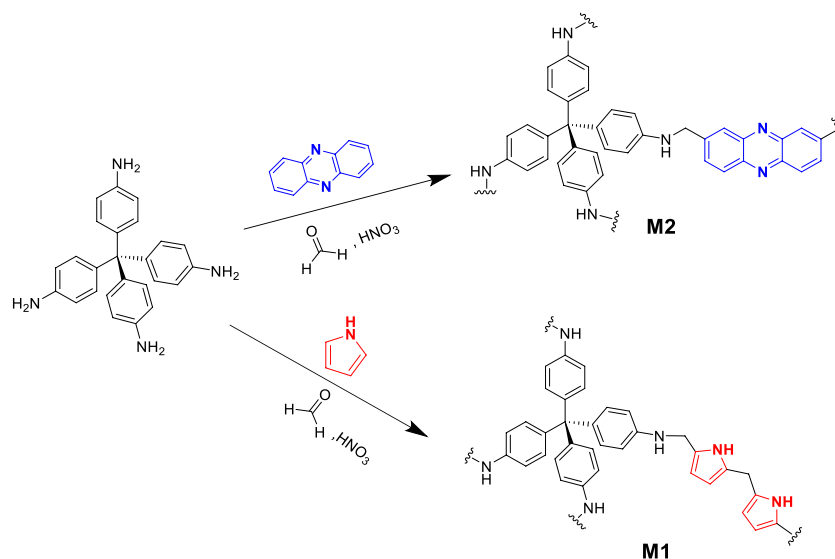
800 ppm within the next 100 years if we continue relying on fossil fuels as a primary energy source (Mercer, 1978; Feldman et al., 2015; Abdelhakim et al., 2022). Fossil fuels, serving as energy sources, are typically divided into three types: natural gas, coal, and petroleum. Upon combustion, they release CO₂, SO_x, and NO_x gases; mercury; and various particulates that cause pollution in the environment and have a large impact on human health (Khraisheh et al., 2020; Perera and Nadeau, 2022). Due to the major concern for the environment and human health, several methods and techniques have been identified to reduce the effect of CO₂ (Taylor et al., 2020; Long et al., 2021). These techniques and methods include finding new sources of energy, such as hydrogen gas, as an alternative energy source, reducing energy consumption by increasing energy efficiency, and finding new methods for capturing CO₂ (Kar et al., 2022; Paramati et al., 2022). Capturing CO₂ is one of these methods and has garnered considerable attention over the years. Two major methods have been used: chemisorption of CO₂, which involves the formation of a chemical bond between CO₂ and the adsorbent. Such an example for chemisorption is the absorption of CO₂ by liquid amines which is the most commonly used method by refineries to capture CO₂ from natural gas streams, their operation is non-costeffective and requires high energy for regeneration. Furthermore, degradation of the liquid amines thermally and oxidatively causes corrosion in refinery setups (Bobek et al., 2016; Dey et al., 2017; Kong et al., 2019). The other major technique that is emerging is capturing CO₂ by physisorption. Physisorption is a process where CO₂ is bonded weakly with the adsorbent by weak van der Waals forces of attraction, which allows the sorbent to be capable of reversibly adsorbing CO₂ from flue gas streams by solid sorbents (Plaza et al., 2007; Oschatz and Antonietti, 2018; Kong et al., 2019). Solid sorbents have been developed through the years, and several key features should be included in the design of these sorbents for

efficient CO₂ capture, such as i) high sorption capacity, ii) selectivity, and iii) adequate stability in the presence of contaminants (Zou et al., 2017; Abdelnaby et al., 2019; Khraisheh et al., 2020). Different classes of solid sorbents have emerged as promising materials for CO₂ reduction, such as metal-organic frameworks (MOFs), covalent organic frameworks (COFs), zeolites, carbonaceous materials, such as activated carbon, and porous organic polymers (POPs) (Cheung and Hedin, 2014; Gadipelli and Guo, 2015; Lohse and Bein, 2018; Zhao et al., 2018; Qasem et al., 2020). POPs are an interesting class of materials that possess excellent features such as low density, high surface area with a tunable pore size distribution, good thermal and chemical stability, and synthetic versatility (Zou et al., 2017; Gao et al., 2019; Gu et al., 2022). These features are considered requirements for the selective removal of CO₂ from flue gas and natural gas streams (Rufford et al., 2012; Ahmed et al., 2015; Alloush et al., 2022). In our endeavor to design and synthesize porous organic polymers for CO₂ capture and hydrogen storage, we demonstrate the design and synthesis of new 3D porous organic polymers with tuned porosity in this study. The synthesized 3D polymers were evaluated for their CO₂ and H₂ adsorption capabilities and for their selectivity of CO₂ over N₂ and CH₄ to assess their potential use in flue gas and natural gas treatment.

2 Experimental

2.1 Materials and methods

Tetrakis (4-aminophenyl) methane (99%), phenazine (99%), and pyrrole (98%) were all purchased from Sigma-Aldrich Co. *p*-Formaldehyde (PF, ≥99.9% purity) was purchased from Fluka™ AG. Nitric acid (65%wt.) and N,N-dimethylformamide



SCHEME 1
Synthesis scheme for 3D porous polymers.

(DMF, 99% purity) were obtained from Alpha Chemika™. Methanol (MeOH, ≥99.9% purity) was acquired from Merck Millipore™. Except for pyrrole, which was distilled at 150°C immediately before use, all chemicals were used as received. Ultrahigh-purity-grade nitrogen (N₂, 99.999%), helium (He, 99.999%), and high-purity carbon dioxide (CO₂, 99.9%) gases were supplied by Abdullah Hashem Industrial Co., Saudi Arabia. Natural abundance solid-state ¹³C-NMR spectra were collected using a Bruker 400 MHz spectrometer set to 125.65 MHz at room temperature (11.74 T). Samples were packed into 4 mm zirconium oxide rotors. Cross-polarization and high-power decoupling were used. The pulse delay was 2.5 s, and the magic angle spinning rate was 10 kHz. A PerkinElmer FT-IR spectrometer was used to obtain FT-IR spectra. FT-IR spectra were obtained in the range of 4,000–400 cm⁻¹ using a PerkinElmer 16F PC FT-IR spectrometer and solid potassium bromide (KBr) pellets (mid-IR region). TGA was performed using the STA 429® (NETZSCH group, Germany) thermal analyzer. All gas uptake measurements were performed on the Quantachrome® Autosorb IQ instrument, and isotherms were obtained at 273 K and 298 K.

2.2 Synthesis

In a typical experiment (Abdelnaby et al., 2018), tetrakis (4-aminophenyl) methane (2.73×10^{-3} mol, 1.0 g) and pyrrole (0.0109 mol, 0.73 g) were stirred in a 50-mL round-bottomed flask equipped with a magnetic bar containing 25 mL DMF until a homogeneous solution was obtained. *p*-Formaldehyde (0.02187 mol, 0.66 g) and nitric acid (10% of *p*-formaldehyde; 0.002187 mol, 0.199 g) were then added to the reaction mixture. The reaction mixture was flushed with N₂ gas and sealed and stirred for 24 h at 90°C. Once the reaction was completed, the product was filtered and washed with methanol for 3 days with continuous

exchange of methanol to ensure the removal of any monomers or unreacted materials left in the reaction. The product was vacuum-dried at 90°C for 24 h to get **M1** as a fine black powder (yield % = 65%). **M2** was obtained as a bright yellow powder (yield % = 49%) under similar reaction conditions with tetrakis (4-aminophenyl) methane, phenazine (**M2**), and *p*-formaldehyde taken at a molar ratio of 1:4:8 and 10 mol% of nitric acid relative to *p*-formaldehyde. The yield of the polymerization reaction was calculated as the mass of the product relative to the mass of all reactants.

2.3 MD simulation procedure

Molecular dynamics simulations (Supplementary Material) were performed to reveal the underlying mechanism of adsorption of CO₂, CH₄, and N₂ gases by the polymers **M1** and **M2**. The structural geometries of the polymers were built and optimized using the smart algorithm in the Forcite module of Materials Studio 8.0 software. The COMPASS II force field (Sun et al., 2016) was adopted, while the self-consistent field (SCF) convergence threshold, maximum force tolerance, and energy tolerance were set to 1.0×10^{-5} Ha, 0.001 Ha/Å, and 1.0×10^{-5} Ha, respectively. Thereafter, using the “Locate” task bar on the Sorption module, the suitable adsorption sites of the gases on **M1** and **M2** were identified, and the adsorption capacities were estimated based on the principle of simulated annealing using the GCMC method (Aljamaan et al., 2017; Song et al., 2018). The adsorption isotherms at 273.15, 298.15, and 313.15 K were calculated using the Langmuir fitting equation:

$$y = \frac{abx}{1 + bx}$$

where *a* is the limit of adsorption capacity in mmol/g and *b* is the adsorption constant in MPa⁻¹. The estimated adsorption capacities

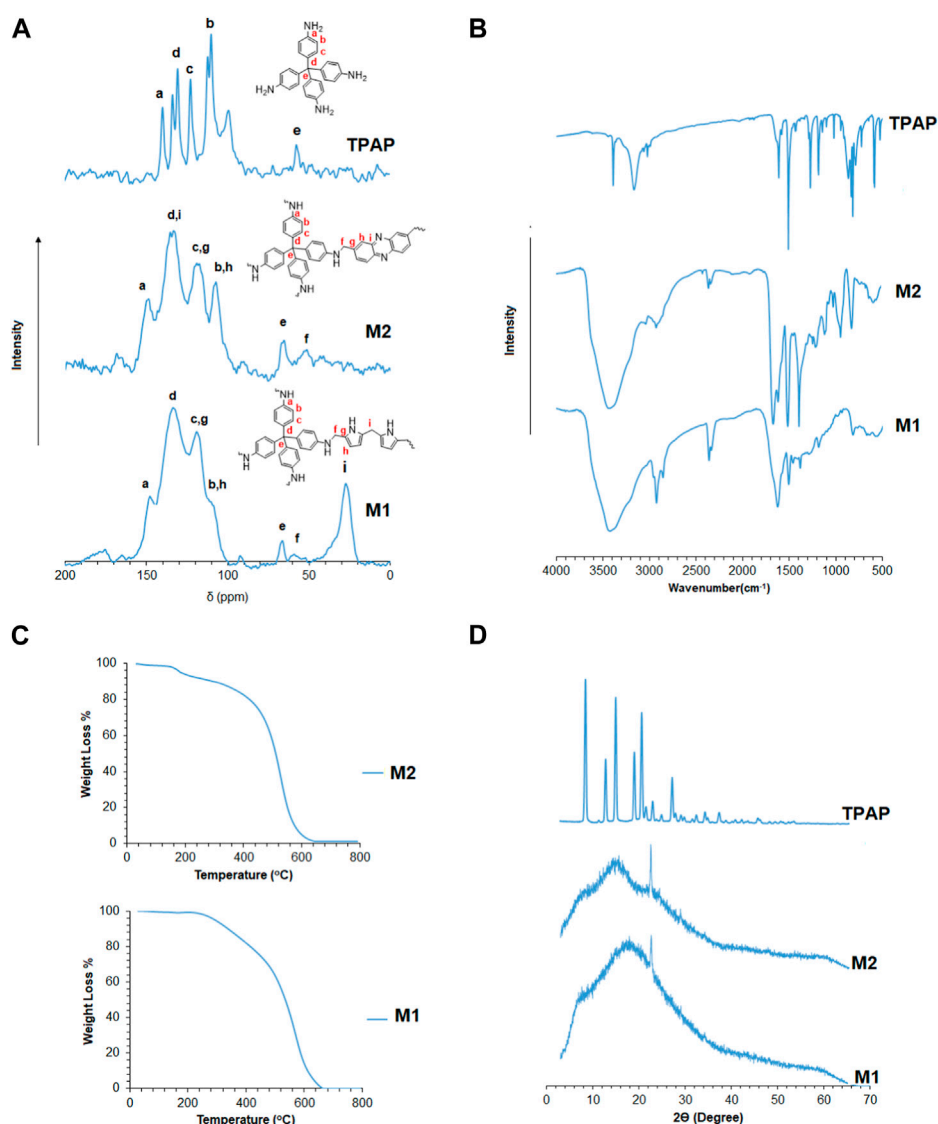


FIGURE 1

(A) Solid ^{13}C -NMR CP/MAS spectra for 3D porous polymers. (B) FT-IR spectra for 3D porous polymers and identification of peaks. (C) Thermogravimetric analysis of 3D porous polymers. (D) Powder X-ray diffraction of 3D porous polymers.

were given in the units of average molecules/cell and were converted to the amount of gas adsorbed in mmol/g using the following equation (Zhang et al., 2021):

$$\text{Amount adsorbed (mmol/g)} = \frac{\text{loading molecules}}{\text{Mw}_{\text{cell}} (\text{g/mol})} \times 1000,$$

where Mw_{cell} is the relative molecular mass of M1 and M2 polymers in the constructed supercell.

3 Results and discussion

3.1 Synthesis and characterization

This paper describes two new 3D porous amine-based polymers. The polymerization method was based on a modified Mannich

polycondensation reaction, with tetrakis (4-aminophenyl) methane added as a common component in the polymers. The polymers were realized by polymerizing tetrakis (4-aminophenyl) methane with pyrrole to obtain M1 and phenazine to form M2. The polymerization reaction was conducted using DMF as a solvent and concentrated HNO_3 as a catalyst (Scheme 1).

The structural features of the polymers were characterized by solid ^{13}C -NMR, as shown in Figure 1A. The peaks residing from 100 ppm to 150 ppm correspond to the aromatic carbons of pyrrole, phenazine, and tetrakis (4-aminophenyl) methane. A peak at 65 ppm corresponds to the quaternary carbon of tetrakis (4-aminophenyl) methane, linking the four aniline moieties. A peak at 55 ppm corresponds to the methylene linkage ($-\text{CH}_2-$) between tetrakis (4-aminophenyl) methane and pyrrole or phenazine. A peak at ~ 30 ppm corresponds to the methylene linkage ($-\text{CH}_2-$) present between pyrrole and pyrrole moieties (Luo et al., 2012; Abdelnaby

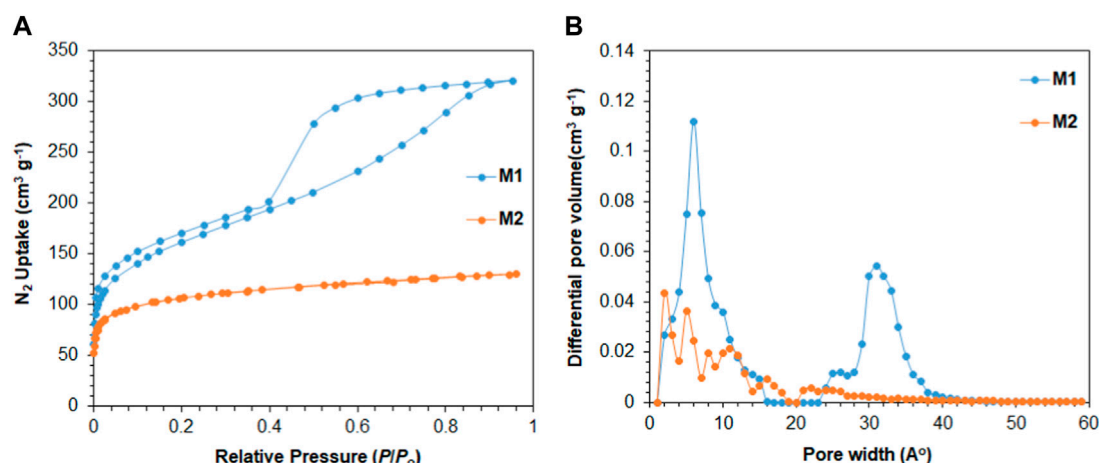


FIGURE 2

(A) Nitrogen adsorption/desorption isotherms of 3D porous polymers at 77 K; (B) pore size distribution using DFT.

et al., 2018). Figure 1B represents the FT-IR spectra for the synthesized polymers. The figure shows a broadband in the region from 3,300 to 3,500 cm^{-1} resulting from the overlap between both the 1° amine ($-\text{NH}_2$) stretching vibrations of the aniline moiety in the tetrakis (4-aminophenyl) methane monomer and the 2° amine ($-\text{NH}-$) stretching band of the pyrrole moiety. The bands between 1,400 and 1,700 cm^{-1} correspond to the aromatic $-\text{C}=\text{C}-$ and $-\text{C}=\text{N}-$ stretching vibrations of phenazine, pyrrole, and aniline moieties. A band at 1,631 cm^{-1} attributed to $-\text{NH}_2$ scissoring can be observed overlapping with the $-\text{C}=\text{C}-$ aromatic vibrational bands that appear in the same region. Both $-\text{NH}_2$ and $-\text{NH}-$ wagging bands are at 694 and 755 cm^{-1} , respectively (Wu et al., 2002; Tian et al., 2009). Figure 1C shows the powder X-ray diffraction patterns of the 3D porous polymers. The powder X-ray diffraction patterns reveal the amorphous nature of the synthesized polymers with a broad signal at $\sim 15^\circ 2\theta$ with some degree of crystallinity shown by the signal at $\sim 22^\circ 2\theta$ present in M1 and M2 (Wei et al., 1992; Errahali et al., 2014). Figure 1D reveals the good thermal stability of the synthesized polymers, which could be related to the stiff cross-linked structures of M1 and M2. The thermograms in Figure 4D show a 5% weight loss of small, trapped molecules in M2 up to 200°C, followed by a second degradation at $\sim 500^\circ\text{C}$, where the degradation of the polymer structure occurs by the loss of the methylene linkages, followed by the degradation of the polymer backbone. On the other hand, M1 begins to thermally degrade at $\sim 300^\circ\text{C}$ up to 440°C, which may be attributed to the loss of the methylene linkages between the moieties, followed by the complete degradation of the polymer structure at $\sim 600^\circ\text{C}$ (Li et al., 2014; Yan et al., 2016).

3.2 Porosity of the 3D porous polymers

As shown in Figure 2A, the nitrogen adsorption/desorption isotherms suggest that M1 and M2 are porous in nature. M1 polymer shows permanent porosity with a BET surface area of 575 m^2/g . The BET isotherm of M1 suggests that the polymer

exhibits Type I characteristics with a steep increase in nitrogen uptake at low relative pressure ($P/P_0 < 0.05$). The hysteresis in the M1 isotherm suggests the high interaction between M1 porous polymer and N_2 molecules, which could be due to the entrapment of N_2 molecules in the pores of M1 that leads to the hysteresis found in the adsorption/desorption isotherm (Li et al., 2022). The pore size distribution analysis based on density functional theory (DFT) calculations reveals two distinct regions in the M2 porous polymer. As shown in Figure 2B, there is a prominent peak at approximately 10 Å, indicating the presence of micropores, and another strong peak at an average pore width of approximately 33 Å, representing the mesoporous region. M2 polymer shows a permanent porosity with a BET surface area of 389 m^2/g . The nitrogen adsorption isotherm of M2 suggests that the polymer is microporous in nature and exhibits Type I characteristics. Further examination using DFT calculations reveals that the apertures of M2 polymer are mainly in the range of micropores with pore widths less than 20 Å, as shown in Figure 2B.

The tuned pore size distribution, accompanied by the good surface areas, encouraged us to investigate the capabilities of M1 and M2 for CO_2 adsorption compared with CH_4 and N_2 for applications in natural gas purification and flue gas treatment. For the polymers to perform well, they should be selective toward CO_2 and that can be produced by enhancing the microporosity of the polymer. As shown in Figure 2B, M2 is microporous in nature, with pore size distributions falling in the microporous region less than 20 Å with a high intensity close to the kinetic diameter of CO_2 (3.3 Å). This is shown by the adsorption capacities observed in Figures 3A–D, where the adsorption capacity at 273 K of CO_2 is higher in M2 (2.1 mmol/g) compared to M1 (1.85 mmol/g). At 298 K, the adsorption capacities behave in a similar manner, where the adsorption capacity of M2 for CO_2 is 1.41 mmol/g, for CH_4 is 0.44 mmol/g, and for N_2 is 0.050 mmol/g, whereas the adsorption capacity of M1 for CO_2 is 1.24 mmol/g, for CH_4 is 0.32 mmol/g, and for N_2 is 0.08 mmol/g. Comparing the efficiency between M1 and M2, it is shown that the adsorption capacity of M2 was higher than

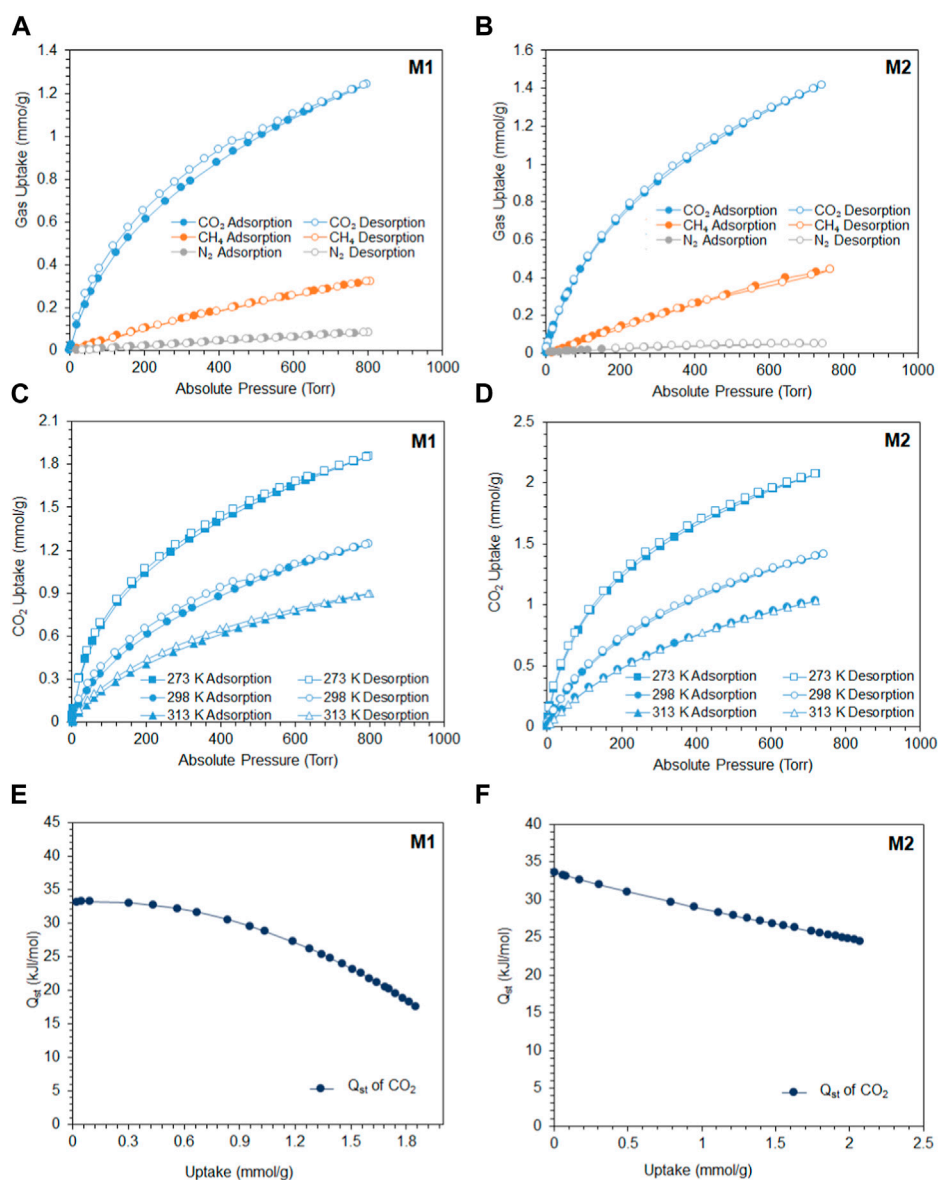


FIGURE 3

(A) Adsorption/desorption of **M1** to CO₂, CH₄, and N₂ at 298 K; (B) adsorption/desorption of **M2** to CO₂, CH₄, and N₂ at 298 K; (C) **M1** adsorption/desorption of CO₂ at 273, 298, and 313 K; (D) **M2** adsorption/desorption of CO₂ at 273, 298, and 313 K (filled circles refer to adsorption, and unfilled circles refer to desorption); (E) **M1** isosteric heat of adsorption (Q_{st}) vs CO₂ uptake (mmol/g); and (F) **M2** isosteric heat of adsorption (Q_{st}) vs CO₂ uptake (mmol/g).

M1, which is attributed to the microporous nature of the pores and the absence of mesopores in **M2** (Song et al., 2022). The isosteric heat of adsorption (Q_{st}) of CO₂ shows the interaction energy between a sorbent and CO₂ gas. Figures 3E, F show the Q_{st} vs uptake of CO₂. The values of Q_{st} decrease with the coverage of the surface of the polymer with CO₂, indicating that the adsorption process occurred on a heterogeneous surface. The Q_{st} values for the adsorption of CO₂ by **M1** and **M2** were found to be 33.1 kJ/mol and 33.6 kJ/mol, respectively. This indicates that the adsorption process is of physisorption in nature (Khosrowshahi et al., 2022; Ravi et al., 2023). Another feature that an adsorbent should possess is high selectivity. As shown in Figures 4A–D, the selectivity was investigated at 298 K to mimic ambient conditions, which is in

agreement with post-combustion treatment conditions. By using the initial slope ratios of Henry's law constants at 298 K, the selectivity of **M1** for CO₂/N₂ is 43 and CO₂/CH₄ is 9, whereas the selectivity of **M2** for CO₂/N₂ is 51 and CO₂/CH₄ is 10. The selectivity of **M2** was higher than that of **M1** even though it has a lower surface area, which could be explained by the microporous nature of the polymer with a similar observation for CO₂/CH₄ selectivity. As shown in Table 1, despite having lower surface areas, **M1** and **M2** exhibit superior adsorption capacity and selectivity for CO₂/CH₄ and CO₂/N₂ compared to reported porous materials with higher surface areas.

The molecular dynamics of the synthesized polymers were studied to correlate the experimental results with the theoretical

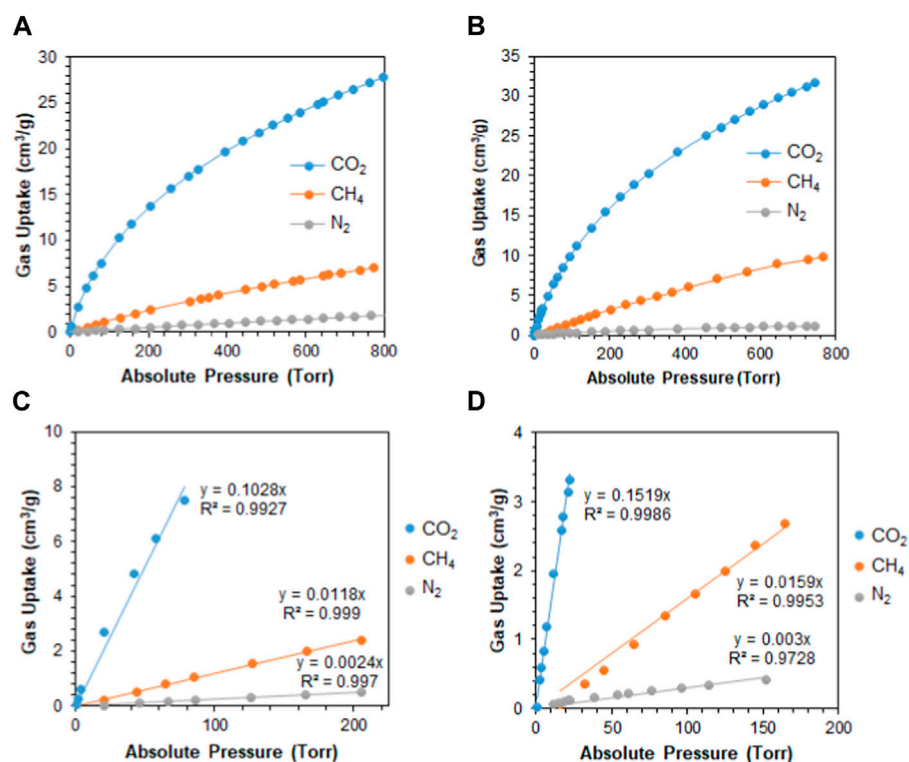


FIGURE 4

(A) Adsorption of CO₂, CH₄, and N₂ by M1 at 298 K; (B) adsorption of CO₂, CH₄, and N₂ by M2 at 298 K; (C) initial slope fitting of M1 at 298 K; and (D) initial slope fitting of M2 at 298 K.

TABLE 1 Comparison of porous materials with M1 and M2 with respect to surface area, CO₂ uptake at 273 K and 298 K, CO₂/N₂ and CO₂/CH₄ selectivity, and Q_{st} (CO₂).

Name	BET (m ² /g)	CO ₂ (mmol/g) 273 K (298 K)	CO ₂ /N ₂ selectivity (298 K)	CO ₂ /CH ₄ selectivity (298 K)	Q _{st} (CO ₂) kJ/mol	Reference
M1	575	1.85 (1.24)	43	9	33.1	This work
M2	389	2.10 (1.41)	51	10	33.6	
P-C	339	1.32 (0.72)	-	20.7	-	Li et al. (2021)
P-N-ET	1,150	4.0 (2.11)	67.4	36.7	-	
P-C-ET	1,031	2.61 (1.57)	28.7	16.5	-	
SNW-1	821	(2.08)	50	15	35	Gao et al. (2014)
P-1	611	2.02	29	4	38.8	Qiao et al. (2014)
P-2	1,222	3.3	8	3	30.9	
Polymer 1	1,168	2.18 (1.09)	56	-	35.5	Wang et al. (2015)
Polymer 2	1,015	2.08 (1.61)	45	-	27.2	
BIPLP-1Cu/BF ₄	1,580	2.30 (1.20)	16	3	32.2	Arab et al. (2015)
BIPLP-1	380	2.5 (1.75)	64	17	32.3	
YBN-CC	579	2 (1.27)	32.25	5.15	24.7	Sadak (2021)
YBN-DMM	784	2.87 (1.75)	25.78	5.14	26.5	
YBN-DMB	957	2.87 (1.68)	23.19	4.96	28.8	

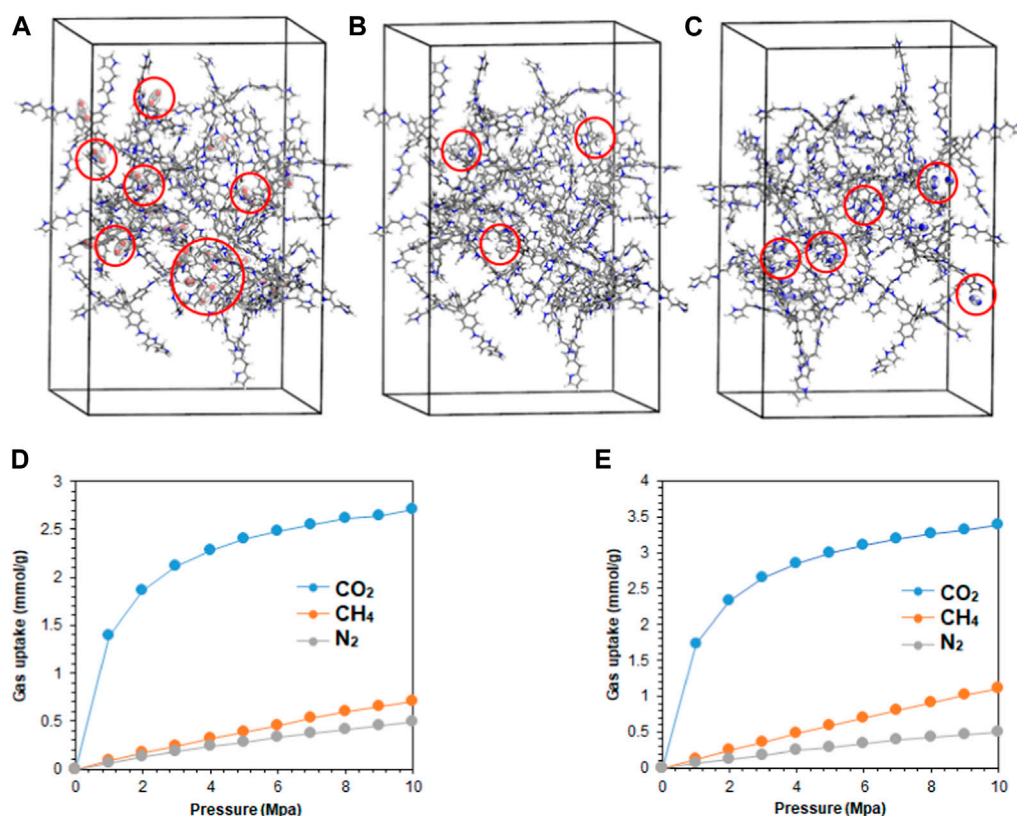


FIGURE 5

(A) CO₂, (B) CH₄, and (C) N₂ adsorption sites located on the **M2** polymer packed in amorphous cells of dimension 30 × 30 × 40 Å, comprising 20 repeating units. The red spheres represent the adsorbed gas molecules. The corresponding simulated adsorption isotherms for both polymers at 298.15 K are presented in (D) **M1** and (E) **M2**.

TABLE 2 Langmuir fitting parameters for the adsorption of CO₂, CH₄, and N₂ on M1 and M2.

Temperature (K)	Polymer	Gas	a (mmol/g)	b (Mpa ⁻¹)	R ²
273.15	M1	CO ₂	3.77	0.12	0.9998
	M2		4.90	0.64	0.9995
298.15	M1	CO ₂	2.99	0.12	0.9994
	M2	CO ₂	3.74	0.12	0.9995
	M1	CH ₄	0.44	0.52	0.9999
	M2	CH ₄	0.98	0.78	0.9999
	M1	N ₂	0.17	0.27	0.9999
	M2	N ₂	0.20	0.30	0.9999
313.15	M1	CO ₂	1.52	0.26	0.9998
	M2		2.34	0.19	0.9994

calculations (Supplementary Material). The adsorption of single-component gases, CO₂, CH₄, and N₂, on **M1** and **M2** polymers at 298.15 K was simulated in supercells of dimension 30 × 30 × 40 Å, comprising of 20 repeating units of the polymer molecules, as presented in Figures 5A–C. The corresponding simulated adsorption isotherms are shown in Figures 5D, E. Both polymers

demonstrated strong van der Waals attraction toward CO₂ molecules via the pyrrolic and pyridinic nitrogen atoms on **M1** and **M2**, respectively. Moreover, CO₂ adsorption binding sites were located on both molecules, with fewer sites for CH₄ and N₂ gases. However, **M2** demonstrated rapid uptake of CO₂ below 2 MPa (20 bar), indicating the presence of microporosity within the

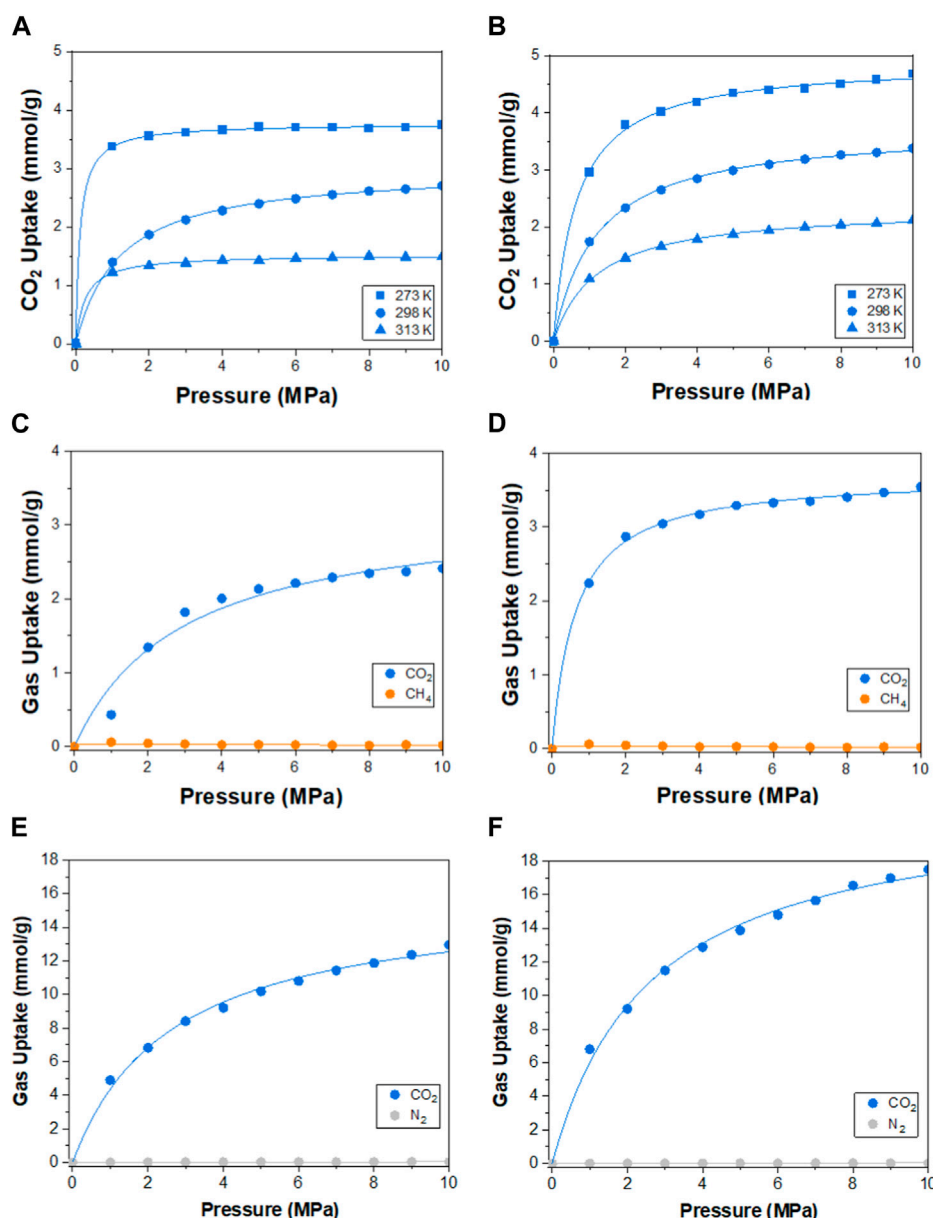


FIGURE 6

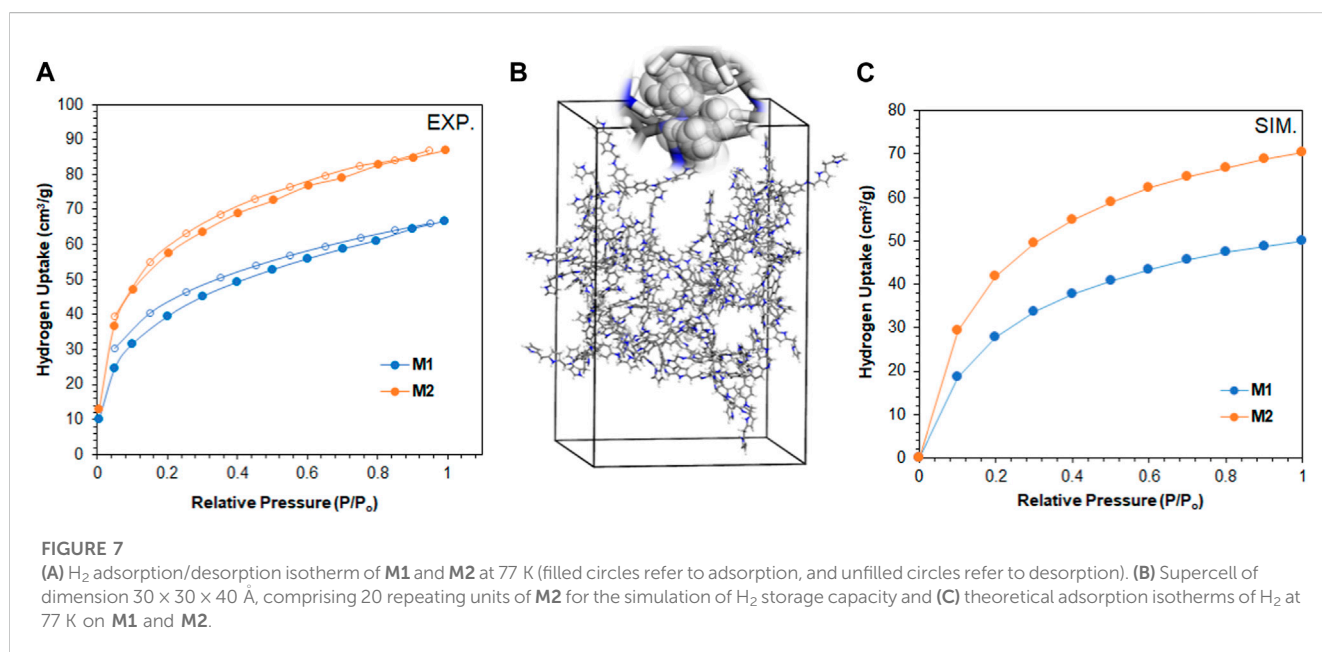
Theoretical adsorption isotherms of CO₂ at 273.15, 298.15, and 313.15 K on (A) M1 and (B) M2. Adsorption isotherms of CO₂/CH₄ in multi-component streams with a molar ratio of 50:50 on (C) M1 and (D) M2 at 298.15 K; and CO₂/N₂ with a molar ratio of 20:80 on (E) M1 and (F) M2 are also presented.

polymer framework (Rizzuto et al., 2017), and the selectivity of the polymer to CO₂ gas is consistent with the experimental findings. Using the Langmuir isotherm model (Table 2), the limit adsorption capacities of CO₂ at 298.15 K on M1 and M2 were estimated as 2.99 and 3.74 mmol/g, while for CH₄ and N₂, the values were 0.44 and 0.17, and 0.98 and 0.20 mmol/g, respectively. Meanwhile, the corresponding theoretical isosteric heat of adsorption (Q_{st}) for CO₂ at 298.15 K was calculated as 43.1 and 43.9 kJ/mol on M1 and M2, respectively. While the theoretical values are slightly higher than the experimental values, which could be ascribed to the overestimation from the general assumptions input into the simulation software (Meng et al., 2018). The order of selectivity of the polymers is in good

agreement with the experimental findings and revealed the preferential selectivity of M2 to CO₂ gas. The adsorption of CO₂ on M1 and M2 at temperatures of 273.15, 298.15, and 313.15 K was further investigated, and the results are presented in Figures 6A, B. A slight decrease in the adsorption capacity of both polymers was observed with increasing temperature. This suggests that the adsorption of the gas molecules is strictly dependent on the van der Waals force of attraction between them and the active sites on the polymers, which tend to weaken with the increase in temperature due to the increase in the inherent kinetic energy of the gas molecules. Thus, M2 experiences less decline in the adsorption capacity, suggesting its greater adsorption preference for CO₂ gas.

TABLE 3 Comparison of porous materials to M1 and M2 for hydrogen storage.

Material	BET (m ² /g)	H ₂ wt% ^a	Reference
M1	575	0.6	This work
M2	389	0.8	
Poly (styrene-co-divinylbenzene)	1,060	0.8	Germain et al. (2009)
PIM-1	760	1.04	McKeown et al. (2006)
Fluoropolymers with intrinsic microporosity	666	0.8	Makhseed et al. (2008)
SCMP1	505	0.77	Cheng et al. (2012)
PCZN-10	391	0.75	Liao et al. (2017)
Bipyridinium array-type porous polymer	-	0.71	Yao et al. (2009)
ZSM-5	431	0.7	Dybtsev et al. (2004)

^aData based on 77 K and 1 bar.

Meanwhile, the selectivity of the polymers toward CO₂ in multi-component gas streams, comprising CO₂ and CH₄ at a molar ratio of 50:50 and CO₂ and N₂ gases at a molar ratio of 20:80, was further explored theoretically, as shown in Figures 6C–F. The presence of equimolar volumes of CH₄ and the abundance of N₂ gases did not impede the selectivity of the polymers to CO₂ gas, as the presence of quadrupole C=O bonds favors the van der Waals attraction to the polymers. On the other hand, CH₄ and N₂ molecules experienced a drastic decrease in adsorption affinity by the polymers due to the strong competition by CO₂ molecules, resulting in fewer molecular interactions, as shown in Figures 6C–F. In all cases, the M2 polymer rapidly adsorbs CO₂ molecules in the presence of competing gas molecules, affirming its selectivity and aligning well with the experimental findings.

In our endeavor to tap into the world of clean energy and seek alternatives to overcome the pollution of petroleum products, we

assessed our polymers for their capability to store hydrogen gas. The results in Figure 7A revealed the adsorption capacity of M1 and M2 toward H₂ at 77 K and 1 atm to be 66 cm³/g (0.6 wt%) and 87 cm³/g (0.8 wt%), respectively. Interestingly, the absence of mesopores in M2 reflected the higher adsorption capacity toward H₂ compared to M1, which is consistent with Rong et al. (2021). The storage capacity is higher and comparable to that of porous polymers with similar or higher surface areas, as shown in Table 3. Finally, we simulate the potential of hydrogen storage on the polymer molecules by constructing supercells and conducting the grand canonical Monte Carlo simulation, as shown in Figures 7B, C. The theoretical H₂ uptake capacities of M1 and M2 at 77 K were calculated to be 61.7 and 83.2 cm³/g, respectively. These values are in good agreement with the experimental adsorption capacities of both polymers and corroborate the microporosity of M2, making it a potential material for H₂ storage.

4 Conclusion

In this study, we report the synthesis of 3D porous polymers with tuned porosity. The choice of reaction conditions and monomers leads to polymers with microporous and meso-/microporous structures. The produced polymers were found to be thermally stable up to temperatures of 400°C. Analysis revealed the porous nature of polymers with a BET surface area of 575 m²/g for **M1** and 389 m²/g for **M2**. The **M1** polymer showed defined micropores of 7 Å and mesopores of 33 Å, whereas **M2** exhibited micropores with a pore size distribution of <20 Å. The study also revealed the effect of microporosity on adsorption ability and selectivity. The results revealed superior performance of **M2** in the absence of mesoporosity. The adsorption capacities at 273 K of CO₂ are higher in **M2** (2.1 mmol/g) compared to **M1** (1.85 mmol/g). In addition, at 298 K, the adsorption capacity of **M2** for CO₂ was 1.41 mmol/g, for CH₄ was 0.44 mmol/g, and for N₂ was 0.050 mmol/g, while the adsorption capacity of **M1** for CO₂ was 1.24 mmol/g, for CH₄ was 0.32 mmol/g, and for N₂ was 0.08 mmol/g. Furthermore, the absence of mesoporosity in **M2** was evidenced by its superior performance in hydrogen storage. The molecular dynamics simulation confirmed the superior performance of **M2** and coincided with the experimental values to prove the efficiency and capability of porous polymers to be a potential adsorbent for selective removal of CO₂ and H₂ storage.

Data availability statement

The original contributions presented in the study are included in the article/**Supplementary Material**; further inquiries can be directed to the corresponding author.

Author contributions

MA-B: Data curation, Investigation, Writing–original draft. IAB: Methodology, Software, Writing–original draft, Writing–review and editing. MA: Data curation, Methodology, Writing–original draft, Writing–review and editing. IAL: Data curation, Writing–original draft, Writing–review and editing. OA: Conceptualization, Data

curation, Formal Analysis, Funding acquisition, Investigation, Methodology, Project administration, Resources, Software, Supervision, Validation, Visualization, Writing–original draft, Writing–review and editing.

Funding

The authors declare that financial support was received for the research, authorship, and/or publication of this article.

Acknowledgments

This article is supported by King Fahd University of Petroleum and Minerals. The Authors at KFUPM acknowledge the Interdisciplinary Research Center for Hydrogen and Energy Storage for the support received under Grant number: INHE2207.

Conflict of interest

The authors declare that the research was conducted in the absence of any commercial or financial relationships that could be construed as a potential conflict of interest.

Publisher's note

All claims expressed in this article are solely those of the authors and do not necessarily represent those of their affiliated organizations, or those of the publisher, the editors, and the reviewers. Any product that may be evaluated in this article, or claim that may be made by its manufacturer, is not guaranteed or endorsed by the publisher.

Supplementary material

The Supplementary Material for this article can be found online at: <https://www.frontiersin.org/articles/10.3389/fchem.2023.1265324/full#supplementary-material>

References

- Abdelhakim, L. O. A., Zhou, R., and Ottosen, C.-O. (2022). Physiological responses of plants to combined drought and heat under elevated CO₂. *Agronomy* 12 (10), 2526. doi:10.3390/agronomy12102526
- Abdelnaby, M. M., Alloush, A. M., Qasem, N. A. A., Al-Maythaly, B. A., Mansour, R. B., Cordova, K. E., et al. (2018). Carbon dioxide capture in the presence of water by an amine-based crosslinked porous polymer. *J. Mater. Chem. A* 6 (15), 6455–6462. doi:10.1039/c8ta00012c
- Abdelnaby, M. M., Qasem, N. A. A., Al-Maythaly, B. A., Cordova, K. E., and Al Hamouz, O. C. S. (2019). A microporous organic copolymer for selective CO₂ capture under humid conditions. *ACS Sustain. Chem. Eng.* 7 (16), 13941–13948. doi:10.1021/acssuschemeng.9b02334
- Ahmed, A., Babarao, R., Huang, R., Medhekar, N., Todd, B. D., Hill, M. R., et al. (2015). Porous aromatic frameworks impregnated with lithiated fullerenes for natural gas purification. *J. Phys. Chem. C* 119 (17), 9347–9354. doi:10.1021/acs.jpcc.5b01144
- Aljamaan, H., Al Ismail, M., and Kovscek, A. R. (2017). Experimental investigation and Grand Canonical Monte Carlo simulation of gas shale adsorption from the macro to the nano scale. *J. Nat. Gas Sci. Eng.* 48, 119–137. doi:10.1016/j.jngse.2016.12.024
- Alloush, A. M., Abdulghani, H., Amasha, H. A., Saleh, T. A., and Al Hamouz, O. C. S. (2022). Microwave-assisted synthesis of novel porous organic polymers for effective selective capture of CO₂. *J. Industrial Eng. Chem.* 113, 215–225. doi:10.1016/j.jiec.2022.05.049
- Arab, P., Verlander, A., and El-Kaderi, H. M. (2015). Synthesis of a highly porous bis(imino)pyridine-linked polymer and its postsynthetic modification with inorganic fluorinated ions for selective CO₂ capture. *J. Phys. Chem. C* 119 (15), 8174–8182. doi:10.1021/acs.jpcc.5b00690
- Bobek, J., Rippel-Pethő, D., Molnár, É., and Bocsi, R. (2016). Selective hydrogen sulphide removal from acid gas by alkali chemisorption in a jet reactor. *Hung. J. Industry Chem.* 44 (1), 51–54. doi:10.1515/hjic-2016-0006

- Cheng, G., Hasell, T., Trewin, A., Adams, D. J., and Cooper, A. I. (2012). Soluble conjugated microporous polymers. *Angew. Chem. Int. Ed.* 51 (51), 12899–12903. doi:10.1002/ange.201205521
- Cheung, O., and Hedin, N. (2014). Zeolites and related sorbents with narrow pores for CO₂ separation from flue gas. *RSC Adv.* 4 (28), 14480–14494. doi:10.1039/c3ra48052f
- Dey, S., Bhunia, A., Boldog, I., and Janiak, C. (2017). A mixed-linker approach towards improving covalent triazine-based frameworks for CO₂ capture and separation. *Microporous Mesoporous Mater.* 241, 303–315. doi:10.1016/j.micromeso.2016.11.033
- Dybtsev, D. N., Chun, H., Yoon, S. H., Kim, D., and Kim, K. (2004). Microporous manganese formate: A simple Metal–Organic porous material with high framework stability and highly selective gas sorption properties. *J. Am. Chem. Soc.* 126 (1), 32–33. doi:10.1021/ja038678c
- Errahali, M., Gatti, G., Tei, L., Paul, G., Rolla, G. A., Canti, L., et al. (2014). Microporous hyper-cross-linked aromatic polymers designed for methane and carbon dioxide adsorption. *J. Phys. Chem. C* 118 (49), 28699–28710. doi:10.1021/jp5096695
- Feldman, D. R., Collins, W. D., Gero, P. J., Torn, M. S., Mlawer, E. J., and Shippert, T. R. (2015). Observational determination of surface radiative forcing by CO₂ from 2000 to 2010. *Nature* 519 (7543), 339–343. doi:10.1038/nature14240
- Gadipelli, S., and Guo, Z. X. (2015). Tuning of ZIF-derived carbon with high activity, nitrogen functionality, and yield – a case for superior CO₂ capture. *ChemSusChem* 8 (12), 2123–2132. doi:10.1002/cssc.201403402
- Gao, X., Zou, X., Ma, H., Meng, S., and Zhu, G. (2014). Highly selective and permeable porous organic framework membrane for CO₂ capture. *Adv. Mater.* 26 (22), 3644–3648. doi:10.1002/adma.201400020
- Gao, H., Li, Q., and Ren, S. (2019). Progress on CO₂ capture by porous organic polymers. *Curr. Opin. Green Sustain. Chem.* 16, 33–38. doi:10.1016/j.cogsc.2018.11.015
- Germain, J., Fréchet, J. M. J., and Svec, F. (2009). Nanoporous polymers for hydrogen storage. *Small* 5 (10), 1098–1111. doi:10.1002/sml.200801762
- Gu, J., Shao, P., Luo, L., Wang, Y., Zhao, T., Yang, C., et al. (2022). Microporous triazine-based ionic hyper-crosslinked polymers for efficient and selective separation of H₂S/CH₄/N₂. *Sep. Purif. Technol.* 285, 120377. doi:10.1016/j.seppur.2021.120377
- Kar, S. K., Harichandan, S., and Roy, B. (2022). Bibliometric analysis of the research on hydrogen economy: An analysis of current findings and roadmap ahead. *Int. J. Hydrogen Energy* 47 (20), 10803–10824. doi:10.1016/j.ijhydene.2022.01.137
- Khosrowshahi, M. S., Abdol, M. A., Mashhadimoslem, H., Khakpour, E., Emrooz, H. B. M., Sadeghzadeh, S., et al. (2022). The role of surface chemistry on CO₂ adsorption in biomass-derived porous carbons by experimental results and molecular dynamics simulations. *Sci. Rep.* 12 (1), 8917. doi:10.1038/s41598-022-12596-5
- Khraisheh, M., Almomani, F., and Walker, G. (2020). Solid sorbents as a retrofit technology for CO₂ removal from natural gas under high pressure and temperature conditions. *Sci. Rep.* 10 (1), 269. doi:10.1038/s41598-019-57151-x
- Kong, X., Li, S., Strømme, M., and Xu, C. (2019). Synthesis of porous organic polymers with tunable amine loadings for CO₂ capture: Balanced physisorption and chemisorption. *Nanomaterials* 9 (7), 1020. doi:10.3390/nano9071020
- Leal, P. P., Hurd, C. L., Sander, S. G., Armstrong, E., Fernández, P. A., Suhrhoff, T. J., et al. (2018). Copper pollution exacerbates the effects of ocean acidification and warming on kelp microscopic early life stages. *Sci. Rep.* 8 (1), 14763. doi:10.1038/s41598-018-32899-w
- Li, G., Zhang, B., Yan, J., and Wang, Z. (2014). Micro- and mesoporous poly(Schiff-base)s constructed from similar building blocks and their adsorption behaviors towards organic vapors and CO₂ gas. *J. Mater. Chem. A* 2 (44), 18881–18888. doi:10.1039/c4ta04429k
- Li, Z., Wang, W., Xu, Y., Zhu, Y., and Guo, X. (2021). Truxene/triazatruxene-based conjugated microporous polymers with flexible/rigid mutualistic symbiosis for efficient CO₂ storage. *J. CO₂ Util.* 49, 101550. doi:10.1016/j.jcou.2021.101550
- Li, M., Jian, Z., Hassanpouryouzband, A., and Zhang, L. (2022). Understanding hysteresis and gas trapping in dissociating hydrate-bearing sediments using pore network modeling and three-dimensional imaging. *Energy and Fuels* 36 (18), 10572–10582. doi:10.1021/acs.energyfuels.2c01306
- Liao, Y., Cheng, Z., Trunk, M., and Thomas, A. (2017). Targeted control over the porosities and functionalities of conjugated microporous polycarbazole networks for CO₂-selective capture and H₂ storage. *Polym. Chem.* 8 (46), 7240–7247. doi:10.1039/c7py01439b
- Lohse, M. S., and Bein, T. (2018). Covalent organic frameworks: Structures, synthesis, and applications. *Adv. Funct. Mater.* 28 (33), 1705553. doi:10.1002/adfm.201705553
- Long, Z., Huang, Y., Zhang, W., Shi, Z., Yu, D., Chen, Y., et al. (2021). Effect of different industrial activities on soil heavy metal pollution, ecological risk, and health risk. *Environ. Monit. Assess.* 193 (1), 20. doi:10.1007/s10661-020-08807-z
- Luo, Y., Li, B., Wang, W., Wu, K., and Tan, B. (2012). Hypercrosslinked aromatic heterocyclic microporous polymers: A new class of highly selective CO₂ capturing materials. *Capturing Mater.* 24 (42), 5703–5707. doi:10.1002/adma.201202447
- Makhseed, S., Samuel, J., Bumajdad, A., and Hassan, M. (2008). Synthesis and characterization of fluoropolymers with intrinsic microporosity and their hydrogen adsorption studies. *J. Appl. Polym. Sci.* 109 (4), 2591–2597. doi:10.1002/app.28372
- McKeown, N. B., Gahnm, B., Msayib, K. J., Budd, P. M., Tattershall, C. E., Mahmood, K., et al. (2006). Towards polymer-based hydrogen storage materials: Engineering ultramicroporous cavities within polymers of intrinsic microporosity. *Angew. Chem. Int. Ed.* 45 (11), 1804–1807. doi:10.1002/anie.200504241
- Meng, J., Zhong, R., Li, S., Yin, F., and Nie, B. (2018). Molecular model construction and study of gas adsorption of zhaozhong coal. *Energy and Fuels* 32 (9), 9727–9737. doi:10.1021/acs.energyfuels.8b01940
- Mercer, J. H. (1978). West antarctic ice sheet and CO₂ greenhouse effect: A threat of disaster. *Nature* 271 (5643), 321–325. doi:10.1038/271321a0
- Oschatz, M., and Antonietti, M. (2018). A search for selectivity to enable CO₂ capture with porous adsorbents. *Energy and Environ. Sci.* 11 (1), 57–70. doi:10.1039/c7ee02110k
- Paramati, S. R., Shahzad, U., and Doğan, B. (2022). The role of environmental technology for energy demand and energy efficiency: Evidence from OECD countries. *Renew. Sustain. Energy Rev.* 153, 111735. doi:10.1016/j.rser.2021.111735
- Perera, F., and Nadeau, K. (2022). Climate change, fossil-fuel pollution, and children's health. *N. Engl. J. Med.* 386 (24), 2303–2314. doi:10.1056/nejmra2117706
- Plaza, M. G., Pevida, C., Arenillas, A., Rubiera, F., and Pis, J. J. (2007). CO₂ capture by adsorption with nitrogen enriched carbons. *Fuel* 86 (14), 2204–2212. doi:10.1016/j.fuel.2007.06.001
- Qasem, N. A. A., Abuelaymen, A., and Ben-Mansour, R. (2020). Enhancing CO₂ adsorption capacity and cycling stability of Mg-MOF-74. *Arabian J. Sci. Eng.* 46, 6219–6228. doi:10.1007/s13369-020-04946-0
- Qiao, S., Du, Z., and Yang, R. (2014). Design and synthesis of novel carbazole-spacer-carbazole type conjugated microporous networks for gas storage and separation. *J. Mater. Chem. A* 2 (6), 1877–1885. doi:10.1039/c3ta14017b
- Ravi, S., Choi, Y., and Bae, Y.-S. (2023). Melamine-functionalized aromatic carbonyl-based polymer with high surface area for efficient CO₂ capture. *Sep. Purif. Technol.* 317, 123828. doi:10.1016/j.seppur.2023.123828
- Rizzuto, C., Caravella, A., Brunetti, A., Park, C. H., Lee, Y. M., Dirolli, E., et al. (2017). Sorption and diffusion of CO₂/N₂ in gas mixture in thermally-rearranged polymeric membranes: A molecular investigation. *J. Membr. Sci.* 528, 135–146. doi:10.1016/j.memsci.2017.01.025
- Rong, M., Yang, L., Yang, C., Yu, J., and Liu, H. (2021). Tetraphenyladamantane-based microporous polyaminals for efficient adsorption of CO₂, H₂ and organic vapors. *Microporous Mesoporous Mater.* 323, 111206. doi:10.1016/j.micromeso.2021.111206
- Rufford, T. E., Smart, S., Watson, G. C. Y., Graham, B. F., Boxall, J., Diniz da Costa, J. C., et al. (2012). The removal of CO₂ and N₂ from natural gas: A review of conventional and emerging process technologies. *J. Petroleum Sci. Eng.* 94–95, 123–154. doi:10.1016/j.petrol.2012.06.016
- Sadak, A. E. (2021). A comparative gas sorption study of dicarbazole-derived microporous hyper-crosslinked polymers. *Microporous Mesoporous Mater.* 311, 110727. doi:10.1016/j.micromeso.2020.110727
- Song, W., Yao, J., Ma, J., Li, A., Li, Y., Sun, H., et al. (2018). Grand canonical Monte Carlo simulations of pore structure influence on methane adsorption in micro-porous carbons with applications to coal and shale systems. *Fuel* 215, 196–203. doi:10.1016/j.fuel.2017.11.016
- Song, K. S., Fritz, P. W., and Coskun, A. (2022). Porous organic polymers for CO₂ capture, separation and conversion. *Chem. Soc. Rev.* 51 (23), 9831–9852. doi:10.1039/d2cs00727d
- Sun, H., Jin, Z., Yang, C., Akkermans, R. L., Robertson, S. H., Spenley, N. A., et al. (2016). Compass II: Extended coverage for polymer and drug-like molecule databases. *J. Mol. Model.* 22 (2), 47. doi:10.1007/s00894-016-2909-0
- Taylor, A. A., Tsuji, J. S., Garry, M. R., McArdle, M. E., Goodfellow, W. L., Adams, W. J., et al. (2020). Critical review of exposure and effects: Implications for setting regulatory health criteria for ingested copper. *Environ. Manag.* 65 (1), 131–159. doi:10.1007/s00267-019-01234-y
- Tian, Q., Yuan, Y. C., Rong, M. Z., and Zhang, M. Q. (2009). A thermally remendable epoxy resin. *J. Mater. Chem.* 19 (9), 1289–1296. doi:10.1039/b811938d
- Wang, J., Wei Yang, J. G., Yi, G., and Zhang, Y. (2015). Phosphonium salt incorporated hypercrosslinked porous polymers for CO₂ capture and conversion. *Chem. Commun.* 51 (86), 15708–15711. doi:10.1039/c5cc06295k

- Wei, Y., Jang, G.-W., Hsueh, K. F., Scherr, E. M., MacDiarmid, A. G., and Epstein, A. J. (1992). Thermal transitions and mechanical properties of films of chemically prepared polyaniline. *Polymer* 33 (2), 314–322. doi:10.1016/0032-3861(92)90988-9
- Wu, Z., Li, C., Wei, Z., Ying, P., and Xin, Q. (2002). FT-IR spectroscopic studies of thiophene adsorption and reactions on Mo2N/ γ -Al2O3 catalysts. *J. Phys. Chem. B* 106 (5), 979–987. doi:10.1021/jp011577l
- Yan, J., Zhang, B., and Wang, Z. (2016). Monodispersed ultramicroporous semi-cycloaliphatic polyimides for the highly efficient adsorption of CO2, H2 and organic vapors. *Polym. Chem.* 7 (47), 7295–7303. doi:10.1039/c6py01734g
- Yao, Q.-X., Pan, L., Jin, X.-H., Li, J., Ju, Z.-F., and Zhang, J. (2009). Bipyridinium array-type porous polymer displaying hydrogen storage, charge-transfer-type guest inclusion, and tunable magnetic properties. *Chem. – A Eur. J.* 15 (44), 11890–11897. doi:10.1002/chem.200901707
- Zakeri, B., Paulavets, K., Barreto-Gomez, L., Echeverri, L. G., Pachauri, S., Boza-Kiss, B., et al. (2022). Pandemic, war, and global energy transitions. *Energies* 15 (17), 6114. doi:10.3390/en15176114
- Zhang, J., Wang, J., Zhang, C., Li, Z., Lu, B., and Zhu, J. (2021). Molecular simulation of C2H4/CO2/N2/O2 adsorption characteristics in lignite and anthracite. *AIP Adv.* 11 (8), 085205. doi:10.1063/5.0057456
- Zhao, H., Luo, X., Zhang, H., Sun, N., Wei, W., and Sun, Y. (2018). Carbon-based adsorbents for post-combustion capture: A review. *Greenh. Gases Sci. Technol.* 8 (1), 11–36. doi:10.1002/ghg.1758
- Zou, L., Sun, Y., Che, S., Yang, X., Wang, X., Bosch, M., et al. (2017). Porous organic polymers for post-combustion carbon capture. *Adv. Mater.* 29 (37), 1700229. doi:10.1002/adma.201700229



OPEN ACCESS

EDITED BY

Daniele Contini,
National Research Council (CNR), Italy

REVIEWED BY

Feiqiang He,
East China University of Technology,
China
Caterina Mapelli,
National Research Council (CNR), Italy

*CORRESPONDENCE

Ngoc T. Bui,
✉ ngoctbui21@ou.edu

[†]These authors have contributed equally
to this work and share first authorship

RECEIVED 19 May 2023

ACCEPTED 21 August 2023

PUBLISHED 08 September 2023

CITATION

Meissner MS, Nguyen VHT, Bousrih I,
Le VTC, Frickenstein A, Le GV and Bui NT
(2023), Thermodynamic insights into
selenium oxyanion removal from
synthetic flue gas desulfurization
wastewater with temperature-swing
solvent extraction.
Front. Chem. 11:1225843.
doi: 10.3389/fchem.2023.1225843

COPYRIGHT

© 2023 Meissner, Nguyen, Bousrih, Le,
Frickenstein, Le and Bui. This is an open-
access article distributed under the terms
of the [Creative Commons Attribution
License \(CC BY\)](#). The use, distribution or
reproduction in other forums is
permitted, provided the original author(s)
and the copyright owner(s) are credited
and that the original publication in this
journal is cited, in accordance with
accepted academic practice. No use,
distribution or reproduction is permitted
which does not comply with these terms.

Thermodynamic insights into selenium oxyanion removal from synthetic flue gas desulfurization wastewater with temperature-swing solvent extraction

Michael S. Meissner^{1†}, Vy H. T. Nguyen^{1†}, Imen Bousrih¹,
Van T. C. Le¹, Alex Frickenstein², Giang V. Le³ and Ngoc T. Bui^{1,4*}

¹School of Chemical, Biological, and Materials Engineering, The University of Oklahoma, Norman, OK, United States, ²Stephenson School of Biomedical Engineering, Norman, OK, United States, ³Central Institute for Natural Resources and Environmental Studies, Vietnam National University, Hanoi, Viet Nam, ⁴School of Civil Engineering and Environmental Science, The University of Oklahoma, Norman, OK, United States

Temperature-swing solvent extraction (TSSE) is a cost-effective, simple, versatile, and industry-ready technology platform capable of desalinating hypersaline brines toward zero liquid discharge. In this work, we demonstrate the potential of TSSE in the effective removal of selenium oxyanions and traces of mercury with the coexistence of high contents of chloride and sulfate often encountered in flue gas desulfurization wastewater streams. We compare the rejection performance of the two common solvents broadly used for TSSE, decanoic acid (DA) and diisopropylamine (DPA), and correlate those with the solvent physicochemical properties (e.g., dielectric constant, polarity, molecular bulkiness, and hydrophobicity) and ionic properties (e.g., hydrated radii and H-bonding). The results show that TSSE can remove >99.5% of selenium oxyanions and 96%–99.6% of mercury traces coexisting with sulfate (at a sixfold Se concentration) and chloride (at a 400-fold Se concentration) in a synthetic wastewater stream. Compared to diisopropylamine, decanoic acid is more effective in rejecting ions for all cases, ranging from a simple binary system to more complex multicomponent systems with highly varied ionic concentrations. Furthermore, the H-bonding interaction with water and the hydrated radii of the oxyanions (i.e., selenate vs. selenite) along with the hindrance effects caused by the molecular bulkiness and hydrophobicity (or lipophilicity) of the solvents play important roles in the favorable rejection of TSSE. This study shows that TSSE might provide a technological solution with a high deionization potential for the industry in complying with the Environmental Protection Agency regulations for discharge streams from coal-fired power facilities.

KEYWORDS

selenate, selenite, mercury, deionization, zero liquid discharge

1 Introduction

Despite being a major contributor to global electricity production, coal-fired power plants (CFPPs) contribute to climate change and induce adverse environmental impact due to air emissions (e.g., carbon dioxide, nitrogen oxides, and sulfur dioxide) (Hu et al., 2000; Bürkle et al., 2018; He et al., 2021a; He et al., 2021b) and aqueous emissions of heavy metals and other bioaccumulative pollutants at these facilities. In the United States, coal accounted for 21.8% of electricity production in 2021, and approximately 25% of the currently operating U.S. coal-fired capacity is due to retire by the end of 2029 (EIA, 2022). While phasing out, effective pollution control is essential for CFPPs to comply with the Effluent Limitations Guidelines (ELGs) for the Steam Electric Power Generating Sector standards. For instance, to limit SO₂ emissions, a toxic environmental pollutant that primarily effectuates acid rain (Kaminski, 2003; Wang and Anthony, 2008), CFPPs are obliged to implement flue gas desulfurization (FGD) techniques to gaseous waste streams before atmospheric release (Srivastava et al., 2001; Kaminski, 2003). These techniques with the division into once-through and regenerative approaches are generally employed under wet (e.g., scrubbing with Ca-, Mg-, and NH₃-based compounds), semi-dry (e.g., using an Na- or Zn-based sorbent), or dry (sorbent injection, circulating fluidized bed, zeolite adsorption, etc.) conditions (Srivastava et al., 2001; Chen et al., 2019; Hanif et al., 2020). Of which, the most commercially profitable practice for FGD in industrial applications is to bring flue gas in contact with a limestone slurry in a wet scrubbing system to capture SO₂ into the aqueous phase as gypsum (CaSO₄·2H₂O) (Carletti et al., 2015; Chen et al., 2019).

Furthermore, it is reported that coal deposits in the earth are contaminated with several trace elements, such as selenium, mercury, and arsenic (Cheng et al., 2009), present at the site of coal formation or delivered via groundwater cycles (Ketris and Yudovich, 2009; Vejehati et al., 2010). Under combustion, these trace elements are released from the coal feeds (Skalnaya and Skalny, 2018; Mehri, 2020) and are, subsequently, partitioned into FGD wastewaters. FGD wastewaters are commonly disposed of via environmental release after treatment (Agency, 2015), turning coal combustion into one of the principal culprits of environmental selenium pollution (Ohlendorf et al., 2011; Gingerich et al., 2018; He et al., 2018). The Environmental Protection Agency (EPA) updated the effluent limits for environmental discharge of FGD waters in 2015 (EPA, 2023), yet engineering challenges involved in meeting the new discharge standards caused the EPA to postpone the compliance date for existing CFPPs (EPA, 2017). In March 2023, the EPA proposed the establishment of more stringent discharge standards for CFPP wastewater (including Se, Hg, As, Ni, and halogen compounds), which would potentially reduce the amount of pollutants discharged through these streams by approximately 584 million pounds per year (Coleman, 2023; EPA, 2023).

It is noteworthy that approximately 30% of selenium found in coal feeds partitions into FGD wastewater (Cheng et al., 2009). These high levels of selenium are reported to pose threats to the environment (Hamilton, 2004; Gingerich et al., 2018) and human health (Skalnaya and Skalny, 2018; Mehri, 2020). The two main species of selenium that exist in the aquatic environment are water-

soluble selenate (SeO₄²⁻) and selenite (SeO₃²⁻) (He et al., 2018; Meher et al., 2020). Removing these selenium oxyanions from water remains challenging (Gingerich et al., 2018), especially the removal of the former ion due to its kinetically non-reactive behavior along with its structural similarity to sulfate (SO₄²⁻)—a co-contaminated anion in most circumstances (Ali and Shrivastava, 2021). Often, sulfate coexists in FGD wastewater at an order of magnitude more prevalent than selenate, which dominates the treatment process, and thus reduces the selenate removal efficiency (Huang et al., 2013; Tokunaga and Takahashi, 2017). Note that FGD wastewater also contains high chloride contents (ranging from 20,000 to 40,000 mg/L), necessitating treatment systems that can effectively function in corrosive environments having high amounts of total dissolved solids (EPA, 2009; Gingerich et al., 2018).

Current industrial efforts for selenium removal are mainly based on biological and chemical approaches, whereas physical methods (e.g., nanofiltration and reverse osmosis) have not captured much attention from industries due to the operational and maintenance costs (Ali and Shrivastava, 2021). Some advanced bioreactors, such as inverse fluidized bed bioreactors, granular sludge reactors, and hybrid bioreactors, displayed excellent Se-reducing bacterial activities, followed by the moderate recovery efficiency of selenium nanoparticles in a single-stage system (Cordoba and Staicu, 2018; Sinharoy and Lens, 2020; Sinharoy et al., 2022). Nevertheless, high sensitivity to variations in feed components and long operating periods of bioremediation unfavorably hinder its practical applications (Gingerich et al., 2018). Coagulation/precipitation, ion exchange, separation, and adsorption dominate the conventional chemical technologies for oxyanion removal. For instance, nano-Al₂O₃ embedded in chitosan beads were reported to be able to combine photooxidation with adsorption to synergistically remove selenate and selenite; however, their performances were moderately thwarted with the presence of competing sulfate ions (Pincus et al., 2019). Co-precipitation of selenium oxyanions with barite followed by a phosphate post-treatment step to minimize selenium leakage in different aqueous environments was also reported (Tokunaga et al., 2023). Other common practices for the concurrent removal of selenate and selenite involve the use of nanosized zero-valent iron (nZVI). In these processes, supplementary oxidants are not required, as selenite inherently activated the reactivity of nZVI, essentially enhancing the removal rate and electron selectivity of selenate (Wu et al., 2021). Recently, electrochemical processes have also been leveraged to drive the conversion of these anions to more treatable forms of selenium through different redox pathways (MeaganMauter, 2021; Zou et al., 2021; Zou and Mauter, 2021). Still, the low tolerance of these technologies with the high range of sulfate and chloride often encountered in FGD wastewater streams may have hindered their widespread use, especially where a pre-treatment process is not equipped. Essentially, while the coexisting sulfate may compete with selenium oxyanions for electrons in cathodic parasitic reactions (Zou et al., 2021), chloride may disrupt Se(IV) reduction pathways by generating strong oxidants on the anode side of the process.

Solvent extraction is a versatile and effective non-evaporative separation process that has been applied in various applications due to its relatively low cost and simplicity, including CO₂ capture, bio-oil fractionation, extraction of metal complexes, and desalination, to name a few (Kumar et al., 2015; Zhang et al., 2022). Temperature-

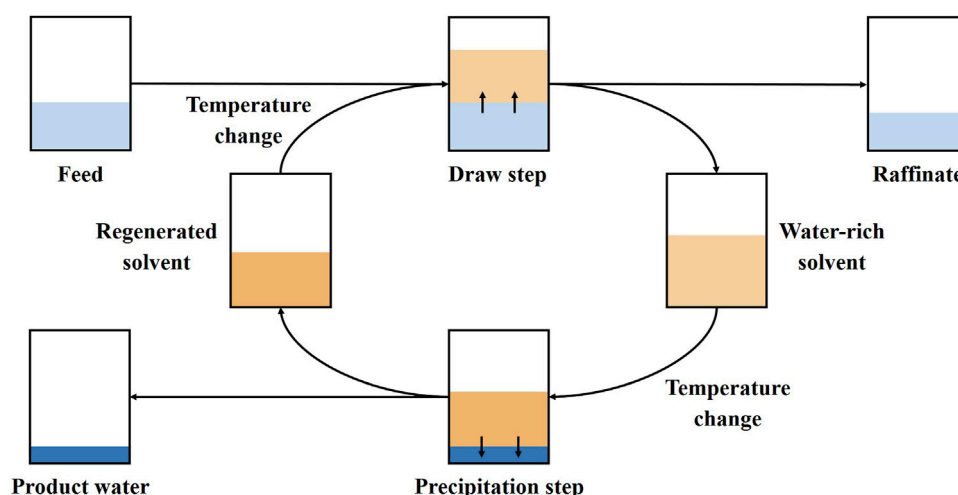


FIGURE 1
General TSSE process diagram.

swing solvent extraction (TSSE) has been recently developed, mainly to meet the incremental demand in desalinating water, with its working principle based on the high thermal sensitivity of water solubility of certain solvents (Zhang et al., 2022). Figure 1 provides a diagram of a standard TSSE process. Essentially, an aqueous feed is equilibrated with an organic solvent at a specific temperature favoring water dissolution into the organic solvent while rejecting other compounds. This creates two distinguished phases, viz., a concentrated raffinate and a water-rich solvent. The latter is then brought to equilibrium at a different temperature that promotes the immiscibility between the water and organic solvent. Finally, phases split, from which the water product is recovered in the aqueous phase, while the organic solvent can be recycled in subsequent extractions and sustainably reused in a recyclable solvent loop, which averts the usage of a large volume of organic extractants, mitigating their influences on the environment (Bajpayee et al., 2011).

Certain gaps in current studies on the employment of the TSSE method and its targeted objectives have been recognized. The TSSE literature has primarily focused on the organic solvents of diisopropylamine (DPA) (Boo et al., 2019; Boo et al., 2020; Sappidi et al., 2021; Zhang et al., 2022) and decanoic acid (DA) (Bajpayee et al., 2011; Rish et al., 2014; Guo et al., 2020). TSSE with DA was shown to attain high rejections (>98%) of all major ions in seawater including Na^+ , K^+ , Ca^{2+} , Mg^{2+} , Cl^- , and SO_4^{2-} , even in the presence of multiple monovalent and divalent cations (Rish et al., 2014), while a single pass of TSSE exhibited the removal efficiencies of 91% for As(III) and 97% for As(V) (Guo et al., 2020). Meanwhile, DPA was reported with the capability of treating feeds containing 4.0 M NaCl (Boo et al., 2019) and impressively achieving zero liquid discharge (Boo et al., 2020). Notwithstanding, apart from a dearth of insight about physicochemical interaction mechanisms between solute–solute and solute–solvent in the TSSE process, how these solvent systems behave in multicomponent feeds with diverse ion concentrations is still unclear. The impact of factors such as solvent physicochemical profiles and ion properties (e.g., hydration radius and atomic charge) on TSSE separating performance has also not

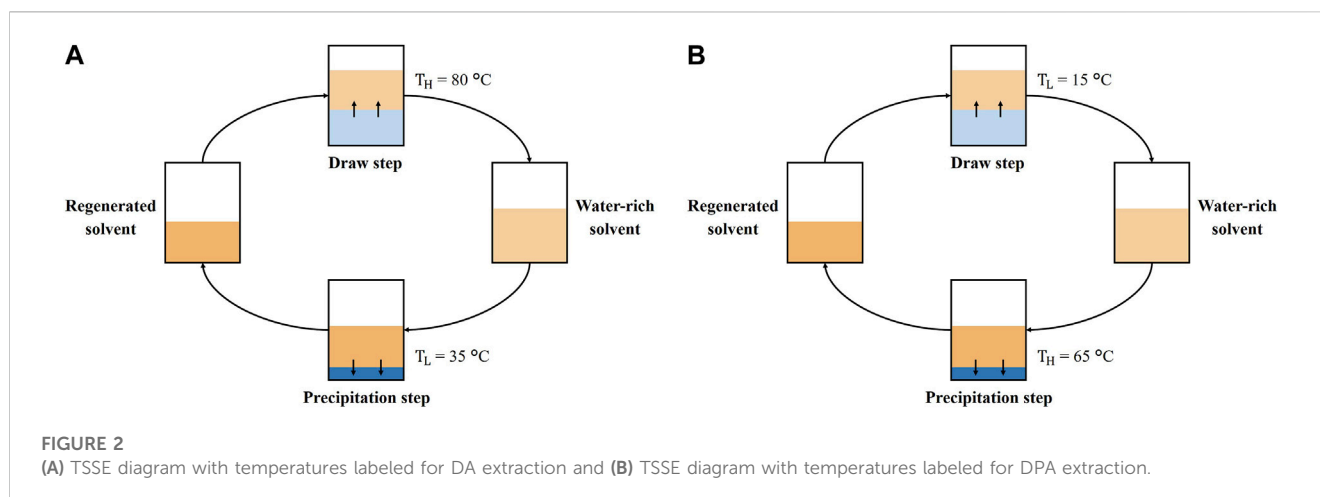
been clarified (Rish et al., 2014). On top of that, the TSSE rejection potential of selenate and selenite, particularly from FGD wastewater produced in CFPPs, has not been thoroughly explored to date.

In this work, we demonstrate the potential of TSSE in the effective removal of selenium oxyanions and mercury traces with the coexistence of high contents of chloride and sulfate often encountered in flue gas desulfurization wastewater streams. We compare the rejection performances of the two common solvents broadly used for TSSE, decanoic acid (DA) and diisopropylamine (DPA), and correlate those with the solvent physicochemical properties (e.g., dielectric constant, polarity, molecular bulkiness, and hydrophobicity) and ionic properties (e.g., hydrated radii and H-bonding). We challenge TSSE to remove selenium oxyanions and mercury traces from complex water streams having a high concentration of competing ions, for example, sulfate (at a sixfold Se concentration) and chloride (at a 400-fold Se concentration). Despite being extensively utilized in liquid–liquid extraction, diisopropylamine and decanoic acid behaviors and their chemical interactions with solutes have rarely been inspected thermodynamically at the molecular level, especially in complex multicomponent systems with highly varied ionic concentrations. Furthermore, we present the important roles of H-bonding interactions with water and the hydrated radii of the oxyanions (i.e., selenate vs. selenite) along with the hindrance effects caused by the solvent bulkiness and hydrophobicity (or lipophilicity) in the rejection tendency of TSSE. The results provide profound thermodynamic insights into the removal of selenium oxyanions from complex water streams using the TSSE technology platform.

2 Experimental

2.1 Chemicals

Diisopropylamine ($\text{C}_6\text{H}_{15}\text{N}$, $\geq 99.5\%$), sodium selenate (Na_2SeO_4 , BioXtra), sodium selenite (Na_2SeO_3 , 99%), mercury(II) chloride (HgCl_2 , $\geq 99.5\%$), decanoic acid ($\text{C}_{10}\text{H}_{20}\text{O}_2$, $\geq 99.5\%$), and



calcium sulfate dihydrate ($\text{CaSO}_4 \cdot 2\text{H}_2\text{O}$, $\geq 99\%$) were purchased from MilliporeSigma. Sodium chloride (NaCl , certified ACS, crystalline) was purchased from Fisher Chemical. For inductively coupled plasma-optical emission spectrometry (ICP-OES) and/or inductively coupled plasma mass spectrometry (ICP-MS) analyses, selenium standard (1 mg L^{-1} Se in nitric acid), mercury standard ($1,000 \text{ mg L}^{-1}$ Hg in nitric acid), and gold standard ($1,000 \text{ mg L}^{-1}$ in hydrochloric acid) were purchased from MilliporeSigma; 28-element ICP calibration/quality control standard and scandium standard ($1,000 \text{ } \mu\text{g mL}^{-1}$ in 7% nitric acid) were purchased from Inorganic Ventures; and yttrium standard ($1,000 \text{ } \mu\text{g mL}^{-1}$ in 2% nitric acid) was purchased from PerkinElmer Pure. Deionized water (DI) was collected from an in-house Milli-Q EQ 7000 ultrapure water purification system.

2.2 Experimental procedure

A total of seven feeds were prepared for temperature-swing solvent extraction with decanoic acid and diisopropylamine each used as solvents. Those include NaCl -only feeds with salt concentrations of 3.5 w/w%, 1.0 M, and 4.0 M; a selenium-only feed consisting of 500 parts per million (ppm) of SeO_4^{2-} and 500 ppm of SeO_3^{2-} ; a synthetic selenium-containing brine consisting of 500 ppm of SeO_4^{2-} and 20 g L^{-1} Cl^- from NaCl ; and two synthetic flue gas desulfurization wastewater samples with different concentrations of mercury composed of 20 g L^{-1} Cl^- from NaCl , 50 ppm of SeO_4^{2-} , 300 ppm of gypsum ($\text{CaSO}_4 \cdot 2\text{H}_2\text{O}$), and 1,000 ppb or 15 ppm of Hg^{2+} from HgCl_2 .

Figure 2A illustrates the procedure for TSSE with DA. In essence, 10 g of DA was transferred into a beaker and heated in an oven at 60°C until completely melted. A measure of 10 mL of the feed solution at an ambient temperature ($\sim 24^\circ\text{C}$) and the melted DA were added to a glass vial and shaken vigorously. The vial was placed in an oil bath at a high temperature (T_H) of 80°C for 24 h. The water-rich organic phase was pipetted into a test tube and placed in a second oil bath at a low temperature (T_L) of 35°C for 72 h to ensure that the aqueous and organic phases split from each other. After precipitation, DA was pipetted into the

original glass vial, and the aqueous phase was recovered as product water.

Figure 2B describes the procedure for TSSE with DPA. A measure of 10 mL of DPA and feed were added to a glass vial at an ambient temperature ($\sim 24^\circ\text{C}$) and shaken vigorously. The vial was placed in an oil bath at a T_L of 15°C for 2 h. The water-rich organic phase was pipetted into another vial and placed into an oil bath at a T_H of 65°C for 2 h. After precipitation, DPA was returned to the original vial, and the aqueous phase was recovered as product water. The chemical structures of DA and DPA are depicted in **Figure 3**.

We determined the salinity (i.e., NaCl concentration) of the product water with conductivity measurements using a Thermo Scientific Orion Star A212 conductivity benchtop meter. The calibration curves were prepared accordingly. The amount of calcium, sulfur, selenium, and mercury in the samples before and after extraction was quantified using an inductively coupled plasma-optical emission spectrometer (Varian Vista-PRO Simultaneous Axial ICP-OES) to determine their residual concentrations in the aqueous phase. The system was calibrated with a multi-element ICP calibration standard solution. Before ICP-OES measurements, all samples were diluted in 2 w/w% nitric acid added with 5 ppm of scandium as an internal standard. When essential, a PerkinElmer NexION 2000 inductively coupled plasma mass spectrometer with a collision-cell analysis capability at the University of Oklahoma Mass Spectroscopy, Proteomics & Metabolomics (MSPM) Core was used to detect trace ionic concentrations to achieve a higher measurement resolution. Specifically, given that Ar_2 dimers interfere with Se ion signals, ICP-MS was run in the kinetic energy discrimination (KED) mode by flowing He gas through the instrument collision/reaction cell (Yamada, 2015). Before ICP-MS measurements, all samples were diluted in 2 w/w% HNO_3 solution to a concentration of approximately ≤ 200 ppm Se/Hg. The dilutions contained 25 ppb of yttrium (Y^{89}) and 50 ppb of gold (Au^{197}). Y^{89} was used as a background signal ion. Au^{197} was used to stabilize ionic Hg in the solution during measurements (Allibone et al., 1999). Commercial selenium and mercury standard solutions were serially diluted and quantified to prepare calibration curves, allowing for the estimation of ionic concentration following the measurement of ion signal intensity.

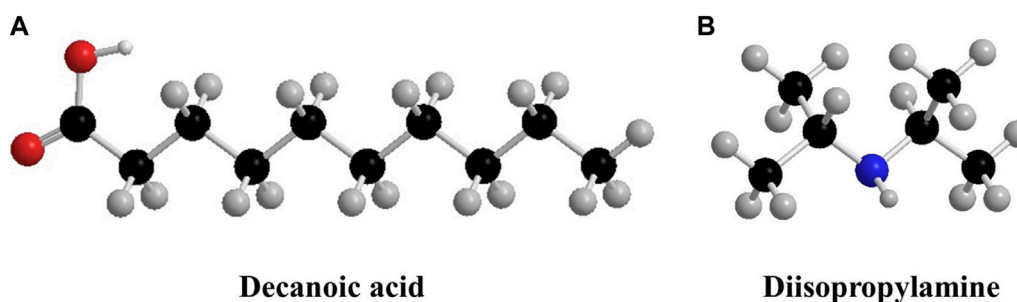


FIGURE 3
Chemical structures of (A) DA and (B) DPA.

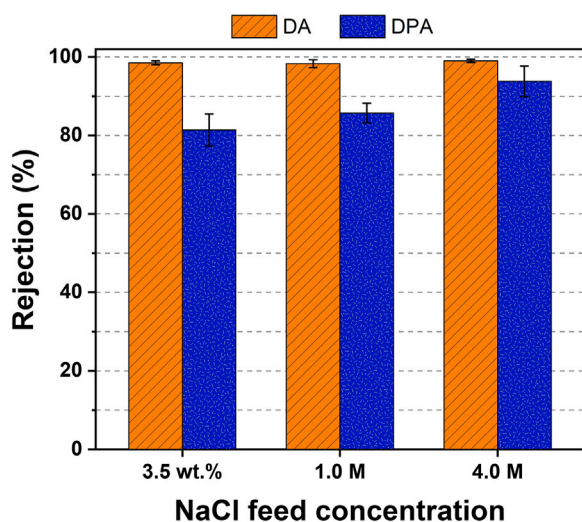


FIGURE 4
NaCl rejection of DA and DPA solvents using TSSE at different feed concentrations.

3 Results and discussion

3.1 Rejection potentials of DA- and DPA-based temperature-swing solvent extraction for feed streams including NaCl, selenate/selenite, and selenate with an NaCl background

Figure 4 demonstrates the salt rejection for different NaCl feed concentrations after extraction with DA and DPA. While DPA removed a greater proportion of NaCl with more concentrated feeds ($R_{NaCl} = 81.4\%–93.8\%$), also reported in the literature (Rish et al., 2014; Boo et al., 2019), DA displayed remarkable NaCl rejection potentials, regardless of the feed concentrations (>98%). The difference in salt extraction capacities of these two solvents could probably be explained with their dielectric constants. The higher the dielectric constants of the solvent, the greater the solvent polarity and the stronger the interactions between dissociated ions and liquid. Therefore, NaCl was more preferably rejected by DA ($\epsilon_{DA} = 2.37$) than by DPA ($\epsilon_{DPA} = 3.04$). Note, that while the

precipitation process of DA occurs at 35°C, that of DPA occurs at 65°C. Precipitating the product water from the water-rich organic phase at an elevated temperature (i.e., 65°C) may also impact the purity of the product water to a certain extent. Future studies are required to further elucidate this thermal influence on the rejection capability of TSSE solvents.

We then assess the rejection potential of DA and DPA against selenium oxyanions with TSSE. The molecular geometry is the principal structural difference between a selenate and selenite oxyanion. A selenate ion is comprised of four oxygens and is therefore tetrahedral, whereas a selenite ion with three oxygens is trigonal pyramidal. These structural dissimilarities bring about the distinction in the hydrated radii of these ions in the solution (Eklund and Persson, 2014). In the presence of water, hydrogen bonds form between the positive dipole of the hydrogen molecule and the negative charge of the oxygen atoms. However, selenite has a hemisphere in which there is no oxygen atom, and this causes a looser association between a selenite anion and a water molecule, creating a larger hydrated radius as a result. Indeed, as can be seen in Figure 5 (with the illustration in a two-dimensional coordinate plane), the hydrated radius of selenite in an aqueous solution is 4.36 Å vs. that of a selenate ion is 3.94 Å (Eklund and Persson, 2014). The larger hydrated radius of selenite may contribute to its more favorable rejection by TSSE. DA with bulky organic sections, as presented in Figure 3A, could render steric interactions and impose a higher energy barrier for selenite partition into the organic phase rather than selenate. Concurring with our theoretical hypotheses, the SeO_4^{2-} and SeO_3^{2-} rejection efficiencies of DA were experimentally examined to be $98.1 \pm 2.9\%$ and $98.8 \pm 0.9\%$, respectively. Interestingly, virtually no selenium oxyanion rejection was observed for DPA in this dilute concentration range. Specifically, DPA rejected only approximately 4.14% and 8.18% of selenate and selenite, respectively, under similar testing conditions. We hypothesize that this is likely due to the hydrogen bonding interactions between the amine groups in DPA and selenium oxyanions. Unlike the carboxylate group in DA, which is under steric hindrance from the long alkyl chain, the amine group in DPA is more accessible through water and oxyanion molecules for H-bonding interactions. As selenate appeared to be more challenging to be removed using TSSE, in the subsequent steps, we assess the potential of TSSE with the chosen solvent systems in separating selenate from synthetic water samples mimicking the complex FGD waste streams.

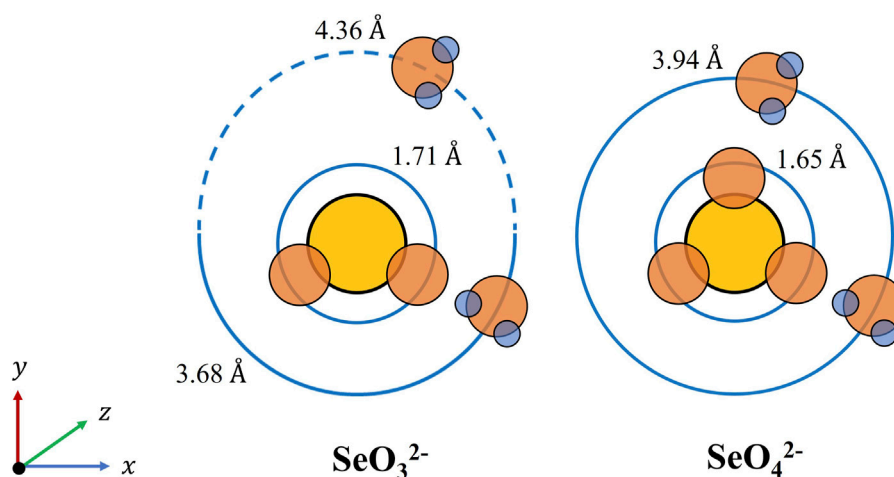


FIGURE 5

2D visualization of molecular structures and hydrated radii of a selenate and selenite anion in an aqueous solution adapted from Eklund and Persson (2014).

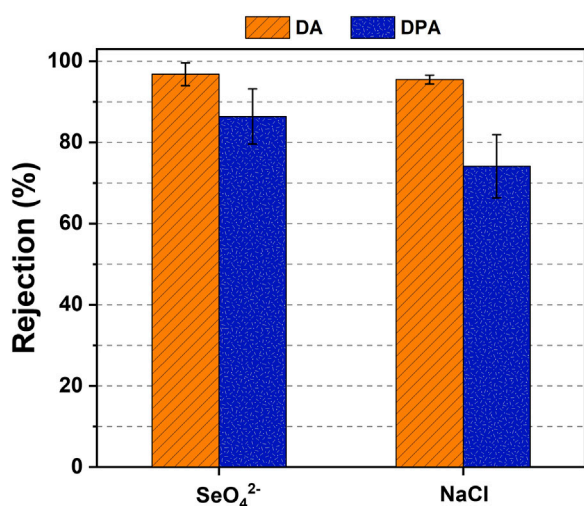


FIGURE 6

Average rejection rate of 500 ppm of selenate and 20 g L⁻¹ Cl⁻ feed of DA and DPA solvents.

Figure 6 displays the ion rejection of DA and DPA from a feed stream having 500 ppm of SeO₄²⁻ and 20 g L⁻¹ of Cl⁻. DA performed a 96.8% ± 2.8% and 95.5% ± 1.1% selenate and NaCl rejection, whereas DPA showed rejections of 86.4% ± 6.8% and 74.1% ± 7.8% for selenate and NaCl, respectively. A higher rejection of selenate as compared to NaCl was observed for both solvents mainly due to the impact of hydrated ion radii on rejection (Marcus, 1988). Notably, unlike previously observed for the virtually no selenium oxyanion rejection behavior of DPA in the selenium-only feed of 500 ppm SeO₄²⁻ and 500 ppm SeO₃²⁻, DPA evinced the selectivity against 500 ppm of selenate in this case, i.e., when there is a coexistence of 20 g L⁻¹ of NaCl. This observation marked that the ion partition between aqueous and organic phases appears to be predominately determined by the solution ionic strength (caused by 500 ppm of selenate and 20 g L⁻¹ of

NaCl) in preference to the concentration of the individual species in the multi-ion systems. We explain the impact of the solution ionic strength on the ion partition behaviors in aqueous and organic phases via thermodynamic models. Essentially, two phases in equilibrium follow the general equilibrium criterion given as follows (Sandler, 2017):

$$f_i^I(T, P, x^I) = f_i^{II}(T, P, x^{II}), \quad (1)$$

where f_i^I represents the fugacity of species i in phase I (water), f_i^{II} represents the fugacity of species i in phase II (organic solvent), T represents the temperature, P represents the pressure, and x represents the mole fraction of species i in phase I or II. Substituting the activity coefficient definition of fugacity into Eq. 1 gives

$$x_i^I \gamma_i^I(T, P, x^I) f_i(T, P) = x_i^{II} \gamma_i^{II}(T, P, x^{II}) f_i(T, P), \quad (2)$$

where γ_i represents the activity coefficient of species i in phase I or II and f_i represents the pure component liquid fugacity. The pure component liquid fugacity for a species is equivalent on both sides of Eq. 2, which is reduced to Eq. 3:

$$x_i^I \gamma_i^I(T, P, x^I) = x_i^{II} \gamma_i^{II}(T, P, x^{II}). \quad (3)$$

Equations 4, 5 introduce two terms: the mean ionic activity coefficient and the solution ionic strength. Briefly, these terms approximate the behavior of all ions within a solution rather than considering individual species.

$$\gamma_{\pm}^v = (\gamma_i^*)^{v+} (\gamma_j^*)^{v-}, \quad (4)$$

$$I = \frac{1}{2} \sum_{i=ions} z_i^2 M_i, \quad (5)$$

where γ_{\pm}^v represents the mean ionic activity coefficient, $(\gamma_i^*)^{v+}$ represents the activity of the cations, $(\gamma_j^*)^{v-}$ represents the activity of the anions, I represents the ionic strength of the solution, z_i represents the charge of ion i , and M_i represents the concentration of ion i . With these terms, Eq. 6 introduces the Debye–Hückel limiting law, which relates the mean ionic activity to the ionic strength.

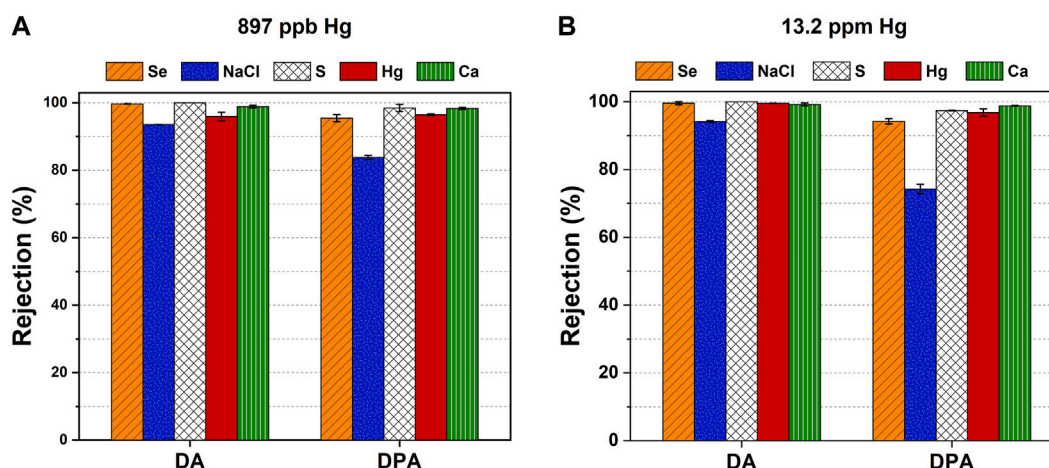


FIGURE 7
Ion rejection of TSSE with DA and DPA solvents for the two synthetic FGD streams having 300 ppm CaSO_4 , 20 g L^{-1} NaCl, 50 ppm SeO_4^{2-} , and (A) 897 ppb of Hg^{2+} or (B) 13.2 ppm of Hg^{2+} .

$$\ln(\gamma_{\pm}) = -\alpha|z_+z_-|\sqrt{I}, \quad (6)$$

where α represents a parameter that depends on the solvent and temperature. Solving Eq. 6 for the mean ionic activity and applying it to Eq. 3 gives Eq. 7:

$$x_i^I \exp(-\alpha|z_+z_-|\sqrt{I}) = x_i^{II} \gamma_i^{II}(T, P, x^{II}). \quad (7)$$

Equation 7 indicates that the higher the ionic strength, the greater the magnitude of the exponential expression, which in turn leads to a reduction in the mean ionic activity of the feed on the left side of Eq. 7. Consequently, a lesser ion concentration will partition into the organic phase, leading to superior solute rejections, which is consistent with the experimental results for DPA. Note, however, that the Debye–Hückel theory is only valid for dilute solutions (<0.01 M), where electrolytes completely dissociate into ions. For DPA, with a selenate rejection of roughly 4%, as discussed previously, the dynamic concentration of ions in the raffinate during the TSSE process remains low, and thus, Eq. 7 remains valid. For DA, however, we do not observe the same trend, i.e., an increase in ion rejection with ionic strength, probably because of the high ionic rejection of DA, and thus the high ionic concentration in the raffinate renders the Debye–Hückel theory invalid. Rather, the rejection behavior of DA is strongly governed by other thermodynamic barriers, such as the hindrance effect of DA, a medium-chain fatty acid that exhibits low or even negligible water miscibility (i.e., a hydrophobic deep eutectic solvent (Aparicio et al., 2023)). Further investigations into the thermodynamic behaviors of ions in biphasic systems, as a function of the concentration, are imperative.

3.2 Rejection potentials of DA- and DPA-based temperature-swing solvent extraction for synthetic flue gas desulfurization feed streams

As described previously, we assess the ion removal capability of TSSE for synthetic FGD wastewater streams having selenate that coexists with sulfate, chloride, and mercury ions. In essence, we

prepared solutions having 300 ppm of gypsum, 20,000 mg L^{-1} of Cl^- , 50 ppm of SeO_4^{2-} , and mercury with the actual concentration of 897 ppb for the first sample (FGD 1) or 13.2 ppm for the second sample (FGD 2). The results show that the medium-chain fatty acid DA performs better rejection for all ions in both FGD streams (Figure 7). Notably, the behaviors of DA and DPA toward NaCl rejection from a multiple-ion mixture remain the same as those shown in single-ion and dual-ion tests. Note that calcium, chloride, and sulfate ions may weakly interact with DA, presumably at their negatively charged carboxylate head groups and through electrostatic forces, covalent bonding, and hydrogen bonding (Yazdani et al., 1990; Yuan et al., 2016; Gao et al., 2023; Zhang et al., 2023). Meanwhile, apart from electrostatic attraction, DPA possibly forms weak coordination complexes with inorganic ligands (i.e., chloride or sulfate) and metal centers (i.e., calcium or mercury ions) (Navarro et al., 1996; Daniele et al., 2008; Akhlaghi et al., 2015). These interactions may interfere with the ion rejection capabilities of DA and DPA to a given extent. Notwithstanding, TSSE was still able to remove $>99.5\%$ of selenium oxyanions and 96% – 99.6% of mercury from a complex environment with a sixfold increase in the concentrations of calcium and sulfate vs. selenate and a background salinity of 20,000 mg L^{-1} NaCl. In contrast, other technologies proposed for the treatment of selenium oxyanions from FGD, such as electrochemical processes or adsorption, have still been hindered due to the lack of capabilities to effectively function without being interrupted by the background chloride level. In addition, the fact that TSSE exhibits a capability to remove traces of mercury (at 897 ppb and 13.2 ppm) reinforces the potential of this technology to provide a treatment solution for FGD wastewater toward meeting the EPA-regulated discharge levels for these toxic compounds. Seemingly, our results lay a foundational understanding essential for TSSE to effectively be integrated for metal removal and recovery and other applications with green extractants (e.g., natural deep eutectic solvents and bio-derived solvents), eventually being transformative for green and clean chemistry.

4 Concluding remarks

In this work, we study the potential of temperature-swing solvent extraction with decanoic acid and diisopropylamine solvents for the removal of species of concern (e.g., selenium oxyanions and mercury) from a synthetic flue gas desulfurization wastewater stream. The results show that compared to diisopropylamine, decanoic acid is more effective in rejecting ions for all cases, ranging from a simple binary system to more complex multicomponent systems with highly varied ionic concentrations, likely due to its lower dielectric constant. Furthermore, the H-bonding interaction with water and the hydrated radii of the oxyanions (i.e., selenate vs. selenite) along with the hindrance effects caused by the molecular bulkiness and hydrophobicity (or lipophilicity) of the solvents play important roles in the favorable rejection of TSSE. It implies that one can tune the selectivity of TSSE with appropriately selected solvents having specific chemical descriptors (e.g., functional groups or ligands). Of note, while DA rejects selenium oxyanions significantly, DPA appears to be more sensitive to the total ionic strength of the solution. Specifically, while DPA can only reject 4%–8% of selenate and selenite from 500 ppm mixed-Se solutions, its rejection rate toward selenate was increased to approximately 86% when there was a coexistence of 20 g L⁻¹ of NaCl. This result is corroborated with our thermodynamic analyses, implying that a higher ionic strength can lead to a reduction in the mean ionic activity in the feed, thereby reducing the amount of ions partitioning into the organic phase, culminating in a superior solute rejection. Furthermore, from this test, although the concentration of NaCl in the feed stream is 400-fold higher than that of selenate, the two solvents exhibit a higher rejection rate of selenate than that of NaCl. Lastly, TSSE shows a great ion-separating performance from synthetic FGD wastewater streams. Specifically, TSSE can remove >99.5% selenium oxyanions and 96%–99.6% mercury from the discharge stream with the coexistence of sulfate at a six-fold increase in the concentration. In summary, we demonstrated that TSSE is promising either as a standalone or a pre-treatment technology to alleviate Se and Hg from FGD discharge streams, helping CFPP facilities to comply with EPA regulations. TSSE is especially efficient and cost-effective in processes where the coexistence of highly varied concentrations of chloride and sulfate is of concern for other technologies due to their low tolerance of these species.

References

- Agency, U. (2015). *Technical development document for the effluent Limitations Guidelines and standards for the Steam electric power generating point source category*. Washington, DC, USA: US Environmental Protection Agency.
- Akhlaghi, S. P., Zaman, M., Mohammed, N., Brinatti, C., Batmaz, R., Berry, R., et al. (2015). Synthesis of amine functionalized cellulose nanocrystals: Optimization and characterization. *Carbohydr. Res.* 409, 48–55. doi:10.1016/j.carres.2015.03.009
- Ali, I., and Shrivastava, V. J. J. O. E. M. (2021). Recent advances in technologies for removal and recovery of selenium from (waste)water: A systematic review. *Recent Adv. Technol. Remov. recovery selenium (waste) water A Syst. Rev.* 294, 112926. doi:10.1016/j.jenvman.2021.112926
- Allibone, J., Fatemian, E., and Walker, P. J. (1999). Determination of mercury in potable water by ICP-MS using gold as a stabilising agent. *J. Anal. Atomic Spectrom.* 14 (2), 235–239. doi:10.1039/a806193i
- Aparicio, S., et al. (2023). Cineole–decanoic acid hydrophobic natural deep eutectic solvent for toluene absorption. *Journal of Molecular Liquids* 384, 122036. doi:10.1016/j.molliq.2023.122036
- Bajpayee, A., Luo, T., Muto, A., and Chen, G. (2011). Very low temperature membrane-free desalination by directional solvent extraction. *Energy Environ. Sci.* 4 (5), 1672–1675. doi:10.1039/c1ee01027a
- Boo, C., Billinge, I. H., Chen, X., Shah, K. M., and Yip, N. Y. (2020). Zero liquid discharge of ultrahigh-salinity brines with temperature swing solvent extraction. *Environ. Sci. Technol.* 54 (14), 9124–9131. doi:10.1021/acs.est.0c02555
- Boo, C., Winton, R. K., Conway, K. M., and Yip, N. Y. (2019). Membrane-less and non-evaporative desalination of hypersaline brines by temperature swing solvent extraction. *Environ. Sci. Technol. Lett.* 6 (6), 359–364. doi:10.1021/acs.estlett.9b00182

Data availability statement

The original contributions presented in the study are included in the article/Supplementary Material; further inquiries can be directed to the corresponding author.

Author contributions

MM defined the scope and methodology of the work, conducted experiments, and wrote a part of the manuscript. VN led the manuscript writing and analytical management. IB conducted the experiments involving FGD. VL conducted the ICP-OES and ICP-MS experiments. AF developed the ICP-MS experimental method. GL provided insights into the work. NB supervised the project, edited the paper, and provided insights into the work. All authors contributed to the article and approved the submitted version.

Acknowledgments

Financial support from the University of Oklahoma (OU) and the Office of the Vice President for Research and Partnerships (OVPRP) is gratefully acknowledged. The authors acknowledge the assistance of Dr. Steven Foster and the OU Mass Spectrometry, Proteomics & Metabolomics (MSPM) Core.

Conflict of interest

The authors declare that the research was conducted in the absence of any commercial or financial relationships that could be construed as a potential conflict of interest.

Publisher's note

All claims expressed in this article are solely those of the authors and do not necessarily represent those of their affiliated organizations, or those of the publisher, the editors, and the reviewers. Any product that may be evaluated in this article, or claim that may be made by its manufacturer, is not guaranteed or endorsed by the publisher.

- Bürkle, S., Becker, L. G., Dreizler, A., and Wagner, S. (2018). Experimental investigation of the flue gas thermochemical composition of an oxy-fuel swirl burner. *Fuel (Lond)*. 231, 61–72. doi:10.1016/j.fuel.2018.05.039
- Carletti, C., Blasio, C. D., Mäkilä, E., Salonen, J., and Westerlund, T. (2015). Optimization of a wet flue gas desulfurization scrubber through mathematical modeling of limestone dissolution experiments. *Ind. Eng. Chem. Res.* 54 (40), 9783–9797. doi:10.1021/acs.iecr.5b02691
- Chen, M., Xie, B., He, F., and Deng, X. (2019). Efficient inhibition of S (IV) oxidation in a novel basic aluminum sulfate regenerative flue gas desulfurization process by ethylene glycol: Kinetics and reaction mechanism. *Energy & Fuels* 33 (2), 1383–1391. doi:10.1021/acs.energyfuels.8b03862
- Cheng, C.-M., Hack, P., Chu, P., Chang, Y. N., Lin, T. Y., Ko, C. S., et al. (2009). Partitioning of mercury, arsenic, selenium, boron, and chloride in a full-scale coal combustion process equipped with selective catalytic reduction, electrostatic precipitation, and flue gas desulfurization systems. *Energy fuels*. 23 (10), 4805–4816. doi:10.1021/ef900293u
- Coleman, L. W. (2023). EPA proposes stronger wastewater discharge standards for coal-fired power plants. <https://ehsdailyadvisor.blr.com/2023/04/epa-proposes-stronger-wastewater-discharge-standards-for-coal-fired-power-plants/>.
- Cordoba, P., and Staicu, L. C. J. F. (2018). Flue gas desulfurization effluents: An unexploited selenium resource. *Flue gas desulfurization effluents unexploited selenium Resour.* 223, 268–276. doi:10.1016/j.fuel.2018.03.052
- Daniele, P. G., Foti, C., Gianguzza, A., Prenesti, E., and Sammartano, S. (2008). Weak alkali and alkaline Earth metal complexes of low molecular weight ligands in aqueous solution. *Coord. Chem. Rev.* 252 (10–11), 1093–1107. doi:10.1016/j.ccr.2007.08.005
- Eia, U. S. E. I. A. (2022). Nearly a quarter of the operating U.S. coal-fired fleet scheduled to retire by 2029. [cited 2022 March 28]; Available from: <https://www.eia.gov/todayinenergy/detail.php?id=54559#:~:text=Of%20the%2055%2C943%20MW%20of,retire%20between%202022%20and%202029.>
- Eklund, L., and Persson, I. J. D. T. (2014). Structure and hydrogen bonding of the hydrated selenite and selenate ions in aqueous solution. *Dalton Trans.* 43 (17), 6315–6321. doi:10.1039/c3dt53468e
- Epa, U. J. W. E. P. A. (2017). Postponement of certain compliance dates for the effluent limitations Guidelines and standards for the Steam electric power generating point source category. *Fed. Register*, 43494–43500. https://www.epa.gov/sites/default/files/2017-09/documents/steam-electric-elg_final_postpone-compliance-dates_fact-sheet_sept-2017.pdf.
- Epa, U. J. W. E. P. A. (2023). Steam electric power generating effluent Guidelines. [cited 2023 April 26]; Available from: <https://www.epa.gov/eg/steam-electric-power-generating-effluent-guidelines>.
- Epa, U. J. W. E. P. A. (2009). Steam electric power generating point source category: Final detailed study report. 2009. <https://nepis.epa.gov/Exe/ZyNET.exe/P1005J8A.TXT?ZyActionD=ZyDocument&Client=EPA&Index=2006+Thru+2010&Docs=&Query=&Time=&EndTime=&SearchMethod=1&TocRestrict=n&Toc=&TocEntry=&QField=&QFieldYear=&QFieldMonth=&QFieldDay=&IntQFieldOp=0&ExtQFieldOp=0&XmlQuery=&File=D%3A%5Czfiles%5CIndex%20Data%5C06thru10%5CTxt%5C00000012%5CP1005J8A.txt&User=ANONYMOUS&Password=anonymous&SortMethod=h%7C-&MaximumDocuments=1&FuzzyDegree=0&ImageQuality=r75g8/r75g8/x150y150g16/i425&Display=hpfr&DefSeekPage=x&SearchBack=ZyActionL&Back=ZyActionS&BackDesc=Results%20page&MaximumPages=1&ZyEntry=1&SeekPage=x&ZyPURL>.
- Gao, J., Dong, M., Xu, T., Bian, H., Wang, S., and Dai, H. (2023). Analysis of causes for high hydration and low drainage rate of wheat straw chemi-thermo-mechanical pulp. *Industrial Crops Prod.* 203, 117103. doi:10.1016/j.indcrop.2023.117103
- Gingerich, D. B., Grol, E., and Mauter, M. S. (2018). Fundamental challenges and engineering opportunities in flue gas desulfurization wastewater treatment at coal fired power plants. *Environ. Sci. Water Res. Technol.* 4 (7), 909–925. doi:10.1039/c8ew00264a
- Guo, J., Luo, S., Liu, Z., and Luo, T. (2020). Direct arsenic removal from water using non-membrane, low-temperature directional solvent extraction. *J. Chem. Eng. Data* 65 (6), 2938–2946. doi:10.1021/acs.jced.9b00936
- Hamilton, S. J. J. S. O. T. T. E. (2004). Review of selenium toxicity in the aquatic food chain. *Rev. selenium Toxic. aquatic food chain* 326 (1–3), 1–31. doi:10.1016/j.scitotenv.2004.01.019
- Hanif, M. A., Ibrahim, N., and Abdul Jalil, A. (2020). Sulfur dioxide removal: An overview of regenerative flue gas desulfurization and factors affecting desulfurization capacity and sorbent regeneration. *Environ. Sci. Pollut. Res.* 27, 27515–27540. doi:10.1007/s11356-020-09191-4
- He, F., Zhu, X., Chen, X., and Ding, J. (2021a). Performance, mechanism, and kinetics of NO removal by combined ascorbic acid and FeII/EDTA reaction systems. *Fuel* 284, 119070. doi:10.1016/j.fuel.2020.119070
- He, F., Zhu, X., Zhong, L., Li, Z., and Qian, Y. (2021b). Nitric oxide removal from flue gas by ferrate (VI)/urea solutions. *Chin. Chem. Lett.* 32 (10), 3175–3179. doi:10.1016/j.ccllet.2021.03.003
- He, Y., Xiang, Y., Zhou, Y., Yang, Y., Zhang, J., Huang, H., et al. (2018). Selenium contamination, consequences and remediation techniques in water and soils: A review. *Environ. Res.* 164, 288–301. doi:10.1016/j.envres.2018.02.037
- Hu, Y., Naito, S., Kobayashi, N., and Hasatani, M. (2000). CO₂, NO_x and SO₂ emissions from the combustion of coal with high oxygen concentration gases. *Fuel (Lond)*. 79 (15), 1925–1932. doi:10.1016/s0016-2361(00)00047-8
- Huang, Y. H., Peddi, P. K., Tang, C., Zeng, H., and Teng, X. (2013). Hybrid zero-valent iron process for removing heavy metals and nitrate from flue-gas-desulfurization wastewater. *Sep. Purif. Technol.* 118, 690–698. doi:10.1016/j.seppur.2013.07.009
- Kaminski, J. J. A. E. (2003). Technologies and costs of SO₂-emissions reduction for the energy sector. *Appl. Energy* 75 (3–4), 165–172. doi:10.1016/s0306-2619(03)00029-1
- Ketris, M. A., and Yudovich, Y. E. J. I. J. O. C. G. (2009). Estimations of Clarks for Carbonaceous bioliths: World averages for trace element contents in black shales and coals. *Int. J. Coal Geol.* 78 (2), 135–148. doi:10.1016/j.coal.2009.01.002
- Kumar, S., Lange, J. P., Van Rossum, G., and Kersten, S. R. (2015). Bio-oil fractionation by temperature-swing extraction: Principle and application. *Biomass Bioenergy* 83, 96–104. doi:10.1016/j.biombioe.2015.09.003
- Marcus, Y. J. C. R. (1988). Ionic radii in aqueous solutions. *Chem. Rev.* 88 (8), 1475–1498. doi:10.1021/cr00090a003
- MeaganMauter, S. S. Z. (2021). *Direct electrochemical reduction method for removing selenium from wastewater*. Stanford, CA, USA: The Board of Trustees of the Leland Stanford Junior University.
- Meher, A. K., Jadhav, A., Labhsetwar, N., and Bansiwala, A. (2020). Simultaneous removal of selenite and selenate from drinking water using mesoporous activated alumina. *Appl. Water Sci.* 10, 10–12. doi:10.1007/s13201-019-1090-x
- Mehri, A. J. I. J. O. P. M. (2020). Trace elements in human nutrition (II)—an update. *Int J Prev Med.* 11 (2). doi:10.4103/ijpvm.IJPVM_48_19
- Navarro, R. R., Sumi, K., Fujii, N., and Matsumura, M. (1996). Mercury removal from wastewater using porous cellulose carrier modified with polyethyleneimine. *Water Res.* 30 (10), 2488–2494. doi:10.1016/0043-1354(96)00143-1
- Ohlendorf, H. M., Covington, S. M., Byron, E. R., and Arenal, C. A. (2011). Conducting site-specific assessments of selenium bioaccumulation in aquatic systems. *Integr. Environ. Assess. Manag.* 7 (3), 314–324. doi:10.1002/ieam.157
- Pincus, L. N., Lounsbury, A. W., and Zimmerman, J. B. J. A. O. C. R. (2019). Toward realizing multifunctionality: Photoactive and selective adsorbents for the removal of inorganics in water treatment. *Acc. Chem. Res.* 52 (5), 1206–1214. doi:10.1021/acs.accounts.8b00668
- Rish, D., Luo, S., Kurtz, B., and Luo, T. (2014). Exceptional ion rejection ability of directional solvent for non-membrane desalination. *Appl. Phys. Lett.* 104 (2), 024102. doi:10.1063/1.4861835
- Sandler, S. I. (2017). *Chemical, biochemical, and engineering thermodynamics*. Hoboken, NJ, USA: John Wiley & Sons.
- Sappidi, P., Barbosa, G., Rabideau, B. D., Weinman, S. T., and Turner, C. H. (2021). Molecular simulation of high-salinity brines in contact with diisopropylamine and tripropylamine solvents. *Ind. Eng. Chem. Res.* 60 (21), 7917–7925. doi:10.1021/acs.iecr.1c01057
- Sinharoy, A., Kumar, M., Chaudhuri, R., Saikia, S., and Pakshirajan, K. (2022). Simultaneous removal of selenite and heavy metals from wastewater and their recovery as nanoparticles using an inverse fluidized bed bioreactor. *J. Clean. Prod.* 376, 134248. doi:10.1016/j.jclepro.2022.134248
- Sinharoy, A., and Lens, P. N. J. C. P. R. (2020). Biological removal of selenate and selenite from wastewater: Options for selenium recovery as nanoparticles. *Curr. Pollut. Rep.* 6, 230–249. doi:10.1007/s40726-020-00146-4
- Skalnaya, M. G., and Skalny, A. V. (2018). Essential trace elements in human health: A physician's view. <https://onlinelibrary.wiley.com/doi/10.1002/9781119133780.ch18#:~:text=Summary,selenium%2C%20and%20zinc%20are%20presented.>
- Srivastava, R. K., Jozewicz, W. J. J. O. T. A., and Association, W. M. (2001). Flue gas desulfurization: The state of the art. *J. Air Waste Manag. Assoc.* 51 (12), 1676–1688. doi:10.1080/10473289.2001.10464387
- Tokunaga, K., Tanaka, K., Takahashi, Y., and Kozai, N. (2023). Improvement of the stability of IO₃[−], SeO₃^{2−}, and SeO₄^{2−}-coprecipitated barite after treatment with phosphate. *Environ. Sci. Technol.* 57 (8), 3166–3175. doi:10.1021/acs.est.2c08939
- Tokunaga, K., and Takahashi, Y. J. E. S. (2017). Effective removal of selenite and selenate ions from aqueous solution by barite. *Environ. Sci. Technol.* 51 (16), 9194–9201. doi:10.1021/acs.est.7b01219
- Vejahati, F., Xu, Z., and Gupta, R. J. F. (2010). Trace elements in coal: Associations with coal and minerals and their behavior during coal utilization—A review. *Fuel (Lond)*. 89 (4), 904–911. doi:10.1016/j.fuel.2009.06.013
- Wang, J., and Anthony, E. J. J. A. E. (2008). Clean combustion of solid fuels. *Clean Combust. solid fuels* 85 (2–3), 73–79. doi:10.1016/j.apenergy.2007.07.002
- Wu, J., Zhao, J., Li, H., Miao, L., Hou, J., and Xing, B. (2021). Simultaneous removal of selenite and selenate by nanosized zerovalent iron in anoxic systems: The overlooked role of selenite. *Environ. Sci. Technol.* 55 (9), 6299–6308. doi:10.1021/acs.est.0c08142
- Yamada, N. (2015). Kinetic energy discrimination in collision/reaction cell ICP-MS: Theoretical review of principles and limitations. *Spectrochim. Acta Part B At. Spectrosc.* 110, 31–44. doi:10.1016/j.sab.2015.05.008

Yazdani, M., Yu, H., and Zografi, G. (1990). Ionic interactions of fatty acid monolayers at the air/water interface. *Langmuir* 6 (6), 1093–1098. doi:10.1021/la00096a012

Yuan, W., Cui, J., and Xu, S. (2016). Mechanical properties and interfacial interaction of modified calcium sulfate whisker/poly (vinyl chloride) composites. *J. Mater. Sci. Technol.* 32 (12), 1352–1360. doi:10.1016/j.jmst.2016.05.016

Zhang, H., Lai, Y., Yang, X., and Dong, Y. Non-evaporative solvent extraction technology applied to water and heat recovery from low-temperature flue gas: Parametric analysis and feasibility evaluation. , 2022. 244: p. 123062, doi:10.1016/j.energy.2021.123062

Zhang, M., Zhao, X., Tang, S., Wu, K., Wang, B., Liu, Y., et al. (2023). Structure-properties relationships of deep eutectic solvents formed between choline chloride and carboxylic acids: Experimental and computational study. *J. Mol. Struct.* 1273, 134283. doi:10.1016/j.molstruc.2022.134283

Zou, S., Mauter, M. S. J. A. E., and Engineering, T. (2021). Competing ion behavior in direct electrochemical selenite reduction. *ACS Es. Trans. Eng.* 1 (6), 1028–1035. doi:10.1021/acsestengg.1c00099

Zou, S., and Mauter, M. S. J. A. S. C. (2021). Direct electrochemical pathways for selenium reduction in aqueous solutions. *Direct Electrochem. Pathw. selenium Reduct. aqueous solutions* 9 (5), 2027–2036. doi:10.1021/acssuschemeng.0c06585

Frontiers in Chemistry

Explores all fields of chemical science across the periodic table

Advances our understanding of how atoms, ions, and molecules come together and come apart. It explores the role of chemistry in our everyday lives - from electronic devices to health and wellbeing.

Discover the latest Research Topics

[See more →](#)

Frontiers

Avenue du Tribunal-Fédéral 34
1005 Lausanne, Switzerland
frontiersin.org

Contact us

+41 (0)21 510 17 00
frontiersin.org/about/contact

